Sheffield Hallam University

Developing high-efficiency multiphase thermoelectric materials

FORTULAN, Raphael Luiz Vicente

Available from the Sheffield Hallam University Research Archive (SHURA) at:

https://shura.shu.ac.uk/33420/

A Sheffield Hallam University thesis

This thesis is protected by copyright which belongs to the author.

The content must not be changed in any way or sold commercially in any format or medium without the formal permission of the author.

When referring to this work, full bibliographic details including the author, title, awarding institution and date of the thesis must be given.

Please visit https://shura.shu.ac.uk/33420/ and http://shura.shu.ac.uk/information.html for further details about copyright and re-use permissions.

Developing high-efficiency multiphase thermoelectric materials

Raphael Luiz Vicente Fortulan

A thesis submitted in partial fulfilment of the requirements of
Sheffield Hallam University
for the degree of Doctor of Philosophy

October 2023

Candidate declaration

I, Raphael Luiz Vicente Fortulan, hereby declare that

1. I have not been enrolled for another award of the University, or other academic or professional organisation, whilst undertaking my research degree
2. None of the material contained in the thesis has been used in any other submission for an academic award
3. I am aware of and understand the University's policy on plagiarism and certify that this thesis is my own work. The use of all published or other sources of material consulted have been properly and fully acknowledged
4. The work undertaken towards the thesis has been conducted in accordance with the SHU Principles of Integrity in Research and the SHU Research Ethics Policy
5. The word count of the thesis is 40341

Name	Raphael Luiz Vicente Fortulan
Date	October 2023
Award	PhD
Research Institute	Materials & Engineering
Director of Studies	Professor Chris Sammon

©2024
Raphael Luiz Vicente Fortulan
All rights reserved

List of publications during doctoral studies

Published manuscripts

(1) Yamini, S. A., Santos, R. and **Fortulan, Raphael** et al. "Room-Temperature Thermoelectric Performance of n-Type Multiphase Pseudobinary Bi2Te3-Bi2S3 Compounds: Synergic Effects of Phonon Scattering and Energy Filtering". ACS Applied Materials & Interfaces 15, no. 15 (Apr. 2023): 19220-19229. doi: 10.1021/acsami.3c01956.

(2) de Camargo, I. L., Erbereli, R., Lovo, J. F. P., **Fortulan, Raphael** et al. "Digital Light Processing Additive Manufacturing of in Situ Mullite-Zirconia Composites". Journal of the European Ceramic Society 42, no. 13 (1st Oct. 2022): 6025-6032. doi: 10.1016/j.jeurceramsoc.2022.06.042.

(3) **Fortulan, Raphael** et al. "Thermoelectric Performance of n-Type Magnetic Element Doped Bi2S3". ACS Applied Energy Materials 5, no. 3 (Mar. 2022): 3845-3853. doi: 10.1021/acsaem.2c00295.

(4) **Fortulan, Raphael** and Yamini, S. A. "Recent Progress in Multiphase Thermoelectric Materials". Materials 14, no. 20 (20 Jan. 2021): 6059. doi: 10.3390/ma14206059.

(5) *__Fortulan, Raphael__. "A Novel Approach for Transient Stability Using Interval Arithmetic and Optimization Methods". International Transactions on Electrical Energy Systems 31, no. 5 (2021): e12851. doi: 10.1002/2050-7038.12851.

(6) **Fortulan, Raphael** et al. "Thermoelectric Properties of Single-Phase n-Type Bi14Te13S8". ACS Applied Electronic Materials, 6(2), pp. 1283–1291. doi:10.1021/acsaelm.3c01615.

Manuscripts under preparation

(1) **Fortulan, Raphael** et al. "Enhanced Thermoelectric Performance of Sulphur added Bi2Te2.7Se0.3 through Synergistic Tailoring of Band Structure and Phonon Transport" (2023).

(2) **Fortulan, Raphael** et al. "CrSb added Bi0.5Sb1.5Te3 Multiphase Thermoelectric Materials" (2023).

Acknowledgments

Everytime we start a journey disappointments and regrets are a part of it and they are mostly due to our own aspirations and naïve views, as St. Francis of Assisi commented:

> *"Lord, grant me the strength to change what can be changed…Acceptance to embrace what cannot be changed…And wisdom to discern one from the other."*
>
> — St. Francis of Assisi

But I was fortunate to have support that aided me through this journey.

I would like to express my gratitude to Sima Aminorroaya Yamini, for her guidance and support throughout my entire doctoral journey. I wish to extend my appreciation to Professor Chris Sammon for providing support in the final months of my doctoral studies.

I also extend my gratitude to the collaborators who provided essential assistance during my research and greatly contributed to the progress of my work. In particular, I extend my heartfelt thanks to Suwei Li and Professor Michael Reece from Queen Mary University, London, and Takahiro Baba, Illia Serhiienko, and Professor Takao Mori from the National Institute for Materials Science (NIMS), Japan.

I wish to recognise and appreciate the technical support from the staff at MERI, in particular Tony Bell, Francis Clegg, and Francis Sweeney, for providing the necessary tools and facilities for my experiments.

Also, I wish to extend my sincere thanks to all the people from University Alliance/DTA for their support.

I would like to express my deepest gratitude to my loving family for their unconditional support during my PhD journey. Their love, encouragement, and constant support were essential to my success. I wholeheartedly thank my parents, brother, grandparents, uncles, and aunts for believing in me and being my source of inspiration. I am truly blessed to have such a loving and united family by my side. *Conce muito obrigado por todo o apoio. Mal posso esperar para tomar um cafezinho com você e a Ana para comemorarmos!*

Your words of wisdom, gestures of affection, and constant presence have strengthened me in times of difficulty. You are my reason to persevere and my source of inspiration. I am eternally grateful for everything you have done for me.

I would like to express my sincere gratitude to my lab mates, Musa and Sarah, for their invaluable help and support throughout my PhD research. Their insightful feedback and constant encouragement pushed me to sharpen my think-

ing and took my work to a higher level. Musa, thank you so much for all your support, help and friendship over the years, since as you always said

"Raphael, I'm telling you, it is not easy!"

— Musa Bilya

I am lucky to have worked with such excellent scientists and friends.

Kris, Joel, Harry - I don't even know where to start. You have all been so supportive throughout my PhD. From research discussion sessions to weekend escapes when I just needed a break, you provided the perfect mix of support, camaraderie, and carefree fun that kept me sane. I could not have crossed the finish line without my three *amigos* cheering me on. You made a sometimes lonely journey feel like a team effort. I am so grateful for your friendship and can't wait to celebrate with you!

Lastly, I would like to acknowledge the financial support provided by European Union's Horizon 2020 research and innovation programme under the Marie Skłodowska-Curie grant agreement No. 801604, which made this research possible.

Having worked with different people during this project, a different phrase from the old master weighs in my thoughts:

"Nobody is perfect enough that they cannot learn from others, and nobody is completely devoid of values that they cannot teach something to someone else."

— St. Francis of Assisi

Thank you all for your contributions to my research project.

Preface

The research presented herein was conducted at the Materials and Engineering Research Institute located at Sheffield Hallam University's City Campus. The research project and associated methods were approved and received ethical clearance from the Research Ethics Board of Sheffield Hallam University, as evidenced by Certificate ER36529528.

A version of chapter 2 has previously been published in the journal Materials published by MDPI, under the reference: Fortulan, R., and Aminorroaya Yamini, S. (2021). Materials, 14(20), 6059. https://doi.org/10.3390/ma14206059. As lead investigator for this publication, I was responsible for all major aspects of study design, data collection, data analysis, and drafting of the manuscript. Dr. Sima Aminorroaya Yamini held the role of senior and corresponding author, contributing to conceptualisation and preparation/review of the manuscript.

A version of chapter 4 has previously been published in the journal ACS Applied Energy Materials, under the reference: Fortulan, R., Aminorroaya Yamini, S., Nwanebu, C., Li, S., Baba, T., Reece, M.J., and Mori, T. (2022). ACS Applied Energy Materials, 5(7), 5899-5909. https://doi.org/10.1021/acsaem.2c00295. As lead investigator, I conducted all major data collection, data analysis, and primary drafting of the manuscript. Mr. Chibuzor Nwanebu was responsible for fabrication of a set of samples utilized in the study. Mr. Suwei Li and Prof. Michael Reece assisted with sample sintering and data collection. Mr. Takahiro Baba and Prof. Takao Mori contributed to additional data collection. Dr. Sima Aminorroaya Yamini served as senior and corresponding author, involved in concept formation and preparation/review of the manuscript.

Data presented in chapter 5 was published in the journal ACS Applied Materials and Interfaces, under the reference: Aminorroaya Yamini, S., Santos, R., Fortulan, R., Gazder, A.A., Malhotra, A., Vashaee, D., Serhiienko, I., and Mori, T. (2023). ACS Applied Materials & Interfaces. https://doi.org/10.1021/acsami.3c01956. I conducted all major data collection, data analysis, and primary drafting of the text in said chapter. Mr. Divyesh Vaya prepared the samples under Dr. Sima Aminorroaya Yamini. The sintering of the samples was carried out at the Henry Royce Institute for Advanced Materials, funded by EPSRC grants EP/R00661X/1, EP/S019367/1, EP/P025021/1, and EP/P025498/1. Prof. Takao Mori and Mr. Illia Serhiiennko were responsible for additional data collection and analysis. Dr. Sima Aminorroaya Yamini was the lead investigator and corresponding author of the published manuscript.

Appropriate permission has been obtained for any reprinting of images, and all permissions for reuse and copyright are documented in the appendix of this work.

Except where reference is made to the work of others, the research presented

in this thesis is the original work of the author, carried out under supervision of the stated collaborators and supervisors.

COVID-19 statement

In light of the unforeseen challenges brought about by the *force majeure* event of the COVID-19 pandemic, my ability to conduct experimental research for my doctoral thesis has been significantly affected. The original methodology involved extensive use of both university laboratories and external research facilities to carry out experiments and collect data over a period of several months or years.

The pandemic necessitated the closure of campuses worldwide in March 2020. Upon commencing my PhD, I did not have access to key facilities housing the specialised equipment required for my research project. This resulted in significant delays in the initial training I required to implement and conduct the experiments for my research endeavour. Switching to a completely remote contingency plan was exceptionally challenging for an *in situ* experimental project. I worked closely with my supervisors to adapt my methodology and thesis objectives to emphasise more computational and analytical facets achievable remotely, as well as feasible experimental goals.

To illustrate, I developed simulations of thermoelectric materials using Python to emulate their transport properties *in silico*. Additionally, I acquired new techniques for the computational analysis of electronic band structures using the Quantum ESPRESSO suite for *ab initio* studies. Although not an ideal substitute, these remote approaches facilitated the further progress of my research. The experience highlighted the necessity for contingency planning and versatile skills in experimental research fields.

I also embarked on an exhaustive literature review of multiphase thermoelectric materials, culminating in the publication of a review paper.

Efforts were made to advocate for the safe reopening of laboratories for critical work, but restrictions remained in place throughout 2020. This had a significant impact on my results and conclusions, as I was unable to obtain training and equipment access to prepare samples in a timely manner. However, the insights I gained through remote computational methods still represent an important scientific contribution and provide the framework for future in-person validation. I aimed to resume hands-on experimental work when feasible, as computational techniques alone cannot fully replace original laboratory data collection and analysis, but this proved challenging to implement.

With the easing of restrictions in 2021, I was able to begin some experimental work. However, access to facilities remained an obstacle. The constant need for COVID-19 tests, with false positives requiring me to stay at home, further cemented the delays in my work. Again, national policies requiring a few people

to be in the same place at the same time created problems with training and running the experiments. The online-only environment for contacting supervisors and collaborators, although increasingly common today, was a novelty at the time and presented difficulties.

My work also relied heavily on external collaborators and facilities, with some critical tasks requiring completion externally due to insufficient equipment in Sheffield Hallam facilities, particularly for laser flash analysis measurements and spark plasma sintering, which were crucial for sample preparation and analysis. However, with the global pandemic, all laboratories worldwide were closed or operating with restrictions, which significantly delayed some experimental work I required. For example, the sintering of the samples used in chapters 6 and 7 took more than eight months (from January 2022 to September 2022). The closed borders also prevented me from directly accessing external facilities.

This experience emphasised the necessity for resilience and flexibility in experimental science. I adapted my methodology by developing simulations and models to supplement the limited original data I had already collected. This enabled me to continue to make progress in data analysis and interpretation remotely. While the pandemic significantly altered my original methodology, it also expanded my skills in adapting to research constraints. I believe that this experience of innovating experimental techniques under difficult circumstances will make me a better researcher, prepared for genuine challenges in the field.

Raphael Luiz Vicente Fortulan
Sheffield, United Kingdom, March 2024

Abstract

This thesis explores strategies for improving the efficiency of thermoelectric materials, with a particular focus on multiphase bismuth chalcogenide compounds. The introduction and literature review provide the necessary background on thermoelectricity and its applications, define key parameters such as the dimensionless figure of merit zT, and outline established methods for optimising single and multiphase thermoelectric materials. The literature review chapter delves into important concepts and mechanisms such as energy filtering, modulation doping, and phonon scattering in multiphase systems. The experimental methods chapter then outlines the different material synthesis techniques used, such as melting, ball milling, and spark plasma sintering, as well as the analytical approaches used to study the materials, including structural, electronic, and thermal transport characterisation.

The subsequent results chapters examine the effects of incorporating magnetic dopants and secondary phases into bismuth sulphide, telluride, and selenide host systems. A notable finding was that magnetic co-doping of Bi_2S_3 with chromium and chlorine significantly increased the thermopower and power factor, attributed to a magnetic drag effect that increases the effective carrier mass. The addition of a $Bi_{14}Te_{13}S_8$ secondary phase to Bi_2Te_3 matrix compounds was also investigated; the presence of this phase led to an energy filtering effect that improved the thermopower but also introduced additional phonon scattering at phase interfaces that reduced the lattice thermal conductivity. Further studies of sulphur-containing $Bi_2Te_{2.7}Se_{0.3}$ revealed that sulphur inclusion dramatically alters the density of states and native defect concentrations in both single and multiphase samples. Interestingly, multiphase $Bi_2Te_{2.7}Se_{0.3}$ samples exhibited complex electronic behaviour, suggesting possible impurity band formation at higher secondary phase contents.

Further investigations $Bi_{0.5}Sb_{1.5}Te_3$ with added CrSb compounds showed that small amounts of the magnetic secondary phase increased the thermopower via an increased effective mass, but higher CrSb contents degraded the performance due to reduced carrier mobility. Finally, iodine doping of single phase $Bi_{14}Te_{13}S_8$, an important component of the multiphase materials studied, was found to effectively optimise the power factor and reduce the lattice thermal conductivity, culminating in an improved figure of merit zT.

In summary, this work provides compelling evidence that strategies such as energy filtering, modulation doping, and phonon scattering can be successfully exploited to improve the efficiency of multiphase bismuth chalcogenide thermoelectric materials. The results provide valuable insights to guide ongoing research and development efforts towards higher performance thermoelectric materials for real-world applications.

Contents

List of figures

List of tables

List of acronyms

ADC
analog-to-digital converter

AFM
antiferromagnetic

BTE
Boltzmann transport equation

DAQ
data acquisition system

DFT
density functional theory

DOS
density of states

DSC
differential scanning calorimetry

FWHM
full width at the half maximum

GGA
generalised gradient approximation

IBVP
initial boundary value problem

LFA
laser flash analysis

LSB
least significant bit

PBE
: Perdew-Burke-Ernzerhof

PF
: power factor

PXRD
: powder X-ray diffraction

RTG
: radioisotope thermoelectric generator

SPB
: single parabolic band

SPS
: spark plasma sintering

TE
: thermoelectric

XRD
: X-ray diffraction

List of symbols

$\langle \cdot \rangle$
: expectation operator or expected value

A
: conductor area

a
: secondary phase radius

B_D
: effective Burger's vector

c_0
: impurity concentration

c_i
: i-th component stoichiometry of a generic compound

C_l
: longitudinal elastic constant

C_m
: magnon specific heat capacity per unit volume

C_p
: heat capacity

c_p
: specific heat capacity

c_p^{sapphire}
: specific heat capacity sapphire standard

D
: thermal diffusivity

d
: density

D_I
: concentration of ionised impurities

E
: carrier energy

e
: elementary charge

E_B
: potential barrier height

E_{BC}
: potential barrier height at the conduction band

E_{BV}
: potential barrier height at the valence band

E_C
: conduction energy or energy at the bottom of the conduction band

E_{def}
: deformation potential for acoustic phonon scattering

E_F
: Fermi level

E_g
: bandgap

k_{B}
: Boltzmann constant

μ_{H}
: Hall mobility

r_{H}
: Hall factor

E_V
: energy at the top of the valence band

f
: volume fraction of the secondary phase

$f(E)$
: Fermi-Dirac distribution

$f_{j,i}$
: site fraction of the j-th species occupying the i-th component of a generic compound

$F_j(\eta)$
: Fermi-Dirac integral for an index j

$g(E)$
: density of states

G_{kl}
: conductivity between nodes k and l

I
: electric current

I_{kl}
: current flowing between nodes k and l

K
: bulk modulus

L
: Lorenz number or average grain size

L_κ
: Kapitza length

$\bar{M}$
: average atomic/stoichiometric mass

$M(E)$
: number of conducting channels

m_b^*
: single valley effective mass

m_{DOS}^*
: density of states effective mass

$\bar{M}_i$
: average mass of the i-th site of a generic compound

m_I^*
: inertial effective mass

$M_{j,i}$
: mass of the j-th species occupying the i-th component of a generic compound

n
: carrier concentration/density

N_D
: density of dislocations

N_v
: valley degeneracy

p
: holes carrier concentration

p_c
: percolation threshold

Q
: heat flow

$\dot{Q}$
: heat transfer rate

q
: elementary charge

r
: reflection energy coefficient

R_{H}
: Hall coefficient

s
: measure of the grain structure and morphology as used in the generalised effective medium theory

T
: absolute temperature

∇T
: temperature gradient

t
: transmission energy coefficient

T_a
: annealing temperature

T_C
: temperature of the cold side/reservoir

T_H
: temperature of the hot side/reservoir

V
: voltage

$\bar{V}$
: average atomic volume

∇V
: voltage gradient

v
: speed of sound in the material

$\mathbb{V}$
: variance

$\mathbb{V}(\boldsymbol{M})$
: stoichiometric average mass variance in the system/composition

V_{H}
: Hall voltage

V_{kl}
: voltage between nodes k and l

v_l
: longitudinal speed of sound

wt.%
: weight percent

x
: reduced frequency

X_i
: i-th component of a generic compound

Y_j
: j-th species occupying the i-th component of a generic compound

Z
: acoustic impedance of a material

$\hbar$
: reduced Planck constant

Γ
: scattering parameter

ΔT
: temperature difference

ΔV
: voltage difference

$\Delta\gamma$
: change in Grüneisen parameter due to impurity atmosphere

Φ
: work function of a material

Φ_M
: work function of a metal

α
: thermopower

α_{md}
: magnon thermopower

α_n
: electron thermopower

α_p
: hole thermopower

γ
: Grüneisen parameter

ε
: reduced energy

η
: reduced Fermi level

η_c
: Carnot efficiency

η_n
: reduced Fermi level for the conduction band

η_p
: reduced Fermi level for the valence band

η_t
: thermoelectric efficiency

θ
: Bragg angle

θ_D
: Debye temperature

κ
: thermal conductivity

κ_b
: bipolar thermal conductivity

κ_e
: electronic thermal conductivity

κ_l
: lattice thermal conductivity

κ_m
: thermal conductivity of the matrix

κ_p
: thermal conductivity of the secondary phase

λ
: wavelength

$\lambda(E)$
: mean free path

λ_κ
: ratio of the Kapitza length and secondary phase radius

μ
: carrier mobility

μ_n
: electron mobility

μ_p
: hole mobility

ν
: Poisson's ratio

ν_i
: volume fraction of phase i of a multiphase material

ξ
: effective property of a multiphase material

ξ_i
: property of phase i of a multiphase material

π
: Peltier coefficient

ρ
: electrical resistivity

σ
: electrical conductivity

σ'
: differential conductivity

σ_n
: electron electrical conductivity

σ_p
: hole electrical conductivity

τ
: relaxation time

τ_C
: combined relaxation time

τ_{dc}
: relaxation time due to dislocation cores

τ_{ds}
: relaxation time due to dislocation strains

τ_{em}
: relaxation time of magnons due to magnon-electron collisions

τ_{gb}
: relaxation time due to grain boundaries

τ_i
: relaxation time for the i-th scattering process

τ_m
: transport mean-free time for the magnons

τ_n
: relaxation time due to normal process

τ_{pd}
: relaxation time due to point defects

τ_u
: relaxation time due to Umklapp process

χ
: electron affinity

χ_S
: electron affinity of a semiconductor

ω
: phonon angular frequency

ω_D
: Debye/cutoff frequency

ϵ
: permittivity of the material

ϵ_g
: reduced bandgap

Colophon

This document was typeset using the XeTeX typesetting system created by the Non-Roman Script Initiative and the memoir class created by Peter Wilson. The body text is set at 12.5 pt with Adobe Caslon Pro. Other fonts include Envy Code R, Optima Regular, and Medici. The bibliography has been processed using BibLaTeX.

1

Introduction

It ought to be remembered that there is nothing more difficult to take in hand, more perilous to conduct, or more uncertain in its success, than to take the lead in the introduction of a new order of things.
— Niccolò Machiavelli, The Prince

Summary
This chapter serves as an introduction to the research, outlining its motivation, main aspects and achievements. It starts by presenting the idea behind the use of thermoelectric materials and the driving force behind the effort to improve their performance. The chapter also looks at the main challenges encountered during the research and provides a brief discussion of these obstacles.
As a whole, this introductory chapter sets the stage for the following sections by providing the reader with a clear understanding of the purpose and significance of the research. It establishes the context for the study and lays the foundation for the exploration of thermoelectric materials and their potential improvements.

1.1 Broad view of thermoelectricity and its applications

Solid-state thermoelectric generators, which reversibly convert heat into electricity, are considered pioneering candidates for industrial waste heat recovery, electronic cooling, and small spacecraft power. This field of study is exciting and has been featured in articles in The New York Times [1, 2] and the Los Angeles Times [3, 4].

The massive reliance on nonrenewable energy sources is straining power systems worldwide. From the perspective of power engineers, thermoelectric (TE) materials can be used to reduce the load on a power system without changing the economic output by converting waste heat from industrial plants into electrical energy. Taking a continental-sized power system such as the United States as an example, approximately 26 quadrillion Btu (or 7.62 trillion kW.h) are wasted annually in transportation and industry [5]. The Sankey diagram shown in figure 1.1 illustrates this concept.

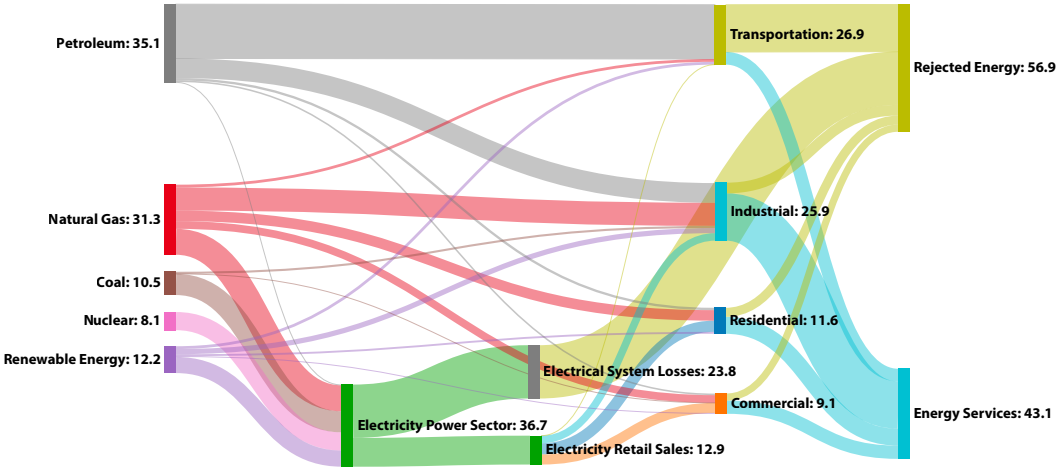

Figure 1.1. Sankey diagram of US energy inputs and outputs in 2022, all values are in quadrillion Btu. 26 quadrillion Btu are lost as waste in industry and transportation. Source: United States Energy Information Administration, Monthly Energy Review (April 2022), tables 1.3 and 2.1-2.6 [5].

Thermoelectric waste heat conversion has been applied to high temperature industrial exhaust systems (e.g. aluminium refining) [6] and medium temperature automotive exhaust systems [7] with limited scope. In these scenarios, TE generators are particularly well suited, as they are both silent and motionless and can be used in areas where a conventional higher efficiency thermal engine would be inaccessible. Excitingly, thermoelectric generation could contribute 10 trillion Btu (2.93 billion kW.h) [6] to the US power system if used at scale.

The best known use of thermoelectric generators is in space applications. For example, NASA's radioisotope thermoelectric generator (RTG) is used to power deep space missions and Mars exploration rovers [8]. Unlike solar cells, RTGs

do not depend on atmospheric conditions to generate power and this, combined with their small size, makes them ideal for this type of application. As the generator is only a small part of the overall cost of the space programme, it is not a budget constraint. However, the development of more efficient and cheaper TE generators is needed for widespread use. An illustration of a thermoelectric unicouple used for energy generation is shown in figure 1.2(a) and an image of the RTG is seen on figure 1.2(b).

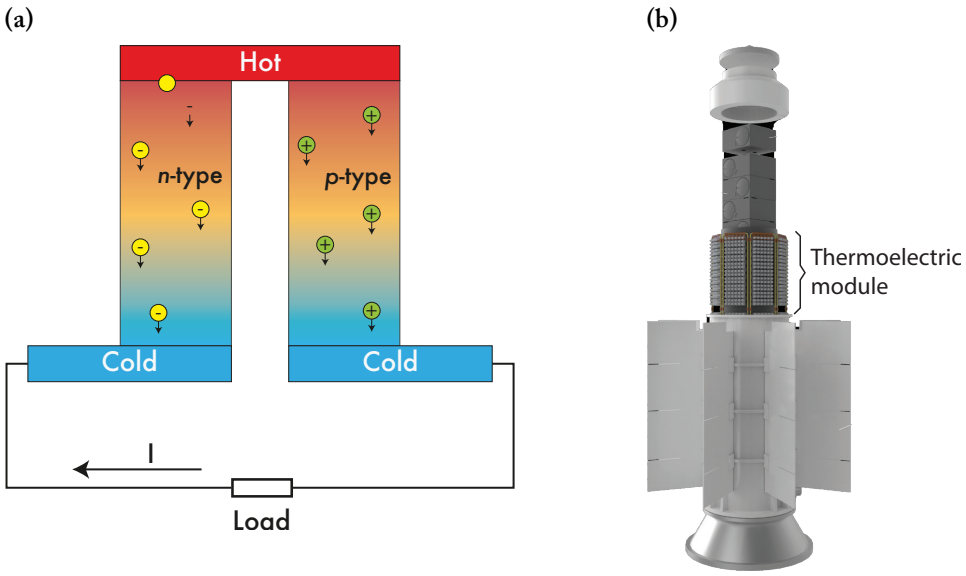

Figure 1.2. (a) Model of a thermoelectric unicouple with the charges transport detailed, and (b) radioisotope thermoelectric generator module. Adapted from NASA. 2014. "MMRTG, or Multi-Mission Radioisotope Thermoelectric Generator." NASA RPS: Radioisotope Power Systems. 2014. Accessed August 21, 2023. https://rps.nasa.gov/power-and-thermal-systems/power-systems/.

1.2 Enhancing the efficiency of thermoelectric materials

Existing TE materials have relatively low conversion efficiency and increasing it is not an easy task as the variables involved in obtaining an efficient generator are not additive and must be considered as a whole when designing new materials. The efficiency of TE materials is characterised by a dimensionless figure of merit, $zT = \alpha^2\sigma T/(\kappa_e + \kappa_l)$, where T, α, σ, κ_e and κ_l are the absolute temperature, the thermopower, the electrical conductivity and the electronic and lattice components of the thermal conductivity (κ), respectively. Most thermoelectric materials used in commercial applications have a zT of about 1 [9], which corresponds to an efficiency of approximately 10 percent in the mid-temperature range [10]. To increase zT it is necessary to increase both α and σ and decrease κ. However, these parameters are correlated. The electronic thermal conduct-

ivity increases with increasing electrical conductivity, and α and σ are inversely proportional [11]. Optimisation of these parameters is therefore very challenging and key to achieving higher efficiency.

Mathematically the "optimisation problem" for enhancing the efficiency of thermoelectric materials can be stated as

$$\max_{x \in X}(|\alpha(x)|, \sigma(x), -\kappa(x)), \tag{1.1}$$

where x denotes the thermoelectric parameters and X denotes the feasible set of parameters. In multi-objective optimisation problems, there is rarely a solution that minimises or maximises all the objective functions; what we are looking for is the Pareto optimal solutions, i.e. solutions that cannot improve any of the objectives without degrading at least one of the other. This argument shows that traditional methods of improving TE require researchers to make concessions when trying to improve zT.

One of the most successful approaches to improve the figure of merit is to reduce the lattice thermal conductivity, and over the years, various phonon engineering approaches have been used to enhance phonon scattering and decrease κ_l by taking advantage of nanoprecipitates [12–14], alloying elements [15–17], nanostructured grain boundaries [18–21], ionised impurities [22, 23], and superlattices [24].

A variety of band structure engineering approaches have also been used to improve electronic properties [25–27]. Strategies such as quantum confinement [28, 29], modulation doping [30–32], the introduction of resonance energy into the electronic density of states (DOS) [33, 34], and energy filtering [35] are actively pursued. These strategies have been adopted to modify the band structure and transport properties of thermoelectric materials by tuning the electrical conductivity and thermopower independently or by increasing them simultaneously. In practice, the best results are obtained with a significant increase in one of these parameters and a slight decrease in the other, resulting in an increase in power factor ($\alpha^2\sigma$) and zT.

The development of highly efficient thermoelectric materials reached a bottleneck when the exploration of single phase alloys was exhausted. Therefore, the investigation of multiphase compounds is the most viable strategy to improve the thermoelectric performance of bulk materials, where higher degrees of freedom are available to design new materials and tune their electronic transport properties [36–38]. Figure 1.3 shows the number of annual publications on thermoelectric materials indexed by the Scopus database compared to the number of papers published on multiphase/composite thermoelectric materials, indicating an increasing interest in this topic by the research community over the last five years.

The combination of multiple phases can improve electrical conductivity, thermopower and thermal conductivity [40]. The main strategies discovered so far

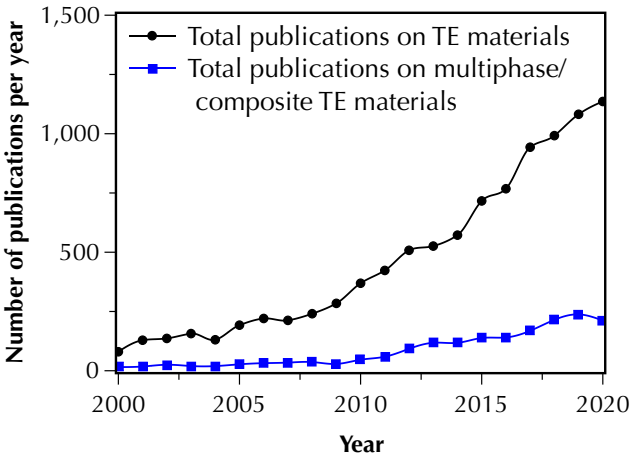

Figure 1.3. Yearly number of publications on thermoelectric materials, compared with publications on multiphase/composite thermoelectric materials. Adapted from [39].

to increase the thermoelectric efficiency of multiphase materials include: (1) energy filtering, which creates potential barriers in the electronic band structure of the main phase via interfaces with the secondary phases. This leads to an increase in the overall thermopower [41–43]; (2) modulation doping, where the heterojunctions between secondary phases with larger bandgaps and higher carrier concentrations than the matrix are used to significantly increase the electrical conductivity of the multiphase compounds [44–46]; (3) phonon scattering by interfaces, grain boundaries, and defects to reduce lattice thermal conductivity [47–50]; and (4) magnetic effects using the magnon-drag mechanism in magnetic materials [51–53], where semiconductors doped with magnetic elements [54–56], or semiconductors containing secondary magnetic phases [57, 58] are used to improve thermoelectric efficiency [59, 60].

1.3 Research aims and objectives

The aim of this research was to investigate the thermoelectric properties of multiphase bismuth sulphide and bismuth telluride materials. Specifically, the following objectives were pursued:

- Synthesis of multiphase bismuth sulphide and bismuth telluride materials using various processing techniques such as zone melting, ball milling, and spark plasma sintering
- Characterisation of the microstructure and phase composition of the synthesised materials using techniques such as X-ray diffraction (XRD)
- Measurement of the thermoelectric properties of the fabricated materials, including electrical conductivity, thermopower, carrier concentration, and

thermal conductivity, using a variety of techniques such as the four-probe method, Hall effect, differential scanning calorimetry (DSC), and the laser flash analysis (LFA) method

- Optimisation of the thermoelectric properties of the synthesised materials by the addition of various dopants and by controlling the microstructure
- Investigation of the underlying mechanisms responsible for the changes in thermoelectric properties through theoretical modelling and simulation

Overall, this thesis aimed to contribute to the development of high-performance thermoelectric materials for energy conversion and waste heat recovery applications. The focus on multiphase bismuth sulphide and bismuth telluride materials was expected to provide new insights into the design and optimisation of thermoelectric materials with enhanced properties.

1.4 Thesis overview

This thesis begins with the motivation for the study and a brief overview of the research.

Chapter 2 reviews thermoelectricity, the thermoelectric effect, and techniques for improving the efficiency of single and multiphase thermoelectric materials. Chapter 3 discusses the synthesis methods used to produce the semiconductor materials studied in this thesis. It also covers the rationale behind the analytical techniques used to study the materials and the mathematical models used to describe their transport properties and band structure.

Chapters 4-8 present the main results of the research. Chapter 4 examines the performance of single phase bismuth sulphide (Bi_2S_3[1]), a key component of the multiphase materials produced here. Chapter 5 focuses on the thermoelectric properties of the multiphase material ($Bi_2Te_{2.75}S_{0.25}$[2]), highlighting the benefits of adding a secondary phase ($Bi_{14}Te_{13}S_8$) to a Bi_2Te_3 matrix. Chapter 6 examines sulphur-added samples of $Bi_2Te_{2.7}Se_{0.3}$[3], while chapter 7 looks at CrSb added to $Bi_{0.5}Sb_{1.5}Te_3$[4] and CrSb added to $Bi_{0.5}Sb_{1.5}Te_{3.3}$[5]. Chapter 8 examines iodine-doped $Bi_{14}Te_{13}S_8$[6]. Finally, chapter 9 concludes with a summary of the main results.

[1] $Bi_{2-x/3}Cr_{x/3}S_{3-x}Cl_x$ (x = 0, 0.005, 0.01, 0.015, and 0.02)
[2] $Bi_2(Te_{2.75-x/3}S_{0.25-x/3})I_x$ x = 0, 0.005, 0.01, and 0.02
[3] $Bi_2(Te_{2.7}Se_{0.3})_{1-x}S_{3x}$ x = (0, 0.003, 0.008, 0.0016, 0.025, 0.05, 0.1, and 0.2)
[4] $Bi_{0.5}Sb_{1.5}Te_3$ with x wt.% CrSb (x = 0, 0.5, 1, 5, 10, 25, and 100)
[5] $Bi_{0.5}Sb_{1.5}Te_{3.3}$ with x wt.% CrSb (x = 0, 0.125, 0.25, 0.5, and 1)
[6] $Bi_2(Te_{1.857}S_{1.142})_{1-x}I_x$ x = 0, 0.005, 0.01, 0.015, and 0.02

References

(1) S. Ashley, *The New York Times, Automobiles*, 2011, https://www.nytimes.com/2011/07/31/automobiles/latest-out-of-tailpipes-electricity-with-exhaust.html (visited on 17/08/2023).

(2) K. Chang, *The New York Times, Business*, 2001, https://www.nytimes.com/2001/11/27/business/technology-a-practical-way-to-make-power-from-wasted-heat.html (visited on 17/08/2023).

(3) A. Khan, *Los Angeles Times, Science & Medicine*, 2017, https://www.latimes.com/science/sciencenow/la-sci-sn-pocket-air-conditioner-20170914-story.html (visited on 17/08/2023).

(4) W. J. Hennigan, *Los Angeles Times, Business*, 2012, https://www.latimes.com/business/la-xpm-2012-aug-07-la-fi-mars-landing-power-source-20120807-story.html (visited on 17/08/2023).

(5) U. S. E. I. A. (EIA), *Monthly Energy Review*, Washington D.C., 2022.

(6) T. Hendricks and W. T. Choate, *Engineering Scoping Study of Thermoelectric Generator Systems for Industrial Waste Heat Recovery*, 1218711, 2006, p. 1218711, doi: 10.2172/1218711.

(7) J. Fairbanks, *US Department of Energy*, 2008.

(8) F. Ritz and C. E. Peterson, 2004 IEEE Aerospace Conference Proceedings (IEEE Cat. No.04TH8720), 2004 IEEE Aerospace Conference Proceedings, IEEE, Big Sky, MT, USA, 2004, pp. 2950–2957, doi: 10.1109/AERO.2004.1368101.

(9) C. B. Vining, *Nat. Mater.*, 2009, **8**, 83–85, doi: 10.1038/nmat2361.

(10) T. M. Tritt, H. Boettner and L. Chen, *Mrs Bull.*, 2008, **33**, 366–368, doi: 10.1557/mrs2008.73.

(11) M. Cutler and N. F. Mott, *Phys. Rev.*, 1969, **181**, 1336–1340, doi: 10.1103/PhysRev.181.1336.

(12) O. Delaire, J. Ma, K. Marty, A. F. May, M. A. McGuire, M. H. Du, D. J. Singh, A. Podlesnyak, G. Ehlers, M. D. Lumsden and B. C. Sales, *Nat. Mater.*, 2011, **10**, 614–9, doi: 10.1038/nmat3035.

(13) Y. Hu, L. Zeng, A. J. Minnich, M. S. Dresselhaus and G. Chen, *Nat. Nanotechnol.*, 2015, **10**, 701–6, doi: 10.1038/nnano.2015.109.

(14) M. E. Siemens, Q. Li, R. Yang, K. A. Nelson, E. H. Anderson, M. M. Murnane and H. C. Kapteyn, *Nat. Mater.*, 2010, **9**, 26–30, doi: 10.1038/nmat2568.

(15) Z. Fan, H. Wang, Y. Wu, X. J. Liu and Z. P. Lu, *Rsc Advances*, 2016, **6**, 52164–52170, doi: 10.1039/c5ra28088e.

(16) L. Hu, Y. Zhang, H. Wu, J. Li, Y. Li, M. McKenna, J. He, F. Liu, S. J. Pennycook and X. Zeng, *Adv. Energy Mater.*, 2018, **8**, 1802116, doi: 10.1002/aenm.201802116.

(17) P. C. Wei, C. N. Liao, H. J. Wu, D. Yang, J. He, G. V. Biesold-McGee, S. Liang, W. T. Yen, X. Tang, J. W. Yeh, Z. Lin and J. H. He, *Adv. Mater.*, 2020, **32**, e1906457, doi: 10.1002/adma.201906457.

(18) G. Joshi, H. Lee, Y. Lan, X. Wang, G. Zhu, D. Wang, R. W. Gould, D. C. Cuff, M. Y. Tang, M. S. Dresselhaus, G. Chen and Z. Ren, *Nano Lett.*, 2008, **8**, 4670–4674, doi: 10.1021/nl8026795.

(19) Y. C. Lan, A. J. Minnich, G. Chen and Z. F. Ren, *Adv. Funct. Mater.*, 2010, **20**, 357–376, doi: 10.1002/adfm.200901512.

(20) Z. Ren, B. E. D. Poudel, G. Chen, Y. Lan, D. Wang, Q. Hao, M. Dresselhaus, Y. I. Ma, X. Yan, X. Chen, X. Wang, R. A. J. Joshi Giri and B. O. Yu, *US Pat.*, 2007/0086291 W, 2008.

(21) X. W. Wang, H. Lee, Y. C. Lan, G. H. Zhu, G. Joshi, D. Z. Wang, J. Yang, A. J. Muto, M. Y. Tang, J. Klatsky, S. Song, M. S. Dresselhaus, G. Chen and Z. F. Ren, *Appl. Phys. Lett.*, 2008, **93**, 193121, doi: 10.1063/1.3027060.

(22) H. Wang, X. Cao, Y. Takagiwa and G. J. Snyder, *Mater. Horiz.*, 2015, **2**, 323–329, doi: 10.1039/c5mh00021a.

(23) B. Yu, M. Zebarjadi, H. Wang, K. Lukas, H. Wang, D. Wang, C. Opeil, M. Dresselhaus, G. Chen and Z. Ren, *Nano Lett.*, 2012, **12**, 2077–82, doi: 10.1021/nl3003045.

(24) M. Thesberg, M. Pourfath, H. Kosina and N. Neophytou, *J. Appl. Phys.*, 2015, **118**, 224301, doi: 10.1063/1.4936839.

(25) J. P. Heremans, V. Jovovic, E. S. Toberer, A. Saramat, K. Kurosaki, A. Charoenphakdee, S. Yamanaka and G. J. Snyder, *Science*, 2008, **321**, 554–7, doi: 10.1126/science.1159725.

(26) J. S. Rhyee, K. H. Lee, S. M. Lee, E. Cho, S. I. Kim, E. Lee, Y. S. Kwon, J. H. Shim and G. Kotliar, *Nature*, 2009, **459**, 965–8, doi: 10.1038/nature08088.

(27) J. Zhou, R. Yang, G. Chen and M. S. Dresselhaus, *Phys. Rev. Lett.*, 2011, **107**, 226601, doi: 10.1103/PhysRevLett.107.226601.

(28) J. Mao, Z. Liu and Z. Ren, *npj Quantum Materials*, 2016, **1**, 1–9, doi: 10.1038/npjquantmats.2016.28.

(29) G. Zeng, J. E. Bowers, J. M. O. Zide, A. C. Gossard, W. Kim, S. Singer, A. Majumdar, R. Singh, Z. Bian, Y. Zhang and A. Shakouri, *Appl. Phys. Lett.*, 2006, **88**, 113502, doi: 10.1063/1.2186387.

(30) Y. Gu, W. Ai, Y. Zhao, L. Pan, C. Lu, P. Zong, X. Hu, Z. Xu and Y. Wang, *J. Mater. Chem.A*, 2021, **9**, 16928–16935, doi: 10 . 1039 / D1TA02812J.

(31) Q. R. Hou, B. F. Gu, Y. B. Chen, Y. J. He and J. L. Sun, *Applied Physics a-Materials Science & Processing*, 2014, **114**, 943–949, doi: 10.1007/s00339-013-7794-0.

(32) M. Zebarjadi, G. Joshi, G. Zhu, B. Yu, A. Minnich, Y. Lan, X. Wang, M. Dresselhaus, Z. Ren and G. Chen, *Nano Lett.*, 2011, **11**, 2225–30, doi: 10.1021/nl201206d.

(33) L. H. Wu, X. Li, S. Y. Wang, T. S. Zhang, J. Yang, W. Q. Zhang, L. D. Chen and J. H. Yang, *Npg Asia Materials*, 2017, **9**, e343–e343, doi: 10.1038/am.2016.203.

(34) Q. Y. Zhang, H. Wang, W. S. Liu, H. Z. Wang, B. Yu, Q. Zhang, Z. T. Tian, G. Ni, S. Lee, K. Esfarjani, G. Chen and Z. F. Ren, *Energy Environ. Sci.*, 2012, **5**, 5246–5251, doi: 10.1039/c1ee02465e.

(35) R. Kim and M. S. Lundstrom, *J. Appl. Phys.*, 2012, **111**, 024508, doi: 10.1063/1.3678001.

(36) S. Aminorroaya Yamini, D. R. Mitchell and M. Avdeev, *Phys. Chem. Chem. Phys.*, 2016, **18**, 32814–32819, doi: 10.1039/c6cp05232k.

(37) J. Byrnes, D. R. G. Mitchell and S. A. Yamini, *Mater. Today Phys.*, 2020, **13**, doi: 10.1016/j.mtphys.2020.100190.

(38) A. Yamini, T. Li, D. R. G. Mitchell and J. M. Cairney, *Nano Energy*, 2016, **26**, 157–163, doi: 10.1016/j.nanoen.2016.05.019.

(39) **Fortulan, Raphael** and S. Aminorroaya Yamini, *Materials*, 2021, **14**, 6059, doi: 10.3390/ma14206059.

(40) Y.-H. Gao, H. Chen, N. Liu and R.-Z. Zhang, *Results Phys.*, 2018, **11**, 915–919, doi: 10.1016/j.rinp.2018.10.034.

(41) Q. Hu, W. Qiu, L. Chen, J. Chen, L. Yang and J. Tang, *ACS Appl. Mater. Interfaces*, 2021, **13**, 38526–38533, doi: 10.1021/acsami.1c12722.

(42) W. Park, H. Hwang, S. Kim, S. Park and K.-S. Jang, *ACS Appl. Mater. Interfaces*, 2021, **13**, 7208–7215, doi: 10/gmkd23.

(43) A. T. T. Pham, P. T. N. Vo, H. K. T. Ta, H. T. Lai, V. C. Tran, T. L. H. Doan, A. T. Duong, C. T. Lee, P. K. Nair, Y. A. Zulueta, T. B. Phan and S. D. N. Luu, *Thin Solid Films*, 2021, **721**, doi: 10.1016/j.tsf.2021.138537.

(44) M. H. Lee, J. H. Yun, G. Kim, J. E. Lee, S.-D. Park, H. Reith, G. Schierning, K. Nielsch, W. Ko, A.-P. Li and J.-S. Rhyee, *ACS Nano*, 2019, **13**, 3806–3815, doi: 10/gmkd25.

(45) C. Wang, S. Lin, H. Chen, Y. Zhao, L. Zhao, H. Wang, D. Huo and X. Chen, *Energy Convers. Manage.*, 2015, **94**, 331–336, doi: 10.1016/j.enconman.2015.01.082.

(46) D. Wu, Y. Pei, Z. Wang, H. Wu, L. Huang, L.-D. Zhao and J. He, *Adv. Funct. Mater.*, 2014, **24**, 7763–7771, doi: 10.1002/adfm.201402211.

(47) K. Ahmad, C. Wan, M. A. Al-Eshaikh and A. N. Kadachi, *Appl. Surf. Sci.*, 2019, **474**, 2–8, doi: 10.1016/j.apsusc.2018.10.163.

(48) T. Manimozhi, S. Kavirajan, S. Harish, J. Archana, K. Kamala Bharathi, E. Senthil Kumar and M. Navaneethan, *Mater. Lett.*, 2021, **304**, 130399, doi: 10.1016/j.matlet.2021.130399.

(49) Z. Wang, G. Wang, R. Wang, X. Zhou, Z. Chen, C. Yin, M. Tang, Q. Hu, J. Tang and R. Ang, *ACS Appl. Mater. Interfaces*, 2018, **10**, 22401–22407, doi: 10.1021/acsami.8b05117.

(50) M. Wolf, K. Menekse, A. Mundstock, R. Hinterding, F. Nietschke, O. Oeckler and A. Feldhoff, *J. Electron. Mater.*, 2019, **48**, 7551–7561, doi: 10.1007/s11664-019-07555-2.

(51) Y. Sun, S. Canulescu, P. J. Sun, F. Steglich, N. Pryds, J. Schou and B. B. Iversen, *Applied Physics a-Materials Science & Processing*, 2011, **104**, 883–887, doi: 10.1007/s00339-011-6431-z.

(52) P. Sun, N. Oeschler, S. Johnsen, B. B. Iversen and F. Steglich, *J. Phys: Conf. Ser.*, 2009, **150**, 012049, doi: 10.1088/1742-6596/150/1/012049.

(53) N. Tsujii, T. Mori and Y. Isoda, *J. Electron. Mater.*, 2014, **43**, 2371–2375, doi: 10.1007/s11664-014-3072-y.

(54) T. Motohashi, E. Naujalis, R. Ueda, K. Isawa, M. Karppinen and H. Yamauchi, *Appl. Phys. Lett.*, 2001, **79**, 1480–1482, doi: 10 . 1063 / 1 . 1400777.

(55) Q. Wen, C. Chang, L. Pan, X. T. Li, T. Yang, H. H. Guo, Z. H. Wang, J. Zhang, F. Xu, Z. D. Zhang and G. D. Tang, *J. Mater. Chem.A*, 2017, **5**, 13392–13399, doi: 10.1039/c7ta03659k.

(56) C. Xiao, K. Li, J. J. Zhang, W. Tong, Y. W. Liu, Z. Li, P. C. Huang, B. C. Pan, H. B. Su and Y. Xie, *Mater. Horiz.*, 2014, **1**, 81–86, doi: 10.1039/c3mh00091e.

(57) K. G. Liu and J. Li, *Frontiers of Green Building, Materials and Civil Engineering, Pts 1-8*, 2011, **71–78**, 3741–3744, doi: 10.4028/www.scientific.net/AMM.71-78.3741.

(58) G. Tan, F. Shi, S. Hao, H. Chi, T. P. Bailey, L. D. Zhao, C. Uher, C. Wolverton, V. P. Dravid and M. G. Kanatzidis, *J. Am. Chem. Soc.*, 2015, **137**, 11507–16, doi: 10.1021/jacs.5b07284.

(59) S. Hébert, R. Daou, A. Maignan, S. Das, A. Banerjee, Y. Klein, C. Bourgès, N. Tsujii and T. Mori, *Sci. Technol. Adv. Mater.*, 2021, **22**, 583–596, doi: 10/gmkd34.

(60) L. Xing, W. Cui, X. Sang, F. Hu, P. Wei, W. Zhu, X. Nie, Q. Zhang and W. Zhao, *Journal of Materiomics*, 2021, **7**, 998–1006, doi: 10/gmkd3z.

2

Literature review

Before getting into the subject for which I find neither a large nor a small door; the best thing to do is to loosen the grip on my pen and let it wander about until it finds an entrance. There must be one – it all depends on the circumstances, a rule that is applicable as much to literary style as to life. Each word draws another one along, one idea another, and that is how books, governments, and revolutions are made.
— Machado de Assis, Primas de Sapucaia!

Summary
This chapter serves as an introductory exploration of the concept of thermoelectricity. It begins with a discussion of the thermoelectric effect, thermopower, and the electrical and thermal conductivity of semiconductors. This is followed by a presentation of various techniques used to improve the thermoelectric efficiency of single phase thermoelectric materials, including approaches aimed at optimising thermopower, electrical conductivity, and thermal conductivity.
This chapter also explains the motivation behind the study of multiphase thermoelectric materials. The potential benefits of incorporating secondary phases into thermoelectric materials to achieve improved performance are explored, and a comprehensive review of research on multiphase thermoelectric materials is presented, highlighting key findings and advances in the field.

2.1 Thermopower

The thermopower is the phenomenon whereby a temperature difference in a material creates a difference in electrical potential. In a conducting material, such as a metal or semiconductor, electrons on the hot side have higher thermal energy and diffuse to the cold side, where they accumulate, creating a difference in charge density that is measured as an electrical potential. The thermopower (α) is defined as

$$\alpha = -\frac{\nabla V}{\nabla T}, \tag{2.1}$$

where ∇V and ∇T are the voltage and temperature gradients, respectively, in the material. It should be noted that the thermopower is also known as the Seebeck coefficient, and S is also used to denote α in some texts.

When a semiconductor is subjected to a temperature gradient, both carriers will diffuse to the cold side, accumulate, and create a charge difference opposite to the temperature difference, the magnitude of which depends on the ratio between the concentrations of majority and minority carriers. Thus, to generate a useful electromotive force, doping is required to achieve a significant difference in carrier type.

At higher temperatures, thermally excited minority carriers can cross the band gap and act as free carriers, contributing negatively to the thermopower. Thermopower is therefore mainly a function of carrier density, temperature, and scattering mechanisms.

2.2 Peltier effect

When an electric current flows through a thermocouple, a heat flow is generated at the junction of the two materials. This is the so-called Peltier effect. The Peltier coefficient is determined as

$$\pi = \frac{\dot{Q}}{I}, \tag{2.2}$$

where $\dot{Q}$ is the heat transfer rate and I is the electric current.

The thermopower is closely related to the Peltier effect since, in a thermoelectric circuit, the thermopower will generate a current, which will in turn transfer heat from the hot to the cold junction via the Peltier effect. This result is analogous to the back electromotive force generated in inductive circuits by Lenz's law.

The thermopower and Peltier coefficient are related by the following expression[1]

$$\pi = \alpha T. \tag{2.3}$$

[1] Also known as Thomson's relation.

2.3 Electrical conductivity and resistivity

The electrical conductivity σ of a material is determined as [61]

$$\sigma = nq\mu, \tag{2.4}$$

where n is the carrier concentration, q is the elementary charge, and μ is the carrier mobility. For semiconductors, equation 2.4 can be modified as follows

$$\sigma = nq\mu_n + pq\mu_p, \tag{2.5}$$

where n and p are, respectively, the concentration of negative and positive carriers; μ_n and μ_p are, respectively, the mobilities of the negative and positive carriers.

The electrical resistivity ρ is the reciprocal of the electrical conductivity

$$\rho = \frac{1}{\sigma}. \tag{2.6}$$

In literature, both properties are used to define the so-called power factor (PF)

$$PF = \frac{\alpha^2}{\rho} = \alpha^2\sigma. \tag{2.7}$$

2.4 Thermal conductivity

In thermoelectric power generation, thermal conductivity plays a crucial role. A low thermal conductivity ensures that the established thermal gradient remains large enough to generate a high voltage. In semiconductors, thermal conduction occurs through two phenomena: electronic conduction (heat transported by electronic charges) and lattice conduction (heat transported by lattice vibrations or phonons). The thermal conductivity (κ) of a thermoelectric material is thus the sum of the electronic thermal conductivity (κ_e) and the lattice thermal conductivity (κ_l). However, in semiconductors, where both positive and negative carriers are present, it is possible for them to move in the same direction and transport energy without an electric current. This effect is known as bipolar, and it leads to an increase in the overall thermal conductivity, so that [62]

$$\kappa = \kappa_e + \kappa_l + \kappa_b, \tag{2.8}$$

$$\kappa_b = \frac{\sigma_n\sigma_p}{\sigma_n + \sigma_p}(\alpha_n - \alpha_p)^2 T, \tag{2.9}$$

where κ_b is the bipolar thermal conductivity, σ_n, σ_p, σ_n, and σ_p are, respectively, the electron conductivity, hole conductivity, the thermopower due to electrons, and the thermopower due to holes. The thermal electronic conductivity is usually determined by the Wiedemann–Franz law [63]

$$\kappa_e = LT\sigma, \tag{2.10}$$

where the proportionality constant L is known as the Lorenz number. The degenerate limit of L is 2.45×10^{-8} $V^2.K^{-2}$.

2.5 Thermoelectric figure of merit zT

Thermoelectric generators are, in essence, heat engines, and their efficiency is limited by the Carnot efficiency [64]

$$\eta_c = 1 - \frac{T_C}{T_H}, \tag{2.11}$$

where T_C and T_H are the absolute temperatures of the hot and cold reservoirs, respectively, and the efficiency η_c is the maximum ratio of the work done by the engine to the heat drawn out of the hot reservoir (to the engine). For thermoelectric materials, the maximum efficiency (η_t) is given by [61]

$$\eta_t = \underbrace{\frac{T_H - T_C}{T_H}}_{\text{Carnot efficiency}} \cdot \underbrace{\frac{\sqrt{1+zT}-1}{\sqrt{1+zT}+\frac{T_C}{T_H}}}_{\text{Thermoelectric weighting}}, \tag{2.12}$$

where zT is known as the figure of merit and is calculated as

$$zT = \frac{\alpha^2\sigma}{\kappa}T = \frac{PF}{\kappa}T. \tag{2.13}$$

Clearly, $\eta_t \propto zT$, so improving zT is the key challenge for increasing the efficiency of thermoelectric materials.

Since zT is temperature dependent, not all materials will operate at all temperature ranges equally. In fact, according to the end application, a family of materials is selected. This phenomenon is illustrated in figure 2.1. In this work, the focus is on thermoelectric materials for low temperature applications, so the family of materials used was BST (Bi, Te, Se, and Sb).

In the next section, the conventional methods used to improve the figure of merit are presented.

2.6 Methods for improving zT

The main mechanisms in which zT have been optimised over the years for single phase compounds are

- optimising the carrier concentration [65];
- band engineering [66–69]; and
- nanostructure engineering [21, 70].

In sequence a brief discussion of each of the mechanisms previously mentioned is shown.

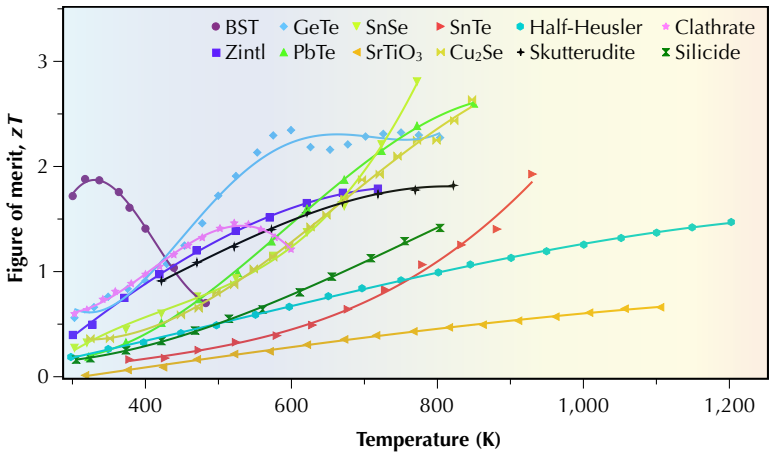

Figure 2.1. State-of-the-art zT for low, mid, and high temperature range thermoelectric materials.

2.6.1 Carrier concentration optimisation

The carrier concentration n of semiconductor material is controlled either by extrinsic doping or by intrinsic defects [71]. Defects in donors donate extra electrons or, in the case of a vacancy, accept fewer electrons into the valence band than without the defect [72].

The challenge in optimising the carrier concentration is that both the conductivity and thermal conductivity increase with it and the thermopower decreases. Therefore, zT will not have a monotonic behaviour with respect to n, but it will reach a maximum value at a certain carrier concentration. In figure 2.2, the behaviour of the thermopower, electrical conductivity, thermal conductivity, and zT with respect to the carrier concentration according to the single parabolic band (SPB) is shown. As can be seen, zT will attain a maximum value at an intermediary carrier concentration.

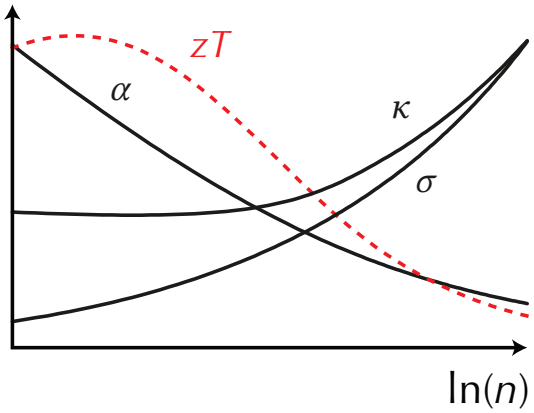

Figure 2.2. Variation of thermoelectric properties with respect to the carrier concentration as evaluated by the single parabolic band model.

2.6.2 Band engineering

Optimising the electron band structure involves two tasks:

- Tuning the band filling to achieve an optimal carrier concentration n
- Enhancing the electron density of states near the Fermi level E_F to increase the thermopower α

One way to control the electron density of states is to increase the gap energy E_g. At higher temperatures, thermal excitation of small carriers can increase the charge density n, which in turn decreases α and increases κ_e. In [25, 67] it can be seen that the energy gap of semiconductors can be tuned by doping, and an enlarged E_g can shift the thermal excitation temperature of minor carriers to a higher temperature range, suppressing the minor carriers.

For Bi_2Te_3, in particular, it was reported in [73] that the figure of merit zT was increased by reducing κ_b and improving α. This result was achieved by increasing the gap energy between the valence and conduction bands. Since κ_b is proportional to temperature according to equation (2.9), reducing its value allows for operation at higher temperatures. The overall result was an increase in the zT from ≈0.76 to ≈0.98 at 450 K.

A formal verification of the band engineering technique is now provided. The carrier concentration is evaluated as [74]

$$n = \int_{E_C}^{+\infty} g(E) f(E) \mathrm{d}E, \tag{2.14}$$

$$f(E) = \frac{1}{1 + \exp\left(\frac{E - E_F}{T}\right)}, \tag{2.15}$$

where E_C is the conduction energy, $g(E)$ is the DOS, and $f(E)$ is the Fermi-Dirac distribution. The Landauer expression for the conductivity is given by [75]

$$\sigma'(E) = \frac{2q^2}{h} \lambda(E) \frac{M(E)}{A} \left(-\frac{\partial}{\partial E} f(E)\right), \tag{2.16}$$

$$\sigma(E) = \int_{-\infty}^{+\infty} \sigma'(E) \mathrm{d}E, \tag{2.17}$$

where σ' is the differential conductivity, $\lambda(E)$ is the mean free path, $M(E)$ is the number of conducting channels at a given energy, and A is the conductor area. The derivative of the Fermi-Dirac distribution is given by

$$\frac{\partial}{\partial E} f(E) = -\frac{\exp(E - E_F)}{\left(1 + \exp(E - E_F)\right)^2}. \tag{2.18}$$

Since $f(E)$ is a sigmoid function, its derivative is a bell-shaped curve centred at E_F. Thus, from equations 2.16 and 2.17, the electrical conductivity will depend on the DOS around the Fermi level.

Besides controlling the bandgap, resonant states and band convergence have been used by researchers to control the band structure and achieve a higher thermopower [25, 66, 69, 76] and higher zT (e.g. from ≈0.2 to ≈1.4 at 750K [77]).

To achieve a resonant state, the dopant energy level is chosen to be in the conduction or valence band of the host band [78]. When this phenomenon occurs, there is a distortion in the band that increases the density of states in the resonant region. As the Fermi level approaches the resonant state, there is an increase in α and consequently in zT.

Finally, the band convergence technique uses the convergence of multiple degenerate valleys to increase the thermopower and achieving high zt≈1.3 at 700 K for $PbTe_{1-x}Se_x$ [79]. This increase occurs because increasing the valley degeneracy N_v also increases the effective mass of thermoelectric materials by a factor of $N_v^{2/3}$ without any noticeable effect on mobility [80]. The overall effect is a large increase in the power factor due to the increase in α, and possibly a reduction in μ due to intervalley scattering.

2.7 Nanostructure engineering

Typically, when the power factor is increased by doping [81] or alloying [82] with other elements, the lattice thermal conductivity κ_l decreases due to the increased phonon scattering introduced by dopant atoms or ions. However, such a reduction is also accompanied by an undesirable side effect: the increase in κ_e due to the increase in carrier concentration. To reduce κ_l, nanostructure engineering has been used as an effective approach to obtain a higher figure of merit zT [19, 83]. The development of low-dimensional nanomaterials [84] has shown that it is possible to enhance zT as a consequence of the quantum confinement of phonons [85], while nanowires have been predicted to exhibit ultra-high zT of up to 14 [86].

2.8 Multiphase materials

Having introduced the techniques for improving zT for single phase thermoelectric materials, this section now provides an overview of those for multiphase thermoelectric materials. The following subsections present the main ways in which the zT of multiphase TE materials can be improved.

2.8.1 Energy filtering

The concept of energy filtering in thermoelectric materials was first introduced and studied in the second half of the last century [87]. Research in this field has been renewed since the 1990s. In general, the thermopower increases with increasing barrier height [88, 89] while the electrical conductivity decreases [90–92]. In the presence of multiple potential barriers, the bipolar effect can be suppressed by reducing the flow of minority charge carriers and reducing the decrease in electrical conductivity [93–96].

Conventionally, the energy filtering effect can be understood by solving the Boltzmann transport equation (BTE) using the relaxation time approximation [97, 98]. The BTE equation expresses all thermoelectric transport coefficients as a function of the energy dependent relaxation times of the carriers $\tau(E)$ and the Fermi level E_F. The energy filtering effect can be easily verified by considering the thermopower expression [99]

$$\alpha = -\frac{1}{qT}\frac{\int (E - E_F)\sigma' \mathrm{d}E}{\int \sigma' \mathrm{d}E}, \tag{2.19}$$

where T is the absolute temperature, E is the charge carrier energy, E_F is the Fermi level, and σ' is the differential conductivity. The thermopower, as shown in equation 2.19, is the energy average weighted by the electrical conductivity

$$\alpha = -\frac{1}{qT}\left\langle E - E_F \right\rangle_{\sigma'}. \tag{2.20}$$

This implies that an asymmetry between the density of states and the Fermi level can produce higher thermopower.

Energy barriers in thermoelectric materials are implemented in the form of nanoparticles or grain boundary interfaces embedded in the bulk host matrix [100]. At these interfaces, carriers with higher energy preferentially pass through the interface, while carriers with lower energy are filtered out. A high density interface ensures a positive carrier filtering effect [101]. Band bending between the two materials creates an energy barrier that reflects the carriers [102, 103]. Figure 2.3 illustrates the energy filtering effect; due to the partial reflection of the low energy electron waves, the high energy electrons contribute most to the thermopower.

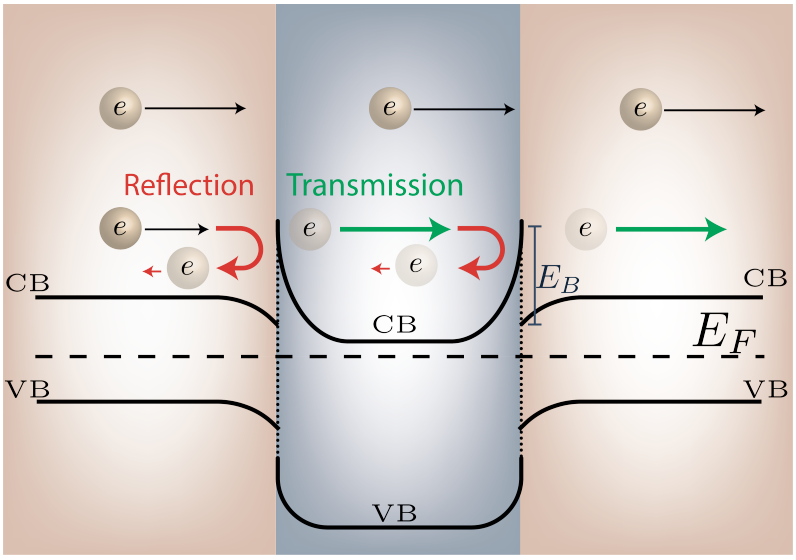

Figure 2.3. Illustration of the energy filtering effect, showing that lower energy electrons are scattered by a potential barrier.

Multiphase materials are viable candidates to take advantage of energy filtering. Due to the possibility of tuning the electronic band structure of each phase, band bending can significantly enhance the energy filtering effect [104–111]. A Schottky or ohmic barrier occurs at the interface with a metallic secondary phase, while a heterojunction barrier occurs at the interface of the thermoelectric material with a semiconducting secondary phase.

2.8.1.1 Energy filtering by metallic secondary phases

For energy filtering effect by metallic phases, the barrier height is proportional to the work function of the metal and to the electron affinity of the semiconductor. The work function Φ is defined as the minimum energy required to remove an electron from the surface of a material, and its value is equal to the energy difference between vacuum and the Fermi level [112]. The electron affinity χ is the energy difference between the vacuum and the bottom of the conduction band. At the metal–semiconductor junction, the Schottky–Mott rule [113] defines the barrier height E_B as the difference between the work function of the metal Φ_M and the electron affinity of the semiconductor χ_S,

$$E_B = \Phi_M - \chi_S. \tag{2.21}$$

Small differences place few restrictions on the movement of electrons, and this barrier is known as an ohmic barrier. Both work function and electron affinity depend on surface impurities and crystallographic orientation.

Theoretically, the presence of metals can strongly influence the carrier relaxation time and consequently both the electrical conductivity and the thermopower [89, 114, 115]. The inclusion of metallic nanoparticles has been shown to

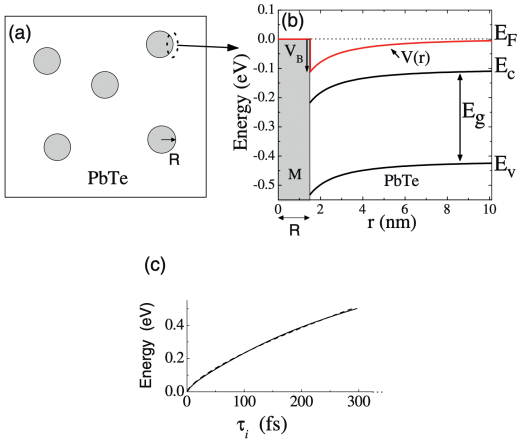

Figure 2.4. (a) Schematic of randomly distributed metallic Pb secondary phase in a PbTe matrix, (b) calculated potential $V(r)$ and energy diagram for PbTe at 300 K, carrier concentration of 2.5×10^{19} cm^{-3}, barrier height of 0.11 eV, and radius of 1.5 nm, where E_F is the Fermi level, E_C is the energy at the bottom of the conduction band, E_g is the band gap, and E_V is the energy at the top of the valence band, and (c) carriers' relaxation time as a function of their energy. Reprinted from [100].

mathematically enhance the thermopower [100]. The interface of n-type PbTe with metallic Pb nanoparticles with a low work function effectively scattered electrons and increased both the thermopower and the electrical resistivity. This mechanism is schematically illustrated in figure 2.4, where spherical metallic nanoparticles are randomly distributed in the host semiconductor. Experimental results proved this concept [116–118], such as Pb precipitates in the matrix of n-type PbTe, intrinsically doped with excess Pb, increased the thermopower and the average resistivity from -98 μV.K^{-1} and 1.2 mΩ.cm for $Pb_{1.03}Te$ to -130 μV.K^{-1} and 3.2 mΩ.cm for $Pb_{1.06}Te$ at 300 K respectively [116]. The addition of metallic Sn and Cr to Cu_2O doubled the thermopower from 700 μV.K^{-1} to 1400 μV.K^{-1}. [118]. Platinum nanocrystals created energy barriers in p-type Sb_2Te_3 thin films [117] and caused a large reduction in carrier mobility of about 2.5 orders of magnitude due to additional carrier scattering compared to Sb_2Te_3 films without Pt nanocrystals. The carrier concentration increased, possibly due to the overlap of energy bands [100]. The band overlap increases the distance between the Fermi energy level and the valence band maximum, thereby increasing the total concentration of holes in the semiconductor matrix.

Silver nanoparticles enhanced the thermopower of CdO–Ag composites [119]—a potential barrier of E_B = 0.1 eV between the work function of Ag and the electron affinity of CdO increasing the resistivity from 1.5 mΩ.cm to 1.7 mΩ.cm for a sample with 0.03% Ag and increasing the thermopower from -120 μV.K^{-1} for the pristine sample to -129 μV.K^{-1} for the sample with 0.03% Ag at 800 K.

2.8.1.2 Energy filtering by semiconducting secondary phases

For a semiconductor secondary phase, the difference between the band gaps and Fermi levels of the two phases gives rise to a potential barrier at their junction [120]. The barrier height will be proportional to the difference between the electron affinity of the two semiconductors (χ_1 and χ_2). Anderson's rule [112] allows a simple estimate of the barrier height at the conduction, E_{BC}, and valence, E_{BV}, bands

$$E_{BC} = \chi_2 - \chi_1, \tag{2.22}$$

$$E_{BV} = (E_{g1} - E_{g2}) - E_{BC}, \tag{2.23}$$

where E_{g1} and E_{g2} are the bandgaps of the two semiconductors. This simple rule has been employed as a rough estimate to design multiphase materials. However, the actual curvature of the band bending can be found using Poisson's equation for the electric potential [121]

$$-\nabla^2 V = \frac{\rho}{\epsilon} = \frac{q(p - n + D_I)}{\epsilon}, \tag{2.24}$$

where ϵ is the permittivity of the material, p and n are the hole and electrons concentrations, respectively, and D_I is the concentration of ionised impurities (extrinsic dopant). The relation between the barrier height and electrical conductivity is suggested as being [122]

$$\sigma \propto T^{-1/2} e^{-\frac{E_B}{k_B T}}. \tag{2.25}$$

It should be noted that this equation was developed for homojunctions [123, 124]. However, the experimental data for heterojunctions fit this equation surprisingly well [125]. Experimental results have shown that energy filtering by dissimilar semiconducting phases can improve the power factor [126–129]. Silicon oxide particles in the $(Bi_2Te_3)_{0.2}(Sb_2Te_3)_{0.8}$ bulk alloy increased the thermopower from 182 $\mu V.K^{-1}$ for the pristine sample to 218 $\mu V.K^{-1}$ for the sample with 1.1% volume of SiO_2 at room temperature [126]. Yttrium oxide (Y_2O_3) particles embedded in a $Bi_{0.5}Sb_{1.5}Te_3$ matrix significantly increase the thermopower [130] and deviate significantly from the ideal Pisarenko relation. The thermopower is inversely proportional to the carrier concentration n for degenerate semiconductors according to the Pisarenko relation [131] with a rate of $n^{-2/3}$. The deviation from this ideal relationship has been used as an indication of changes in the electronic band structure of a material [132].

Randomly dispersed titanium dioxide nanoparticles (from 10 to 25 nm) in a $Ba_{0.22}Co_4Sb_{12}$ matrix increase the thermopower [133]. Although the bandgap for $Ba_{0.22}Co_4Sb_{12}$ is unknown, given the large bandgap of TiO_2 (3.2 eV [134]), the influence of energy filtering was assumed. At 300 K the electrical conductivity decreased from 2.9×10^5 $S.m^{-1}$ to 2.8×10^5 $S.m^{-1}$ and the thermopower increased from -105 $\mu V.K^{-1}$ for the pristine sample to -110 $\mu V.K^{-1}$ for the sample

with 0.8% volume of TiO_2. The TiO_2 particles in the Bi_2Se_3 based materials increased the overall power factor of the composite from 0.75×10^{-3} W.m^{-1}.K to 1.07×10^{-3} W.m^{-1}.K for the sample containing 10 wt.% titanium dioxide [135]. The carrier concentration varied significantly with the concentration of TiO_2, possibly due to the formation of Ti^{2+} ions during hot pressing under vacuum.

A double filtering effect has been reported for TiO_2 deposited on $Ti_{1-x}O_x$ @ TiO_y ($x < 1, 1 < y < 2$) heterostructures [136]. $TiC_{1-x}O_x$, with a narrow bandgap and high electrical conductivity, in combination with TiO_y and TiO_2 nanoparticles with wide bandgaps, provided an effective barrier height for energy filtering. The thermopower and the resistivity of the samples increase as a larger amount of TiO_2 is deposited. The maximum value obtained for the thermopower at 973 K was -156 μV.K^{-1} with an electrical conductivity of $\approx 4 \times 10^4$ S.m^{-1}.

Silicon-based materials, although not commonly used as thermoelectric materials, have also been shown to benefit from energy filtering [137–144]. For instance, heavily doped silicon with boron and nanoparticles of Si have shown increased thermopower and electrical conductivity in a particular range of dopant concentrations [145]. The increased Fermi level of the bulk material explains the increase in electrical conductivity, and the energy filtering effect justifies the increased thermopower.

A half-Heusler compound of $(Hf_{0.6}Zr_{0.4})NiSn_{0.99}Sb_{0.01}$ with added nanoparticles of tungsten (W) showed a maximum zT of 1.4 at 873 K and an average zT of 0.9 in the temperature range of 300—973 K for the alloy with 5 wt.% tungsten nanoparticles [146].

Table 2.1 summarises the compositions and fabrication methods of recent studies that reported energy filtering effects in multiphase thermoelectric materials.

2.8.2 Modulation doping

Modulation doping is a well established concept for increasing the conductivity of heterojunction devices [161]. The basic idea behind modulation doping is to use the offset in the band structure between two semiconductors in combination with heavy doping of the material with the wider band gap, so that there is a transfer of carriers from the material with the wide band gap material with the narrow band gap material. The transferred carriers create a two-dimensional electron gas that is essentially separated from the donor phase, thereby increasing the carrier mobility [162]. Conventionally, this strategy has been used to create p-channel devices called modulation-doped field-effect transistors (MODFETs) [163]. The difference between energy filtering and modulation doping is shown schematically in figure 2.5. In the case of modulation doping, the secondary phase increases the conductivity by donating electrons to the host semi-

Table 2.1. Compositions, fabrication methods, and corresponding references of multiphase materials that benefited from the energy-filtering effect. Adapted from [39]

Composition	Fabrication method	Ref.
$Bi_{0.5}Sb_{1.5}Te_3$ + (0, 1.0, 2.0, 4.0, and 6.0 wt.%) nanoparticles of Sb_2O_3	Casting $Bi_{0.5}Sb_{1.5}Te_3$ + ball milling $Bi_{0.5}Sb_{1.5}Te_3$ and commercial powder of Sb_2O_3+ sintering	[147]
$Bi_2Te_{2.7}Se_{0.3}$ powder + 2 nm layer of film of ZnO	Solution-based synthesis of Bi-Te-Se powder + atomic layer deposition of ZnO + hot pressing	[148]
$Bi_{1-x}Sb_x$ (x = 0, 0.10, 0.12, 0.13, 0.14, and 0.2) + 3 wt.% carbon nanotubes	Ball milling + cold pressing + annealing	[149]
$Bi_{0.46}Sb_{1.54}Te_3$ + (0, 0.1, 0.2, and 0.3 wt.%) SiC	Ball milling + sintering	[110]
$Bi_{0.4}Sb_{1.6}Te_3$ + (0.1, 0.2, and 0.3 wt.%) $CuInTe_2$	Casting each phase separately + ball milling + sintering	[150]
$Lu_{0.1}Bi_{1.9}Te_3$ + (0, 0.0, 0.05, 1 wt.%) carbon nanotubes	Hydrothermal synthesis + grinding + hot pressing	[151]
$Bi_{0.5}Sb_{1.5}Te$ + (0, 0.1, 0.2, 0.3, 0.4 wt.%) $BaTiO_3$	Hydrothermally synthesised $BaTiO_3$ + Commercial ingots of $Bi_{0.5}Sb_{1.5}Te_3$ were ground and sintered	[111]
$Bi_{0.5}Sb_{1.5}Te_3$ + $SrTiO_3$	$Bi_{0.5}Sb_{1.5}Te_3$ films were grown on $SrTiO_3$ substrates by co-sputtering	[152]
Bi_2Te_3 + $Bi_{0.5}Sb_{1.5}Te_3$ thin films	Radio-frequency magnetron sputtering of Bi_2Te_3 / $Bi_{0.5}Sb_{1.5}Te_3$ layers on a SiO_2/Si(001) substrate	[153]
$Bi_{0.4}Sb_{1.6}Te_3$ + (0, 0.2, 0.4, and 0.6 vol.%) $CuGaTe_2$	Vacuum melting + hot pressing	[154]
$Bi_{0.5}Sb_{1.5}Te_3$ + 2 wt.% (Gd_2O_3, $Gd_{1.98}Bi_{0.02}O_3$)	Powders for each phase were prepared by induction melting then mixed by spray pyrolysis + sintering	[155]
Bi_2Te_3 + (1, 2, and 5 wt.%) SnS	Commercial powders were mixed, cold pressed, and annealed	[156]
$Bi_{0.3}Sb_{1.7}Te_3$+ (0, 0.25, 0.50, and 0.75 wt.%) TiC	Ball milling + sintering	[157]
Bi_2Te_3 + ≈4 wt.% of $Cu_{1.5}Te$	Solution-based synthesis (each phase separately) + hot pressing	[158]
Coated grains of SnTe with $CuInTe_2$	$CuInTe_2$ was formed by cation exchange of Sn by Cu and In on the surface of ball-milled SnTe powder	[159]
$Bi_{0.5}Sb_{1.5}Te_3$-$Cu_{0.07}$ + (0, 0.5, and 1.0 wt.%) HfO_2	Water atomisation + ball milling + sintering	[160]
SiGe + (2, 4, 6, 8, 10 wt.%) TiB_2	Ball milling + hot pressing	[137]

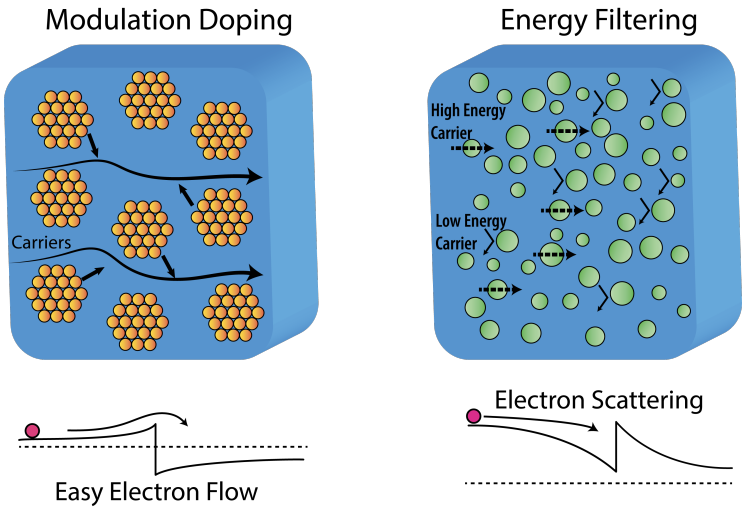

Figure 2.5. Comparison between a modulated doped semiconductor and a multiphase compound benefiting from energy filtering.

conductor, whereas in the case of energy filtering, the secondary phase scatters electrons and reduces mobility.

The thermoelectric research community has also used this mechanism to enhance the thermoelectric performance of materials [23, 30, 32, 38, 46]. For thermoelectric materials, a combination of two effects has improved thermoelectric efficiency in modulated doped materials: first, a large increase in electrical conductivity and carrier mobility [164] and second, a reduction in lattice thermal conductivity as a result of phonon scattering by nanostructuring [32, 165].

Some attempts have also been made to explore the possibility of using modulation doping in structures similar to field-effect transistors (FETs) [163]. In this structure, the thermoelectric semiconductor nanowire (channel) is enclosed by a heavily doped layer (gate) [166–170]. A modest increase in power factor has been achieved with this approach. Table 2.2 summarises the sample compositions, fabrication methods, and corresponding references of recent studies that have used modulation doping to enhance the thermoelectric performance of multiphase materials.

2.8.3 Phonon scattering

When designing a thermoelectric material, the main goal is to maintain a high electrical conductivity while reducing the thermal conductivity [181]. Phonon transport plays an important role in the thermal conductivity [182, 183]. Increasing phonon scattering has therefore emerged as a key strategy to improve the efficiency of thermoelectric materials [184]. This is achieved mainly by nanostructuring the material [80], introducing grains with sizes larger than the mean free path of the carriers but smaller than the mean free path of the phonons [185], alloy scattering with additional mass or strain fluctuation [186–188], nanocom-

Table 2.2. Sample compositions and fabrication methods of references that employed modulation doping to enhance the thermoelectric performance of multiphase materials. Adapted from [39]

Composition	Fabrication method	Ref.
$Ba_8(Al_xGa_{1-x})_{16}Ge_{30}$ (x = 0, 0.20, 0.23, 0.25, 0.33, 0.50, and 1)	Casting (each phase separately) + ball milling + sintering	[171]
$AgBiSe_2 + Bi_4Se_3$	Casting (each phase separately) + ball milling + sintering	[172]
Cu_2SnS_3 + (0, 1, 3, and 5) mol% $CuCo_2S_4$	Casting (each phase separately) + ball milling + sintering	[30, 173]
$Si_a(Mg_2Si + x$ at.% $Bi)_{1-a}$	Bi-doped Mg_2Si fabricated using induction melting +	
a = 0.39, 0.50, 0.56, 0.59, and 0.67; x = 0.3, 0.8, 1.3, 1.8, and 2.5	melt spinning + sintering	[174]
p-type organic conducting polymer PEDOT:PSS + Ge	PEDOT:PSS coated with Ge layer	[175]
$(Ge_2Te_2)_x(CuInTe_2)_{1-x}$	Casting + hand milling + hot pressing	[176]
x = 98, 95, 90, 87.5, 85, 70, 30, and 10%		
$BiCuSeO + Bi_{0.8}Pb_{0.2}Cu_{0.8}Ni_{0.2}SeO$	Each phase was fabricated by Mechanical alloying + ball milling of mixture + sintering	[177]
$BiCuSeO + Bi_{0.8}Er_{0.2}CuSeO$	Each phase was fabricated by ball milling + sintering. The final composition was obtained by ball milling + sintering	[178]
$BiCuSeO + Bi_{0.8}Ba_{0.2}CuSe_{0.8}Te_{0.2}O$	Each phase was fabricated by mechanical alloying + milling the mixture + sintering	[179]
$Pb_{1-x}Na_xTe_{0.65}S_{0.25}Se_{0.1}$ (x = 0.005, 0.01, 0.0015, 0.02, 0.025, and 0.03)	Casting PbSe and PbS + mixing stoichiometric amounts of PbSe, PbS, Pb, Te, and Na (casting) + sintering	[38]
$Pb_{0.97}Na_{0.03}Te_{1-x}S_x$ (x = 0.1, 0.15, 0.2, 0.25, 0.3, and 0.35)	Casting + hand milling + sintering	[180]

posites [189–192], and embedding interfaces by creating a texture between the two materials [193].

Effective medium approximation can be used to assess the effect of a secondary phase in the material. The traditional mathematical treatment for TE materials incorporates an interface resistance, called Kapitza resistance (R_κ), in series with the intergrain resistance [194]. This model is further developed to consider the shapes, orientations, volume fractions, and thermal conductivities of the phases [193]. For instance, the thermal conductivity of a two-phase material with spherical inclusions is expressed by

$$\kappa^* = \frac{\kappa_p(1+2\lambda) + 2\kappa_m + 2f\left[\kappa_p(1-\lambda) - \kappa_m\right]}{\kappa_p(1+2\lambda) + 2\kappa_m - 2f\left[\kappa_p(1-\lambda) - \kappa_m\right]}, \tag{2.26}$$

where κ_m is the thermal conductivity of the matrix, κ_p is the thermal conductivity of the secondary phase, and f is the volume fraction of the secondary phase. The non-dimensional parameter, λ_κ, is the ratio of the Kapitza length, L_κ, and the secondary phase radius, a

$$\lambda = \frac{L_\kappa}{a} = \frac{\kappa_m R_\kappa}{a}. \tag{2.27}$$

An even simpler model than that has been used to describe the scattering in multiphase materials is impedance mismatch [185]. The acoustic impedance (Z) of a material is the analogue of the electrical impedance for electrical circuits. In this case, the acoustic impedance measures the opposition of a system when acoustic pressure is applied to it, and it is calculated as

$$Z = d \cdot v, \tag{2.28}$$

where d is the density of the medium and v is the speed of the sound in the medium. At the interface of two materials, the reflection (r) and transmission (t) energy coefficients are [195]

$$r = \left[\frac{Z_2 - Z_1}{Z_2 + Z_1}\right]^2, \tag{2.29}$$

$$t = \frac{4Z_1Z_2}{(Z_1 + Z_2)^2}, \tag{2.30}$$

where Z_1 and Z_2 are the acoustic impedances of the two materials. Figure 2.6 illustrates phonon transmission and reflection between two dissimilar materials.

Experimentally, impedance mismatch between phases has been shown to reduce the thermal conductivity of the bulk material. The impedance mismatch between the PbTe and PbS rich phases in $(Pb_{0.95}Sn_{0.05}Te)_{1-x}(PbS)_x$ samples led to an inhibition of the heat flow, with the lattice thermal conductivity reaching 0.4 $W.m^{-1}.K^{-1}$ for the sample with 8% PbS, an 80% reduction in the reported values for the bulk material [196].

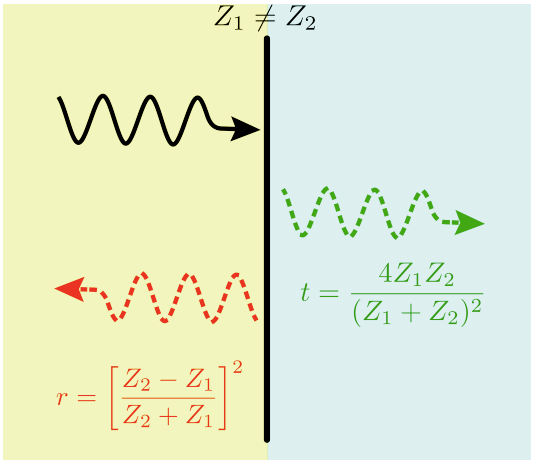

Figure 2.6. Phonon transmission and reflection due to impedance mismatch.

In general, phonon scattering has proven to be an effective strategy to reduce the lattice thermal conductivity in multiphase lead telluride-based materials [197–200] and bismuth telluride-based [201–203] materials. For instance, nano-engineered multiphase PbTe-x% InSb compounds showed an exceptionally low minimum lattice thermal conductivity of ≈0.3 W.m^{-1}.K^{-1} at ≈770 K for 4% InSb and consequently a zT value of ≈1.83 at 770 K [204]. Even higher zT values of ≈2 were observed for $Pb_{1-x}Na_xTe_{0.65}S_{0.25}Se_{0.1}$ compounds [36, 37], where the combined effects of phonon scattering at nanoprecipitates and the increase in the power factor due to the heterogeneous distribution of dopants between phases were recognised to be responsible for the high TE efficiency. Nano and micro-sized precipitates in $Pb_{1-x}Ga_xTe$ ($x = 0.01, 0.02, 0.03,$ and 0.04) compounds have shown a reduction in the lattice thermal conductivity, reaching 1.6 W.m^{-1}.K^{-1}. The lattice thermal conductivity of multiphase half-Heusler $(Hf_{0.6}Zr_{0.4})NiSn_{0.99}Sb_{0.01}$ material was reduced from ≈4.5 W.m^{-1}.K^{-1} for the pristine sample to 2.9 W.m^{-1}.K^{-1} for the sample with 20 wt.% of tungsten at 300 K [146]; the combined effects of phonon scattering and energy filtering due to the presence of metallic tungsten improved the zT by 55%.

In contrast, a large fraction of a secondary phase with high thermal conductivity can increase the thermal conductivity of the bulk material, as reported for PbTe−Ge_x [205]. Five percent of GeTe reduced the lattice thermal conductivity to 1.1 W.m^{-1}.K^{-1}, while a sample with $x = 0.2$ showed a lattice thermal conductivity similar to the pristine sample. Adding a secondary phase of TiO_2 to a Bi_2Se_3 host increased the thermopower by energy filtering and simultaneously reduced the lattice thermal conductivity by 45% [135].

The lattice thermal conductivity values of several single-phase chalcogenides are compared with their multiphase counterparts in figure 2.7. The data for single phase materials was manually extracted from the Materials Research Laborat-

ory Energy Materials Datamining website [206, 207]. This dataset contains information on 573 thermoelectric materials from various combinations of host materials and dopants, along with several thermoelectric properties measured experimentally at 300 K, 400 K and 700 K. Here, the lattice thermal conductivity of chalcogenides measured at 300 K has been chosen for comparison. Where the lattice thermal conductivity was not available, its value was evaluated using the Wiedemann–Franz law (see equation 2.10) and the Sommerfeld limit of 2.45×10^{-8} $V^2.K^{-2}$ for the Lorenz number. Both the bar and box plots show that the multiphase materials have consistently lower values of the lattice thermal conductivity. In particular, the box plot shows that the multiphase materials have, on average, lower values of lattice thermal conductivity.

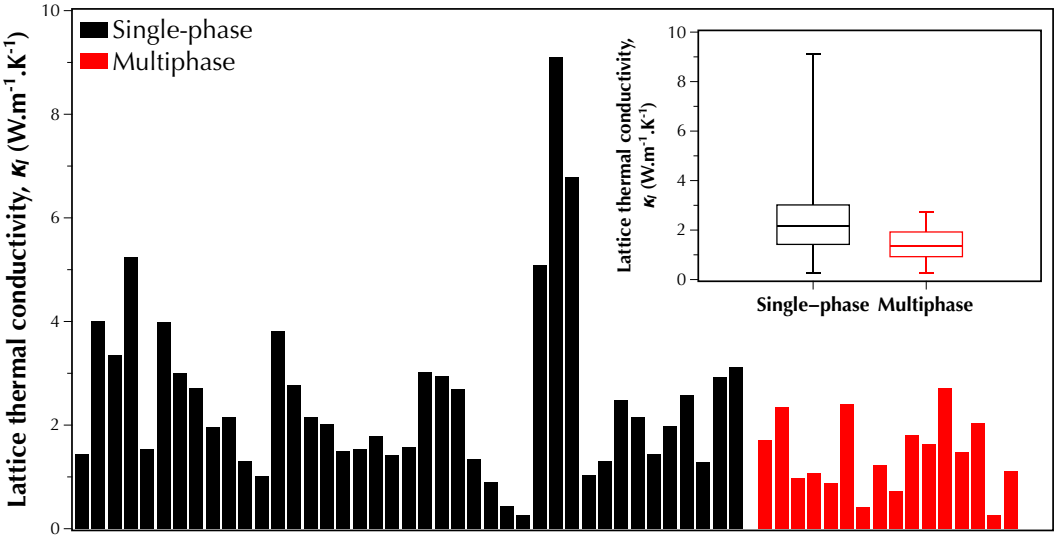

FIGURE 2.7. The lattice thermal conductivity of multiphase thermoelectric materials compared with single phase counterparts, data extracted from [36–38, 49, 79, 135, 165, 204, 205, 208–239]. The inset shows a box plot of the same data.

2.8.4 Estimating the transport properties of multiphase thermoelectric materials

In general, multiphase materials can increase phonon scattering, increase the thermopower due to energy filtering, and increase electrical conductivity due to modulation doping. These micro and nano effects clearly influence the material on a macroscale. It is, however, of interest to have simplified expressions to predict the behaviour of these materials from based on their composition.

Effective medium theory allows us to approximate the effective thermopower and the electrical conductivity of multiphase materials [240]. There are two main equations to evaluate these properties. The most common equation is the one

derived from the usual effective medium theory [241]

$$\sum_i \nu_i \frac{\xi_i - \xi}{\xi + 2\xi} = 0, \tag{2.31}$$

where ν_i and ξ_i are the volume fraction and property of phase i, respectively, and ξ is the effective material property. The electrical conductivity can be calculated by setting $\xi = \sigma$, and the thermopower can be calculated by setting $\xi = \alpha/\sigma$ [242]. The second equation is based on the generalised effective medium theory

$$\sum_i \nu_i \frac{\xi_i^{1/s} - \xi^{1/s}}{\xi^{1/s} + A_c \cdot \xi^{1/s}} = 0, \tag{2.32}$$

where s is a measure of the grain structure and morphology, and $A_c = (1-p_c)/p_c$, where p_c is the percolation threshold. Both parameters can be determined by fitting experimental data, and p_c is estimated from the lattice type and dimensions of the network [243]. The thermopower and the conductivity are estimated similarly to the previous equation [244].

Recently, models based on electrical networks have also been introduced to estimate the electronic properties [240, 245, 246]. These models divide the material into pixel (for a 2D analysis) or voxel (for a 3D analysis) grids, where each node corresponds to a fraction of the total volume. Each voxel or pixel is required to be larger than the mean free paths of the carriers and phonons so that the transport is diffusive. Each node is connected to its neighbours by a resistance that is an electric resistance (to calculate the electrical conductivity) and a thermal resistance (to calculate the thermal conductivity) in series with an interface resistance if needed.

Following the construction of the grids, a nodal analysis will be conducted [247] to determine the temperature and voltage profiles of the grids. The thermopower is estimated by assigning each node in the electric grid to a local voltage source in series, representing the local Seebeck voltage. By using a Norton equivalent of the voltage source [248], the usual nodal formulation can be applied, and the bulk thermopower will be estimated. The general expression is presented as [246]

$$0 = \sum_{k \neq l} V_{kl} G_{kl} + \sum_{k \neq l} I_{kl}, \tag{2.33}$$

where V_{kl} is the voltage (or temperature) difference between nodes k and l, I_{kl} is the current flowing between nodes k and l, and G_{kl} is the conductivity between nodes k and l. The conductivity will be determined by the local thermoelectric properties of the voxels or pixels as

$$\sigma_{kl}^{-1} = \sigma_k^{-1} + \sigma_l^{-1}, \tag{2.34}$$

$$\kappa_{kl}^{-1} = \kappa_k^{-1} + \kappa_l^{-1}, \tag{2.35}$$

where σ_k, σ_l is the electrical conductivity of nodes k and l, respectively, and κ_k, κ_l is the thermal resistivity of nodes k and l.

The main advantage of this approach is that this linear system of equations can easily be solved by electric circuit solvers, and the results can be directly interpreted by engineers. However, quantum effects are not approximated by this model, so it provides similar accuracy to the more simple models described earlier [245].

Overall, from a design perspective, these equations suggest that the incorporation of highly conductive phases (both thermally and electrically) results in an overall increase in the conductivity of materials. This effect has been experimentally proven for several materials. Graphene, a zero-bandgap material [249], has been successfully used to create thermoelectric materials with high conductivity [250–252], while the electrical conductivity of $CoSb_3$ reached 1.3×10^6 S.m^{-1}, four times larger than the pristine sample at 300 K [251]. Copper telluride in $Bi_{0.5}Sb_{1.5}Te_3$ [253] and a composite of ZnSb matrix with minority phases of Zn_4Sb_3, Zn_3P_2, and Cu_5Zn_8 [254] have shown higher electrical conductivity. High-temperature, oxide-based thermoelectric materials have also been shown to benefit from the presence of secondary phases. A multiphase compound of $Ca_3Co_4O_9$, matrimid polymer + Ag, and carbon black [50] showed a reduction in the electrical conductivity compared to the porous $Ca_3Co_4O_9$, while the highly conductive phase of Ag reduced a significant deterioration of conductivity. It should be noted that the values of electronic transport properties are greatly dependent on the fabrication methods [255], quality of the raw materials, and oxidisation of the material [256–258].

The equations described in this subsection do not take into account quantum effects such as magnetic scattering, modulation doping, and energy filtering. For more information, please refer to the rest of this chapter.

2.8.5 Magnetic effects

The effects of magnetism on the performance of thermoelectric materials have been investigated for some time, but with less detailed analysis. The idea of spin-wave scattering and magnon drag was proposed in the middle of the last century, where magnon scattering was shown to contribute to an increase in the thermopower [259]. Magnons are bosonic quasiparticles, the quanta associated with spin waves [260]. When a magnetic material is subjected to a temperature gradient, the hotter side contains a higher density of magnons that will diffuse towards the cooler side; this magnon flux "drags" the free charge carriers due to the electron–magnon collisions and gives rise to a second contribution to the thermopower, called the magnon thermopower [261]. A hydrodynamical, Ga-

lilean based expression for the magnon thermopower is [262]

$$\alpha_{md} = \frac{2}{3} \cdot \frac{c_m}{nq} \cdot \frac{1}{1 + \frac{\tau_{em}}{\tau_m}}, \tag{2.36}$$

where c_m is the magnon specific heat capacity per unit volume, τ_m is the transport mean-free time for the magnons, τ_{em} is the relaxation time of magnons due to magnon-electron collisions, q is the elementary charge, and n is the carrier concentration.

When dealing with magnetism in semiconductors, three main strategies have been proposed to improve the thermoelectric efficiency: (1) optimise thermoelectric properties of magnetic materials using strategies known for non-magnetic materials [51–53, 263, 264]; (2) introduce a magnetic dopant in a non-magnetic material [54–56, 265–268]; and (3) introduce a magnetic secondary phase in a non-magnetic material [57, 58].

2.8.5.1 Magnetic semiconductors

Examples of magnetic semiconductors include $FeSb_2$ [269, 270], MnTe [271–273], $Cr_2Ge_2Te_6$ [274], MgAgSb [275], MnSe [276], and FeSe [277]. Experimental results have demonstrated their potential as thermoelectric materials. For instance, a large thermopower of ≈27 $mV.K^{-1}$ has been reported for $FeSb_2$ (albeit at a low temperature of ≈12 K) [278]. However, it is difficult to establish a causal relationship between the magnetism and thermopower. A common method is to check whether a heavily doped sample with a high carrier concentration shows a large thermopower [279], since this indicates a possible effect of electron–magnon scattering, which increases the thermopower. Fitting mathematical models to experimental data has also been proposed as a method to identify magnetic thermopower [280]. However, measuring the transport properties as a function of the magnetic field is the best method for determining magnetic thermopower [261, 281, 282].

A spin-dependent thermopower can also occur in magnetic semiconductors [283] since the thermopower for the two spin channels of spin-up ($\alpha\uparrow$) and spin-down ($\alpha\downarrow$) are not equal, a spin current proportional to the difference between $\alpha\uparrow$ and $\alpha\downarrow$ flows through the magnetic material even in the absence of a charge current [284]. The literature refers to spintronics as the field of study that investigates devices that exploit the properties of electron spins. In thermoelectricity, this process is known as spin caloritronics [285]. This new field of research has attracted the interest of the thermoelectric research community [286–288].

2.8.5.2 Magnetic dopants in non-magnetic semiconductors

Doping non-magnetic thermoelectric materials with magnetic elements has been shown to improve the power factor. Magnetic doping of $CuGaTe_2$ with

manganese ions (Mn^{2+}) increased the effective mass of the carriers owing to the interaction of the magnetic ions and charge carriers and, consequently, increased the thermopower [289]. This effect has also been reported for chromium-doped Bi_2Te_3 [290]. The negative side effect of magnetic ion dopants is a decrease in charge carrier mobility, which results in a reduction in electrical conductivity. But, overall, it has been seen that the power factor increases [291–293].

2.8.5.3 Secondary magnetic phases

The natural extension of magnetic elements involves the inclusion of magnetic phases to enhance the performance of thermoelectric materials [289, 294, 295]. The magnetic particles of $BaFe_{12}O_{19}$ in $Ba_{0.3}In_{0.3}Co_4Sb_{12}$ formed a magnetic composite. $BaFe_{12}O_{19}$ nanoparticles trap electrons in the ferromagnetic phase due to the spiral motion of electrons generated by non-uniform spherical magnetic fields. This effectively suppresses the deterioration of thermoelectric efficiency in the intrinsic excitation region [296]. In the paramagnetic phase (at temperatures above the Curie temperature), the nanoparticles release the trapped electrons to increase the carrier concentration in the intrinsic excitation. This effect enhances the overall performance of the thermoelectric material.

Coherent magnetic full-Heusler nanoparticles of $Ti(Ni_{4/3}Fe_{2/3})Sn$ in a half-Heusler matrix composed of $Ti_{0.25}Zr_{0.25}Hf_{0.5}NiSn_{0.975}Sb_{0.025}$ showed significant enhancements in both carrier mobility and thermopower [297]. The magnetic nanoparticles interact with the spin of itinerant carriers, leading to charge localisation (which consequently leads to a decrease in the charge density) and the formation of overlapping bound magnetic polarons (which leads to an increase in mobility).

Some magnetic phenomena occur only when the particles are smaller than a certain size [298]. Nanoparticles provide a good platform to take advantage of these magnetic phenomena to optimise the thermoelectric performance of materials. If the size of a ferromagnetic nanoparticle is small enough to have only several magnetic domains, it can be magnetised similarly to a paramagnet under an external magnetic field, except for a much greater magnetisation. This mechanism is known as superparamagnetism (magnetisation of nanoparticles can randomly flip direction under the influence of temperature, and they can be magnetised similarly to a paramagnet under an external magnetic field [299]). Experimentally, soft magnetic transition metal (Fe, Co, or Ni) nanoparticles were embedded in a $Ba_{0.3}In_{0.3}Co_4Sb_{12}$ matrix [300]. The superparamagnetic fluctuations of the nanoparticles resulted in the multiple scattering of electrons and enhanced phonon scattering. These effects increased the overall thermoelectric efficiency of the material.

In general, secondary magnetic phases introduce a new degree of freedom to enhance thermoelectric materials. The effects of magnetism in semiconductors are not yet fully understood, and general expressions for the contribution

of magnon-drag on the thermopower are not yet available. The need for further experimental and theoretical investigations presents an opportunity for the development of thermoelectric materials, which is studied in this thesis (see chapter 7)

Table 2.3 summarises the sample composition and fabrication techniques of recent studies that reported magnetic effects in thermoelectric materials.

Table 2.3. Sample composition, fabrication technique, and corresponding references that studied magnetic effects in thermoelectric materials. Adapted from [39]

System	Fabrication method	Type	Ref.
$CuGa_{1-x}Mn_xTe_2$ (x = 0, 0.01, 0.02, and 0.03)	Casting + hand milling + sintering	Magnetic dopant	[289]
$Bi_{2-x}Cr_xTe_3$ (x = 0, 0.01, 0.02, 0.05, and 0.10)	Casting + hand milling + sintering	Magnetic dopant	[290]
$Fe_{3-x}Ti_xSn$ (x = 0, 0.25, 0.5, and 0.75)	Casting	Magnetic material	[264]
$Sn_{1.03-x}Mn_xTe$ (x = 0, 0.05, 0.07, and 0.1)	Casting + cold pelletising	Magnetic dopant	[291]
$Ba_{0.3}In_{0.3}Co_4Sb_{12}$ + x $BaFe_{12}O_{19}$) (x = 0.15, 0.25, 0.35, and 0.45%)	Ball milling + sintering	Magnetic phase	[296]
$Ti_{0.25}Zr_{0.25}Hf_{0.5}(Ni,Fe_x)Sn_{0.975}Sb_{0.025}$ (x = 0, 0.05, 0.01, and 0.15)	Casting + hand milling + sintering	Magnetic phase	[297]
$Mn_{1-x}Na_xSe$ ($0 \leq x \leq 0.03$)	Ball milling + annealing + hot pressing	Magnetic material	[276]
$FeSb_2$	Hand milling + annealing + hot pressing	Magnetic material	[269]

References

(19) Y. C. Lan, A. J. Minnich, G. Chen and Z. F. Ren, *Adv. Funct. Mater.*, 2010, **20**, 357–376, doi: 10.1002/adfm.200901512.

(21) X. W. Wang, H. Lee, Y. C. Lan, G. H. Zhu, G. Joshi, D. Z. Wang, J. Yang, A. J. Muto, M. Y. Tang, J. Klatsky, S. Song, M. S. Dresselhaus, G. Chen and Z. F. Ren, *Appl. Phys. Lett.*, 2008, **93**, 193121, doi: 10.1063/1.3027060.

(23) B. Yu, M. Zebarjadi, H. Wang, K. Lukas, H. Wang, D. Wang, C. Opeil, M. Dresselhaus, G. Chen and Z. Ren, *Nano Lett.*, 2012, **12**, 2077–82, doi: 10.1021/nl3003045.

(25) J. P. Heremans, V. Jovovic, E. S. Toberer, A. Saramat, K. Kurosaki, A. Charoenphakdee, S. Yamanaka and G. J. Snyder, *Science*, 2008, **321**, 554–7, doi: 10.1126/science.1159725.

(30) Y. Gu, W. Ai, Y. Zhao, L. Pan, C. Lu, P. Zong, X. Hu, Z. Xu and Y. Wang, *J. Mater. Chem.A*, 2021, **9**, 16928–16935, doi: 10.1039/D1TA02812J.

(32) M. Zebarjadi, G. Joshi, G. Zhu, B. Yu, A. Minnich, Y. Lan, X. Wang, M. Dresselhaus, Z. Ren and G. Chen, *Nano Lett.*, 2011, **11**, 2225–30, doi: 10.1021/nl201206d.

(36) S. Aminorroaya Yamini, D. R. Mitchell and M. Avdeev, *Phys. Chem. Chem. Phys.*, 2016, **18**, 32814–32819, doi: 10.1039/c6cp05232k.

(37) J. Byrnes, D. R. G. Mitchell and S. A. Yamini, *Mater. Today Phys.*, 2020, **13**, doi: 10.1016/j.mtphys.2020.100190.

(38) A. Yamini, T. Li, D. R. G. Mitchell and J. M. Cairney, *Nano Energy*, 2016, **26**, 157–163, doi: 10.1016/j.nanoen.2016.05.019.

(39) **Fortulan, Raphael** and S. Aminorroaya Yamini, *Materials*, 2021, **14**, 6059, doi: 10.3390/ma14206059.

(46) D. Wu, Y. Pei, Z. Wang, H. Wu, L. Huang, L.-D. Zhao and J. He, *Adv. Funct. Mater.*, 2014, **24**, 7763–7771, doi: 10.1002/adfm.201402211.

(49) Z. Wang, G. Wang, R. Wang, X. Zhou, Z. Chen, C. Yin, M. Tang, Q. Hu, J. Tang and R. Ang, *ACS Appl. Mater. Interfaces*, 2018, **10**, 22401–22407, doi: 10.1021/acsami.8b05117.

(50) M. Wolf, K. Menekse, A. Mundstock, R. Hinterding, F. Nietschke, O. Oeckler and A. Feldhoff, *J. Electron. Mater.*, 2019, **48**, 7551–7561, doi: 10.1007/s11664-019-07555-2.

(51) Y. Sun, S. Canulescu, P. J. Sun, F. Steglich, N. Pryds, J. Schou and B. B. Iversen, *Applied Physics a-Materials Science & Processing*, 2011, **104**, 883–887, doi: 10.1007/s00339-011-6431-z.

(52) P. Sun, N. Oeschler, S. Johnsen, B. B. Iversen and F. Steglich, *J. Phys: Conf. Ser.*, 2009, **150**, 012049, doi: 10.1088/1742-6596/150/1/012049.

(53) N. Tsujii, T. Mori and Y. Isoda, *J. Electron. Mater.*, 2014, **43**, 2371–2375, doi: 10.1007/s11664-014-3072-y.

(54) T. Motohashi, E. Naujalis, R. Ueda, K. Isawa, M. Karppinen and H. Yamauchi, *Appl. Phys. Lett.*, 2001, **79**, 1480–1482, doi: 10.1063/1.1400777.

(55) Q. Wen, C. Chang, L. Pan, X. T. Li, T. Yang, H. H. Guo, Z. H. Wang, J. Zhang, F. Xu, Z. D. Zhang and G. D. Tang, *J. Mater. Chem.A*, 2017, **5**, 13392–13399, doi: 10.1039/c7ta03659k.

(56) C. Xiao, K. Li, J. J. Zhang, W. Tong, Y. W. Liu, Z. Li, P. C. Huang, B. C. Pan, H. B. Su and Y. Xie, *Mater. Horiz.*, 2014, **1**, 81–86, doi: 10.1039/c3mh00091e.

(57) K. G. Liu and J. Li, *Frontiers of Green Building, Materials and Civil Engineering, Pts 1-8*, 2011, **71–78**, 3741–3744, doi: 10.4028/www.scientific.net/AMM.71-78.3741.

(58) G. Tan, F. Shi, S. Hao, H. Chi, T. P. Bailey, L. D. Zhao, C. Uher, C. Wolverton, V. P. Dravid and M. G. Kanatzidis, *J. Am. Chem. Soc.*, 2015, **137**, 11507–16, doi: 10.1021/jacs.5b07284.

(61) H. J. Goldsmid, *Introduction to Thermoelectricity*, Springer Berlin Heidelberg, Berlin, Heidelberg, 2016, vol. 121, pp. 339–357, doi: 10.1007/978-3-662-49256-7.

(62) P. Hofmanm, *Solid State Physics, an Introduction*, John Wiley & Sons, 2nd edn., 2015, 267 pp.

(63) R. Franz and G. Wiedemann, *Annalen der Physik und Chemie*, 1853, **165**, 497–531, doi: 10.1002/andp.18531650802.

(64) T. L. Bergman, A. S. Lavine and F. P. Incropera, *Fundamentals of Heat and Mass Transfer, 7th Edition*, John Wiley & Sons, Incorporated, 2011, 1076 pp.

(65) Y. Z. Pei, Z. M. Gibbs, A. Gloskovskii, B. Balke, W. G. Zeier and G. J. Snyder, *Adv. Energy Mater.*, 2014, **4**, 1400486, doi: 10.1002/aenm.201400486.

(66) J. P. Heremans, B. Wiendlocha and A. M. Chamoire, *Energy Environ. Sci.*, 2012, **5**, 5510–5530, doi: 10.1039/c1ee02612g.

(67) Y. Z. Pei, A. LaLonde, S. Iwanaga and G. J. Snyder, *Energy Environ. Sci.*, 2011, **4**, 2085–2089, doi: 10.1039/c0ee00456a.

(68) H. J. Wu, L. D. Zhao, F. S. Zheng, D. Wu, Y. L. Pei, X. Tong, M. G. Kanatzidis and J. Q. He, *Nat. Commun.*, 2014, **5**, 4515, doi: 10.1038/ncomms5515.

(69) Y. Pei, H. Wang and G. J. Snyder, *Adv. Mater.*, 2012, **24**, 6125–35, doi: 10.1002/adma.201202919.

(70) A. Soni, Z. Yanyuan, Y. Ligen, M. K. K. Aik, M. S. Dresselhaus and Q. Xiong, *Nano Letters*, 2012, **12**, 1203–1209, doi: 10.1021/nl2034859.

(71) T. Zhu, Y. Liu, C. Fu, J. P. Heremans, J. G. Snyder and X. Zhao, *Adv. Mater.*, 2017, **29**, 1605884, doi: 10.1002/adma.201605884.

(72) T. Zhu, L. Hu, X. Zhao and J. He, *Adv Sci (Weinh)*, 2016, **3**, 1600004, doi: 10.1002/advs.201600004.

(73) M. Hong, Z. G. Chen, L. Yang and J. Zou, *Nanoscale*, 2016, **8**, 8681–6, doi: 10.1039/c6nr00719h.

(74) C. Kittel, *Introduction to Solid State Physics*, John Wiley & Sons, New York, NY, 8th edn., 2018, 712 pp.

(75) C. Jeong, R. Kim and M. S. Lundstrom, *J. Appl. Phys.*, 2012, **111**, 113707, doi: 10.1063/1.4727855.

(76) K. H. Lee, S. I. Kim, H. S. Kim and S. W. Kim, *Acs Applied Energy Materials*, 2020, **3**, 2214–2223, doi: 10.1021/acsaem.9b02131.

(77) S. Ahmad, A. Singh, S. Bhattacharya, M. Navaneethan, R. Basu, R. Bhatt, P. Sarkar, K. N. Meshram, A. K. Debnath, K. P. Muthe and D. K. Aswal, *ACS Appl. Energy Mater.*, 2020, **3**, 8882–8891, doi: 10.1021/acsaem.0c01359.

(78) C. M. Jaworski, V. Kulbachinskii and J. P. Heremans, *Phys. Rev. B*, 2009, **80**, 233201, doi: 10.1103/PhysRevB.80.233201.

(79) Y. Pei, X. Shi, A. LaLonde, H. Wang, L. Chen and G. J. Snyder, *Nature*, 2011, **473**, 66–9, doi: 10.1038/nature09996.

(80) M. S. Dresselhaus, G. Chen, M. Y. Tang, R. G. Yang, H. Lee, D. Z. Wang, Z. F. Ren, J. P. Fleurial and P. Gogna, *Adv. Mater.*, 2007, **19**, 1043–1053, doi: 10.1002/adma.200600527.

(81) E. S. Toberer, A. Zevalkink and G. J. Snyder, *J. Mater. Chem.*, 2011, **21**, 15843–15852, doi: 10.1039/c1jm11754h.

(82) J. E. Parrott, *J. Phys. C: Solid State Phys.*, 1969, **2**, 147–151, doi: 10.1088/0022-3719/2/1/320.

(83) J. P. Heremans, M. S. Dresselhaus, L. E. Bell and D. T. Morelli, *Nat. Nanotechnol.*, 2013, **8**, 471–3, doi: 10.1038/nnano.2013.129.

(84) Q. Wang, M. Safdar, Z. Wang and J. He, *Adv. Mater.*, 2013, **25**, 3915–21, doi: 10.1002/adma.201301128.

(85) A. Balandin and K. L. Wang, *Phys. Rev. B*, 1998, **58**, 1544–1549, doi: 10.1103/PhysRevB.58.1544.

(86) L. D. Hicks and M. S. Dresselhaus, *Phys. Rev. B Condens. Matter*, 1993, **47**, 16631–16634, doi: 10.1103/physrevb.47.16631.

(87) A. F. Ioffe, L. S. Stil'bans, E. K. Iordanishvili, T. S. Stavitskaya, A. Gelbtuch and G. Vineyard, *Phys. Today*, 1959, **12**, 42–42, doi: 10.1063/1.3060810.

(88) D. L. Medlin and G. J. Snyder, *Curr. Opin. Colloid Interface Sci.*, 2009, **14**, 226–235, doi: 10.1016/j.cocis.2009.05.001.

(89) A. Popescu, L. M. Woods, J. Martin and G. S. Nolas, *Phys. Rev. B*, 2009, **79**, 205302, doi: 10.1103/PhysRevB.79.205302.

(90) J. P. Heremans, C. M. Thrush and D. T. Morelli, *Phys. Rev. B*, 2004, **70**, 115334, doi: 10.1103/PhysRevB.70.115334.

(91) Q. J. Hu, Y. Zhang, Y. W. Zhang, X. J. Li and H. Z. Song, *J. Alloys Compd.*, 2020, **813**, 152204, doi: 10.1016/j.jallcom.2019.152204.

(92) K. Kishimoto, K. Yamamoto and T. Koyanagi, *Japanese Journal of Applied Physics Part 1-Regular Papers Short Notes & Review Papers*, 2003, **42**, 501–508, doi: 10.1143/Jjap.42.501.

(93) Y. L. D. L. S. Ali Shakouri Edwin, *Microscale Thermophys. Eng.*, 1998, **2**, 37–47, doi: 10.1080/108939598200097.

(94) J. H. Bahk, Z. X. Bian and A. Shakouri, *Phys. Rev. B*, 2013, **87**, 075204, doi: 10.1103/PhysRevB.87.075204.

(95) D. M. Rowe and G. Min, AIP Conference Proceedings, The Thirteenth International Conference on Thermoelectrics, AIP, Kansas City, Missouri (USA), 1994, vol. 316, pp. 339–342, doi: 10.1063/1.46827.

(96) L. W. Whitlow and T. Hirano, *J. Appl. Phys.*, 1995, **78**, 5460–5466, doi: 10.1063/1.359661.

(97) X. Zianni and D. Narducci, *J. Appl. Phys.*, 2015, **117**, 035102, doi: 10.1063/1.4905674.

(98) J. M. Ziman, *Electrons and Phonons: The Theory of Transport Phenomena in Solids*, Oxford University Press, 2001, doi: 10.1093/acprof:oso/9780198507796.001.0001/acprof-9780198507796.

(99) C. Jeong, R. Kim, M. Luisier, S. Datta and M. Lundstrom, *J. Appl. Phys.*, 2010, **107**, 023707, doi: 10.1063/1.3291120.

(100) S. V. Faleev and F. Leonard, *Phys. Rev. B*, 2008, **77**, 214304, doi: 10.1103/PhysRevB.77.214304.

(101) C. Gayner and Y. Amouyal, *Adv. Funct. Mater.*, 2019, **30**, 1901789, doi: 10.1002/adfm.201901789.

(102) D. Narducci, E. Selezneva, G. Cerofolini, S. Frabboni and G. Ottaviani, *J. Solid State Chem.*, 2012, **193**, 19–25, doi: 10.1016/j.jssc.2012.03.032.

(103) A. Singha and B. Muralidharan, *Sci. Rep.*, 2017, **7**, 7879, doi: 10.1038/s41598-017-07935-w.

(104) H. An, M. Pusko, D. Chun, S. Park and J. Moon, *Chem. Eng. J.*, 2019, **357**, 547–558, doi: 10.1016/j.cej.2018.09.200.

(105) H. Cho, S. Y. Back, J. H. Yun, S. Byeon, H. Jin and J. S. Rhyee, *ACS Appl. Mater. Interfaces*, 2020, **12**, 38076–38084, doi: 10.1021/acsami.0c09529.

(106) Q. H. Jiang, S. W. Li, Y. B. Luo, J. W. Xin, S. H. Li, W. Li, G. L. Zhao and J. Y. Yang, *Acs applied materials & interfaces*, 2020, **12**, 54653–54661, doi: 10.1021/acsami.0c15877.

(107) X. Y. Jiang, Q. K. Zhang, S. P. Deng, B. Zhou, B. Wang, Z. Q. Chen, N. Qi and X. F. Tang, *J. Electron. Mater.*, 2020, **49**, 2371–2380, doi: 10.1007/s11664-019-07935-8.

(108) X. X. Li, Z. K. Yu, H. B. Zhou, F. Yang, F. Zhong, X. H. Mao, B. Z. Li, H. Xin, C. M. Gao and L. Wang, *Acs Sustainable Chemistry & Engineering*, 2021, **9**, 1891–1898, doi: 10.1021/acssuschemeng.0c08403.

(109) S. Q. Liu, J. H. Kong, H. M. Chen and C. B. He, *Acs Applied Energy Materials*, 2019, **2**, 8843–8850, doi: 10.1021/acsaem.9b01834.

(110) D. Zhang, J. Lei, W. Guan, Z. Ma, C. Wang, L. Zhang, Z. Cheng and Y. Wang, *J. Alloys Compd.*, 2019, **784**, 1276–1283, doi: 10.1016/j.jallcom.2019.01.084.

(111) Z. Zhang, W. Zhao, W. Zhu, S. Ma, C. Li, X. Mu, P. Wei, X. Nie, Q. Zhang and W. Zhao, *J. Electron. Mater.*, 2020, **49**, 2794–2801, doi: 10.1007/s11664-019-07851-x.

(112) J. H. Davies, *The Physics of Low-Dimensional Semiconductors: An Introduction*, Cambridge University Press, 1st edn., 1997.

(113) Y. Liu, J. Guo, E. Zhu, L. Liao, S. J. Lee, M. Ding, I. Shakir, V. Gambin, Y. Huang and X. Duan, *Nature*, 2018, **557**, 696–700, doi: 10.1038/s41586-018-0129-8.

(114) M. Liu and X. Y. Qin, *Appl. Phys. Lett.*, 2012, **101**, 132103, doi: 10.1063/1.4755768.

(115) D. Vashaee and A. Shakouri, *Phys. Rev. Lett.*, 2004, **92**, 106103, doi: 10.1103/PhysRevLett.92.106103.

(116) J. P. Heremans, C. M. Thrush and D. T. Morelli, *J. Appl. Phys.*, 2005, **98**, 063703, doi: 10.1063/1.2037209.

(117) D. K. Ko, Y. Kang and C. B. Murray, *Nano Lett.*, 2011, **11**, 2841–4, doi: 10.1021/nl2012246.

(118) Y. Zhou, M. Y. Zhang and S. Liang, *Chem. Phys. Lett.*, 2021, **777**, 138722, doi: 10.1016/j.cplett.2021.138722.

(119) L. Gao, S. Wang, R. Liu, X. Zha, N. Sun, S. Wang, J. Wang and G. Fu, *Dalton Trans.*, 2016, **45**, 12215–20, doi: 10.1039/c6dt02348g.

(120) A. G. Milnes and D. L. Feucht, *Heterojunctions and Metal Semiconductor Junctions*, Elsevier, 1972, doi: 10.1016/B978-0-12-498050-1.X5001-6.

(121) I. D. Mayergoyz, *J. Appl. Phys.*, 1986, **59**, 195–199, doi: 10.1063/1.336862.

(122) H. J. Wu, J. Carrete, Z. Y. Zhang, Y. Q. Qu, X. T. Shen, Z. Wang, L. D. Zhao and J. Q. He, *Npg Asia Materials*, 2014, **6**, e108–e108, doi: 10.1038/am.2014.39.

(123) J. Y. W. Seto, *J. Appl. Phys.*, 1975, **46**, 5247–5254, doi: 10.1063/1.321593.

(124) W. E. Taylor, N. H. Odell and H. Y. Fan, *Phys. Rev.*, 1952, **88**, 867–875, doi: 10.1103/PhysRev.88.867.

(125) Z. W. Zhou, J. Y. Yang, Q. H. Jiang, D. Zhang, J. W. Xin, X. Li, Y. Y. Ren and X. He, *J. Am. Ceram. Soc.*, 2017, **100**, 5723–5730, doi: 10.1111/jace.15088.

(126) Y. C. Dou, X. Y. Qin, D. Li, L. L. Li, T. H. Zou and Q. Q. Wang, *J. Appl. Phys.*, 2013, **114**, 7, doi: 10.1063/1.4817074.

(127) T. Fang, X. Li, C. Hu, Q. Zhang, J. Yang, W. Zhang, X. Zhao, D. J. Singh and T. Zhu, *Adv. Funct. Mater.*, 2019, **29**, 1900677, doi: 10.1002/adfm.201900677.

(128) Y. Li, Y. Dou, X. Qin, J. Zhang, H. Xin, D. Li, C. Song, T. Zou, Y. Liu and C. Li, *RSC Adv.*, 2016, **6**, 12243–12248, doi: 10.1039/c5ra25012a.

(129) T. H. Nguyen, J. Enju and T. Ono, *J. Electrochem. Soc.*, 2019, **166**, D508, doi: 10.1149/2.1011912jes.

(130) B. Madavali, H. S. Kim, K. H. Lee and S. J. Hong, *Intermetallics*, 2017, **82**, 68–75, doi: 10.1016/j.intermet.2016.11.002.

(131) I. I. Ravich, *Semiconducting Lead Chalcogenides*, Springer US, 1970, doi: 10.1007/978-1-4684-8607-0.

(132) T. Zou, X. Qin, Y. Zhang, X. Li, Z. Zeng, D. Li, J. Zhang, H. Xin, W. Xie and A. Weidenkaff, *Sci. Rep.*, 2015, **5**, 17803, doi: 10.1038/srep17803.

(133) Z. Xiong, X. Chen, X. Zhao, S. Bai, X. Huang and L. Chen, *Solid State Sci.*, 2009, **11**, 1612–1616, doi: 10.1016/j.solidstatesciences.2009.06.007.

(134) C. Dette, M. A. Perez-Osorio, C. S. Kley, P. Punke, C. E. Patrick, P. Jacobson, F. Giustino, S. J. Jung and K. Kern, *Nano Lett.*, 2014, **14**, 6533–8, doi: 10.1021/nl503131s.

(135) Y.-X. Yang, Y.-H. Wu, Q. Zhang, G.-S. Cao, T.-J. Zhu and X.-B. Zhao, *Rare Metals*, 2020, **39**, 887–894, doi: 10.1007/s12598-020-01414-4.

(136) C. Ou, J. Hou, T.-R. Wei, B. Jiang, S. Jiao, J.-F. Li and H. Zhu, *NPG Asia Mater.*, 2015, **7**, e182–e182, doi: 10.1038/am.2015.36.

(137) S. Ahmad, R. Basu, P. Sarkar, A. Singh, A. Bohra, S. Bhattacharya, R. Bhatt, K. N. Meshram, S. Samanta, P. Bhatt, M. Navaneethan, Y. Hayakawa, A. K. Debnath, S. K. Gupta, D. K. Aswal, K. P. Muthe and S. C. Gadkari, *Materialia*, 2018, **4**, 147–156, doi: 10.1016/j.mtla.2018.09.029.

(138) J. C. Felizco, M. Uenuma, M. N. Fujii and Y. Uraoka, *IEEE Electron Device Lett.*, 2021, **42**, 1236–1239, doi: 10.1109/LED.2021.3093036.

(139) Q. Hu, K. Wang, Y. Zhang, X. Li and H. Song, *Mater. Res. Express*, 2018, **5**, doi: 10.1088/2053-1591/aabca8.

(140) F. Solá and F. W. Dynys, *J. Alloys Compd.*, 2015, **633**, 165–169, doi: 10.1016/j.jallcom.2015.01.246.

(141) Y. Xia, J. Park, F. Zhou and V. Ozoliņš, *Phys. Rev. Appl.*, 2019, **11**, doi: 10.1103/PhysRevApplied.11.024017.

(142) X. Yang, S. Chen, H. Zhang, F. Lv, W. Fan, W. Wang and Z. A. Munir, *Physica Status Solidi (A) Applications and Materials Science*, 2018, **215**, doi: 10.1002/pssa.201700742.

(143) W. Zhang, K. Zhu, J. Liu, J. Wang, K. Yan, P. Liu and Y. Wang, *Funct. Mater. Lett.*, 2019, **12**, doi: 10.1142/S1793604719500097.

(144) Z. Zhou, J. Li, Y. Fan, Q. Zhang, X. Lu, S. Fan, K. Kikuchi, N. Nomura, A. Kawasaki, L. Wang and W. Jiang, *Scr. Mater.*, 2019, **162**, 166–171, doi: 10.1016/j.scriptamat.2018.11.015.

(145) N. Neophytou, X. Zianni, H. Kosina, S. Frabboni, B. Lorenzi and D. Narducci, *Proc. Spie.*, 2013, **24**, 205402, doi: 10.1088/0957-4484/24/20/205402.

(146) H. B. Kang, B. Poudel, W. Li, H. Lee, U. Saparamadu, A. Nozariasbmarz, M. G. Kang, A. Gupta, J. J. Heremans and S. Priya, *Mater. Today*, 2020, **36**, 63–72, doi: 10.1016/j.mattod.2020.01.002.

(147) A. Pakdel, Q. Guo, V. Nicolosi and T. Mori, *J. Mater. Chem.A*, 2018, **6**, 21341–21349, doi: 10.1039/c8ta08238c.

(148) S. Li, Y. Liu, F. Liu, D. He, J. He, J. Luo, Y. Xiao and F. Pan, *Nano Energy*, 2018, **49**, 257–266, doi: 10.1016/j.nanoen.2018.04.047.

(149) E. Güneş, M. S. Wickleder, E. Müller, M. T. Elm and P. J. Klar, *AIP Adv.*, 2018, **8**, doi: 10.1063/1.5034525.

(150) Y. S. Wang, L. L. Huang, D. Li, J. Zhang and X. Y. Qin, *J. Alloys Compd.*, 2018, **758**, 72–77, doi: 10.1016/j.jallcom.2018.05.035.

(151) R. Cao, Z. Zhu, X.-J. Li, X. Hu and H. Song, *Applied Physics A: Materials Science and Processing*, 2019, **125**, doi: 10.1007/s00339-019-2427-x.

(152) X. Y. Wan, Z. M. Liu, L. Sun, P. Jiang and X. H. Bao, *Journal Of Materials Chemistry A*, 2020, **8**, 10839–10844, doi: 10.1039/d0ta04296j.

(153) N.-W. Park, W.-Y. Lee, Y.-S. Yoon, G.-S. Kim, Y.-G. Yoon and S.-K. Lee, *ACS Applied Materials and Interfaces*, 2019, **11**, 38247–38254, doi: 10.1021/acsami.9b11042.

(154) Y. Li, X. Wang, G. Liu, B. Shin and F. Shan, *Scr. Mater.*, 2019, **172**, 88–92, doi: 10.1016/j.scriptamat.2019.07.016.

(155) M. L. Lwin, P. Dharmaiah, B. H. Min, G. Song, K. Y. Jung and S.-J. Hong, *Int. J. Energy Res.*, 2021, **n/a**, doi: 10.1002/er.7148.

(156) M. Ahmad, N. Kodan, A. Ghosh and B. R. Mehta, *J. Alloys Compd.*, 2020, **847**, 156233, doi: 10.1016/j.jallcom.2020.156233.

(157) L. Zhao, W. Qiu, Y. Sun, L. Chen, H. Deng, L. Yang, X. Shi and J. Tang, *J. Alloys Compd.*, 2021, **863**, doi: 10.1016/j.jallcom.2020.158376.

(158) Y. Zhang, C. Xing, Y. Liu, M. Li, K. Xiao, P. Guardia, S. Lee, X. Han, A. Ostovari Moghaddam, J. Josep Roa, J. Arbiol, M. Ibáñez, K. Pan, M. Prato, Y. Xie and A. Cabot, *Chem. Eng. J.*, 2021, **418**, doi: 10.1016/j.cej.2021.129374.

(159) J. Hwang, M. Lee, B.-K. Yu, M.-K. Han, W. Kim, J. Kim, R. Al Rahal Al Orabi, H. Wang, S. Acharya, J. Kim, Y. Jin, H. Park, S. Kim, S.-H. Yang and S.-J. Kim, *J. Mater. Chem.A*, 2021, **9**, 14851–14858, doi: 10.1039/d1ta02893f.

(160) P. Dharmaiah, C. Nagarjuna, P. Sharief and S.-J. Hong, *Appl. Surf. Sci.*, 2021, **556**, doi: 10.1016/j.apsusc.2021.149783.

(161) Y. L. Pei, H. Wu, D. Wu, F. Zheng and J. He, *J. Am. Chem. Soc.*, 2014, **136**, 13902–8, doi: 10.1021/ja507945h.

(162) R. Dingle, H. L. Störmer, A. C. Gossard and W. Wiegmann, *Appl. Phys. Lett.*, 1978, **33**, 665–667, doi: 10.1063/1.90457.

(163) T. Mimura, S. Hiyamizu, T. Fujii and K. Nanbu, *Jpn. J. Appl. Phys.*, 1980, **19**, L225–L227, doi: 10.1143/JJAP.19.L225.

(164) L. Pfeiffer, K. W. West, H. L. Stormer and K. W. Baldwin, *Appl. Phys. Lett.*, 1998, **55**, 1888, doi: 10.1063/1.102162.

(165) S. A. Yamini, D. R. G. Mitchell, Z. M. Gibbs, R. Santos, V. Patterson, S. Li, Y. Z. Pei, S. X. Dou and G. J. Snyder, *Adv. Energy Mater.*, 2015, **5**, 1501047, doi: 10.1002/aenm.201501047.

(166) B. M. Curtin, E. A. Codecido, S. Krämer and J. E. Bowers, *Nano Lett.*, 2013, **13**, 5503–5508, doi: 10.1021/nl403079a.

(167) W. Liang, A. I. Hochbaum, M. Fardy, O. Rabin, M. Zhang and P. Yang, *Nano Lett.*, 2009, **9**, 1689–1693, doi: 10.1021/nl900377e.

(168) J. Moon, J.-H. Kim, Z. C. Y. Chen, J. Xiang and R. Chen, *Nano Lett.*, 2013, **13**, 1196–1202, doi: 10.1021/nl304619u.

(169) N. Neophytou and M. Thesberg, *J. Comput. Electron.*, 2016, **15**, 16–26, doi: 10.1007/s10825-016-0792-7.

(170) Y. Tian, M. R. Sakr, J. M. Kinder, D. Liang, M. J. MacDonald, R. L. J. Qiu, H.-J. Gao and X. P. A. Gao, *Nano Lett.*, 2012, **12**, 6492–6497, doi: 10.1021/nl304194c.

(171) Y. Zhang, J. Brorsson, R. Qiu and A. E. C. Palmqvist, *Adv. Electron. Mater.*, 2021, **7**, 2000782, doi: 10.1002/aelm.202000782.

(172) E. Rathore, S. N. Guin and K. Biswas, *Bull. Mater. Sci.*, 2020, **43**, 315, doi: 10.1007/s12034-020-02285-2.

(173) Y. Peng, H. J. Lai, C. Y. Liu, J. Gao, M. Kurosawa, O. Nakatsuka, T. Takeuchi, S. Zaima, S. Tanemura and L. Miao, *APPLIED PHYSICS LETTERS*, 2020, **117**, doi: 10.1063/5.0012087.

(174) D. Souda, K. Shimizu, Y. Ohishi, H. Muta, T. Yagi and K. Kurosaki, *ACS Appl. Energy Mater.*, 2020, **3**, 1962–1968, doi: 10.1021/acsaem.9b02395.

(175) D. Lee, J. Zhou, G. Chen and Y. Shao-Horn, *Adv. Electron. Mater.*, 2019, **5**, 1800624, doi: 10.1002/aelm.201800624.

(176) S. Hui, W. Gao, X. Lu, A. Panda, T. P. Bailey, A. A. Page, S. R. Forrest, D. T. Morelli, X. Pan, K. P. Pipe and C. Uher, *Adv. Energy Mater.*, 2017, **8**, doi: 10.1002/aenm.201701623.

(177) B. Feng, G. Q. Li, Z. Pan, X. M. Hu, P. H. Liu, Z. He, Y. W. Li and X. A. Fan, *JOURNAL OF SOLID STATE CHEMISTRY*, 2019, **271**, 1–7, doi: 10.1016/j.jssc.2018.12.001.

(178) B. Feng, G. Q. Li, Z. Pan, X. M. Hu, P. H. Liu, Y. W. Li, Z. He and X. Fan, *CERAMICS INTERNATIONAL*, 2019, **45**, 4493–4498, doi: 10.1016/j.ceramint.2018.11.130.

(179) B. Feng, G. Li, Z. Pan, X. Hu, P. Liu, Z. He, Y. Li and X. Fan, *J. Solid State Chem.*, 2018, **266**, 297–303, doi: 10.1016/j.jssc.2018.07.034.

(180) D. Wu, L.-D. Zhao, X. Tong, W. Li, L. Wu, Q. Tan, Y. Pei, L. Huang, J.-F. Li, Y. Zhu, M. G. Kanatzidis and J. He, *Energy Environ. Sci.*, 2015, **8**, 2056–2068, doi: 10.1039/C5EE01147G.

(181) *Thermoelectrics Handbook*, ed. D. Rowe, CRC Press, 1st edn., 2006, doi: 10.1201/9781420038903.

(182) D. Y. Bao, J. Chen, Y. Yu, W. D. Liu, L. S. Huang, G. Han, J. Tang, D. L. Zhou, L. Yang and Z. G. Chen, *Chem. Eng. J.*, 2020, **388**, doi: 10.1016/j.cej.2020.124295.

(183) M. Hong, Y. Wang, T. Feng, Q. Sun, S. Xu, S. Matsumura, S. T. Pantelides, J. Zou and Z. G. Chen, *J. Am. Chem. Soc.*, 2019, **141**, 1742–1748, doi: 10.1021/jacs.8b12624.

(184) H. Alam and S. Ramakrishna, *Nano Energy*, 2013, **2**, 190–212, doi: 10.1016/j.nanoen.2012.10.005.

(185) X. Chen, D. Parker and D. J. Singh, *Phys. Rev. B*, 2013, **87**, 045317, doi: 10.1103/PhysRevB.87.045317.

(186) H. Xie, H. Wang, C. Fu, Y. Liu, G. J. Snyder, X. Zhao and T. Zhu, *Sci. Rep.*, 2014, **4**, 6888, doi: 10.1038/srep06888.

(187) X. Yan, W. S. Liu, H. Wang, S. Chen, J. Shiomi, K. Esfarjani, H. Z. Wang, D. Z. Wang, G. Chen and Z. F. Ren, *Energy Environ. Sci.*, 2012, **5**, 7543–7548, doi: 10.1039/c2ee21554c.

(188) J. Yang, G. P. Meisner and L. Chen, *Appl. Phys. Lett.*, 2004, **85**, 1140–1142, doi: 10.1063/1.1783022.

(189) S. Bhattacharya, M. J. Skove, M. Russell, T. M. Tritt, Y. Xia, V. Ponnambalam, S. J. Poon and N. Thadhani, *Phys. Rev. B*, 2008, **77**, 184203, doi: 10.1103/PhysRevB.77.184203.

(190) S. Bhattacharya, T. M. Tritt, Y. Xia, V. Ponnambalam, S. J. Poon and N. Thadhani, *Appl. Phys. Lett.*, 2002, **81**, 43–45, doi: 10.1063/1.1488698.

(191) G. Joshi, X. Yan, H. Wang, W. Liu, G. Chen and Z. Ren, *Adv. Energy Mater.*, 2011, **1**, 643–647, doi: 10.1002/aenm.201100126.

(192) X. Yan, G. Joshi, W. Liu, Y. Lan, H. Wang, S. Lee, J. W. Simonson, S. J. Poon, T. M. Tritt, G. Chen and Z. F. Ren, *Nano Lett.*, 2011, **11**, 556–60, doi: 10.1021/nl104138t.

(193) P. Jiang, L. Lindsay, X. Huang and Y. K. Koh, *Phys. Rev. B*, 2018, **97**, 195308, doi: 10.1103/PhysRevB.97.195308.

(194) C.-W. Nan and R. Birringer, *Phys. Rev. B*, 1998, **57**, 8264–8268, doi: 10.1103/PhysRevB.57.8264.

(195) L. E. Kinsler, A. R. Frey, A. B. Coppens and J. V. Sanders, *Fundamentals of Acoustics, 4th Edition*, 1999, 560 pp.

(196) D. James, X. Lu, A. C. Nguyen, D. Morelli and S. L. Brock, *J. Phys. Chem. C*, 2015, **119**, 4635–4644, doi: 10.1021/jp5127046.

(197) K. Ahmad, Z. Almutairi and C. Wan, *J. Mater. Sci.: Mater. Electron.*, 2020, **31**, 20996–21004, doi: 10.1007/s10854-020-04613-y.

(198) S. Aminorroaya Yamini, H. Wang, Z. M. Gibbs, Y. Pei, D. R. G. Mitchell, S. X. Dou and G. J. Snyder, *Acta Mater.*, 2014, **80**, 365–372, doi: 10.1016/j.actamat.2014.06.065.

(199) O. Falkenbach, A. Schmitz, D. Hartung, T. Dankwort, G. Koch, L. Kienle, P. J. Klar, E. Mueller and S. Schlecht, *J. Appl. Phys.*, 2016, **119**, 214310, doi: 10.1063/1.4952982.

(200) O. Falkenbach, D. Hartung, P. J. Klar, G. Koch and S. Schlecht, *J. Electron. Mater.*, 2013, **43**, 1674–1680, doi: 10.1007/s11664-013-2832-4.

(201) M. K. Keshavarz, D. Vasilevskiy, R. A. Masut and S. Turenne, *Mater. Charact.*, 2014, **95**, 44–49, doi: 10/f6d6jz.

(202) B. Trawiński, B. Bochentyn, N. Gostkowska, M. Łapiński, T. Miruszewski and B. Kusz, *Mater. Res. Bull.*, 2018, **99**, 10–17, doi: 10.1016/j.materresbull.2017.10.043.

(203) G. Yang, L. Sang, F. F. Yun, D. R. G. Mitchell, G. Casillas, N. Ye, K. See, J. Pei, X. Wang, J.-F. Li, G. J. Snyder and X. Wang, *Adv. Funct. Mater.*, 2021, **31**, 2008851, doi: 10.1002/adfm.202008851.

(204) J. Zhang, D. Wu, D. He, D. Feng, M. Yin, X. Qin and J. He, *Adv. Mater.*, 2017, **29**, 1703148, doi: 10.1002/adma.201703148.

(205) J. R. Sootsman, J. Q. He, V. P. Dravid, C. P. Li, C. Uher and M. G. Kanatzidis, *J. Appl. Phys.*, 2009, **105**, 083718, doi: 10.1063/1.3093833.

(206) M. W. Gaultois, T. D. Sparks, C. K. H. Borg, R. Seshadri, W. D. Bonificio and D. R. Clarke, *Chem. Mater.*, 2013, **25**, 2911–2920, doi: 10.1021/cm400893e.

(207) M. R. Laboratory, *Energy Materials Datamining*, 2021.

(208) K. Biswas, J. He, I. D. Blum, C. I. Wu, T. P. Hogan, D. N. Seidman, V. P. Dravid and M. G. Kanatzidis, *Nature*, 2012, **489**, 414–8, doi: 10.1038/nature11439.

(209) D. Y. Chung, T. Hogan, P. Brazis, M. Rocci-Lane, C. Kannewurf, M. Bastea, C. Uher and M. G. Kanatzidis, *Science*, 2000, **287**, 1024–1027, doi: 10.1126/science.287.5455.1024.

(210) D.-Y. Chung, K.-S. Choi, L. Iordanidis, J. L. Schindler, P. W. Brazis, C. R. Kannewurf, B. Chen, S. Hu, C. Uher and M. G. Kanatzidis, *Chem. Mater.*, 1997, **9**, 3060–3071, doi: 10.1021/cm970397e.

(211) F. Gascoin and A. Maignan, *Chem. Mater.*, 2011, **23**, 2510–2513, doi: 10.1021/cm200581k.

(212) K. F. Hsu, S. Loo, F. Guo, W. Chen, J. S. Dyck, C. Uher, T. Hogan, E. K. Polychroniadis and M. G. Kanatzidis, *Science*, 2004, **303**, 818–21, doi: 10.1126/science.1092963.

(213) T. Jungwirth, J. Wunderlich and K. Olejnik, *Nat. Mater.*, 2012, **11**, 382–90, doi: 10.1038/nmat3279.

(214) M. G. Kanatzidis, T. J. McCarthy, T. A. Tanzer, L.-H. Chen, L. Iordanidis, T. Hogan, C. R. Kannewurf, C. Uher and B. Chen, *Chem. Mater.*, 1996, **8**, 1465–1474, doi: 10.1021/cm9600182.

(215) K. Kurosaki, A. Kosuga and S. Yamanaka, *J. Alloys Compd.*, 2003, **351**, 208–211, doi: 10.1016/S0925-8388(02)01002-2.

(216) K. Kurosaki, A. Kosuga, H. Muta, M. Uno and S. Yamanaka, *Appl. Phys. Lett.*, 2005, **87**, 061919, doi: 10.1063/1.2009828.

(217) S. Larouche, Y. J. Tsai, T. Tyler, N. M. Jokerst and D. R. Smith, *Nat. Mater.*, 2012, **11**, 450–4, doi: 10.1038/nmat3278.

(218) H. Liu, X. Shi, F. Xu, L. Zhang, W. Zhang, L. Chen, Q. Li, C. Uher, T. Day and G. J. Snyder, *Nat. Mater.*, 2012, **11**, 422–5, doi: 10.1038/nmat3273.

(219) C. D. Martin, A. Costa, B. Dering, N. Hoshino, Y. J. Wu and G. Thierry, *Brain Lang.*, 2012, **120**, 61–5, doi: 10.1016/j.bandl.2011.10.003.

(220) A. F. May, E. Flage-Larsen and G. J. Snyder, *Phys. Rev. B*, 2010, **81**, 125205, doi: 10.1103/PhysRevB.81.125205.

(221) M. A. McGuire, T. K. Reynolds and F. J. DiSalvo, *Chem. Mater.*, 2005, **17**, 2875–2884, doi: 10.1021/cm050412c.

(222) M. Ohta, A. Yamamoto and H. Obara, *J. Electron. Mater.*, 2010, **39**, 2117–2121, doi: 10.1007/s11664-009-0975-0.

(223) J. Orava, A. L. Greer, B. Gholipour, D. W. Hewak and C. E. Smith, *Nat. Mater.*, 2012, **11**, 279–83, doi: 10.1038/nmat3275.

(224) E. T. Rogers, J. Lindberg, T. Roy, S. Savo, J. E. Chad, M. R. Dennis and N. I. Zheludev, *Nat. Mater.*, 2012, **11**, 432–5, doi: 10.1038/nmat3280.

(225) S. Scherrer, H. Scherrer and D. Rowe, in *CRC Handbook of Thermoelectrics*, CRC Press, 1995, doi: 10.1201/9781420049718.ch19.

(226) J. W. Sharp, B. C. Sales, D. G. Mandrus and B. C. Chakoumakos, *Appl. Phys. Lett.*, 1999, **74**, 3794–3796, doi: 10.1063/1.124182.

(227) E. Skrabek, D. Trimmer and D. Rowe, in *CRC Handbook of Thermoelectrics*, CRC Press, 1995, doi: 10.1201/9781420049718.ch22.

(228) C. Wan, Y. Wang, N. Wang and K. Koumoto, *Materials*, 2010, **3**, 2606–2617, doi: 10.3390/ma3042606.

(229) W. H. Wang, *Nat. Mater.*, 2012, **11**, 275–6, doi: 10.1038/nmat3277.

(230) S. C. Warren, M. R. Perkins, A. M. Adams, M. Kamperman, A. A. Burns, H. Arora, E. Herz, T. Suteewong, H. Sai, Z. Li, J. Werner, J. Song, U. Werner-Zwanziger, J. W. Zwanziger, M. Gratzel, F. J. DiSalvo and U. Wiesner, *Nat. Mater.*, 2012, **11**, 460–7, doi: 10.1038/nmat3274.

(231) J. L. Cui, H. F. Xue and W. J. Xiu, *Intermetallics*, 2007, **15**, 1466–1470, doi: 10.1016/j.intermet.2007.05.004.

(232) C. Gayner and N. Nandihalli, *Materialia*, 2020, **14**, 100912, doi: 10.1016/j.mtla.2020.100912.

(233) C.-C. Chang, C.-H. Liu, C.-C. Wu, P. Bag and Y.-K. Kuo, *Mater. Res. Bull.*, 2020, **129**, 110916, doi: 10.1016/j.materresbull.2020.110916.

(234) N. Nandihalli, Y.-H. Pai and C.-J. Liu, *Ceram. Int.*, 2020, **46**, 18683–18689, doi: 10.1016/j.ceramint.2020.04.182.

(235) C. Zhu, J. Zhang, H. Ming, X. Lou, L. Huang, T. Chen, B. Zhang, D. Li, H. Xin and X. Qin, *Appl. Phys. Lett.*, 2020, **117**, 042105, doi: 10.1063/5.0013039.

(236) Z.-R. Yang and C.-J. Liu, *J. Electron. Mater.*, 2020, **49**, 2954–2961, doi: 10.1007/s11664-020-07994-2.

(237) T. Zhu, H. Xie, C. Zhang, X. Cheng, J. Zhang, P. F. P. Poudeu, G. Tan, Y. Yan, W. Liu, X. Su and X. Tang, *ACS Appl. Mater. Interfaces*, 2019, **11**, 41472–41481, doi: 10.1021/acsami.9b10019.

(238) J. Gao, T. Mao, T. Lv, Z. Li and G. Xu, *J. Mater. Sci.: Mater. Electron.*, 2018, **29**, 5327–5336, doi: 10.1007/s10854-017-8498-6.

(239) D. Ginting, C.-C. Lin, L. Rathnam, J. Hwang, W. Kim, R. A. rahal Al Orabi and J.-S. Rhyee, *Data in Brief*, 2017, **13**, 233–241, doi: 10.1016/j.dib.2017.05.041.

(240) A. G. Rösch, F. Giunta, M. M. Mallick, L. Franke, A. Gall, J. Aghassi-Hagmann, J. Schmalian and U. Lemmer, *Advanced Theory and Simulations*, 2021, **4**, doi: 10.1002/adts.202000284.

(241) D. A. G. Bruggeman, *Annalen der Physik.*, 1935, **416**, 636–664, doi: 10.1002/andp.19354160705.

(242) R. Landauer, *J. Appl. Phys.*, 1952, **23**, 779–784, doi: 10.1063/1.1702301.

(243) J. B. Vaney, A. Piarristeguy, V. Ohorodniichuck, O. Ferry, A. Pradel, E. Alleno, J. Monnier, E. B. Lopes, A. P. Goncalves, G. Delaizir, C. Candolfi, A. Dauscher and B. Lenoir, *J. Mater. Chem. C*, 2015, **3**, 11090–11098, doi: 10.1039/c5tc02087e.

(244) J. Sonntag, *J. Mater. Chem. C*, 2016, **4**, 10973–10976, doi: 10.1039/c6tc03140d.

(245) S. Angst and D. E. Wolf, *New J. Phys.*, 2016, **18**, doi: 10.1088/1367-2630/18/4/043004.

(246) F. Gather, C. Heiliger and P. J. Klar, *Prog. Solid State Chem.*, 2011, **39**, 97–107, doi: 10.1016/j.progsolidstchem.2011.10.001.

(247) A. Monticelli, *State Estimation in Electric Power Systems: A Generalized Approach*, Springer Science & Business Media, 1st edn., 1999.

(248) B. Razavi, *Fundamentals of Microelectronics*, Wiley, 2nd edn., 2013.

(249) S. Roche, *Nat. Nanotechnol.*, 2010, **6**, 8–9, doi: 10.1038/nnano.2010.262.

(250) D. Suh, S. Lee, H. Mun, S. H. Park, K. H. Lee, S. W. Kim, J. Y. Choi and S. Baik, *Nano Energy*, 2015, **13**, 67–76, doi: 10.1016/j.nanoen.2015.02.001.

(251) S. Yadav, S. Chaudhary and D. K. Pandya, *Ceram. Int.*, 2018, **44**, 10628–10634, doi: 10.1016/j.ceramint.2018.03.090.

(252) Y. Zhang, H. Ma, B. Sun, B. Liu, H. Liu, L. Kong, B. Liu, X. Jia and X. Chen, *J. Alloys Compd.*, 2017, **715**, 344–348, doi: 10.1016/j.jallcom.2017.05.004.

(253) Y. He, T. S. Zhang, X. Shi, S. H. Wei and L. D. Chen, *Npg Asia Materials*, 2015, **7**, e210–e210, doi: 10.1038/am.2015.91.

(254) J. Sottmann, K. Valset, O. B. Karlsen and J. Tafto, *J. Electron. Mater.*, 2013, **42**, 1820–1826, doi: 10.1007/s11664-012-2441-7.

(255) S. A. Yamini, M. Brewis, J. Byrnes, R. Santos, A. Manettas and Y. Z. Pei, *J. Mater. Chem. C*, 2015, **3**, 10610–10615, doi: 10.1039/C5TC02210J.

(256) S. Aminorroaya Yamini, D. R. G. Mitchell, H. Wang, Z. M. Gibbs, Y. Pei, S. X. Dou and G. J. Snyder, *AIP Adv.*, 2015, **5**, doi: 10.1063/1.4913992.

(257) J. J. Shen, L. P. Hu, T. J. Zhu and X. B. Zhao, *Appl. Phys. Lett.*, 2011, **99**, 124102, doi: 10.1063/1.3643051.

(258) X. B. Zhao, X. H. Ji, Y. H. Zhang, T. J. Zhu, J. P. Tu and X. B. Zhang, *Appl. Phys. Lett.*, 2005, **86**, 062111, doi: 10.1063/1.1863440.

(259) M. Bailyn, *Phys. Rev.*, 1962, **126**, 2040–2054, doi: 10.1103/PhysRev.126.2040.

(260) A. Hirohata, K. Yamada, Y. Nakatani, I. L. Prejbeanu, B. Dieny, P. Pirro and B. Hillebrands, *J. Magn. Magn. Mater.*, 2020, **509**, 166711, doi: 10.1016/j.jmmm.2020.166711.

(261) M. V. Costache, G. Bridoux, I. Neumann and S. O. Valenzuela, *Nat. Mater.*, 2011, **11**, 199–202, doi: 10.1038/nmat3201.

(262) S. J. Watzman, R. A. Duine, Y. Tserkovnyak, S. R. Boona, H. Jin, A. Prakash, Y. H. Zheng and J. P. Heremans, *Phys. Rev. B*, 2016, **94**, 144407, doi: 10.1103/PhysRevB.94.144407.

(263) T. Saito and D. Nishio-Hamane, *Phys. B Condens. Matter*, 2021, **603**, doi: 10.1016/j.physb.2020.412761.

(264) T. Saito and S. Kamishima, *IEEE Trans. Magn.*, 2019, **55**, 1–4, doi: 10.1109/TMAG.2018.2874631.

(265) S. Das, S. M. Valiyaveettil, K.-H. Chen, S. Suwas and R. C. Mallik, *Mater. Res. Express*, 2019, **6**, doi: 10.1088/2053-1591/aaf710.

(266) A. Jena, S.-C. Lee and S. Bhattacharjee, *Phys. Rev. Appl.*, 2021, **15**, doi: 10.1103/PhysRevApplied.15.064023.

(267) G. Solomon, E. Song, C. Gayner, J. A. Martinez and Y. Amouyal, *ACS Appl. Nano Mater.*, 2021, **4**, 4419–4431, doi: 10.1021/acsanm.0c03472.

(268) Vikram, D. D. Johnson and A. Alam, *Phys. Rev. B*, 2018, **98**, doi: 10.1103/PhysRevB.98.115204.

(269) M. S. Diakhate, R. P. Hermann, A. Mochel, I. Sergueev, M. Sondergaard, M. Christensen and M. J. Verstraete, *Phys. Rev. B*, 2011, **84**, 125210, doi: 10.1103/PhysRevB.84.125210.

(270) P. Sun, N. Oeschler, S. Johnsen, B. B. Iversen and F. Steglich, *Dalton Trans.*, 2010, **39**, 1012–9, doi: 10.1039/b918909b.

(271) H. Franzen and C. Sterner, *J. Solid State Chem.*, 1978, **25**, 227–230, doi: 10.1016/0022-4596(78)90107-X.

(272) M. Podgorny and J. Oleszkiewicz, *J. Phys. C: Solid State Phys.*, 1983, **16**, 2547–2557, doi: 10.1088/0022-3719/16/13/017.

(273) J. D. Wasscher and C. Haas, *Phys. Lett. B*, 1964, **8**, 302–304, doi: 10.1016/s0031-9163(64)80006-8.

(274) C. Peng, G. Zhang, C. Wang, Y. Yan, H. Zheng, Y. Wang and M. Hu, *physica status solidi (RRL) - Rapid Research Letters*, 2018, **12**, 1800172, doi: 10.1002/pssr.201800172.

(275) M. J. Kirkham, A. M. dos Santos, C. J. Rawn, E. Lara-Curzio, J. W. Sharp and A. J. Thompson, *Phys. Rev. B*, 2012, **85**, 144120, doi: 10.1103/PhysRevB.85.144120.

(276) L. Zheng, J. Li, B. Zhou, H. Liu, Z. Bu, B. Chen, R. Ang and W. Li, *J. Alloys Compd.*, 2019, **789**, 953–959, doi: 10.1016/j.jallcom.2019.03.140.

(277) S. Shimizu, J. Shiogai, N. Takemori, S. Sakai, H. Ikeda, R. Arita, T. Nojima, A. Tsukazaki and Y. Iwasa, *Nat. Commun.*, 2019, **10**, 825, doi: 10.1038/s41467-019-08784-z.

(278) H. Takahashi, R. Okazaki, S. Ishiwata, H. Taniguchi, A. Okutani, M. Hagiwara and I. Terasaki, *Nat. Commun.*, 2016, **7**, 12732, doi: 10.1038/ncomms12732.

(279) N. Tsujii and T. Mori, *Appl. Phys. Express*, 2013, **6**, 043001, doi: 10.7567/Apex.6.043001.

(280) R. Ang, A. U. Khan, N. Tsujii, K. Takai, R. Nakamura and T. Mori, *Angew. Chem. Int. Ed. Engl.*, 2015, **54**, 12909–13, doi: 10.1002/anie.201505517.

(281) T. Kikkawa, D. Reitz, H. Ito, T. Makiuchi, T. Sugimoto, K. Tsunekawa, S. Daimon, K. Oyanagi, R. Ramos, S. Takahashi, Y. Shiomi, Y. Tserkovnyak and E. Saitoh, *Nat. Commun.*, 2021, **12**, 4356, doi: 10.1038/s41467-021-24623-6.

(282) K. Uchida, S. Takahashi, K. Harii, J. Ieda, W. Koshibae, K. Ando, S. Maekawa and E. Saitoh, *Nature*, 2008, **455**, 778–81, doi: 10.1038/nature07321.

(283) Y. Wang, N. S. Rogado, R. J. Cava and N. P. Ong, *Nature*, 2003, **423**, 425–8, doi: 10.1038/nature01639.

(284) G. E. Bauer, E. Saitoh and B. J. van Wees, *Nat. Mater.*, 2012, **11**, 391–9, doi: 10.1038/nmat3301.

(285) H. M. Yu, S. D. Brechet and J. P. Ansermet, *Phys. Lett. A*, 2017, **381**, 825–837, doi: 10.1016/j.physleta.2016.12.038.

(286) M. Erekhinsky, F. Casanova, I. K. Schuller and A. Sharoni, *Appl. Phys. Lett.*, 2012, **100**, 212401, doi: 10.1063/1.4717752.

(287) N. Marchal, T. da Camara Santa Clara Gomes, F. Abreu Araujo and L. Piraux, *Nanoscale Res. Lett.*, 2020, **15**, 137, doi: 10.1186/s11671-020-03343-8.

(288) K. Yamanoi, M. Yafuso, K. Miyazaki and T. Kimura, *J. Phys. Mater.*, 2019, **3**, doi: 10.1088/2515-7639/ab45cc.

(289) F. Ahmed, N. Tsujii and T. Mori, *J. Mater. Chem.A*, 2017, **5**, 7545–7554, doi: 10.1039/C6TA11120C.

(290) J. B. Vaney, S. A. Yamini, H. Takaki, K. Kobayashi, N. Kobayashi and T. Mori, *Mater. Today Phys.*, 2019, **9**, 100090, doi: 10.1016/j.mtphys.2019.03.004.

(291) S. Acharya, S. Anwar, T. Mori and A. Soni, *J. Mater. Chem. C*, 2018, **6**, 6489–6493, doi: 10.1039/C8TC00788H.

(292) J. He, X. Tan, J. Xu, G.-Q. Liu, H. Shao, Y. Fu, X. Wang, Z. Liu, J. Xu, H. Jiang and J. Jiang, *J. Mater. Chem.A*, 2015, **3**, 19974–19979, doi: 10.1039/C5TA05535K.

(293) W. Li, Z. W. Chen, S. Q. Lin, Y. J. Chang, B. H. Ge, Y. Chen and Y. Z. Pei, *Journal of Materiomics*, 2015, **1**, 307–315, doi: 10.1016/j.jmat.2015.09.001.

(294) T. Graf, J. Barth, C. G. F. Blum, B. Balke, C. Felser, P. Klaer and H.-J. Elmers, *Phys. Rev. B*, 2010, **82**, 104420, doi: 10.1103/PhysRevB.82.104420.

(295) Z. Liu, J. Zhu, P. Wei, W. Zhu, W. Zhao, A. Xia, D. Xu, Y. Lei and J. Yu, *ACS Appl. Mater. Interfaces*, 2019, **11**, 45875–45884, doi: 10.1021/acsami.9b16309.

(296) W. Zhao, Z. Liu, P. Wei, Q. Zhang, W. Zhu, X. Su, X. Tang, J. Yang, Y. Liu, J. Shi, Y. Chao, S. Lin and Y. Pei, *Nat. Nanotechnol.*, 2017, **12**, 55–60, doi: 10.1038/nnano.2016.182.

(297) R. Lu, J. S. Lopez, Y. Liu, T. P. Bailey, A. A. Page, S. Wang, C. Uher and P. F. P. Poudeu, *J. Mater. Chem.A*, 2019, **7**, 11095–11103, doi: 10.1039/c9ta01156k.

(298) S. Vandendriessche, W. Brullot, D. Slavov, V. K. Valev and T. Verbiest, *Appl. Phys. Lett.*, 2013, **102**, 161903, doi: 10.1063/1.4801837.

(299) V. Marghussian, in *Nano-Glass Ceramics*, Elsevier, 2015, pp. 181–223, doi: 10.1016/B978-0-323-35386-1.00004-9.

(300) W. Zhao, Z. Liu, Z. Sun, Q. Zhang, P. Wei, X. Mu, H. Zhou, C. Li, S. Ma, D. He, P. Ji, W. Zhu, X. Nie, X. Su, X. Tang, B. Shen, X. Dong, J. Yang, Y. Liu and J. Shi, *Nature*, 2017, **549**, 247–251, doi: 10.1038/nature23667.

3

Experimental techniques

If I learned anything, I would need to learn more, and I would never be satisfied.
— Graciliano Ramos, Vidas Secas

Summary
This chapter presents a discussion of the synthesis and characterisation techniques used in this work. A discussion of each step of the fabrication process is included in this chapter, as well as a brief mathematical derivation of the characterisation techniques.

In this chapter, the experimental techniques used in this work are discussed. For the knowledgeable reader, this chapter provides an insight into the theory of characterisation techniques used to measure the transport properties of thermoelectric materials and how to model them concisely. The body of the text is divided into three main sections:

1. Characterisation techniques: where a discussion of all the characterisation methods used in this work is performed
2. Modelling thermoelectric materials: where the models employed in this work to study the transport properties of the material are discussed
3. Synthesis: where an overall discussion of the synthesis procedure used in this work is discussed

3.1 Characterisation techniques

The characterisation techniques used for thermoelectric materials are divided into two groups. One that characterises the structural properties of the materials: XRD; and one that measures the transport properties of the materials: thermopower and resistivity measurements, Hall effect, laser flash analysis, and differential scanning calorimetry.

The equipment used for characterising the materials synthesised in this work changed in every chapter, thus, the information regarding each measurement device was added on a chapter basis.

3.1.1 Thermopower measurement

The procedure for measuring the thermopower is as follows: a bar-shaped or cylindrical sample is placed vertically between the upper and lower blocks in a heating furnace. While the sample is heated and held at a specified temperature, the lower part of the sample is heated by a heater in the lower block to provide a temperature gradient. The thermopower is then calculated by measuring the upper and lower temperatures, T_1 and T_2, and the thermal voltage, ΔV. The schematic of the measurements is shown in figure 3.1.

To understand how the thermopower is calculated, one first needs to find its integral form. From equation 2.1, it is possible to write

$$-\nabla V = \alpha \nabla T. \tag{3.1}$$

Since α is measured one-dimensionally, the partial differential equation can be substituted by an ordinary differential equation as follows

$$\alpha = -\frac{\mathrm{d}V}{\mathrm{d}T} \rightarrow -\alpha \mathrm{d}T = \mathrm{d}V. \tag{3.2}$$

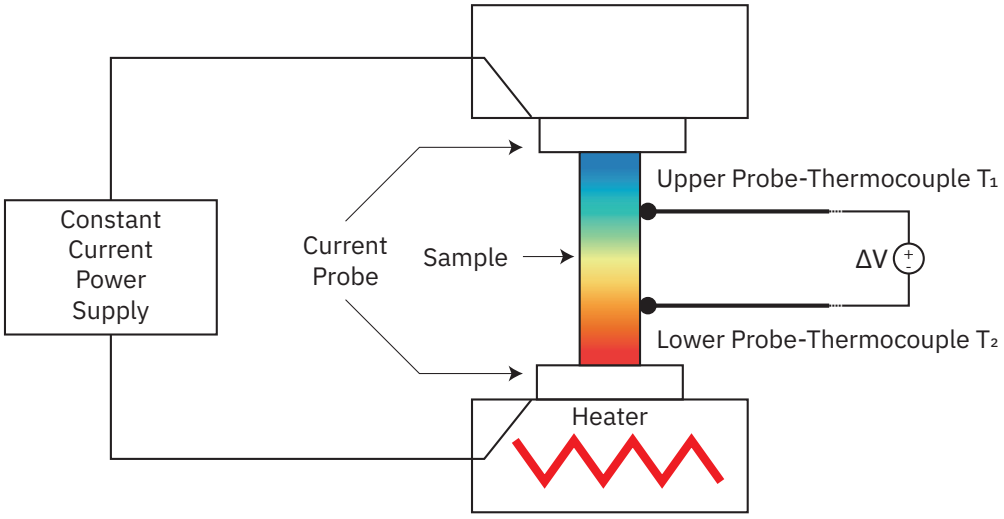

Figure 3.1. Schematic of a thermopower and bulk resistivity measurement device.

Integrating both sides of equation 3.2, the potential difference between the probes is given by

$$V_2 - V_1 := \Delta V = -\int_{T_1}^{T_2} \alpha \mathrm{d}T. \tag{3.3}$$

In a real experimental scenario, the voltage is measured by the same thermocouples that measure the temperature. Therefore, the measured voltage ΔV_m is not the actual voltage induced in the material, but rather the difference between the voltage induced in the material ΔV and the voltage induced in the positive and negative legs of the thermocouple $\Delta V_{\pm}$, or

$$\Delta V_m = \Delta V + \Delta V_{\pm} = -\int_{T_1}^{T_2} \alpha \mathrm{d}T + \int_{T_1}^{T_2} \alpha_{\pm} \mathrm{d}T, \tag{3.4}$$

$$\Delta V_m = -\int_{T_1}^{T_2} \alpha - \alpha_{\pm} \mathrm{d}T, \tag{3.5}$$

where $\alpha_{\pm}$ is the thermopower of the thermocouple. The integral of equation 3.5 can be approximated by using the midpoint rule [301] where we would obtain

$$\Delta V_m \approx (T_2 - T_1) \left[\alpha(\bar{T}) - \alpha_{\pm}(\bar{T})\right], \tag{3.6}$$

where $\bar{T} = \frac{T_1+T_2}{2}$.

Since both the positive and negative legs can be used to measure the voltage, the expression for the voltage measured in each leg is

$$\Delta V_m^- = \left(T_2 - T_1\right) \left[\alpha\left(\bar{T}\right) - \alpha_-\left(\bar{T}\right)\right], \tag{3.7}$$

$$\Delta V_m^+ = \left(T_2 - T_1\right) \left[\alpha\left(\bar{T}\right) - \alpha_+\left(\bar{T}\right)\right], \tag{3.8}$$

where ΔV_m^- is the voltage measured by the negative legs, ΔV_m^+ is the voltage measured by the positive legs, $\alpha_-\left(\bar{T}\right)$ is the thermopower of the negative legs, and $\alpha_+\left(\bar{T}\right)$ is the thermopower of the negative legs. Solving each equation for α wields

$$\alpha(\bar{T})_{neg} = -\frac{\Delta V_m^-}{T_2 - T_1} + \alpha_-\left(\bar{T}\right), \tag{3.9}$$

$$\alpha(\bar{T})_{pos} = -\frac{\Delta V_m^+}{T_2 - T_1} + \alpha_+\left(\bar{T}\right), \tag{3.10}$$

where $\alpha(\bar{T})_{neg}$ and $\alpha(\bar{T})_{pos}$ are the thermopowers found using the negative and positive legs, respectively.

In a practical scenario, a number of points with different temperature gradients will be measured, so equations 3.9 and 3.10 can be rewritten as

$$\alpha(\bar{T})_{neg} = -\frac{\partial V_m^-}{\partial T} + \alpha_-\left(\bar{T}\right), \tag{3.11}$$

$$\alpha(\bar{T})_{pos} = -\frac{\partial V_m^+}{\partial T} + \alpha_+\left(\bar{T}\right). \tag{3.12}$$

The slope of both equations can be obtained using a linear regression of the data.

3.1.2 Resistivity measurement

The resistance is measured with the same probe used to measure the thermopower. The method used to evaluate the resistance of semiconductors is known as the Kelvin method or the 4-point probe method [302]. This technique is particularly useful for measuring small resistances or loads distant from the current source. To understand why, it is necessary to compare a 2-point probe measurement with a 4-point probe measurement.

In figure 3.2, the resistance is measured using (a) an ohmmeter and (b) a combination of an ammeter and voltmeter. In the first case, the ohmmeter measures the resistance of the probe summed with the resistance of the wire. Generally, this is not an issue, as the wire resistance is usually very small in comparison to the resistance being measured. However, since semiconductor samples have a low resistance comparable to that of the wire, the measurement error introduced by the wire resistance is significant. In the second case, this error is avoided because the current flow to the voltmeter is negligible, so the measured resistance has no influence on the wire resistance value.

When measuring the resistance of semiconductor samples, the usual setup is as shown in the figure 3.3 [303]. The R_W term represents the wire resistance, R_C represents the contact resistance, and R_S represents the resistance of the sample.

To derive an expression for the resistance measured by the four probes, consider that the sample dimensions are much larger than the distance between the

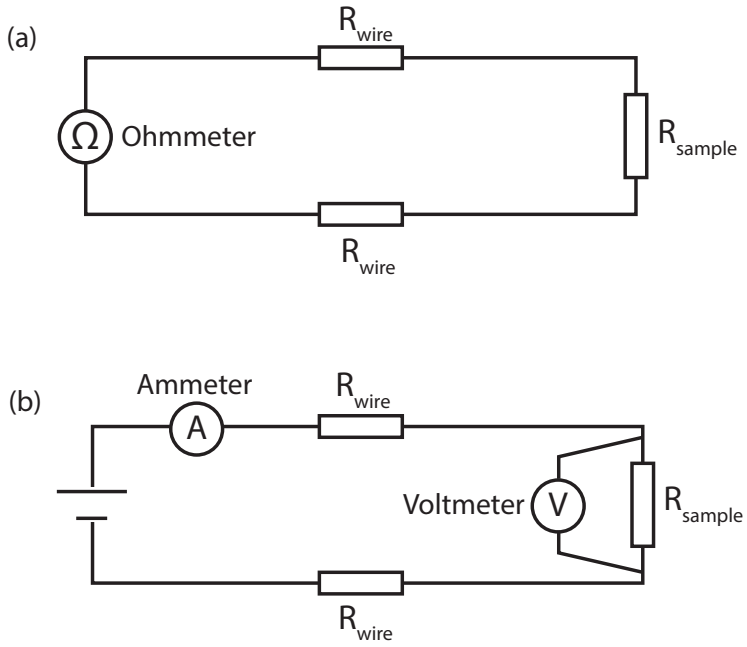

Figure 3.2. Resistance measurement using a (a) 2-point probe and (b) 4-point probe scheme.

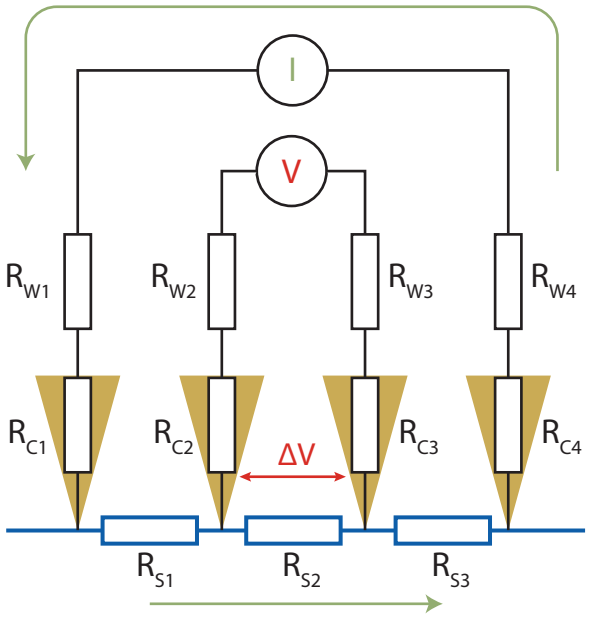

Figure 3.3. 4-point probe scheme to measure resistance of semiconductor samples.

probes, so that the simple sample geometry shown in figure 3.4 can be used [304]. Assuming an infinitesimal point probe and a radial current distribution, the current density can be evaluated as

$$\vec{J} = \frac{I}{2\pi r^2}\hat{r}. \tag{3.13}$$

The electric field and voltage will be

$$\vec{E} = \rho\vec{J}, \tag{3.14}$$

$$E = -\frac{\mathrm{d}V}{\mathrm{d}r}. \tag{3.15}$$

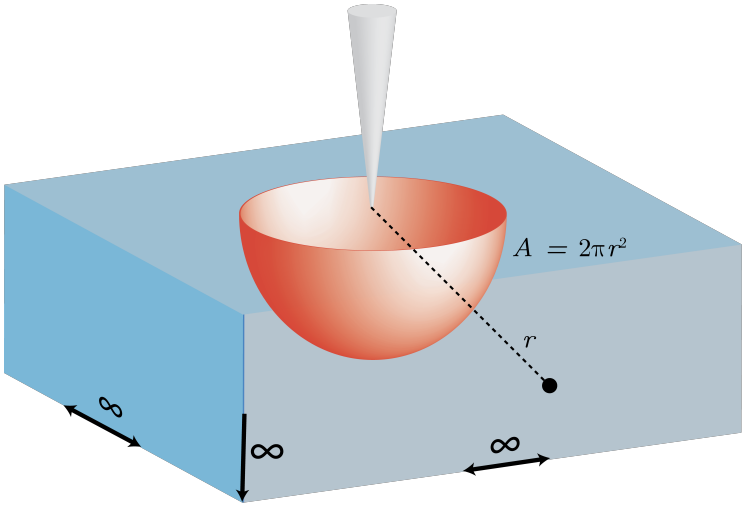

Figure 3.4. Idealised current distribution for thick samples.

Using the boundary condition of a zero potential at infinity [305], the voltage at a distance r from the probe will be

$$V = -\int_0^r \frac{I\rho}{2\pi r^2}\mathrm{d}r \rightarrow V = \frac{I\rho}{2\pi r}. \tag{3.16}$$

For a four-point probe scheme with spacings of s_1, s_2, ands_3 between probes, the voltage measured by probes 2 and 3 for a current flowing from probes 1 and 4 will be

$$V_2 = \frac{I\rho}{2\pi}\left(\frac{1}{s_1} - \frac{1}{s_2 + s_3}\right), \tag{3.17}$$

$$V_3 = \frac{I\rho}{2\pi}\left(\frac{1}{s_1 + s_2} - \frac{1}{s_3}\right), \tag{3.18}$$

where the minus sign accounts for the current leaving probe 4. Finally, the measured voltage $V_{23} = V_2 - V_3$ becomes

$$V_{23} = \frac{I\rho}{2\pi}\left(\frac{1}{s_1} - \frac{1}{s_2 + s_3} - \frac{1}{s_1 + s_2} + \frac{1}{s_3}\right), \tag{3.19}$$

and the resistivity is given by

$$\rho_{23,14} = \frac{2\pi}{\frac{1}{s_1} - \frac{1}{s_2+s_3} - \frac{1}{s_1+s_2} + \frac{1}{s_3}} \cdot \frac{V_{23}}{I_{14}}. \tag{3.20}$$

Equation 3.20 is defined for a semi-infinite semiconductor slab, and it is only valid if the sample thickness t is much larger than the probe spacing and the four probes are far from the sample edge. For cases where these conditions do not hold, the following expression is used [304]

$$\rho = F\ 2\pi s \frac{V}{I}, \tag{3.21}$$

where F is a correction factor and $s = s_1 = s_2 = s_3$.

Correction factors accounting, probe location near sample edges, sample thickness, sample diameter, probe placement, sample temperature, and unequal probe spacing have been calculated using the method of images [306, 307], Laplace's equation [308], and conformal mappings [309]. Each of these factors is evaluated independently and the overall correction is obtained by multiplying them.

The correction factor used for most measurements is the one that accounts for a non-infinite thickness and is given as [310]

$$F = \frac{t/s}{2\ln\left(\frac{\sinh(t/s)}{\sinh(t/2s)}\right)}. \tag{3.22}$$

For non-uniform samples, the formula devised in appendix C can be employed.

3.1.3 Uncertainty analysis in thermopower and resistivity measurements

In this work, samples containing volatile elements have been studied. It is therefore essential to be able to assess the difference between compositional changes and measurement errors. The first step is to review the common sources of error for each type of measurement.

For resistivity measurements, the most common sources of uncertainty are due to

1. Probes spacing → Arising from length measurements using a calliper
2. Sample dimensions → Arising from length measurements using a calliper
3. Voltage values → Arising from the data acquisition system (DAQ) for voltage measurements
4. Current values → Arising from the DAQ for current measurement

Errors in length measurements are due to the precision of the equipment used, and it is common practice to assume the error to be ± the precision of the equipment. For callipers, this will be ± 0.1 mm.

Voltage and current measurement errors are due to the accuracy of the DAQ equipment used. There are two main components of measurement accuracy: gain error and offset value. The gain error is expressed as a percentage and is defined as the error in the measurement at full scale. The offset error is measured as the difference between the ideal transfer function of the analog-to-digital converter (ADC) and the measured function. This is illustrated in figure3.5(a).

The offset values are due to the accuracy of the conversion; as ADCs convert analogue signals to digital bytes, the values to be acquired are in fact discrete, and the accuracy of the discretisation is related to the number of bits of the ADC. The offset value is assumed to be the least significant bit (LSB) of the converter and is shown in figure 3.5 (b).

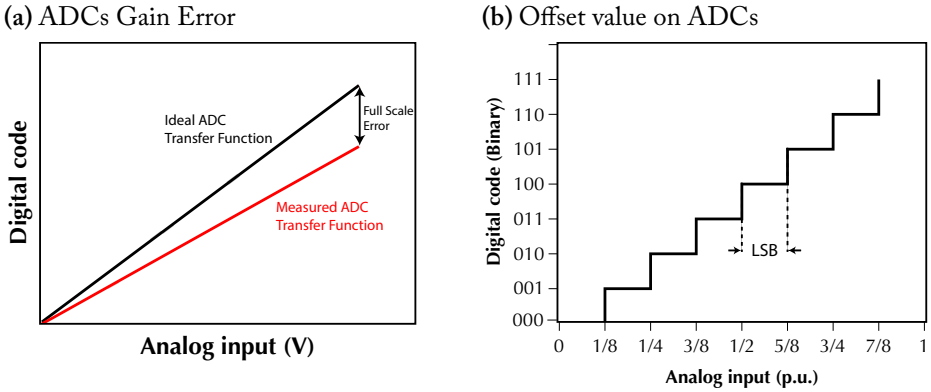

Figure 3.5. Illustration of the sources of errors on analog-to-digital converters.

For thermopower measurements, the most common source of error is due to

1. Cold-finger effect → Arising from the temperature difference between the thermocouple and sample temperature
2. Voltage values → Arising from the DAQ for voltage measurement
3. Absolute temperature values → Arising from thermopower from the wire
4. Estimate of the standard error from the slope approach method → Arising from the least-squares method

The cold finger effect is caused by the thermal difference between a cooler thermocouple and a hot surface being measured. Heat is transferred into the thermocouple, creating a thermal gradient. Due to the thermal resistance of the wire, this results in a slight underestimation of the actual surface temperature. Equations modelling this effect can be found at [311] and are derived from a finite element analysis of the system. Voltage errors are due to the same reasons

as for resistivity measurements. The uncertainty in the temperature values is due to the mismatch between the standard values for the thermocouples and those used in the measurement. Finally, there is the error associated with slope estimation when using ordinary least squares to calculate the thermopower, as in equations 3.12 and 3.11 (for more details see [301]).

For assessing the final error values, error propagation techniques [312] or Monte Carlo methods [313] can be employed. In this work the following sources of error were considered

1. Resistivity: I) Probe spacing (±0.1 mm), II) bar dimensions (±0.01 mm), III) voltage (±5%), and III) current (0.2% + 0.3 mA)

2. Thermopower: I) Cold-finger effect ($1 \times 10^4\,W^2.m^{-1}.K^{-1}$), II) voltage (±3%), III) absolute temperature (±2 K), and IV) estimate standard error from the slope approach method

3.1.4 Hall Effect measurement

The Hall effect is the production of a voltage across an electrical conductor or semiconductor when a magnetic field is applied in a direction perpendicular to that of the flow of current [314] and it is used to measure the sheet resistance and carrier concentration of materials. In figure 3.6, the Hall effect is illustrated for a semiconductor slab when a magnetic field B_z is applied transversally to the current I.

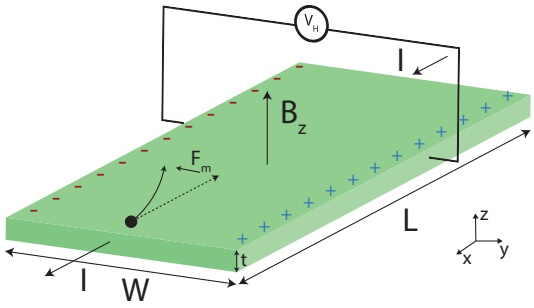

Figure 3.6. Hall effect for a semiconductor slab.

Due to the presence of a magnetic field, the carriers will experience a force called the Lorenz force

$$\vec{F} = q\left(\vec{E} + \vec{v} \times \vec{B}\right). \tag{3.23}$$

Assuming that the motions of the carriers are damped owing to scattering and the average scattering time is τ, Newton's second law for the carriers will be [315] as follows

$$m\frac{\mathrm{d}\vec{v}}{\mathrm{d}t} = q\left(\vec{E} + \vec{v} \times \vec{B}\right) - \frac{m\vec{v}}{\tau}. \tag{3.24}$$

Following the convention determined in figure 3.6, the negative carriers are flowing in the negative x-axis direction with a drift velocity v_x. In a steady state scenario, the net force is zero, thus

$$\begin{bmatrix}0\\0\\0\end{bmatrix} = q\left(\begin{bmatrix}E_x\\E_y\\E_z\end{bmatrix} + \begin{bmatrix}v_x\\v_y\\v_z\end{bmatrix} \times \begin{bmatrix}0\\0\\B_z\end{bmatrix}\right) - \frac{m}{\tau}\begin{bmatrix}v_x\\v_y\\v_z\end{bmatrix}, \tag{3.25}$$

$$\begin{bmatrix}0\\0\\0\end{bmatrix} = q\left(\begin{bmatrix}E_x\\E_y\\0\end{bmatrix} + \begin{bmatrix}v_yB_z\\v_xB_z\\0\end{bmatrix}\right) - \frac{m}{\tau}\begin{bmatrix}v_x\\v_y\\v_z\end{bmatrix}, \tag{3.26}$$

Rearranging equation 3.26, it can be seen that

$$\begin{bmatrix}v_x\\v_y\\v_z\end{bmatrix} = \begin{bmatrix}\frac{q\tau}{m}E_x + \frac{q\tau}{m}B_zv_y\\\frac{q\tau}{m}E_y - \frac{q\tau}{m}B_zv_x\\0\end{bmatrix}. \tag{3.27}$$

The current density in the y-axis direction is zero, thus the electric field is

$$\begin{bmatrix} E_x \\ E_z \end{bmatrix} = \begin{bmatrix} \frac{m}{q\tau} v_x \\ \frac{q\tau}{m} B_z E_x \end{bmatrix}. \tag{3.28}$$

The Hall voltage, defined as $V_H = -\frac{E_y}{W}$, is then given as

$$V_H = -\frac{q\tau}{m} \frac{E_x}{W} B_z. \tag{3.29}$$

The current flowing in the x-axis direction is $I_x = tWJ_x = tWE_x\sigma$, where $\sigma = \frac{nq^2\tau}{m}$ is the electrical conductivity. Plugging this expression in equation 3.29, we find that

$$V_H = -\frac{I_x B_z}{ntq}. \tag{3.30}$$

Interestingly, the sign of V_H allows us to determine if the semiconductor is p-type or n-type. Since the carrier is always deflected to the left side, the build-up charge will be the opposite for n-type and p-type materials.

A quantity of interest called the Hall coefficient can also be evaluated from these measurements, and it is defined as

$$R_H = \frac{E_y}{J_x B_z} = \frac{V_H t}{I_x B_z} = \frac{1}{nq}. \tag{3.31}$$

Until now, it was assumed that the current flowing through the material was due to only holes or electrons. In semiconductors, however, both carriers contribute to the current, and the current density on the x-axis takes the following form [315]

$$J_x = J_{hx} + J_{ex} = e(p\mu_h + n\mu_e)E_x, \tag{3.32}$$

where $\mu_h = \frac{e\tau}{m_h}$ and $\mu_e = \frac{e\tau}{m_e}$ are the hole and electron mobilities, respectively; p is the hole carrier concentration; and n is the electron carrier concentration. Using this new J_x in the Hall coefficient expression, we obtain

$$R_H = \frac{p\mu_h - n\mu_e}{e\left(p\mu_h + n\mu_h\right)^2}. \tag{3.33}$$

Experimentally, V_H, t and W are measured, and the values of B_z and I are set. Thus, it is possible to calculate n and R_H. The mobility can be evaluated by noting that

$$R_H = \rho\mu. \tag{3.34}$$

The only step now is to find the resistivity. For this, the usual approach is to employ a methodology known as the van der Pauw method. This method is explained in the following section.

3.1.5 Van der Pauw method

The van der Pauw method is used to evaluate the resistivity of a sample of arbitrary shape (shown in fig. 3.7), as long as the sample is approximately two-dimensional (i.e. it is much thinner than it is wide), solid (no holes), and the probes are placed on its perimeter [316].

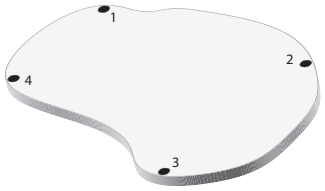

Figure 3.7. Sample with arbitrary shape for van der Pauw measurements.

For simplicity, let us assume a simpler geometry of an infinity half-plane as seen in figure 3.8, where p_1, p_2, p_3 and p_4 are the locations of the four probes arbitrarily spaced.

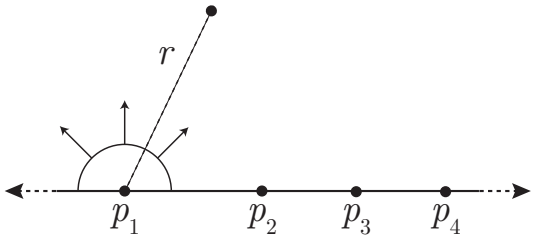

Figure 3.8. Probes location and current distribution in a semi-infinite half-plane.

The current will propagate radially in semicircles centred around the probe's location, as illustrated in figure 3.8, so the current density can be expressed as

$$\vec{J} = \frac{I}{\pi r t}\hat{r}. \tag{3.35}$$

Once again, assuming the boundary condition of a zero potential at infinity, the voltage at a point r distant from the current source is

$$V = -\int_0^r \frac{I\rho}{\pi t r}\mathrm{d}r \rightarrow V = -\frac{I\rho}{\pi t}\ln r. \tag{3.36}$$

Assuming a current flowing from points p_1 and p_2, the voltage in points p_3 and p_4, will be

$$V_3 = -\frac{I\rho}{\pi t}\left(\ln d_{31} - \ln d_{32}\right),\ V_4 = -\frac{I\rho}{\pi t}\left(\ln d_{41} - \ln d_{42}\right), \tag{3.37}$$

where $d_{ij} = \|p_i - p_j\|$.

The voltage between points p_4 and p_3 is

$$V_{43} = V_4 - V_3 = -\frac{I\rho}{\pi t}\left(\ln d_{41} - \ln d_{42} - \ln d_{31} + \ln d_{32}\right). \tag{3.38}$$

The resistance $R_{43,12}$ is defined as

$$R_{43,12} = \frac{V_{43}}{I} = -\frac{\rho}{\pi t}\ln\frac{d_{41}d_{32}}{d_{42}d_{31}} = \frac{\rho}{\pi t}\ln\frac{d_{42}d_{31}}{d_{41}d_{32}}. \tag{3.39}$$

Now, we assume a current flowing from points p_2 and p_3. Following the same procedure as before, the voltage between points p_1 and p_4 is

$$V_{14} = V_1 - V_4 = -\frac{I\rho}{\pi t}\left(\ln d_{12} - \ln d_{13} - \ln d_{42} + \ln d_{43}\right). \tag{3.40}$$

The resistance $R_{14,23}$ is defined as

$$R_{14,23} = \frac{V_{14}}{I} = -\frac{\rho}{\pi t}\ln\frac{d_{12}d_{43}}{d_{13}d_{42}} = \frac{\rho}{\pi t}\ln\frac{d_{13}d_{42}}{d_{12}d_{43}}. \tag{3.41}$$

Exponentiating both equations 3.39 and 3.41 and adding them [304], we find

$$e^{-\frac{\pi t}{\rho}R_{14,23}} + e^{-\frac{\pi t}{\rho}R_{43,12}} = \frac{d_{12}d_{43}}{d_{13}d_{42}} + \frac{d_{41}d_{32}}{d_{42}d_{31}}. \tag{3.42}$$

Since $d_{ij} = d_{ji}$ and $p_1 < p_2 < p_3 < p_4$,

$$e^{-\frac{\pi t}{\rho}R_{14,23}} + e^{-\frac{\pi t}{\rho}R_{43,12}} = 1. \tag{3.43}$$

Equation 3.43 is referred in some texts as the van der Pauw formula.

In practice, equation 3.43 is modified as follows

$$e^{-\frac{\pi R_-}{R_s}} + e^{-\frac{\pi R_|}{R_s}} = 1, \tag{3.44}$$

where

$$R_- = \frac{R_{23,41} + R_{41,23} + R_{32,14} + R_{14,23}}{4}, \tag{3.45a}$$

$$R_| = \frac{R_{12,34} + R_{34,12} + R_{21,43} + R_{43,21}}{4}. \tag{3.45b}$$

R_- and $R_|$ are known as the horizontal and vertical resistances, while R_s denotes the sheet resistance. An advantage of this method is that the resistance values are averaged and offset voltages are cancelled. Since equation 3.44 is transcendental, R_s is numerically found. This result holds for arbitrary shaped samples and is denoted as the van der Pauw theorem, as stated in sequence.

Theorem 3.1.1 (van der Pauw theorem). *On an arbitrary simply connected region* Ω *with a positively oriented boundary,* $\partial\Omega$*, take points* w_1, w_2, w_3, w_4 *and measure the quantities* $\boldsymbol{R}_{14,23}$ *and* $\boldsymbol{R}_{43,12}$ *as defined above, then* ρ *satisfies*

$$e^{-\frac{\pi t}{\rho}R_{14,23}} + e^{-\frac{\pi t}{\rho}R_{43,12}} = 1. \tag{3.46}$$

Proof. To show that this result holds for a sample of arbitrary shape, we proceed as follows: Let $H = \{p \in \mathbb{C} : \Im(p) > 0\}$ be the semi-infinite half-plane with $p_1 < p_2 < p_3 < p_4 \in \mathbb{R} = \partial H$, and $U = \{l \in \mathbb{C} : |l| < 1\}$ be the unit disc in the complex plane.
From the Riemann mapping theorem [317], there is a conformal mapping $f : \Omega \to U$ from Ω onto U and a conformal mapping $g : H \to U$ from H onto U. Since conformal mappings are bijective [318], there is a conformal mapping $f \cdot g^{-1} : \Omega \to H$ from Ω onto H, so that $w_1, w_2, w_3, w_4 \in \partial\Omega \xrightarrow{f\cdot g^{-1}} p_1, p_2, p_3, p_4 \in \partial H$. This result is illustrated in figure 3.9.

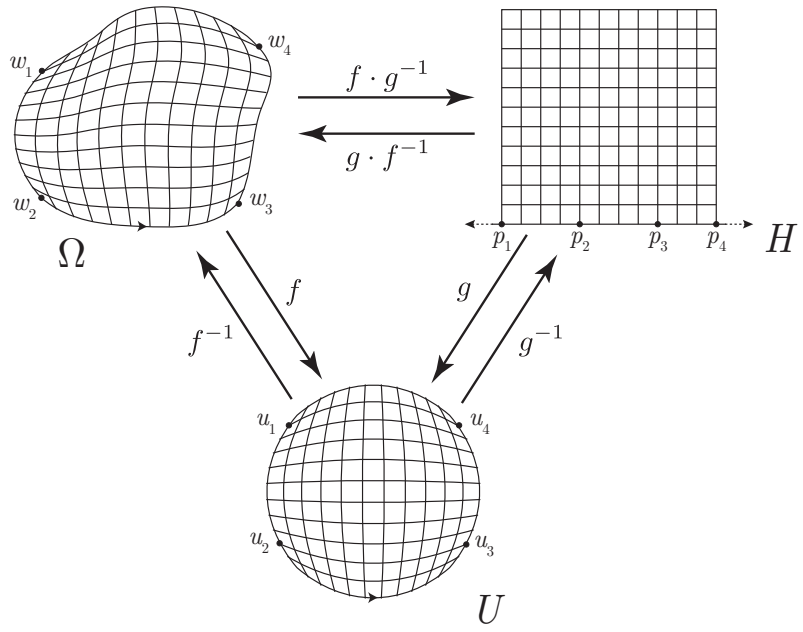

Figure 3.9. Conformal mapping between regions Ω, U and H.

The current flowing from points w_i, w_j will be the same as the current flowing from p_i, p_j. Furthermore, by the invariance of the electric potential under conformal mappings [319, 320], the potential difference between points w_k, w_l and p_k, p_l will be the same. Thus, the resistance $\boldsymbol{R}_{kl,ij}$ will be the same whether evaluated on Ω or H, and the formulation previously shown can be applied to a sample of arbitrary shape. QED

In practice, the following sample shapes are used in measurements, as seen in figure 3.10

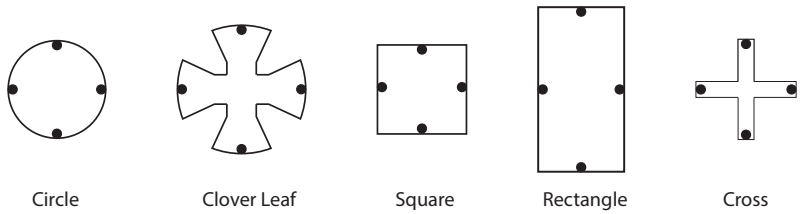

Figure 3.10. Usual samples shapes for van der Pauw measurements.

3.1.6 X-ray diffraction analysis

XRD analysis is a non-destructive tool to analyse materials. The primary function of a XRD analysis is to identify the phases in the samples. The fundamental idea behind this method is that at certain angles, the X-ray beams are scattered in a mirror-like reflection, and the interference from successive crystallographic planes is constructive [321]. The condition for this happening is given by Bragg's law [322]

$$n\lambda = 2d \sin\theta, \tag{3.47}$$

where n is the diffraction order, λ wavelength of the X-ray beam, d is the spacing of the crystallographic planes, and θ Bragg angle. Bragg's law is illustrated in figure 3.11.

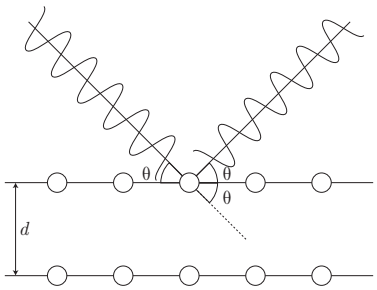

Figure 3.11. Mirror-like reflection of an X-ray beam following Bragg's law.

Experimentally, the result of Bragg's law is the X-ray diffraction pattern of the phase, where the intensities of the scattered X-rays are plotted at different angles. This is usually obtained by following the arrangement shown in figure 3.12. At each 2θ, the position of the rotating detector is recorded along with the number of X-rays detected. This value is known as the intensity and is usually recorded as counts or counts per second. This result is commonly presented as a diffraction pattern containing 2θ values in the x-axis and intensity values in the y-axis.

In real measurement data, the diffraction pattern contains noise and a superimposed background (due to X-ray scattering from the equipment), and the peaks are broadened due to the sample microstructure and equipment [323].

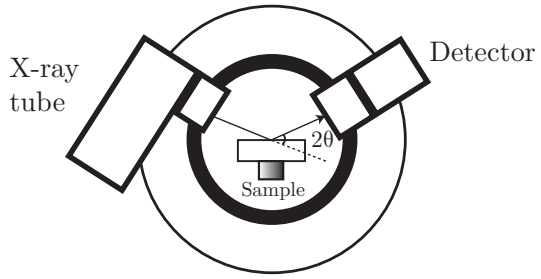

Figure 3.12. Illustration of an X-ray diffractometer.

Systematic errors due to sample displacement and diffractometer misalignment (known as zero-point errors) can also be observed in diffraction patterns [323].

In practice, researchers use specialised software to analyse the diffraction patterns. These programmes use data analysis to correct for the systematic errors described above. The locations of all peaks are determined using profile fitting, where the peaks are usually modelled as Gaussian, Lorentzian, Pseudo-Voigt, or Pearson VII shapes [301] and the background is usually fitted using Chebyshev polynomials [301].

After phase identification, the unit cell dimensions can be determined using the Miller indices (hkl) of the diffraction peaks and the appropriate equation relating d to the lattice parameters [321]. This type of profile fitting is useful for indexing materials, but to accurately estimate the crystal structure of the sample, a different type of profile fitting is used, called Rietveld refinement.

In Rietveld refinement, the profile is fitted by considering structural parameters (lattice parameters, fractional atomic coordinates, atomic site occupancies, atomic displacement parameters, and preferred orientation), parameters describing the instrument calibration parameters (e.g. 2θ zero-point offset), parameters describing the 2θ-dependent intensity correction (e.g. due to absorption), parameters describing the peak shape, and parameters describing the background between the Bragg peaks [324]. This fitting is typically done using the nonlinear least-squares method [301].

Given the large number of variables, the refinement is performed iteratively following a greedy algorithm structure [325]; where at each refinement cycle, certain variables are fixed, and a minimisation routine is executed to improve the model. This process continues until all the variables are optimised. Unfortunately, the heuristic behind the local optimal choice for each cycle is user-dependent. Therefore, the quality of the model is not only dependent on the initial guess and the quality of the data but also on the experience of the user. Commonly used software packages for Rietveld refinement are GSAS-II [326] and FullProf [327].

3.1.7 Laser flash analysis

LFA is a technique used to measure the thermal diffusivity, D, of a sample. This technique uses a short laser pulse that is absorbed by the front surface of the sample while the temperature of the rear surface is recorded as a function of time. From the evolution of the temperature signal, the thermal diffusivity D can be determined. The LFA technique is illustrated in figure 3.13.

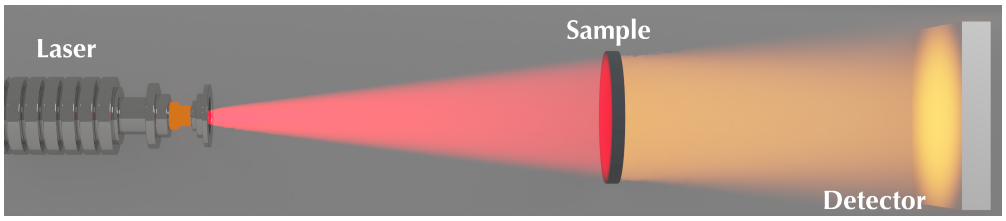

Figure 3.13. Illustration of the laser flash analysis technique.

Fundamentally, the idea behind the LFA technique comes from the heat equation [64]

$$\frac{\partial u\left(x,y,z,t\right)}{\partial t} = D\nabla^2 u\left(x,y,z,t\right), \tag{3.48}$$

where $u(\cdot)$ is the temperature as a function of space and time.

The samples used for this type of measurement are thin (with thickness h) and small, so it is possible to assume a one-dimensional heat flow. In addition, since the measurements are done in a short span of time, the ends of the material are assumed to be thermally insulated. With these assumptions, the initial boundary value problem (IBVP) can be defined as [328]

$$\frac{\partial u\left(x,t\right)}{\partial t} = D\frac{\partial^2 u\left(x,t\right)}{\partial x^2} \quad x \in (0,h)\,,\ t > 0, \tag{3.49}$$

$$\frac{\partial u\left(0,t\right)}{\partial x} = \frac{\partial u\left(h,t\right)}{\partial x} = 0 \quad t > 0, \tag{3.50}$$

$$u\left(x,\ 0\right) = f\left(x\right) \quad x \in (0,h)\,. \tag{3.51}$$

The general solution of the IBVP is given by [329]

$$u\left(x,t\right) = \frac{1}{h}\int_0^h f\left(x\right)\mathrm{d}x + \frac{2}{h}\sum_{n=1}^{\infty}\exp\left(-\frac{Dn^2\pi^2}{h^2}t\right)\cos\frac{n\pi x}{h}\int_0^h f\left(x\right)\cos\frac{n\pi x}{h}\mathrm{d}x. \tag{3.52}$$

For LFA measurements, it is assumed that a pulse with radiant energy Q_e is instantaneously and uniformly absorbed in a small depth δ, so that $f(x)$ can be written as [330]

$$f(x) = \begin{cases} \frac{Q_e}{dc_p\delta} & , x = (0,\delta) \\ 0 & , x = (\delta,h) \end{cases}, \tag{3.53}$$

where d is the density of the material and c_p is the specific heat capacity of the material. Now, equation 3.52 can be written

$$u(x,t) = \frac{1}{h}\int_0^{\delta} \frac{Q_e}{dc_p\delta}\mathrm{d}x + \frac{2}{h}\sum_{n=1}^{\infty} \exp\left(-\frac{Dn^2\pi^2}{h^2}t\right)\cos\frac{n\pi x}{h}\int_0^{\delta}\frac{Q_e}{dC_p\delta}\cos\frac{n\pi x}{h}\mathrm{d}x, \tag{3.54}$$

$$u(x,t) = \frac{Q_e}{dc_p h}\left[1 + 2\sum_{n=1}^{\infty}\exp\left(-\frac{Dn^2\pi^2}{h^2}t\right)\cos\frac{n\pi x}{h}\frac{\sin n\pi\delta/h}{n\pi\delta/h}\right]. \tag{3.55}$$

Since it was assumed that δ is small, $\sin\pi\delta/h \approx \pi\delta/h$, we can rewrite equation 3.55 as

$$u(x,t) = \frac{Q_e}{dc_p h}\left[1 + 2\sum_{n=1}^{\infty}\exp\left(-\frac{Dn^2\pi^2}{h^2}t\right)\cos\frac{n\pi x}{h}\right]. \tag{3.56}$$

Following equation 3.56, the time dependent temperature at a depth h is expressed as

$$u(x=h,t) = \frac{Q_e}{dc_p h}\left[1 + 2\sum_{n=1}^{\infty}\exp\left(-\frac{Dn^2\pi^2}{h^2}t\right)\cos n\pi\right] \rightarrow$$

$$u(x=h,t) = \frac{Q_e}{dc_p h}\left[1 + 2\sum_{n=1}^{\infty}(-1)^n\exp\left(-\frac{Dn^2\pi^2}{h^2}t\right)\right]. \tag{3.57}$$

Since the maximum temperature at $x = h$ is $T_{\max} = Q_e \cdot d \cdot c_p \cdot h$, the temperature at $u(h,t)$ can be normalised as follows

$$\tilde{u}(h,t) = \frac{u(h,t)}{T_{max}} = 1 + 2\sum_{n=1}^{\infty}(-1)^n\exp\left(-\frac{Dn^2\pi^2}{h^2}t\right). \tag{3.58}$$

Initially, Parker [330] proposed to calculate D from a first order approximation of the normalised temperature when $\tilde{u}(h,t) = 0.5$ as follows

$$D = \frac{\ln 1/4}{\pi^2}\frac{h^2}{t_{1/2}}, \tag{3.59}$$

where $t_{1/2}$ is the time when $\tilde{u}(h,t) = 0.5$.

If Q_e is known, then both specific heat capacity and thermal conductivity can be calculated as

$$c_p = \frac{Q_e}{dhT_{max}}, \tag{3.60}$$

$$\kappa = D \cdot d \cdot c_p. \tag{3.61}$$

Over the years, this simple model has been extended to include heat losses due to radiation and convection, such as Cowan's [331], Cape and Lehman's [332],

and Clark and Taylor's [333] models, and non-instantaneous energy transfer (see Larson and Koyama model [334]). For transparent and semi-transparent samples, where the laser causes a near-instantaneous rise in the temperature on the rear side, a method called the Radiation model [335] is employed.

In LFA measurements the estimated error for the thermal diffusivity is around ±3%

3.1.8 Differential scanning calorimetry

DSC is an important technique for measuring the thermal properties of a material. DSC measures the changes in the physical properties of a material with temperature and time. In this technique, the thermal apparatus measures the heat flow radiated or absorbed by the sample based on the temperature difference between the sample and the reference material. Two main schemes are used in DSC: heat-flux DSC and power compensated DSC. In the first one, the sample and reference are connected by a low thermal resistance path and enclosed in a furnace. Due to the heat capacity of the sample, a temperature difference ΔT is created between the sample and reference pans, which is recorded. The heat flow, Q, is then evaluated as

$$Q = \frac{\Delta T}{R_p}, \tag{3.62}$$

where R_p is resistance of the thermal path.

In power-compensated DSC, the sample and reference are thermally insulated and controlled separately using identical furnaces. The temperatures of the sample and reference are controlled to be identical using a feedback loop that varies the power input to the two furnaces. The thermal energy required to achieve this condition is recorded and used as a measure of the enthalpy change in the sample relative to the reference. This technique is illustrated in figure 3.14.

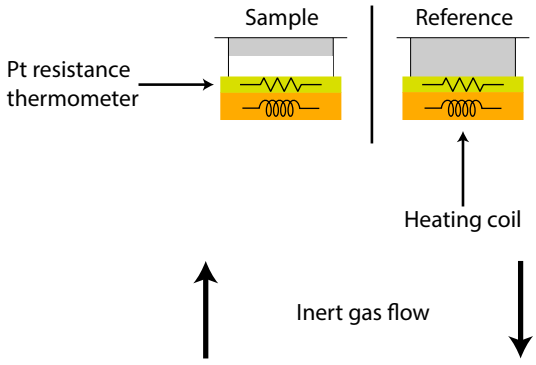

FIGURE 3.14. Power-compensated differential scanning calorimetry scheme.

3.1.8.1 Heat capacity measurements

In this work, the primary use of the DSC is to measure the heat capacity (C_p) and specific heat capacity (c_p) of semiconductor materials. Since the samples are either enclosed or in contact with aluminium or alumina pans, the C_p can be calculated as

$$C_p = \frac{Q_{\text{sample}} - Q_{\text{empty}}}{\dot{Q}}, \tag{3.63}$$

where Q_{sample} and Q_{empty} are the heat flows of the sample and empty pan, respectively, and $\dot{Q}$ is the heating rate. Clearly, equation 3.63 assumes a perfect calibration of the system. In reality, this is rarely the case, and it is desirable to have a reference material to calibrate the heat flow measurements. The procedures for doing this are described in ISO 11357-4 [336], Japanese Industrial Standard K 7123 [337] and ASTM E1269-11 [338]. The ASTM standard was the one primarily used in this study and uses a sapphire reference for the analysis. The method can be described as follows

1. Purge the DSC with an inert gas at a flow rate of 10 to 50 L.min^{-1} during the experiment
2. Weigh a clean, empty specimen holder plus lid to a precision of ± 0.01 mg. Record the weight and use as tare
3. Heat or cool the DSC test chamber to the initial temperature for the experiment at 20 °C.min^{-1}
4. Hold the DSC chamber isothermally at the initial temperature for at least 4 min to establish equilibrium
5. Heat the empty specimen from the initial to the final temperature at a rate of 20 °C.min^{-1}
6. Record a steady-state isothermal baseline at the upper temperature limit
7. Cool the DSC test chamber to ambient temperature
8. Weigh the sapphire standard and the specimen holder plus lid if using a different one
9. Follow steps 3-7
10. Weigh the test sample and the specimen holder plus lid if using a different one
11. Follow steps 3-7
12. Finish the experiment

The specific heat capacity can then be calculated as

$$c_p = c_p^{\text{sapphire}} \frac{Q_{\text{sample}} - Q_{\text{empty}}}{Q_{\text{sapphire}} - Q_{\text{empty}}} \cdot \frac{W_{\text{sapphire}}}{W_{\text{sample}}} + \Delta W c_p^{\text{pan}}, \tag{3.64}$$

where c_p is the specific heat capacity of the test sample, $Q_{\text{sample}}, Q_{\text{sapphire}}, Q_{\text{empty}}$ are the heat flows for the test sample, sapphire standard, and empty pan, respectively, W_{sample}, W_{sapphire}, are the weights of the sample and sapphire standard, respectively, ΔW is the weight difference between the sapphire and test sample pans, and c_p^{pan} is the pan specific heat capacity.

3.1.9 Modulated DSC

In this study, the modulated DSC technique was employed for higher temperature measurements. This technique follows the previously discussed heat-flux DSC scheme. The main difference is that, instead of applying a linear heating hate, the heating profile is a straight line with a superimposed sinusoidal wave. The standard used for this measurement is ASTM E2716-23 [339]. Since the signal is being modulated, the resulting effect is that with a single run, two experiments are being run at the same time, and the heat capacity can be evaluated as

$$c_p = \frac{K_{c_p}}{W} \cdot \frac{A_{hf}}{A_{hr}}, \tag{3.65}$$

where K_{c_p} is the calibration constant evaluated from the sapphire standard, A_{hf} is the heating flow amplitude, A_{hr} is the heating rate amplitude, and W is the sample weight.

As covered by the measurements standards referenced in this chapter, the estimated error for the calculated specific heat ranges from $\pm 2 - 5\%$.

3.2 Modelling thermoelectric materials

3.2.1 Thermopower, electrical conductivity, and carrier concentration

In this section, the models used in this work to study the several transport mechanisms of the thermoelectric materials are described. First, let us assume that the material can be modelled by the SPB model as illustrated in figure 3.15.

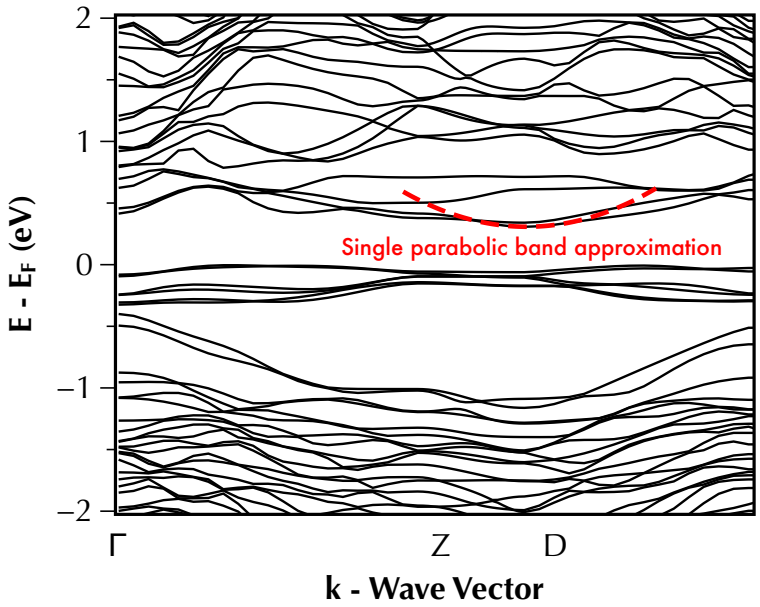

FIGURE 3.15. Illustration of the single parabolic band approximation.

For the SPB model with acoustic phonons as the main scattering mechanisms, the thermopower, carrier concentration, Hall mobility (μ_{H}), and Lorenz number are evaluated as

$$\alpha = \pm\frac{k_{\mathrm{B}}}{e}\left(\frac{2F_1(\eta)}{F_0(\eta)} - \eta\right), \tag{3.66a}$$

$$n = \frac{\left(2m^*_{\mathrm{DOS}}k_{\mathrm{B}}T\right)^{3/2}}{2\pi^2\hbar^3}F_{1/2}(\eta), \tag{3.66b}$$

$$\mu_{\mathrm{H}} = \frac{e\pi\hbar^4 C_l}{\sqrt{2}\left(k_{\mathrm{B}}T\right)^{3/2}E^2_{def}m^*_I\left(m^*_b\right)^{3/2}}, \tag{3.66c}$$

$$L = \left(\frac{k_{\mathrm{B}}}{e}\right)^2\frac{3F_0(\eta)F_2(\eta) - 4F_1(\eta)^2}{F_0(\eta)^2}, \tag{3.66d}$$

where e is the elementary charge, k_{B} is the Boltzmann constant, $\varepsilon = \frac{E}{k_{\mathrm{B}}T}$ is the reduced energy, $\eta = \frac{E_F}{k_{\mathrm{B}}T}$ is the reduced Fermi level, $\hbar$ is the reduced Planck constant, m^*_{DOS} is the DOS effective mass, m^*_b is the single valley effective mass,

m_I^* is the inertial effective mass, E_{def} is the deformation potential for acoustic phonon scattering, $C_l = d v_l^2$ is the longitudinal elastic constant of the material, which is related to its density d and longitudinal speed of sound v_l. The DOS effective mass is related to the single valley effective mass by $m^*_{\text{DOS}} = N_v^{2/3} m_b^*$, where N_v is the valley degeneracy. $F_j(\eta)$ is the Fermi-Dirac integral for an index j and is defined as

$$F_j(\eta) \coloneqq \int_0^\infty \frac{\varepsilon^j}{\exp(\varepsilon - \eta) + 1} \mathrm{d}\varepsilon. \tag{3.67}$$

Note that the Fermi-Dirac integral as defined above does not contain the normalisation factor $1/\Gamma(j+1)$ as seen in other texts.

The Hall mobility is related to the carrier mobility by the Hall factor

$$r_{\text{H}} = \frac{\mu}{\mu_{\text{H}}} = \frac{3}{2} F_{1/2}(\eta) \frac{F_{-1/2}(\eta)}{2 F_0(\eta)^2}. \tag{3.68}$$

At higher temperatures, r_{H} is close to 1, and it is often omitted.

Since equation 3.66a is independent of 3.66b, the usual procedure for estimating the DOS effective mass is to first calculate the reduced Fermi level from the thermopower measurement and then estimate m^*_{DOS} from the measured carrier concentration.

3.2.1.1 Beyond the single band model

If more than one band is necessary to explain the behaviour of the material, it is possible to extend the SPB model to accommodate several parabolic bands. This multiband model is described by the following set of equations

$$\alpha = \frac{\sum_i \alpha_i \sigma_i}{\sum_i \sigma_i}, \tag{3.69a}$$

$$n = \sum_i n_i, \tag{3.69b}$$

$$\sigma = \sum_i \sigma_i = \sum_i n_i \mu_i e, \tag{3.69c}$$

where the index i represents the contribution of the i-th band.

The bipolar and electronic contributions to the thermal conductivity in this model are described by

$$\kappa_e = T \sum_i L_i \sigma_i, \tag{3.70a}$$

$$\kappa_b = T \left[\sum_i \sigma_i \alpha_i^2 - \frac{\left(\sum_i \sigma_i \alpha_i \right)^2}{\sum_i \sigma_i} \right]. \tag{3.70b}$$

In the case of only one valence and one conduction band, the model is simplified to

$$\alpha = \frac{\alpha_n \sigma_n + \alpha_p \sigma_p}{\sigma_n + \sigma_p}, \tag{3.71a}$$

$$\sigma = \sigma_n + \sigma_p \tag{3.71b}$$

$$\sigma_n = n \mu_n e, \tag{3.71c}$$

$$\sigma_p = p \mu_p e, \tag{3.71d}$$

$$\kappa_e = \sum_{i=p,n} L_i \sigma_i T, \tag{3.71e}$$

$$\kappa_b = \frac{\sigma_p \sigma_n}{\sigma_p + \sigma_n} \left(\alpha_p - \alpha_n\right)^2 T, \tag{3.71f}$$

where α_n, α_p, σ_n, σ_p are, respectively, the partial thermopower and electrical conductivity of electrons and holes; μ_n, μ_p, n, p are, respectively, the carrier mobility and carrier concentration of electrons and holes. For this case, the reduced Fermi level of the valence band is $\eta_p = -\eta_n - \epsilon_g$, where η_n is the reduced Fermi level for the conduction band, and $\epsilon_g = \frac{E_g}{k_B T}$ is the reduced bandgap. Notably, the expressions for κ and κ_b are the same as defined in equations 2.8 and 2.9, respectively.

3.2.2 Thermal transport

The lattice thermal conductivity of thermoelectric materials is usually modelled using the Debye-Callaway model

$$\kappa_l = \frac{k_B}{2\pi^2 v} \left(\frac{k_B T}{\hbar}\right)^3 \int_0^{\frac{\theta_D}{T}} \frac{x^4 \exp(x)}{\tau_c^{-1} \left(\exp(x) - 1\right)^2} \mathrm{d}x, \tag{3.72}$$

where $x = \frac{\hbar\omega}{k_B T}$ is the reduced frequency, ω is the phonon angular frequency, v is the average speed of sound in the material, θ_D is the Debye temperature, and τ_c the combined phonon relaxation time. The average speed of sound in the materials is calculated as

$$v = \left(\frac{v_l^{-3}}{3} + \frac{2 v_t^{-3}}{3}\right)^{-1/3}, \tag{3.73}$$

where v_l and v_t are the longitudinal and transversal speed of the sound in the material, respectively.

Matthiessen's rule [340] is commonly employed to find the combined phonon relaxation time as

$$\tau_c^{-1} = \sum_i \tau_i^{-1}, \tag{3.74}$$

where τ_i is the relaxation time of the i-th scattering process. The scattering mechanisms used in this work are discussed in sequence.

The effect of phonon-phonon scattering from Umklapp processes was accounted for as defined by Slack [341, 342]

$$\tau_u^{-1} = \frac{\hbar\gamma^2 T}{\bar{M} v^2 \theta_D}\omega^2 \exp\left(-\frac{\theta_D}{3T}\right), \tag{3.75}$$

where $\bar{M}$ is the average atomic mass and γ is the Grüneisen parameter.

The phonon-phonon scattering arising from normal processes can be expressed analytically, but experimentally, the following approximation has successfully been used to determine its contribution to the relaxation time

$$\tau_n^{-1} \approx \beta\tau_u^{-1}. \tag{3.76}$$

The relaxation time arising from the scattering due to point defects (τ_{pd}) assumed the form as defined by Klemens [343]

$$\tau_{pd}^{-1} = \frac{\bar{V}\omega^4}{4\pi v^3}\Gamma, \tag{3.77a}$$

$$\Gamma = \frac{\langle \mathbb{V}(M)\rangle}{\left\langle \bar{M}\right\rangle^2}, \tag{3.77b}$$

where $\bar{V}$ is the average atomic volume, Γ is known as the scattering parameter, $\left\langle \mathbb{V}(\bar{M})\right\rangle$ is the stoichiometric average mass variance in the system, and $\bar{M}$ is the stoichiometric average mass. The mass variance at a site i ($\langle \mathbb{V}(M)\rangle_i$) for a generic compound composed by a set of $\left\{X_i\right\}_{c_i}, i = 1, 2, 3, \ldots, n$, components with c_i stoichiometry, occupied by a set of $\left\{Y_j\right\}_i$ species, including the host atom and defects, can be expressed as [344]

$$\mathbb{V}\left(M\right)_i = \sum_j f_{j,i}\left(M_{j,i} - \bar{M}_j\right)^2, \tag{3.78a}$$

$$\bar{M}_i = \sum_j f_{j,i} M_{j,i}, \tag{3.78b}$$

where $f_{j,i}$ and $M_{j,i}$ are, respectively, the j-th species site fraction and mass, $\bar{M}_i$ is the i-th site average mass. Finally, $\langle \mathbb{V}\left(M\right)\rangle$ and $\left\langle \bar{M}\right\rangle$ are evaluated as

$$\langle \mathbb{V}\left(M\right)\rangle = \frac{\sum_i c_i \mathbb{V}\left(M\right)_i}{\sum_i c_i}, \tag{3.79a}$$

$$\left\langle \bar{M}\right\rangle = \frac{\sum_i c_i \bar{M}_i}{\sum_i c_i}. \tag{3.79b}$$

The relaxation time due to grain boundaries scattering (τ_{gb}) was assumed to have a Casimir [345] like form

$$\tau_{gb}^{-1} = \frac{v}{L}, \tag{3.80}$$

where L is the average grain size.

The scattering due to dislocation cores τ_{dc} and dislocation strain τ_{ds} were found as [346, 347]

$$\tau_{dc}^{-1} = N_D \frac{\bar{V}^{4/3}}{v^2} \omega^3, \tag{3.81}$$

$$\tau_{ds}^{-1} = 0.6 \cdot B_D^2 N_D (\gamma + \Delta\gamma)^2 \omega \left(\frac{1}{2} + \frac{1}{24} \left(\frac{1-2\nu}{1-\nu} \right)^2 \left[1 + \sqrt{2} \left(\frac{v_l}{v_t} \right)^2 \right]^2 \right), \tag{3.82}$$

where the N_D and B_D are the density of dislocations and effective Burger's vector, respectively, ν is the Poisson's ratio and $\Delta\gamma$ is the change in Grüneisen parameter due to impurity atmosphere [348]

$$\Delta\gamma = \frac{\bar{V}_0 c_0 K}{k_B T_a} \left(\gamma A^2 - A\xi \right), \tag{3.83a}$$

$$A = \frac{\bar{V}_i - \bar{V}_0}{\bar{V}_0}, \tag{3.83b}$$

$$\xi = \frac{\bar{M}_0 - \bar{M}_i}{2\bar{M}_0}, \tag{3.83c}$$

where the indexes i and 0 refer to the impurity and host, $\bar{M}$ is the average atomic mass, $\bar{V}$ is the average atomic volume, K is the bulk modulus, T_a is the annealing temperature, and c_0 is the impurity concentration.

The Debye-Callaway model is frequency limited, and its maximum frequency is evaluated as

$$\omega_D = \left(\frac{6\pi^2}{\bar{V}} \right)^{1/3} v, \tag{3.84}$$

where v is the average speed of sound in the material. To understand the frequency dependency of the lattice thermal conductivity over the phonon's frequency, the spectral lattice thermal conductivity (κ_s) can be employed, and it is evaluated as [81]

$$\kappa_s = \frac{k_B}{2\pi^2 v} \left(\frac{k_B T}{\hbar} \right)^3 \frac{x^4 \exp(x)}{\left(\exp(x) - 1 \right)^2} \tau_c(x). \tag{3.85}$$

The Debye temperature used in the model is evaluated as

$$\theta_D = \frac{\hbar}{k_B} \left(\frac{6n\pi^2}{V} \right)^{1/3} v, \tag{3.86}$$

where V is the unity cell volume and n is the number of atoms in the unity cell.

3.2.3 Clarke model for the minimum value for the thermal conductivity

Generally, the thermal conductivity of the materials decreases to a minimum value as the temperature increases. Several models exist to calculate a theoretical value for the minimum thermal conductivity, with the most famous ones being the ones by Cahill [349] and Clarke [350]. In Clarke's model, the minimum thermal conductivity (κ_{min}) is assumed to be the limit of the average phonon mean free path (interatomic spacing) and is evaluated as

$$\kappa_{\text{min}} \approx 0.93 \cdot \bar{V}^{-\frac{2}{3}} \cdot k_{\text{B}} \cdot \frac{1}{3} \left(2 \cdot v_t + v_l\right), \tag{3.87}$$

where $\bar{V}$ is the average volume per atom, v_t and v_l are the transversal and longitudinal speed of sound in the material, respectively.

3.2.4 Density functional theory

To gain insight into the atomic interactions and electronic structure of the materials, one needs to study the materials at their most fundamental description. In principle, this can be done by solving the many body Schrödinger equation [351]

$$\hat{H}\Psi = E\Psi(\mathbf{r}_i), \tag{3.88}$$

where $\hat{H}$ is the Hamiltonian operator, E is the total ground state energy, and Ψ is the many body wave function for the N electronic eigenstates with $\{\mathbf{r}_i : 1, \ldots, N\}$ electronic coordinates. Upon adding atoms to the system, this procedure becomes computationally prohibitive. Density functional theory (DFT) has been used as a method for an *ab initio* description of matter due to its accuracy and numerical efficiency. The main idea behind DFT analysis comes from the two Hohenberg-Kohn theorems [352], where it was established that, given an external potential, the electronic structure of a material with N electronic eigenstates can be studied as a set of N one-electron Schrödinger equations, known as Kohn-Sham equations [353]. The drawback of DFT analysis is that an exchange-correlation potential needs to be used to force the N non-interacting electrons to have the same density of N interacting electrons under the same potential; however, although it is shown that the functional exists, it is generally unknown and an approximation needs to be used.

In this work, DFT analysis was employed to study the bandstructure of thermoelectric materials using the Quantum ESPRESSO suite [354].

3.3 Synthesis

In this work, all the samples followed a similar fabrication route as described in sequence. In every chapter, however, details such as composition, processing time, and temperatures used are discussed individually and in detail.

3.3.1 Ingot fabrication

The ingots in this study were fabricated via the direct reaction of the raw materials. In a controlled atmosphere glove box, high-purity raw elements were weighed according to compound stoichiometry and placed inside a quartz tube. The tube was then temporarily sealed with a valve, removed from the glovebox, evacuated, and permanently sealed with a flame. The tube was then placed in a tube furnace for the melting process. The tube containing the melted materials was removed from the furnace and quickly quenched in cold water to maintain the composition of the ingot. The fabricated material was then annealed in a muffle furnace at a certain temperature to optimise its crystal structure and eliminate stress. The as-cast ingots were then ground inside a controlled-atmosphere glovebox using an agate mortar and pestle to prepare the powders for sintering.

3.3.2 Ball milling

Ball milling is a grinding method used to grind powders into fine particles and has been widely utilised in the fabrication of thermoelectric materials [250, 355–357]. In this study, a planetary ball mill was employed. In this setup, the jar (or bowl) is attached to a disc that rotates around its central axis, while the jar simultaneously rotates around its own axis (see fig.3.16(a))[358]. In the cataracting regime of the mill, the milling balls are carried along by the jar wall and then detach due to the centrifugal force of the rotating disc, subsequently impacting the opposite wall with high energy (as illustrated in fig.3.16(b))[359].

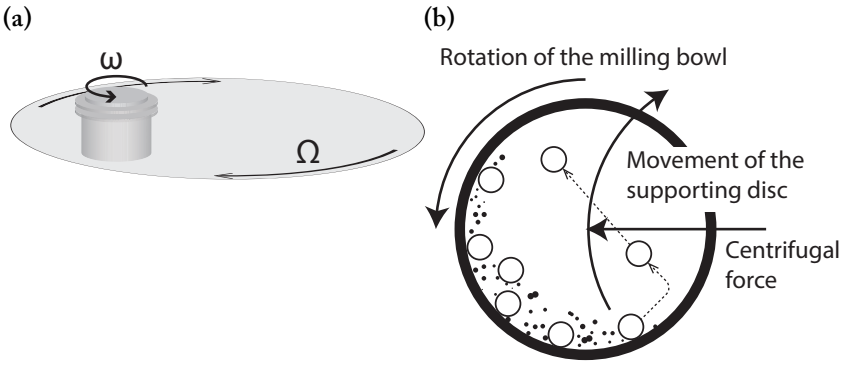

Figure 3.16. (a) Schematic configuration of a planetary ball mill and (b) schematic view of motion of the balls and powder mixture.

3.3.3 Spark plasma sintering

The spark plasma sintering (SPS) process uses specially designed mechanical and electrical systems to produce small samples. The process uses an electrically conductive die and punch system to sinter the desired material under controlled conditions [360, 361]. Figure 3.17(a) shows a typical setup for the SPS process. During sintering, a compaction force ranging from 40–300 kN and an electric current ranging from 1–10 kA are applied to the punch as required. The SPS process achieves fast heating, shorter processing times, and uniform densification at lower temperatures. By increasing the compaction pressure, small powder agglomerates can be effectively eliminated, resulting in more uniform densification and grain growth. Figure 3.17(b) shows a typical circuit for current generation in SPS machines [362].

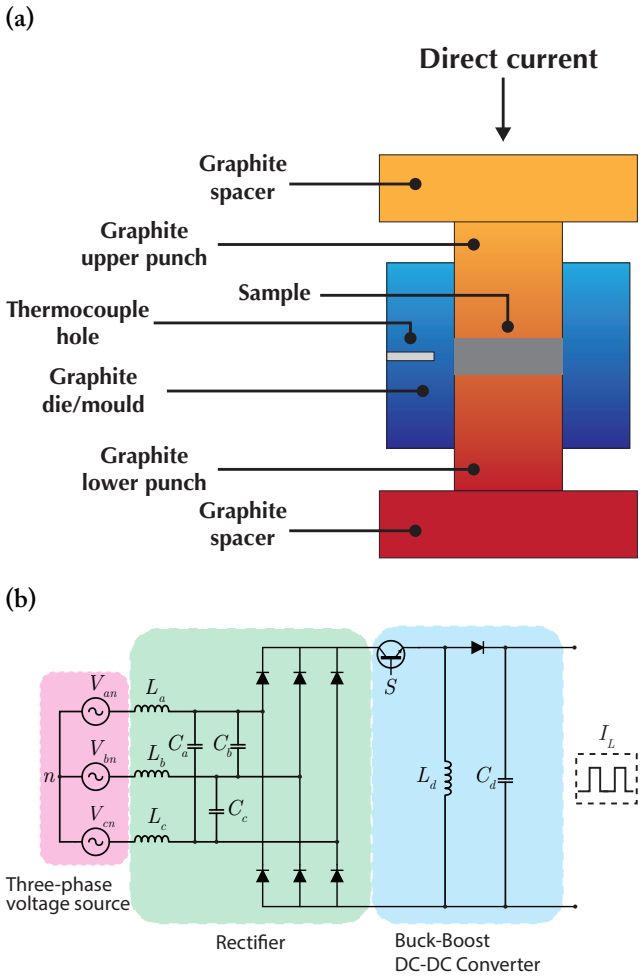

FIGURE 3.17. (a) Working schematic representation of a spark plasma sintering apparatus and (b) example of a current generation scheme used for spark plasma sintering.

3.3.4 Sample cutting

The sintered samples were cut into the shapes illustrated in figure 3.18.

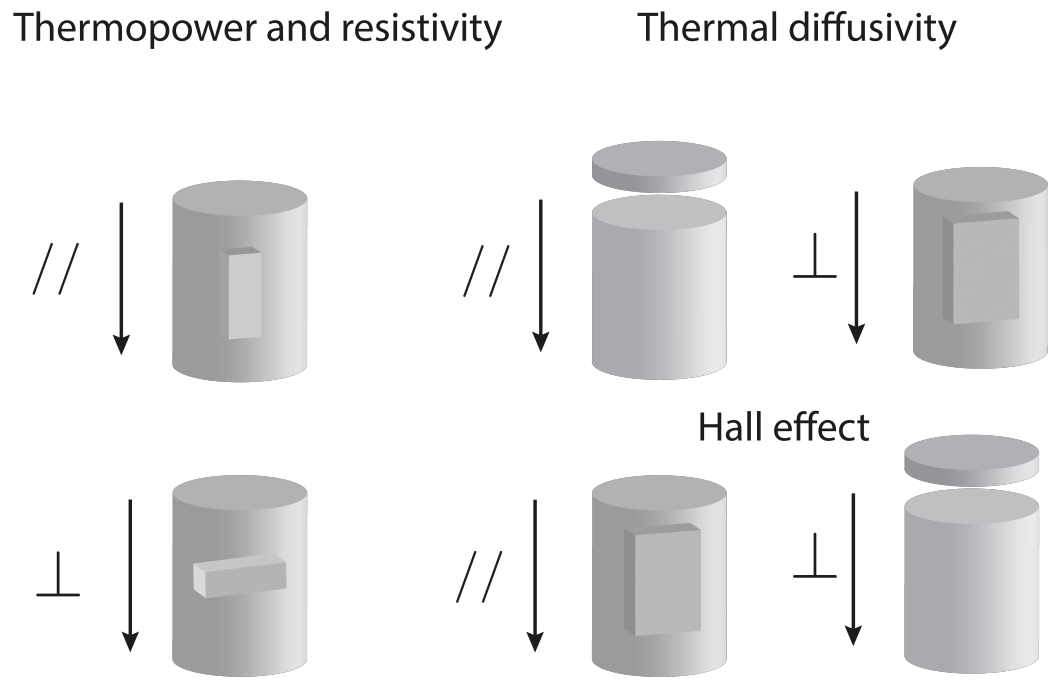

Figure 3.18. Shapes for the transport properties measurements of the sintered materials along the parallel (//) and (⊥) directions to the sintering direction.

References

(64) T. L. Bergman, A. S. Lavine and F. P. Incropera, *Fundamentals of Heat and Mass Transfer, 7th Edition*, John Wiley & Sons, Incorporated, 2011, 1076 pp.

(81) E. S. Toberer, A. Zevalkink and G. J. Snyder, *J. Mater. Chem.*, 2011, **21**, 15843–15852, doi: 10.1039/c1jm11754h.

(250) D. Suh, S. Lee, H. Mun, S. H. Park, K. H. Lee, S. W. Kim, J. Y. Choi and S. Baik, *Nano Energy*, 2015, **13**, 67–76, doi: 10.1016/j.nanoen.2015.02.001.

(301) R. L. Burden and J. D. Faires, *Numerical Analysis*, Cengage Learning, 2010.

(302) I. Miccoli, F. Edler, H. Pfnür and C. Tegenkamp, *J. Phys.: Condens. Matter*, 2015, **27**, 223201, doi: 10.1088/0953-8984/27/22/223201.

(303) L. J. Swartzendruber, *Calculations for Comparing Two-Point and Four-Point Probe Resistivity Measurements on Rectangular Bar-Shaped Semiconductor Samples*, U.S. Department of Commerce, National Bureau of Standards, 1964.

(304) D. K. Schroder, *Semiconductor Material and Device Characterization*, Wiley, 2015.

(305) D. J. Griffiths, *Introduction to Electrodynamics*, American Association of Physics Teachers, 2005.

(306) M. G. Buehler and W. R. Thurber, *Solid-State Electron.*, 1977, **20**, 403–406, doi: 10.1016/0038-1101(77)90130-7.

(307) L. B. Valdes, *Proc. IRE*, 1954, **42**, 420–427, doi: 10.1109/JRPROC.1954.274680.

(308) S. Zolfaghar Tehrani, W. L. Lim and L. Lee, *Measurement*, 2012, **45**, 219–225, doi: 10.1016/j.measurement.2011.11.019.

(309) A. Mircea, *J. Sci. Instrum.*, 1964, **41**, 679–681, doi: 10.1088/0950-7671/41/11/307.

(310) J. Albers and H. L. Berkowitz, *J. Electrochem. Soc.*, 1985, **132**, 2453, doi: 10.1149/1.2113598.

(311) J. Mackey, F. Dynys and A. Sehirlioglu, *Rev. Sci. Instrum.*, 2014, **85**, 085119, doi: 10.1063/1.4893652.

(312) W. C. Navidi, *Statistics for Engineers and Scientists*, McGraw-Hill, 2011.

(313) C. P. Robert and G. Casella, *Monte Carlo Statistical Methods*, Springer New York, New York, NY, 2004, doi: 10.1007/978-1-4757-4145-2.

(314) R. A. Serway and J. W. Jewett, *Physics for Scientists and Engineers*, Cengage Learning, 2013.

(315) C. Kittel, *Introduction to Solid State Physics*, John Wiley & Sons, New York, NY, 4th edn., 2004.

(316) L. J. Van Der Pauw, *Philips Tech. Rev.*, 1958, **20**, 220–224.

(317) J. Bak and D. J. Newman, in *Complex Analysis*, ed. J. Bak and D. J. Newman, Springer, New York, NY, 2010, pp. 195–214, doi: 10.1007/978-1-4419-7288-0_14.

(318) E. M. Stein and R. Shakarchi, *Complex Analysis*, Princeton University Press, 2003.

(319) H. Bateman, *Proceedings of the London Mathematical Society*, 1910, **s2-8**, 223–264, doi: 10.1112/plms/s2-8.1.223.

(320) E. Cunningham, *Proceedings of the London Mathematical Society*, 1910, **s2-8**, 77–98, doi: 10.1112/plms/s2-8.1.77.

(321) B. D. Cullity, *Elements of X-Ray Diffraction*, Addison-Wesley Publishing Company, 1956, 534 pp.

(322) N. W. Ashcroft, W. AshcroftNeil, i. W. Ashcroft and N. D. Mermin, *Solid State Physics*, Holt, Rinehart and Winston, 1976, 868 pp.

(323) C. Suryanarayana and M. G. Norton, *X-Ray Diffraction: A Practical Approach*, Springer US, 1998, doi: 10.1007/978-1-4899-0148-4.

(324) *Rietveld Refinement in the Characterization of Crystalline Materials*, MDPI, 2019, doi: 10.3390/books978-3-03897-528-1.

(325) T. H. Cormen, C. E. Leiserson, R. L. Rivest and C. Stein, *Introduction to Algorithms*, MIT Press, Cambridge, MA, USA, 3rd edn., 2009, 1312 pp.

(326) B. H. Toby and R. B. Von Dreele, *J. Appl. Crystallogr.*, 2013, **46**, 544–549, doi: 10.1107/S0021889813003531.

(327) J. Rodriguez-Carvajal, Satellite Meeting on Powder Diffraction of the XV Congress of the IUCr, Toulouse, France:[sn], 1990, vol. 127.

(328) W. A. Strauss, *Partial Differential Equations: An Introduction*, Wiley & Sons Ltd, 2nd edn., 2008.

(329) H. S. Carslaw and J. C. Jaeger, *Conduction of Heat in Solids*, Oxford University Press, Oxford, New York, Second Edition, 1986, 522 pp.

(330) W. J. Parker, R. J. Jenkins, C. P. Butler and G. L. Abbott, *J. Appl. Phys.*, 1961, **32**, 1679–1684, doi: 10.1063/1.1728417.

(331) R. D. Cowan, *J. Appl. Phys.*, 1963, **34**, 926–927, doi: 10.1063/1.1729564.

(332) J. A. Cape and G. W. Lehman, *J. Appl. Phys.*, 1963, **34**, 1909–1913, doi: 10.1063/1.1729711.

(333) L. M. Clark III and R. E. Taylor, *J. Appl. Phys.*, 1975, **46**, 714–719, doi: 10.1063/1.321635.

(334) K. B. Larson and K. Koyama, *J. Appl. Phys.*, 1968, **39**, 4408–4416, doi: 10.1063/1.1656985.

(335) H. Mehling, G. Hautzinger, O. Nilsson, J. Fricke, R. Hofmann and O. Hahn, *Int. J. Thermophys.*, 1998, **19**, 941–949, doi: 10.1023/A:1022611527321.

(336) *ISO 11357-4:2021 Plastics — Differential Scanning Calorimetry (DSC) — Part 4: Determination of Specific Heat Capacity*, ISO/TC 61/SC 5 Physical-chemical properties, 2021.

(337) H. Kanetsuna, *Polymer*, 1988, **37**, 282–283.

(338) A. International, *ASTM E1269-11*, 2018, doi: 10.1520/E1269-11R18.

(339) A. International, *ASTM E2716-09*, 2014, doi: 10.1520/E2716-23.

(340) A. Matthiessen and C. Vogt, *Annalen der Physik und Chemie*, 1864, **198**, 19–78, doi: 10.1002/andp.18641980504.

(341) G. A. Slack and S. Galginaitis, *Physical Review*, 1964, **133**, A253–A268, doi: 10.1103/physrev.133.a253.

(342) C. J. Glassbrenner and G. A. Slack, *Physical Review*, 1964, **134**, A1058–A1069, doi: 10.1103/physrev.134.a1058.

(343) P. G. Klemens and F. E. Simon, *Proceedings of the Royal Society of London. Series A. Mathematical and Physical Sciences*, 1951, **208**, 108–133, doi: 10.1098/rspa.1951.0147.

(344) R. Gurunathan, R. Hanus, M. Dylla, A. Katre and G. J. Snyder, *Physical Review Applied*, 2020, **13**, 034011, doi: 10.1103/physrevapplied.13.034011.

(345) H. B. G. Casimir, *Physica*, 1938, **5**, 495–500, doi: 10.1016/s0031-8914(38)80162-2.

(346) H.-S. Kim, S. D. Kang, Y. Tang, R. Hanus and G. J. Snyder, *Materials Horizons*, 2016, **3**, 234–240, doi: 10.1039/c5mh00299k.

(347) S. I. Kim, K. H. Lee, H. A. Mun, H. S. Kim, S. W. Hwang, J. W. Roh, D. J. Yang, W. H. Shin, X. S. Li, Y. H. Lee, G. J. Snyder and S. W. Kim, *Science*, 2015, **348**, 109–14, doi: 10.1126/science.aaa4166.

(348) A. J. Friedman, T. K. Chu, P. G. Klemens and C. A. Reynolds, *Physical Review B*, 1972, **6**, 356–363, doi: 10.1103/PhysRevB.6.356.

(349) D. G. Cahill, S. K. Watson and R. O. Pohl, *Physical Review B*, 1992, **46**, 6131–6140, doi: 10.1103/PhysRevB.46.6131.

(350) D. R. Clarke, *Surface and Coatings Technology*, 2003, **163–164**, 67–74, doi: 10.1016/S0257-8972(02)00593-5.

(351) D. J. Griffiths and D. F. Schroeter, *Introduction to quantum mechanics*, Cambridge University Press, Cambridge ; New York, NY, Third edition, 2018.

(352) S. Kurth, M. A. L. Marques and E. K. U. Gross, 2005, 395–402, doi: 10.1016/B0-12-369401-9/00445-9.

(353) W. Kohn and L. J. Sham, *Physical Review*, 1965, **140**, A1133–A1138, doi: 10.1103/PhysRev.140.A1133.

(354) P. Giannozzi, O. Baseggio, P. Bonfà, D. Brunato, R. Car, I. Carnimeo, C. Cavazzoni, S. de Gironcoli, P. Delugas, F. Ferrari Ruffino, A. Ferretti, N. Marzari, I. Timrov, A. Urru and S. Baroni, *J. Chem. Phys.*, 2020, **152**, 154105, doi: 10.1063/5.0005082.

(355) G. Zhang, B. Kirk, L. A. Jauregui, H. Yang, X. Xu, Y. P. Chen and Y. Wu, *Nano Letters*, 2011, **12**, 56–60, doi: 10.1021/nl202935k.

(356) A. Kanatzia, C. Papageorgiou, C. Lioutas and T. Kyratsi, *Journal of Electronic Materials*, 2012, **42**, 1652–1660, doi: 10.1007/s11664-012-2362-5.

(357) B. Poudel, Q. Hao, Y. Ma, Y. Lan, A. Minnich, B. Yu, X. Yan, D. Wang, A. Muto, D. Vashaee, X. Chen, J. Liu, M. S. Dresselhaus, G. Chen and Z. Ren, *Science*, 2008, **320**, 634–8, doi: 10.1126/science.1156446.

(358) C. F. Burmeister and A. Kwade, *Chemical Society Reviews*, 2013, **42**, 7660, doi: 10.1039/C3CS35455E.

(359) S. Rosenkranz, S. Breitung-Faes and A. Kwade, *Powder Technology*, 2011, **212**, 224–230, doi: 10.1016/j.powtec.2011.05.021.

(360) N. Saheb, Z. Iqbal, A. Khalil, A. S. Hakeem, N. Al Aqeeli, T. Laoui, A. Al-Qutub and R. Kirchner, *J. Nanomater.*, 2012, **2012**, 983470, doi: 10.1155/2012/983470.

(361) O. Guillon, J. Gonzalez-Julian, B. Dargatz, T. Kessel, G. Schierning, J. Räthel and M. Herrmann, *Adv. Eng. Mater.*, 2014, **16**, 830–849, doi: 10.1002/adem.201300409.

(362) M. H. Rashid, *Power electronics : circuits, devices, and applications*, Pearson/Prentice Hall, Upper Saddle River, NJ, 3rd ed., 2004.

4

Thermoelectric performance of n-type magnetic element doped Bi_2S_3

Not all those who wander are lost.
— J. R. R. Tolkien, Lord of the Rings

Summary
In this chapter, Bi_2S_3 is co-doped with Cr and Cl to enhance its thermoelectric properties is reported. An enhanced conductivity was achieved due to an increase in the carrier concentration by the substitution of S with Cl. High values of the thermopower were obtained despite high carrier concentrations, this is attributed to an increase in the effective mass, resulted from the magnetic drag introduced by the magnetic Cr dopant. A peak power factor of 566 $\mu W.m^{-1}.K^{-2}$ was obtained for the cast sample of $Bi_{2-x/3}Cr_{x/3}S_{3-x}Cl_x$ with $x = 0.01$ at 320 K, as high as the largest values reported in literature for the sintered samples. These results support the success of co-doping thermoelectric materials with isovalent magnetic and carrier concentration tuning elements to enhance the thermoelectric properties of eco-friendly materials.

4.1 Introduction

Magnetic interactions, as discussed with more details in chapter 2, have been proposed as a strategy to enhance the thermopower in thermoelectric materials such as Bi_2Te_3 [279, 289, 291, 363–365]. Carriers interact with the local magnetic moments, effectively dragging the carriers, which results in an increased effective mass, increasing the thermopower, and decreasing carrier mobility. Overall, this has resulted in an increased power factor [279, 289–291, 363–365].

Tellurium based thermoelectric materials such as Bi_2Te_3 have been employed as power generators and refrigerators in lower temperature applications (<500 K). However, tellurium is expensive and rare, which can hinder the movement towards mass adoption of TE generators. Sulphur, another element from Group IV, is inexpensive, non-toxic, and a sustainable alternative. Bismuth sulphide (Bi_2S_3), in particular, has low thermal conductivity and a large thermopower [366, 367]. However, its high resistivity results in a low zT [368]. Several dopants have been used to optimise the electronic transport properties of Bi_2S_3, including $CuBr_2$ [369], Sb [370], Cu [371], Ag [372], I [373], Cl [374], Se [374, 375], $InCl_3$ [376], $BiCl_3$ [377], and $NbCl_5$ [378]. A lower thermal conductivity was also obtained in Bi_2S_3 by nano structuring [371, 379–381].

The thermoelectric figure-of-merit of pristine Bi_2S_3 was also increased to 0.11 from 0.09 at 623 K by texturing through hot forging and introducing sulphur vacancies [382]. $PbBr_2$ doping of bulk Bi_2S_3 has significantly improved its electrical conductivity by modulation doping and reduced the lattice thermal conductivity by introducing nanoprecipitates, resulting in a peak zT value of 0.8 at 673 K [383].

It has been widely shown that the charge density is increased when halogen group elements (Cl, Br, and I) are doped at the sulphur sites [369, 373, 374]. Here, bismuth sulphide was doped with chromium chloride ($CrCl_3$) to obtain samples of $Bi_{2-x/3}Cr_{x/3}S_{3-x}Cl_x$ (x = 0, 0.005, 0.01, 0.015, and 0.02). Doping with chlorine increases the number of free carriers in the material, leading to a reduction in the electrical resistivity, while the magnetic effect of chromium results in an increase in the carrier effective mass and, consequently, in the thermopower.

4.2 Experimental details

4.2.1 Synthesis

Ultra-high purity bismuth pieces (99.999%, Sigma Aldrich), sulphur pieces (99.9995%, Alfa Aesar Puratronic) and chromium chloride powder (99.99%, Sigma Aldrich) were mixed stoichiometrically to obtain $Bi_{2-x/3}Cr_{x/3}S_{3-x}Cl_x$ (x = 0, 0.005, 0.01, 0.015, and 0.02) [1] in vacuum-sealed quartz ampoules, prepared

[1] One sample was prepared for each composition.

in an inert atmosphere (nitrogen) glove box. In a tube furnace, the tubes were heated up to 350 °C at a rate of 87.5 $K.h^{-1}$, maintained at this temperature for 4 h, heated up to 850 °C at a rate of 150 $K.h^{-1}$, held at this temperature for 4 h, heated up to 1000 °C at a rate of 37.5 $K.h^{-1}$, held at this temperature for 2 h, and, finally, quenched in cold water. The samples were then annealed at 450 °C for 2 days.

The cylindrical ingot samples of 10 mm diameter were then cut into disc shapes of 10 mm in diameter and ≈1.5 mm thickness for Hall effect measurements and bars of $2 \times 2 \times 10$ mm^3 for electrical properties measurements. The electrical resistivity and thermopower were measured simultaneously under 0.1 bar of helium from room temperature to 483 K using an LSR-3 Linseis unit. Hall effect measurements were performed on an Ecopia HMS-3000 Hall Measurement System at room temperature. The density of the samples was determined from the bar-shaped samples using their dimensions and mass. All samples were then manually ground to fine powders by using an agate mortar and pestle. Three samples with $x = 0, 0.005,$ and 0.01 were sintered in a 10 mm diameter graphite die under an axial pressure of 63 MPa at 450 °C for 5 min under vacuum, and the sample with $x = 0.01$ broke during sintering. To avoid this repeating, the sintering temperature was reduced to 350 °C for the samples with composition of $x = 0.015$ and 0.02. The measured density is shown in tables 4.1(a) and (b) for the cast and sintered samples, respectively. The relative density was calculated using the theoretical density of 6.8 $g.cm^{-3}$ [384].

Table 4.1. Density/Relative density of $Bi_{2-x/3}Cr_{x/3}S_{3-x}Cl_x$ ($x = 0, 0.005, 0.01, 0.015,$ and 0.02) samples

(a) Cast samples

x	Density ($g.cm^{-3}$)	Relative density (%)
0	6.59	96.9
0.005	6.55	96.3
0.01	6.65	97.8
0.015	6.45	94.9
0.02	6.68	98.2

(b) Sintered samples

x	Density ($g.cm^{-3}$)	Relative density (%)
0	6.65	97.8
0.005	6.70	98.5
0.015	6.48	95.3
0.02	6.63	97.5

4.2.2 Material characterisation

powder X-ray diffraction (PXRD) analysis was performed via an X'Pert PRO, PANalytical diffractometer using Cu-Kα1 radiation (λ = 1.540 59 Å) to identify the crystal structure of each sample. Rietveld refinement was performed using GSAS-II [326] to obtain the lattice parameters for all samples.

4.2.3 Thermoelectric transport properties

To investigate the electrical and thermal transport properties parallel and perpendicular to the sintering direction, the sintered samples were cut and polished into discs (10 mm in diameter and ≈1.5 mm in thickness, perpendicular to the pressing direction) and slabs of $8 \times 8 \times 2$ mm^3, parallel to the pressing direction for Hall effect and thermal diffusivity measurements, and bars of $2 \times 2 \times 10$ mm^3 (parallel and perpendicular to the pressing direction) for electrical properties measurements. The thermal conductivity (κ) was calculated from the thermal diffusivity (D), specific heat capacity (c_p), and density (d); $\kappa = D \cdot c_p \cdot d$. The temperature-dependent thermal diffusivity D was measured on disc-shaped samples using the laser flash diffusivity method in LFA-467 Hyperflash®(Netzsch). The temperature-dependent heat capacity was derived using a standard sample (Pyroceram-9060). Thermopower and resistivity measurements were carried out at three different thermal gradients: 3 K, 5 K and 8 K, three times each. The resulting thermopower was evaluated using equation 3.11. LFA measurements were taken in both the heating and cooling cycles, with three measurements taken at each temperature. The directions of measurement and sample shapes are illustrated in figure 4.1[2].

4.2.4 Electronic structure calculation

DFT calculations were employed to qualitatively study the electronic band structure of the doped and pristine samples. The Perdew-Burke-Ernzerhof (PBE) and generalised gradient approximation (GGA) exchange-correlation functionals were used [385]. Monkhorst-Pack procedure was used to generate 12×12×12 k-points for the Brillouin zone [386]. The plane wave/pseudopotential approach was employed, with a kinetic energy cut-off of 45 Ry for the wavefunctions and 360 Ry for the electron density. Spin polarisation was considered for the materials doped with Cr.

[2]The sample shapes and measurement directions are the same as seen in chapter 3 figure 3.18 and have been redrawn here simply to emphasise the difference in the measurements made on the cast and sintered samples.

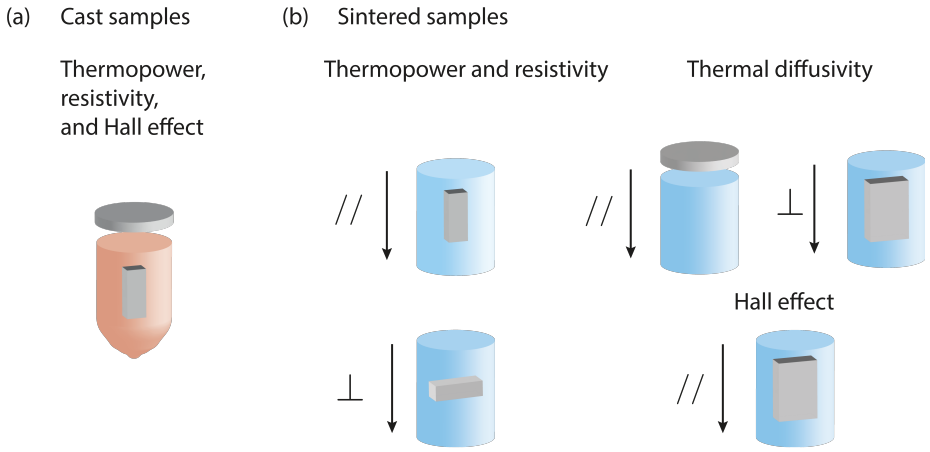

Figure 4.1. Shapes of (a) cast and (b) sintered samples used for measurement of the properties of the samples.

4.3 Results and discussion

4.3.1 Structural analysis

Figure 4.2 shows the PXRD patterns of both the cast and sintered samples. All patterns confirm the presence of a single phase Bi_2S_3 (Materials Project ID mp-22856), orthorhombic crystal structure in the Pnma space group. The diffraction patterns did not show any Cr or Cl due to the low percentage of dopant. The lattice parameters and cell volume of all the samples were determined by the Rietveld refinement of the PXRD patterns (shown in tables 4.2 and 4.3 for the cast and sintered samples, respectively). No variation of the lattice parameters was detected due to comparable ionic radius values of S^{2-} (1.84 Å) and Cl^{1-} (1.81 Å) [387]. Although there is a difference in the ionic radii of Bi^{3+} (1.03 Å) and $Cr^{3+/}$ (0.615 Å) [387], the amount of chromium introduced to Bi_2S_3 is one-third of the chlorine atomic ratio, and therefore no noticeable difference was detected in the lattice parameters. In figure 4.3, the lattice parameter variation with dopant presence is shown graphically.
The lattice parameter values are consistent with the values reported in the literature (a = 11.269 Å, b = 3.972Å, and c = 11.129 Å) [388].

The intensity of the peaks corresponding to the {111} crystal plane for the $x = 0.015$ sample was higher than for the other samples. This might be attributed to the preferred orientation caused by the non-uniform hand milling of the samples used for the PXRD analysis.

4.3.2 Band structure analysis

To understand the effect of dopants on the electronic band structure of Bi_2S_3, the band structure of Bi_2S_3 and doped sample of $Bi_{23}Cr_1S_{33}Cl_3$, for spin-up

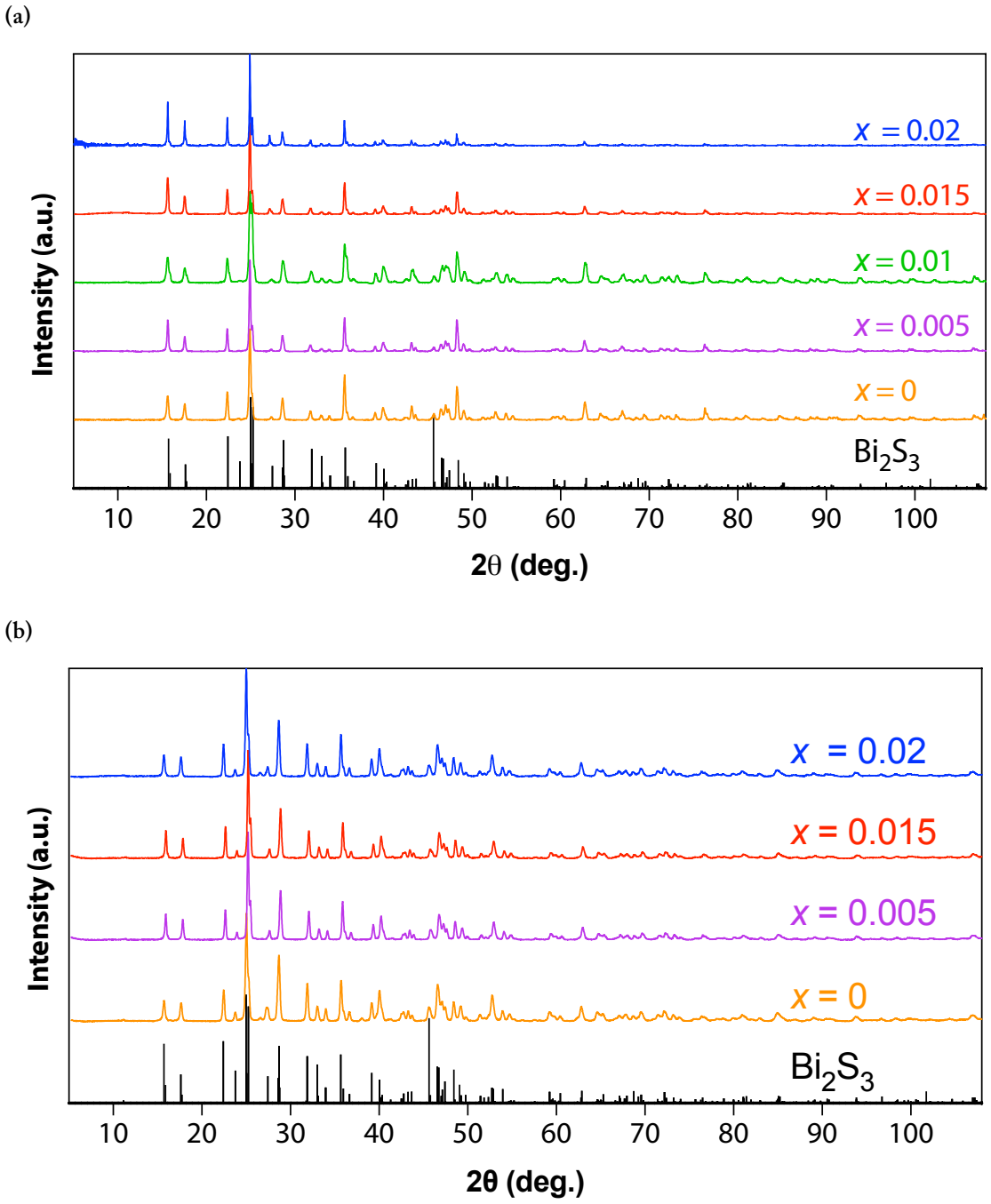

FIGURE 4.2. Powder X-ray diffraction patterns of (a) cast $Bi_{2-x/3}Cr_{x/3}S_{3-x}Cl_x$ (x = 0, 0.005, 0.01, 0.015, and 0.02) and (b) sintered $Bi_{2-x/3}Cr_{x/3}S_{3-x}Cl_x$ (x = 0, 0.005, 0.015, and 0.02) in the range of 5° to 108°.

Table 4.2. Rietveld refined lattice parameters of cast $Bi_{2-x/3}Cr_{x/3}S_{3-x}Cl_x$ (x = 0, 0.005, 0.01, 0.015, and 0.02)

x	a (Å)	b (Å)	c (Å)	V (Å^3)
0	11.290 00(8)	3.980 00(1)	11.1400(1)	500.567(6)
0.005	11.2900(2)	3.9900(8)	11.1400(3)	501.8(1)
0.01	11.2800(5)	3.990 00(3)	11.1400(5)	501.38(3)
0.015	11.2900(2)	3.9800(1)	11.1400(3)	500.57(2)
0.02	11.2900(2)	3.9800(2)	11.1400(4)	500.57(3)

Table 4.3. Rietveld refined lattice parameters of sintered $Bi_{2-x/3}Cr_{x/3}S_{3-x}Cl_x$ (x = 0, 0.005, 0.015, and 0.02)

x	a (Å)	b (Å)	c (Å)	V (Å^3)
0	11.2900(3)	3.9800(1)	11.1400(4)	500.57(3)
0.005	11.2900(2)	3.990 00(9)	11.1400(2)	501.82(2)
0.015	11.2900(2)	3.980 00(8)	11.1400(2)	500.57(2)
0.02	11.2900(2)	3.9800(2)	11.1400(5)	500.57(3)

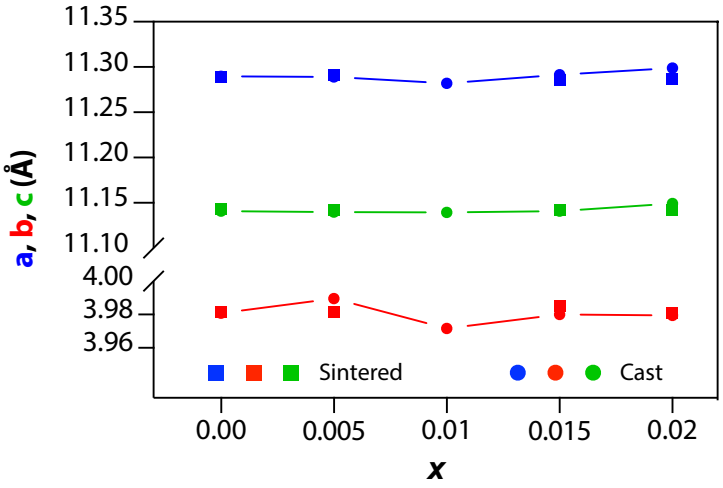

Figure 4.3. Rietveld refined lattice parameters of $Bi_{2-x/3}Cr_{x/3}S_{3-x}Cl_x$ (x = 0, 0.005, 0.01, 0.015, and 0.02) samples as a function of the dopant concentration.

and spin-down states, were calculated (figs. 4.4(a), (b), and (c), respectively).

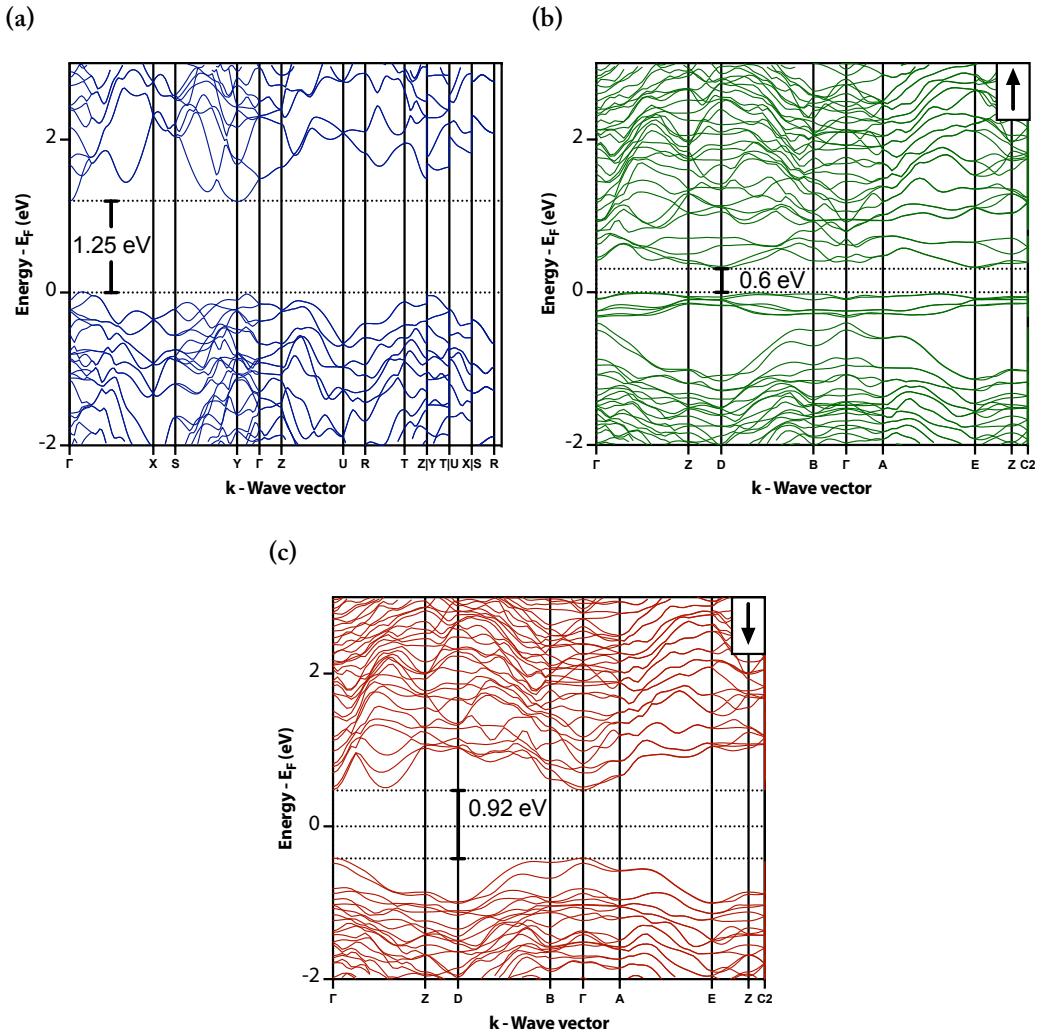

Figure 4.4. Electronic band structure of (a) Bi_2S_3, (b) $Bi_{23}Cr_1S_{33}Cl_3$ spin-up (↑) state, and (c) $Bi_{23}Cr_1S_{33}Cl_3$ spin-down (↓) state.

The calculated bandgap of the pristine material is ≈1.25 eV, which is in good agreement with the reported experimental values of ≈1.3 eV [376, 389, 390]. Both spin-up and spin-down states showed a reduced value of ≈0.6 eV and ≈0.92 eV for the band gap, respectively. The reduction in the band gap for the spin-up state was due to the presence of an additional impurity band.

It is worth noting that these numerical results should only be discussed qualitatively due to the rather high concentration of dopant. The effective masses were calculated for both heavy and light bands in the spin-up (D point) and spin-down (Γ point) band structures using a parabolic band approximation for the band extrema and are shown in figure 4.5.

The electrons of both heavy and light bands show similar values of effective

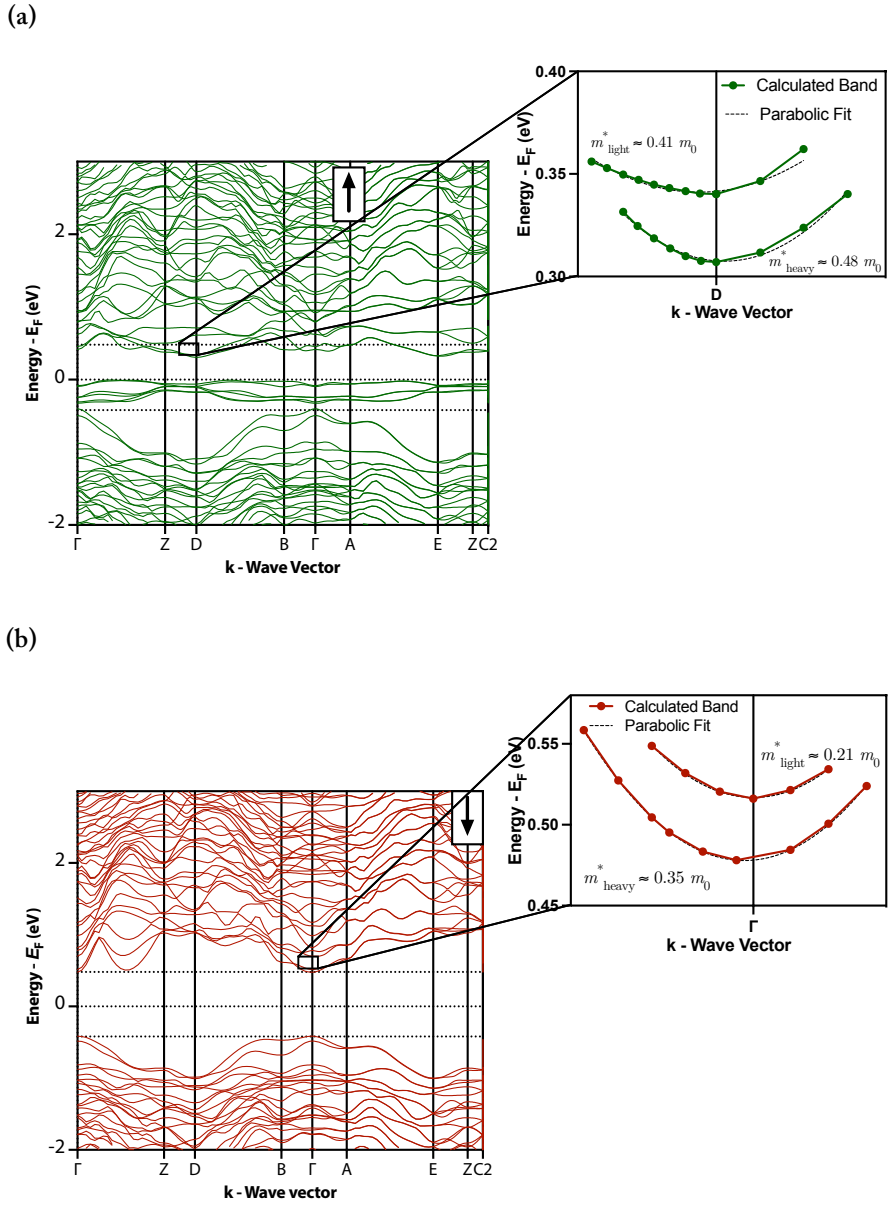

Figure 4.5. Parabolic approximation for the conduction band minimum of (a) $Bi_{23}Cr_1S_{33}Cl_3$ spin-up (↑) state and (b) $Bi_{23}Cr_1S_{33}Cl_3$ spin-down (↓) state.

mass ($m^*_{heavy} \approx 0.48m_0$ and $m^*_{light} \approx 0.41m_0$ for the spin-up band diagram, and $m^*_{heavy} \approx 0.35m_0$ and $m^*_{light} \approx 0.21m_0$ for the spin-down band diagram, where m_0 is the electron rest mass), so band degeneracy does not play a key role in the transport properties of the material.

4.3.3 Transport properties analysis

The thermopower, the electrical resistivity, and the carrier concentration of the cast samples of $Bi_{2-x/3}Cr_{x/3}S_{3-x}Cl_x$ with (x = 0, 0.005, 0.01, 0.015, and 0.02) and sintered samples with (x = 0, 0.005, 0.01, 0.015, and 0.02) measured parallel to the direction of sintering are presented in figure 4.6. The negative thermopower indicates an n-type semiconductor behaviour (figs. 4.6(a) and (b)). The thermopower for the cast pristine Bi_2S_3 sample ranges from −96 μV.K^{-1} at ≈320 K to −135 μV.K^{-1} at ≈480 K. These values are considerably smaller than the reported values of -380 to −498 μV.K^{-1} for Bi_2S_3 seen in the literature [367, 381].

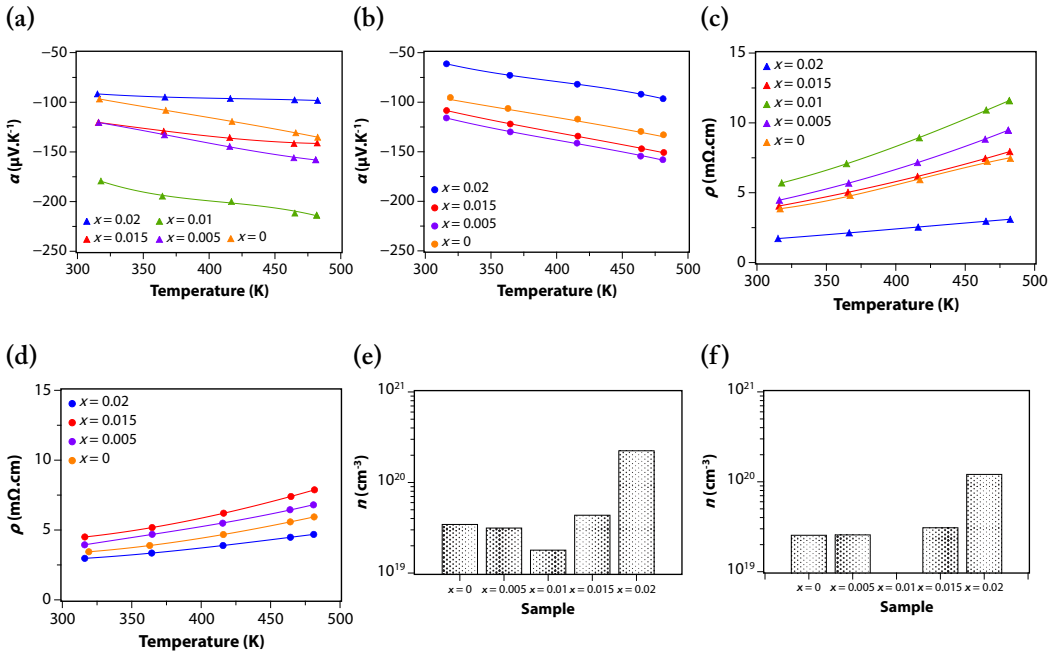

Figure 4.6. The (a), (b) thermopower; (c), (d) electrical resistivity; and (e), (f) Hall carrier concentration of cast $Bi_{2-x/3}Cr_{x/3}S_{3-x}Cl_x$ (x = 0, 0.005, 0.01, 0.015, and 0.02) and of sintered $Bi_{2-x/3}Cr_{x/3}S_{3-x}Cl_x$ (x = 0, 0.005, 0.015, and 0.02), parallel to the direction of sintering as a function of temperature, respectively.

Following Mott's formula for the thermopower[3] [391], the sharp decrease in the thermopower can be explained by an increase in the carrier density in the

[3] $\alpha = \left(\frac{\pi^2 k_B T}{3q}\right)\left\{\frac{dn(E)}{dE} + \frac{d\mu(E)}{dE}\frac{1}{\mu}\right\}_{E=E_F}$.

material. This is supported by the electrical resistivity values for these samples, which varied from 3.16 mΩ.cm at ≈320 K to 4.82 mΩ.cm at ≈480 K (fig. 4.6(c)). These values, including for $x = 0$, are significantly smaller than the reported values of ≈2400 mΩ.cm [382] and ≈7460 mΩ.cm [392] for the pristine sample of Bi_2S_3. These results can be explained by the volatile nature of sulphur during sample fabrication, as a single sulphur atom vacancy donates two free electrons to the bulk material. Vacancies in bismuth sulphide have been previously reported [378, 381] and they commonly occur in chalcogenides [393, 394]. This is supported by the high carrier concentrations measured for both cast and sintered samples (figs. 4.6(e) and (f)). This also greatly reduces the resistivity for the heavily doped samples, reaching 4.82 mΩ.cm at circa 480 K for $x = 0.02$ compared to 7.46 mΩ.cm for the pristine sample at room temperature. The increase in carrier concentration with the addition of dopants may be due to the successful substitution of S with Cl.

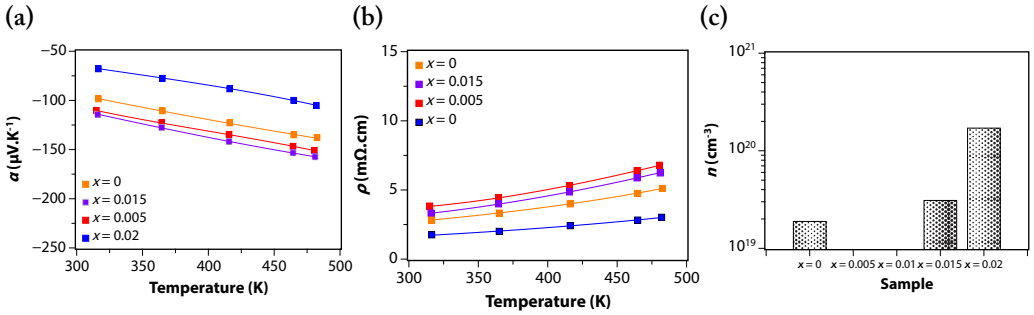

Figure 4.7. The (a) thermopower, (b) electrical resistivity, and (c) Hall carrier concentration of sintered $Bi_{2-x/3}Cr_{x/3}S_{3-x}Cl_x$ (x = 0, 0.005, 0.015, and 0.02), perpendicular to the direction of sintering as a function of temperature, respectively.

No significant difference was observed in the thermopower values of the sintered samples for both measurement directions. However, the electrical resistivity of the samples parallel to the direction of sintering is slightly lower than the ones perpendicular to the sintering direction (fig. 4.7(a)). The thermopower values of sintered samples are very similar to the values obtained from ingots (figs. 4.6(a) and (b)), except for the thermopower of the sample with $x = 0.02$, for which the thermopower was reduced from ≈−100 μV.K^{-1} to ≈−60 μV.K^{-1}. Overall, the electrical resistivities of the sintered samples are lower than those of their cast counterparts. This is attributed to the improved mechanical integrity of sintered samples relative to cast samples. The sintered samples with $x = 0.015$ and 0.02 showed a smaller reduction in resistivity compared to the ones with $x = 0$ and 0.005, due to the changes in the sintering conditions that made the former samples less dense than the latter (the sintering temperature was reduced from 723 K to 623 K for the samples with $x = 0.015$ and 0.02).

To check if there was any influence of the volatile sulphur in the resistivity

and thermopower, the reproducibility of the results was verified by repeating the experiments several times, as shown in figure 4.8. The error bars were estimated using the error analysis discussed in chapter 3 using a Monte Carlo sampling algorithm with 1×10^4 samples[4]. The measured values fall within the estimated error bar, indicating that the difference between the measurements is due to errors in the measurement rather than changes in the transport properties of the material.

[4]The term sample is used here in the statistical sense: "a subset of data from a larger group of data (called the population)". In this case, the samples were generated numerically based on the measurements and sources of error presented in chapter 3.

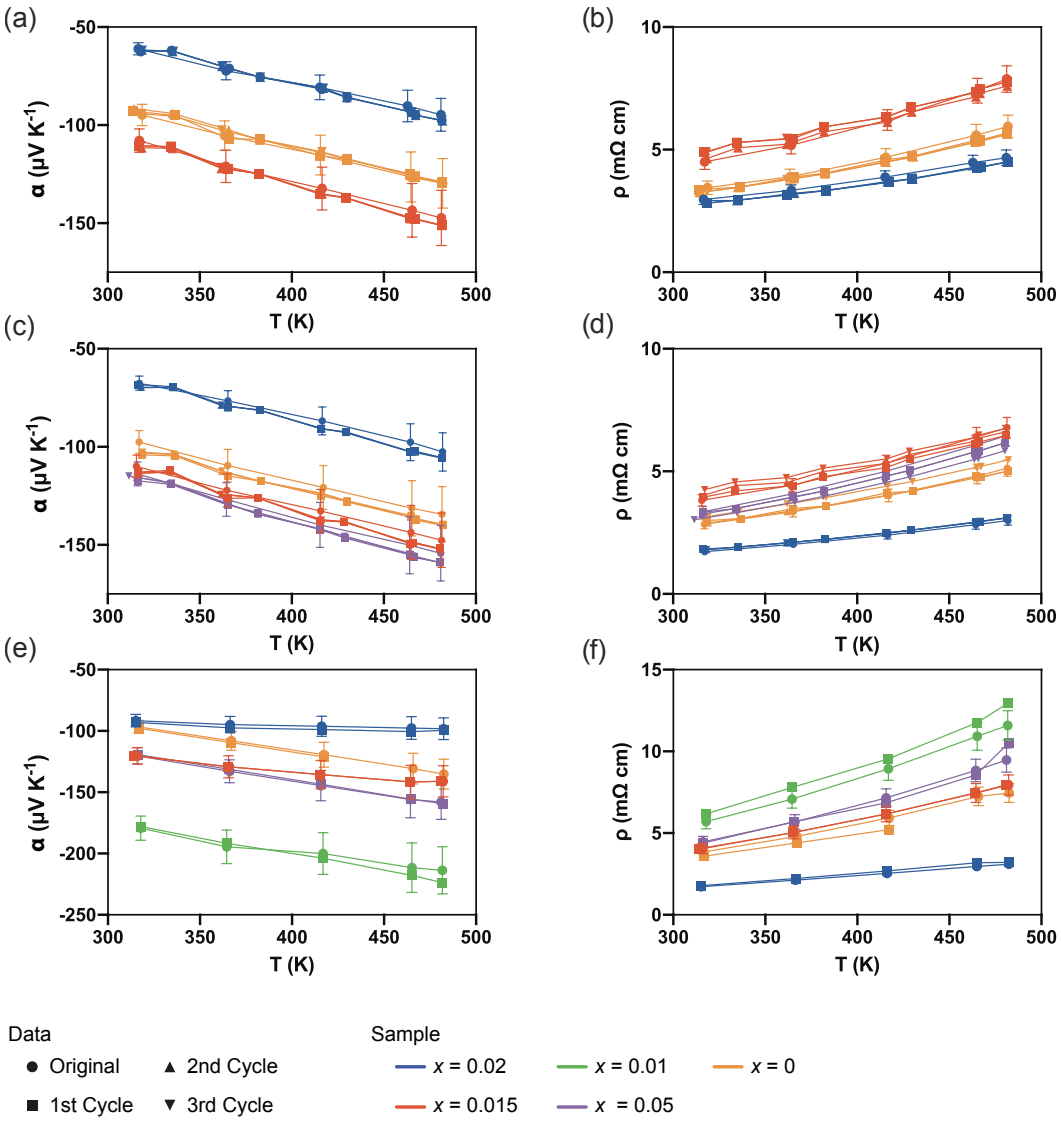

Figure 4.8. Cyclic measurements and errors bars for the (a) thermopower and (b) electrical resistivity of sintered $Bi_{2-x/3}Cr_{x/3}S_{3-x}Cl_x$ (x = 0, 0.005, 0.015, and 0.02) perpendicular to the direction of sintering as a function of temperature; (c) thermopower and (d) electrical resistivity of sintered $Bi_{2-x/3}Cr_{x/3}S_{3-x}Cl_x$ (x = 0, 0.005, 0.015, and 0.02) parallel to the direction of sintering as a function of temperature; (e) thermopower and (f) electrical resistivity of cast $Bi_{2-x/3}Cr_{x/3}S_{3-x}Cl_x$ (x = 0, 0.005, 0.01, 0.015, and 0.02) as a function of temperature.

The power factor (PF) of the cast and sintered samples was measured parallel to the direction of sintering (fig. 4.9). The PF values of the doped samples are much higher than those of the pristine samples due to the optimisation of the electrical conductivity and thermopower. The cast Bi_2S_3 sample with moderate doping ($x = 0.01$) exhibited the highest PF value (about 566 $\mu W.m^{-1}.K^{-2}$ at 320 K), which was circa 2.3 times higher than that of the undoped Bi_2S_3 sample (about 243 $\mu W.m^{-1}.K^{-2}$ at 320 K). The sintered sample with $x = 0.01$ was unavailable for measurement, though. The highest power factor for the sintered sample ($x = 0.005$), measured along the parallel direction to the sintering pressure, was of ≈367 $\mu W.m^{-1}.K^{-2}$ at 480 K (fig. 4.9(b)).

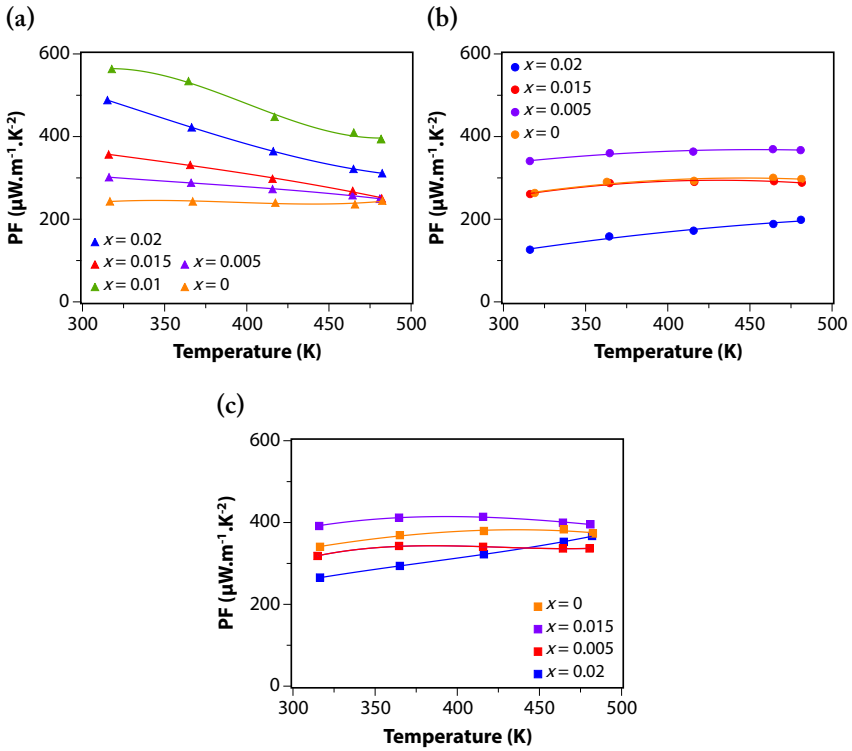

Figure 4.9. The (a), (b), and (c) power factor of cast $Bi_{2-x/3}Cr_{x/3}S_{3-x}Cl_x$ (x = 0, 0.005, 0.01, 0.015, and 0.02) and of sintered $Bi_{2-x/3}Cr_{x/3}S_{3-x}Cl_x$ (x = 0, 0.005, 0.015, and 0.02) along the parallel and perpendicular directions of the sintering pressure as a function of temperature, respectively.

The PFs obtained in this work are compared with the data reported in the literature (fig. 4.10). The results presented here are comparable with the highest values reported in the literature at the same temperature.

Since the samples in the current study have been co-doped with Cr and Cl, the relation between the measured thermopower and carrier concentration from the cast samples is now compared with previous studies of Bi_2S_3 doped with $BiCl_3$ [377], $InCl_3$ [376], $LaCl_3$ [390], $CuBr_2$ [369], and Cl [395], to illustrate

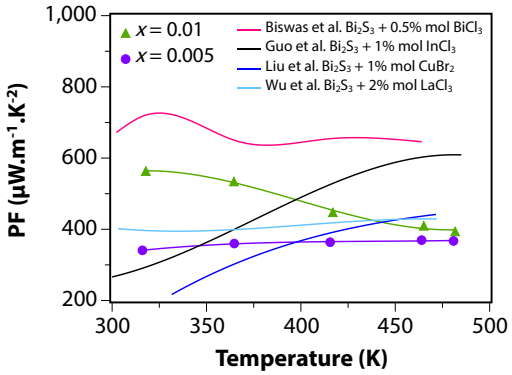

FIGURE 4.10. Power factor comparison of n-type Bi_2S_3 with those reported in the literature of Bi_2S_3 doped with $BiCl_3$, $LaCl_3$, $CuBr_2$, and Cl.

the effect of doping with chromium [396] (see fig. 4.11). The effective mass was evaluated using the SPB model (see chapter 3).

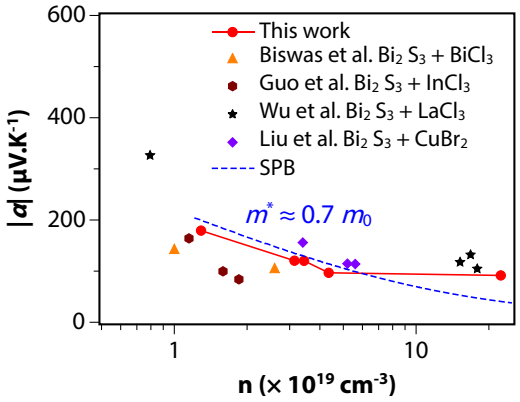

FIGURE 4.11. Hall carrier concentration dependence of room temperature thermopower of n-type cast $Bi_{2-x/3}Cr_{x/3}S_{3-x}Cl_x$ compared to those reported in the literature of Bi_2S_3 doped with $BiCl_3$, $LaCl_3$, $CuBr_2$, and Cl.

For degenerate semiconductors, according to the Pisarenko relation [131], the thermopower is inversely proportional to the carrier concentration with a dependence of $n^{-2/3}$. The experimental data of this study deviates from this ideal relationship, which indicates the changes in the electronic band structure of the material [132]. In particular, the thermopower values of the current study are higher than values predicted by the SPB model and experimental data of samples doped only with Cl [376, 377] (as seen in fig. 4.11).This can also be seen in samples doped with La [376] (due to the presence of La nanoprecipitates) and $CuBr_2$ (due to the energy filtering effect [114]).

The higher values of the thermopower obtained in the current study could be attributed to a magnetic drag effect generated by the magnetic chromium dopant [279, 289, 291, 363–365]. For example, it has been shown that in the

case of magnetic materials, an additional contribution to the thermopower is observed when the materials are subjected to a temperature gradient due to the flux of magnons [261, 262]. The interaction between magnons and carriers leads to an overall increase in the effective mass and, consequently, in the thermopower [280]. Similar enhancement has been observed for non-magnetic materials doped with magnetic elements [289–291, 364]. A more detailed discussion is seen in chapter 2.

In the present study, the effective mass of the cast samples increased significantly from $0.7m_0$ for the pristine sample to $2.1m_0$ for the sample with $x = 0.02$ (see table 4.4), where m_0 is the electron rest mass. This enhanced mass contributed to the higher thermopower compared to materials doped only with Cl [377, 395] and supports the hypothesis of carrier interactions with magnetic elements.

The carrier mobilities also decreased with the increase in the concentration of chromium (as seen in table 4.4). The decrease in carrier mobility is responsible for a decrease in the electrical conductivity [397, 398]. However, the overall effect was an increase in the power factor for the lightly doped sample due to the enhanced thermopower from the increased effective mass.

Table 4.4. Carrier concentration, mobility, and calculated effective mass of cast $Bi_{2-x/3}Cr_{x/3}S_{3-x}Cl_x$

x	n ($\times 10^{19}$ cm^{-3})	μ (cm^2.V^{-1}.s^{-1})	m^*/m_0
0	3.44	15.1	0.76
0.005	3.14	28.2	0.79
0.01	1.79	24.5	0.83
0.015	4.35	16.7	0.75
0.02	22.4	7.59	2.10

The measured carrier concentrations were of 2.54×10^{19}, 2.56×10^{19}, 3.08×10^{19}, and 1.2×10^{20} cm^{-3} and the mobilities were of 60.4, 47.8, 40, and 53.3 cm^2.V^{-1}.s^{-1} for the sintered $Bi_{2-x/3}Cr_{x/3}S_{3-x}Cl_x$ (x = 0, 0.005, 0.015, and 0.02) (see table 4.5).

Table 4.5. Carrier concentration and mobility of sintered $Bi_{2-x/3}Cr_{x/3}S_{3-x}Cl_x$

x	n ($\times 10^{19}$ cm^{-3})	μ (cm^2.V^{-1}.s^{-1})
0	2.44	60.4
0.005	2.56	47.8
0.015	3.08	40
0.02	12.0	53.3

The temperature dependence of κ, κ_e and κ_l for sintered $Bi_{2-x/3}Cr_{x/3}S_{3-x}Cl_x$ (x = 0, 0.005, 0.015 and 0.02) samples measured parallel to the sintering direction are shown in figure 4.14. The measured specific heat capacity is shown in figure 4.13.

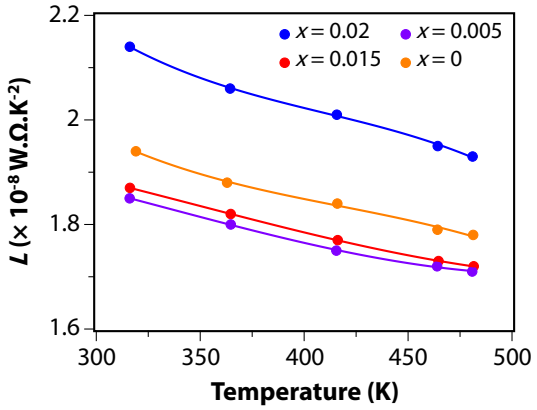

FIGURE 4.12. The Lorenz number of $Bi_{2-x/3}Cr_{x/3}S_{3-x}Cl_x$ (x = 0, 0.005, 0.015, and 0.02) parallel to the direction of sintering as a function of temperature.

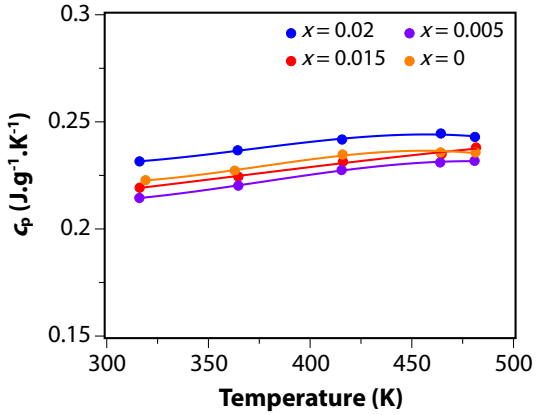

FIGURE 4.13. The specific heat capacity and $Bi_{2-x/3}Cr_{x/3}S_{3-x}Cl_x$ (x = 0, 0.005, 0.015, and 0.02) parallel to the direction of sintering as a function of temperature.

The electronic thermal conductivity was calculated according to the Wiedemann-Franz law as presented in chapter 3 (see equation 2.10) with the Lorenz number (see in figure 4.12) evaluated using the SPB model.

The electronic thermal conductivity values (fig. 4.14(b)) are larger for the doped samples due to their higher carrier concentrations (fig. 4.6(f)). The lattice thermal conductivity values for all samples are very close to the κ values (fig. 4.14(c) and (a)), due to a small contribution of the electronic thermal conductivity to the thermal conductivity of Bi_2S_3. The measurements in the perpendicular direction are shown in figure 4.15.

The κ values of all samples ranged from 0.8 $\sim$ 1.1 $W.m^{-1}.K^{-1}$ at 320 K and from 0.6 $\sim$ 0.8 $W.m^{-1}.K^{-1}$ at 480 K (fig. 4.14(a)). The samples sintered at a lower temperature of 673 K (x = 0.015 and x = 0.02) have higher thermal conductivity. Nevertheless, all samples have similar values of lattice thermal conductivity (fig. 4.14(c)).

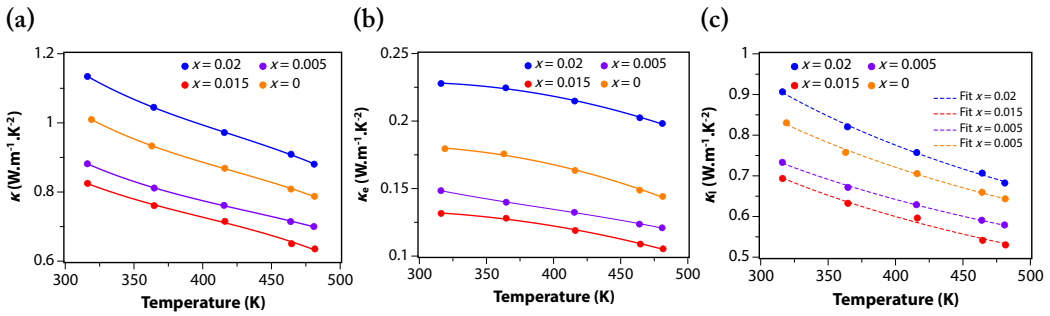

Figure 4.14. The (a) thermal conductivity; (b) electronic thermal conductivity; and (c) lattice thermal conductivity (the dashed lines are the calculations based on the Debye-Callaway model) of sintered $Bi_{2-x/3}Cr_{x/3}S_{3-x}Cl_x$ (x = 0, 0.005, 0.015, and 0.02) parallel to the direction of sintering as a function of temperature.

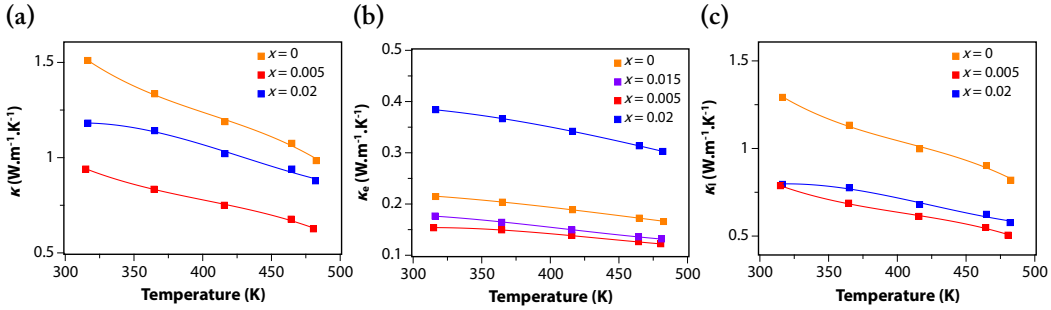

Figure 4.15. The (a) total thermal conductivity; (b) electronic thermal conductivity; and (c) lattice thermal conductivity of sintered $Bi_{2-x/3}Cr_{x/3}S_{3-x}Cl_x$ (x = 0, 0.005, 0.015, and 0.02) perpendicular to the direction of sintering as a function of temperature.

To further study the changes in κ for all samples and the effect of the dopant on the scattering mechanism of phonons in these samples, the Debye-Callaway model was adopted to evaluate the thermal conductivity as previously discussed in chapter 3 (see equations 3.72 and 3.74). For this set of samples, the combined relaxation time (τ_c) expression was simplified to

$$\tau_c^{-1} = \tau_{pd}^{-1} + \tau_n^{-1} + \tau_u^{-1} + \tau_{gb}^{-1} = A\omega^4 + \beta\tau_u^{-1} + B_u T\omega^2 e^{-\frac{\theta_D}{3T}} + \frac{\upsilon}{L}, \qquad (4.1)$$

where τ_{pd}, τ_n, τ_u and τ_{gb} are, respectively, the relaxation times for points defects scattering, normal three phonon process, Umklapp process, and grain-boundary scattering, L is the average grain size, and the coefficients A, β, and B_u are fitting parameters. The values of θ_D = 283 K and υ = 2775 m.s^{-1} were adopted from the literature [399].

Table 4.6 presents the calculated parameters for all sintered samples parallel to the direction of sintering. The average grain size was obtained from the Rietveld

refinement of the PXRD patterns. The fitted values are shown as dashed lines in figure 4.14(c).

Table 4.6. Calculated parameters for the Debye-Callaway model for sintered $Bi_{2-x/3}Cr_{x/3}S_{3-x}Cl_x$ (x = 0, 0.005, 0.015, and 0.02) samples parallel to the direction of sintering.

x	A (10^{-41} s^3)	β	B_u (10^{-18} s.K)	L (μm)
0	4.9	2.2	3.6	1.3
0.005	7.3	6.3	1.4	1.4
0.015	5.6	6.4	2.0	1.3
0.02	3.5	2.4	3.9	1.5

The results show a significant increase in point defect scattering with increasing dopant concentration. In general, the thermal conductivity values of the sintered samples are similar for all samples. The changes in β and B_u indicate that the main mechanism causing these differences is due to changes in phonon-phonon scattering.

Again, the reproducibility of the results was verified by repeating the experiment several times, and the results are shown in figure 4.16. There was no noticeable change in the measured thermal conductivity values, again indicating that no changes in material composition occurred during heating and cooling.

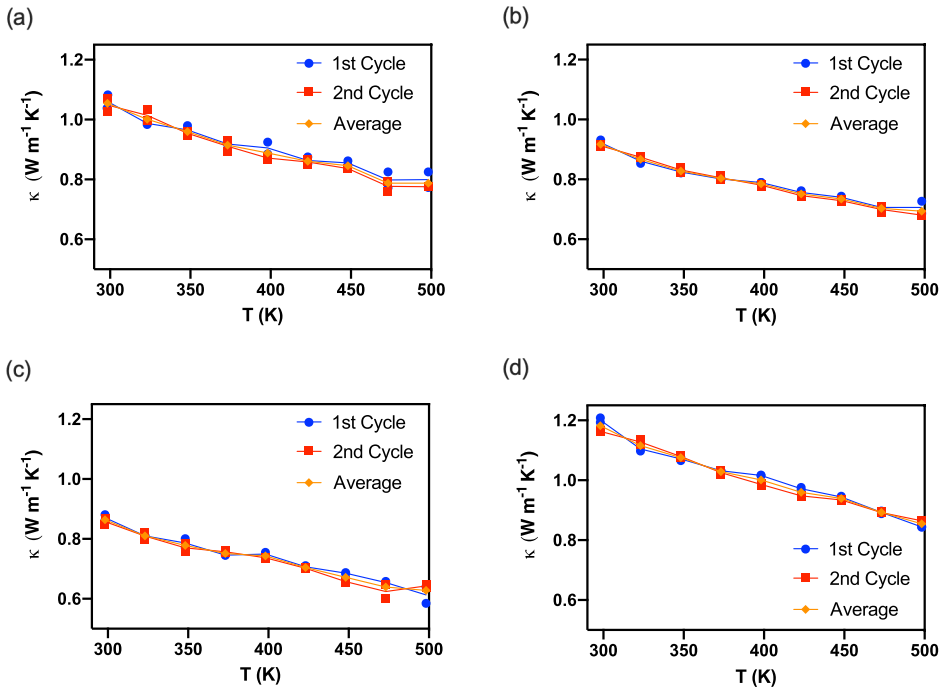

Figure 4.16. Cyclic measurements for the thermal conductivity of $Bi_{2-x/3}Cr_{x/3}S_{3-x}Cl_x$ for (a) x = 0, (b) x = 0.005, (b) x = 0.015, and (d) x = 0.02 parallel to the direction of sintering as a function of temperature.

4.3.4 Figure of merit zT

Figure 4.17(a) shows the zT values for the sintered samples (measured parallel to the sintering direction). The maximum zT value of ≈0.25 was obtained for the sample with x = 0.005 at 480 K. It is worth noting that the sample $Bi_{2-x/3}Cr_{x/3}S_{3-x}Cl_x$ (x = 0.01), with the potentially highest zT value, was not available for measurement in the sintered form. Figure 4.17(b) compares the zT values of the samples in the current study with the highest values reported in the literature at the same temperature. There is a difference in the zT values obtained from measurements performed parallel and perpendicular to the direction of sintering due to the crystal structure of Bi_2S_3 (fig. 4.17(c)).

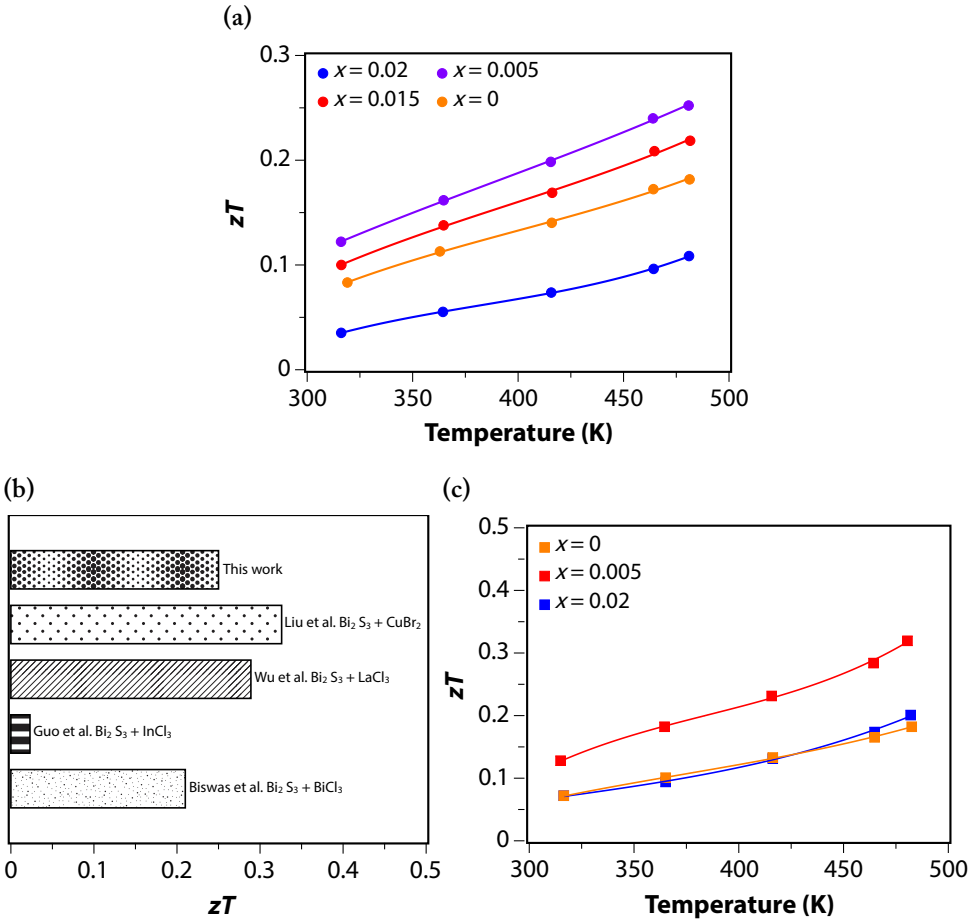

FIGURE 4.17. (a) zT values of sintered $Bi_{2-x/3}Cr_{x/3}S_{3-x}Cl_x$ (x = 0, 0.005, 0.015, and 0.02) parallel to the direction of sintering as a function of temperature; (b) zT of sintered $Bi_{2-x/3}Cr_{x/3}S_{3-x}Cl_x$ (x = 0.005) at 480 K compared to Bi_2S_3 doped with $BiCl_3$ [377], $InCl_3$ [376], $LaCl_3$ [390], and $CuBr_2$ [369]; and (c) zT values of sintered $Bi_{2-x/3}Cr_{x/3}S_{3-x}Clx$ (x = 0, 0.005, 0.015, and 0.02) perpendicular to the direction of sintering as a function of temperature.

4.4 Conclusion

In this chapter, Bi_2S_3 with added $CrCl_3$ was fabricated using a melt annealing technique followed by sintering via SPS. The electronic properties of both the cast and sintered samples were measured. Compared to samples with non-magnetic dopants, the thermopower increased at a similar carrier concentration. This increase might be attributed to the magnetic drag effect, where the interaction between magnetic moments and carriers effectively increases the effective mass of the carriers and consequently the thermopower. The increase in effective mass resulted in a decrease in carrier mobility and electrical conductivity in samples with higher carrier concentrations. Thermal conductivity measurements of the sintered samples showed similar values for all samples, with variations due

to carrier concentration and increased scattering caused by impurities. The zT values obtained in this study are comparable to the highest values reported in the literature and provide experimental evidence that the inclusion of magnetic dopants can improve the overall efficiency of thermoelectric materials. It should be noted that the samples studied in this chapter were codoped with Cr and Cl, which means that the conclusions drawn here regarding the contributions of each individual dopant are only indicative. In order to have a complete picture, samples containing only Cr would have to be prepared, as samples prepared with only Cl have already been seen in the literature and have been discussed in this text.

References

(114) M. Liu and X. Y. Qin, *Appl. Phys. Lett.*, 2012, **101**, 132103, doi: 10.1063/1.4755768.

(131) I. I. Ravich, *Semiconducting Lead Chalcogenides*, Springer US, 1970, doi: 10.1007/978-1-4684-8607-0.

(132) T. Zou, X. Qin, Y. Zhang, X. Li, Z. Zeng, D. Li, J. Zhang, H. Xin, W. Xie and A. Weidenkaff, *Sci. Rep.*, 2015, **5**, 17803, doi: 10.1038/srep17803.

(261) M. V. Costache, G. Bridoux, I. Neumann and S. O. Valenzuela, *Nat. Mater.*, 2011, **11**, 199–202, doi: 10.1038/nmat3201.

(262) S. J. Watzman, R. A. Duine, Y. Tserkovnyak, S. R. Boona, H. Jin, A. Prakash, Y. H. Zheng and J. P. Heremans, *Phys. Rev. B*, 2016, **94**, 144407, doi: 10.1103/PhysRevB.94.144407.

(279) N. Tsujii and T. Mori, *Appl. Phys. Express*, 2013, **6**, 043001, doi: 10.7567/Apex.6.043001.

(280) R. Ang, A. U. Khan, N. Tsujii, K. Takai, R. Nakamura and T. Mori, *Angew. Chem. Int. Ed. Engl.*, 2015, **54**, 12909–13, doi: 10.1002/anie.201505517.

(289) F. Ahmed, N. Tsujii and T. Mori, *J. Mater. Chem.A*, 2017, **5**, 7545–7554, doi: 10.1039/C6TA11120C.

(290) J. B. Vaney, S. A. Yamini, H. Takaki, K. Kobayashi, N. Kobayashi and T. Mori, *Mater. Today Phys.*, 2019, **9**, 100090, doi: 10.1016/j.mtphys.2019.03.004.

(291) S. Acharya, S. Anwar, T. Mori and A. Soni, *J. Mater. Chem. C*, 2018, **6**, 6489–6493, doi: 10.1039/C8TC00788H.

(326) B. H. Toby and R. B. Von Dreele, *J. Appl. Crystallogr.*, 2013, **46**, 544–549, doi: 10.1107/S0021889813003531.

(363) H. Takaki, K. Kobayashi, M. Shimono, N. Kobayashi, K. Hirose, N. Tsujii and T. Mori, *Mater. Today Phys.*, 2017, **3**, 85–92, doi: 10.1016/j.mtphys.2017.12.006.

(364) T. Mori, *Small*, 2017, **13**, 1702013, doi: 10.1002/smll.201702013.

(365) N. Tsujii, A. Nishide, J. Hayakawa and T. Mori, *Sci. Adv.*, **5**, eaat5935, doi: 10.1126/sciadv.aat5935.

(366) W. Liu, K. C. Lukas, K. McEnaney, S. Lee, Q. Zhang, C. P. Opeil, G. Chen and Z. Ren, *Energy Environ. Sci.*, 2013, **6**, 552–560, doi: 10.1039/c2ee23549h.

(367) Y. Guo, X. Du, Y. Wang and Z. Yuan, *J. Alloys Compd.*, 2017, **717**, 177–182, doi: 10.1016/j.jallcom.2017.05.067.

(368) B. Chen, C. Uher, L. Iordanidis and M. G. Kanatzidis, *Chem. Mater.*, 1997, **9**, 1655–1658, doi: 10.1021/cm970033m.

(369) Z. H. Liu, Y. L. Pei, H. Y. Geng, J. C. Zhou, X. F. Meng, W. Cai, W. S. Liu and J. H. Sui, *Nano Energy*, 2015, **13**, 554–562, doi: 10.1016/j.nanoen.2015.03.036.

(370) Y. Kawamoto and H. Iwasaki, *J. Electron. Mater.*, 2014, **43**, 1475–1479, doi: 10.1007/s11664-013-2742-5.

(371) Z. H. Ge, B. P. Zhang, Y. Liu and J. F. Li, *Phys. Chem. Chem. Phys.*, 2012, **14**, 4475–81, doi: 10.1039/c2cp23955h.

(372) Y. Q. Yu, B. P. Zhang, Z. H. Ge, P. P. Shang and Y. X. Chen, *Mater. Chem. Phys.*, 2011, **131**, 216–222, doi: 10.1016/j.matchemphys.2011.09.010.

(373) J. Yang, G. W. Liu, J. N. Yan, X. Z. Zhang, Z. Q. Shi and G. J. Qiao, *J. Alloys Compd.*, 2017, **728**, 351–356, doi: 10.1016/j.jallcom.2017.08.148.

(374) X. L. Du, F. S. Cai and X. W. Wang, *J. Alloys Compd.*, 2014, **587**, 6–9, doi: 10.1016/j.jallcom.2013.10.185.

(375) Y. Chen, D. Wang, Y. Zhou, Q. Pang, J. Shao, G. Wang, J. Wang and L.-D. Zhao, *Front. Phys-beijing.*, 2018, **14**, 13, doi: 10.1007/s11467-018-0845-4.

(376) J. Guo, Z. H. Ge, F. Qian, D. H. Lu and J. Feng, *J. Mater. Sci.*, 2020, **55**, 263–273, doi: 10.1007/s10853-019-04008-3.

(377) K. Biswas, L. D. Zhao and M. G. Kanatzidis, *Adv. Energy Mater.*, 2012, **2**, 634–638, doi: 10.1002/aenm.201100775.

(378) Z. Y. Wang, J. Guo, J. Feng and Z. H. Ge, *J. Solid State Chem.*, 2021, **297**, 122043, doi: 10.1016/j.jssc.2021.122043.

(379) Z. H. Ge, B. P. Zhang, P. P. Shang and J. F. Li, *J. Mater. Chem.*, 2011, **21**, 9194–9200, doi: 10.1039/c1jm11069a.

(380) Z.-H. Ge, B.-P. Zhang and J.-F. Li, *J. Mater. Chem.*, 2012, **22**, 17589, doi: 10.1039/c2jm33603k.

(381) L. J. Zhang, B. P. Zhang, Z. H. Ge and C. G. Han, *Solid State Commun.*, 2013, **162**, 48–52, doi: 10.1016/j.ssc.2013.03.013.

(382) L. D. Zhao, B. P. Zhang, W. S. Liu, H. L. Zhang and J. F. Li, *J. Solid State Chem.*, 2008, **181**, 3278–3282, doi: 10.1016/j.jssc.2008.08.022.

(383) J. Guo, Y. X. Zhang, Z. Y. Wang, F. S. Zheng, Z. H. Ge, J. C. Fu and J. Feng, *Nano Energy*, 2020, **78**, 105227, doi: 10.1016/j.nanoen.2020.105227.

(384) H. Mizoguchi, H. Hosono, N. Ueda and H. Kawazoe, *Journal of Applied Physics*, 1995, **78**, 1376–1378, doi: 10.1063/1.360315.

(385) J. P. Perdew, K. Burke and M. Ernzerhof, *Phys. Rev. Lett.*, 1996, **77**, 3865–3868, doi: 10.1103/PhysRevLett.77.3865.

(386) H. J. Monkhorst and J. D. Pack, *Phys. Rev. B*, 1976, **13**, 5188–5192, doi: 10.1103/PhysRevB.13.5188.

(387) L. Pauling, *The Nature of the Chemical Bond and the Structure of Molecules and Crystals: An Introduction to Modern Structural Chemistry*, Cornell University Press, Third, 1960, 664 pp.

(388) L. F. Lundegaard, E. E. Makovicky, T. Boffa-Ballaran and T. Balic-Zunic, *Phys. Chem. Miner.*, 2005, **32**, 578–584, doi: 10.1007/s00269-005-0033-2.

(389) W. Ji, X.-L. Shi, W.-D. Liu, H. Yuan, K. Zheng, B. Wan, W. Shen, Z. Zhang, C. Fang, Q. Wang, L. Chen, Y. Zhang, X. Jia and Z.-G. Chen, *Nano Energy*, 2021, **87**, 106171, doi: 10.1016/j.nanoen.2021.106171.

(390) Y. Wu, Q. Lou, Y. Qiu, J. Guo, Z. Y. Mei, X. Xu, J. Feng, J. Q. He and Z. H. Ge, *Inorg. Chem. Front.*, 2019, **6**, 1374–1381, doi: 10.1039/c9qi00213h.

(391) M. Jonson and G. D. Mahan, *Phys. Rev. B*, 1980, **21**, 4223–4229, doi: 10.1103/PhysRevB.21.4223.

(392) J. Guo, Q. Lou, Y. Qiu, Z.-Y. Wang, Z.-H. Ge, J. Feng and J. He, *Appl. Surf. Sci.*, 2020, **520**, 146341, doi: 10.1016/j.apsusc.2020.146341.

(393) S. Chen, H. Bai, J. Li, W. Pan, X. Jiang, Z. Li, Z. Chen, Y. Yan, X. Su, J. Wu, C. Uher and X. Tang, *ACS Appl. Mater. Interfaces*, 2020, **12**, 19664–19673, doi: 10.1021/acsami.0c02155.

(394) X. F. Tan, X. J. Tan, G. Q. Liu, J. T. Xu, H. Z. Shao, H. Y. Hu, M. Jin, H. C. Jiang and J. Jiang, *J. Mater. Chem. C*, 2017, **5**, 7504–7509, doi: 10.1039/c7tc02162c.

(395) J. Guo, J. Yang, Z.-H. Ge, B. Jiang, Y. Qiu, Y.-K. Zhu, X. Wang, J. Rong, X. Yu, J. Feng and J. He, *Adv. Funct. Mater.*, 2021, **31**, 2102838, doi: 10.1002/adfm.202102838.

(396) S. D. Kang and G. J. Snyder, *arXiv*, 2018, doi: 10.48550/arXiv.1710.06896.

(397) B. Ge, Z. Shi, C. Zhou, J. Hu, G. Liu, H. Xia, J. Xu and G. Qiao, *Journal of Alloys and Compounds*, 2019, **809**, 151717, doi: 10.1016/j.jallcom.2019.151717.

(398) Y. Xiao, D. Wang, Y. Zhang, C. Chen, S. Zhang, K. Wang, G. Wang, S. J. Pennycook, G. J. Snyder, H. Wu and L.-D. Zhao, *Journal of the American Chemical Society*, 2020, **142**, 4051–4060, doi: 10.1021/jacs.0c00306.

(399) H. Koc, H. Ozisik, E. Deligöz, A. M. Mamedov and E. Ozbay, *J. Mol. Model.*, 2014, **20**, 2180, doi: 10.1007/s00894-014-2180-1.

5

Multiphase iodine doped Bi_2Te_3-$Bi_{14}Te_{13}S_8$: effects of phonon scattering and bipolar effect suppression

Do not disturb thyself by thinking of the whole of thy life. Let not thy mind wander up and down, and heap together in her thoughts the many troubles and grievous calamities which thou art as subject unto as any other. But on every occasion, put this question unto thyself, and say: What is it that in this present matter, seems unto thee so intolerable? For thou wilt be ashamed to confess it. Then upon this presently call to mind, that neither that which is future nor that which is past can hurt thee; but that only which is present.
— Marcus Aurelius, Meditations. 8.36

Summary
Bismuth telluride based alloys are known to have the highest efficiencies for low temperature (<500K) applications among thermoelectric materials. Despite significant progress in improving the efficiency of p-type Bi_2Te_3-based materials by engineering the electronic band structure via the convergence of multiple bands, the n-type counterparts still suffer from poor efficiency. In this chapter, multiphase Bi_2Te_3-$Bi_{14}Te_{13}S_8$ compounds have been fabricated to take advantage of phonon scattering to improve the overall efficiency of these materials.
The inclusion of a secondary phase, $Bi_{14}Te_{13}S_8$, within the Bi_2Te_3 matrix resulted in the formation of an energy barrier at the interface, leading to higher thermopower and consequently higher power factor in the multiphase compounds compared to the single phase alloys.

5.1 Introduction

Bismuth telluride alloys have the highest efficiencies among thermoelectric materials for room/low temperature applications. Significant progress has been made in improving the efficiency of p-type Bi_2Te_3-based materials, in particular $(Bi,Sb)_2Te_3$, by introducing secondary phases [60, 110, 154, 203, 252, 400, 401], nanostructuring [357, 402, 403], and liquid phase sintered $Bi_{0.5}Sb_{1.5}Te_3$ [347]. The development of n-type Bi_2Te_3 alloys has not enjoyed the same level of improvement as its n-type counterpart, mainly due to the fact that the band structure of bismuth telluride favours the development of p-type materials, since the band degeneracy of the valence band is three times greater than that of the conduction band [404].

In this chapter, a series of multiphase samples of Bi_2Te_3-$Bi_{14}Te_{13}S_8$ with a composition of $Bi_2(Te_{2.75-x/3}S_{0.25-x/3})I_x$ (x = 0, 0.005, 0.01 and 0.02) are investigated. This work was motivated by the results presented in the first section of [405],where multiphase pseudobinary compounds of Bi_2Te_3 and Bi_2S_3 were studied, and the best composition was $Bi_2Te_{2.75}S_{0.25}$.

5.2 Experimental details

5.2.1 Synthesis

A set of $Bi_2(Te_{2.75-x/3}S_{0.25-x/3})I_x$ (x = 0, 0.005, 0.01, and 0.02) samples were synthesised by direct reaction of stoichiometric amounts of high purity Bi (99.999%, Alfa Aesar), Te (99.999%, Alfa Aesar) shots, dried S (99.99%, Alfa Aesar) powder, and BiI_3 (99.999%, Alfa Aesar Puratronic®) powder in vacuum sealed quartz tubes in an inert atmosphere glovebox. The tubes were homogenised at 850 °C for 16 h, quenched in cold water, and annealed at 450 °C for 72 h. The resulting ingots were ground by hand into fine powders using an agate mortar and pestle housed in an inert atmosphere glovebox. The powders were then loaded into a graphite die and sintered under vacuum to produce 11 mm diameter rods using SPS at 400 °C and an axial pressure of 50 MPa for 5 min. The relative density of the sintered samples, calculated from the weight and dimensions of the rods, was ≤92% for all the samples.

5.2.2 Materials characterisation

Phase purity and crystal structure of the sintered samples were characterised by PXRD using a PANalytical X'Pert PRO X-ray diffractometer with Cu-Kα1 radiation (λ = 1.54059 Å, 40 kV, 40 mA). Rietveld refinements were performed on the acquired diffraction patterns using the GSAS-II software [326].

The electronic transport properties of the sintered samples were investigated in parallel to the sintering direction by cutting $\approx 2 \times 2 \times 8$ mm^3 bars from the

sintered rods. Measurements were carried out from room temperature to 530 K under a helium atmosphere using a Linseis LSR-3 apparatus.

The thermal transport properties of the samples were also investigated in the parallel direction to the sintering direction by cutting discs of ≈10 mm of diameter and ≈1.5 mm of thickness. The thermal conductivities (κ) were calculated from the thermal diffusivity (D), specific heat capacity (c_p), and density (d) of the samples: $\kappa = D \cdot c_p \cdot d$. The thermal diffusivity was measured using a Netzsch LFA-467 Hyperflash®instrument. The specific heat capacity was measured using the sapphire standard test ASTM E1269-11(2018) (see section 3.1.8.1) with a PerkinElmer-DSC 8000 differential scanning calorimeter.

The disc-shaped samples were also used to measure the carrier concentration and electronic mobilities using the van der Pauw technique with an ECOPIA HMS 3000 Hall measurement system.

5.3 Results and discussion

5.3.1 Structural and phase analysis

Figure 5.1 shows the diffraction patterns of these samples. All patterns confirm the presence of a primary phase of trigonal Bi_2Te_3 belonging to the $R\bar{3}m$ space group (Materials Projec ID mp-568390) and a secondary phase of rhombohedral $Bi_{14}Te_{13}S_8$ belonging to the $R\bar{3}$ space group (Materials Projec ID mp-557619).

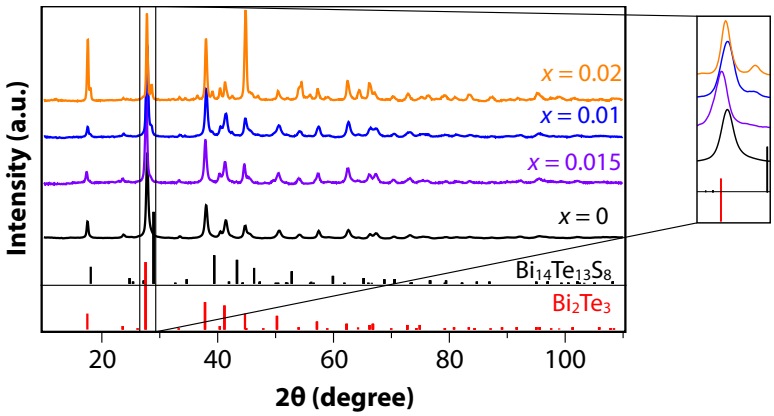

Figure 5.1. Room temperature XRD patterns of $Bi_2(Te_{2.75-x/3}S_{0.25-x/3})I_x$ (x = 0, 0.005, 0.01, and 0.02) in the range of 5° to 108°. Inset shows a zommed area between 27° and 29°.

The quantitative phase compositions obtained from the Rietveld refinement of the diffraction patterns and the weighted profile R-factor[1] (Rwp) are given in table 5.1. The Rwp values are within the acceptable range [407] and given the phase percentage estimates and attributed errors, all samples can be assumed to have the same phase composition[2].

Table 5.1. Quantitative phase analysis of $Bi_2(Te_{2.75-x/3}S_{0.25-x/3})I_x$ (x = 0, 0.005, 0.01, and 0.02) obtained from the Rietveld refinement of the diffraction patterns

x	Bi_2Te_3 (wt.%)	$Bi_{14}Te_{13}S_8$ (wt.%)	Rwp (%)
0	75.3(18)	24.7(15)	8.95
0.005	75.1(21)	24.9(5)	12.15
0 .01	78.8(17)	21.2(10)	10.78
0.02	78.3(21)	21.7(15)	12.43

Refinement plots are shown in figure 5.2.

[1] See definition in [406].
[2] The lattice parameters and unit cell volumes are all presented in the appendix E

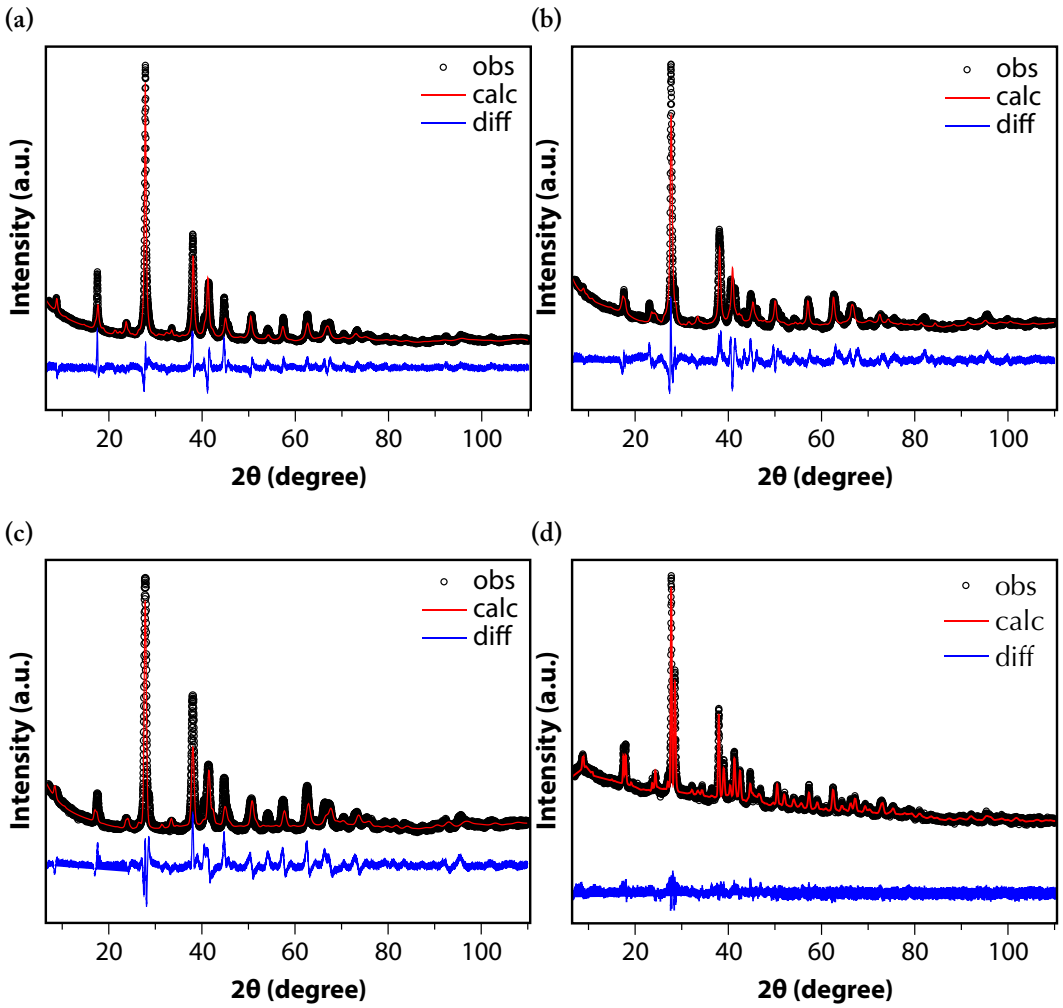

FIGURE 5.2. Rietveld refinement plots of $Bi_2(Te_{2.75-x/3}S_{0.25-x/3})I_x$, x = (a) 0, (b) 0.01, (c) 0.015, and (d) 0.02.

5.3.1.1 Control of the sintering procedure

The sintering machine used for these samples (KCE FCT-H HP D-25 SD, FCT Systeme GmbH, Rauenstein, Germany) has a suboptimal force control for the desired pressure range used in this set of samples. This resulted in a lower effective pressure than the set one, resulting in low density samples (less than 92% of nominal). However, the sintering temperature was accurately controlled. Figures 5.3(a) and (b) show the measured sintering temperature and force for sample $x = 0.005$. The inset in figure 5.3(a) shows that the temperature of the process was accurately controlled, while the sporadic behaviour of the measured force seen in figure 5.3(b) demonstrates the poor pressure control applied by the SPS machine. The non-oscillatory overshoot behaviour of the temperature is indicative of a closed-loop system with a PI controller and a stable open-loop

transfer function, so it is not surprising that the closed-loop system is stable [3].

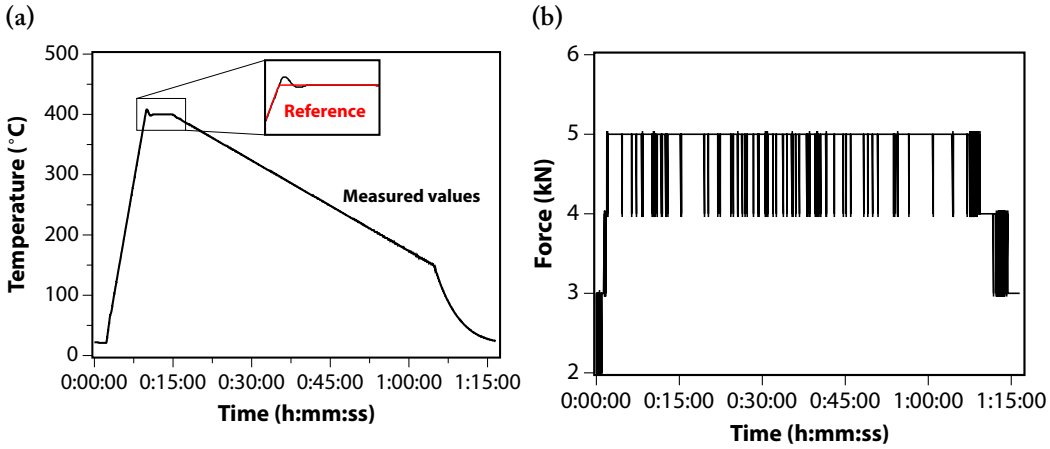

FIGURE 5.3. Measured (a) temperature during the sintering process with the inset showing the accurate temperature control and (b) force applied during the sintering process for $x = 0.005$.

5.3.2 Transport properties analysis and figure of merit zT

The Hall carrier concentration and mobility measured at room temperature of all samples are shown in table 5.2.

Table 5.2. Room-temperature Hall carrier concentration (n_H) and Hall mobility (μ_H)

x	$n_H(\times 10^{19}\,cm^{-3})$	$\mu_H\,(cm^2.V^{-1}.s^{-1})$
0	0.95	55.0
0.005	−1.7	232.9
0.01	−4.1	314.2
0.02	−4.3	374.5

The temperature dependent thermopower, electrical conductivity, thermal conductivity, and figure of merit zT of the iodine-doped multiphase $Bi_2Te_{2.75}S_{0.25}$ compound measured parallel to the sintering direction in the temperature range of 300 to 530 K are shown in figures 5.4(a)-(d). The samples are labelled with their Hall carrier concentrations in figure 5.4 for ease of comparison.

The positive sign of the thermopower of $x = 0$ indicates that it is a p-type material, and conversely, the negative sign of the thermopower for the doped samples indicates that the samples are n-type. Both the undoped sample (0.95E19) and the doped $x = 0.005$ sample (1.7E19) display non-degenerate semiconductor behaviour (positive $d\sigma/dT$), probably due to their low carrier

[3] For a more detailed explanation, see appendix D.

concentrations. The lower density of these samples also induced an increase in carrier scattering at the pores [267, 408], resulting in a decrease in their conductivity but a decrease in their thermal conductivity. The low carrier concentration of the doped samples and the p-type behaviour of the undoped sample indicate the presence of hole-generating defects in the material, in particular antisite defects from Bi atom hopping to Te atom sites [409].

This compound of Bi_2Te_3-$Bi_{14}Te_{13}S_8$ has a peak thermopower of ≈−162 μV.K^{-1} for the sample $x = 0.005$ (the one with the lowest carrier concentration of 1.7×10^{19} cm^{-3}), a value much higher than that of the single phase Bi_2Te_3 (≈−120 μV.K^{-1}) prepared by a similar procedure [405].

The higher values of the thermopower (see fig. 5.4(a)) and low values of thermal conductivity (see fig. 5.4(c)) led to the highest value of zT (see fig. 5.4(d)) for $x = 0.005$. The overall efficiency of was limited due to its low electrical conductivity (fig. 5.4(b)).

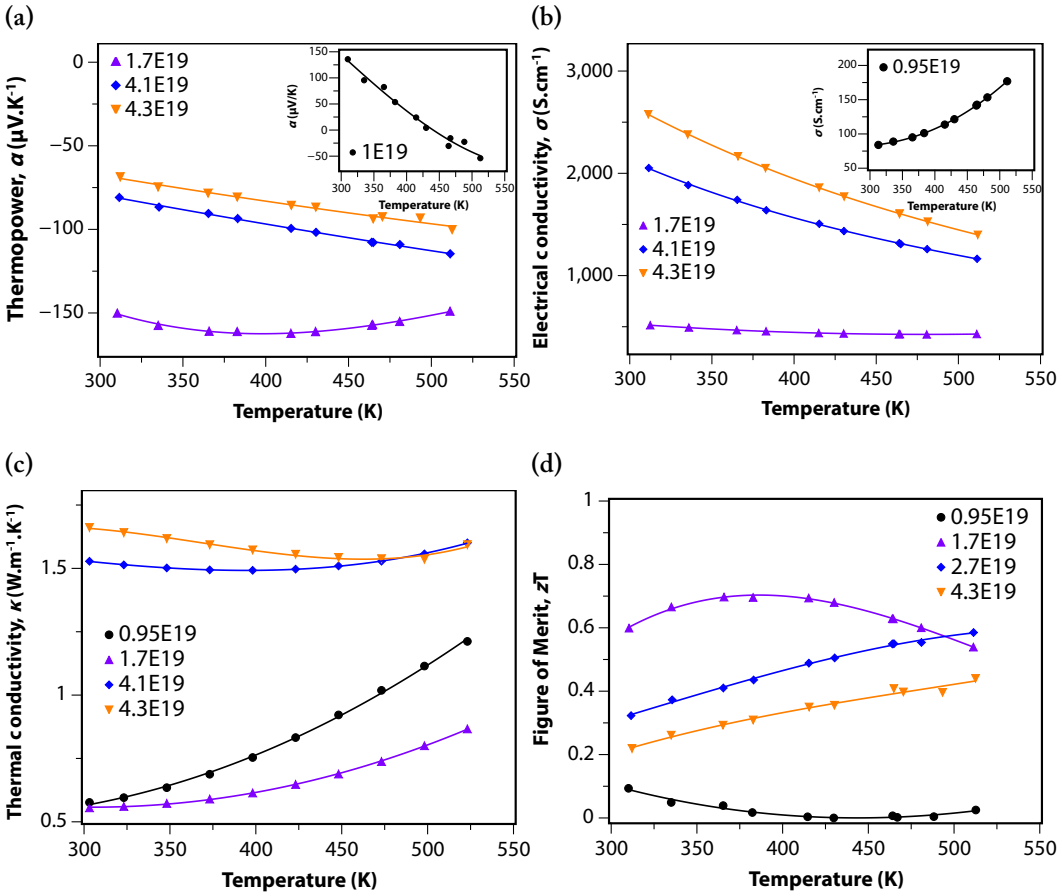

FIGURE 5.4. Temperature dependence of the (a) thermopower, (b) electrical conductivity, (c) thermal conductivity, and (d) figure of merit zT, of $Bi_2(Te_{2.75-x/3}S_{0.25-x/3})I_x$ (x = 0, 0.005, 0.01, and 0.02) samples between 300 and 530 K measured parallel to the sintering direction.

In order to understand the optimum carrier concentration range for this set of samples, the transport properties of the doped samples are compared with those of an intrinsic sample prepared by a similar procedure [405] and shown in figure 5.5. The sintering of this intrinsic sample was performed on a different SPS furnace which led to a higher density (≥99% of the nominal density).

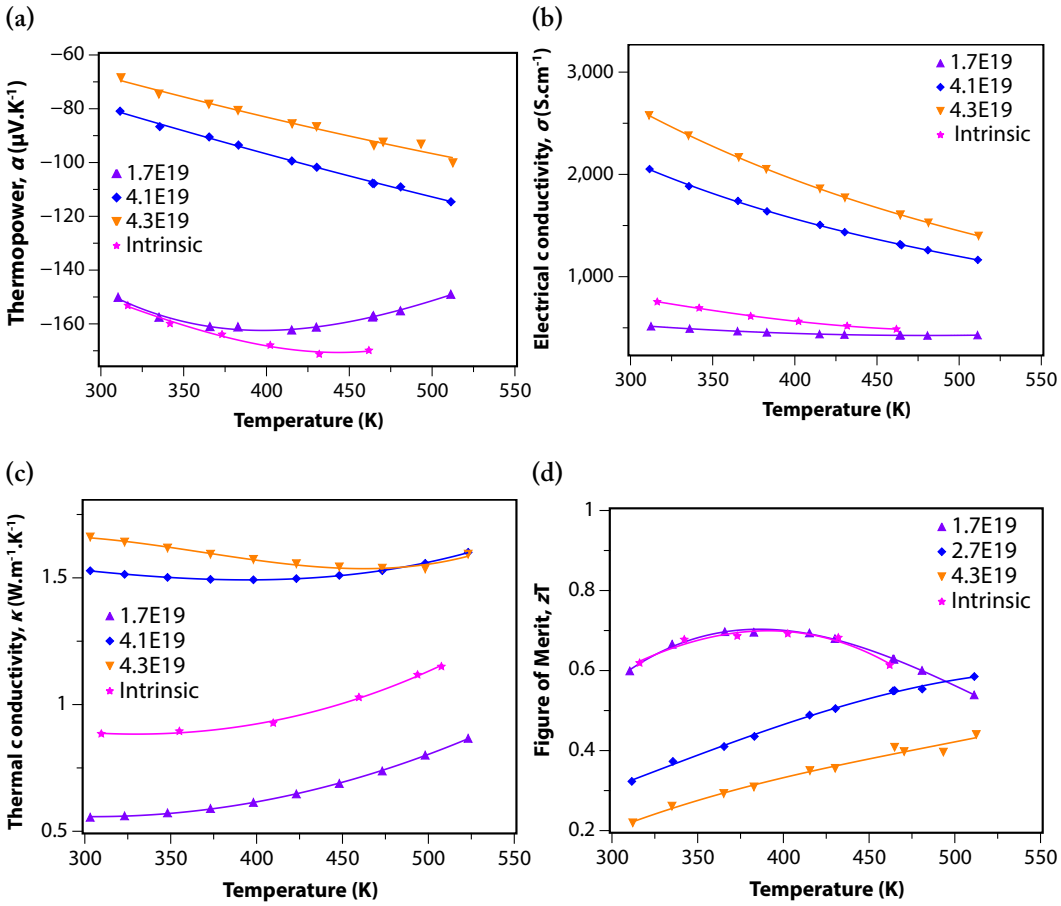

Figure 5.5. Temperature dependence of the (a) thermopower, (b) electrical conductivity, (c) thermal conductivity, and (d) figure of merit zT, of $Bi_2(Te_{2.75-x/3}S_{0.25-x/3})I_x$ (x = 0.005, 0.01, and 0.02) samples between 300 and 530 K measured parallel to the sintering direction, compared with the intrinsic sample of [405].

The intrinsic sample has a slightly lower carrier concentration (1.2×10^{19} cm^{-3}) [405] than the lightly doped sample (1.7×10^{19} cm^{-3}), resulting in a similar value of thermopower (fig. 5.5(a)), while the electrical conductivity of the lightly doped sample was lower, despite having a higher carrier concentration, due to the increased carrier scattering at the pores (fig. 5.5(b)).

The high porosity of the sample also led to an increase in phonon scattering, resulting in a lower thermal conductivity (fig. 5.5(c)). Overall, this resulted in a similar zT for both the intrinsic and lightly doped samples (fig. 5.5(d)), indic-

ating that the optimal carrier concentration for this composition is in the lower range of $\times 10^{19}$.

To understand the effects of structure on the behaviour of the optimal sample, both the intrisic sample and the single phase Bi_2Te_3 were modelled using the multiband model described in chapter 3. In this chapter, the inertial effective mass (m_I^*) was assumed to have the same value as the single valley effective mass (m_b^*). Since the effective mass of the density of states (m_{DOS}^*) is related to m_b^* by $m_{\mathrm{DOS}}^* = {N_v}^{2/3} m_b^*$, where N_v is the valley degeneracy, the model is simplified to calculate only either m_b^* or m_{DOS}^*. For the model used in this chapter, only the influence of the maximum valence and minimum conduction bands on the transport properties of the material has been considered.

The measurements of the thermopower, carrier concentration, and electrical conductivity (as seen in [405]) were used to estimate the density of states effective mass m_{DOS}^* for both hole and electrons, deformation potential (E_{def}), and reduced Fermi level for both samples. The bandgap (E_g) and valley degeneracy of both Bi_2Te_3 and $Bi_{14}Te_{13}S_8$ were obtained from literature and are shown in table 5.3. The longitudinal elastic constant was calculated following $C_l = d \cdot {v_l}^2$, where the density (d) and longitudinal speed of sound (v_l) were obtained from the literature and are also shown in table 5.3. These values were linearly interpolated considering the sample phase composition determined by the Rietveld refinement of the powder diffraction data (see table 5.1).

Table 5.3. Parameters used for the multiband modelling of Bi_2Te_3 and $Bi_{14}Te_{13}S_8$

Composition	E_g (eV)	N_v (VB)	N_v (CB)	d (g.cm^{-3})	v_l (m.s^{-1})	C_l (GPa)
Bi_2Te_3	0.15 [410]	2 [411]	6 [411]	7.80 [412]	2668 [413]	55.52
$Bi_{14}Te_{13}S_8$	0.28 [414]	2 [411]	6 [411]	7.55 [415]	2693 [413]	54.75

The measured thermal conductivity of the intrinsic $Bi_2Te_{2.75}S_{0.25}$ and Bi_2Te_3 is shown in figure 5.6(a), while the modelled electronic, bipolar, and lattice thermal conductivities are shown in figures 5.6(b)-(d), respectively.

The thermal conductivities of the samples exhibit a behaviour typical of intrinsic narrow-gap semiconductors with a large bipolar contribution [416, 417]. In addition, they exhibit distinct trends as a function of temperature and secondary phase fraction (figs. 5.6(a)-(d)). In particular, the bipolar thermal conductivity experiences a decrease with increasing secondary phase fraction (see fig. 5.6 (c)). As discussed in chapter 2, bipolar conduction occurs due to the presence of excited minority charges and is, in fact, exponentially proportional to the bandgap [418] as can be seen in the following equation [419]

$$\kappa_b \propto \exp\left(-\frac{E_g}{2k_{\mathrm{B}T}}\right) \rightarrow \frac{\partial \kappa_b}{\partial E_g} \leq 0. \tag{5.1}$$

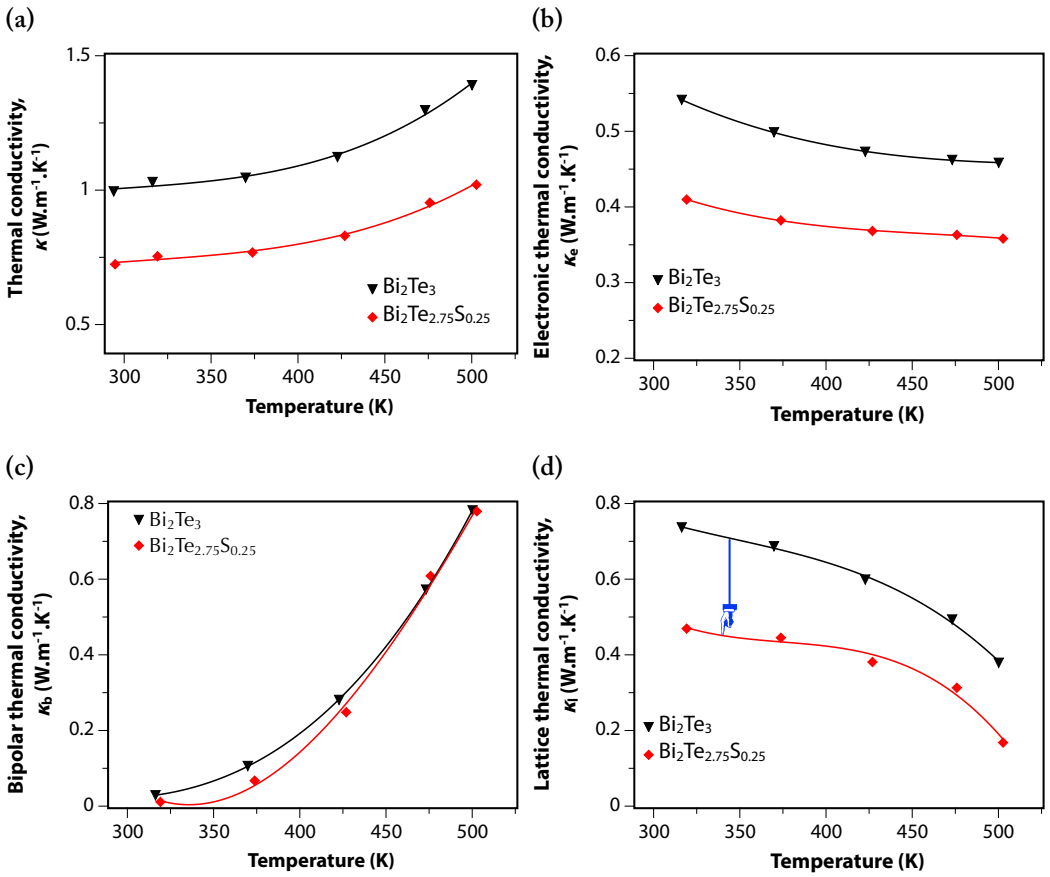

Figure 5.6. Temperature dependence of the (a) thermal conductivity, (b) electronic thermal conductivity, (c) bipolar thermal conductivity, and (d) lattice thermal conductivity, of Bi_2Te_3 and $Bi_2Te_{2.75}S_{0.25}$ samples between 300 and 530 K measured parallel to the sintering direction.

The negative sensitivity of κ_b with respect to E_g implies that larger bandgaps have a diminishing effect on bipolar conduction. The small bandgap of Bi_2Te_3 is therefore the culprit for the observed large bipolar effect in this sample set. As already discussed, the heterostructure of the band structure of the two-phase material caused scattering of the majority carriers and increased the bulk thermopower. The downward trend of the bipolar thermal conductivity with increasing secondary phase shows that the minority charges were also filtered, contributing to its decrease.

The multiphase sample displayed a lower lattice thermal conductivity (fig. 5.6) compared to Bi_2Te_3, mainly due to additional phonon scattering at defects, grain boundaries, and interfaces between the two phases [420–423]. This result is in agreement with the experimental results discussed in chapter 2, where it was seen that multiphase thermoelectric materials can indeed be used to reduce the lattice thermal conductivity of materials.

5.3.3 Average zT comparison

The average zT over 300-500 K ($\langle zT \rangle$) [4] of the best sample (1.7E19) was compared with results seen in literature and commercially available material [366, 424–426] and are seen figure 5.7. Our results are lower than the best seen in literature, but better than those seen in commercial Bi_2Te_3.

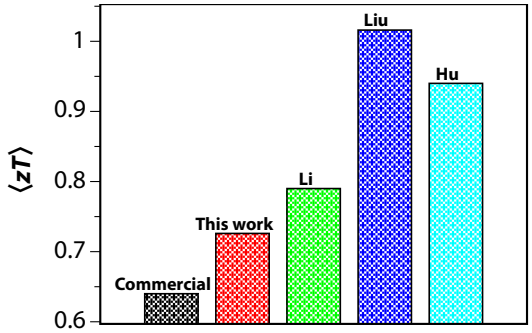

Figure 5.7. Average zT comparison of best sample (1.7E19) with the ones seem in literature and commercial Bi_2Te_3 [366, 424–426].

5.4 Conclusions

In conclusion, the results show that the inclusion of a secondary phase increases the overall performance of Bi_2Te_3 with a nearly constant value of zT in the temperature range 300 $\sim$ 530 K. The average zT over 300-500 K are lower than the best seen in literature, but better than those seen in commercial Bi_2Te_3.The origin of the lower higher values of zT was the enhancement of the thermopower and lower lattice thermal conductivity due to additional scattering interfaces in the multiphase material. The iodine doped samples confirmed the results obtained for a previous pristine sample of $Bi_2Te_{2.75}S_{0.25}$ and showed that the optimal carrier concentration for this compound was in the lower range of 10^{19} cm^{-3}.

[4] The average zT is defined as $\langle zT \rangle = \frac{1}{T_h - T_c} \int_{T_c}^{T_h} zT dT$, where T_h is the hot side temperature and T_c is the cold side temperature in a given temperature range.

References

(60) L. Xing, W. Cui, X. Sang, F. Hu, P. Wei, W. Zhu, X. Nie, Q. Zhang and W. Zhao, *Journal of Materiomics*, 2021, **7**, 998–1006, doi: 10/gmkd3z.

(110) D. Zhang, J. Lei, W. Guan, Z. Ma, C. Wang, L. Zhang, Z. Cheng and Y. Wang, *J. Alloys Compd.*, 2019, **784**, 1276–1283, doi: 10.1016/j.jallcom.2019.01.084.

(154) Y. Li, X. Wang, G. Liu, B. Shin and F. Shan, *Scr. Mater.*, 2019, **172**, 88–92, doi: 10.1016/j.scriptamat.2019.07.016.

(203) G. Yang, L. Sang, F. F. Yun, D. R. G. Mitchell, G. Casillas, N. Ye, K. See, J. Pei, X. Wang, J.-F. Li, G. J. Snyder and X. Wang, *Adv. Funct. Mater.*, 2021, **31**, 2008851, doi: 10.1002/adfm.202008851.

(252) Y. Zhang, H. Ma, B. Sun, B. Liu, H. Liu, L. Kong, B. Liu, X. Jia and X. Chen, *J. Alloys Compd.*, 2017, **715**, 344–348, doi: 10.1016/j.jallcom.2017.05.004.

(267) G. Solomon, E. Song, C. Gayner, J. A. Martinez and Y. Amouyal, *ACS Appl. Nano Mater.*, 2021, **4**, 4419–4431, doi: 10.1021/acsanm.0c03472.

(326) B. H. Toby and R. B. Von Dreele, *J. Appl. Crystallogr.*, 2013, **46**, 544–549, doi: 10.1107/S0021889813003531.

(347) S. I. Kim, K. H. Lee, H. A. Mun, H. S. Kim, S. W. Hwang, J. W. Roh, D. J. Yang, W. H. Shin, X. S. Li, Y. H. Lee, G. J. Snyder and S. W. Kim, *Science*, 2015, **348**, 109–14, doi: 10.1126/science.aaa4166.

(357) B. Poudel, Q. Hao, Y. Ma, Y. Lan, A. Minnich, B. Yu, X. Yan, D. Wang, A. Muto, D. Vashaee, X. Chen, J. Liu, M. S. Dresselhaus, G. Chen and Z. Ren, *Science*, 2008, **320**, 634–8, doi: 10.1126/science.1156446.

(366) W. Liu, K. C. Lukas, K. McEnaney, S. Lee, Q. Zhang, C. P. Opeil, G. Chen and Z. Ren, *Energy Environ. Sci.*, 2013, **6**, 552–560, doi: 10.1039/c2ee23549h.

(400) C. Tan, X. J. Tan, F. F. Shi, Y. N. Yin, G. Q. Liu, C. L. Xiong, H. X. Wang, G. Q. Luo, B. Yu, J. G. Noudem, B. Liang and J. Jiang, *Ceram. Int.*, 2021, **47**, 725–731, doi: 10.1016/j.ceramint.2020.08.182.

(401) W. H. Shin, J. W. Roh, B. Ryu, H. J. Chang, H. S. Kim, S. Lee, W. S. Seo and K. Ahn, *ACS Applied Materials & Interfaces*, 2018, **10**, 3689–3698, doi: 10.1021/acsami.7b18451.

(402) W. Xie, X. Tang, Y. Yan, Q. Zhang and T. M. Tritt, *Applied Physics Letters*, 2009, **94**, 102111, doi: 10.1063/1.3097026.

(403) S. Fan, J. Zhao, J. Guo, Q. Yan, J. Ma and H. H. Hng, *Applied Physics Letters*, 2010, **96**, 182104, doi: 10.1063/1.3427427.

(404) P. Larson, S. D. Mahanti and M. G. Kanatzidis, *Physical Review B*, 2000, **61**, 8162–8171, doi: 10.1103/PhysRevB.61.8162.

(405) S. A. Yamini, R. Santos, **Fortulan, Raphael**, A. A. Gazder, A. Malhotra, D. Vashaee, I. Serhiienko and T. Mori, *ACS Applied Materials & Interfaces*, 2023, **15**, 19220–19229, doi: 10.1021/acsami.3c01956.

(406) R. A. Young, *The Rietveld method*, International union of crystallography, 1993, vol. 5.

(407) B. H. Toby, *Powder Diffraction*, 2006, **21**, 67–70, doi: 10 . 1154 / 1 . 2179804.

(408) Y. Wang, C. Bourgès, R. Rajamathi, C. Nethravathi, M. Rajamathi and T. Mori, *Materials*, 2021, **15**, 53, doi: 10.3390/ma15010053.

(409) W.-S. Liu, Q. Zhang, Y. Lan, S. Chen, X. Yan, Q. Zhang, H. Wang, D. Wang, G. Chen and Z. Ren, *Advanced Energy Materials*, 2011, **1**, 577–587, doi: 10.1002/aenm.201100149.

(410) M. Michiardi, I. Aguilera, M. Bianchi, V. E. de Carvalho, L. O. Ladeira, N. G. Teixeira, E. A. Soares, C. Friedrich, S. Blügel and P. Hofmann, *Physical Review B*, 2014, **90**, 075105, doi: 10 . 1103 / PhysRevB . 90 . 075105.

(411) I. T. Witting, F. Ricci, T. C. Chasapis, G. Hautier and G. J. Snyder, *Research*, 2020, **2020**, 1–15, doi: 10.34133/2020/4361703.

(412) N. C. for Biotechnology Information, *PubChem Compound Summary for CID 6379155*.

(413) Q. Tao, F. Meng, Z. Zhang, Y. Cao, Y. Tang, J. Zhao, X. Su, C. Uher and X. Tang, *Materials Today Physics*, 2021, **20**, 100472, doi: 10.1016/j.mtphys.2021.100472.

(414) L.-L. Wang and D. D. Johnson, *Physical Review B*, 2011, **83**, 241309, doi: 10.1103/PhysRevB.83.241309.

(415) L. Pauling, *American Mineralogist: Journal of Earth and Planetary Materials*, 1975, **60**, 994–997.

(416) Y. Xiao, H. Wu, J. Cui, D. Wang, L. Fu, Y. Zhang, Y. Chen, J. He, S. J. Pennycook and L.-D. Zhao, *Energy & Environmental Science*, 2018, **11**, 2486–2495, doi: 10.1039/C8EE01151F.

(417) R. Al Rahal Al Orabi, N. A. Mecholsky, J. Hwang, W. Kim, J.-S. Rhyee, D. Wee and M. Fornari, *Chemistry of Materials*, 2016, **28**, 376–384, doi: 10.1021/acs.chemmater.5b04365.

(418) J.-H. Bahk and A. Shakouri, *Applied Physics Letters*, 2014, **105**, doi: 10.1063/1.4892653.

(419) J.-H. Bahk and A. Shakouri, *Physical Review B*, 2016, **93**, 165209, doi: 10.1103/PhysRevB.93.165209.

(420) T. Parashchuk, R. Knura, O. Cherniushok and K. T. Wojciechowski, *ACS Applied Materials & Interfaces*, 2022, **14**, 33567–33579, doi: 10.1021/acsami.2c08686.

(421) Z. Zhou, Y. Xu, M. Zou, C. Liu, J. Lan, Y.-H. Lin and C. Nan, *J. Am. Ceram. Soc.*, 2021, **104**, 1370–1378, doi: 10.1111/jace.17530.

(422) B. Zhu, W. Wang, J. Cui and J. He, *Small*, 2021, **17**, 2101328, doi: 10.1002/smll.202101328.

(423) Y.-K. Zhu, J. Guo, Y.-X. Zhang, J.-F. Cai, L. Chen, H. Liang, S.-W. Gu, J. Feng and Z.-H. Ge, *Acta Materialia*, 2021, **218**, 117230, doi: 10.1016/j.actamat.2021.117230.

(424) A. Nozariasbmarz, B. Poudel, W. Li, H. B. Kang, H. Zhu and S. Priya, *iScience*, 2020, **23**, 101340, doi: 10.1016/j.isci.2020.101340.

(425) F. Li, R. Zhai, Y. Wu, Z. Xu, X. Zhao and T. Zhu, *Journal of Materiomics*, 2018, **4**, 208–214, doi: 10.1016/j.jmat.2018.05.008.

(426) L. Hu, H. Wu, T. Zhu, C. Fu, J. He, P. Ying and X. Zhao, *Advanced Energy Materials*, 2015, **5**, 1500411, doi: 10.1002/aenm.201500411.

6

Enhanced thermoelectric performance of sulphur added $Bi_2Te_{2.7}Se_{0.3}$ compounds through synergistic tailoring of band structure and phonon transport

Life is the art of encounter, although there is so much misencounter throughout life.
— Vinicius de Moraes, Samba da Benção

Summary
This chapter examines the thermoelectric performance of $Bi_2Te_{2.7}Se_{0.3}$ compounds with added sulphur. Since $Bi_2(Te,Se)_3$ materials are the best performers for room temperature applications, this study is a natural progression from the previous chapter where sulphur was added to Bi_2Te_3. Here it is shown that the inclusion of sulphur changes the bandstructure of the material, increasing the thermopower while providing additional scattering mechanisms for phonons and reducing the thermal conductivity.

6.1 Introduction

Alloys of chalcogenide (Te and Se) and pnictogenide (Bi and Sb) materials have shown the best thermoelectric performance for thermoelectric refrigeration and power generation [411, 427, 428]. In particular, binary p-type $(Bi,Sb)_2Te_3$ and n-type $Bi_2(Te,Se)_3$ compounds are the best performing materials at around room temperature [429–431]. The presence of Se at Te sites in $Bi_2(Te,Se)_3$ creates donor levels that increase the carrier concentration, and alloying decreases the thermal conductivity [80, 88]. The anisotropy of the layered crystal structure also plays an important role in its efficiency [432, 433].

The addition of dopants such as Cl [420], Cu [409], Zn [434], I [435], and CuI [436] has been shown to improve the power factor of $Bi_2(Te,Se)_3$, while nanoinclusions have also been proposed as a method to decrease the thermal conductivity and increase zT [437–440]. Isovalent substitutions have been utilised to make profound changes in the thermopower and electrical resistivity with band structure changes [428], enhanced effective mass [441], and changes in the presence of defects [442]. Recently, there has been great interest in the use of sulphur as an isovalent substitution for Te sites in p-type [443, 444] and n-type [428, 445] pnictogen chalcogenides. The presence of sulphur effects the presence of naturally occurring defect antisites and vacant Te sites, which increase the carrier concentration of these alloys [428]. The presence of secondary phases owing to the addition of sulphur has also been verified in these materials [366, 446]. The compounds with secondary phases showed a decrease in thermal conductivity but also a decrease in mobility, which increased the electrical resistivity of the samples [366]. Secondary phase of Bi_2S_3 [423, 439] has been used to introduce multiscale scattering of phonons and decrease the thermal conductivity of the compounds.

This chapter investigates the thermoelectric performance of compounds incorporating sulphur in $Bi_2Te_{2.7}Se_{0.3}$. The previous chapter focused on sulphur addition to Bi_2Te_3 due to its excellent performance in room-temperature applications. As a natural progression, this chapter demonstrates that the introduction of sulphur alters the bandstructure of the material. This alteration leads to an improvement in thermopower while also introducing additional scattering mechanisms for phonons, thereby reducing thermal conductivity.

6.2 Experimental details

6.2.1 Synthesis

High purity elements of bismuth shots (Bi, 99.999%, Alfa Aesar), tellurium chunks (Te, 99.999%, Alfa Aesar), selenium shots (Se, 99.999%, Alfa Aesar), and sulphur pieces (S, 99.99%, Alfa Aesar) were weighted according to the stoichiometry of $Bi_{2-y/3}Cr_{y/3}[(Te_{2.7}Se_{0.3})_{1-x}S_x]Cl_y$, where x = (0, 0.003,

0.008, 0.0016, 0.025, 0.05, 0.1, and 0.2) and y = 0.05. Since the dopant concentration remained constant, these samples are referred to in the text as $Bi_2(Te_{2.7}Se_{0.3})_{1-x}S_x$. The raw elements were loaded into vacuum sealed quartz ampoules in a glove box and sealed under vacuum. The ampoules were heated to 850 °C, held at this temperature for 12 h, quenched in cold water, and annealed at 450 °C for 72 h. The resulting ingots were then ground by hand into fine powders in an agate mortar and pestle housed in a glove box and sintered under vacuum to produce 11 mm diameter rods using SPS (KCE FCT-H HP D-25 SD, FCT Systeme GmbH, Rauenstein, Germany) at a pressure of 50 MPa and a temperature of 400 °C for 5 min. The densities of all samples were measured from the dimensions and weight of the rods. The average density of the samples was approximately 85% of their theoretical density. The samples exhibited a significant degree of porosity due to the low force applied by the SPS equipment, resulting in an effective pressure lower than the set pressure and consequently a low density. Figure 6.1 illustrates the poor force control of the SPS apparatus for the samples $Bi_2(Te_{2.7}Se_{0.3})_{1-x}S_x$ with x = 0.1 with the measured temperature (shown in black) and the applied force (shown in pink). The applied force shows that once again (as discussed in chapter 5) it was not properly controlled.

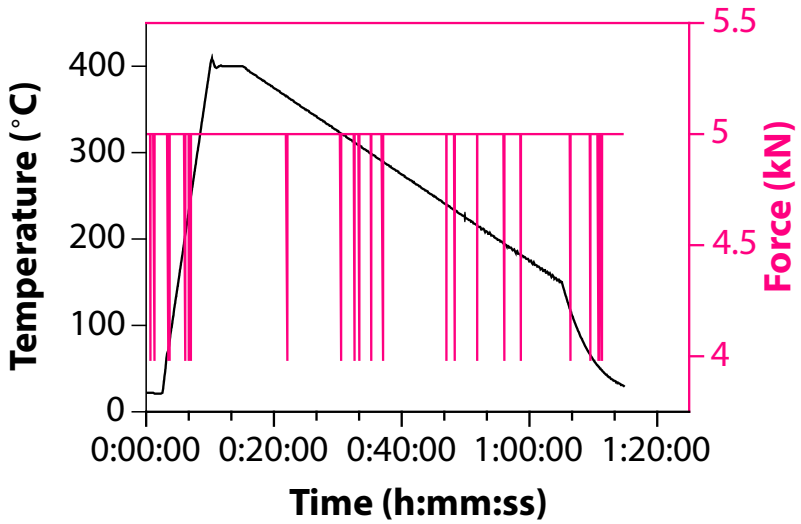

Figure 6.1. Measured temperature (shown in black) and applied force (shown in pink) for the sintering process of $Bi_2(Te_{2.7}Se_{0.3})_{1-x}S_x$ with x = 0.1.

6.2.2 Materials characterisation

PXRD measurements were conducted on a PANalytical X'Pert Pro diffractometer with Cu-Kα1 radiation (λ =1.5406 Å, 40 kV, 40 mA). The lattice parameters, atomic sites, and quantitative phase percentages were determined by

the Rietveld refinement method, which was performed using the GSAS-II software [326].

6.2.3 Thermoelectric transport properties

The simultaneous measurement of electrical resistivity and thermopower coefficient was conducted on a commercial system (LSR-3, Linseis). Thermal conductivity was calculated as $\kappa = D \cdot c_p \cdot d$, where D, c_p, and d are the thermal diffusivity, specific heat capacity, and density, respectively. Thermal diffusivity was measured by the LFA method using an LFA 467 HyperFlash®, Netzsch. The specific heat capacity was determined using a differential scanning calorimeter (DSC 8000, PerkinElmer) following the sapphire standard method (ASTM Standard E1269 [338]), as described in chapter 3.

The room temperature Hall coefficient (R_H) measurement was carried out on an ECOPIA 3000 Hall Effect Measurement System with a magnetic field of 0.55 T.

The longitudinal speed of sound was measured using the pulse-echo method at room temperature via an ultrasonic thickness gauge (38DL PLUS, Olympus).

6.3 Results and discussion

6.3.1 Structural and phase analysis

The PXRD patterns of $Bi_2(Te_{2.7}Se_{0.3})_{1-x}S_{3x}$, x = (0, 0.003, 0.008, 0.0016, 0.025, 0.05, 0.1, and 0.2) are shown in figure 6.2. All samples showed a hexagonal $Bi_2Te_{2.7}Se_{0.3}$ primary phase (space group $R\bar{3}m$) and samples with $x > 0.025$ contained an orthorhombic crystal structure of Bi_2S_3 secondary phase[1] (space group Pnma). The estimated phase composition is given in table 6.1, the refined lattice parameters are presented in table 6.2[2], and refinement plots are presented in figure 6.3.

6.3.2 Transport properties analysis

The temperature dependence of electrical resistivity (ρ), thermopower (α) and thermal conductivity (κ) was measured in both perpendicular (in-plane) and parallel (cross-plane) directions relative to the sintering direction. The thermoelectric properties of the samples along the in-plane direction are discussed in this text, while the cross-plane data are presented at the end of the chapter.

Figure 6.4 shows the electrical resistivity, thermopower, power factor (PF, α^2/ρ), and thermal conductivity[3] of $Bi_2(Te_{2.7}Se_{0.3})_{1-x}S_{3x}$, x = (0, 0.003, 0.008, 0.0016, 0.025, 0.05, 0.1, and 0.2) samples. The electrical resistivities of the single

[1] Materials Project ID mp-22856.

[2] The unit cell volumes of all samples are presented in appendix F.

[3] Measurements of thermal conductivity for x = 0.0016 and 0.1 were unavailable.

Table 6.1. Quantitative phase analysis of $Bi_2(Te_{2.7}Se_{0.3})_{1-x}S_{3x}$, x = (0, 0.003, 0.008, 0.0016, 0.025, 0.05, 0.1, and 0.2) obtained from the Rietveld refinement of the powder X-ray diffraction patterns

x	$Bi_2Te_{2.7}Se_{0.3}$ (wt.%)	Bi_2S_3 (wt.%)
0	100	…
0.003	100	…
0.008	100	…
0.016	100	…
0.025	94.9(4)	5.1(4)
0.05	88.4(16)	11.6(16)
0.1	83.9(13)	16.1(13)
0.2	77.0(4)	23.0(4)

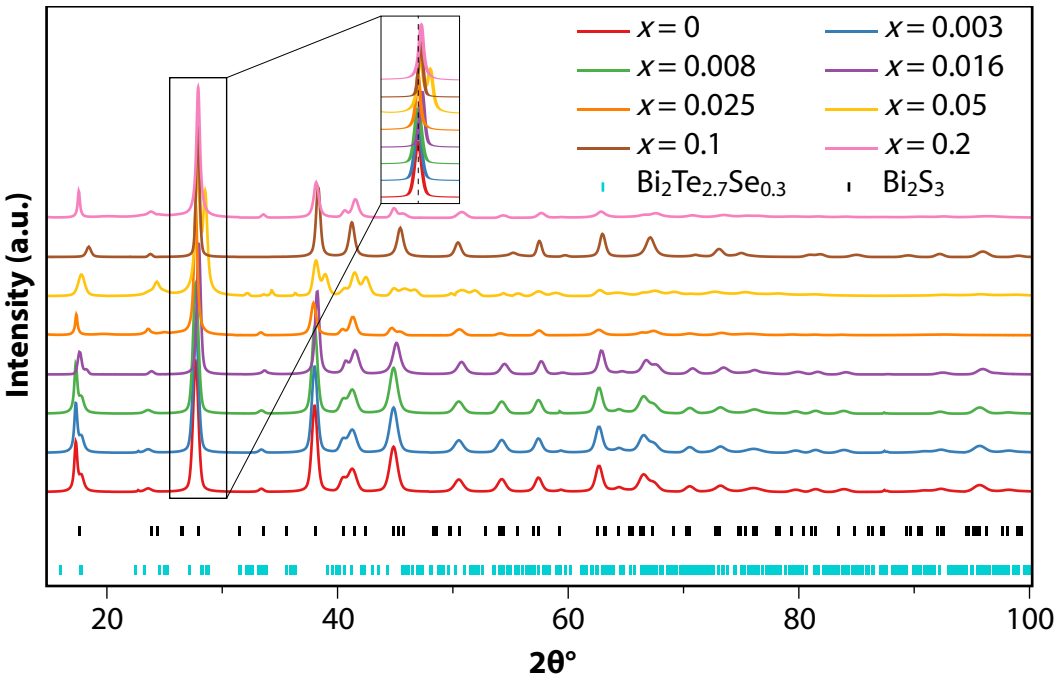

Figure 6.2. Powder X-ray diffraction patterns of $Bi_2(Te_{2.7}Se_{0.3})_{1-x}S_{3x}$, x = (0, 0.003, 0.008, 0.0016, 0.025, 0.05, 0.1, and 0.2). The inset shows the zoomed area around the largest peak.

Table 6.2. Refined lattice parameters of $Bi_2(Te_{2.7}Se_{0.3})_{1-x}S_{3x}$, x = (0, 0.003, 0.008, 0.0016, 0.025, 0.05, 0.1, and 0.2)

	$Bi_2Te_{2.7}Se_{0.3}$		Bi_2S_3		
x	a = b (Å)	c (Å)	a (Å)	b (Å)	c (Å)
0	4.3605(5)	30.2661(19)	…	…	…
0.003	4.3751(4)	30.3880(18)	…	…	…
0.008	4.3844(7)	30.2565(28)	…	…	…
0.016	4.3803(5)	30.3250(26)	…	…	…
0.025	4.3492(3)	30.3002(22)	11.505(13)	4.090(5)	11.142(15)
0.05	4.3600(29)	30.153(15)	11.446(30)	4.159(12)	10.687(21)
0.1	4.3988(5)	30.0163(27)	11.756(15)	3.8969(27)	11.667(6)
0.2	4.3733(7)	30.416(5)	11.239(10)	4.0609(15)	11.492(8)

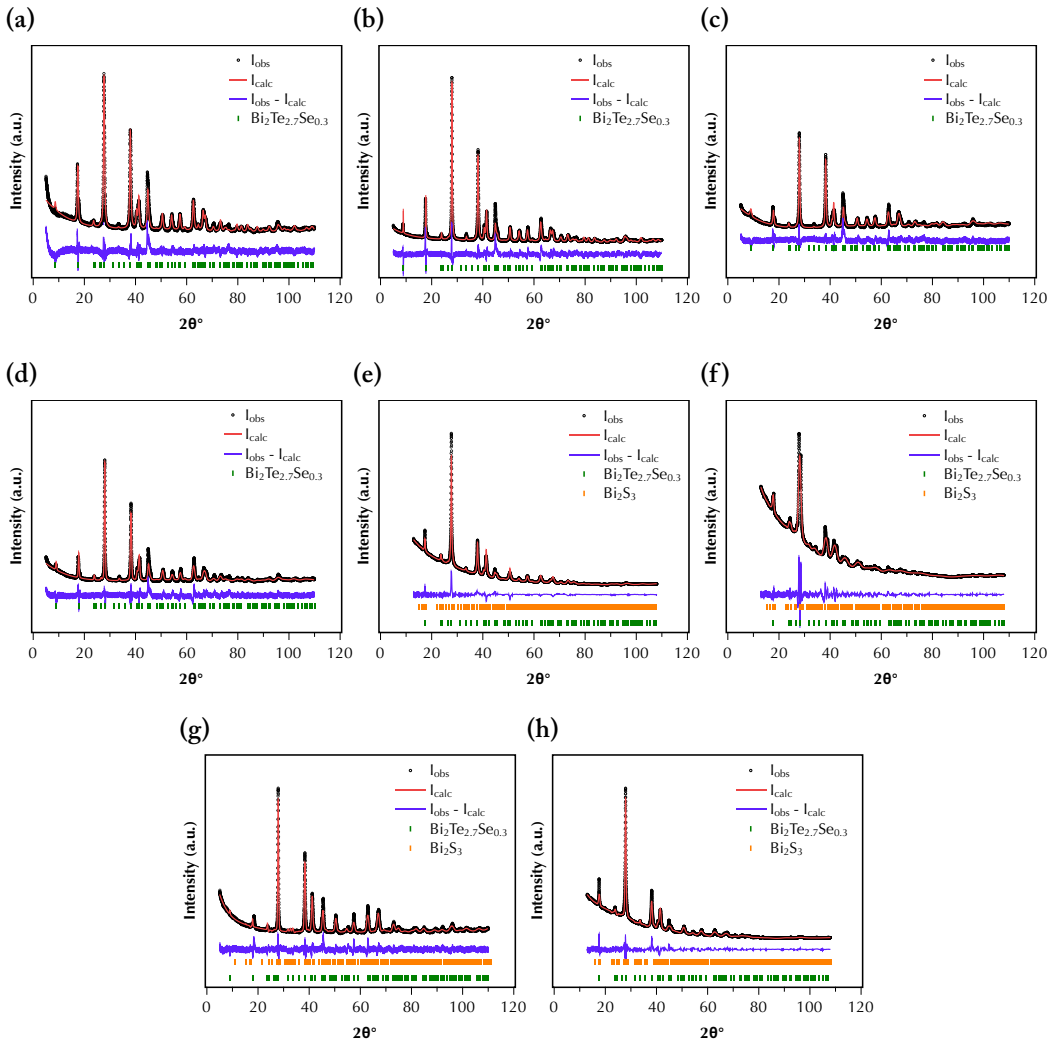

Figure 6.3. Refinement plots of $Bi_2(Te_{2.7}Se_{0.3})_{1-x}S_{3x}$, x = (a) 0, (b) 0.003, (c) 0.008, (d) 0.0016, (e) 0.025, (f) 0.05, (g) 0.1, and (h) 0.2 samples.

phase x = 0, 0.003, 0.008, and 0.0016 samples (see fig. 6.4(a)) display intrinsic semiconductor behaviour with values decreasing with temperature [447]. The electrical resistivity of the multiphase samples with x = 0.025, 0.05, and 0.1 shows the same intrinsic behaviour as the single phase samples, whereas the resistivity curve of the sample with x = 0.2 shows a weak metallic behaviour with a small positive slope of $d\rho/dT$ [447]. The low carrier concentrations (as seen in table 6.3) explain the intrinsic character of the samples.

The addition of sulphur to the samples increases the electrical resistivity of the samples at concentrations of x = 0.003, 0.008, 0.0016, 0.025, and 0.05. The resistivity values reported here are larger than those reported in the literature for $Bi_2Te_{2.7}Se_{0.3}$ [448, 449] but similar for porous samples [70]. The density of our sintered samples was approximately 85%, indicating the presence of a high

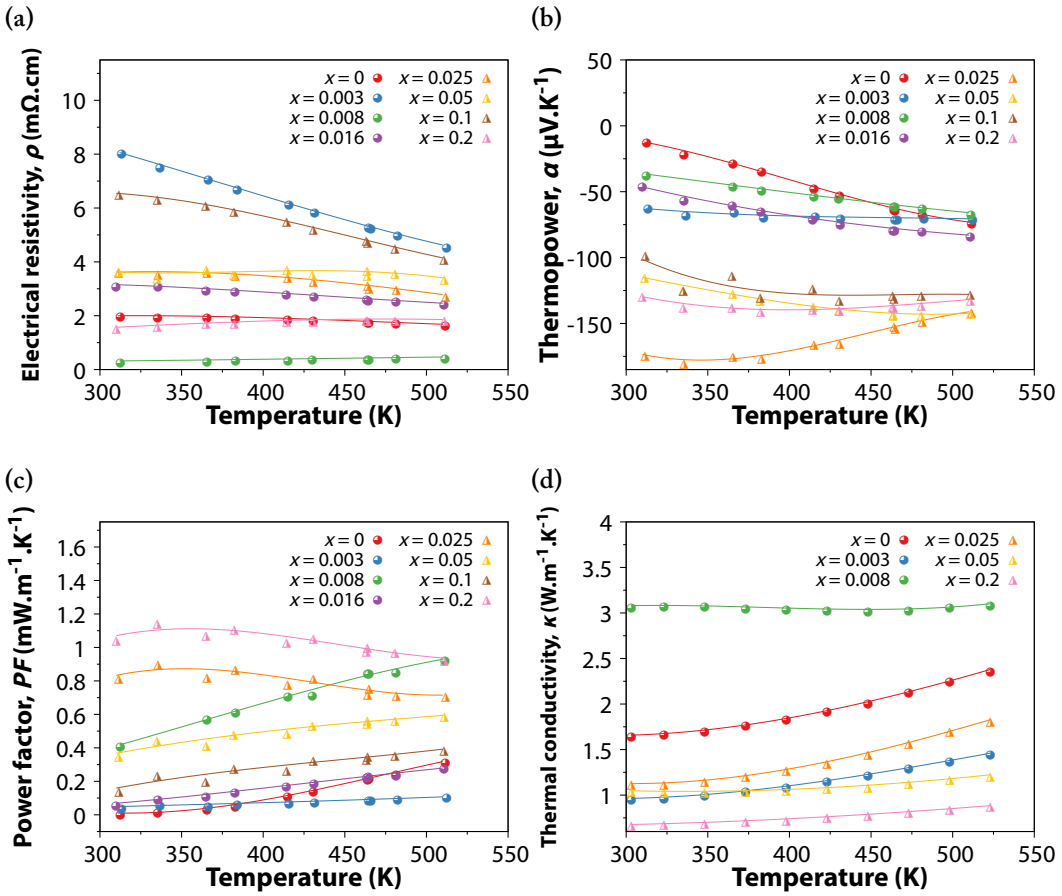

Figure 6.4. Temperature dependence of the (a) electrical resistivity, (b) thermopower, (c) power factor, and (d) thermal conductivity of $Bi_2(Te_{2.7}Se_{0.3})_{1-x}S_{3x}$, x = (0, 0.003, 0.008, 0.0016, 0.025, 0.05, 0.1, and 0.2) samples. Measurements of thermal conductivity for x = 0.0016 and 0.1 were unavailable.

Table 6.3. Hall carrier concentration and mobility for $Bi_2(Te_{2.7}Se_{0.3})_{1-x}S_{3x}$, x = (0, 0.003, 0.008, 0.0016, 0.025, 0.05, 0.1, and 0.2) samples

x	n_H($\times 10^{19}$ cm^{-3})	μ_H (cm^2.V^{-1}.s^{-1})
0	1.57	224.0
0.003	2.74	81.19
0.008	2.58	131.0
0.016	1.29	120.7
0.025	1.42	76.75
0.05	1.88	73.06
0.1	1.11	82.76
0.2	7.73	47.55

proportion of porosity. These pores scatter charge carriers, resulting in reduced carrier mobility and consequently increased electrical resistivity [450].

The observed changes in the carrier concentration of the sulphur alloyed samples can be explained by the defect control in the system. Bismuth telluride alloys typically exhibit three major atomic defects [409]: antisite defects of Bi at Te sites (Bi'_{Te}, which contributes one hole per defect); vacancies at Te sites ($V^{\bullet\bullet}_{Te}$, which contributes two electrons per defect); and vacancies at Bi sites (V'''_{Bi}, which contributes three holes per defect) [451, 452] (represented using the Kröger-Vink notation [453]). The presence of selenium in these alloys tends to increase the number of vacancies in the material (Te ($V^{\bullet\bullet}_{Te}$) and Se ($V^{\bullet\bullet}_{Se}$)) since the enthalpy of evaporation of Se (95.48 kJ.mol^{-1} [454]) and Te (114.1 kJ.mol^{-1} [454]) is much lower than that of Bi (178.632 kJ.mol^{-1} [455]); this increases the carrier concentration of electrons and contributes to the n-type behaviour of these materials with high carrier concentrations [456, 457]. The low value of the thermopower (fig. 6.4(b)) for the sample with $x = 0$ at room temperature ($\approx$–12.5 μV.K^{-1}) indicates that vacancy of Te and Se is not the most prevalent mechanism in our samples, but most likely antisite defects are responsible for the changes in carrier concentration of single phase samples in our study [428, 443, 458, 459]. However, the mechanisms are different for the multiphase samples.

The general effective medium theory (see equations 2.31 and 2.32) can be used to estimate the behaviour of the mixture of different phases [460]. Figure 6.5(a) shows the variation of the electrical resistivity values as a function of the weight fraction of the secondary phase in samples with $x = 0$[4], 0.025, 0.05, 0.1, and 0.2 extracted from XRD analysis at 512 K. The simple composite rule [461], is shown to be able to fit the data for $x = 0.025$, 0.05, and 0.1. This confirms that the addition of a phase with high electrical resistivity, in this case Bi_2S_3 [462], increases the overall resistivity of the medium as expected. Despite this, the rule fails to predict ρ for $x = 0.2$, suggesting that additional mechanisms are involved in this sample.

The sudden decrease in electrical resistivity for the sample with $x = 0.2$ suggests either the formation of a new phase with a different composition and electronic band structure or a sharp change in the band structures in both phases. XRD analysis did not reveal any compositional changes, suggesting band structure changes were due to the increased presence of the secondary phase rather than formation of a distinct new phase.

To investigate this, Hall effect measurements were performed at 300 K to measure the Hall coefficient of the samples and to evaluate their Hall carrier concentration ($n_H = 1/(R_H \cdot e)$) and Hall carrier mobility ($\mu_H = R_H/\rho$), as shown in table 6.3. The single phase sample $x = 0$ shows a carrier concentration of 1.57×10^{19} cm^{-3} and a carrier mobility of 224 cm^2.V^{-1}.s^{-1} at 300 K.

[4]Single-phase sample.

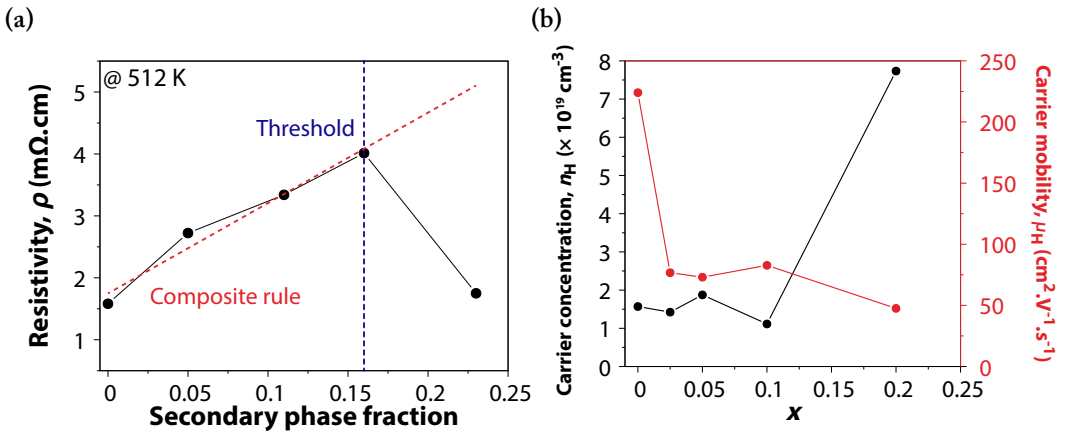

FIGURE 6.5. (a) Electrical resistivity at 512 K versus secondary phase fraction. The red dashed line indicates a simple composite rule for a binary mixture and the blue dashed line indicates the threshold at which the rule fails to predict the mixture behaviour. (b) Carrier concentration and carrier mobility.

The observed trend of the mobility is one of decreasing values, with the secondary phase inclusion reaching the lowest value of 47.55 $cm^2.V^{-1}.s^{-1}$ for the multiphase sample $x = 0.2$, probably due to the increased scattering at the interfaces between the two phases. On the other hand, the carrier concentration shows the opposite trend to the resistivity, with its maximum value of 7.73×10^{19} cm^{-3} for the sample with the largest secondary phase inclusion sample $x = 0.2$. Figure 6.5(b) shows this dependence of the carrier concentration and mobility on the sulphur concentration.

The relationship shown in figure 6.5(b) provides some insight and indicates that the deterioration in electrical resistivity is due to the decrease in carrier mobility, while the large improvement for $x = 0.2$ is due to the increase in carrier concentration.

This unique electronic behaviour suggests that high energy donors are now accessible from the conduction band of the $Bi_2Te_{2.7}Se_{0.3}$ matrix and contribute to the electronic conduction. A possible explanation for this effect is that the interplay between the two phases forms an intermediate band of impurity states. It can then be concluded that the presence of this impurity band is responsible for the deviation from the monotonic change in electrical resistivity.

The plateau-like nature of the carrier concentration for $0.025 \leqslant x \leqslant 0.2$ can be explained by noting that as the secondary phase fraction reaches the percolation limit, $x = 0.025$, the sulphur defects ($V_S^{\bullet\bullet}$, which contribute to two electrons per defect) on the sulphur rich phase appear to balance out the reduction (fractional) of the $V_{Te}^{\bullet\bullet}$ and $V_{Se}^{\bullet\bullet}$ defects present on the $Bi_2Te_{2.7}Se_{0.3}$ phase, maintaining a relatively constant carrier concentration.

The electrical resistivity of the samples $x = 0.025$, 0.05, and 0.1 follows an

Arrhenius like form [463]

$$\rho = \rho_0 \exp\left(\frac{E_a}{k_B T}\right), \tag{6.1}$$

where ρ_0 is the resistivity prefactor and E_a the activation energy. The value of the activation energy increases with the presence of the secondary phase, with a minimum of 10.8 meV for x = 0 and a maximum of 28.8 meV for x = 0.1, implying that the effective band gap of the samples increases as the secondary phase inclusion increases, explaining the different $d\rho/dT$ of the samples.

The thermopower for all samples has negative values at room temperature, indicating n-type conduction (fig. 6.4(b)). The linear dependence of thermopower on temperature up to 350 K for all samples indicates that in this temperature range the main parameter of thermopower generation is the thermal diffusion of electrons, as predicted by Mott's formula [391]. This linear relationship between thermopower and temperature is observed over the temperature range for the concentrations of the sulphur-free and sulphur-alloyed samples: x = 0, 0.003, 0.008, and 0.0016.

It is well known that the thermopower is strongly dependent on the band structure and the DOS around the Fermi level (E_F) [65, 220] and given the high sensitivity of the thermopower values to the sulphur concentration, it can be inferred that the presence of sulphur in the materials dramatically changes the DOS around E_F. This significant dependence of DOS on sulphur content was previously observed in a $Bi_{0.5}Sb_{1.5}Te_3$ alloy [458]. The magnitude of the thermopower of the samples with added sulphur was generally higher than that of the sample without sulphur. ($\approx$-12.5 $\mu V.K^{-1}$) and ranged from $\approx$-46.8 $\mu V.K^{-1}$ for the sample with x = 0.008 to $\approx$-173.9 $\mu V.K^{-1}$ for the sample with x = 0.025.

The set of multiphase samples x = 0.025, 0.05, 0.1, and 0.2 were those with the highest values of α, comparable to those found in the literature [431, 436, 464], and exhibited nonlinear behaviour at higher temperatures, consistent with the presence of bipolar conduction in the material [465]. The observed improvement in the secondary phase materials can be explained by a twofold mechanism [405]. First, using the same approach as previously used to analyse the resistivity of the samples, effective medium theory shows that the inclusion of a phase with large negative thermopower values will naturally increase the thermopower of the bulk material. In this case Bi_2S_3 shows large values of α, up to $\approx$-183 $\mu V.K^{-1}$, as discussed in chapter 4 [462], which confirms the previous argument.

Secondly, similar to what has been discussed in previous chapters, the presence of additional phases in a material with highly mismatched band structures can introduce the energy filtering effect. This effect screens out low energy carriers using a potential barrier that is proportional to the difference in electron affinity of the materials, resulting in an increased thermopower of the bulk material [110, 111, 114, 405].

In figures 6.6(a) and (b), the electrical resistivity and carrier concentration/-mobility of the single-phase samples are plotted as a function of sulphur concentration. Compared to the multiphase samples, the resistivity of the sulphur alloyed samples does not follow a clear trend. As can be seen in figure 6.6(b), the presence of sulphur ions decreases carrier mobility due to increased carrier scattering. The carrier concentration of this set of samples does not follow a clear trend, as can also be seen in figure 6.6(b). The carrier concentration in these samples appears to be primarily a function of the defects in the system; alloying with sulphur causes changes in the DOS but it does not appear to follow a clear trend or relationship.

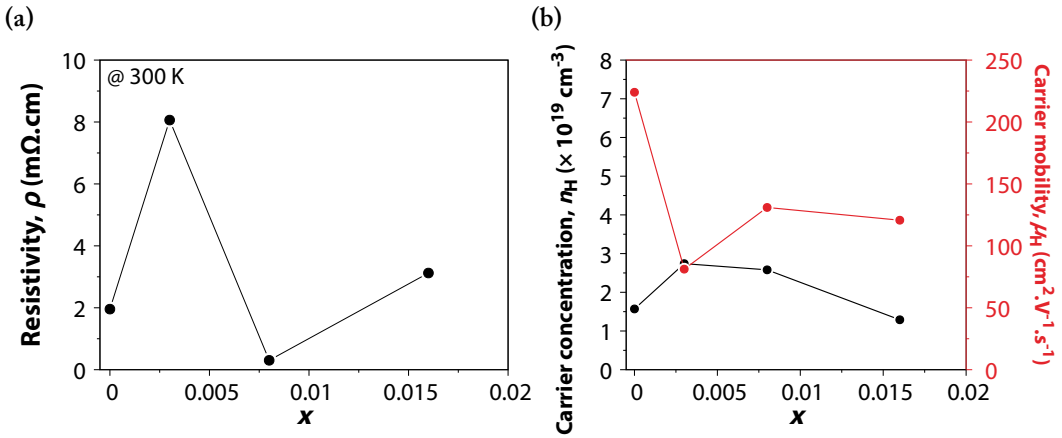

Figure 6.6. (a) Electrical resistivity at 300 K versus sulphur concentration in the material fraction, (b) carrier concentration and carrier mobility as a function of the sulphur concentration on the material.

Given the low values of α for the sulphur-free sample, the power factor of all samples with added sulphur was higher than that of the sulphur-free sample (fig. 6.4(c)). The combination of low resistivity and relatively high thermopower of the sample with $x = 0.02$ resulted in the highest PF for this sample.

In general, the thermal conductivity of the sulphur-containing samples is lower than that of the single-phase sulphur-free sample, except for the sample with $x = 0.08$, as shown in figure 6.4(d). To understand the contribution of phonons and both majority and minority carriers to the heat transport mechanisms in the materials, the two-band model shown in chapter 2 was used to evaluate the lattice thermal conductivity of the material.

Measurements of the thermopower, carrier concentration, and electrical resistivity were used to estimate the density of states effective mass m^*_{DOS} for both holes and electrons, the deformation potential E_{def} of the conduction and valence bands, and the reduced Fermi level. The valley degeneracies of the valence and conduction bands were obtained from the literature (shown in table 6.4), and these values were linearly interpolated considering the composi-

Table 6.4. Longitudinal speed of sound and valley degeneracy of Bi_2Te_3, Bi_2Se_3, Bi_2S_3

Material	v_l (m.s^{-1})	N_v (VB)	N_v (CB)
Bi_2Te_3	2668 [413]	6 [433]	2 [433]
Bi_2Se_3	3390 [466]	1 [433]	1 [433]
Bi_2S_3	4267 [399]	3 [467]	2 [467]

tion of each sample.

The calculated values of the electronic, bipolar and lattice contributions to the thermal conductivity of the samples are shown in figures 6.7(a), (b) and (c) respectively. The electronic contribution, κ_e, follows the same behaviour as the electrical resistivity, with the low resistivity samples showing higher values. The bipolar thermal conductivity values show an exponential increase with temperature due to the thermal activation of minority carriers [465]. The presence of sulphur reduced the values of κ_{bp}, with lower values for the samples with added sulphur up to ≈450 K, possibly due to the presence of additional majority carriers in these materials.

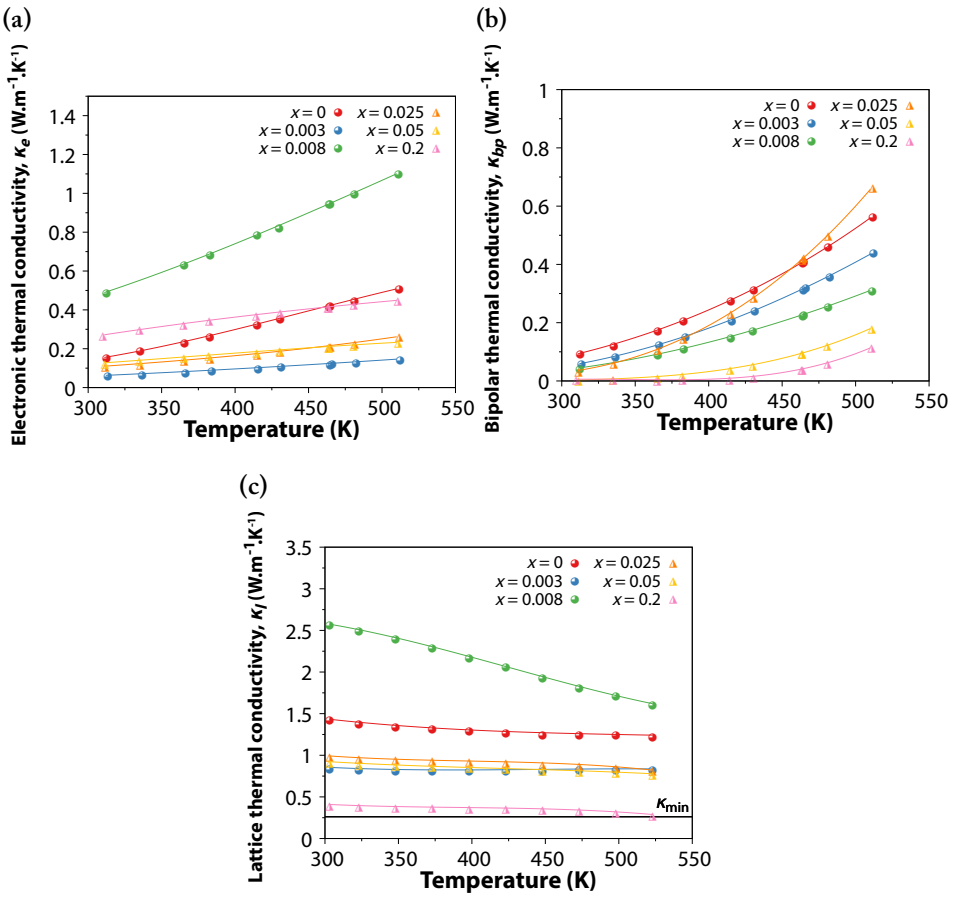

Figure 6.7. Temperature dependence of the (a) electronic, (b) bipolar, and (c) lattice thermal conductivities (estimated from the two-band model and the Wiedemann-Franz law; see text for details) of $Bi_2(Te_{2.7}Se_{0.3})_{1-x}S_{3x}$, x = (0, 0.003, 0.008, 0.0016, 0.025, 0.05, 0.1, and 0.2).

The lattice thermal conductivity of the samples with added sulphur decreased significantly compared to the single-phase sulphur-free sample, except for the sample with x = 0.008. It is noteworthy that the multiphase sample with the highest sulphur concentration and the largest proportion of secondary phase, x = 0.2, had a surprisingly low value for κ_l, approaching Clarke's limit [350] of $\kappa_{min} \approx 0.261\,W.m^{-1}.K^{-1}$ for Bi_2Te_3 at higher temperatures (calculated as shown in chapter 2). The behaviour of κ_l is mainly determined by the phonon scattering mechanisms that occur in the materials, including phonon-phonon normal/Umklapp process scattering, boundary scattering and pore scattering [468].

The two main reasons for the remarkably low values of lattice thermal conductivity in these sample sets are: 1) the porosity of the samples due to the low density of the samples, which created additional scattering centres [220, 469]; and 2) the presence of a secondary phase, which created additional boundary

scattering (as discussed in chapter 2).

To understand these changes in the lattice thermal conductivity of the sample, the material was modelled using the Debye-Callaway model for κ_l. The scattering mechanisms used to model these materials were Umklapp processes, normal processes, point defects, grain boundaries, and dislocations. The measured longitudinal speed of sound and calculated Debye (calculated as seen in chapter 3) are given in table 6.5. The used value of for the transverse speed of sound was $1600\,\mathrm{m.s^{-1}}$ [470] and the average speed of sound was calculated using equation 3.73.

Table 6.5. Longitudinal speed of sound and Debye temperature of $Bi_2(Te_{2.7}Se_{0.3})_{1-x}S_{3x}$, x = (0, 0.003, 0.008, 0.0016, 0.025, 0.05, 0.1, and 0.2).

x	v_l ($\mathrm{m.s^{-1}}$)	θ_D (K)
0	2320	166
0.003	2286	163
0.008	2012	151
0.016	2300	164
0.025	2203	158
0.05	2256	161
0.1	2195	157
0.2	2320	166

The parameters used in the Debye-Callaway model are shown in tables 6.6 and 6.7.

Table 6.6. Parameters used in the lattice thermal conductivity model for $Bi_2Te_{2.7}Se_{0.3}$

Parameters	Description	Value	Reference
v_l	longitudinal speed of sound ($m.s^{-1}$)	2320	Experimental
v_t	transverse speed of sound ($m.s^{-1}$)	1570	[471]
v	average phonon speed ($m.s^{-1}$)	1712	Calculated
γ	Grüneisen parameter	1.51	Fitted
Γ	scattering factor	1.55×10^{-3}	Calculated
$\bar{M}_{Bi_2Te_{2.7}Se_{0.3}}$	average atomic mass of $Bi_2Te_{2.7}Se_{0.3}$ (kg)	2.61×10^{-25}	…
β	proportionality constant for normal process	0.18	Fitted
$\bar{V}_{Bi_2Te_{2.7}Se_{0.3}}$	average atomic volume of $Bi_2Te_{2.7}Se_{0.3}$ (m^3)	3.45×10^{-29}	…
L	average grain size (μm)	5	Fitted
N_D	density of dislocations (cm^{-2})	2.3×10^{10}	Fitted
B_D	effective Burger's vector (nm)	1.2	[472]
ν	Poisson's ratio	0.26	Calculated
K	bulk modulus of Bi_2Te_3 (GPa)	37.4	[470]
c_0	concentration of Bi_2Se_3 in $Bi_2Te_{2.7}Se_{0.3}$	0.1	Calculated
T_a	sample annealing temperature (K)	723.15	…
$M_{Bi_2Te_3}$	average atomic mass of Bi_2Te_3 (kg)	2.66×10^{-25}	…
$M_{Bi_2Se_3}$	average atomic mass of Bi_2Se_3 (kg)	2.17×10^{-25}	…
M_{Bi}	atomic mass of Bi (kg)	3.47×10^{-25}	…
M_{Te}	atomic mass of Te (kg)	2.12×10^{-25}	…
M_{Se}	atomic mass of Se (kg)	1.31×10^{-25}	…
Bi_2Te_3	average atomic volume of Bi_2Te_3 (m^3)	3.39×10^{-29}	…
Bi_2Se_3	average atomic volume of Bi_2Te_3 (m^3)	2.82×10^{-29}	…
V	volume of the unit cell (m^3)	5.04×10^{-28}	…
θ_D	Debye temperature (K)	166	Experimental

Table 6.7. Parameters used in the lattice thermal conductivity model for $Bi_2Te_{2.16}Se_{0.24}S_{0.6}$

Parameters	Description	Value	Reference
v_l	longitudinal speed of sound ($m.s^{-1}$)	2320	Experimental
v_t	transverse speed of sound ($m.s^{-1}$)	1570	[471]
v	average phonon speed ($m.s^{-1}$)	1712	Calculated
γ	Grüneisen parameter	0.124	Fitted
Γ	scattering factor	5.69	Calculated
$\bar{M}_{Bi_2Te_{2.16}Se_{0.24}S_{0.6}}$	average atomic mass of $Bi_2Te_{2.16}Se_{0.24}S_{0.6}$ (kg)	2.43×10^{-25}	…
β	proportionality constant for normal process	0.36	Fitted
$\bar{V}_{Bi_2Te_{2.16}Se_{0.24}S_{0.6}}$	average atomic volume of $Bi_2Te_{2.16}Se_{0.24}S_{0.6}$ (m^3)	3.3261×10^{-29}	…
L	average grain size (μm)	5	Fitted
N_D	density of dislocations (cm^{-2})	6.99×10^9	Fitted
B_D	effective Burger's vector (nm)	1.2	[472]
ν	Poisson's ratio	0.26	Calculated
K	bulk modulus of Bi_2Te_3 (GPa)	37.4	[470]
c_0	concentration of Bi_2Se_3 in $Bi_2Te_{2.7}Se_{0.3}$	0.1	Calculated
T_a	sample annealing temperature (K)	723.15	…
$M_{Bi_2Te_3}$	average atomic mass of Bi_2Te_3 (kg)	2.66×10^{-25}	…
$M_{Bi_2Se_3}$	average atomic mass of Bi_2Se_3 (kg)	2.17×10^{-25}	…

Table 6.7 (continued)

Parameters	Description	Value	Reference
M_{Bi}	atomic mass of Bi (kg)	3.47×10^{-25}	…
M_{Te}	atomic mass of Te (kg)	2.12×10^{-25}	…
M_{Se}	atomic mass of Se (kg)	1.31×10^{-25}	…
M_S	atomic mass of S (kg)	0.532×10^{-25}	…
Bi_2Te_3	average atomic volume of Bi_2Te_3 (m^3)	3.39×10^{-29}	…
Bi_2Se_3	average atomic volume of Bi_2Te_3 (m^3)	2.82×10^{-29}	…
V	volume of the unit cell (m^3)	5.04×10^{-28}	…
θ_D	Debye temperature (K)	166	Experimental

Figure 6.8(a) shows the fitted lattice thermal conductivity with the scattering mechanisms as described above. The relaxation times of all scattering mechanisms are seen in figure 6.8(b) while the spectral thermal conductivity is seen in figure 6.8(c) considering U (Umklapp processes), N (Normal processes), PD (point defects), GB (grain boundaries), and D (dislocations). As can be seen in figures 6.8(b) and (c), U + N + PD introduces high-frequency phonon scattering, while GB introduces low-frequency scattering. D improves the scattering with wide-frequency phonon scattering. Therefore, point defects, grain boundaries, and dislocations play major roles in the thermal conductivity in this sample.

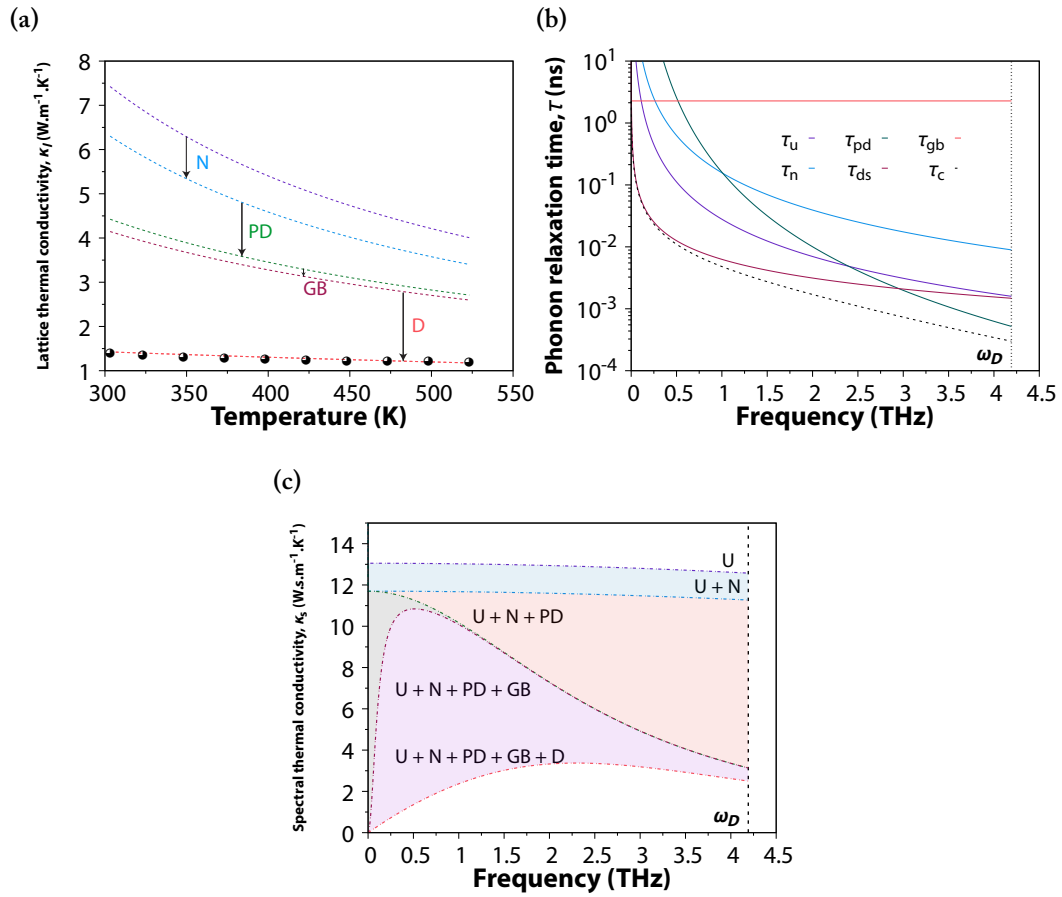

Figure 6.8. (a) Fitted lattice thermal conductivity, (b) relaxation times for the various scattering mechanisms, and (c) calculated spectral thermal conductivity for the various scattering mechanisms for $Bi_2Te_{2.7}Se_{0.3}$

Figure 6.9(a) shows the fitted lattice thermal conductivity with the scattering mechanisms as described above for $Bi_2(Te_{2.7}Se_{0.3})_{1-x}S_{3x}$ with $x = 0.2$. The relaxation times of all scattering mechanisms are seen in figure 6.9(b) while the spectral thermal conductivity is seen in figure 6.9(c) considering U (Umklapp processes), N (Normal processes), PD (point defects), GB (grain boundaries), and D (dislocations). Differently from the sample with no sulphur, this sample has a higher contribution of PD scattering, which is consistent with the introduction of the secondary phase of sulphur and can be observed in the increased Γ value. As can be seen in figures 6.9(b) and (c), U + N + PD introduces high-frequency phonon scattering, while GB introduces low-frequency scattering. D improves the scattering with a wide-frequency phonon scattering similar to the sample with no sulphur.

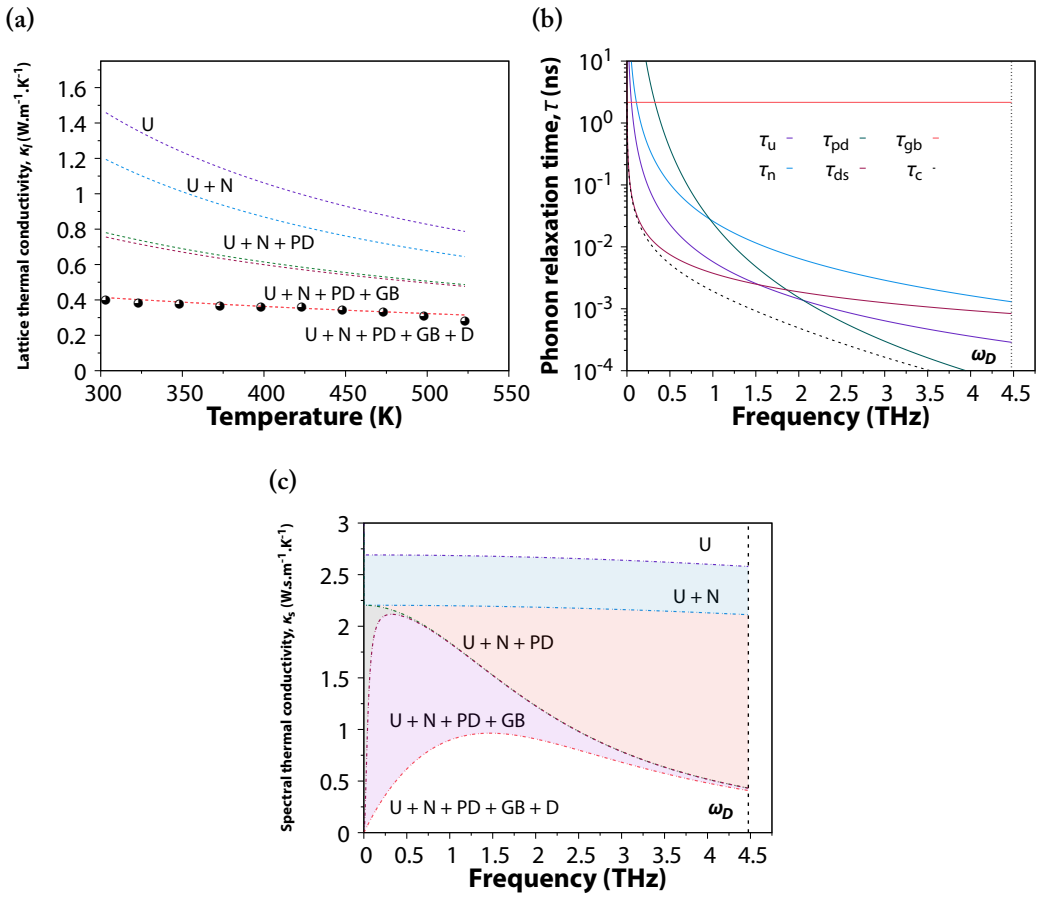

Figure 6.9. (a) Fitted lattice thermal conductivity, (b) relaxation times for the various scattering mechanisms, and (c) calculated spectral thermal conductivity for the various scattering mechanisms for $Bi_2(Te_{2.7}Se_{0.3})_{1-x}S_{3x}$, x = 0.2.

6.3.3 Figure of merit zT

The temperature dependence of zT is shown in figure 6.10. It is clear that zT is significantly increased in the sulphur-added samples compared to the sulphur-free sample. The maximum value of about 0.55 was obtained for the sample with x = 0.2. The increase in the figure of merit is due to the simultaneous improvement in the thermopower and decrease in the thermal conductivity.

These samples showed low values of zT when compared to those reported in the literature, which can reach up to 1.2 [41, 148, 409, 423, 437, 438, 440, 448, 473, 474]. The main reason for this low performance was the low density of the samples, which caused the high resistivity values. It should be stated, however, that the samples have the same conditions and that the conclusions and arguments of the text remain valid.

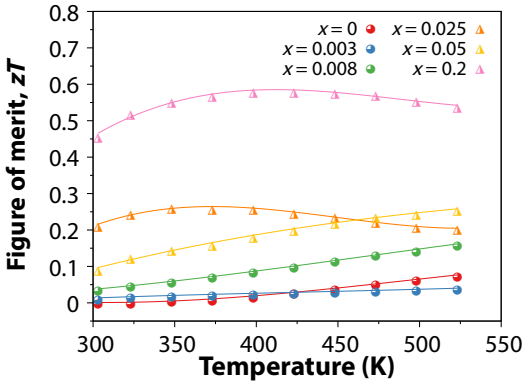

Figure 6.10. Temperature dependence of zT for $Bi_2(Te_{2.7}Se_{0.3})_{1-x}S_{3x}$, x = (0, 0.003, 0.008, 0.025, 0.05, and 0.2) samples.

6.4 Conclusion

Chapter 6 shows that adding sulphur to $Bi_2Te_{2.7}Se_{0.3}$ samples altered their thermoelectric properties significantly. When low sulphur concentrations were added to the composition, it changed the density of states and defect chemistry, thus inducing major changes in electrical resistivity and thermopower.

At higher sulphur concentrations, a secondary phase of Bi_2S_3 developed[5]. The bulk electrical transport properties of the multiphase samples followed a simple composite rule (given by the effective medium theory) at lower fractions, increasing electrical resistivity and thermopower as expected. However, at the maximum sulphur level, the transport properties departed from this simple principle, probably due to the formation of an impurity band between the two phases, which increased electron donation and, by consequence, reduced electrical resistivity.

The use of multiphase samples with a Bi_2S_3 secondary phase was shown to be highly effective for reducing thermal conductivity. The sample with the highest fraction of the Bi_2S_3 phase displayed remarkably low lattice thermal conductivities, approaching the theoretical minimum for Bi_2Te_3. This significant reduction was attributed to the introduction of the secondary phase, which substantially increased phonon scattering at the boundaries. Additional defects, such as porosity, further suppressed lattice thermal conductivity.

Overall, sulphur inclusion successfully reduces thermal conductivity while enhancing thermopower in both single-phase and multiphase samples. The highest figure of merit zT of 0.55 was achieved at $x = 0.2$.

This chapter demonstrates how sulphur alloying can improve band struc-

[5]The composition of the samples was estimated from their diffraction patterns; however, XRD analysis does not provide information on the distribution of the secondary phase or the elemental composition. Therefore, the conclusions presented here are limited by the scope of the experiments conducted in this chapter.

ture and phonon transport to enhance the thermoelectric performance of $Bi_2Te_{2.7}Se_{0.3}$-based compounds. The presence of a secondary phase has been found to significantly alter the electrical resistivity, thermopower, and thermal conductivity of the material, potentially enabling the development of highly efficient thermoelectric materials. The significant reduction in thermal conductivity obtained by incorporating a secondary phase highlights the advantage of using multiphase thermoelectric materials to achieve higher zT.

The set of samples studied in this chapter demonstrate rather low thermoelectric transport properties compared to values reported in literature. This is attributed to the poor mechanical properties of the samples investigated here. While the conclusions drawn are valid for these specific low-quality samples, they may not extend to higher quality samples with improved mechanical properties and transport characteristics.

References

(41) Q. Hu, W. Qiu, L. Chen, J. Chen, L. Yang and J. Tang, *ACS Appl. Mater. Interfaces*, 2021, **13**, 38526–38533, doi: 10.1021/acsami.1c12722.

(65) Y. Z. Pei, Z. M. Gibbs, A. Gloskovskii, B. Balke, W. G. Zeier and G. J. Snyder, *Adv. Energy Mater.*, 2014, **4**, 1400486, doi: 10.1002/aenm.201400486.

(70) A. Soni, Z. Yanyuan, Y. Ligen, M. K. K. Aik, M. S. Dresselhaus and Q. Xiong, *Nano Letters*, 2012, **12**, 1203–1209, doi: 10.1021/nl2034859.

(80) M. S. Dresselhaus, G. Chen, M. Y. Tang, R. G. Yang, H. Lee, D. Z. Wang, Z. F. Ren, J. P. Fleurial and P. Gogna, *Adv. Mater.*, 2007, **19**, 1043–1053, doi: 10.1002/adma.200600527.

(88) D. L. Medlin and G. J. Snyder, *Curr. Opin. Colloid Interface Sci.*, 2009, **14**, 226–235, doi: 10.1016/j.cocis.2009.05.001.

(110) D. Zhang, J. Lei, W. Guan, Z. Ma, C. Wang, L. Zhang, Z. Cheng and Y. Wang, *J. Alloys Compd.*, 2019, **784**, 1276–1283, doi: 10.1016/j.jallcom.2019.01.084.

(111) Z. Zhang, W. Zhao, W. Zhu, S. Ma, C. Li, X. Mu, P. Wei, X. Nie, Q. Zhang and W. Zhao, *J. Electron. Mater.*, 2020, **49**, 2794–2801, doi: 10.1007/s11664-019-07851-x.

(114) M. Liu and X. Y. Qin, *Appl. Phys. Lett.*, 2012, **101**, 132103, doi: 10.1063/1.4755768.

(148) S. Li, Y. Liu, F. Liu, D. He, J. He, J. Luo, Y. Xiao and F. Pan, *Nano Energy*, 2018, **49**, 257–266, doi: 10.1016/j.nanoen.2018.04.047.

(220) A. F. May, E. Flage-Larsen and G. J. Snyder, *Phys. Rev. B*, 2010, **81**, 125205, doi: 10.1103/PhysRevB.81.125205.

(326) B. H. Toby and R. B. Von Dreele, *J. Appl. Crystallogr.*, 2013, **46**, 544–549, doi: 10.1107/S0021889813003531.

(338) A. International, *ASTM E1269-11*, 2018, doi: 10.1520/E1269-11R18.

(350) D. R. Clarke, *Surface and Coatings Technology*, 2003, **163–164**, 67–74, doi: 10.1016/S0257-8972(02)00593-5.

(366) W. Liu, K. C. Lukas, K. McEnaney, S. Lee, Q. Zhang, C. P. Opeil, G. Chen and Z. Ren, *Energy Environ. Sci.*, 2013, **6**, 552–560, doi: 10.1039/c2ee23549h.

(391) M. Jonson and G. D. Mahan, *Phys. Rev. B*, 1980, **21**, 4223–4229, doi: 10.1103/PhysRevB.21.4223.

(399) H. Koc, H. Ozisik, E. Deligöz, A. M. Mamedov and E. Ozbay, *J. Mol. Model.*, 2014, **20**, 2180, doi: 10.1007/s00894-014-2180-1.

(405) S. A. Yamini, R. Santos, **Fortulan, Raphael**, A. A. Gazder, A. Malhotra, D. Vashaee, I. Serhiienko and T. Mori, *ACS Applied Materials & Interfaces*, 2023, **15**, 19220–19229, doi: 10.1021/acsami.3c01956.

(409) W.-S. Liu, Q. Zhang, Y. Lan, S. Chen, X. Yan, Q. Zhang, H. Wang, D. Wang, G. Chen and Z. Ren, *Advanced Energy Materials*, 2011, **1**, 577–587, doi: 10.1002/aenm.201100149.

(411) I. T. Witting, F. Ricci, T. C. Chasapis, G. Hautier and G. J. Snyder, *Research*, 2020, **2020**, 1–15, doi: 10.34133/2020/4361703.

(413) Q. Tao, F. Meng, Z. Zhang, Y. Cao, Y. Tang, J. Zhao, X. Su, C. Uher and X. Tang, *Materials Today Physics*, 2021, **20**, 100472, doi: 10.1016/j.mtphys.2021.100472.

(420) T. Parashchuk, R. Knura, O. Cherniushok and K. T. Wojciechowski, *ACS Applied Materials & Interfaces*, 2022, **14**, 33567–33579, doi: 10.1021/acsami.2c08686.

(423) Y.-K. Zhu, J. Guo, Y.-X. Zhang, J.-F. Cai, L. Chen, H. Liang, S.-W. Gu, J. Feng and Z.-H. Ge, *Acta Materialia*, 2021, **218**, 117230, doi: 10.1016/j.actamat.2021.117230.

(427) N. S. Chauhan, S. V. Pyrlin, O. I. Lebedev, L. S. A. Marques, M. M. D. Ramos, T. Maiti, K. Kovnir, B. A. Korgel and Y. V. Kolen'ko, *The Journal of Physical Chemistry C*, 2021, **125**, 20184–20194, doi: 10.1021/acs.jpcc.1c05375.

(428) Devender, P. Gehring, A. Gaul, A. Hoyer, K. Vaklinova, R. J. Mehta, M. Burghard, T. Borca-Tasciuc, D. J. Singh, K. Kern and G. Ramanath, *Advanced Materials*, 2016, **28**, 6436–6441, doi: 10.1002/adma.201601256.

(429) X. Wu, Z. Wang, R. Jiang, Y. Tian, Y. Liu, J. Shi, W. Zhao and R. Xiong, *Materials Today Physics*, 2022, **29**, 100904, doi: 10.1016/j.mtphys.2022.100904.

(430) C. Zhang, Z. Peng, Z. Li, L. Yu, K. A. Khor and Q. Xiong, *Nano Energy*, 2015, **15**, 688–696, doi: 10.1016/j.nanoen.2015.05.022.

(431) B. Zhu, X. Liu, Q. Wang, Y. Qiu, Z. Shu, Z. Guo, Y. Tong, J. Cui, M. Gu and J. He, *Energy & Environmental Science*, 2020, **13**, 2106–2114, doi: 10.1039/D0EE01349H.

(432) M. Carle, P. Pierrat, C. Lahalle-Gravier, S. Scherrer and H. Scherrer, *Journal of Physics and Chemistry of Solids*, 1995, **56**, 201–209, doi: 10.1016/0022-3697(94)00166-9.

(433) S. K. Mishra, S. Satpathy and O. Jepsen, *Journal of Physics: Condensed Matter*, 1997, **9**, 461, doi: 10.1088/0953-8984/9/2/014.

(434) S. Wang, H. Li, R. Lu, G. Zheng and X. Tang, *Nanotechnology*, 2013, **24**, 285702, doi: 10.1088/0957-4484/24/28/285702.

(435) J. H. Kim, S. Y. Back, J. H. Yun, H. S. Lee and J.-S. Rhyee, *Materials*, 2021, **14**, 1564, doi: 10.3390/ma14061564.

(436) J. H. Kim, H. Cho, S. Y. Back, J. H. Yun, H. S. Lee and J.-S. Rhyee, *Journal of Alloys and Compounds*, 2020, **815**, 152649, doi: 10.1016/j.jallcom.2019.152649.

(437) B. Jabar, X. Qin, A. Mansoor, H. Ming, L. Huang, M. H. Danish, J. Zhang, D. Li, C. Zhu, H. Xin and C. Song, *Nano Energy*, 2021, **80**, 105512, doi: 10.1016/j.nanoen.2020.105512.

(438) S. Li, X. Liu, Y. Liu, F. Liu, J. Luo and F. Pan, *Nano Energy*, 2017, **39**, 297–305, doi: 10.1016/j.nanoen.2017.07.011.

(439) Y.-X. Zhang, Y.-K. Zhu, D.-S. Song, J. Feng and Z.-H. Ge, *Chemical Communications*, 2021, **57**, 2555–2558, doi: 10.1039/D1CC00119A.

(440) J. Zhang, H. Ming, D. Li, X. Qin, J. Zhang, L. Huang, C. Song and L. Wang, *ACS Applied Materials & Interfaces*, 2020, **12**, 37155–37163, doi: 10.1021/acsami.0c09338.

(441) A. Saji, S. Ampili, S.-H. Yang, K. J. Ku and M. Elizabeth, *Journal of Physics: Condensed Matter*, 2005, **17**, 2873, doi: 10.1088/0953-8984/17/19/005.

(442) J.-D. Musah, X. Yanjun, A. M. Ilyas, T. G. Novak, S. Jeon, C. Arava, S. V. Novikov, D. S. Nikulin, W. Xu, L. Liu, A. Md, K.-H. Lam, X. Chen, C.-M. L. Wu and V. A. L. Roy, *ACS Applied Materials & Interfaces*, 2019, **11**, 44026–44035, doi: 10.1021/acsami.9b11344.

(443) J. Kennedy, P. P. Murmu, P. Kumar and G. Ramanath, *Materials Research Bulletin*, 2021, **142**, 111426, doi: 10.1016/j.materresbull.2021.111426.

(444) K. H. Lee, H.-S. Kim, M. Kim, J. W. Roh, J.-H. Lim, W. J. Kim, S.-i. Kim and W. Lee, *Acta Materialia*, 2021, **205**, 116578, doi: 10.1016/j.actamat.2020.116578.

(445) I. Malik, T. Srivastava, K. K. Surthi, C. Gayner and K. K. Kar, *Materials Chemistry and Physics*, 2020, **255**, 123598, doi: 10.1016/j.matchemphys.2020.123598.

(446) E. J. Ahmadov, D. M. Babanly, S. Z. Imamaliyeva, D. B. Tagiev and M. B. Babanly, *Inorganic Materials*, 2021, **57**, 227–233, doi: 10.1134/S0020168521030018.

(447) E. Abrahams, S. V. Kravchenko and M. P. Sarachik, *Reviews of Modern Physics*, 2001, **73**, 251–266, doi: 10.1103/RevModPhys.73.251.

(448) C.-L. Chen, T.-H. Wang, Z.-G. Yu, Y. Hutabalian, R. K. Vankayala, C.-C. Chen, W.-P. Hsieh, H.-T. Jeng, D.-H. Wei and Y.-Y. Chen, *Advanced Science*, 2022, **9**, 2201353, doi: 10.1002/advs.202201353.

(449) D. Li, J. M. Li, J. C. Li, Y. S. Wang, J. Zhang, X. Y. Qin, Y. Cao, Y. S. Li and G. D. Tang, *Journal of Materials Chemistry A*, 2018, **6**, 9642–9649, doi: 10.1039/C8TA00525G.

(450) B. Du, J. Su, M. Tian, T. Han and J. Li, *Scientific Reports*, 2018, **8**, 8481, doi: 10.1038/s41598-018-26773-y.

(451) J. Navrátil, Z. Starý and T. Plechácek, *Materials Research Bulletin*, 1996, **31**, 1559–1566, doi: 10.1016/S0025-5408(96)00149-3.

(452) Q. Zhang, B. Gu, Y. Wu, T. Zhu, T. Fang, Y. Yang, J. Liu, B. Ye and X. Zhao, *ACS Applied Materials & Interfaces*, 2019, **11**, 41424–41431, doi: 10.1021/acsami.9b15198.

(453) F. A. Kröger and H. J. Vink, 1956, 307–435, doi: 10.1016/S0081-1947(08)60135-6.

(454) *CRC Handbook of Chemistry and Physics*, ed. W. M. Haynes, CRC Press, 0th edn., 2014, doi: 10.1201/b17118.

(455) F. Habashi, in *Encyclopedia of Metalloproteins*, ed. R. H. Kretsinger, V. N. Uversky and E. A. Permyakov, Springer, New York, NY, 2013, pp. 283–284, doi: 10.1007/978-1-4614-1533-6_413.

(456) H. Fang, J.-H. Bahk, T. Feng, Z. Cheng, A. M. S. Mohammed, X. Wang, X. Ruan, A. Shakouri and Y. Wu, *Nano Research*, 2016, **9**, 117–127, doi: 10.1007/s12274-015-0892-x.

(457) P. Lošťák, Č. Drašar, D. Bachan, L. Beneš and A. Krejčová, *Radiation Effects and Defects in Solids*, 2010, **165**, 211–215, doi: 10.1080/10420151003616663.

(458) R. J. Mehta, Y. Zhang, C. Karthik, B. Singh, R. W. Siegel, T. Borca-Tasciuc and G. Ramanath, *Nature Materials*, 2012, **11**, 233–240, doi: 10.1038/nmat3213.

(459) R. J. Mehta, Y. Zhang, H. Zhu, D. S. Parker, M. Belley, D. J. Singh, R. Ramprasad, T. Borca-Tasciuc and G. Ramanath, *Nano Letters*, 2012, **12**, 4523–4529, doi: 10.1021/nl301639t.

(460) D. Stroud, *Physical Review B*, 1975, **12**, 3368–3373, doi: 10.1103/PhysRevB.12.3368.

(461) D. S. McLachlan, M. Blaszkiewicz and R. E. Newnham, *Journal of the American Ceramic Society*, 1990, **73**, 2187–2203, doi: 10.1111/j.1151-2916.1990.tb07576.x.

(462) **Fortulan, Raphael**, S. A. Yamini, C. Nwanebu, S. Li, T. Baba, M. J. Reece and T. Mori, *ACS Applied Energy Materials*, 2022, **5**, 3845–3853, doi: 10.1021/acsaem.2c00295.

(463) A. D. McNaught and A. Wilkinson, *The IUPAC Compendium of Chemical Terminology*, ed. V. Gold, International Union of Pure and Applied Chemistry (IUPAC), 2019, doi: 10.1351/goldbook.

(464) M. Hong, T. C. Chasapis, Z.-G. Chen, L. Yang, M. G. Kanatzidis, G. J. Snyder and J. Zou, *ACS Nano*, 2016, **10**, 4719–4727, doi: 10.1021/acsnano.6b01156.

(465) S. Wang, J. Yang, T. Toll, J. Yang, W. Zhang and X. Tang, *Scientific Reports*, 2015, **5**, doi: 10.1038/srep10136.

(466) X. Gao, M. Zhou, Y. Cheng and G. Ji, *Philosophical Magazine*, 2016, **96**, 208–222, doi: 10.1080/14786435.2015.1128126.

(467) P. Larson, V. A. Greanya, W. C. Tonjes, R. Liu, S. D. Mahanti and C. G. Olson, *Physical Review B*, 2002, **65**, 085108, doi: 10.1103/PhysRevB.65.085108.

(468) J. A. Perez-Taborda, M. Muñoz Rojo, J. Maiz, N. Neophytou and M. Martin-Gonzalez, *Scientific Reports*, 2016, **6**, 32778, doi: 10.1038/srep32778.

(469) A. Banik, B. Vishal, S. Perumal, R. Datta and K. Biswas, *Energy & Environmental Science*, 2016, **9**, 2011–2019.

(470) J. O. Jenkins, J. A. Rayne and R. W. Ure, *Physical Review B*, 1972, **5**, 3171–3184, doi: 10.1103/PhysRevB.5.3171.

(471) Q. Zhang, Y. Lin, N. Lin, Y. Yu, F. Liu, C. Fu, B. Ge, O. Cojocaru-Mirédin, T. Zhu and X. Zhao, *Materials Today Physics*, 2022, **22**, 100573, doi: 10.1016/j.mtphys.2021.100573.

(472) D. L. Medlin, K. J. Erickson, S. J. Limmer, W. G. Yelton and M. P. Siegal, *Microscopy and Microanalysis*, 2014, **20**, 1088–1089, doi: 10.1017/S1431927614007168.

(473) D. H. Kim, H.-S. Kim, S. Hong, J. H. Lee, J. G. Han, H. S. Cho, S. W. Lee and S.-I. Kim, *Electron. Mater. Lett.*, 2021, **17**, 436–442, doi: 10.1007/s13391-021-00300-0.

(474) S. F. Ma, C. C. Li, L. Xing, X. Mu, W. T. Zhu, X. L. Nie, X. H. Sang, P. Wei, Q. J. Zhang and W. Y. Zhao, *J. Electron. Mater.*, 2020, **49**, 2881–2889, doi: 10.1007/s11664-020-07956-8.

7

Thermoelectric performance of CrSb added $Bi_{0.5}Sb_{1.5}Te_3$ compounds

Let no one be discouraged because their cradle was not generous, let no one consider themselves ill-fated because they lack in birthright wealth and qualities. In all of this, there are no surprises that cannot be expected from tenacity and sanctity in work.
— Rui Barbosa, Oração aos Moços

Summary
This chapter investigated the effects of the inclusion of a secondary magnetic phase on the thermoelectric performance of BiSbTe materials and was divided into two parts. In the first part, samples with varying percentages (0.5 to 25 wt.%) of the CrSb phase in a $Bi_{0.5}Sb_{1.5}Te_3$ matrix were prepared by direct reaction of the raw elements and SPS. The inclusion of small amounts of CrSb was found to improve the thermal performance due to an increased effective mass due to the presence of magnetic drag effects. However, higher percentages of CrSb resulted in reduced carrier mobility and an overall decrease in zT and power factor, probably due to increased carrier scattering. The optimum composition contained 0.5 wt.% CrSb and showed improved thermopower without a significant decrease in electrical conductivity. In the second, a new set of samples with lower CrSb contents were prepared by ball milling followed by SPS and confirmed these initial results. This work demonstrates the complex interactions between magnetic phases, charge carriers and thermoelectric properties. While small additions of secondary phases can improve performance through magnetic drag effects, larger percentages are detrimental, highlighting the need for precise control of multiphase compositions.

7.1 First part - mixing and melting raw elements

7.1.1 Introduction

As mentioned earlier in this thesis, bismuth telluride alloys are considered to be the most efficient thermoelectric materials for room temperature applications. Alloying Bi_2Te_3 with Sb_2Te_3 can tune the carrier concentration, reduce the lattice contribution to the thermal conductivity and induce band convergence, which contributes to an increase in zT [411, 475].

In chapter 4 it was shown that magnetic dopants have been proposed as a more recent strategy to increase the thermopower in thermoelectric materials, with the same result also observed in the literature [279, 289, 291] (see chapter 2 for more details). In summary, the carriers interact with the local magnetic moments, which effectively drag the carriers, resulting in increased carrier effective mass, increased thermopower, and decreased carrier mobility. However, the overall effect is an increase in power factor [290, 365]. Also, as discussed in the literature review chapter (see chapter 2), the addition of secondary magnetic phases has also been proposed to improve thermoelectric properties [294, 295, 297], as the combination of several phases can improve electrical conductivity, thermopower, and thermal conductivity [40, 157].

In this study, a series of samples of $Bi_{0.5}Sb_{1.5}Te_3$ with x wt.% CrSb (x = 0, 0.5, 1, 5, 10, 25, and 100) were first prepared by casting and powder processing using SPS. CrSb was chosen because it is a p-type antiferromagnetic semiconductor with a high Néel temperature (680 $\sim$ 710 K), which makes it suitable for studying its magnetic properties in the low temperature range of thermoelectric applications. Here, it is shown that by adding small percentages of a magnetic secondary phase, it is possible to increase the thermoelectric power of the composites. However, the electrical conductivity of the composite sample is significantly reduced. In the next section of this chapter, a new series of samples of $Bi_{0.5}Sb_{1.5}Te_{3.3}$ with x wt.% CrSb (x = 0, 0.125, 0.25, 0.5, and 1) have been prepared by ball milling and SPS to verify the conclusions drawn in this first part.

This chapter builds on the foundations laid by the previous ones. The inclusion of the magnetic secondary phase is a natural extension of the results presented in chapter 4 and is consistent with the review presented in chapter 2.

7.1.2 Experimental details

7.1.2.1 Synthesis

A series of polycrystalline samples of $Bi_{0.5}Sb_{1.5}Te_3$ with x wt.% CrSb (x = 0, 0.5, 1, 5, 10, and 25) were synthesised by direct reaction of stoichiometric amounts of high purity elements of Bi shots (99. 999%, Alfa Aesar), Te pieces (99.999%, Alfa Aesar), Sb shots (99.999%, Alfa Aesar), and Cr 60 mesh powder (99.95%,

Alfa Aesar) in vacuum sealed quartz ampoules loaded in an inert atmosphere glove box. The ampoules were heated up 850 °C for 12 hours, homogenised at 1000 °C, quenched in cold water, and then annealed at 400 °C for 72 h. The resulting ingots were ground by hand into fine powders in an agate mortar and pestle in an inert glove box. The powders were then loaded into a graphite die and sintered under vacuum to produce 11 mm diameter rods using SPS (KCE FCT-H HP D-25 SD, FCT Systeme GmbH, Rauenstein, Germany) at a pressure of 50 MPa for 5 min and a temperature of 400 °C. The densities of all samples were measured from the dimensions and weight of the rod. The average density of the samples was approximately 85% of their nominal density.

The suboptimal force control of the SPS equipment resulted in an effective pressure lower than the set one, which caused the powders to be consolidated only by Joule heating of the particles, resulting in a high degree of porosity in the samples and,consequently, a low density [476, 477]. In figure 7.1 the temperature (in black) and the applied force (in pink) are shown for the sintering process of $Bi_{0.5}Sb_{1.5}Te_3$ with 0.5 wt.% CrSb. As can be seen, similarly to chapter 5, the temperature control was stable and the force control was poor.

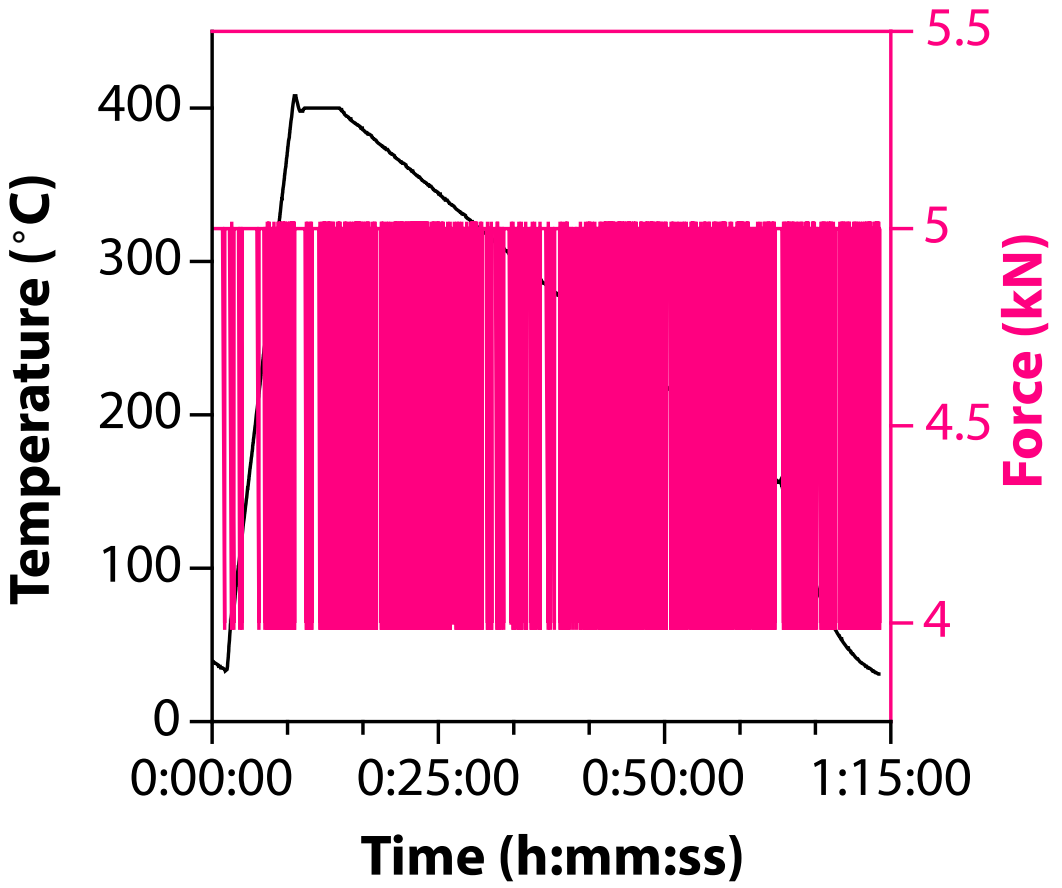

Figure 7.1. Temperature (shown in black) and applied force (shown in pink) curves versus time for the sintering process of $Bi_{0.5}Sb_{1.5}Te_3$ with 0.5 wt.% CrSb.

A pristine CrSb sample was also synthesised by loading stoichiometric amounts of Cr 60 mesh powder (99.95%, Alfa Aesar) and Sb shots (99.999%, Alfa Aesar) into a vacuum sealed quartz ampoule. The ampoule was heated to 850 °C for 24 hours, mixed every 4 hours, homogenised at 1160 °C for 1 hour, and allowed to cool naturally in the furnace. The resulting ingot was ground by hand with an agate mortar and pestle housed in a glove box, loaded into a vacuum sealed quartz tube, and annealed at 900 °C for 24 hours to eliminate the presence of a $CrSb_2$ impurity phase. The annealed powder was then loaded into a graphite die and sintered under vacuum to produce 11 mm diameter rods using SPS (KCE FCT-H HP D-25 SD, FCT Systeme GmbH, Rauenstein, Germany) at a pressure of 50 MPa for 20 min at a temperature of 1173 K. The sample had a density of 99.9% of the nominal value. The selected temperatures are shown in the Cr-Sb phase diagram in figure 7.2 [478].

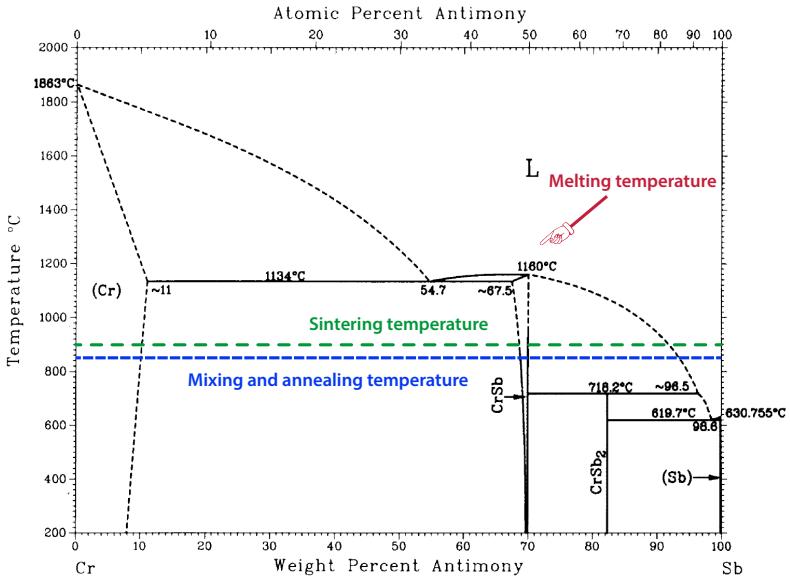

Figure 7.2. Cr-Sb binary phase diagram. Adapted from [478].

7.1.2.2 Materials characterisation

Phase purity and crystal structure of the sintered samples were characterised by PXRD using a PANalytical X'Pert Pro diffractometer with Cu-Kα1 radiation (λ = 1.5406 Å, 40 kV, 40 mA).

7.1.2.3 Thermoelectric transport properties

Electrical conductivity (σ) and thermopower (α) were measured parallel to the sintering direction of the samples by cutting $\approx 2 \times 2 \times 8$ mm^3 bar specimens from the rods. Measurements were conducted from room temperature to 523 K under a helium atmosphere using a Linseis LSR-3 apparatus.

The thermal diffusivity (D) of all samples was measured by the LFA method using a NETZSCH LFA 467 HyperFlash®instrument. Heat capacity measurements were conducted from room temperature to 473 K using a PerkinElmer DSC 8000 according to ASTM sapphire standard method E1269 and from 473 K to 773 K using a TA Instruments SDT 650 simultaneous thermal analyser according to ASTM modulated DSC method E2716 (both discussed in chapter 3).

Slab-shaped samples were also cut to measure the room temperature Hall coefficient (R_{H}) under a ± 0.55 T magnetic field using an ECOPIA 3000 Hall Effect Measurement System. The Hall carrier concentration (n_{H}) was calculated as $n_{\mathrm{H}} = 1/(e \cdot R_{\mathrm{H}})$.

The speed of sound was measured for the sintered pellets using the pulse-echo method at room temperature with an Olympus 38DL PLUS apparatus.

7.1.3 Results and discussion

7.1.3.1 Structural and phase analysis

The phase purity and crystal structure of all samples were determined by indexing their PXRD patterns (see fig. 7.3). Two distinct phases were identified: a primary rhombohedral $Bi_{0.5}Sb_{1.5}Te_3$ phase, and a secondary hexagonal CrSb phase[1]. The mixing ratio between the phases was extrapolated using the full-pattern summation method [479] on the PANalytical X'Pert HighScore Plus software package, as shown in table 7.1.

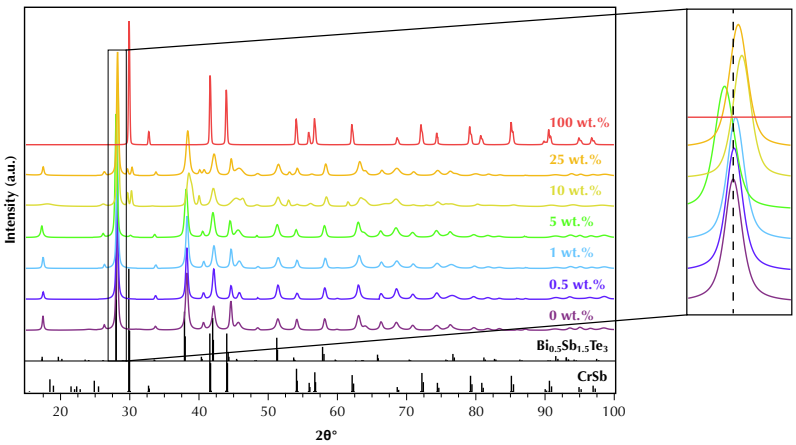

Figure 7.3. Powder X-ray diffraction patterns of $Bi_{0.5}Sb_{1.5}Te_3$ with x wt.% CrSb (x = 0, 0.5, 1, 5, 10, 25, and 100). The inset shows the zoomed area around the peak with highest intensity.

Table 7.1. Mixture ratio of $Bi_{0.5}Sb_{1.5}Te_3$ with x wt.% CrSb (x = 0, 0.5, 1, 5, 10, 25, and 100)

x	$Bi_{0.5}Sb_{1.5}Te_3$ (wt.%)	CrSb (wt.%)
0	100	0
0.5	100	0
1	100	0
5	94.5	5.5
10	87.2	12.8
25	73.3	26.7
100	0	100

[1]Materials Project ID mp-1641

7.1.3.2 Transport properties analysis

Figure 7.4 shows the temperature dependent electrical transport properties of the $Bi_{0.5}Sb_{1.5}Te_3$ with x wt.% CrSb (x = 0, 0.5, 1, 5, 10, 25, and 100) samples measured perpendicularly to the sintering direction. The electrical conductivity of all samples decreases with the temperature, typical behaviour of degenerate semiconductors (see fig. 7.4(b)) and the conductivity of all samples decreased with the increase in the secondary phase.

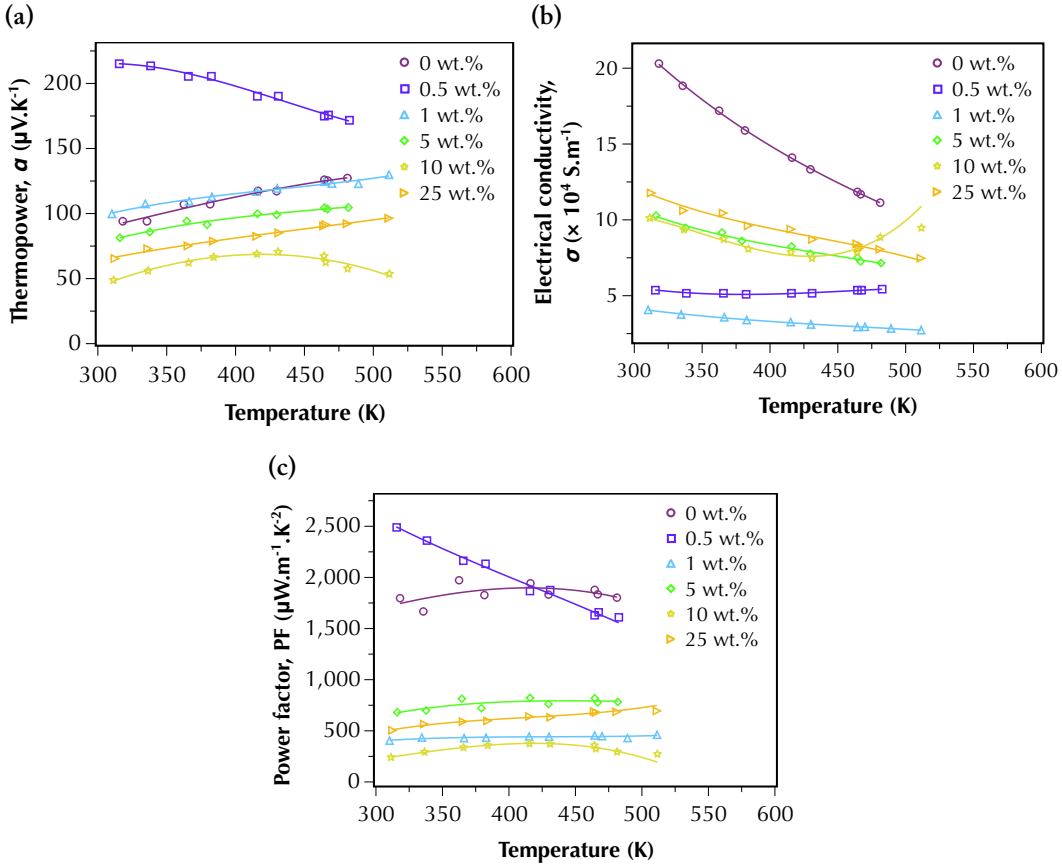

Figure 7.4. Temperature dependence of the (a) thermopower, (b) electrical conductivity, and (c) power factor of $Bi_{0.5}Sb_{1.5}Te_3$ with x wt.% CrSb (x = 0, 0.5, 1, 5, 10, and 25) samples.

A first attempt to understand the behaviour of the electrical conductivity can be by using the effective medium approximation discussed in more details in chapter 2. From equation 2.31, the electrical conductivity of two phase material can be expressed as

$$v_1 \frac{\sigma_1 - \sigma_e}{\sigma_1 + 2\sigma_e} + v_2 \frac{\sigma_2 - \sigma_e}{\sigma_2 + 2\sigma_e} = 0, \tag{7.1}$$

where v_i is the volume fraction of phase i, σ_i is electrical conductivity of phase i

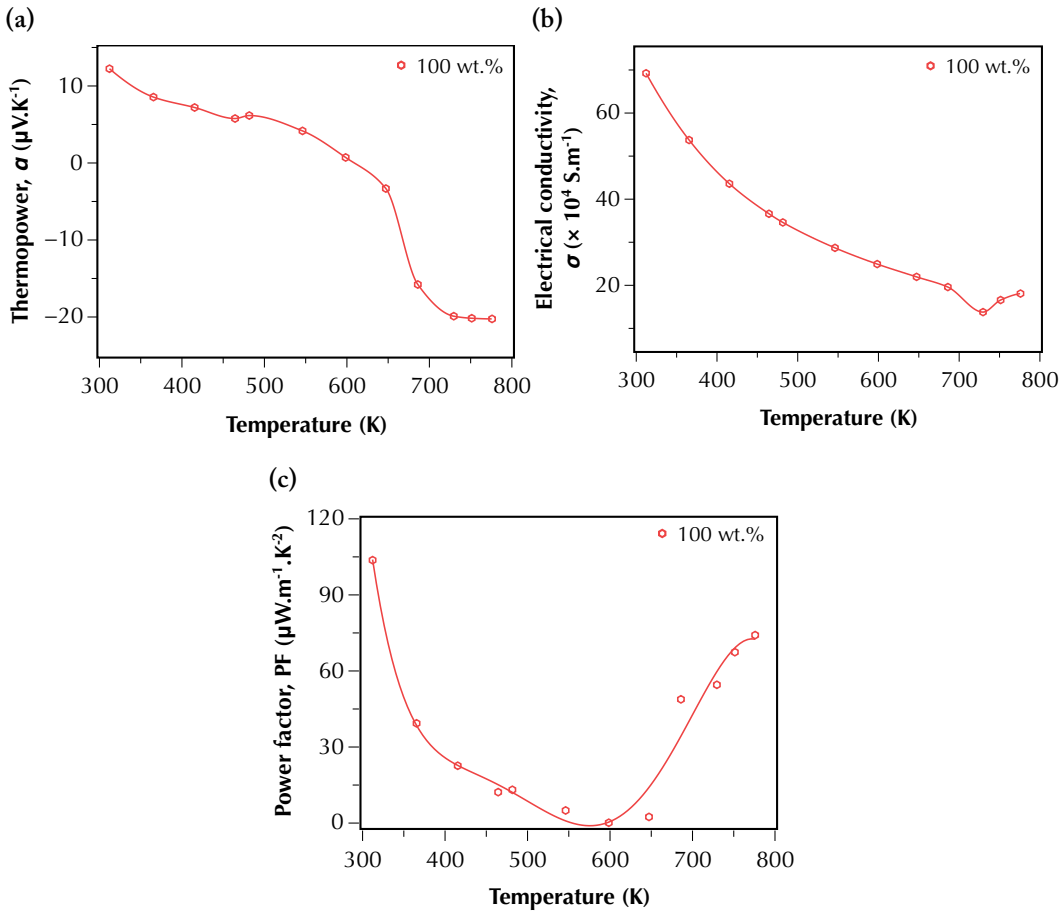

FIGURE 7.5. Temperature dependence of the (a) thermopower, (b) electrical conductivity, and (c) power factor of the pristine CrSb sample.

and the identity matrix, and σ_e is the effective electrical conductivity.

Equation 7.1 indicates that the effective conductivity of the material is proportional to both the volume fraction of phase i and its conductivity ($\sigma_e \propto \|nu_i\sigma_i\|$). Given the high conductivity values of the secondary phase (see fig. 7.5(b)), it was expected that the multiphase samples would show higher electrical conductivity values, which does not happen. This implies that there are additional transport mechanisms that are not accounted for by the effective medium approach.

To gain insight into this, Hall effect measurements were carried out on these samples at room temperature and are shown in table 7.2. It was observed that the non-pristine samples exhibited lower values of Hall mobility (μ_H) compared to the pristine $Bi_{0.5}Sb_{1.5}Te_3$ sample. The reduction in electrical conductivity can be explained by a twofold mechanism: first, the introduction of a secondary phase into the material creates additional scattering centres for the charges and reduces their mobility. This mechanism has been widely discussed and is a common occurrence in multiphase thermoelectric materials [50, 480]. Secondly, according

to the results presented in chapter 4 and in [279, 289, 365], the presence of magnetic phases, particles, and dopants in the materials can adversely affect the carrier mobility. The combination of these two effects was hypothesised to be responsible for the changes in Hall mobility.

The Hall carrier concentration of the composite samples showed higher values compared to the $Bi_{0.5}Sb_{1.5}Te_3$ sample, as it seems that the presence of an additional phase with a higher carrier concentration (11.5×10^{19} cm^{-3} in CrSb compared to 1.57×10^{19} cm^{-3} for pristine $Bi_{0.5}Sb_{1.5}Te_3$) has increased the carrier concentration of the bulk material. This is evidenced by the overall trend of increasing n_H with respect to secondary phase inclusion.

This discussion suggests that the reduction in electrical mobility was the primary factor that led to the decrease of the electrical conductivity in the samples.

Table 7.2. Hall carrier concentration, Hall carrier mobility, thermopower, and effective mass of $Bi_{0.5}Sb_{1.5}Te_3$ with x wt.% CrSb (x = 0, 0.5, 1, 5, 10, 25, and 100) measured at room temperature

x (wt.%)	n_H ($\times 10^{19}$)	μ_H (cm^2.V^{-1}.s^{-1})	α (μV.K^{-1})	m^*/m_0
0	1.57	285	94	0.28
0.5	1.77	221	215	0.57
1	2.24	109	99	0.38
5	4.04	159	81	0.45
10	3.36	215	44	0.24
25	5.12	143	65	0.42
100	11.5	383	12	0.13

All samples showed a positive thermopower α (figs. 7.4(a) and 7.5(a)), which indicates p-type semiconductors and is consistent with the Hall effect measurements (table 7.2). The low values of the thermopower for the samples ($\approx$95 μV.K^{-1}) are in agreement with experimental [481] and *ab initio* calculations [427] where no Te excess was added to the material.

The change in the slope of the thermopower and electrical conductivity of the pure CrSb sample (fig. 7.5(a) and (b)) is due to a change in the magnetic regime of the material. As discussed in chapter 2, the thermopower due to the presence of magnons is dependent of the scattering rates of carriers and magnons and the magnons specific heat which follows a T^3 [482]. Around 680 K, the material changes from an ordered antiferromagnetic (AFM) regime, where magnons exist, to a disordered magnetic regime, where magnons do not exist and there is no contribution to the thermopower, changing the slope of both α and σ.

Except for the sample with 0.5 wt.% CrSb, all multiphase samples showed lower power factors as a result of lower thermopower and electrical conductivity (see fig. 7.4(c)). The power factor showed a higher value for the sample with

0.5 wt.% CrSb compared to pristine $Bi_{0.5}Sb_{1.5}Te_3$ at room temperature due to its higher thermopower ($\approx$2500 $\mu W.m^{-1}.K^{-1}$) compared to the latter's value of ($\approx$1750 $\mu W.m^{-1}.K^{-1}$).

To examine the influence of the secondary phase on thermopower, the materials were modelled using the SPB model as discussed in chapter 3. Table 7.2 lists the calculated hole effective mass (m^*). The sample with the lowest CrSb concentration (0.5 wt.%) revealed an increase of around 46% in m^*, consistent with what was observed in chapter 4 and [289, 290]. However, in the samples with a higher percentage of the secondary phase, an increase in effective mass does not overwrite the impact of an increased carrier concentration, leading to lower values of thermopower.

To gain more insight of the band structure of the materials the weighted mobility μ_W of the materials was calculated with the following expression [483]

$$\mu_W = \frac{3h^3\sigma}{8\pi e(2m_0 k_B T)^{3/2}} = \left[\frac{\exp\left(\frac{|\alpha|}{k_B/e} - 2\right)}{1 + \exp\left(-5\left(\frac{|\alpha|}{k_B/e} - 1\right)\right)} + \frac{\frac{3}{\pi^2}\frac{|\alpha|}{k_B/e}}{1 + \exp\left(5\left(\frac{|\alpha|}{k_B/e} - 1\right)\right)}\right] \approx \mu\left(\frac{m^*}{m_0}\right)^{3/2}, \quad (7.2)$$

and their values are plotted in figure 7.6.

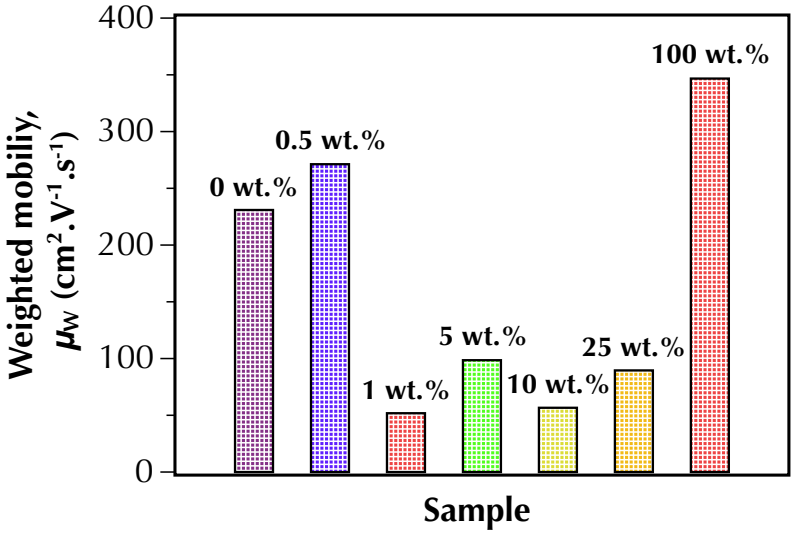

Figure 7.6. Room temperature weighted mobility of $Bi_{0.5}Sb_{1.5}Te_3$ with x wt.% CrSb (x = 0, 0.5, 1, 5, 10, 25, 100) samples.

Equation 7.2 is based on the SPB model. However, this equation provides an independent method of evaluating the band structure of the material, as it

does not rely on the Hall effect measurements. The weighted mobility increases significantly for the samples with a low percentage of the secondary phase. This suggests that there is a notable increase in the effective mass $(m^*)^{3/2}$ of the density of states. However, as the percentage of the secondary phase increases, μ_W declines rapidly and falls below the values of pristine $Bi_{0.5}Sb_{1.5}Te_3$. These results agree with the Hall effect measurements, but they are independent of them. Therefore, they support the conclusions reached previously.

Heat capacity measurements were carried out for all the samples, and they are displayed in figure 7.7. The behaviour of the heat capacity of the CrSb sample can be understood by recognising that, for temperatures below the Néel temperature of the material [482], the magnon contribution in the AFM regime followed a T^3 law [280], whereas the lattice contribution at higher temperatures was almost constant, as predicted by the Dulong and Petit law (proof in the appendix). Figure 7.7(b) readily shows this finding. At temperatures exceeding roughly 680 K, which is the Néel temperature of the material [482], the magnon contribution is insignificant, and only the lattice contribution is observed. It should be noted that CrSb exhibits mostly linear behaviour in the specific heat capacity for temperatures up to 450 K. This behaviour provides an explanation for the linear relationship observed in the set of samples with x wt.% CrSb (x = 0.5, 1, 5, 10, and 25) in $Bi_{0.5}Sb_{1.5}Te_3$.

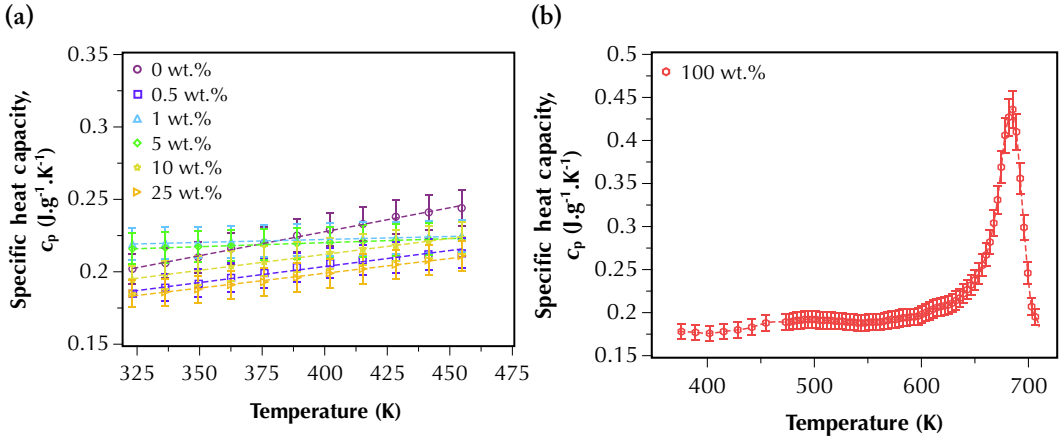

Figure 7.7. Temperature-dependent specific heat capacity of (a) $Bi_{0.5}Sb_{1.5}Te_3$ with x wt.% CrSb (x = 0, 0.5, 1, 5, 10, and 25) and (b) CrSb samples. The dashed line represents a linear fit of the data for (a) and a cubic Hermite spline for (b).

The thermal conductivity (κ) of the samples is shown in figure 7.8(a). As the temperature increases, the thermal conductivity (κ) of all samples begin to increase. The electronic contribution to the thermal conductivity (κ_e) is shown in figure 7.8(b), and it was estimated using the Wiedemann-Franz law [391] ($\kappa_e = L\sigma T$) as discussed in chapter 3, where L represents the Lorenz number.

The values of L were calculated using the SPB model and are depicted in figure 7.8(d). Since multiphase samples have a lower electrical conductivity, κ_e is reduced accordingly. The bipolar (κ_b) and lattice (κ_l) contributions to the thermal conductivity were computed as $\kappa_l + \kappa_b = \kappa - \kappa_e$, and are shown in figure 7.8(c). All samples show an exponential pattern with $\kappa_l + \kappa_b$, indicating a significant bipolar contribution to the thermal conductivity [429, 465].

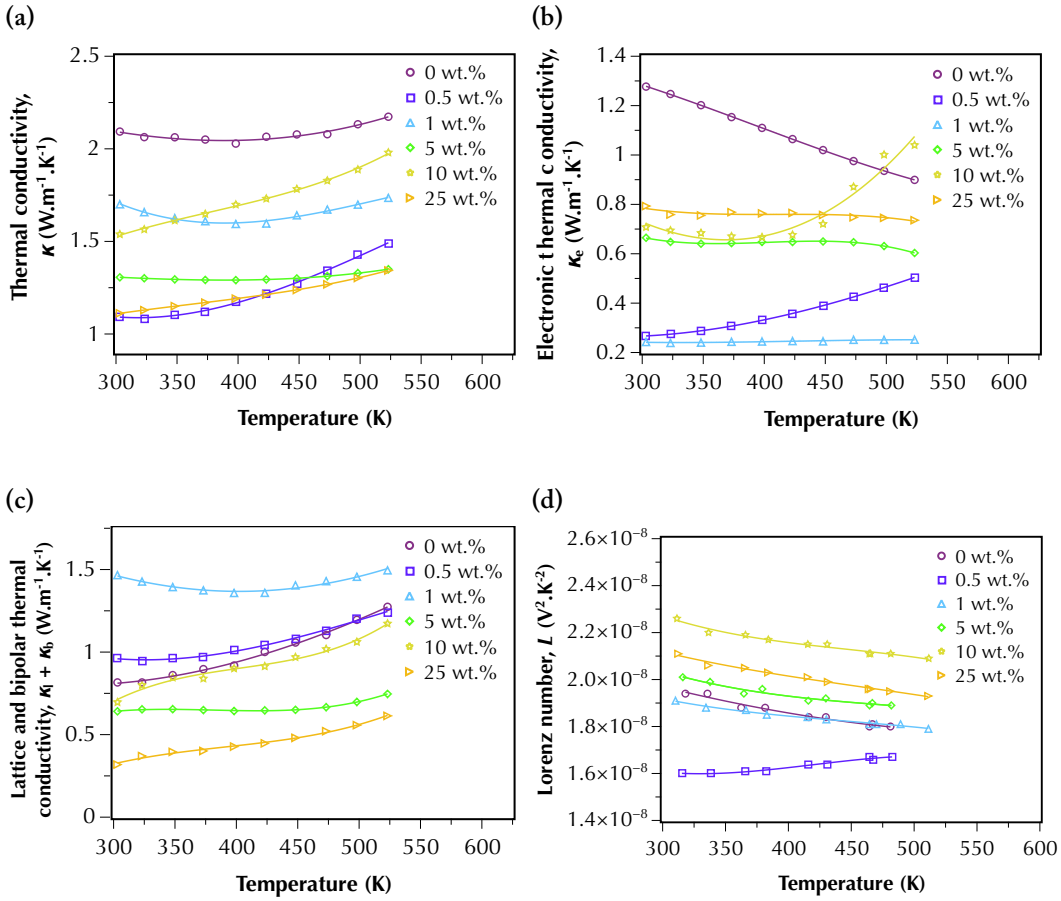

Figure 7.8. Temperature dependence of the (a) thermal conductivity, (b) electronic thermal conductivity, (c) lattice and bipolar thermal conductivity, and (d) Lorenz number of $Bi_{0.5}Sb_{1.5}Te_3$ with x wt.% CrSb (x = 0, 0.5, 1, 5, 10, and 25) samples.

The measured longitudinal speed of sound (v_l) of all samples is given in table 7.3. Transversal measurements were not available, so the average speed of sound was estimated (according to equation 3.73) using the literature value of 1533 $m.s^{-1}$ [484]. The Debye temperature is also given in the table 7.3 and was estimated using the equation 3.86.

All samples had similar average speed of sound and therefore Debye temperature values. This clarifies the similar values of heat capacity for $Bi_{0.5}Sb_{1.5}Te_3$ with x wt.% CrSb (x = 0, 0.5, 1, 5, 10 and 25) (see figure 7.7(a)).

Table 7.3. Measured longitudinal speed of sound at room temperature, calculated average speed of sound, and calculated Debye temperature of $Bi_{0.5}Sb_{1.5}Te_3$ with x wt.% CrSb (x = 0, 0.5, 1, 5, 10, and 25)

x (wt.%)	v_l (m.s^{-1})	v (m.s^{-1})	θ_D (K)
0	1750	1593	195
0.5	2140	1658	203
1	2230	1668	204
5	2270	1673	206
10	1890	1621	200
25	1960	1633	205

Due to their higher carrier concentrations, the samples with lower CrSb content (x = 0.5 and 1) have suppressed the bipolar conduction up to about 350 K (see figure 7.8(c)), which allowed the use of the Debye-Callaway model [485, 486] to understand the lattice thermal conductivity behaviour of these two samples. For this set of samples, the expression for the combined relaxation time (τ_c) followed the same expression as seen in chapter 4

$$\tau_c^{-1} = \tau_{pd}^{-1} + \tau_n^{-1} + \tau_u^{-1} + \tau_{gb}^{-1} = A\omega^4 + \beta\tau_u^{-1} + B_u T\omega^2 e^{-\frac{\theta_D}{3T}} + \frac{v_s}{L}, \qquad (7.3)$$

where τ_{pd}, τ_n, τ_u and τ_{gb} are the relaxation times for point defect scattering, normal three phonon process, Umklapp process, and grain boundary scattering respectively, L is the mean grain size and the coefficients A, β and B_u are fitting parameters. The values of the speed of sound and the Debye temperature have been measured (see table 7.3) while L has been estimated from the fitted diffraction pattern. Table 7.4 shows the fitted parameters and the average grain size.

The sample containing 0.5 wt.% of CrSb had a more significant point defect scattering than the sample containing 1 wt.% of CrSb, which explains the lower values of the lattice thermal conductivity. As per [344, 486], point defect scattering is directly proportional to the mass fluctuations in the material. Therefore, it is likely that the changes in the secondary phase distribution on the material led to this effect. Currently, microscopy data is unavailable, but it will be investigated in future studies.

Table 7.4. Calculated parameters for the Debye-Callaway model for $Bi_{0.5}Sb_{1.5}Te_3$ with x wt.% CrSb (x = 0.5 and 1)

x	A (10^{-40} s^3)	β	B_u (10^{-20} s.K)	L (μm)
0.5	283	1.0	1.02	0.1367
1	135	0.9	0.88	0.1276

Figure 7.9 depicts the modelled lattice thermal conductivity and the measured values. The dashed lines represent the values calculated by the Debye-Callaway model, and the arrows indicate the point at which bipolar conduction begins to make a significant contribution to the thermal conductivity, causing the model to fail in predicting the behaviour of $\kappa_l + \kappa_b$.

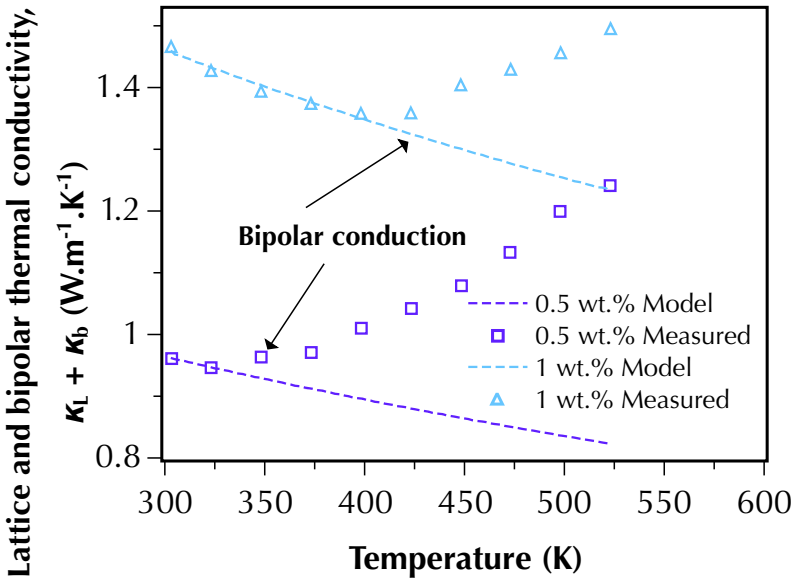

Figure 7.9. Modelled lattice and bipolar thermal conductivity of $Bi_{0.5}Sb_{1.5}Te_3$ with x wt.% CrSb (x = 0.5 and 1) samples. The dashed lines represent the values calculated by the Debye-Callaway model.

7.1.3.3 Figure of merit zT

The dimensionless figure of merit zT of $Bi_{0.5}Sb_{1.5}Te_3$ with x wt.% CrSb (x = 0, 0.5, 1, 5, 10 and, 25) is shown in figure 7.10. The higher power factor of the sample containing 0.5 wt.% of CrSb enabled a higher figure of merit up to 375 K compared to the single phase $Bi_{0.5}Sb_{1.5}Te_3$. Due to the combination of lower power factor and higher thermal conductivity, the rest of the multiphase samples exhibit reduced values.

It is worth noting that the zT values of this sample set are lower than previously reported in the literature, where values greater than 1 have been observed [154, 402, 484, 487]. The main reasons for the low efficiency are the non-doped nature and low density of these samples. In the next part of this chapter, these two factors will be addressed by doping the samples with excess Te and sintering them on a different SPS furnace (to obtain denser samples).

7.1.4 Partial conclusion

In this first part of the study, multiphase samples of $Bi_{0.5}Sb_{1.5}Te_3$ with x wt.% CrSb (x = 0, 0.5, 1, 5, 10 and 25) were successfully prepared by melting the

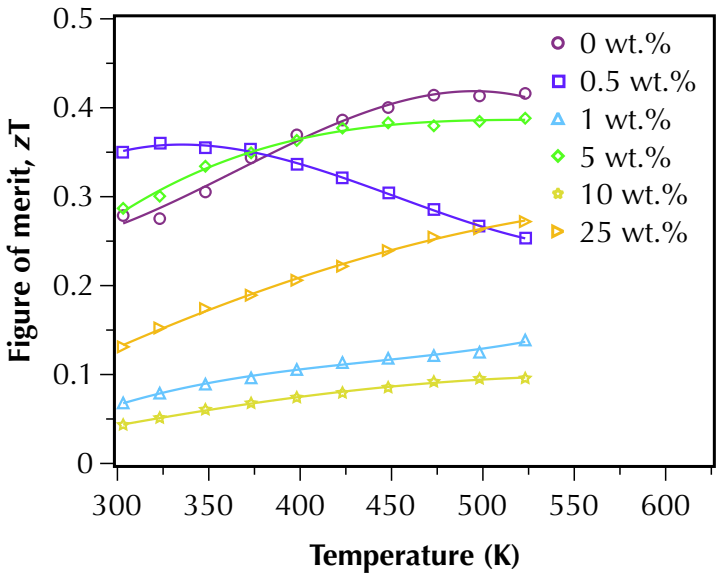

FIGURE 7.10. Temperature dependence of zT of $Bi_{0.5}Sb_{1.5}Te_3$ with x wt.% CrSb (x = 0, 0.5, 1, 5, 10, and 25) samples.

raw elements and sintering. Electronic transport measurements showed that the sample with a lower percentage of magnetic phase exhibited a large increase in thermopower due to an increased effective mass. The conductivity of the multiphase samples is significantly reduced compared to their single phase counterparts due to the greatly reduced mobility. The thermal conductivities of the multiphase samples are slightly reduced. The sample containing a low percentage of CrSb (x = 0.5) showed a larger zT at room temperature. However, samples with higher percentages showed a deterioration in performance.

7.2 Second part - ball milling

7.2.1 Introduction

After preparing a set of samples by direct mixing of all the raw elements, it was found that the optimum composition was between 0 and 1 wt.% CrSb in $Bi_{0.5}Sb_{1.5}Te_3$. To verify the assumption that the addition of small amounts of CrSb improves the thermoelectric properties and to avoid a *non sequitur*, a new set of samples was prepared by wet ball milling of stoichiometric $Bi_{0.5}Sb_{1.5}Te_3$ 10 at.% Te-rich and CrSb. Wet ball milling was used as it provides smaller particles [488–491], sharper particle size distribution [491], and it hinders the oxidation process as the powder is not in contact with the atmosphere. Excess tellurium was added to the system as Te-rich bismuth telluride and bismuth antimony telluride alloys have shown high thermoelectric performance with a significant reduction in lattice thermal conductivity and suppression of defects in the system [427, 477, 487, 492, 493].

The impact of defects, such as tellurium vacancies ($V_{Te}^{\bullet\bullet}$, which are electron donor defects), on thermoelectric properties is addressed in chapter 6. Inclusion of excess Te suppresses the defects caused by its easy volatilisation during the SPS process [494]. This strategy was shown to result in more efficient thermoelectric materials [427].

7.2.2 Experimental details

A set of multiphase polycrystalline samples of $Bi_{0.5}Sb_{1.5}Te_{3.3}$ with x wt.% CrSb (x = 0, 0.125, 0.25, 0.5, and 1) were synthesised by ball milling previously prepared $Bi_{0.5}Sb_{1.5}Te_{3.3}$ and CrSb following the same procedures as described in the first part of this chapter. The cast ingots were manually pre-milled by hand using an agate mortar and pestle housed inside a glovebox.

The powders were weighed and placed in a 250 mL agate jar along with 20 mm agate balls and ethanol absolute (99.97%, VWR). The ball to powder ratio was 15:1, and the ratio of solvent to powder used was 100 ml to 10 g [356].

The milling process was conducted using a Retsch Planetary Ball Mill PM 100 at 300 rpm for 4 h in 15 min intervals with a 5 min break and a change of direction half way through the milling process. The purpose of the breaks and intervals was to prevent heat buildup and breakage of the jar's seal. The change in direction was made to ensure the milling process was more uniform.

Following the milling, the jar was opened, the balls were removed with the help of a forceps and washed with isopropyl alcohol (99%, VWR) to minimise powder loss. Subsequently, the jar was placed in a desiccator for a minimum of 15 h. The dried powders were then placed into a graphite die and sintered under vacuum to fabricate 11 mm diameter rods utilising SPS. Samples were sintered at a pressure of 50 MPa for 5 min at a temperature of 400 °C. The densities of

all samples were measured from the rod dimensions and weight. The samples had an average density of approximately 95% of their nominal density.

7.2.3 Materials characterisation and thermoelectric transport properties

The samples were characterised and their properties measured using the same procedure as described in the first part of the chapter. The diffraction patterns of the ball-milled samples were obtained using a PANalytical Empyrean diffractometer with Co-Kα1 radiation ($\lambda = 1.7889$ Å, 40 kV, 40 mA). Bar-shaped specimens ($\approx 2 \times 2 \times 8$ mm^3), cut perpendicular to the direction of sintering pressure, were used to measure their electrical conductivity (σ) and thermopower (α). Measurements were performed from room temperature to 523 K under a helium atmosphere using a Linseis LSR-3 apparatus.

Additionally, circular samples were cut to measure the room temperature Hall coefficient (R_{H}) under a ± 0.55 T magnetic field using an ECOPIA 3000 Hall Effect Measurement System. The Hall carrier concentration (n_{H}) was calculated as $n_{\mathrm{H}} = 1/(e \cdot R_{\mathrm{H}})$.

7.2.4 Results and discussion

7.2.4.1 Selection of the ball milling parameters

Ball milling experiments for thermoelectric materials can range from $1 \sim 60$ h at $100 \sim 500$ rpm [495–497]. From a practical perspective, one would assume that these variables (or factors) are discrete, with certain "levels", and could use a full factorial experiment to determine the effects of the factors on the particle size [498]. However, the number of runs (or trials) required to complete a full factorial experiment increases rapidly; in fact, the number of runs required for a no repetition experiment with X, Y, Z, …factors with x, y, z, …levels is $x \cdot y \cdot z \cdot \ldots$, which makes the experimental design logistically infeasible. A more sensible approach would be to use previous experimental results as a guide, and this was the approach taken in this work.

To obtain an indication of the best values for speed and milling time of the experiment, the values of particle size, speed and milling time from the references [356, 499, 500] were normalised[2] and analysed. As can be seen in figure 7.11(a), the relationship between milling time and particle size follows approximately an exponential decay followed by a plateau like behaviour, indicating that long milling times do not necessarily lead to smaller values of particle size in a feasible time. On the other hand, the relationship between rpm and particle size follows an inverted bell curve, i.e. as rpm increases, particle size initially decreases (for the same milling time) until it reaches a minimum value

[2] Here, normalisation is defined as $x \leftarrow \frac{x - x_{\min}}{x_{\max} - x_{\min}}$.

and then starts to increase; thus, the lowest particle size values are obtained for intermediate rpm.

Therefore, an optimal experiment would be in the middle range for rpm and the middle range for milling time (as shown by the heat map in figure 7.11(b)). Following this analysis, the chosen levels were 150 and 300 rpm and 4 and 8 h. The full factorial design is shown in table 7.5.

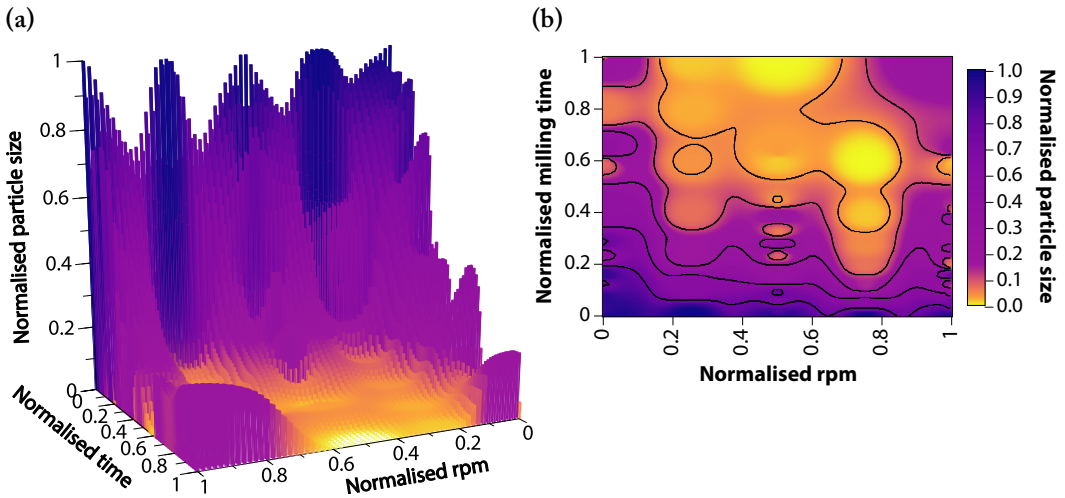

FIGURE 7.11. (a) 3D surface plot of normalised rpm, milling time, and particle size and (b) heatmap of normalised rpm, milling time, and particle size. All data was extracted from [356, 499, 500].

Table 7.5. Design of experiments table for ball milling

Trial	rpm	Milling time
1	300	4
2	150	4
3	300	8
4	150	8

The results of each trial are shown in sequence.

7.2.4.2 Crystallite size

The crystallite size of the powder were estimated using XRD. A silicon standard was used to determine the instrument contribution for the peaks shapes. Scherrer equation

$$L_c = \frac{K\lambda}{\beta_{struct}\cos\theta}, \tag{7.4}$$

where L_c is the crystallite size, K is the Scherrer constant (0.9), λ is the X-ray beam wavelength, β_{struct} is the full width at the half maximum (FWHM) of the peak, and θ is the Bragg angle, was used to calculate the crystallite size [501].

Table 7.6. Measured parameters used in Scherrer equation and calculated crystallite size for ball-milled $Bi_{0.5}Sb_{1.5}Te_{3.3}$ for 300 rpm and 4 h of milling time

Number	β_{obs} (°)	β_{inst} (°)	2θ (°)	β_{struct} (°)	Crystallite size (nm)
1	0.263	0.086	10.198	0.177	52.27
2	0.186	0.086	20.426	0.100	93.46
3	0.357	0.086	32.412	0.271	35.45
4	0.498	0.086	44.500	0.412	24.22
5	1.013	0.087	59.365	0.926	11.47
6	1.438	0.103	87.556	1.335	9.57
7	1.120	0.112	98.329	1.009	13.99
					Average crystallite size = 34 nm

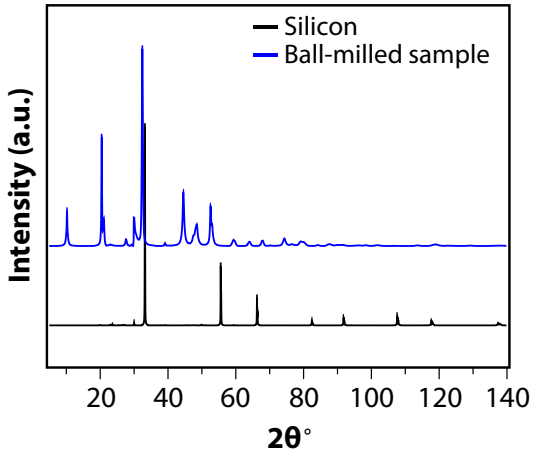

Figure 7.12. X-ray diffraction patterns of silicon standard and ball-milled $Bi_{0.5}Sb_{1.5}Te_3$ using 300 rpm and 4 h of milling time from 5°to 140°.

The instrument contribution to the measured FWHM (β_{obs}) was corrected by subtracting the value of the FWHM silicon standard (β_{inst}); thus, $\beta_{struct} = \beta_{obs} - \beta_{inst}$.

Detailed values are presented in table 7.6 and the diffraction patterns are shown in figure 7.12 for the first trial using 300 rpm and 4 h of milling time. This analysis was repeated for the rest of the trials and the results are presented in table 7.7.

Table 7.7. Trial results for the designed experiments

Trial	rpm	Milling time	Result
1	300	4	34
2	150	4	84
3	300	8	37
4	150	8	72

Table 7.8 displays the two-way ANOVA analysis of the data presented in table 7.7. Changes in the rpm factor account for approximately 96% of the

total variation, indicating that the crystallite size for the hand-milled sample was already at the tail of the decaying exponential curve for the 150 rpm trials; hence, attaining a bigger change would take more time. Nevertheless, slight variations observed in the 300 rpm trials indicate that the plateau value for the employed setup is around 34 ∼ 37 nm. The p-value of the rpm factor is 0.11, slightly higher than the usual value of 5%. However, this result is reasonable given the lack of repetition in the study [502].

Table 7.8. Two-way ANOVA of ball milling

Source of variation	% of total variation	p-value
rpm	95.94	0.1112
Milling time	1.076	0.6560

7.2.4.3 Structural and phase analysis

PXRD measurements were conducted on a PANalytical X'Pert Pro diffractometer with Cu-Kα1 radiation (λ =1.5406 Å, 40 kV, 40 mA). The phase purity and crystal structure of all samples were determined by indexing their PXRD patterns, as shown in figure 7.13. All samples matched a single phase rhombohedral $Bi_{0.5}Sb_{1.5}Te_3$ phase, with no impurity phases detected. It should be noted that the detection range for XRD phase analysis is typically 5 ∼ 10% [503]. Therefore, given the low concentration of this set of samples, it was already expected that no CrSb peaks would be observed. The refinement of the diffraction patterns was not carried out for the same reason.

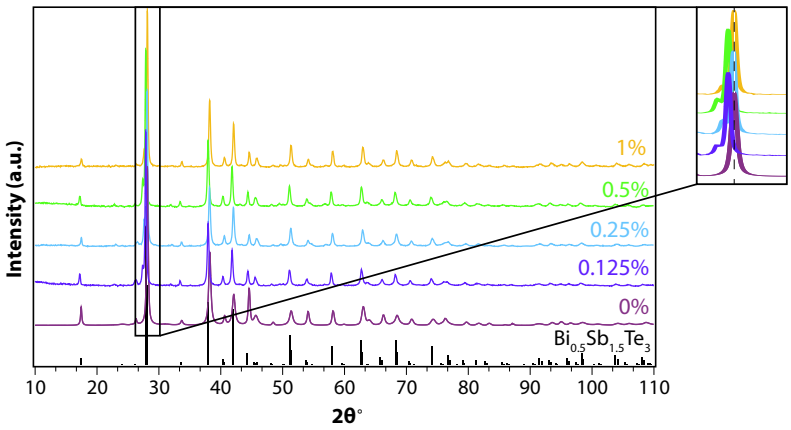

Figure 7.13. Powder X-ray diffraction patterns of $Bi_{0.5}Sb_{1.5}Te_{3.3}$ with x wt.% CrSb (x = 0, 0.125, 0.25, 0.5, and 1) samples. The inset shows the zommed area around the highest intensity peak.

7.2.4.4 Transport properties

Figure 7.14 displays the thermopower, electrical conductivity, and power factor of $Bi_{0.5}Sb_{1.5}Te_{3.3}$ with x wt.% CrSb (x = 0, 0.125, 0.25, 0.5, and 1), which were measured perpendicular to the direction of sintering. All samples showed a positive thermopower (fig. 7.14(a)), indicating a p-type semiconductor behaviour. The electrical conductivity exhibits metallic behaviour, with decreasing values at higher temperatures, as shown in figure 7.14(b). At higher temperatures, the samples containing an added secondary phase showed a large contribution from the bipolar effect, as observed by the upward trend of the electrical conductivity [418].

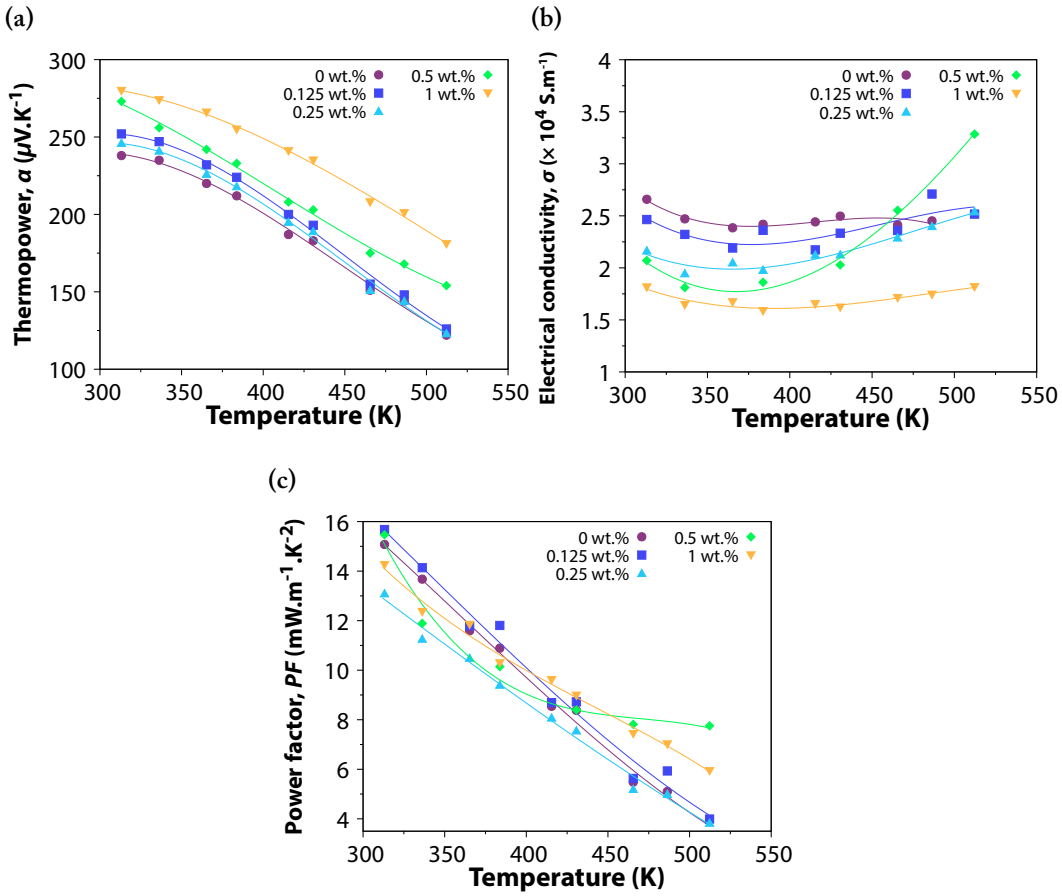

FIGURE 7.14. Temperature dependence of the (a) thermopower, (b) electrical conductivity, and (c) power factor of ball milled $Bi_{0.5}Sb_{1.5}Te_{3.3}$ with x wt.% CrSb (x = 0, 0.125, 0.25, 0.5, and 1) samples.

The thermopower of this new set of samples is greatly increased compared to the non-excess Te samples seen in the first part of this chapter. The room temperature values of α increase from ≈94 $\mu V.K^{-1}$ to ≈238 $\mu V.K^{-1}$ for the single phase sample and from ≈215 $\mu V.K^{-1}$ to ≈270 $\mu V.K^{-1}$ for the 0.5 wt.% CrSb.

Introducing Te into the system decreases the electrical conductivity of the single phase sample from $\approx 20 \times 10^4$ S.m^{-1} to $\approx 2.7 \times 10^4$ S.m^{-1} and from $\approx 5 \times 10^4$ S.m^{-1} to $\approx 2.1 \times 10^4$ S.m^{-1}.

Table 7.9 shows the Hall carrier concentration and mobility of the samples. The carrier concentrations are lower than those observed in the literature (e.g. $\approx 1 \times 10^{19}$ cm^{-3} [427]) and the non-excess Te ones, explains the lower overall electrical conductivity of the samples. The mobility value of 232 cm^2.V^{-1}.s^{-1} of the single phase samples are similar to the ones reported in literature (e.g. 248 cm^2.V^{-1}.s^{-1} [487]).

The values for n range from $7.7 \sim 7.1\ 10^{18}$ cm^{-3}, indicating that the addition of Te to the system has stabilised the carrier concentration for the samples. However, the mobility decreased with the inclusion of the secondary phase, which is a consistent behaviour of multiphase materials [117, 439] and it was seen in chapter 6 and 5.

Table 7.9. Hall carrier concentration and mobility of ball milled $Bi_{0.5}Sb_{1.5}Te_{3.3}$ with x wt.% CrSb (x = 0, 0.125, 0.25, 0.5, and 1) samples

x	n_H($\times 10^{18}$ cm^{-3})	μ_H (cm^2.V^{-1}.s^{-1})
0	7.7	232.0
0.125	7.7	203.9
0.25	7.6	203.7
0.5	7.3	185.5
1	7.1	161.6

The thermopower of the CrSb added samples shows an overall increase with secondary phase inclusion. Since the carrier concentration of all samples has similar values, these changes cannot simply be attributed to changes in the values of n.

The behaviour of the band structure with the CrSb inclusion was analysed by modelling the thermopower and Hall carrier concentration using the SPB model. The single parabolic band method described in chapter 3 may not fully and accurately determine the behaviour of $Bi_{0.5}Sb_{0.5}Te_{3.3}$ due to the presence of bipolar conduction, complex scattering processes, and the non-parabolic nature of the valence band. However, this approach can provide an indication of a trend in the calculated effective mass m^* of the fabricated samples [484, 504–506]. The calculated effective mass for all samples is listed in table 7.10.

The effective mass of the samples increases overall with the presence of the secondary phase in alignment with the trend of the thermopower. This trend is visible in both table 7.10 and in the dependence between thermopower α, carrier concentration n and m^* shown in the Pisarenko plot in figure 7.15.

As discussed in chapters 3 and 4, the thermopower for a degenerate semiconductor, with a parabolic band and energy-independent scattering approximation,

Table 7.10. Room temperature thermopower, Hall carrier concentration, and effective mass of ball milled $Bi_{0.5}Sb_{1.5}Te_{3.3}$ with x wt.% CrSb (x = 0, 0.125, 0.25, 0.5, and 1) samples

x	α (μV.K^{-1})	n ($\times 10^{18}$ cm^{-3})	m^*/m_0
0	238	7.7	0.90
0.125	252	7.7	1.16
0.25	246	7.6	0.96
0.5	273	7.3	1.06
1	280	7.1	1.21

can be written as [507]

$$\alpha = \frac{8\pi^2 k_B}{3qh^2} m^* T \left(\frac{\pi}{3n}\right)^{2/3}, \tag{7.5}$$

where m^* is the effective mass of the density of states.

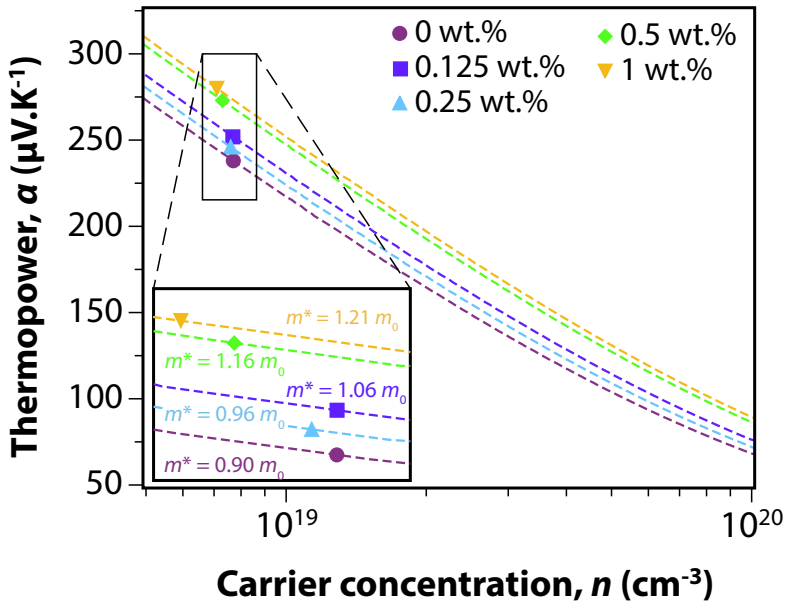

Figure 7.15. The Pisarenko plots (thermopower versus Hall carrier concentration) at room temperature for ball milled $Bi_{0.5}Sb_{1.5}Te_{3.3}$ with x wt.% CrSb (x = 0, 0.125, 0.25, 0.5, and 1). The dashed lines represent the calculated values from the single parabolic band model using the effective masses as shown in the inset.

Equation 7.5 shows a direct proportionality between the thermopower and the effective mass. Drawing a parallel analysis from chapter 4, we observe a striking similarity between the results presented here and those of the single-phase samples of Bi_2S_3 codoped with Cr. This suggests that the presence of a magnetic phase within the material can lead to an increase in the effective mass of the sample and consequently an increase in the thermopower, similar to what occurred in the presence of a magnetic dopant.

The combined decrease in carrier mobility due to the presence of an additional phase and the possible dragging effect caused by the magnetic phase, however, severely degrades the electrical conductivity of the multiphase samples. As a result, there was only a marginal increase in the power factor PF (as shown in fig. 7.14(c)).

For comparison with the first part of this chapter, in figure 7.16, the Hall carrier concentration (in purple), the Hall mobility (in green) and the weighted mobility (in orange; calculated using the equation 7.2) are plotted against the weight percent of CrSb in the samples. Due to the lower effective mass, the 0.25 wt.% CrSb sample also has lower weighted mobility, but the overall trend is an increase in μ_W due to the increased effective mass. This result is similar to that seen for the no-excess Te samples (see fig. 7.6).

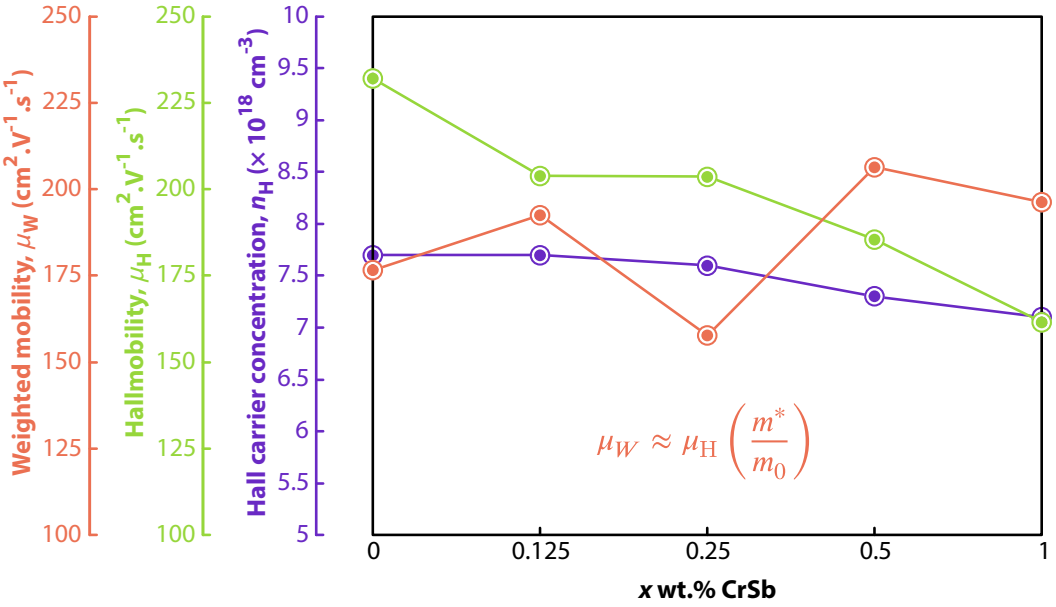

FIGURE 7.16. Hall carrier concentration (in purple), the Hall mobility (in green) and the weighted mobility (in orange; calculated using the equation 7.2) of ball milled $Bi_{0.5}Sb_{1.5}Te_{3.3}$ with x wt.% CrSb (x = 0, 0.125, 0.25, 0.5, and 1).

7.2.5 Partial conclusion

In the second part of this study, a series of multiphase samples of $Bi_{0.5}Sb_{1.5}Te_{3.3}$ with varying CrSb content were synthesised and analysed. The samples were successfully prepared using a combination of ball milling and sintering techniques, ensuring control over their composition and microstructure. The main goal of this study was to systematically investigate the impact of low CrSb concentrations on the thermoelectric properties of the material. It aimed to validate and extend the preliminary conclusions from the initial stage of this chapter.

In the first part of the study, it was found that the sample with the lowest magnetic phase content (0.5 wt.%) showed a significant enhancement in thermoelectric performance. This leads to the hypothesis that the incorporation of lower concentrations of CrSb could yield similarly advantageous results. Consequently, a new set of samples with low CrSb concentrations was synthesised for analysis. In addition, excess Te was added to the samples to improve the material's thermoelectric performance.

The results obtained from this new set of samples provided evidence to support the conclusions drawn in the first part of the study, in particular, that the presence of small amounts of magnetic phases can in fact enhance the thermoelectric performance. The inclusion of the secondary phase was found to significantly increase the thermopower of the samples by enhancing the effective mass of the charge carriers similarly as it was seen in the first party of this study. However, it was observed that the introduction of the secondary phase had a detrimental effect on the electrical conductivity of the samples. Despite similar carrier concentrations, the carrier mobility was significantly reduced, leading to lower electrical conductivity values.

The interplay between the enhanced thermopower and the degraded electrical conductivity resulted in only marginal gains in power factor, highlighting the delicate balance required to optimise thermoelectric efficiency in such multiphase systems.

7.3 Final remarks

This study was conducted in two parts. In the first part, a set of samples was fabricated by melting the raw elements of Bi, Sb, Te, and Cr, followed by hand milling the resulting ingots and sintering the materials. The XRD analysis revealed the presence of two phases: $Bi_{0.5}Sb_{1.5}Te_3$ and CrSb. The samples were designed to cover a wide range of second-phase contents, spanning from 0.5 wt.% to 25 wt.%. Notably, the thermoelectric performance of the samples with higher percentages of CrSb exhibited significant degradation, resulting in reduced values of the figure of merit (zT) and power factor. The sample with the best performance was the one with the lowest percentage of secondary phase inclusion, specifically 0.5 wt.%. For this sample, the thermopower was enhanced due to an increase in the effective mass.

Based on these initial findings, a new set of multiphase samples, featuring lower percentages of CrSb, was fabricated using ball-milling and SPS. The results from this new set corroborated those obtained in the first part of the study.

Interestingly, the results presented here in this chapter allow for a parallel analysis with those in chapter 4. In the previous chapter, the addition of a magnetic dopant resulted in an increase in thermopower due to the presence of magnetic drag. Analogously, this effect seems to manifest in the samples investigated in this chapter. Indeed, this current chapter was inspired by the previous one, representing a natural extension, where instead of a magnetic co-dopant, a magnetic phase was introduced. The inclusion of a secondary magnetic phase, in small amounts, similarly influenced the material by enhancing the thermopower through an increased effective mass. However, the presence of this drag effect, combined with carrier scattering introduced by the secondary phase, reduced the carrier mobility of the materials, leading to lower electrical conductivities and consequently only modest enhancements in the power factors.

Including large amounts of the CrSb magnetic phase resulted in an overall decrease in the performance of the material. It was concluded that adding significant amounts of CrSb failed to enhance the overall performance of the multiphase material. These findings underline the complex interplay between magnetic phases, charge carriers, and thermoelectric properties, providing useful insights to optimise the development of advanced thermoelectric materials.

References

(40) Y.-H. Gao, H. Chen, N. Liu and R.-Z. Zhang, *Results Phys.*, 2018, **11**, 915–919, doi: 10.1016/j.rinp.2018.10.034.

(50) M. Wolf, K. Menekse, A. Mundstock, R. Hinterding, F. Nietschke, O. Oeckler and A. Feldhoff, *J. Electron. Mater.*, 2019, **48**, 7551–7561, doi: 10.1007/s11664-019-07555-2.

(117) D. K. Ko, Y. Kang and C. B. Murray, *Nano Lett.*, 2011, **11**, 2841–4, doi: 10.1021/nl2012246.

(154) Y. Li, X. Wang, G. Liu, B. Shin and F. Shan, *Scr. Mater.*, 2019, **172**, 88–92, doi: 10.1016/j.scriptamat.2019.07.016.

(157) L. Zhao, W. Qiu, Y. Sun, L. Chen, H. Deng, L. Yang, X. Shi and J. Tang, *J. Alloys Compd.*, 2021, **863**, doi: 10.1016/j.jallcom.2020.158376.

(279) N. Tsujii and T. Mori, *Appl. Phys. Express*, 2013, **6**, 043001, doi: 10.7567/Apex.6.043001.

(280) R. Ang, A. U. Khan, N. Tsujii, K. Takai, R. Nakamura and T. Mori, *Angew. Chem. Int. Ed. Engl.*, 2015, **54**, 12909–13, doi: 10.1002/anie.201505517.

(289) F. Ahmed, N. Tsujii and T. Mori, *J. Mater. Chem.A*, 2017, **5**, 7545–7554, doi: 10.1039/C6TA11120C.

(290) J. B. Vaney, S. A. Yamini, H. Takaki, K. Kobayashi, N. Kobayashi and T. Mori, *Mater. Today Phys.*, 2019, **9**, 100090, doi: 10.1016/j.mtphys.2019.03.004.

(291) S. Acharya, S. Anwar, T. Mori and A. Soni, *J. Mater. Chem. C*, 2018, **6**, 6489–6493, doi: 10.1039/C8TC00788H.

(294) T. Graf, J. Barth, C. G. F. Blum, B. Balke, C. Felser, P. Klaer and H.-J. Elmers, *Phys. Rev. B*, 2010, **82**, 104420, doi: 10.1103/PhysRevB.82.104420.

(295) Z. Liu, J. Zhu, P. Wei, W. Zhu, W. Zhao, A. Xia, D. Xu, Y. Lei and J. Yu, *ACS Appl. Mater. Interfaces*, 2019, **11**, 45875–45884, doi: 10.1021/acsami.9b16309.

(297) R. Lu, J. S. Lopez, Y. Liu, T. P. Bailey, A. A. Page, S. Wang, C. Uher and P. F. P. Poudeu, *J. Mater. Chem.A*, 2019, **7**, 11095–11103, doi: 10.1039/c9ta01156k.

(344) R. Gurunathan, R. Hanus, M. Dylla, A. Katre and G. J. Snyder, *Physical Review Applied*, 2020, **13**, 034011, doi: 10.1103/physrevapplied.13.034011.

(356) A. Kanatzia, C. Papageorgiou, C. Lioutas and T. Kyratsi, *Journal of Electronic Materials*, 2012, **42**, 1652–1660, doi: 10.1007/s11664-012-2362-5.

(365) N. Tsujii, A. Nishide, J. Hayakawa and T. Mori, *Sci. Adv.*, **5**, eaat5935, doi: 10.1126/sciadv.aat5935.

(391) M. Jonson and G. D. Mahan, *Phys. Rev. B*, 1980, **21**, 4223–4229, doi: 10.1103/PhysRevB.21.4223.

(402) W. Xie, X. Tang, Y. Yan, Q. Zhang and T. M. Tritt, *Applied Physics Letters*, 2009, **94**, 102111, doi: 10.1063/1.3097026.

(411) I. T. Witting, F. Ricci, T. C. Chasapis, G. Hautier and G. J. Snyder, *Research*, 2020, **2020**, 1–15, doi: 10.34133/2020/4361703.

(418) J.-H. Bahk and A. Shakouri, *Applied Physics Letters*, 2014, **105**, doi: 10.1063/1.4892653.

(427) N. S. Chauhan, S. V. Pyrlin, O. I. Lebedev, L. S. A. Marques, M. M. D. Ramos, T. Maiti, K. Kovnir, B. A. Korgel and Y. V. Kolen'ko, *The Journal of Physical Chemistry C*, 2021, **125**, 20184–20194, doi: 10.1021/acs.jpcc.1c05375.

(429) X. Wu, Z. Wang, R. Jiang, Y. Tian, Y. Liu, J. Shi, W. Zhao and R. Xiong, *Materials Today Physics*, 2022, **29**, 100904, doi: 10.1016/j.mtphys.2022.100904.

(439) Y.-X. Zhang, Y.-K. Zhu, D.-S. Song, J. Feng and Z.-H. Ge, *Chemical Communications*, 2021, **57**, 2555–2558, doi: 10.1039/D1CC00119A.

(465) S. Wang, J. Yang, T. Toll, J. Yang, W. Zhang and X. Tang, *Scientific Reports*, 2015, **5**, doi: 10.1038/srep10136.

(475) I. T. Witting, T. C. Chasapis, F. Ricci, M. Peters, N. A. Heinz, G. Hautier and G. J. Snyder, *Adv. Electron. Mater.*, 2019, **5**, doi: 10.1002/aelm.201800904.

(476) R. M. German, *Critical Reviews in Solid State and Materials Sciences*, 2010, **35**, 263–305, doi: 10.1080/10408436.2010.525197.

(477) I. T. Witting, J. A. Grovogui, V. P. Dravid and G. J. Snyder, *Journal of Materiomics*, 2020, **6**, 532–544, doi: 10.1016/j.jmat.2020.04.001.

(478) In *Alloy Phase Diagrams*, ASM International, 2016, doi: 10.31399/asm.hb.v03.a0006157.

(479) S. J. Chipera and D. L. Bish, *Advances in Materials Physics and Chemistry*, 2013, **3**, 47–53, doi: 10.4236/ampc.2013.31A007.

(480) R. A. Downie, D. A. MacLaren and J. W. G. Bos, *J. Mater. Chem. A*, 2014, **2**, 6107–6114, doi: 10.1039/c3ta13955g.

(481) Z. Wei, C. Wang, L. You, S. Zhao, K. Yang, H. Chen, J. Luo and X. Chen, *RSC Advances*, 2017, **7**, 41111–41116, doi: 10.1039/C7RA06277J.

(482) M. M. H. Polash, F. Mohaddes, M. Rasoulianboroujeni and D. Vashaee, *Journal of Materials Chemistry C*, 2020, **8**, 4049–4057, doi: 10.1039/C9TC06330G.

(483) G. J. Snyder, A. H. Snyder, M. Wood, R. Gurunathan, B. H. Snyder and C. Niu, *Advanced Materials*, 2020, **32**, 2001537, doi: 10.1002/adma.202001537.

(484) Y. Zheng, Q. Zhang, X. Su, H. Xie, S. Shu, T. Chen, G. Tan, Y. Yan, X. Tang, C. Uher and G. J. Snyder, *Advanced Energy Materials*, 2015, **5**, 1401391, doi: 10.1002/aenm.201401391.

(485) P. Al-Alam, G. Pernot, M. Isaiev, D. Lacroix, M. De Vos, N. Stein, D. Osenberg and L. Philippe, *Phys. Rev. B*, 2019, **100**, 115304, doi: 10.1103/PhysRevB.100.115304.

(486) G.-K. Ren, J.-L. Lan, K. J. Ventura, X. Tan, Y.-H. Lin and C.-W. Nan, *npj Comput. Mater.*, 2016, **2**, 1–9, doi: 10.1038/npjcompumats.2016.23.

(487) H.-L. Zhuang, J. Pei, B. Cai, J. Dong, H. Hu, F.-H. Sun, Y. Pan, G. J. Snyder and J.-F. Li, *Advanced Functional Materials*, 2021, **31**, 2009681, doi: 10.1002/adfm.202009681.

(488) S. C. Chelgani, M. Parian, P. S. Parapari, Y. Ghorbani and J. Rosenkranz, *Journal of Materials Research and Technology*, 2019, **8**, 5004–5011, doi: 10.1016/j.jmrt.2019.07.053.

(489) A. Ozkan, M. Yekeler and M. Calkaya, *International Journal of Mineral Processing*, 2009, **90**, 67–73, doi: 10.1016/j.minpro.2008.10.006.

(490) H. J. Jung, Y. Sohn, H. G. Sung, H. S. Hyun and W. G. Shin, *Powder Technology*, 2015, **269**, 548–553, doi: 10.1016/j.powtec.2014.03.058.

(491) N. Kotake, M. Kuboki, S. Kiya and Y. Kanda, *Advanced Powder Technology*, 2011, **22**, 86–92, doi: 10.1016/j.apt.2010.03.015.

(492) Y. Liu, Y. Zhang, S. Ortega, M. Ibáñez, K. H. Lim, A. Grau-Carbonell, S. Martí-Sánchez, K. M. Ng, J. Arbiol, M. V. Kovalenko, D. Cadavid and A. Cabot, *Nano Letters*, 2018, **18**, 2557–2563, doi: 10.1021/acs.nanolett.8b00263.

(493) R. Deng, X. Su, Z. Zheng, W. Liu, Y. Yan, Q. Zhang, V. P. Dravid, C. Uher, M. G. Kanatzidis and X. Tang, *Science Advances*, 2018, **4**, eaar5606, doi: 10.1126/sciadv.aar5606.

(494) H.-S. Kim, N. A. Heinz, Z. M. Gibbs, Y. Tang, S. D. Kang and G. J. Snyder, *Mater. Today*, 2017, **20**, 452–459, doi: 10.1016/j.mattod.2017.02.007.

(495) A. Sankhla, A. Patil, H. Kamila, M. Yasseri, N. Farahi, E. Mueller and J. de Boor, *ACS Applied Energy Materials*, 2018, **1**, 531–542, doi: 10.1021/acsaem.7b00128.

(496) P. Khade, T. Bagwaiya, S. Bhattacharaya, A. Singh, P. Jha and V. Shelke, 2018, doi: 10.1063/1.5029035.

(497) O. Raihan, S. M. Said, M. F. M. Sabri, S. Rozali, B. D. Long, K. Kimura, K. Tobita, Fitriani, M. F. M. Salleh and M. B. A. Bashir, *Materials Research Express*, 2018, **5**, 105008, doi: 10.1088/2053-1591/aada92.

(498) D. Montgomery, *Design and Analysis of Experiments*, John Wiley & Sons Ltd., New York, 5th edn., 2001.

(499) H. Mio, J. Kano and F. Saito, *Chemical Engineering Science*, 2004, **59**, 5909–5916, doi: 10.1016/j.ces.2004.07.020.

(500) S. Biyik and M. Aydin, *Acta Physica Polonica A*, 2015, **127**, 1255–1260, doi: 10.12693/APhysPolA.127.1255.

(501) A. L. Patterson, *Physical Review*, 1939, **56**, 978–982, doi: 10.1103/PhysRev.56.978.

(502) R. L. Wasserstein and N. A. Lazar, *The American Statistician*, 2016, **70**, 129–133, doi: 10.1080/00031305.2016.1154108.

(503) C. F. Holder and R. E. Schaak, *ACS Nano*, 2019, **13**, 7359–7365, doi: 10.1021/acsnano.9b05157.

(504) L.-P. Hu, T.-J. Zhu, Y.-G. Wang, H.-H. Xie, Z.-J. Xu and X.-B. Zhao, *NPG Asia Materials*, 2014, **6**, e88–e88, doi: 10.1038/am.2013.86.

(505) W. Liu, X. Tang, H. Li, K. Yin, J. Sharp, X. Zhou and C. Uher, *Journal of Materials Chemistry*, 2012, **22**, 13653–13661, doi: 10.1039/C2JM31919E.

(506) X. Su, H. Li, Y. Yan, H. Chi, X. Tang, Q. Zhang and C. Uher, *Journal of Materials Chemistry*, 2012, **22**, 15628–15634, doi: 10.1039/C2JM31677C.

(507) G. J. Snyder and E. S. Toberer, *Nature Materials*, 2008, **7**, 105–114, doi: 10.1038/nmat2090.

8

Thermoelectric properties of single phase n-type $Bi_{14}Te_{13}S_8$

Remember ye not the former things, neither consider the things of old. Behold, I will do a new thing; now shall it spring forth; shall ye not know it? I will even make a way in the wilderness, and rivers in the desert.
— Isaiah, 43:18-19

Summary
This chapter investigates the thermoelectric properties of iodine-doped $Bi_{14}Te_{13}S_8$ single phase samples. $Bi_{14}Te_{13}S_8$ is an important thermoelectric material in this work that has been relatively unexplored compared to the widely studied Bi_2Te_3 and Bi_2S_3. The $Bi_2(Te_{1.857}S_{1.142})_{1-x}I_x$ (x = 0 to 0.02) samples were synthesised by direct reaction and spark plasma sintering. X-ray diffraction analysis confirmed the single-phase rhombohedral structure. First-principles calculations revealed a direct bandgap semiconductor with a bandgap of ≈0.14 eV. The electronic transport properties showed optimised electrical conductivity and thermopower at an iodine doping level of x = 0.01 to 0.015, although Hall measurements indicated that the carrier concentration was only significantly increased above x = 0.02. This highlights the relative ineffectiveness of iodine doping in this system. Analysis of the effective density of states and the Pisarenko plot suggests a lighter band structure compared to Bi_2Te_3. The lattice thermal conductivity has been reduced by increased point defect phonon scattering from the iodine dopant atoms. An improved figure of merit zT of ≈0.29 at 520 K was obtained for x = 0.01 and 0.015, mainly due to the reduced lattice thermal conductivity. Overall, this work demonstrates that the thermoelectric performance of the relatively unexplored $Bi_{14}Te_{13}S_8$ system can be improved by optimising the carrier concentration and reducing the lattice thermal conductivity. The results provide insight into the improvement of the multiphase thermoelectric materials containing this phase shown in this thesis.

8.1 Introduction

In this chapter, the properties of single phase samples of iodine doped $Bi_{14}Te_{13}S_8$ are investigated. In a previous chapter of this thesis (chapter 5), the characteristics of the multiphase Bi_2T_3-$Bi_{14}Te_{13}S_8$ system were examined. It is therefore a natural progression that the properties of the single phase compounds should now be studied. Bi_2Te_3 has been the focus of extensive research within the thermoelectric community for many decades, and its properties have been thoroughly documented since the 1950s, as evidenced by numerous studies (e.g. [47, 73, 78, 485, 508–510]). In contrast, the properties of $Bi_{14}Te_{13}S_8$ have rarely been explored experimentally (as discussed in [413]), and a comprehensive investigation of this phase spanning from electronic band structure calculations to experimentally measured figure of merit zT values has not yet been reported in the literature, to the best of my knowledge. Therefore, this chapter focuses on studying the thermoelectric properties of $Bi_{14}Te_{13}S_8$.

8.2 Experimental details

8.2.1 Synthesis

A set of $Bi_2(Te_{1.857}S_{1.142})_{1-x}I_x$ (x = 0, 0.005, 0.01, 0.015, and 0.02) samples were synthesised by direct reaction of stoichiometric amounts of high purity Bi (99.999%, Alfa Aesar), Te (99.999%, Alfa Aesar) shots, dried S (99.99%, Alfa Aesar) powder, and BiI_3 (99.999%, Alfa Aesar Puratronic®) powder in vacuum sealed quartz tubes in an inert atmosphere glovebox. The tubes were homogenised at 850 °C for 16 h, quenched in cold water, and annealed at 450 °C for 72 h. The obtained ingots were hand-ground into fine powders in an agate mortar and pestle housed inside an inert atmosphere glovebox. The powders were then loaded into a graphite die and sintered under vacuum to produce 11 mm diameter rods using SPS (Dr. Sinter-1080 SPS system, Fuji-SPS, Japan) at 400 °C and an axial pressure of 50 MPa for 5 min. The relative density of the sintered samples, calculated from the weight and dimensions of the rods, was ≥99% for all the samples.

8.2.2 Materials characterisation

Phase purity and crystal structure of sintered samples were characterised by PXRD using a PANalytical X'Pert PRO X-ray diffractometer with Cu-Kα1 radiation (λ = 1.54059 Å, 40 kV, 40 mA). Rietveld refinements were performed on the acquired diffraction patterns using the GSAS-II software [326].

The electronic transport properties of the sintered samples were investigated in the parallel direction to the sintering pressure by cutting $\approx 2 \times 2 \times 8$ mm^3 bars from the sintered rods. The measurements were carried out from room temperature to 520 K under a helium atmosphere using a Linseis LSR-3 apparatus.

The thermal transport properties of the samples were investigated parallel to the sintering pressure by cutting out a disc with a diameter and thickness of approximately 10 mm and 1.5 mm, respectively, from the sintered rods. The thermal conductivities (κ) were calculated using the thermal diffusivity (D), specific heat capacity (c_p), and density (d) of the samples, $\kappa = D \cdot c_p \cdot d$. The thermal diffusivity was measured using a Netzsch LFA-467 Hyperflash®instrument. The specific heat capacity was measured using a PerkinElmer-DSC 8000 differential scanning calorimeter in compliance with the sapphire standard ASTM E1269-11(2018) test (refer to section 3.1.8.1).

The disc-shaped samples were also used to measure carrier concentration and electronic mobility using the van der Pauw technique with an ECOPIA HMS 3000 Hall measurement system.

8.2.3 Electronic structure calculation

DFT calculations were employed to qualitatively study the electronic band structure of the pristine sample. The PBE and GGA exchange-correlation functionals were used [385]. Monkhorst-Pack procedure was used to generate 10×10×10 k-points for the Brillouin zone [386]. The plane wave/pseudopotential approach was employed, with a kinetic energy cut-off of 45 Ry for the wavefunctions and 360 Ry for the electron density. The crystal structure used was that of the Rietveld refined pristine sample.

8.3 Results and discussion

8.3.1 Structural and phase analysis

Figure 8.1 depicts the XRD patterns of all samples analysed. The diffraction patterns confirm the existence of a single rhombohedral phase of $Bi_{14}Te_{13}S_8$ crystal, which belongs to the space group $R\bar{3}$ (PDF Card - 04-009-4602).

The lattice parameters for each sample were determined using Rietveld refinement of the XRD patterns and are presented in table 8.1. As shown in figure 8.3, the lattice parameters exhibit considerable variation with the presence of the dopant, where a = b parameters show an overall decreasing trend, while the c parameter fluctuates, decreasing and increasing with the dopant concentration. These changes in the lattice parameters can be attributed to the differences in ionic radii of S^{2-} (1.84 Å), Te^{2-} (2.21 Å), and I^{1-} (2.2 Å) [511]. Similar behaviour was observed in iodine-doped Bi_2Te_3, albeit to a lesser extent due to the relatively similar radii of Te^{2-} and I^{1-} [435, 512]. Nevertheless, the obtained values are consistent with literature-reported values (a = b = 11.269 Å and c = 11.129 Å) [415].

It is worth noticing that all samples exhibited a preferred orientation in the {006} lattice plane, as illustrated in figure 8.4. This was already seen for samples of $Bi_2Te_{2-x}S_{1-x}$ [413] and it is likely due to the preferred crystal growth in the basal plane parallel to the ingot growth direction [508, 513]. This indicates that the samples show a large degree of anisotropy of the transport properties with a preferred orientation of the layers of the materials. Much like Bi_2T_3, $Bi_{14}Te_{13}S_8$ exhibits three covalently bonded quintuple layers of $\left[Te^{(1)}/S^{(1)} - Bi - S^{(2)} - Bi - Te^{(1)}/S^{(1)}\right]$ sheets stacked along the c-axis [508, 514–516]. These sheets interact weakly through van der Waals interactions [513]. Here, the superscripts (1) and (2) were used to distinguish the two types of atomic bonding, where (1) denotes a weak van der Waals attraction and (2) denotes a covalent bonding [517]. Note that this crystal structure has been erroneously referred to as "Bi_2Te_2S" in some works [518, 519]. Historically, in the 1970s, Linus Pauling [415] realised that the "Bi_2Te_2S" crystal structure was unlikely to be stable at this stoichiometry due to a substantial strain localised on the internal sulphur layer within the stacking sequence. This strain is due to the considerable difference in ionic radii between S and Te, which would result in a large size mismatch between the hexagonal, closely packed S and Te layers. To relieve this strain and stabilise the structure, Pauling suggested that the formula should incorporate S atoms into the Te layers (and Te into the S layers), resulting in the proposed formula of $Bi_{14}Te_{13}S_8$.

Figure 8.2 presents the refinement plots. As pointed out earlier, the samples have a preferred orientation along the {006} lattice plane, represented by the elongated peak corresponding to this plane. This effect was corrected in the

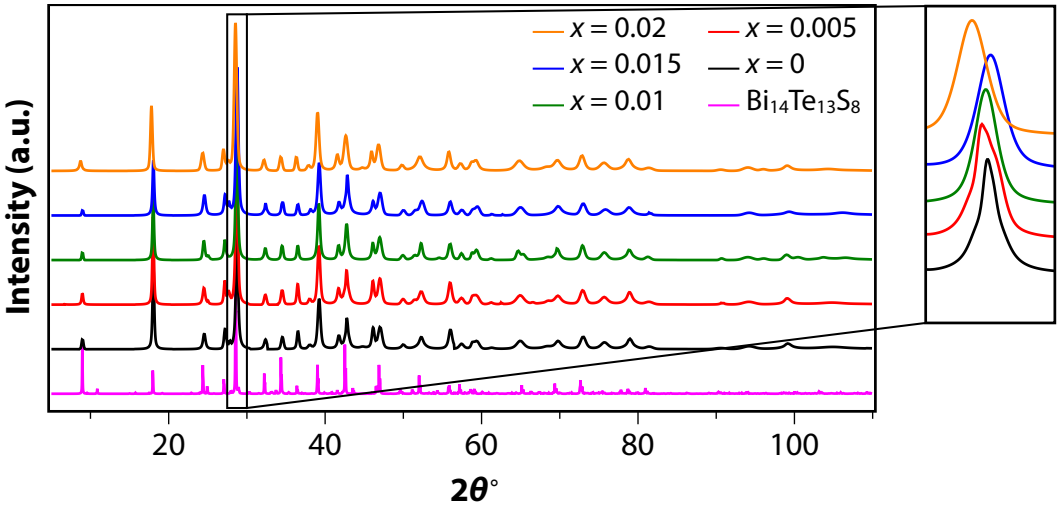

Figure 8.1. X-ray diffraction patterns of $Bi_2(Te_{1.857}S_{1.142})_{1-x}I_x$ (x = 0, 0.005, 0.01, 0.015, and 0.02) in the range of 5° to 108°. The inset shows the zoomed area around the largest intensity peak.

Rietveld refinement procedure by applying the March-Dollase preferred orientation model [520, 521] as implemented in GSAS-II [326]. Despite applying the model, the R_{wp} values remained high, but the overall fitness was reasonable [407].

Table 8.1. Refined lattice parameters of $Bi_2(Te_{1.857}S_{1.142})_{1-x}I_x$ (x = 0, 0.005, 0.01, 0.015, and 0.02)

x	a = b (Å)	c (Å)
0	11.219 83(12)	29.653 97(29)
0.005	11.2174(12)	29.6318(27)
0.01	11.2210(10)	29.6279(26)
0.015	11.2140(9)	29.6473(26)
0.02	11.2128(12)	29.6494(31)

8.3.2 Bandstructure analysis

The calculated electronic band structure of $Bi_{14}Te_{13}S_8$ using the refined lattice parameters for the original sample as described in table 8.1 is shown in figure 8.5. The band structure shows that this is a direct bandgap semiconductor, with the conduction band minimum and the valence band maximum centred around the Γ point in reciprocal space.

The band gap obtained for $Bi_{14}Te_{13}S_8$ was about 0.14 eV. Note, however, that it is well known that traditional DFT calculations such as PBE (used in this work) underestimate the value of the band gap [522–526], with the errors mainly due to: (1) self-interaction errors due to interactions of an electron with

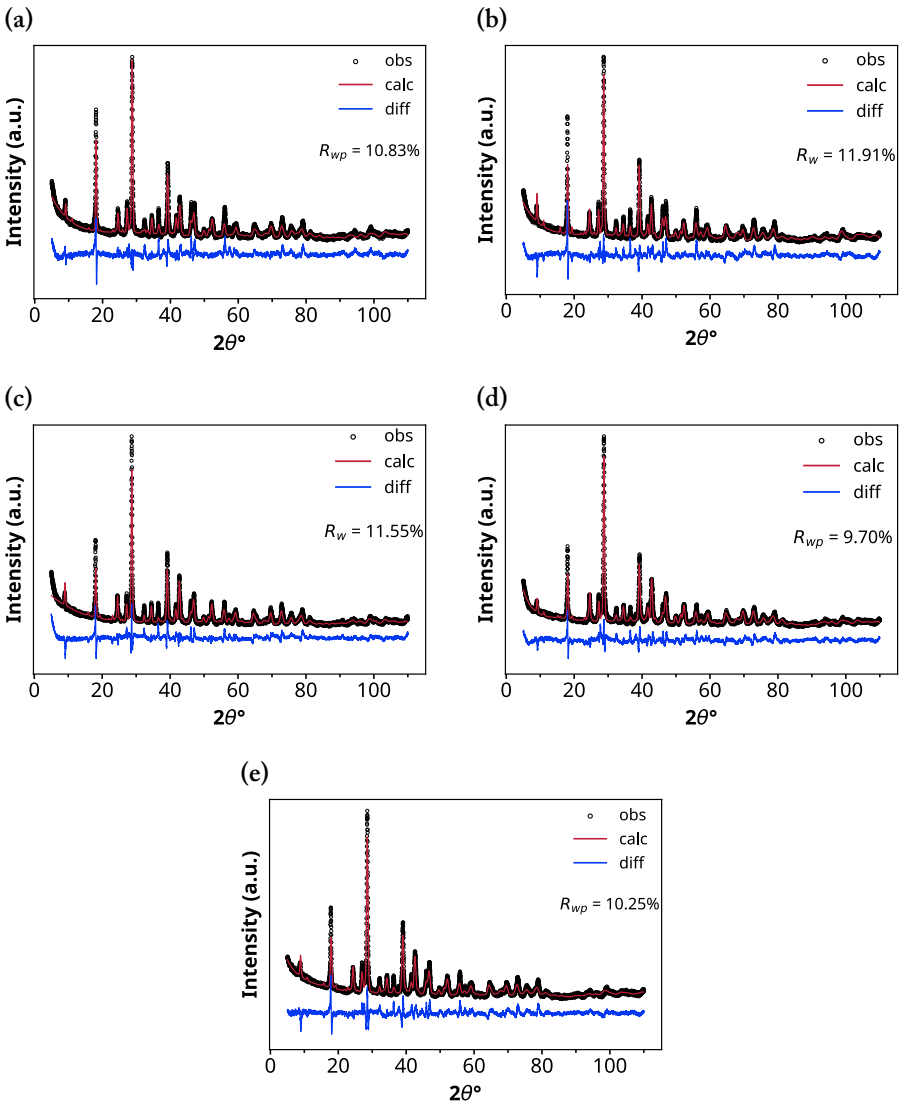

Figure 8.2. Rietveld refinement plots of $Bi_2(Te_{1.857}S_{1.142})_{1-x}I_x$, x = (a) 0, (b) 0.005, (c) 0.01, (d) 0.015, and (e) 0.02.

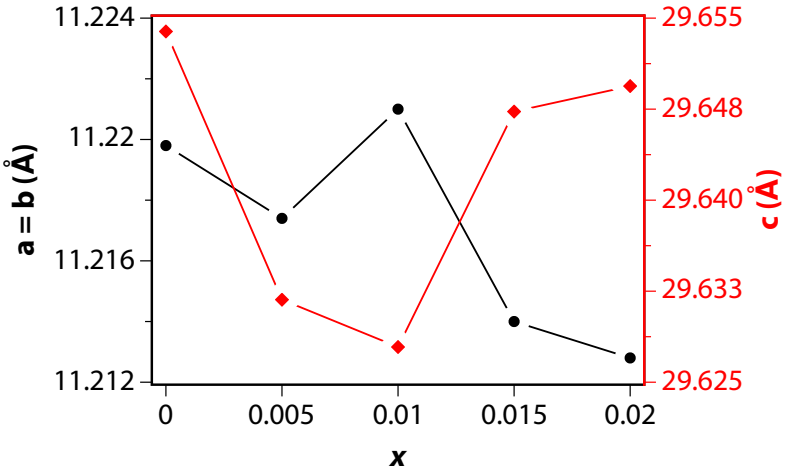

FIGURE 8.3. Variation of lattice parameters a = b and c with the dopant concentration x.

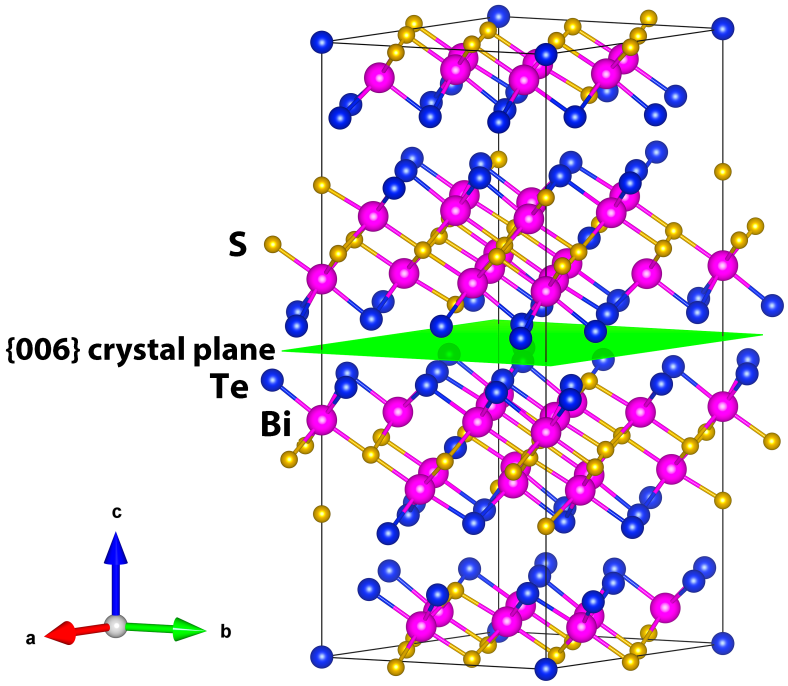

FIGURE 8.4. Crystal structure of $Bi_{14}Te_{13}S_8$ and {006} crystal plane.

itself in the Coulomb repulsion term of the density functional [525, 527]; and (2) the Kohn-Sham eigenvalues, which stem from using the differences of the ground state energies of the Kohn-Sham system as the band gap [528, 529].

The value calculated here is smaller than those presented in the Open Quantum Materials (≈0.5 eV) [530], JARVIS-DFT (≈0.36 eV) [531], and Materials Project (≈0.55 eV) [532, 533] databases, and it also differs from those presented in [534] of ≈0.9 eV, in [515] of ≈0.34 eV using PBE +

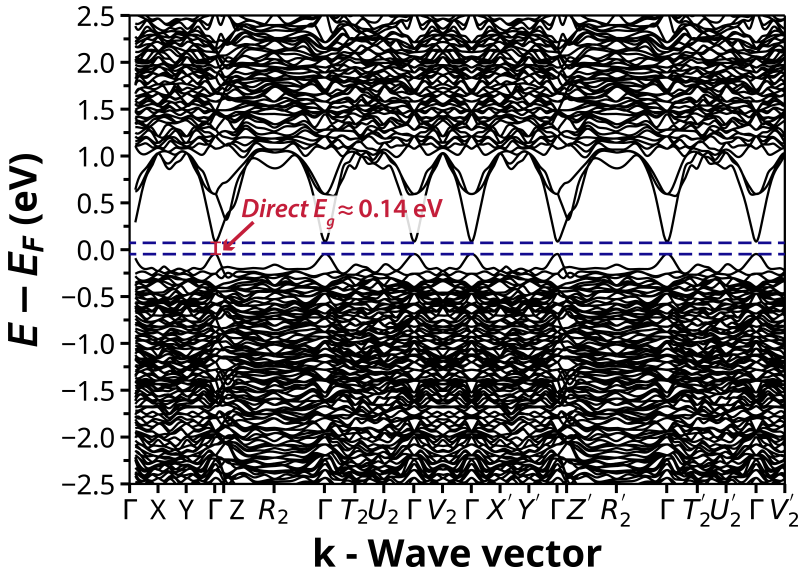

Figure 8.5. Bandstructure of $Bi_{14}Te_{13}S_8$.

spin-orbit coupling [535, 536], and of ≈0.68 eV using hybrid functionals [537] + spin-orbit coupling. However, the overall trend points out that $Bi_{14}Te_{13}S_8$ is a narrow band semiconductor with a larger band gap compared to Bi_2Te_3, in agreement with the fact that the higher electronegativity of S (compared to Te) should reduce the valence band maximum of the material [538].

8.3.3 Transport properties analysis and figure of merit zT

The temperature dependent thermopower and electrical resistivity of all samples are shown in figures 8.6(a) and (b). All samples show a negative value for the thermopower, indicating n-type semiconductor behaviour. At room temperature, the values of the thermopower vary between ≈−130 $\mu V.K^{-1}$ for the undoped sample to ≈−44 $\mu V.K^{-1}$ for the heavily doped sample with $x = 0.02$.

The electrical resistivity showed an inverse trend if compared to the thermopower, with the highest value of about 5.8 mΩ.cm for the undoped sample and the lowest value of about 1.2 mΩ.cm for the heavily doped sample with $x = 0.02$. All samples exhibited a metallic behaviour, with the electrical resistivity increasing with temperature. In particular, the thermopower and electrical resistivity showed similar values for the samples with $x = 0.005$, $x = 0.01$, and $x = 0.015$.

The choice of iodine as a dopant in Bi_2Te_3 is typically effective, leading to noticeable changes in electrical resistivity due to controlled variations in carrier concentration [512, 539–541], given to the similarity in radii between Te^{2-} and I^{1-}. In the case of Bi_2S_3, doping with iodine does increase the conductivity and carrier concentration; however the effect does not follow a clear trend [373].

In this set of samples, both Te and S are present, and both have been accounted for by substitution with I. Assuming that the changes are caused by the

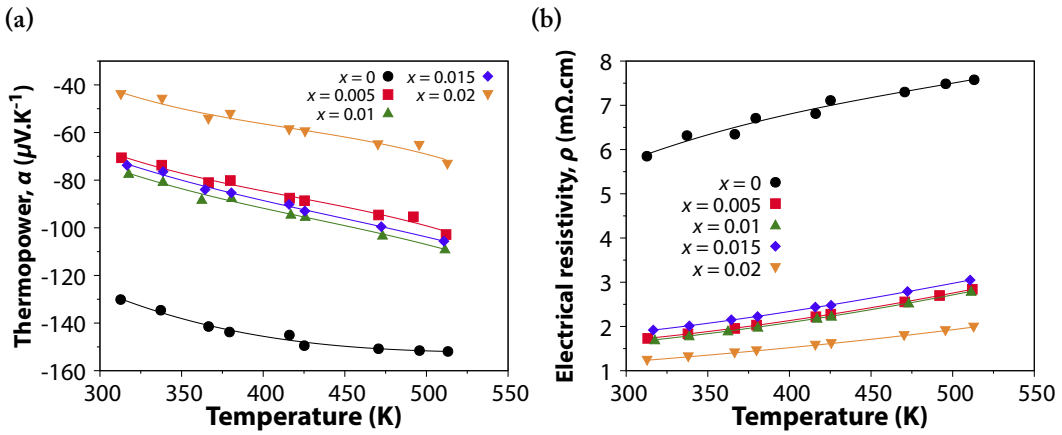

Figure 8.6. Temperature dependence of the (a) thermopower and (b) electrical resistivity of $Bi_2(Te_{1.857}S_{1.142})_{1-x}I_x$ (x = 0, 0.005, 0.01, 0.015, and 0.02) from 300 and 520 K.

Table 8.2. Room-temperature Hall carrier concentration (n_H) and Hall mobility (μ_H) of $Bi_2(Te_{1.857}S_{1.142})_{1-x}I_x$ (x = 0, 0.005, 0.01, 0.015, and 0.02)

x	n_H ($\times 10^{19}$ cm^{-3})	μ_H (cm^2.V^{-1}.s^{-1})
0	−1.41	75.24
0.005	−5.3	68.50
0.01	−5.47	68.22
0.015	−5	64.68
0.02	−22.8	22.29

incorporation of I at the sites of both Te and S, the carrier concentration would be governed by the following defect chemistry defect reaction

$$Bi_{14}Te_{13-1.85\frac{x}{3}}S_{8-1.15\frac{x}{3}}I_x \longrightarrow \left(1.85\frac{x}{3}I_{Te}^{\bullet} + 1.85\frac{x}{3}e'\right) + \left(1.15\frac{x}{3}I_S^{\bullet} + 1.15\frac{x}{3}e'\right). \tag{8.1}$$

Equation 8.1 predicts that the incorporation of high concentrations x of iodine will increase the carrier concentration in $Bi_{14}Te_{13}S_8$. To test this hypothesis, room temperature Hall effect measurements were conducted on samples with varying iodine doping levels. The results, summarised in table 8.2, reveal that while carrier mobility (μ_H) decreases monotonically with increasing iodine concentration from a maximum of 75.24 cm^2.V^{-1}.s^{-1} at $x = 0$ to a minimum of 22.29 cm^2.V^{-1}.s^{-1} at $x = 0.02$, the dependence of carrier concentration on iodine doping is more complex. Specifically, the carrier concentration remains relatively constant for $x = 0.005$, 0.01, and 0.015 before increasing significantly at $x = 0.02$. These data suggest that iodine doping increases the carrier concentration only above a critical threshold between $0.015 < x < 0.02$.

The trends in electrical resistivity (see fig. 8.6(b)) further illustrate the effect

of doping on the carrier concentration. The resistivity ρ shows a marked decrease from its maximum value for the undoped sample, maintaining similar values of $\approx$1.7 mΩ.cm for $0.05 \leq x \leq 0.015$ before dropping abruptly to its minimum at $x = 0.02$.

Similarly, given the inverse relationship between carrier concentration and thermopower α, the undoped sample has the largest thermopower magnitude due to its lowest carrier concentration, whereas the $x = 0.02$ sample has the smallest thermopower magnitude corresponding to its highest carrier density. Since the samples with $x = 0.005$, 0.01, and 0.015 have comparable carrier concentrations, they achieve similar thermopower values of $-80 \sim -70$ μV.K^{-1}. Overall, the transport data confirm the existence of a critical iodine doping threshold between $0.015 < x < 0.02$.

At room temperature and with similar carrier concentrations, the thermopower value for Bi_2Te_3 ($\approx$–238 μV.K^{-1} at $n_H = 1 \times 10^{19}$ cm^{-3} [475]) is larger than the one presented here, which indicates that this compound has a lower effective mass than both Bi_2Te_3. However, thermopower measurements of Bi_2S_3 of $\approx$–320 μV.K^{-1} at lower carrier concentrations of $n_H = 0.45 \times 10^{19}$ cm^{-3} [542] suggests a similar density of state effective mass between the samples and Bi_2S_3.

To understand the influence of the band structure on the thermopower, the SPB model was used to analyse the measured transport and carrier concentration data. The fitted density of state effective mass was found to be $m^* \approx 0.65m_0$. The measured thermopower and carrier concentrations follow the trend predicted by the SPB model, as shown in the Pisarenko plot in figure 8.7. Understandably, the relatively low effective mass of $Bi_{14}Te_{13}S_8$ compared to Bi_2T_3 ($m^* \approx 1.06m_0$ [411, 475]) can explain the low thermopower values observed even at lower carrier concentrations as predicted by Mott's rule.

For comparison, data from pristine Bi_2Te_3 samples [475, 509, 510] and Bi_2S_3 samples [368, 462, 509, 542], and samples of similar composition to that used in this work of chlorine doped $Bi_2Te_{1.93}S_{1.07-y}Cl_y$ and $Bi_2Te_{1.83}S_{1.17}$ [413] was added to the plot. As can be seen from the Pisarenko plot, $Bi_{14}Te_{13}S_8$ closely follows the band structure of both Bi_2S_3 and similar compositions of $Bi_2Te_{1.93}S_{1.07-y}Cl_y$ and $Bi_2Te_{1.83}S_{1.17}$.

Figure 8.8 shows the power factor ($\boldsymbol{PF}$) values for all samples. Despite the reduced electrical resistivity, the reduced thermopower at higher doping concentrations resulted in similar, modest power factor values of approximately 2.8 mW.m^{-2}.K^{-1} for the undoped, $x = 0.005$, and $x = 0.015$ samples. The heavily doped $x = 0.02$ sample exhibited the lowest power factor of $\approx$1.5 mW.m^{-2}.K^{-1}, while $x = 0.01$ gave the optimum $\boldsymbol{PF}$ of $\approx$3.5 mW.m^{-2}.K^{-1}.

To understand the heat transport mechanisms existent in the material, high temperature measurements of the specific heat capacity of pristine $Bi_{14}Te_{13}S_8$ were conducted and are exhibited in figure 8.9(a). At this temperature range of 300 $\sim$ 500 K, the specific heat capacity has values very close to those predicted

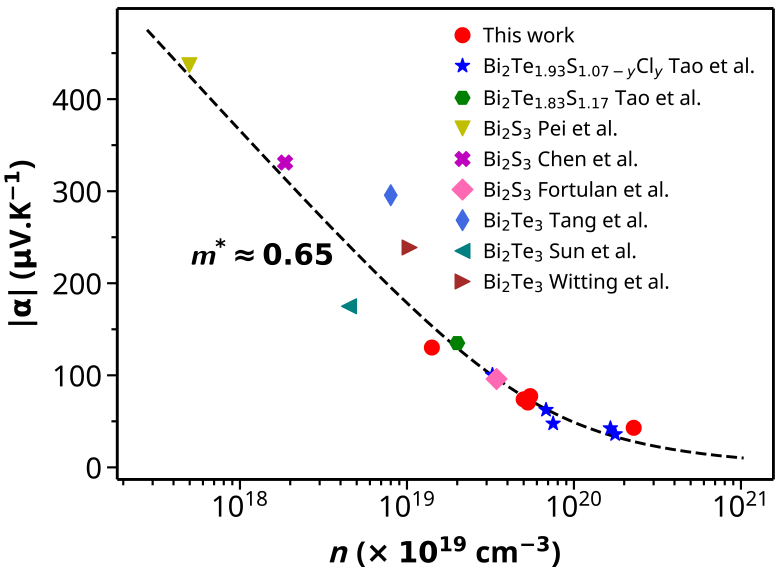

FIGURE 8.7. The Pisarenko plot (thermopower versus Hall carrier concentration) at room temperature of $Bi_2(Te_{1.857}S_{1.142})_{1-x}I_x$. The dashed line represents the calculated values from the single parabolic band model using the fitted effective mass. Data from Bi_2Te_3 [475, 509, 510], Bi_2S_3 [368, 462, 509, 542], $Bi_2Te_{1.93}S_{1.07-y}Cl_y$ and $Bi_2Te_{1.83}S_{1.17}$ [413] are included for comparison.

by the Dulong-Petit law [543][1], with a linear trend ($c_p = 0.16500(8) + 1.769(19)$

[1]A formal derivation of this law from the Debye model can be found in the Appendix.

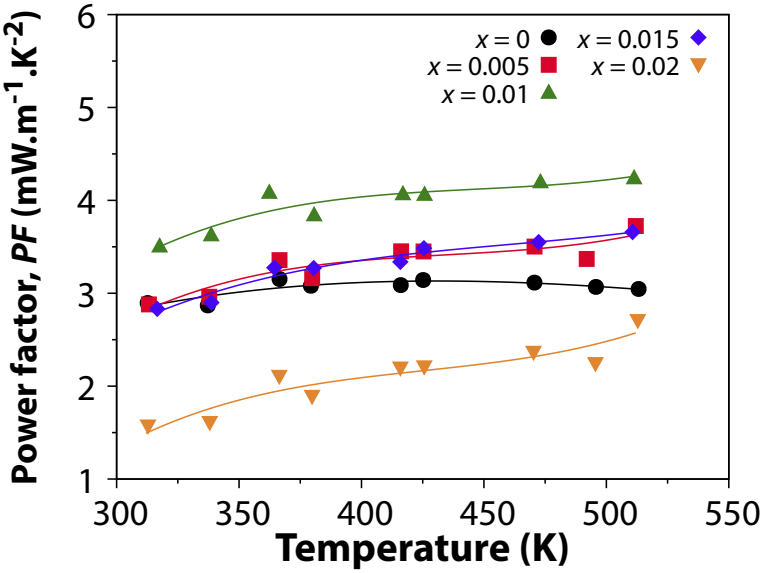

FIGURE 8.8. Temperature dependence of the power factor of $Bi_2(Te_{1.857}S_{1.142})_{1-x}I_x$ (x = 0, 0.005, 0.01, 0.015, and 0.02) from 300 and 520 K.

$\times 10^{-5}T$ J.g^{-1}.K^{-1}). At this temperature range, the specific heat capacity can be fitted using the Debye model as seen in chapter 3, which leads to a Debye temperature of $\theta_D = 190.0(2.3)$ K and an average speed of sound of $v = 2001(24)$ m.s^{-1}. The fitted model versus the measured values is shown in figure 8.9(b). It is worth noticing that due to the non-availability of lower temperature measurements to fit the specific heat capacity, these values can only be understood as approximations [544, 545].

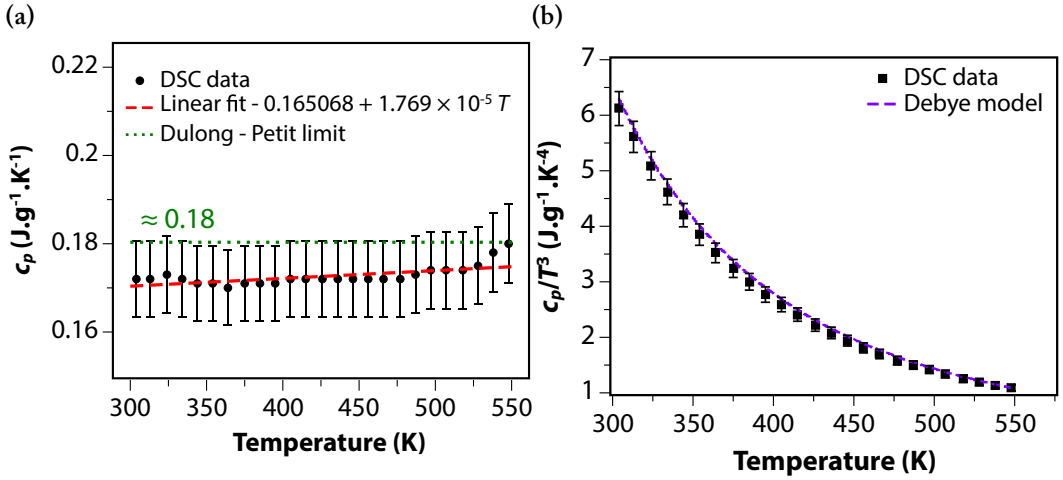

Figure 8.9. (a) Temperature dependence of the specific heat capacity of $Bi_{14}Te_{13}S_8$ between 300 and 550 K. The linear fit of the data is shown in red and the Dulong-Petit limit value for the hear capacity is shown in green. (b) The specific heat plotted as c_p/T^3 versus T, the modelled heat capacity is shown in purple.

It is worth mentioning that the curve fitting problem used to find the Debye temperature and the speed of sound in the material involves fitting a parameter used in the limits of an integral, which can be computationally taxing, especially since we need the numerical derivative of c_p when using gradient-based optimisation methods. A common approach in numerical analysis is to first simplify the problem, find an approximate solution, and use this initial guess to solve the full problem. Since the approximate solution is assumed to be close to the true solution, the more complex model typically converges within a few iterations. In this case, the integral in the expression of c_p can be approximated using a Newton-Cotes quadrature such as Simpson's rule [301] to obtain an initial guess

as follows

$$\int_0^{\theta_D/T} \frac{x^4 \exp(x)}{(\exp(x)-1)^2} \mathrm{d}x \approx$$
$$\frac{1}{3}\left[\frac{\theta_D}{2T}\left(4\frac{(\theta_D/2T)^4 \exp(\theta_D/2T)}{(\exp(\theta_D/2T)-1)^2} + \frac{(\theta_D/T)^4 \exp(\theta_D/T)}{(\exp(\theta_D/T)-1)^2}\right)\right] + \mathcal{O}\left((\theta_D/T)^6\right) \rightarrow$$
$$c_p \approx \frac{3}{2} N k_\mathrm{B} \left(\frac{T}{\theta_D}\right)^2 \left[4\frac{(\theta_D/2T)^4 \exp(\theta_D/2T)}{(\exp(\theta_D/2T)-1)^2} + \frac{(\theta_D/T)^4 \exp(\theta_D/T)}{(\exp(\theta_D/T)-1)^2}\right] \quad (8.2)$$

The thermal conductivity (κ) as a function of the temperature is shown figure 8.10(a). The thermal conductivity of the samples increases with the presence of the dopant. The electronic contribution to the thermal conductivity, i.e. the electronic thermal conductivity κ_e, was determined from the Wiedemann-Franz law (see chapter 3) using the Lorenz number estimated using the SPB model and is exhibited in figure 8.10(b). As expected, with the increase in electrical conductivity with the dopant addition, the electronic thermal conductivity also increased for the doped samples. The lattice thermal conductivity was estimated from the relation $\kappa_l = \kappa - \kappa_e$ as it is plotted in figure 8.10(c). With the presence of the dopant, the lattice thermal conductivity was reduced. This kind of behaviour can be readily found in literature [546–550] and the reason behind it is that dopants act as point defects in the system, scattering phonons and, thus, reducing κ_l (for more details of the relation between the relaxation time and point defects, see chapter 3).

At room temperature, the maximum value of κ_l was seen for the undoped sample with $\approx$0.69 $\mathrm{W.m^{-1}.K^{-1}}$ and a minimum of $\approx$0.47 $\mathrm{W.m^{-1}.K^{-1}}$ for the sample with $x = 0.015$ (as seen in fig. 8.10(c)). The values exhibited by this material are in the lower range of the ones observed for telluride materials, as can be seen in the violin plot shown in figure 8.10(d) [67, 68, 79, 204, 208, 357, 416, 417, 431, 469, 551–635]. Specifically, the κ_l values for the iodine-doped $Bi_2(Te_{1.857}S_{1.142})_{1-x}I_x$ compositions lie below the first quartile of the lattice thermal conductivity data compiled from the references.

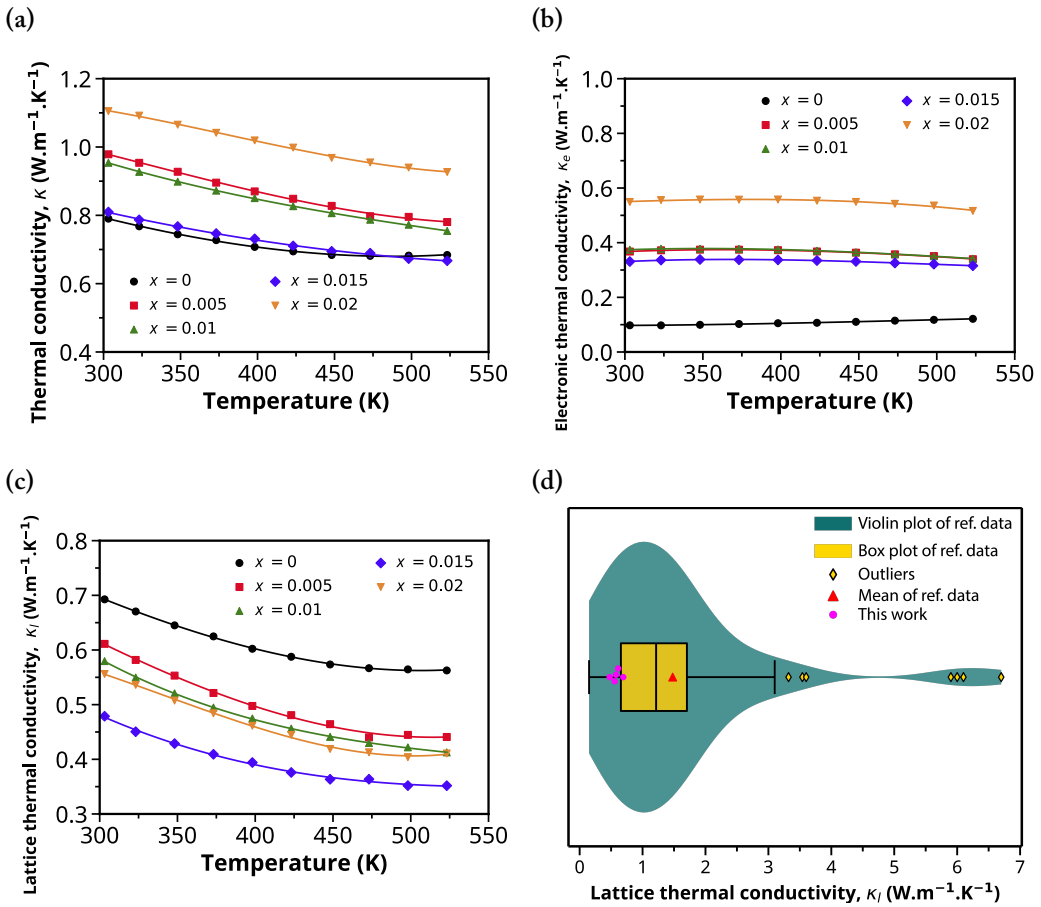

FIGURE 8.10. Temperature dependence of the (a) thermal conductivity, (b) electronic thermal conductivity, and (c) lattice thermal conductivity of $Bi_2(Te_{1.857}S_{1.142})_{1-x}I_x$ (x = 0, 0.005, 0.01, 0.015, and 0.02) between 300 to 520 K; (d) violin plot of lattice thermal conductivity data of literature data compared with this work, all values are at room temperature.

8.3.4 Figure of merit zT

The figure of merit zT for the samples can be observed in figure 8.11. The samples with $x = 0.01$ and 0.015 achieved a maximum value of zT of ≈0.289 at 520 K. The presence of dopants resulted in a shift of the higher value of zT towards higher temperatures. The increase in figure of merit was mainly due to the optimised power factor and a sharp reduction in the lattice thermal conductivity when compared to the undoped sample.

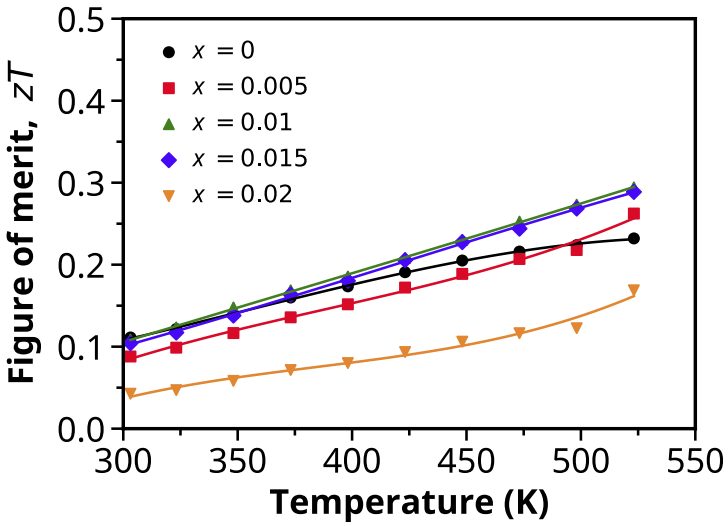

Figure 8.11. Figure of merit zT of $Bi_2(Te_{1.857}S_{1.142})_{1-x}I_x$ (x = 0, 0.005, 0.01, 0.015, and 0.02) between 300 to 520 K.

8.4 Conclusions

This chapter presents an investigation of the thermoelectric properties of iodine-doped $Bi_{14}Te_{13}S_8$ single-phase samples. The $Bi_{14}Te_{13}S_8$ compound, which has remained largely unexplored, was produced, and its structure was confirmed through X-ray diffraction as single-phased with the rhombohedral crystal structure. First principles calculations revealed $Bi_{14}Te_{13}S_8$ to be a direct bandgap semiconductor with a calculated bandgap of approximately 0.14 eV.

The electronic transport properties demonstrated enhanced electrical resistivity and thermopower upon iodine doping levels of x = 0.01 to 0.015. Nevertheless, carrier concentration was only significantly increased above x = 0.02 according to Hall effect measurements, illustrating the limited effectiveness of iodine as a dopant when substituting both tellurium and sulphur in this system. The Pisarenko plot and single parabolic band model were employed to analyse the experimental data, which revealed that $Bi_{14}Te_{13}S_8$ has a lower effective mass for density of states compared to Bi_2Te_3. This explains the low thermopower values even at the lower carrier concentrations.

The lattice thermal conductivity decreased with increasing iodine doping as a result of enhanced phonon scattering from point defects introduced by the dopant atoms. A peak zT of approximately 0.29 was obtained at 520 K for x values of 0.01 and 0.015. This was primarily due to the lowered electrical resistivity and lattice thermal conductivity.

Overall, this chapter has demonstrated that the thermoelectric properties of the relatively unexplored $Bi_{14}Te_{13}S_8$ system can be enhanced by targeted tuning

of the carrier concentration, resulting in an increased power factor, and by reducing the lattice thermal conductivity via iodine doping. These findings provide a blueprint for optimising complex multiphase thermoelectric materials containing the $Bi_{14}Te_{13}S_8$ phase.

References

(47) K. Ahmad, C. Wan, M. A. Al-Eshaikh and A. N. Kadachi, *Appl. Surf. Sci.*, 2019, **474**, 2–8, doi: 10.1016/j.apsusc.2018.10.163.

(67) Y. Z. Pei, A. LaLonde, S. Iwanaga and G. J. Snyder, *Energy Environ. Sci.*, 2011, **4**, 2085–2089, doi: 10.1039/c0ee00456a.

(68) H. J. Wu, L. D. Zhao, F. S. Zheng, D. Wu, Y. L. Pei, X. Tong, M. G. Kanatzidis and J. Q. He, *Nat. Commun.*, 2014, **5**, 4515, doi: 10.1038/ncomms5515.

(73) M. Hong, Z. G. Chen, L. Yang and J. Zou, *Nanoscale*, 2016, **8**, 8681–6, doi: 10.1039/c6nr00719h.

(78) C. M. Jaworski, V. Kulbachinskii and J. P. Heremans, *Phys. Rev. B*, 2009, **80**, 233201, doi: 10.1103/PhysRevB.80.233201.

(79) Y. Pei, X. Shi, A. LaLonde, H. Wang, L. Chen and G. J. Snyder, *Nature*, 2011, **473**, 66–9, doi: 10.1038/nature09996.

(204) J. Zhang, D. Wu, D. He, D. Feng, M. Yin, X. Qin and J. He, *Adv. Mater.*, 2017, **29**, 1703148, doi: 10.1002/adma.201703148.

(208) K. Biswas, J. He, I. D. Blum, C. I. Wu, T. P. Hogan, D. N. Seidman, V. P. Dravid and M. G. Kanatzidis, *Nature*, 2012, **489**, 414–8, doi: 10.1038/nature11439.

(301) R. L. Burden and J. D. Faires, *Numerical Analysis*, Cengage Learning, 2010.

(326) B. H. Toby and R. B. Von Dreele, *J. Appl. Crystallogr.*, 2013, **46**, 544–549, doi: 10.1107/S0021889813003531.

(357) B. Poudel, Q. Hao, Y. Ma, Y. Lan, A. Minnich, B. Yu, X. Yan, D. Wang, A. Muto, D. Vashaee, X. Chen, J. Liu, M. S. Dresselhaus, G. Chen and Z. Ren, *Science*, 2008, **320**, 634–8, doi: 10.1126/science.1156446.

(368) B. Chen, C. Uher, L. Iordanidis and M. G. Kanatzidis, *Chem. Mater.*, 1997, **9**, 1655–1658, doi: 10.1021/cm970033m.

(373) J. Yang, G. W. Liu, J. N. Yan, X. Z. Zhang, Z. Q. Shi and G. J. Qiao, *J. Alloys Compd.*, 2017, **728**, 351–356, doi: 10.1016/j.jallcom.2017.08.148.

(385) J. P. Perdew, K. Burke and M. Ernzerhof, *Phys. Rev. Lett.*, 1996, **77**, 3865–3868, doi: 10.1103/PhysRevLett.77.3865.

(386) H. J. Monkhorst and J. D. Pack, *Phys. Rev. B*, 1976, **13**, 5188–5192, doi: 10.1103/PhysRevB.13.5188.

(407) B. H. Toby, *Powder Diffraction*, 2006, **21**, 67–70, doi: 10.1154/1.2179804.

(411) I. T. Witting, F. Ricci, T. C. Chasapis, G. Hautier and G. J. Snyder, *Research*, 2020, **2020**, 1–15, doi: 10.34133/2020/4361703.

(413) Q. Tao, F. Meng, Z. Zhang, Y. Cao, Y. Tang, J. Zhao, X. Su, C. Uher and X. Tang, *Materials Today Physics*, 2021, **20**, 100472, doi: 10.1016/j.mtphys.2021.100472.

(415) L. Pauling, *American Mineralogist: Journal of Earth and Planetary Materials*, 1975, **60**, 994–997.

(416) Y. Xiao, H. Wu, J. Cui, D. Wang, L. Fu, Y. Zhang, Y. Chen, J. He, S. J. Pennycook and L.-D. Zhao, *Energy & Environmental Science*, 2018, **11**, 2486–2495, doi: 10.1039/C8EE01151F.

(417) R. Al Rahal Al Orabi, N. A. Mecholsky, J. Hwang, W. Kim, J.-S. Rhyee, D. Wee and M. Fornari, *Chemistry of Materials*, 2016, **28**, 376–384, doi: 10.1021/acs.chemmater.5b04365.

(431) B. Zhu, X. Liu, Q. Wang, Y. Qiu, Z. Shu, Z. Guo, Y. Tong, J. Cui, M. Gu and J. He, *Energy & Environmental Science*, 2020, **13**, 2106–2114, doi: 10.1039/D0EE01349H.

(435) J. H. Kim, S. Y. Back, J. H. Yun, H. S. Lee and J.-S. Rhyee, *Materials*, 2021, **14**, 1564, doi: 10.3390/ma14061564.

(462) **Fortulan, Raphael**, S. A. Yamini, C. Nwanebu, S. Li, T. Baba, M. J. Reece and T. Mori, *ACS Applied Energy Materials*, 2022, **5**, 3845–3853, doi: 10.1021/acsaem.2c00295.

(469) A. Banik, B. Vishal, S. Perumal, R. Datta and K. Biswas, *Energy & Environmental Science*, 2016, **9**, 2011–2019.

(475) I. T. Witting, T. C. Chasapis, F. Ricci, M. Peters, N. A. Heinz, G. Hautier and G. J. Snyder, *Adv. Electron. Mater.*, 2019, **5**, doi: 10.1002/aelm.201800904.

(485) P. Al-Alam, G. Pernot, M. Isaiev, D. Lacroix, M. De Vos, N. Stein, D. Osenberg and L. Philippe, *Phys. Rev. B*, 2019, **100**, 115304, doi: 10.1103/PhysRevB.100.115304.

(508) S. Shigetomi and S. Mori, *Journal of the Physical Society of Japan*, 1956, **11**, 915–919, doi: 10.1143/JPSJ.11.915.

(509) C. Tang, Z. Huang, J. Pei, B.-P. Zhang, P.-P. Shang, Z. Shan, Z. Zhang, H. Gu and K. Wen, *RSC Advances*, 2019, **9**, 14422–14431, doi: 10.1039/C9RA01738K.

(510) Y. Sun, H. Qin, W. Wang, F. Guo, W. Cai and J. Sui, *ACS Applied Energy Materials*, 2021, **4**, 4986–4992, doi: 10.1021/acsaem.1c00546.

(511) R. D. Shannon, *Acta crystallographica section A: crystal physics, diffraction, theoretical and general crystallography*, 1976, **32**, 751–767.

(512) F. Wu, W. Wang, X. Hu and M. Tang, *Progress in Natural Science: Materials International*, 2017, **27**, 203–207, doi: 10.1016/j.pnsc.2017.02.009.

(513) A. Tamtögl, D. Campi, M. Bremholm, E. M. J. Hedegaard, B. B. Iversen, M. Bianchi, P. Hofmann, N. Marzari, G. Benedek, J. Ellis and W. Allison, *Nanoscale*, 2018, **10**, 14627–14636, doi: 10.1039/C8NR03102A.

(514) C. B. Satterthwaite and R. W. Ure, *Phys. Rev.*, 1957, **108**, 1164–1170, doi: 10.1103/PhysRev.108.1164.

(515) Z. Rashid, A. S. Nissimagoudar and W. Li, *Physical Chemistry Chemical Physics*, 2019, **21**, 5679–5688, doi: 10.1039/C8CP05793A.

(516) J. Nagao, M. Ferhat, E. Hatta and K. Mukasa, *physica status solidi (b)*, 2000, **219**, 347–349, doi: 10.1002/1521-3951(200006)219:2<347::AID-PSSB347>3.0.CO;2-F.

(517) Y. Hosokawa, K. Tomita and M. Takashiri, *Scientific Reports*, 2019, **9**, 10790, doi: 10.1038/s41598-019-47356-5.

(518) J. B. Byrnes, A. A. Gazder and S. A. Yamini, *Rsc Advances*, 2018, **8**, 7457–7464, doi: 10.1039/c7ra08594j.

(519) D. C. Grauer, Y. S. Hor, A. J. Williams and R. J. Cava, *Materials Research Bulletin*, 2009, **44**, 1926–1929, doi: 10.1016/j.materresbull.2009.05.002.

(520) D. Li, B. H. O'Connor and H. Sitepu, *Journal of Applied Crystallography*, 2005, **38**, 158–167, doi: 10.1107/S0021889804031231.

(521) W. A. Dollase, *Journal of Applied Crystallography*, 1986, **19**, 267–272, doi: 10.1107/S0021889886089458.

(522) J. M. Crowley, J. Tahir-Kheli and W. A. Goddard, *The Journal of Physical Chemistry Letters*, 2016, **7**, 1198–1203, doi: 10.1021/acs.jpclett.5b02870.

(523) P. Mori-Sánchez, A. J. Cohen and W. Yang, *Physical Review Letters*, 2008, **100**, 146401, doi: 10.1103/PhysRevLett.100.146401.

(524) J. P. Perdew and M. Levy, *Physical Review Letters*, 1983, **51**, 1884–1887, doi: 10.1103/PhysRevLett.51.1884.

(525) J. P. Perdew and A. Zunger, *Physical Review B*, 1981, **23**, 5048–5079, doi: 10.1103/PhysRevB.23.5048.

(526) L. J. Sham and M. Schlüter, *Physical Review Letters*, 1983, **51**, 1888–1891, doi: 10.1103/PhysRevLett.51.1888.

(527) A. Pribram-Jones, D. A. Gross and K. Burke, *Annual Review of Physical Chemistry*, 2015, **66**, 283–304, doi: 10.1146/annurev-physchem-040214-121420.

(528) L. J. Sham and W. Kohn, *Physical Review*, 1966, **145**, 561–567, doi: 10.1103/PhysRev.145.561.

(529) C. Fiolhais, F. Nogueira and M. A. L. Marques, *A Primer in Density Functional Theory*, Springer Science & Business Media, 2003, 290 pp.

(530) K. S. A. M. M. B. Saal, J. E. and C. Wolverton, *Bi14Te13S8*, The Open Quantum Materials Database (OQMD).

(531) National Institute of Standards and Technology (NIST), *JVASP-29442_Bi14Te13S8*, JARVIS-DFT.

(532) *Mp-557619: Bi14Te13S8 (Trigonal, R-3, 148)*, Materials Project.

(533) A. Jain, S. P. Ong, G. Hautier, W. Chen, W. D. Richards, S. Dacek, S. Cholia, D. Gunter, D. Skinner, G. Ceder and K. A. Persson, *APL Materials*, 2013, **1**, 011002, doi: 10.1063/1.4812323.

(534) S. Lebègue, T. Björkman, M. Klintenberg, R. M. Nieminen and O. Eriksson, *Physical Review X*, 2013, **3**, 031002, doi: 10.1103/PhysRevX.3.031002.

(535) T. Thonhauser, D. Ceresoli, D. Vanderbilt and R. Resta, *Physical Review Letters*, 2005, **95**, 137205, doi: 10.1103/PhysRevLett.95.137205.

(536) M. P. Surh, M.-F. Li and S. G. Louie, *Physical Review B*, 1991, **43**, 4286–4294, doi: 10.1103/PhysRevB.43.4286.

(537) A. V. Krukau, O. A. Vydrov, A. F. Izmaylov and G. E. Scuseria, *The Journal of Chemical Physics*, 2006, **125**, 224106, doi: 10.1063/1.2404663.

(538) R. J. Cava, H. Ji, M. K. Fuccillo, Q. D. Gibson and Y. S. Hor, *Journal of Materials Chemistry C*, 2013, **1**, 3176–3189, doi: 10.1039/C3TC30186A.

(539) H. J. Goldsmid, *Materials (Basel)*, 2014, **7**, 2577–2592, doi: 10.3390/ma7042577.

(540) H. J. Goldsmid, *Proceedings of the Physical Society*, 1958, **71**, 633–646, doi: 10.1088/0370-1328/71/4/312.

(541) M.-K. Han, B.-G. Yu, Y. Jin and S.-J. Kim, *Inorganic Chemistry Frontiers*, 2017, **4**, 881–888, doi: 10.1039/C6QI00544F.

(542) J. Pei, L.-J. Zhang, B.-P. Zhang, P.-P. Shang and Y.-C. Liu, *Journal of Materials Chemistry C*, 2017, **5**, 12492–12499, doi: 10.1039/C7TC04082B.

(543) L. D. Landau and E. M. Lifshitz, *Statistical Physics: Volume 5*, Elsevier, 2013, 563 pp.

(544) B. A. Danilchenko, T. Paszkiewicz, S. Wolski, A. Jeżowski and T. Plackowski, *Applied Physics Letters*, 2006, **89**, 061901, doi: 10.1063/1.2335373.

(545) Y. Du, Z. X. Cheng, S. X. Dou, X. L. Wang, H. Y. Zhao and H. Kimura, *Applied Physics Letters*, 2010, **97**, 122502, doi: 10.1063/1.3490221.

(546) O. Zapata-Arteaga, A. Perevedentsev, S. Marina, J. Martin, J. S. Reparaz and M. Campoy-Quiles, *ACS Energy Letters*, 2020, **5**, 2972–2978, doi: 10.1021/acsenergylett.0c01410.

(547) P. Zhang, W. Liao, Z. Zhu, M. Qin, Z. Zhang, D. Jin, Y. Liu, Z. Wang, Z. Lu and R. Xiong, *Physical Chemistry Chemical Physics*, 2023, **25**, 15422–15432, doi: 10.1039/D3CP00999H.

(548) Y.-L. Pei, J. He, J.-F. Li, F. Li, Q. Liu, W. Pan, C. Barreteau, D. Berardan, N. Dragoe and L.-D. Zhao, *NPG Asia Materials*, 2013, **5**, e47–e47, doi: 10.1038/am.2013.15.

(549) M. Fava, N. H. Protik, C. Li, N. K. Ravichandran, J. Carrete, A. van Roekeghem, G. K. H. Madsen, N. Mingo and D. Broido, *npj Computational Materials*, 2021, **7**, 1–7, doi: 10.1038/s41524-021-00519-3.

(550) B. Dongre, J. Carrete, S. Wen, J. Ma, W. Li, N. Mingo and G. K. H. Madsen, *Journal of Materials Chemistry A*, 2020, **8**, 1273–1278, doi: 10.1039/C9TA11424F.

(551) K. Biswas, J. He, G. Wang, S.-H. Lo, C. Uher, V. P. Dravid and M. G. Kanatzidis, *Energy & Environmental Science*, 2011, **4**, 4675–4684, doi: 10.1039/C1EE02297K.

(552) A. D. LaLonde, Y. Pei and G. J. Snyder, *Energy & Environmental Science*, 2011, **4**, 2090–2096, doi: 10.1039/C1EE01314A.

(553) X. Xu, J. Cui, Y. Yu, B. Zhu, Y. Huang, L. Xie, D. Wu and J. He, *Energy & Environmental Science*, 2020, **13**, 5135–5142, doi: 10.1039/D0EE02638G.

(554) L. Zheng, W. Li, S. Lin, J. Li, Z. Chen and Y. Pei, *ACS Energy Letters*, 2017, **2**, 563–568.

(555) L.-D. Zhao, X. Zhang, H. Wu, G. Tan, Y. Pei, Y. Xiao, C. Chang, D. Wu, H. Chi and L. Zheng, *Journal of the American Chemical Society*, 2016, **138**, 2366–2373.

(556) L.-D. Zhao, H. J. Wu, S. Q. Hao, C.-I. Wu, X. Y. Zhou, K. Biswas, J. Q. He, T. P. Hogan, C. Uher and C. Wolverton, *Energy & Environmental Science*, 2013, **6**, 3346–3355.

(557) K. Zhao, K. Liu, Z. Yue, Y. Wang, Q. Song, J. Li, M. Guan, Q. Xu, P. Qiu and H. Zhu, *Advanced Materials*, 2019, **31**, 1903480.

(558) X. Zhang, D. Wang, H. Wu, M. Yin, Y. Pei, S. Gong, L. Huang, S. J. Pennycook, J. He and L.-D. Zhao, *Energy & Environmental Science*, 2017, **10**, 2420–2431.

(559) Q. Zhang, Q. Song, X. Wang, J. Sun, Q. Zhu, K. Dahal, X. Lin, F. Cao, J. Zhou and S. Chen, *Energy & Environmental Science*, 2018, **11**, 933–940.

(560) Q. Zhang, F. Cao, W. Liu, K. Lukas, B. Yu, S. Chen, C. Opeil, D. Broido, G. Chen and Z. Ren, *Journal of the American chemical society*, 2012, **134**, 10031–10038.

(561) J. Zhang, R. Liu, N. Cheng, Y. Zhang, J. Yang, C. Uher, X. Shi, L. Chen and W. Zhang, *Advanced Materials*, 2014, **26**, 3848–3853.

(562) A. Yusufu, K. Kurosaki, A. Kosuga, T. Sugahara, Y. Ohishi, H. Muta and S. Yamanaka, *Applied Physics Letters*, 2011, **99**.

(563) X. Yan, B. Poudel, Y. Ma, W. S. Liu, G. Joshi, H. Wang, Y. Lan, D. Wang, G. Chen and Z. F. Ren, *Nano letters*, 2010, **10**, 3373–3378.

(564) Z. Xu, H. Wu, T. Zhu, C. Fu, X. Liu, L. Hu, J. He, J. He and X. Zhao, *NPG Asia Materials*, 2016, **8**, e302–e302.

(565) Y. Xu, W. Li, C. Wang, J. Li, Z. Chen, S. Lin, Y. Chen and Y. Pei, *Journal of Materials Chemistry A*, 2017, **5**, 19143–19150.

(566) H. Xie, S. Hao, S. Cai, T. P. Bailey, C. Uher, C. Wolverton, V. P. Dravid and M. G. Kanatzidis, *Energy & Environmental Science*, 2020, **13**, 3693–3705.

(567) Y. Xiao, D. Wang, B. Qin, J. Wang, G. Wang and L.-D. Zhao, *Journal of the American Chemical Society*, 2018, **140**, 13097–13102.

(568) Y. Wu, Z. Chen, P. Nan, F. Xiong, S. Lin, X. Zhang, Y. Chen, L. Chen, B. Ge and Y. Pei, *Joule*, 2019, **3**, 1276–1288.

(569) L. Wang, X. Tan, G. Liu, J. Xu, H. Shao, B. Yu, H. Jiang, S. Yue and J. Jiang, *ACS Energy Letters*, 2017, **2**, 1203–1207.

(570) P. Vaqueiro, G. Guélou, M. Stec, E. Guilmeau and A. V. Powell, *Journal of Materials Chemistry A*, 2013, **1**, 520–523.

(571) Y.-F. Tsai, P.-C. Wei, L. Chang, K.-K. Wang, C.-C. Yang, Y.-C. Lai, C.-R. Hsing, C.-M. Wei, J. He and G. J. Snyder, *Advanced Materials*, 2021, **33**, 2005612.

(572) G. Tan, F. Shi, S. Hao, L.-D. Zhao, H. Chi, X. Zhang, C. Uher, C. Wolverton, V. P. Dravid and M. G. Kanatzidis, *Nature communications*, 2016, **7**, 12167.

(573) G. Tan, F. Shi, S. Hao, H. Chi, L.-D. Zhao, C. Uher, C. Wolverton, V. P. Dravid and M. G. Kanatzidis, *Journal of the American Chemical Society*, 2015, **137**, 5100–5112.

(574) G. Tan, F. Shi, J. W. Doak, H. Sun, L.-D. Zhao, P. Wang, C. Uher, C. Wolverton, V. P. Dravid and M. G. Kanatzidis, *Energy & Environmental Science*, 2015, **8**, 267–277.

(575) X. Su, N. Zhao, S. Hao, C. C. Stoumpos, M. Liu, H. Chen, H. Xie, Q. Zhang, C. Wolverton and X. Tang, *Advanced Functional Materials*, 2019, **29**, 1806534.

(576) D. Sarkar, T. Ghosh, A. Banik, S. Roychowdhury, D. Sanyal and K. Biswas, *Angewandte Chemie International Edition*, 2020, **59**, 11115–11122.

(577) M. Samanta, K. Pal, U. V. Waghmare and K. Biswas, *Angewandte Chemie International Edition*, 2020, **59**, 4822–4829.

(578) M. Samanta, T. Ghosh, R. Arora, U. V. Waghmare and K. Biswas, *Journal of the American Chemical Society*, 2019, **141**, 19505–19512.

(579) M. Samanta and K. Biswas, *Journal of the American Chemical Society*, 2017, **139**, 9382–9391.

(580) S. Roychowdhury, R. Panigrahi, S. Perumal and K. Biswas, *ACS Energy Letters*, 2017, **2**, 349–356.

(581) S. Roychowdhury, M. K. Jana, J. Pan, S. N. Guin, D. Sanyal, U. V. Waghmare and K. Biswas, *Angewandte Chemie*, 2018, **130**, 4107–4111.

(582) S. Roychowdhury, T. Ghosh, R. Arora, M. Samanta, L. Xie, N. K. Singh, A. Soni, J. He, U. V. Waghmare and K. Biswas, *Science*, 2021, **371**, 722–727.

(583) S. Roychowdhury, R. K. Biswas, M. Dutta, S. K. Pati and K. Biswas, *ACS Energy Letters*, 2019, **4**, 1658–1662.

(584) Y. Ren, J. Yang, Q. Jiang, D. Zhang, Z. Zhou, X. Li, J. Xin and X. He, *Journal of Materials Chemistry C*, 2017, **5**, 5076–5082.

(585) Y. Qiu, Y. Liu, J. Ye, J. Li and L. Lian, *Journal of Materials Chemistry A*, 2018, **6**, 18928–18937.

(586) P. F. P. Poudeu, J. D'Angelo, A. D. Downey, J. L. Short, T. P. Hogan and M. G. Kanatzidis, *Angewandte Chemie International Edition*, 2006, **45**, 3835–3839.

(587) T. Plirdpring, K. Kurosaki, A. Kosuga, T. Day, S. Firdosy, V. Ravi, G. J. Snyder, A. Harnwunggmoung, T. Sugahara and Y. Ohishi, *Advanced Materials*, 2012, **24**, 3622–3626.

(588) S. Perumal, M. Samanta, T. Ghosh, U. S. Shenoy, A. K. Bohra, S. Bhattacharya, A. Singh, U. V. Waghmare and K. Biswas, *Joule*, 2019, **3**, 2565–2580.

(589) S. Perumal, S. Roychowdhury, D. S. Negi, R. Datta and K. Biswas, *Chemistry of Materials*, 2015, **27**, 7171–7178.

(590) S. Perumal, S. Roychowdhury and K. Biswas, *Inorganic Chemistry Frontiers*, 2016, **3**, 125–132.

(591) S. Perumal, P. Bellare, U. S. Shenoy, U. V. Waghmare and K. Biswas, *Chemistry of Materials*, 2017, **29**, 10426–10435.

(592) Y. Pei, A. D. LaLonde, N. A. Heinz, X. Shi, S. Iwanaga, H. Wang, L. Chen and G. J. Snyder, *Advanced materials*, 2011, **23**, 5674–5678.

(593) Y. Z. Pei, N. A. Heinz and G. J. Snyder, *J. Mater. Chem.*, 2011, **21**, 18256–18260, doi: 10.1039/c1jm13888j.

(594) Y. Pan, Y. Qiu, I. Witting, L. Zhang, C. Fu, J.-W. Li, Y. Huang, F.-H. Sun, J. He and G. J. Snyder, *Energy & Environmental Science*, 2019, **12**, 624–630.

(595) M. Ohta, K. Biswas, S.-H. Lo, J. He, D. Y. Chung, V. P. Dravid and M. G. Kanatzidis, *Advanced Energy Materials*, 2012, **2**, 1117–1123.

(596) Y. Niu, S. Li, J. Mao, C. Yang, Q. Zhang, Q. Zhang, J. Jiang, C. Wang and Z. Ren, *Nano Energy*, 2020, **77**, 105297.

(597) Z.-Z. Luo, S. Cai, S. Hao, T. P. Bailey, X. Su, I. Spanopoulos, I. Hadar, G. Tan, Y. Luo and J. Xu, *Journal of the American Chemical Society*, 2019, **141**, 16169–16177.

(598) Y. Luo, J. Yang, Q. Jiang, W. Li, D. Zhang, Z. Zhou, Y. Cheng, Y. Ren and X. He, *Advanced Energy Materials*, 2016, **6**, 1600007.

(599) Y. Luo, Q. Jiang, J. Yang, W. Li, D. Zhang, Z. Zhou, Y. Cheng, Y. Ren, X. He and X. Li, *Nano Energy*, 2017, **32**, 80–87.

(600) W. Liu, K. C. Lukas, K. McEnaney, S. Lee, Q. Zhang, C. P. Opeil, G. Chen and Z. Ren, *Energy & Environmental Science*, 2013, **6**, 552–560.

(601) R. Liu, L. Xi, H. Liu, X. Shi, W. Zhang and L. Chen, *Chemical Communications*, 2012, **48**, 3818–3820.

(602) Y. Li, Q. Meng, Y. Deng, H. Zhou, Y. Gao, Y. Li, J. Yang and J. Cui, *Applied Physics Letters*, 2012, **100**.

(603) W. Li, L. Zheng, B. Ge, S. Lin, X. Zhang, Z. Chen, Y. Chang and Y. Pei, *Advanced Materials*, 2017, **29**, 1605887.

(604) J. Li, X. Zhang, Z. Chen, S. Lin, W. Li, J. Shen, I. T. Witting, A. Faghaninia, Y. Chen and A. Jain, *Joule*, 2018, **2**, 976–987.

(605) A. Kosuga, T. Plirdpring, R. Higashine, M. Matsuzawa, K. Kurosaki and S. Yamanaka, *Applied Physics Letters*, 2012, **100**.

(606) S. I. Kim, K. H. Lee, H. A. Mun, H. S. Kim, S. W. Hwang, J. W. Roh, D. J. Yang, W. H. Shin, X. S. Li and Y. H. Lee, *Science*, 2015, **348**, 109–114.

(607) P. Jood, M. Ohta, A. Yamamoto and M. G. Kanatzidis, *Joule*, 2018, **2**, 1339–1355.

(608) M. Hong, Y. Wang, W. Liu, S. Matsumura, H. Wang, J. Zou and Z.-G. Chen, *Advanced Energy Materials*, 2018, **8**, 1801837.

(609) M. Hong, Y. Wang, T. Feng, Q. Sun, S. Xu, S. Matsumura, S. T. Pantelides, J. Zou and Z.-G. Chen, *Journal of the American Chemical Society*, 2018, **141**, 1742–1748.

(610) M. Hong, W. Lyv, M. Li, S. Xu, Q. Sun, J. Zou and Z.-G. Chen, *Joule*, 2020, **4**, 2030–2043.

(611) M. Hong, Z.-G. Chen, L. Yang, Y.-C. Zou, M. S. Dargusch, H. Wang and J. Zou, *Advanced materials*, 2018, **30**, 1705942.

(612) M. Hong, Z.-G. Chen, L. Yang, Z.-M. Liao, Y.-C. Zou, Y.-H. Chen, S. Matsumura and J. Zou, *Advanced Energy Materials*, 2018, **8**, 1702333.

(613) M. Hong, T. C. Chasapis, Z.-G. Chen, L. Yang, M. G. Kanatzidis, G. J. Snyder and J. Zou, *ACS nano*, 2016, **10**, 4719–4727.

(614) Y. He, P. Lu, X. Shi, F. Xu, T. Zhang, G. J. Snyder, C. Uher and L. Chen, *Advanced Materials*, 2015, **27**, 3639–3644.

(615) F. Hao, P. Qiu, Y. Tang, S. Bai, T. Xing, H.-S. Chu, Q. Zhang, P. Lu, T. Zhang and D. Ren, *Energy & Environmental Science*, 2016, **9**, 3120–3127.

(616) S. N. Girard, J. He, X. Zhou, D. Shoemaker, C. M. Jaworski, C. Uher, V. P. Dravid, J. P. Heremans and M. G. Kanatzidis, *Journal of the American Chemical Society*, 2011, **133**, 16588–16597.

(617) R. Deng, X. Su, S. Hao, Z. Zheng, M. Zhang, H. Xie, W. Liu, Y. Yan, C. Wolverton and C. Uher, *Energy & Environmental Science*, 2018, **11**, 1520–1535.

(618) H. Deng, X. Lou, W. Lu, J. Zhang, D. Li, S. Li, Q. Zhang, X. Zhang, X. Chen and D. Zhang, *Nano Energy*, 2021, **81**, 105649.

(619) J. Cui, Y. Li, Z. Du, Q. Meng and H. Zhou, *Journal of Materials Chemistry A*, 2013, **1**, 677–683.

(620) D. Cheikh, B. E. Hogan, T. Vo, P. Von Allmen, K. Lee, D. M. Smiadak, A. Zevalkink, B. S. Dunn, J.-P. Fleurial and S. K. Bux, *Joule*, 2018, **2**, 698–709.

(621) H.-C. Chang, T.-H. Chen, R. Sankar, Y.-J. Yang, L.-C. Chen and K.-H. Chen, *Materials Today Physics*, 2020, **15**, 100248.

(622) Y. Cao, X. Su, F. Meng, T. P. Bailey, J. Zhao, H. Xie, J. He, C. Uher and X. Tang, *Advanced Functional Materials*, 2020, **30**, 2005861.

(623) A. Banik, U. S. Shenoy, S. Saha, U. V. Waghmare and K. Biswas, *Journal of the American Chemical Society*, 2016, **138**, 13068–13075.

(624) A. Banik, U. S. Shenoy, S. Anand, U. V. Waghmare and K. Biswas, *Chemistry of Materials*, 2015, **27**, 581–587.

(625) A. Banik, T. Ghosh, R. Arora, M. Dutta, J. Pandey, S. Acharya, A. Soni, U. V. Waghmare and K. Biswas, *Energy & Environmental Science*, 2019, **12**, 589–595.

(626) A. Banik and K. Biswas, *Journal of Materials Chemistry A*, 2014, **2**, 9620–9625.

(627) S. Ballikaya, H. Chi, J. R. Salvador and C. Uher, *Journal of Materials Chemistry A*, 2013, **1**, 12478–12484.

(628) K. Ahn, M.-K. Han, J. He, J. Androulakis, S. Ballikaya, C. Uher, V. P. Dravid and M. G. Kanatzidis, *Journal of the American Chemical Society*, 2010, **132**, 5227–5235.

(629) P. Acharyya, S. Roychowdhury, M. Samanta and K. Biswas, *Journal of the American Chemical Society*, 2020, **142**, 20502–20508.

(630) K. Park, K. Ahn, J. Cha, S. Lee, S. I. Chae, S.-P. Cho, S. Ryee, J. Im, J. Lee, S.-D. Park, M. J. Han, I. Chung and T. Hyeon, *Journal of the American Chemical Society*, 2016, **138**, 14458–14468, doi: 10.1021/jacs.6b09222.

(631) B. Liao, B. Qiu, J. Zhou, S. Huberman, K. Esfarjani and G. Chen, *Physical Review Letters*, 2015, **114**, 115901, doi: 10.1103/PhysRevLett.114.115901.

(632) G. Tan, L.-D. Zhao, F. Shi, J. W. Doak, S.-H. Lo, H. Sun, C. Wolverton, V. P. Dravid, C. Uher and M. G. Kanatzidis, *Journal of the American Chemical Society*, 2014, **136**, 7006–7017, doi: 10.1021/ja500860m.

(633) T. Zhu, H. Bai, J. Zhang, G. Tan, Y. Yan, W. Liu, X. Su, J. Wu, Q. Zhang and X. Tang, *ACS Appl. Mater. Interfaces*, 2020, **12**, 39425–39433, doi: 10.1021/acsami.0c10932.

(634) Y. Z. Pei, A. D. LaLonde, H. Wang and G. J. Snyder, *Energy Environ. Sci.*, 2012, **5**, 7963–7969, doi: 10.1039/c2ee21536e.

(635) Y. Z. Pei, H. Wang, Z. M. Gibbs, A. D. LaLonde and G. J. Snyder, *Npg Asia Materials*, 2012, **4**, e28–e28, doi: 10.1038/am.2012.52.

9

Final conclusions and remarks

Ignorance, the root and stem of all evil.
— Plato, The Republic

This thesis has shown that the integration of secondary phases into thermoelectric materials can be a viable approach to developing high efficiency materials suitable for room temperature applications.

The research began with the study of magnetically doped bismuth sulphide, specifically Bi_2S_3 co-doped with chromium and chlorine. It was found that the magnetic dopants increased the thermopower and power factor of Bi_2S_3 due to a magnetic drag effect that increased the effective mass of the charge carriers. This initial finding highlighted the potential of magnetic dopants and phases to beneficially manipulate the thermoelectric transport behaviour. In addition, the promising performance of doped Bi_2S_3 suggested that sulphur-containing materials warranted further exploration.

In sequence, the properties of multiphase Bi_2Te_3-$Bi_{14}Te_{13}S_8$ compounds were investigated in detail. The incorporation of the secondary phase $Bi_{14}Te_{13}S_8$ resulted in the presence of the energy filtering effect where charge carriers are scattered by potential energy barriers, increasing the thermopower and power factor of the multiphase material. Furthermore, the additional interfaces between the phases introduced phonon scattering which reduced the lattice thermal conductivity. Taken together, these effects improved the figure of merit zT compared to single phase Bi_2Te_3.

Based on the promising results for the Bi_2Te_3-based system, an investigation of similar sulphur-containing multiphase materials based on $Bi_2Te_{2.7}Se_{0.3}$ was undertaken. Both single phase and multiphase $Bi_2Te_{2.7}Se_{0.3}$ samples with varying sulphur contents were synthesised using direct reaction and spark plasma sintering techniques. Characterisation revealed that in the single phase alloys, sulphur incorporation significantly altered the density of states and helped to modulate native defect concentrations arising from antisite disorder and chalcogen vacancies. The multiphase samples exhibited a unique bandstructure behaviour at higher secondary phase contents, suggesting the possible formation of impurity bands with high energy states accessible to carriers. In both the single and multiphase cases, the addition of sulphur favourably increased the thermopower and reduced the thermal conductivity.

The effects of integrating magnetic phases have been studied by adding antiferromagnetic CrSb to $Bi_{0.5}Sb_{1.5}Te_3$ matrix compounds. Small amounts of the CrSb secondary phase (0.5 wt%) increased the thermopower as a result of an increased effective mass attributed to magnetic drag effects. However, higher percentages of CrSb degraded performance due to decreasing carrier mobility associated with additional scattering at phase boundaries. This highlights the delicate balance and complex interdependencies involved in optimising multiphase thermoelectric materials.

Finally, single-phase iodine-doped $Bi_{14}Te_{13}S_8$, an important component of the multiphase compounds, was also studied. Iodine doping optimised the power factor and reduced the lattice thermal conductivity, resulting in

an improved figure of merit zT. This shows that the relatively unexplored $Bi_{14}Te_{13}S_8$ system is promising for thermoelectric applications.

In summary, this thesis has systematically investigated various multiphase bismuth chalcogenide systems and demonstrated that mechanisms such as energy filtering, modulation doping and phonon scattering can be advantageously exploited to improve thermoelectric efficiency. The results provide valuable insights into the synergistic phenomena that govern the transport properties in multiphase thermoelectric materials, paving the way for further advances in this promising class of materials.

9.1 Future work

While I am confident that the results presented in this thesis encompass a comprehensive analysis of the thermoelectric materials under study and reflect our utmost efforts, it is important to acknowledge the potential for further experiments. Nevertheless, it was my inherent curiosity as a researcher that led to the inclusion of this section.

Ab initio simulations were carried out using the Quantum ESPRESSO suite and the band structures of pristine Bi_2S_3, doped Bi_2S_3 and pristine $Bi_{14}Te_{13}S_8$ were evaluated in this work. For $Bi_{14}Te_{13}S_8$, the transport properties calculation using a Boltzmann transport relaxation approximation may be something that can be explored further, as it is a material that is relatively unexplored in the thermoelectric community. A theoretical analysis of the phonon dispersion may also be of interest, as it was found in this study that this material has a lattice thermal conductivity comparable to that of Bi_2Te_3. Unfortunately, these calculations demand a long computing time as they are extremely intensive, requiring the use of larger clusters or supercomputers, which made their inclusion in the scope of this study unfeasible.

Chapter 7 shows that the presence of a magnetic phase was shown to increase the power factor and zT. This preliminary result is an indication that this can be a promising area for advancement in thermoelectricity. New multiphase materials using different kinds of magnetic phases can drive a new generation of thermoelectric materials. Particularly, focusing on n-type materials holds interest but poses challenges of its own, such as identifying magnetic semiconductors with high Curie or Néel temperatures.

Experimentally, scanning electron microscopy (SEM) combined with elemental analysis using electron energy spectra (EDX) could also be used to critically analyse the phase and grain distribution of the materials discussed here. Magnetic measurements could also be used to provide direct evidence of the magnetic moments introduced by the magnetic dopants and magnetic phases.

Appendices

A

Licences

American Physical Society
Reuse and Permissions License

26-May-2023

This license agreement between the American Physical Society ("APS") and Raphael Luiz Vicente Fortulan ("You") consists of your license details and the terms and conditions provided by the American Physical Society and SciPris.

Licensed Content Information

License Number:	**RNP/23/MAY/066800**
License date:	26-May-2023
DOI:	10.1103/PhysRevB.77.214304
Title:	Theory of enhancement of thermoelectric properties of materials with nanoinclusions
Author:	Sergey V. Faleev and François Léonard
Publication:	Physical Review B
Publisher:	American Physical Society
Cost:	USD $ 0.00

Request Details

Does your reuse require significant modifications: No

Specify intended distribution locations:	UK & Commonwealth (excluding Canada)
Reuse Category:	Reuse in a thesis/dissertation
Requestor Type:	Student
Items for Reuse:	Figures/Tables
Number of Figure/Tables:	1
Figure/Tables Details:	Figure 1
Format for Reuse:	Print and Electronic
Total number of print copies:	Up to 1000

Information about New Publication:

University/Publisher:	Sheffield Hallam University
Title of dissertation/thesis:	Developing high-efficiency multiphase thermoelectric materials
Author(s):	Raphael Luiz Vicente Fortulan
Expected completion date:	Aug. 2023

License Requestor Information

Name:	Raphael Luiz Vicente Fortulan
Affiliation:	Individual
Email Id:	b9044884@my.shu.ac.uk
Country:	United Kingdom

American Physical Society
Reuse and Permissions License

TERMS AND CONDITIONS

The American Physical Society (APS) is pleased to grant the Requestor of this license a non-exclusive, non-transferable permission, limited to Print and Electronic format, provided all criteria outlined below are followed.

1. You must also obtain permission from at least one of the lead authors for each separate work, if you haven't done so already. The author's name and affiliation can be found on the first page of the published Article.
2. For electronic format permissions, Requestor agrees to provide a hyperlink from the reprinted APS material using the source material's DOI on the web page where the work appears. The hyperlink should use the standard DOI resolution URL, http://dx.doi.org/{DOI}. The hyperlink may be embedded in the copyright credit line.
3. For print format permissions, Requestor agrees to print the required copyright credit line on the first page where the material appears: "Reprinted (abstract/excerpt/figure) with permission from [(FULL REFERENCE CITATION) as follows: Author's Names, APS Journal Title, Volume Number, Page Number and Year of Publication.] Copyright (YEAR) by the American Physical Society."
4. Permission granted in this license is for a one-time use and does not include permission for any future editions, updates, databases, formats or other matters. Permission must be sought for any additional use.
5. Use of the material does not and must not imply any endorsement by APS.
6. APS does not imply, purport or intend to grant permission to reuse materials to which it does not hold copyright. It is the requestor's sole responsibility to ensure the licensed material is original to APS and does not contain the copyright of another entity, and that the copyright notice of the figure, photograph, cover or table does not indicate it was reprinted by APS with permission from another source.
7. The permission granted herein is personal to the Requestor for the use specified and is not transferable or assignable without express written permission of APS. This license may not be amended except in writing by APS.
8. You may not alter, edit or modify the material in any manner.
9. You may translate the materials only when translation rights have been granted.
10. APS is not responsible for any errors or omissions due to translation.
11. You may not use the material for promotional, sales, advertising or marketing purposes.
12. The foregoing license shall not take effect unless and until APS or its agent, Aptara, receives payment in full in accordance with Aptara Billing and Payment Terms and Conditions, which are incorporated herein by reference.
13. Should the terms of this license be violated at any time, APS or Aptara may revoke the license with no refund to you and seek relief to the fullest extent of the laws of the USA. Official written notice will be made using the contact information provided with the permission request. Failure to receive such notice will not nullify revocation of the permission.
14. APS reserves all rights not specifically granted herein.
15. This document, including the Aptara Billing and Payment Terms and Conditions, shall be the entire agreement between the parties relating to the subject matter hereof.

RightsLink

Help

Live Chat

SPRINGER NATURE

High thermoelectric performance of all-oxide heterostructures with carrier double-barrier filtering effect

Author: Chunlin Ou et al
Publication: NPG Asia Materials
Publisher: Springer Nature
Date: May 22, 2015

Copyright © 2015, The Author(s)

Creative Commons

This is an open access article distributed under the terms of the Creative Commons CC BY license, which permits unrestricted use, distribution, and reproduction in any medium, provided the original work is properly cited.

You are not required to obtain permission to reuse this article.

To request permission for a type of use not listed, please contact Springer Nature

© 2023 Copyright - All Rights Reserved | Copyright Clearance Center, Inc. | Privacy statement | Data Security and Privacy | For California Residents | Terms and Conditions
Comments? We would like to hear from you. E-mail us at customercare@copyright.com

Attribution 4.0 International (CC BY 4.0)

This is a human-readable summary of (and not a substitute for) the license. Disclaimer.

You are free to:

Share — copy and redistribute the material in any medium or format

Adapt — remix, transform, and build upon the material
for any purpose, even commercially.

The licensor cannot revoke these freedoms as long as you follow the license terms.

Under the following terms:

Attribution — You must give appropriate credit, provide a link to the license, and indicate if changes were made. You may do so in any reasonable manner, but not in any way that suggests the licensor endorses you or your use.

No additional restrictions — You may not apply legal terms or technological measures that legally restrict others from doing anything the license permits.

Notices:

You do not have to comply with the license for elements of the material in the public domain or where your use is permitted by an applicable exception or limitation.

No warranties are given. The license may not give you all of the permissions necessary for your intended use. For example, other rights such as publicity, privacy, or moral rights may limit how you use the material.

B

Specific heat capacity behaviour at high temperatures

The specific heat capacity in the Debye model is given by

$$c_p = 9Nk_{\mathrm{B}}\left(\frac{T}{\theta_D}\right)^3 \int_0^{\theta_D/T} \frac{x^4 \exp(x)}{(\exp(x)-1)^2}\mathrm{d}x \tag{B.1}$$

where θ_D is the Debye temperature, N is the number of atoms in 1 g of the material, k_{B} is the Boltzmann constant, and T is the absolute temperature.

The integrand in equation B.1 can be rewritten as

$$\frac{x^4 \exp(x)}{(\exp(x)-1)^2} = \frac{x^4 \exp(x)}{\exp(2x) - 2\exp(x) + 1} = \frac{x^4}{\exp(x) - 2 + \frac{1}{\exp(x)}}. \tag{B.2}$$

Using the power series for the exponential function, we can write

$$\frac{x^4}{(\exp(x)-1)+(\exp(-x)-1)} = \frac{x^4}{\sum_{k=0}^{\infty}\frac{x^k}{k!} - 1 + \sum_{k=0}^{\infty}\frac{(-x)^k}{k!} - 1}. \tag{B.3}$$

Looking at the denominator of equation B.3, we have

$$\begin{aligned} -1 + \left(1 + x + \frac{x^2}{2} + \frac{x^3}{6} + \frac{x^4}{24} + \frac{x^5}{720} + \mathcal{O}(x^6)\right) \\ -1 + \left(1 - x + \frac{x^2}{2} - \frac{x^3}{6} + \frac{x^4}{24} - \frac{x^5}{720} + \mathcal{O}(x^6)\right), \end{aligned} \tag{B.4}$$

which simplifies to

$$2\left(\frac{x^2}{2} + \frac{x^4}{24} + \mathcal{O}(x^8)\right). \tag{B.5}$$

Plugging this result in equation B.2 yields

$$\frac{x^4}{2\left(\frac{x^2}{2}+\frac{x^4}{24}+\mathcal{O}(x^8)\right)} = \frac{1}{2}\frac{1}{\left(\frac{1}{2x^2}+\frac{1}{24}+\mathcal{O}(x^4)\right)}, \tag{B.6}$$

which can be compactly written as

$$\frac{1}{2}\left(\sum_{k=0,2,\ldots}^{\infty}\frac{x^{k-2}}{(k+2)!}\right)^{-1}. \tag{B.7}$$

Using only the first term of equation B.7 we get

$$\frac{x^4\exp(x)}{(\exp(x)-1)^2} \approx x^2. \tag{B.8}$$

Thus, the heat capacity is approximately given by

$$c_p \approx 9Nk_\mathrm{B}\left(\frac{T}{\theta_D}\right)^3\int_0^{T/\theta_D}x^2\mathrm{d}x = 9Nk_\mathrm{B}T\left(\frac{T}{\theta_D}\right)^3\cdot\frac{1}{3}\left(\frac{\theta_D}{T}\right)^3, \tag{B.9}$$

or

$$c_p \approx 3Nk_\mathrm{B}. \tag{B.10}$$

This result is known as the Dulong-Petit limit for c_p.

C

Non-uniform samples in resistivity measurements

Let a, b, c, and d be the sides and L the length of the rectangular cuboid shown in figure C.1.

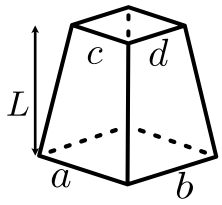

Figure C.1. Rectangular cuboid with sides a, b, c, d and length L.

In general, the resistance R is given by

$$R = \int \mathrm{d}R = \rho \frac{L}{A}. \tag{C.1}$$

Assuming a uniform variation between the opposite sides of the rectangular cuboid, we can write the area as a function of the length

$$A = \left(\frac{c-a}{L}y + a\right) \cdot \left(\frac{d-b}{L}y + d\right). \tag{C.2}$$

The infinitesimal resistance is then given by

$$\mathrm{d}R = \rho \frac{\mathrm{d}y}{\left(\frac{c-a}{L}y + a\right) \cdot \left(\frac{d-b}{L}y + d\right)}, \tag{C.3}$$

and the overall resistance is given by

$$R = \int_0^L \rho \frac{\mathrm{d}y}{\left(\frac{c-a}{L}y + a\right) \cdot \left(\frac{d-b}{L}y + d\right)}. \tag{C.4}$$

Solving the integral above wields

$$\frac{R}{\rho} = \frac{L\log(b/d)}{bc-ad} - \frac{L\log(a/c)}{bc-ad}. \tag{C.5}$$

Simplifying, we obtain

$$\frac{R}{\rho} = L\frac{\log\left(\frac{ad}{bc}\right)}{ad-bc}. \tag{C.6}$$

Equation C.6 holds for rectangular cuboid with equal sides. To prove this statement, let

$$\lim_{\alpha\to c}\lim_{\beta\to d} L\frac{\log\left(\frac{\alpha d}{\beta c}\right)}{\alpha d-\beta c}. \tag{C.7}$$

From the monotone convergence theorem [636], each limit can be evaluated separately and in any order, thus

$$\lim_{\beta\to d}\left(\lim_{\alpha\to c} L\frac{\log\left(\frac{\alpha d}{\beta c}\right)}{\alpha d-\beta c}\right) = L\lim_{\beta\to d}\frac{\log\frac{d}{\beta}}{cd-\beta c} = \frac{L}{cd}. \tag{C.8}$$

Finally, the resistance for this case is

$$R = \rho\frac{L}{cd}, \tag{C.9}$$

that is the usual result for sides with same length, QED.

References

(636) J. Yeh, *Real Analysis: Theory of Measure and Integration Second Edition*, World Scientific Publishing Company, 2006.

D

SPS furnace control loop

A temperature controlled system can be modelled as [64]

$$\tau \dot{T} = -T + Bu + c, \tag{D.1}$$

where T is the temperature, u is the control signal, B is the constant that relates the temperature control signal to the heat flow, c is a constant that relates the ambient temperature to the controlled system, and τ is the time constant that relates the stored energy to the thermal resistance.

The Laplace transform of D.1 is given by

$$\tau s T(s) = -T(s) + Bu(s) + \frac{c}{s}. \tag{D.2}$$

Ignoring the constant c, we obtain

$$G(s) = \frac{T(s)}{u(s)} = \frac{B}{\tau s + 1}. \tag{D.3}$$

The pole of $G(s)$ is $p = -1/\tau$, which implies that the open-loop response is stable since $\tau > 0$ [637].

A PI controller have the following transfer function

$$C(s) = K_p \left(1 + \frac{K_i}{s}\right), \tag{D.4}$$

where K_p and K_i are, respectively, the proportional and integral constants of the controller.

The transfer function of the controlled closed-loop is as follows

$$H_{cl}(s) = \frac{G(s)C(s)}{1 + G(s)C(s)} = \frac{BK_p s + BK_p K_i}{\tau s^2 + (BK_p + 1)s + BK_p K_i} \tag{D.5}$$

Using the System Identification Toolbox on MATLAB and fitting the SPS data, the following transfer function was obtained

$$H_{cl}(s) = \frac{0.04609s + 0.005239}{s^2 + 0.04817s + 0.005329}. \tag{D.6}$$

The poles of $H_{cl}(s)$ are $p_{1,2} = -0.024085 \pm 0.0689124j$. Note that since $\mathrm{Re}(p_{1,2}) < 0$, the system is stable [637]. The complex component of the poles are the responsible for the oscillation seen in the controlled temperature.

In figure D.1, the fitted model of the sintering furnace compared to measured temperature values as exhibited in chapter 5.

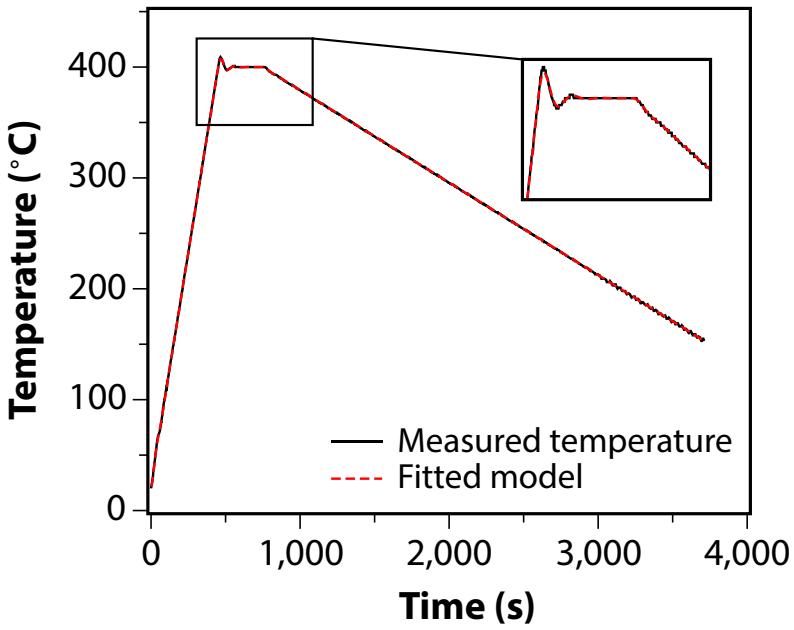

Figure D.1. Fitted model of the sintering furnace compared to measured temperature values.

References

(64) T. L. Bergman, A. S. Lavine and F. P. Incropera, *Fundamentals of Heat and Mass Transfer, 7th Edition*, John Wiley & Sons, Incorporated, 2011, 1076 pp.

(637) H. K. Khalil, *Nonlinear Systems*, Prentice Hall, 2002.

E

Additional data for chapter 5

In table E.1, the lattice parameters and unit cell volumes of the samples of chapter 5 are shown.

Table E.1. Lattice parameters and unit cell volume of $Bi_2(Te_{2.75-x/3}S_{0.25-x/3})I_x$ (x = 0, 0.005, 0.01, and 0.02) obtained from the Rietveld refinement of the diffraction patterns

	Bi_2Te_3			$Bi_{14}Te_{13}S_8$		
x	a = b (Å)	c (Å)	V (Å^3)	a = b (Å)	c (Å)	V (Å^3)
0	4.40	30.45	510.00	11.24	29.60	3238.19
0.005	4.40	30.46	509.98	11.24	29.60	3238.93
0.01	4.40	30.46	509.85	11.25	29.67	3249.89
0.02	4.40	30.40	508.62	11.25	29.62	3246.46

F

Additional data for chapter 6

F.1 Additional XRD data

In table F.1, the unit cell volumes of the samples of chapter 6 are shown.

Table F.1. Unit cell volumes of $Bi_2(Te_{2.7}Se_{0.3})_{1-x}S_{3x}$, x = (0, 0.003, 0.008, 0.0016, 0.025, 0.05, 0.1, and 0.2)

	$Bi_2Te_{2.7}Se_{0.3}$	Bi_2S_3
x	V (Å^3)	V (Å^3)
0	575.48(14)	…
0.003	581.67(11)	…
0.008	581.62(19)	…
0.016	581.85(14)	…
0.025	573.14(9)	524.3(11)
0.05	573.2(8)	508.7(22)
0.1	580.80(14)	534.5(8)
0.2	581.73(21)	524.5(6)

F.2 Measurements along the parallel direction

In the main body of the text, the thermoelectric properties along the perpendicular direction to the sintering direction of the materials have been discussed. Subsequently, the transport properties measured along the parallel direction to the sintering direction are presented in figure F.1. The discussion remains the same as the trends are the same for both directions and the data are included for completeness.

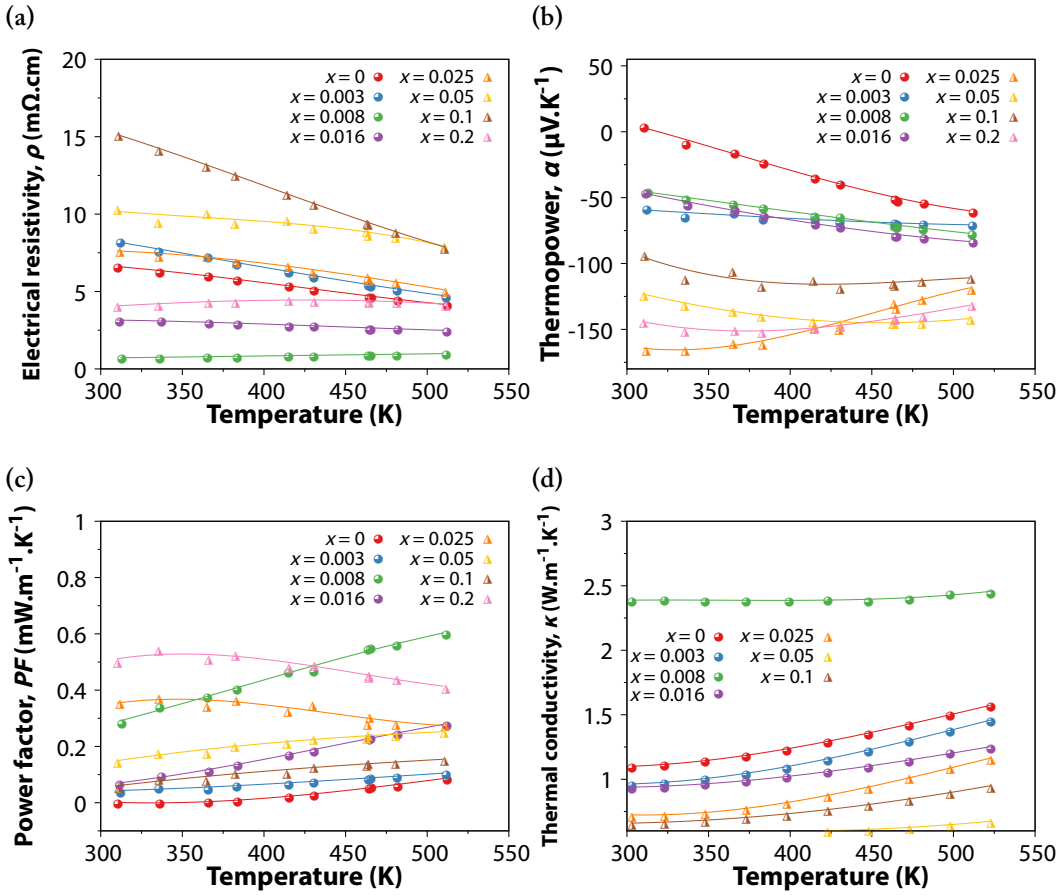

Figure F.1. Temperature dependence of the (a) electrical resistivity, (b) thermopower, (c) power factor, and (d) thermal conductivity of $Bi_2(Te_{2.7}Se_{0.3})_{1-x}S_{3x}$, x = (0, 0.003, 0.008, 0.0016, 0.025, 0.05, 0.1, and 0.2) samples measured along the parallel direction to the sintering direction.

F.3 Specific heat capacity measurements

The specific heat capacity was measured using DSC for x = (0, 0.025 and 0.2), i.e. the extreme values and the median, and is shown in figure F.2, where the dashed lines represent a linear fit of the data. Taking into account a measurement error of 5% [338], the values are similar.

By calculating the theoretical specific heat capacity using the Debye model (see appendix B) using the measured longitudinal speed of sound in the material given in table 6.5, it can again be verified that c_p is similar for all samples, as shown in figure F.3.

Therefore, the value of c_p used to calculate the thermal conductivity was x = 0.2, as it was the intermediate range of measured specific heat capacities of x = 0 and 0.025.

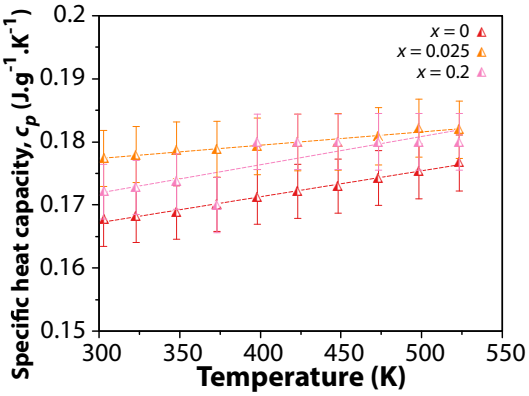

Figure F.2. Measured specific heat capacity of $Bi_2(Te_{2.7}Se_{0.3})_{1-x}S_{3x}$, x = (0, 0.025, and 0.2) samples. The dashed lines represent a linear fit of the data.

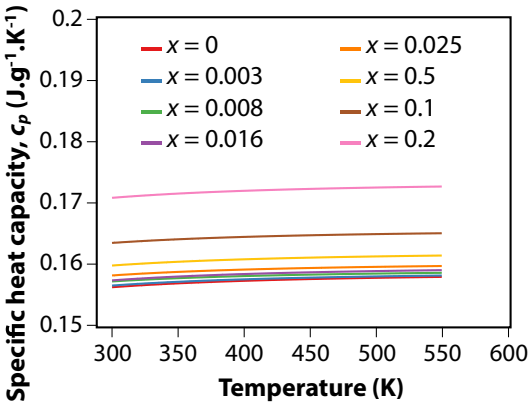

Figure F.3. Modelled specific heat capacity of $Bi_2(Te_{2.7}Se_{0.3})_{1-x}S_{3x}$, x = (0, 0.003, 0.008, 0.0016, 0.025, 0.05, 0.1, and 0.2) samples using the Debye model.

G

My publications

ACS APPLIED MATERIALS & INTERFACES

www.acsami.org

Research Article

Room-Temperature Thermoelectric Performance of n-Type Multiphase Pseudobinary Bi_2Te_3–Bi_2S_3 Compounds: Synergic Effects of Phonon Scattering and Energy Filtering

Sima Aminorroaya Yamini,* Rafael Santos, Raphael Fortulan, Azdiar A. Gazder, Abhishek Malhotra, Daryoosh Vashaee, Illia Serhiienko, and Takao Mori

Cite This: *ACS Appl. Mater. Interfaces* 2023, 15, 19220–19229

Read Online

ACCESS | Metrics & More | Article Recommendations | Supporting Information

ABSTRACT: Bismuth telluride-based alloys possess the highest efficiencies for the low-temperature-range (<500 K) applications among thermoelectric materials. Despite significant advances in the efficiency of p-type Bi_2Te_3-based materials through engineering the electronic band structure by convergence of multiple bands, the n-type pair still suffers from poor efficiency due to a lower number of electron pockets near the conduction band edge than the valence band. To overcome the persistent low efficiency of n-type Bi_2Te_3-based materials, we have fabricated multiphase pseudobinary Bi_2Te_3–Bi_2S_3 compounds to take advantages of phonon scattering and energy filtering at interfaces, enhancing the efficiency of these materials. The energy barrier generated at the interface of the secondary phase of $Bi_{14}Te_{13}S_8$ in the Bi_2Te_3 matrix resulted in a higher Seebeck coefficient and consequently a higher power factor in multiphase compounds than the single-phase alloys. This effect was combined with low thermal conductivity achieved through phonon scattering at the interfaces of finely structured multiphase compounds and resulted in a relatively high thermoelectric figure of merit of ∼0.7 over the 300–550 K temperature range for the multiphase sample of n-type $Bi_2Te_{2.75}S_{0.25}$, double the efficiency of single-phase Bi_2Te_3. Our results inform an alternative alloy design to enhance the performance of thermoelectric materials.

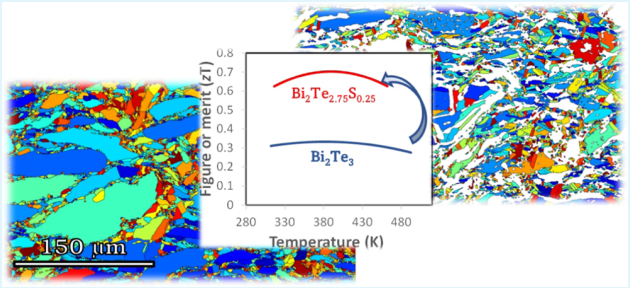

KEYWORDS: *multiphase, thermoelectric, energy filtering, phonon scattering, bismuth telluride-based*

1. INTRODUCTION

Two-thirds of the world's energy is wasted as heat, with low-grade waste heat, up to 500 K, accounting for 60% of this lost energy.[1] Thermoelectric generators (TEGs) that convert thermal energy to electricity and vice versa are a pioneer recovery technique for low-grade waste heat; several promising materials have been explored for power generation applications including GeTe,[2] PbTe,[3] and silicide.[4] However, there are only a few thermoelectric materials that perform relatively well in TEGs within this temperature range, with a conversation efficiency of <10% over a narrow temperature range.[5] Therefore, further development is required to improve the conversion efficiency of current thermoelectric materials, defined by the dimensionless figure of merit, $zT = \frac{\alpha^2\sigma}{\kappa_e + \kappa_l}T$, where α, σ, κ_e, and κ_l are the Seebeck coefficient, the electrical conductivity, the electronic thermal conductivity, and the lattice thermal conductivity, respectively.

The state-of-the-art thermoelectric material for the low-temperature range (<500 K) is based on Bi_2Te_3 alloys. Despite significant advances in the conversion efficiency of p-type Bi_2Te_3-based materials, upon reaching zT of ∼1.5 at room temperature,[6,7] the n-type pair still suffers from poor efficiency, and the zT of ∼0.9 is still the highest value at room temperature,[8] resulting in low generated power by the TEG. This is associated with the lower number of electron pockets near the conduction band edge of Bi_2Te_3 than the valence band, failing to take advantages of the power factor, $S^2\sigma$, enhancement through engineering the electronic band structure by convergence of multiple bands.[9] Therefore, a new approach is required to tackle its persistent low zT.

Recently, multiphase thermoelectric materials have attracted the attention of the thermoelectric research community[10] due to higher degrees of freedoms that these materials provide to design high-performance compounds through phonon scattering at interfaces,[11,12] energy filtering,[12,13] modulation doping,[14,15] and potentially benefiting from incorporating mag-

Received: February 12, 2023
Accepted: March 27, 2023
Published: April 4, 2023

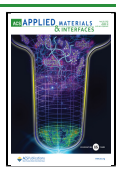

Downloaded via SHEFFIELD HALLAM UNIV on September 15, 2023 at 10:46:41 (UTC).
See https://pubs.acs.org/sharingguidelines for options on how to legitimately share published articles.

ACS Publications

© 2023 The Authors. Published by American Chemical Society

netic interaction.[16,17] The energy filtering effect creates potential barriers in the electronic band structure of the matrix through interfaces with the secondary phases, resulting in an increase in the overall Seebeck coefficient.[13,18] The secondary phases with the larger band gaps and higher carrier concentrations than the matrix can increase the electrical conductivity of the multiphase compounds called modulation doping.[15,19] These strategies are adopted to improve the thermoelectric performance, mostly by enhancing the power factor ($\alpha^2\sigma$); however, the lattice thermal conductivity is influenced at the presence of secondary phases.[17,20]

Here, we have selected a pseudobinary Bi_2Te_3−Bi_2S_3 system, which contains multiphase compounds of Bi_2Te_2S and Bi_2Te_3 or Bi_2S_3 phases. Both phases of Bi_2Te_2S (~0.28 eV)[21] and Bi_2S_3 (1.3 eV)[22] have higher band gaps than Bi_2Te_3 (~0.15 eV).[23] We have shown that n-type multiphase pseudobinary Bi_2Te_2S−Bi_2Te_3 compounds possess a higher power factor and simultaneously provide lower total thermal conductivities than single-phase counterparts, resulting in a relatively high thermoelectric figure of merit of ~0.7 over the temperature range of 300−550 K, compared to ~0.3 for the Bi_2Te_3 sample. These new findings will inform the design of next-generation, multiphase compounds with enhanced thermoelectric performance for low-grade waste heat recovery applications.

2. MATERIALS AND METHODS

2.1. Synthesis. A set of polycrystalline $Bi_2Te_{3-x}S_x$ (x = 0, 0.25, 0.5, 0.75, and 1.0) samples were synthesized by direct reaction of stoichiometric amounts of high-purity Bi (99.999%, Alfa Aesar), Te (99.999%) shots, and dried S (99.99%) powder in vacuum-sealed quartz ampoules in an Ar glove box. The ampoules were homogenized at 1123 K for 10 h, quenched in cold water, and annealed at 673 K for 72 h. The obtained ingots were hand-ground to fine powders in an agate mortar and pestle housed inside an Ar atmosphere glove box. The powders were then loaded into a graphite die and sintered under vacuum to produce rods of 6 mm in diameter and 12−14 mm in length, using spark plasma sintering at 633 K and an axial pressure of 50 MPa for 5 min. The density (ρ) of samples was measured via the Archimedes method such that the relative densities were ≥99% for all samples.

The multiphase samples of $Bi_2Te_{2.75(1-\frac{y}{3})}S_{0.25(1-\frac{y}{3})}I_y$ (y = 0.005, 0.01, and 0.02) that are iodine-doped samples of multiphase $Bi_2Te_{2.75}S_{0.25}$ were fabricated to ingots by direct reaction of stoichiometric amounts of high-purity Bi (99.999%, Alfa Aesar), Te (99.999%) shots, dried S (99.99%) powder, and BiI_3 (99.999%, Alfa Aesar Puratronic), using the abovementioned heat treatment procedure. The hand-ground powders were then loaded into a graphite die and sintered under vacuum to produce pellets using spark plasma sintering (FCT System GmbH, KCE FCT-H HP D-25 SD, Rauenstein, Germany) at 673 K and an axial pressure of 50 MPa for 5 min, obtaining samples with 11 mm in diameter and ~12 mm height. Although the same sintering parameters were used to sinter these samples, the change in the SPS equipment resulted in samples with densities (ρ) of >90% of the relative densities, lower that the densities of >99% of the theoretical density for previous samples.

2.2. Material Characterization. The phase purity and crystal structure of sintered samples were characterized by powder X-ray diffraction (XRD) using a PANalytical X'Pert PRO X-ray diffractometer with Cu Kα radiation (λ = 1.5406 Å, 40 kV, 25 mA). The lattice parameters were determined by Rietveld refinement of the collected diffraction patterns using the FullProf program.

For the microstructure and chemical mapping, samples were cut from the sintered disk cross section of $Bi_2Te_{3-x}S_x$ (x = 0 and 0.5) ingots such that the compression direction was parallel to the sample surface. The sample surface was polished up to 1 μm diamond and then subjected to Ar-ion milling on a Leica EM RES101 at 4 kV for 1 h. The grain and phase distribution and chemical composition of samples were characterized using a JEOL JSM-7001F field emission gun scanning electron microscope (SEM), equipped with an Oxford Instruments 80 mm^2 X-Max energy-dispersive spectroscopy (EDS) detector and a Nordlys-S(II) electron backscattering diffraction (EBSD) detector working concurrently with the OI Aztec acquisition software. Combined EBSD and EDS maps were collected from 480 × 360 μm^2 areas at an accelerating voltage of 15 kV, a probe current of ~5.5 nA, and a step size of 0.24 μm. In the Bi_2Te_3 and $Bi_2Te_{2.5}S_{0.5}$ samples, overall indexing rates of ~91.5 and 92.2% were obtained such that most zero solutions were located at grain boundary regions. The maps were cleaned by removing wild orientation spikes and filling-in zero solutions via cyclic extrapolation down to five neighbors and processed using the OI HKL Channel-5 analytical software suite. The parameters used to collect and process the combined EBSD and EDS maps are detailed in our previous study.[24]

2.3. Electronic Transport Property Measurements. The electrical conductivity and Seebeck coefficient were measured perpendicular and parallel to the compression/sintering direction of the pellet and rod samples, respectively, by cutting ~2 × 2 × 9 mm^3 specimens from the pellet. The measurements were carried out from room temperature to 523 K under a helium atmosphere by using a Linseis LSR-3 apparatus.

The laser flash diffusivity method (Linseis LFA 1000) was used to measure the thermal diffusivity of the pellet and rod samples. The thermal diffusivity (D) of all samples was measured parallel to the compression/sintering direction. The thermal conductivities (κ) were calculated by $\kappa = D \times C_p \times \rho$. The heat capacity ($C_p$) of all samples was measured according to the ASTM-E1269-11 standard test using a differential scanning calorimeter (PerkinElmer-DSC 8000). The density (ρ) of samples was measured via the Archimedes method.

The samples were cut with their long axis perpendicular to the sintering direction of samples to measure the Hall coefficient (R_H) from transverse electrical resistivity measurements using the DC transport option of a Quantum Design physical property measurement system (PPMS) at temperatures between 5 and 400 K under a ±2 T magnetic field. The Hall carrier concentration (n_H) and Hall carrier mobility (μ_H) were calculated using $n_H = 1/(R_H \cdot e)$ and $\mu_H = \sigma/(n_H \cdot e)$, respectively. The room-temperature Hall coefficient (R_H) of doped samples was measured through van der Pauw method, using an ECOPIA-HMS-3000 apparatus to obtain the room-temperature Hall carrier concentrations and electronic mobilities.

3. RESULTS AND DISCUSSION

3.1. Composition and Microstructure Analysis. According to the pseudobinary phase diagram of Bi_2Te_3−Bi_2S_3[25] (Figure 1), $Bi_2Te_{3-x}S_x$ (x = 0.25, 0.5, and 0.75) compounds comprise two phases, namely, Bi_2Te_3 and Bi_2Te_2S.

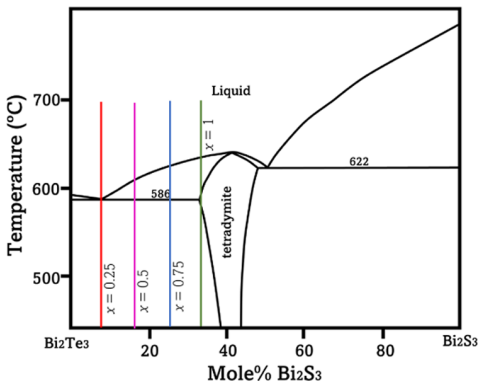

Figure 1. Phase diagram of Bi_2Te_3−Bi_2S_3, adapted from ref 25, indicating the composition of samples $Bi_2Te_{3-x}S_x$ (x = 0, 0.25, 0.5, 0.75, and 1).

https://doi.org/10.1021/acsami.3c01956
ACS Appl. Mater. Interfaces 2023, 15, 19220−19229

The purity and crystal structure of the undoped $Bi_2Te_{3-x}S_x$ (x = 0, 0.25, 0.5, 0.75, and 1) samples are determined by indexing the powder X-ray diffraction (XRD) patterns, shown in Figure 2. All samples exhibit trigonal crystal structures. The

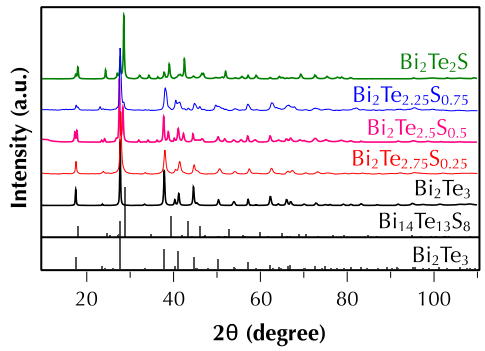

Figure 2. Room-temperature X-ray diffraction patterns of $Bi_2Te_{3-x}S_x$ (x = 0, 0.25, 0.5, 0.75, and 1).

Bi_2Te_3 sample is a single phase belonging to the $R\bar{3}m$ space group with the lattice parameters $a = b = 4.39$ Å, $c = 30.47$ Å, $\alpha = \beta = 90°$, and $\gamma = 120°$. However, the sample stoichiometrically referred to as Bi_2Te_2S comprises two phases, namely, Bi_2Te_3 and $Bi_{14}Te_{13}S_8$. The latter phase belongs to the $R\bar{3}$ space group with the lattice parameters $a = b = 4.18$ Å, $c = 29.45$ Å, $\alpha = \beta = 90°$, and $\gamma = 120°$. The tetradymites Bi_2Te_3 are based on five layers in three blocks in a $[Te_2-Bi-Te_1-Bi-Te_2]_0 - [Te_2-Bi-Te_1-Bi-Te_2]_{1/3} - [Te_2-Bi-Te_1-Bi-Te_2]_{2/3}$ sequence with the subscripts indicating the z translation of the blocks within the hexagonal unit cell.[26]

In the case of Bi_2Te_2S, it was initially proposed that the S atoms substituted at Te sites.[27] However, this structure was unstable at that composition due to the high strains on the internal sulfur layer caused by the electronegative anion of sulfur and the very different ionic radii of Te and S, resulting in a large size mismatch of the hexagonal-close-packed Te and S layers. Therefore, a more complex formula, $Bi_{14}Te_{13}S_8$, was suggested for the single-phase structure where S only occupies the Te_1 sites in the Bi_2Te_3 structure.[26,28] This phase has an orthorhombic crystal structure, belongs to the $R\bar{3}$ space group with lattice parameters of $a = b = 11.24$ Å and $\alpha = \beta = \gamma = 56.83°$ or a corresponding hexagonal structure with lattice parameters of $a = 4.25$ Å, $c = 29.6$ Å, $\alpha = \beta = 90°$, and $\gamma = 120°$.[28] The stoichiometrically prepared sample of Bi_2Te_2S contains less sulfur than single-phase $Bi_{14}Te_{13}S_8$, and therefore, as XRD results indicate, it contains a secondary Bi_2Te_3 phase within the $Bi_{14}Te_{13}S_8$ matrix.

It is worth noting that this crystal structure has been indexed as Bi_2Te_2S in the XRD databases of the Inorganic Crystal Structure Database (ICSD) and Open Quantum Materials Database (OQMD). Consequently, we used this to identify phases in our previous work,[24] and in fact, the phase labeled the Bi_2Te_2S phase in our previous report[24] is the $Bi_{14}Te_{13}S_8$ phase. We acknowledge the incorrect labeling of the $Bi_{14}Te_{13}S_8$ phase as Bi_2Te_2S in our previous study and refer to it as $Bi_{14}Te_{13}S_8$ in this work. Rietveld refinement was also employed via the FullProf software suite to determine the proportion of phases, summarized in Table 1.

The electronic transport properties of bismuth chalcogenides are affected by the fraction of individual phases.[7,29] Therefore, we employed a combination of an EBSD technique and EDS mapping to discriminate the Bi_2Te_3 and $Bi_{14}Te_{13}S_8$ phases.[24]

Figure 3a,c shows the band contrast maps of the $Bi_2Te_{3-x}S_x$ (x = 0 and 0.5) sample cross section, the surface parallel to the sintering direction, respectively. The low-angle grain boundaries (LAGBs) are defined as misorientations between $2 \leq \theta \leq 15°$ in blue and high-angle grain boundaries (HAGBs) as misorientations >15° in black. Since the powder was hand-ground from an annealed ingot in an agate mortar and pestle, it resulted in a large variation in grain sizes, with some grains exceeding 100 μm. In general, most large grains are elongated perpendicular to the direction of sintering. The latter is along the map vertically.

Figure 3d shows the phase distribution maps of Bi_2Te_3 (red) and $Bi_{14}Te_{13}S_8$ (blue) phases in the multiphase sample of $Bi_2Te_{2.5}S_{0.5}$. Although the same fabrication method was employed to prepare these samples, the grain sizes in the multiphase $Bi_2Te_{2.5}S_{0.5}$ sample are much smaller than in single-phase Bi_2Te_3 (compare Figure 3a,c). The phase diagram of $Bi_2Te_3-Bi_2S_3$[25] (Figure 1) shows that there is a eutectic transformation between Bi_2Te_3 and $Bi_{14}Te_{13}S_8$, following which a lamellar structure is expected in the final ingot. This has resulted in much finer grain size in the multiphase sample of $Bi_2Te_{2.5}S_{0.5}$ than in the single-phase Bi_2Te_3 sample.

Figure 3b shows the EBSD image of the Bi_2Te_3 phase in a single-phase sample of Bi_2Te_3, and Figure 3e,f shows the EBSD image of Bi_2Te_3 and $Bi_{14}Te_{13}S_8$ phases, respectively, in the multiphase sample of $Bi_2Te_{2.5}S_{0.5}$. These images show the orientation of the unit cells' c-axis of each phase relative to the compression axis. The grains sizes of both phases in the $Bi_2Te_{2.5}S_{0.5}$ sample are very similar and elongated perpendicular to the sintering direction, similar to the single-phase sample.

3.2. Electronic Transport Properties of $Bi_2Te_{3-x}S_x$ (x = 0, 0.25, 0.5, 0.75, and 1) Samples. Figure 4 shows the temperature-dependent thermoelectric properties of the undoped $Bi_2Te_{3-x}S_x$ (x = 0, 0.25, 0.5, 0.75, and 1) samples between 300 K and 500 K. All thermoelectric properties of this set of samples were measured parallel to the sintering direction.

All samples show negative Seebeck coefficient values, which indicates that electrons compose most charge carriers. The Seebeck coefficient (Figure 4a) of all samples with x = 0.5 and 0.75 decreases with temperature, exhibiting a temperature dependence behavior typical of intrinsic semiconductors. The Bi_2Te_2S and Bi_2Te_3 samples show a bipolar effect within the range of 400−500 K that is typical behavior of narrow band gap degenerate semiconductors[30] where the intrinsic carriers

Table 1. Estimated Mass Ratio of the Phases in the $Bi_2Te_{3-x}S_x$ (x = 0, 0.25, 0.5, 0.75, and 1) Samples Obtained by Rietveld Refinement

x	0	0.25	0.5	0.75	1
Bi_2Te_3	100	83.9 ± 1.5	55.4 ± 0.7	33.4 ± 1.8	18.9 ± 0.3
$Bi_{14}Te_{13}S_8$		16.1 ± 0.8	44.6 ± 0.5	66.6 ± 0.7	81.1 ± 0.8

https://doi.org/10.1021/acsami.3c01956
ACS Appl. Mater. Interfaces 2023, 15, 19220−19229

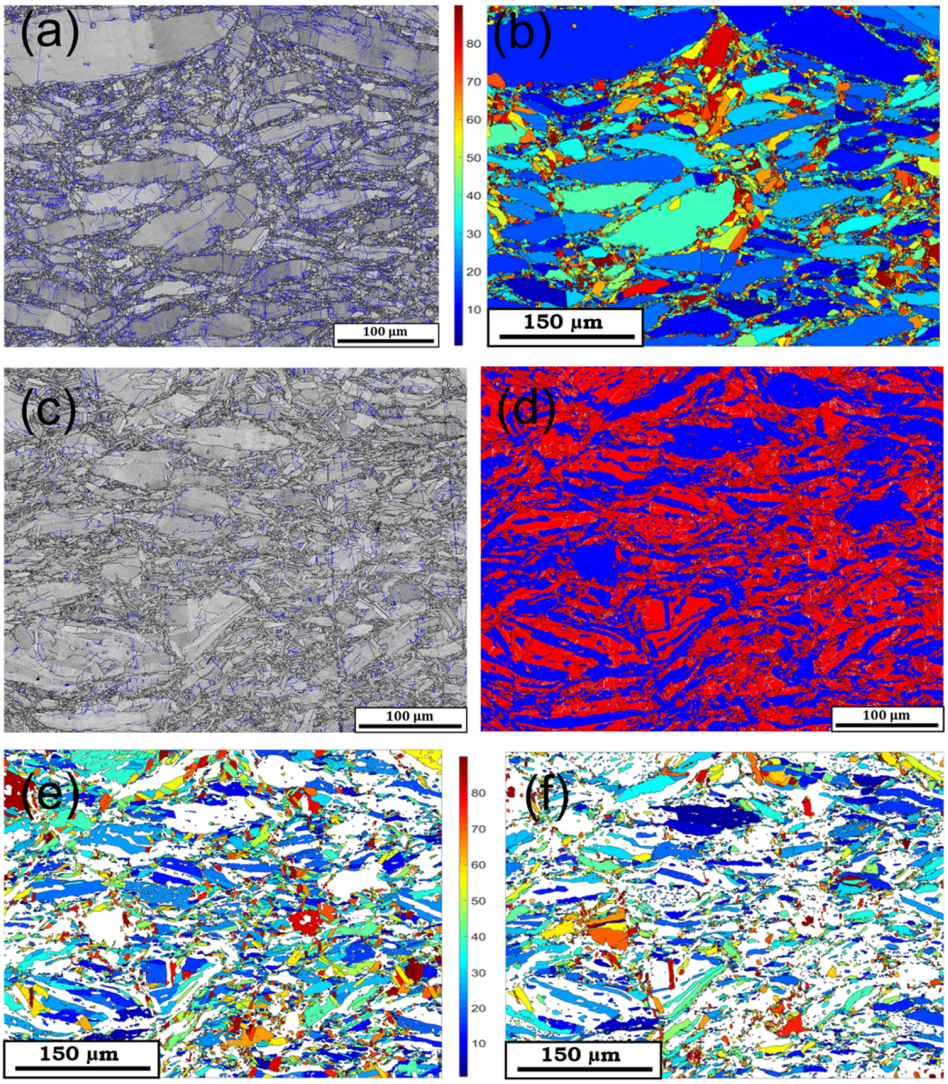

Figure 3. (a) Band contrast and (b) EBSD image of the Bi_2Te_3 sample, indicating a single-phase compound with grains elongated normal to the direction of sintering. (c) Band contrast, (d) phase distribution map of Bi_2Te_3 (red) and $Bi_{14}Te_{13}S_8$ (blue), (e) EBSD image of the Bi_2Te_3 phase, and (f) EBSD image of the $Bi_{14}Te_{13}S_8$ phase in the $Bi_2Te_{2.5}S_{0.5}$ sample, showing the sample containing both phases with grains sizes much smaller than the single-phase Bi_2Te_3 sample. EBSD images indicate the orientation of the unit cells' c-axis of each phase relative to the compression axis.

are excited and compete with the extrinsic carriers, which in turn decreases the Seebeck coefficient with increasing the temperature as a result of the combined contribution of negative and positive charge carriers.

The electrical conductivity (Figure 4b) of all samples, except for samples with x = 0 and 0.25, increases with temperature and exhibits a temperature dependence behavior, typical of intrinsic semiconductors. The highest value of power factors, ~1.75 mW/m·K^2 (Figure 4c) was obtained in the multiphase $Bi_2Te_{2.75}S_{0.25}$ sample (containing roughly 16 wt % of $Bi_{14}Te_{13}S_8$ in the matrix of Bi_2Te_3) at around room temperature with a Seebeck coefficient of ~150 μV/K and above 1.5 mW/m·K^2 over the whole temperature range. This marks a significant increase from ~1.25 mW/m·K^2 for the single-phase Bi_2Te_3.

The temperature-dependent Hall coefficient, R_H, of $Bi_2Te_{3-x}S_x$ (x = 0, 0.25, 0.5, 0.75, and 1) samples between 10 and 400 K (Figure 5) shows that the Hall coefficient of multiphase samples with x = 0.5 and 0.75 decreases with temperature, while the values are constant over the whole temperature range for the rest of samples. The Hall carrier concentrations (n_H) of all samples were calculated at 350 K and are summarized in Table 2. These samples are all undoped and the charge carriers are caused by the structural defects. The multiphase samples of $Bi_2Te_{3-x}S_x$ (x = 0.5, 0.75, and 1) with a larger fraction of the $Bi_{14}Te_{13}S_8$ secondary phase show very low charge carrier concentrations (~10^{18} cm^{-3}), while the carrier concentration of the multiphase sample of $Bi_2Te_{2.75}S_{0.25}$ is ~1.2 × 10^{19}, similar to the charge carrier concentration of Bi_2Te_3 (~1 × 10^{19}), explaining the higher electrical conductivity and the behavior, typical of a degenerate semiconductor. The optimum thermoelectric performance of n-type Bi_2Te_3 is usually achieved at carrier concentrations in the lower range of ×10^{19} cm^{-3},[31] similar to the single-phase sample of Bi_2Te_3 and the multiphase sample of $Bi_2Te_{2.75}S_{0.25}$. All samples of this study are undoped, and these results suggest that the variations in the charge carrier concentrations in these materials might not be solely due to a substitutional effect of Te with S in Bi_2Te_3 but likely due to the random formation of antisites and vacancy defects and various ratios of each phase in these samples. Table 2 summarizes the Seebeck coefficient,

https://doi.org/10.1021/acsami.3c01956
ACS Appl. Mater. Interfaces 2023, 15, 19220−19229

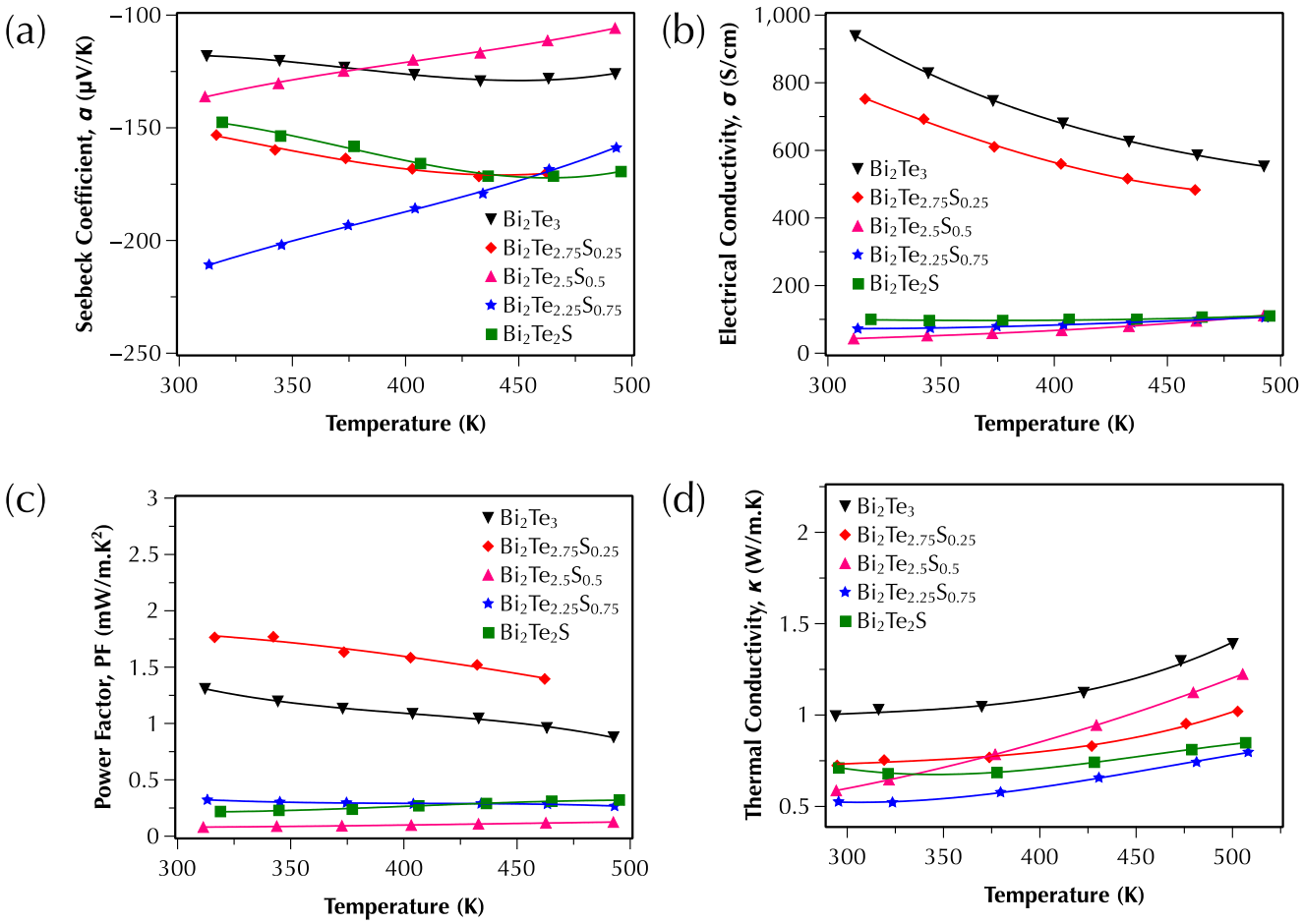

Figure 4. Temperature dependence between 300 and 500 K of (a) the Seebeck coefficient, (b) the electrical conductivity, (c) the power factor, and (d) the total thermal conductivity of $Bi_2Te_{3-x}S_x$ (x = 0, 0.25, 0.5, 0.75, and 1) samples parallel to the sintering direction.

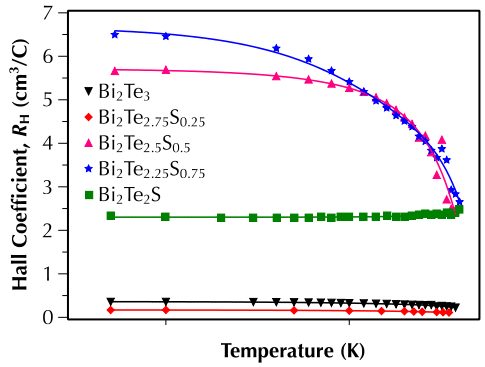

Figure 5. Temperature dependence of the Hall coefficient, R_H, for $Bi_2Te_{3-x}S_x$ (x = 0, 0.25, 0.5, 0.75, and 1) samples between 5 and 400 K.

carrier concentration, and mobility of $Bi_2Te_{3-x}S_x$ (x = 0, 0.25, 0.5, 0.75, and 1) samples at room temperature.

Although the point defects have controlled the carrier concentration of samples and effects on their electrical conductivity significantly, regardless of the carrier concentrations, all multiphase samples of $Bi_{14}Te_{13}S_8$−Bi_2Te_3 ($Bi_2Te_{3-x}S_x$ (x = 0.25, 0.5, 0.75, and 1)) show much higher Seebeck coefficients than the single-phase Bi_2Te_3. The $Bi_2Te_{2.75}S_{0.25}$ sample with carrier concentration similar to Bi_2Te_3 (~1.0×10^{19}) have shown the Seebeck coefficient of

Table 2. Room-Temperature Resistivity (ρ), Seebeck Coefficient (α), Hall Charge Carrier Concentration (n_H), and Hall Mobility (μ_H) of $Bi_2Te_{3-x}S_x$ (x = 0, 0.25, 0.5, 0.75, and 1) Samples

x	resistivity, ρ (mΩ·cm)	Seebeck coefficient, α (μV/K)	Hall carrier concentration, n_H (cm^{-3})	Hall mobility, μ_H (cm^2/V·s)
0	0.94	−118	1.0×10^{19}	655
0.25	1.80	−153	1.2×10^{19}	284
0.5	17.9	−136	1.9×10^{18}	183
0.75	17.2	−210	1.7×10^{18}	213
1	14.3	−147	2.7×10^{18}	161

~150 μV/K, much higher than the value of ~120 μV/K for single-phase Bi_2Te_3 at room temperature (Figure 4a). This can be explained by the energy filtering effect, where the potential barriers generated in the electronic band structure of the matrix through interfaces with the secondary phases increases the overall Seebeck coefficient.[13,18] In this effect, low energy carriers are scattered by potential barriers formed at the junction of the two phases. The barrier height can be approximated as a function of the difference between the electron affinity of two phases. The multiphase samples of $Bi_{14}Te_{13}S_8$−Bi_2Te_3 ($Bi_2Te_{3-x}S_x$ (x = 0.25, 0.5, 0.75, and 1)) have an estimated barrier height of ≈ 0.7 eV, considering the electron affinity, χ, of ≈5.26 eV for $Bi_{14}Te_{13}S_8$[32] and ≈4.5 eV for Bi_2Te_3,[33] schematically demonstrated in Figure 6.

https://doi.org/10.1021/acsami.3c01956
ACS Appl. Mater. Interfaces 2023, 15, 19220−19229

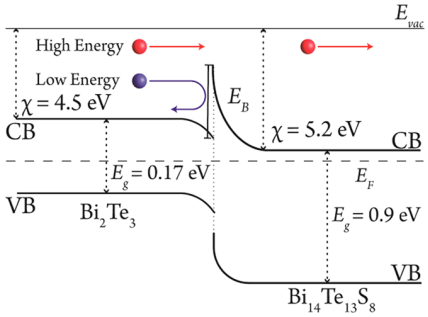

Figure 6. Schematic diagram of the energy filtering effect at the interface between Bi_2Te_3 and $Bi_{14}Te_{13}S_8$.

The temperature dependence of the total thermal conductivity, κ, between 300 and 500 K for all $Bi_2Te_{3-x}S_x$ (x = 0, 0.25, 0.5, 0.75, and 1) samples is presented in Figure 4d. The total thermal conductivity of all samples increases with temperature, indicating low carrier concentrations in these samples. In general. all multiphase samples of $Bi_2Te_{3-x}S_x$ (x = 0.25, 0.5, 0.75, and 1) show the total thermal conductivities much lower than the single-phase Bi_2Te_3 sample. The total thermal conductivity of the highly conductive multiphase $Bi_2Te_{2.75}S_{0.25}$ sample, with similar charge carrier concentration to Bi_2Te_3, is below ~1.1 W/m·K over the temperature range as a result of the finer microstructure (Figure 3).

To understand the effect of the microstructure on the lattice thermal conductivity of these samples, a multiband parabolic model with one electron (n) band and one hole (p) band was employed to calculate the electronic and bipolar contributions of the thermal conductivity for all samples.[34] The multiband model considers both holes and electrons, and the overall Seebeck coefficient and electrical conductivity of samples can be described by

$$S = \frac{\alpha_n\sigma_n + \alpha_p\sigma_p}{\sigma_n + \sigma_p} \quad (1)$$

$$\sigma = \sigma_n + \sigma_p \quad (2)$$

where α_n, α_p, σ_n, and σ_p are the partial Seebeck coefficient and electrical conductivity of electrons and holes, respectively. The electronic (κ_e) and bipolar (κ_b) contributions of the thermal conductivity are given as

$$\kappa_e = (L_n\sigma_n + L_p\sigma_p)T \quad (3)$$

$$\kappa_b = \frac{\sigma_n\sigma_p}{\sigma_n + \sigma_p}(\alpha_n - \alpha_p)^2 T \quad (4)$$

where L_n and L_p are the Lorenz numbers of the conduction and valence bands, respectively. More details of the calculations are provided in the Supporting Information. The electronic (κ_e), bipolar (κ_b), and lattice ($\kappa_L = \kappa - \kappa_e - \kappa_b$) thermal conductivities of $Bi_2Te_{3-x}S_x$ (x = 0, 0.25, 0.5, 0.75, and 1) samples are presented in Figure 7. The most electrically conductive samples (x = 0 and 0.25) show higher values of electronic contribution to the total lattice thermal conductivities than the less conductive ones (Figure 7a). The bipolar thermal conductivity of all samples increases with temperature and decreases with an increase in the fraction of the secondary phase (Figure 7b) due to the larger band gap of $Bi_{14}Te_{13}S_8$. The lattice thermal conductivity of all samples decreases with the temperature, indicating the phonon scattering mechanisms.[35] All multiphase samples with a fine microstructure (x = 0.25, 0.5, and 0.75) show lower lattice thermal conductivity than Bi_2Te_3, most likely due to additional scattering of phonons at the defects, the grain boundaries, and the interfaces between two phases. The bipolar and lattice thermal conductivities of samples are calculated according to the multiband model. This model is developed for single-phase compounds, whereas there is a significant fraction of secondary phase existing in the samples of the current study; this introduces substantial errors in the calculated values of bipolar and lattice thermal conductivities of multiphase samples. Overall, the combination of low total thermal conductivity and high power factor in the highly conductive multiphase $Bi_2Te_{2.75}S_{0.25}$ sample results in a reasonably high figure of merit of ~0.7 (Figure 8) with values higher than 0.6 over the full temperature range of 300−500 K.

The multiphase samples of $Bi_2Te_{2.75}S_{0.25}$, containing $Bi_{14}Te_{13}S_8$ and Bi_2Te_3, were doped with iodine to obtain samples of $Bi_2Te_{2.75(1-\frac{y}{3})}S_{0.25(1-\frac{y}{3})}I_y$ (y = 0.005, 0.01, and 0.02), with various charge carrier concentrations. The thermoelectric performance of these samples was measured for both directions parallel and perpendicular to the sintering orientation.

3.3. Electronic Transport Properties of (y = 0.005, 0.01, and 0.02) Samples. The temperature-dependent Seebeck coefficient, electrical conductivity, total thermal conductivity, and figure of merit of iodine-doped multiphase $Bi_2Te_{2.75}S_{0.25}$ compound, measured parallel to the sintering direction at the temperature range of 300−530 K, are shown in Figure 9a−d, respectively. The thermoelectric performance of

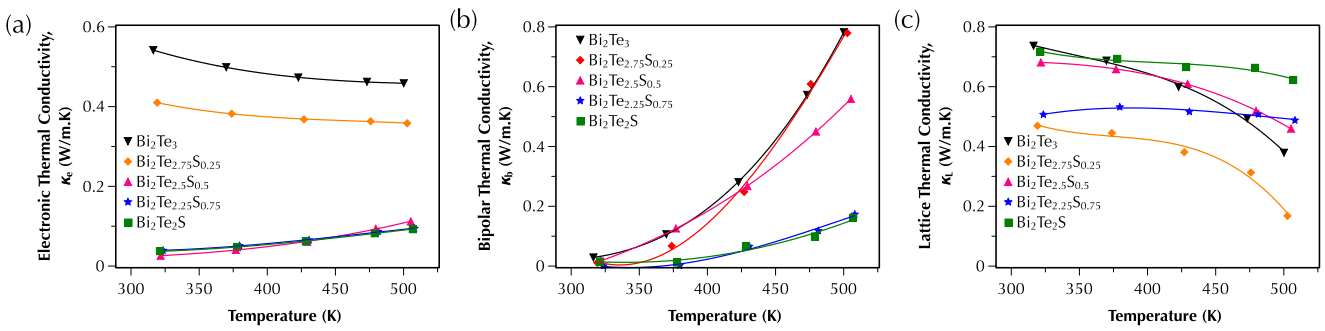

Figure 7. Temperature dependence of the (a) electronic thermal conductivity; (b) bipolar thermal conductivity; and (c) lattice thermal conductivity for $Bi_2Te_{3-x}S_x$ (x = 0, 0.25, 0.5, 0.75, and 1) samples between 300 and 500 K measured parallel to the sintering direction.

https://doi.org/10.1021/acsami.3c01956
ACS Appl. Mater. Interfaces 2023, 15, 19220−19229

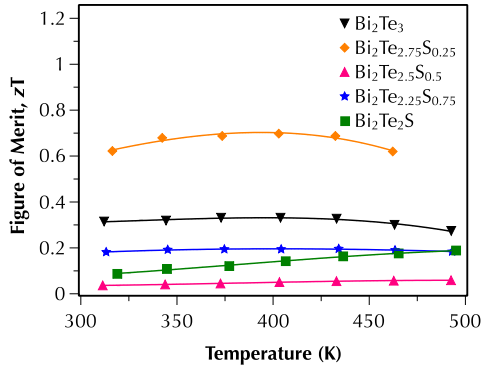

Figure 8. Temperature dependence of the figure of merit, zT, for $Bi_2Te_{3-x}S_x$ (x = 0, 0.25, 0.5, 0.75, and 1) samples between 300 and 500 K measured parallel to the sintering direction.

these samples was also measured at the direction perpendicular to the sintering direction (detailed in the Supporting Information). The electronic transport properties of these samples are compared with the intrinsic sample, shown in Figure 4. The samples are named with their Hall carrier concentrations in Figure 9 for simplicity of comparison. The electrical conductivity has been increased and the Seebeck coefficient has been reduced by the increase in the carrier concentration, as expected; the intrinsic sample has shown only slightly lower charge carrier concentrations (1.2×10^{19} cm^{-3}) than the slightly doped sample (1.7×10^{19} cm^{-3}); however, it has higher electrical conductivity and higher thermal conductivity than the slightly doped samples. We have used the same fabrication method to prepare doped samples as the intrinsic ones; however, the SPS equipment used to sinter these samples was changed, which had lower accuracy in the pressure control system at lower ranges, resulting in samples with densities (ρ) more than 90% of the relative densities, much lower than the density of intrinsic samples (>99% of the theoretical density) that were prepared by different equipment. The porosities in the doped samples resulted in lower electrical conductivity of samples with the same chemistry and carrier concentrations due to scattering of electrons.[36] However, it also reduced the thermal conductivity (Figure 9c) of samples due to the scattering of phonons in the porous structure. This resulted in a similar figure of merit for both samples, showing that optimum charge carrier concentrations for this composition is also in the lower range of $\times 10^{19}$ cm^{-3}, similar to the single-phase n-type Bi_2Te_3 sample.[31] The intrinsic Bi_2Te_3 sample prepared in this study (Table 2 and Figure 4) showed the charge carrier concentrations at the lower range of $\times 10^{19}$

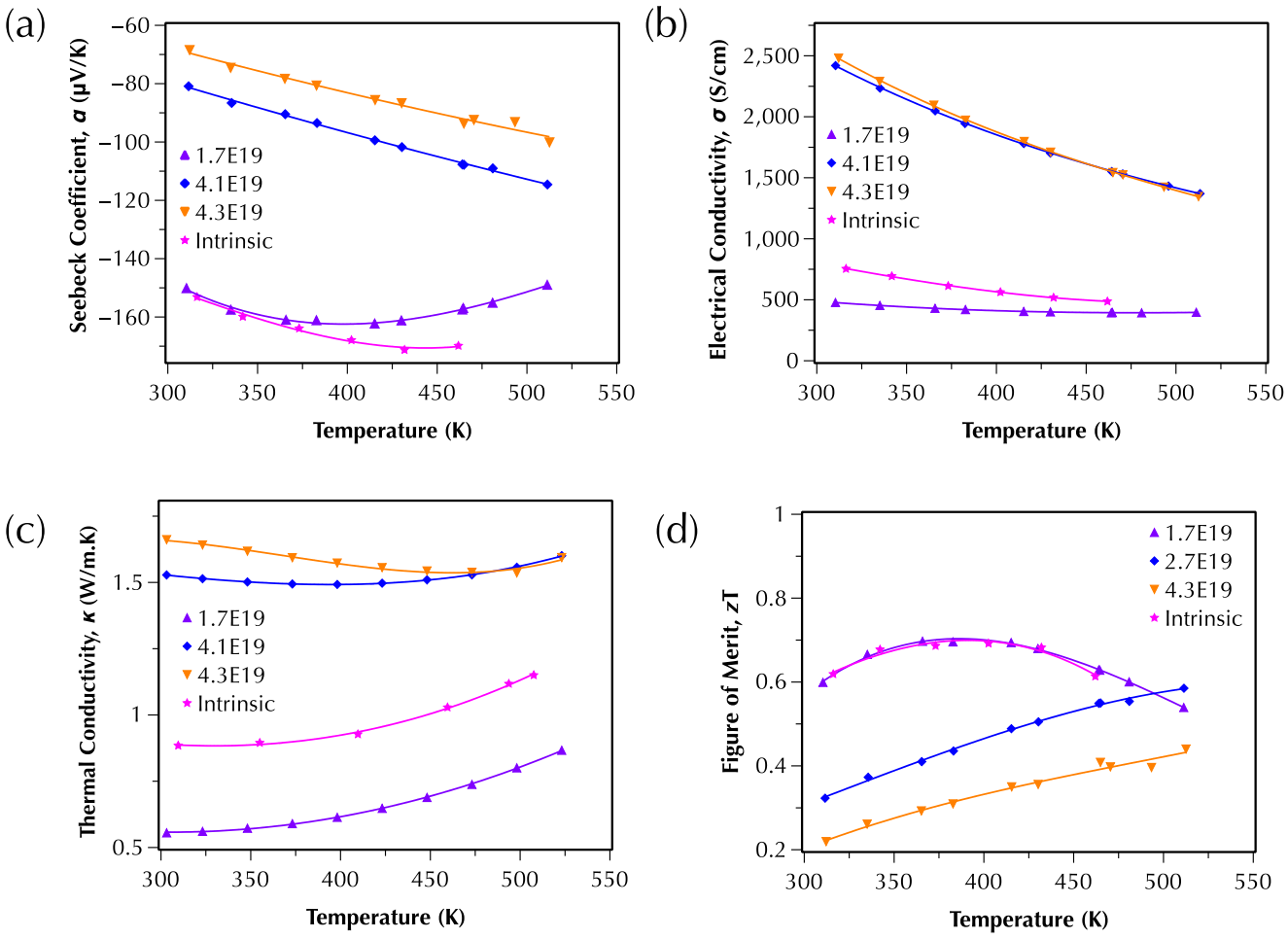

Figure 9. Temperature dependence of (a) the Seebeck coefficient; (b) the electrical conductivity; (c) the total lattice thermal conductivity; and (d) the figure of merit, zT, of $Bi_2Te_{2.75(1-\frac{y}{3})}S_{0.25(1-\frac{y}{3})}I_y$ (y = 0.005, 0.01, and 0.02) samples between 300 and 500 K measured parallel to the sintering direction, compared with the intrinsic sample shown in Figure 4.

https://doi.org/10.1021/acsami.3c01956
ACS Appl. Mater. Interfaces 2023, 15, 19220−19229

cm^{-3}, proving a reasonable comparison of the thermoelectric performance of multiphase samples with the single-phase n-type Bi_2Te_3.

These results suggest that there is a possibility to obtain high room temperature and/or over a wide temperature range thermoelectric performance in the multiphase pseudobinary $Bi_{14}Te_{13}S_8$–Bi_2Te_3 alloys. These samples exhibit a high power factor and simultaneously provide low total thermal conductivities.

4. CONCLUSIONS

In summary, multiphase pseudobinary $Bi_{14}Te_{13}S_8$–Bi_2Te_3 compounds are promising high-performance thermoelectric materials around room temperature. We have shown that the finely distributed secondary phase of $Bi_{14}Te_{13}S_8$ with a larger band gap and electron affinity than the matrix Bi_2Te_3 increased the Seebeck coefficient through the energy filtering effect. This resulted in a higher power factor of multiphase compounds relative to single-phase Bi_2Te_3. Simultaneously, the increased number of interfaces between the two phases formed through eutectic transformation during solidification of the compounds added additional scattering centers for phonons, leading to a decrease in the lattice thermal conductivity of multiphase samples. The combination of these beneficial effects resulted in a reasonably high figure of merit of ~0.7 over the temperature range of 300–550 K for the multiphase sample of $Bi_2Te_{2.75}S_{0.25}$, doubling the efficiency of single-phase Bi_2Te_3.

■ ASSOCIATED CONTENT

Supporting Information

The Supporting Information is available free of charge at https://pubs.acs.org/doi/10.1021/acsami.3c01956.

More detailed information including XRD results, heat capacities, electronic transport properties of samples perpendicular to the direction of sintering, and detailed multiband model used to define bipolar and lattice thermal conductivities of samples (PDF)

■ AUTHOR INFORMATION

Corresponding Author

Sima Aminorroaya Yamini – *Department of Engineering and Mathematics, Sheffield Hallam University, Sheffield S1 1 WB, U.K.; Materials and Engineering Research Institute, Sheffield Hallam University, Sheffield S1 1WB, U.K.;* orcid.org/0000-0002-2312-8272; Email: S.Aminorroaya@shu.ac.uk

Authors

Rafael Santos – *Australian Institute for Innovative Materials (AIIM), University of Wollongong, North Wollongong, New South Wales 2500, Australia*

Raphael Fortulan – *Materials and Engineering Research Institute, Sheffield Hallam University, Sheffield S1 1WB, U.K.*

Azdiar A. Gazder – *Australian Institute for Innovative Materials (AIIM), University of Wollongong, North Wollongong, New South Wales 2500, Australia*

Abhishek Malhotra – *Department of Materials Science and Engineering, North Carolina State University, Raleigh, Raleigh, North Carolina 27606, United States*

Daryoosh Vashaee – *Department of Materials Science and Engineering, North Carolina State University, Raleigh, Raleigh, North Carolina 27606, United States;* orcid.org/0000-0003-3667-3672

Illia Serhiienko – *International Centre for Materials Nanoarchitectonics (WPI-MANA), National Institute for Materials Science, Tsukuba 305-0044, Japan;* orcid.org/0000-0002-3072-9412

Takao Mori – *International Centre for Materials Nanoarchitectonics (WPI-MANA), National Institute for Materials Science, Tsukuba 305-0044, Japan; Graduate School of Pure and Applied Science, University of Tsukuba, Tsukuba 305-8577, Japan;* orcid.org/0000-0003-2682-1846

Complete contact information is available at: https://pubs.acs.org/10.1021/acsami.3c01956

Author Contributions

The manuscript was written through contributions of all authors. All authors have given approval to the final version of the manuscript.

Notes

The authors declare no competing financial interest.

■ ACKNOWLEDGMENTS

The study has received partial funding from the European Union's Horizon 2020 research and innovation programme under the Marie Skłodowska-Curie Grant Agreement No. 801604; the Henry Royce Institute for Advanced Materials, funded through EPSRC Grants EP/R00661X/1, EP/S019367/1, EP/P025021/1, and EP/P025498/1; the Air Force Office of Scientific Research (AFOSR), Contract Number FA9550-19-1-0363; the National Science Foundation (NSF), Grant Number CBET-2110603. T.M. would like to thank JST Mirai Program Grant Number JPMJMI19A1. The JEOL JSM-7001F was funded by the Australian Research Council–Linkage Infrastructure, Equipment and Facilities Grant LE0882813.

■ REFERENCES

(1) Kishore, R. A.; Priya, S. Low-grade waste heat recovery using the reverse magnetocaloric effect. *Sustainable Energy Fuels* **2017**, *1*, 1899–1908.

(2) Jiang, B.; Wang, W.; Liu, S.; Wang, Y.; Wang, C.; Chen, Y.; Xie, L.; Huang, M.; He, J. High figure-of-merit and power generation in high-entropy GeTe-based thermoelectrics. *Science* **2022**, *377*, 208–213.

(3) Liu, H.-T.; Sun, Q.; Zhong, Y.; Deng, Q.; Gan, L.; Lv, F.-L.; Shi, X.-L.; Chen, Z.-G.; Ang, R. High-performance in n-type PbTe-based thermoelectric materials achieved by synergistically dynamic doping and energy filtering. *Nano Energy* **2022**, *91*, No. 106706.

(4) Sadia, Y.; Elegrably, M.; Ben-Nun, O.; Marciano, Y.; Gelbstein, Y. Submicron features in higher manganese silicide. *J. Nanomater.* **2013**, *2013*, No. 4.

(5) Shi, X.; Sun, C.; Bu, Z.; Zhang, X.; Wu, Y.; Lin, S.; Li, W.; Faghaninia, A.; Jain, A.; Pei, Y. Revelation of Inherently High Mobility Enables Mg3Sb2 as a Sustainable Alternative to n-Bi2Te3 Thermoelectrics. *Adv. Sci.* **2019**, *6*, No. 1802286. Liu, Z.; Gao, W.; Oshima, H.; Nagase, K.; Lee, C.-H.; Mori, T. Maximizing the performance of n-type Mg3Bi2 based materials for room-temperature power generation and thermoelectric cooling. *Nat. Commun.* **2022**, *13*, No. 1120.

(6) Kim, S. I.; Lee, K. H.; Mun, H. A.; Kim, H. S.; Hwang, S. W.; Roh, J. W.; Yang, D. J.; Shin, W. H.; Li, X. S.; Lee, Y. H.; et al. Dense dislocation arrays embedded in grain boundaries for high-performance bulk thermoelectrics. *Science* **2015**, *348*, 109–114. Mehta, R. J.; Zhang, Y.; Karthik, C.; Singh, B.; Siegel, R. W.; Borca-Tasciuc, T.; Ramanath, G. A new class of doped nanobulk high-figure-of-merit thermoelectrics by scalable bottom-up assembly. *Nat. Mater.* **2012**, *11*, 233–240.

(7) Pan, Y.; Aydemir, U.; Grovogui, J. A.; Witting, I. T.; Hanus, R.; Xu, Y.; Wu, J.; Wu, C.-F.; Sun, F.-H.; Zhuang, H.-L.; et al. Melt-Centrifuged (Bi,Sb)2Te3: Engineering Microstructure toward High Thermoelectric Efficiency. *Adv. Mater.* **2018**, *30*, No. 1802016.
(8) Liu, W.; Lukas, K. C.; McEnaney, K.; Lee, S.; Zhang, Q.; Opeil, C. P.; Chen, G.; Ren, Z. Studies on the Bi2Te3-Bi2Se3-Bi2S3 system for mid-temperature thermoelectric energy conversion. *Energy Environ. Sci.* **2013**, *6*, 552−560. Wu, Y.; Zhai, R.; Zhu, T.; Zhao, X. Enhancing room temperature thermoelectric performance of n-type polycrystalline bismuth-telluride-based alloys via Ag doping and hot deformation. *Mater. Today Phys.* **2017**, *2*, 62−68. Meroz, O.; Gelbstein, Y. Thermoelectric Bi2Te3−xSex alloys for efficient thermal to electrical energy conversion. *Phys. Chem. Chem. Phys.* **2018**, *20*, 4092−4099.
(9) Pei, Y.; LaLonde, A. D.; Heinz, N. A.; Shi, X.; Iwanaga, S.; Wang, H.; Chen, L.; Snyder, G. J. Stabilizing the Optimal Carrier Concentration for High Thermoelectric Efficiency. *Adv. Mater.* **2011**, *23*, 5674−5678. Lee, Y.; Lo, S.-H.; Androulakis, J.; Wu, C.-I.; Zhao, L.-D.; Chung, D.-Y.; Hogan, T. P.; Dravid, V. P.; Kanatzidis, M. G. High-Performance Tellurium-Free Thermoelectrics: All-Scale Hierarchical Structuring of p-Type PbSe−MSe Systems (M = Ca, Sr, Ba). *J. Am. Chem. Soc.* **2013**, *135*, 5152−5160. (acccessed 2013/06/19) Ahn, K.; Biswas, K.; He, J.; Chung, I.; Dravid, V.; Kanatzidis, M. G. Enhanced thermoelectric properties of p-type nanostructured PbTe-MTe (M = Cd, Hg) materials. *Energy Environ. Sci.* **2013**, *6*, 1529−1537. Tang, Y.; Gibbs, Z. M.; Agapito, L. A.; Li, G.; Kim, H.-S.; Nardelli, M. B.; Curtarolo, S.; Snyder, G. J. Convergence of multi-valley bands as the electronic origin of high thermoelectric performance in CoSb3 skutterudites. *Nat. Mater.* **2015**, *14*, 1223−1228.
(10) Fortulan, R.; Aminorroaya Yamini, S. Recent Progress in Multiphase Thermoelectric Materials. *Materials* **2021**, *14*, No. 6059. Jia, N.; Tan, X. Y.; Xu, J.; Yan, Q.; Kanatzidis, M. G. Achieving Enhanced Thermoelectric Performance in Multiphase Materials. *Acc. Mater. Res.* **2022**, *3*, 237−246.
(11) Qian, X.; Zhou, J.; Chen, G. Phonon-engineered extreme thermal conductivity materials. *Nat. Mater.* **2021**, *20*, 1188−1202. Kim, W. Strategies for engineering phonon transport in thermoelectrics. *J. Mater. Chem. C* **2015**, *3*, 10336−10348. Dado, B.; Gelbstein, Y.; Dariel, M. P. Nucleation of nanosize particles following the spinodal decomposition in the pseudo-ternary Ge0.6Sn0.1Pb0.3Te compound. *Scr. Mater.* **2010**, *62*, 89−92.
(12) Lan, Y.; Minnich, A. J.; Chen, G.; Ren, Z. Enhancement of Thermoelectric Figure-of-Merit by a Bulk Nanostructuring Approach. *Adv. Funct. Mater.* **2010**, *20*, 357−376.
(13) Lin, Y.; Wood, M.; Imasato, K.; Kuo, J. J.; Lam, D.; Mortazavi, A. N.; Slade, T. J.; Hodge, S. A.; Xi, K.; Kanatzidis, M. G.; et al. Expression of interfacial Seebeck coefficient through grain boundary engineering with multi-layer graphene nanoplatelets. *Energy Environ. Sci.* **2020**, *13*, 4114−4121. Madavali, B.; Kim, H.-S.; Lee, K.-H.; Hong, S.-J. Enhanced Seebeck coefficient by energy filtering in Bi-Sb-Te based composites with dispersed Y2O3 nanoparticles. *Intermetallics* **2017**, *82*, 68−75.
(14) Yu, B.; Zebarjadi, M.; Wang, H.; Lukas, K.; Wang, H.; Wang, D.; Opeil, C.; Dresselhaus, M.; Chen, G.; Ren, Z. Enhancement of Thermoelectric Properties by Modulation-Doping in Silicon Germanium Alloy Nanocomposites. *Nano Lett.* **2012**, *12*, 2077−2082. (acccessed 2014/02/13) Pei, Y.-L.; Wu, H.; Wu, D.; Zheng, F.; He, J. High Thermoelectric Performance Realized in a BiCuSeO System by Improving Carrier Mobility through 3D Modulation Doping. *J. Am. Chem. Soc.* **2014**, *136*, 13902−13908.
(15) Aminorroaya Yamini, S.; Mitchell, D. R. G.; Gibbs, Z.; Santos, R.; Patterson, V.; Li, S.; Pei, Y. Z.; Dou, S. X.; Snyder, G. J. Heterogeneous distribution of sodium for high thermoelectric performance of p-type multiphase lead-chalcogenides. *Adv. Energy Mater.* **2015**, *5*, No. 1501047.
(16) Li, C.; Ma, S.; Wei, P.; Zhu, W.; Nie, X.; Sang, X.; Sun, Z.; Zhang, Q.; Zhao, W. Magnetism-induced huge enhancement of the room-temperature thermoelectric and cooling performance of p-type BiSbTe alloys. *Energy Environ. Sci.* **2020**, *13*, 535−544. Matsuura, H.; Ogata, M.; Mori, T.; Bauer, E. Theory of huge thermoelectric effect based on a magnon drag mechanism: Application to thin-film Heusler alloy. *Phys. Rev. B: Condens. Matter Mater. Phys.* **2021**, *104*, No. 214421.
(17) Byrnes, J.; Mitchell, D. R. G.; Aminorroaya Yamini, S. Thermoelectric performance of thermally aged nanostructured bulk materials—a case study of lead chalcogenides. *Mater. Today Phys.* **2020**, *13*, No. 100190.
(18) Bahk, J.-H.; Bian, Z.; Shakouri, A. Electron energy filtering by a nonplanar potential to enhance the thermoelectric power factor in bulk materials. *Phys. Rev. B: Condens. Matter Mater. Phys.* **2013**, *87*, No. 075204.
(19) Zebarjadi, M.; Joshi, G.; Zhu, G.; Yu, B.; Minnich, A.; Lan, Y.; Wang, X.; Dresselhaus, M.; Ren, Z.; Chen, G. Power Factor Enhancement by Modulation Doping in Bulk Nanocomposites. *Nano Lett.* **2011**, *11*, 2225−2230. (acccessed 2011/12/06) Wu, D.; Pei, Y.; Wang, Z.; Wu, H.; Huang, L.; Zhao, L.-D.; He, J. Significantly Enhanced Thermoelectric Performance in n-type Heterogeneous BiAgSeS Composites. *Adv. Funct. Mater.* **2014**, *24*, 7763−7771. Yamini, A.; Li, T.; Mitchell, D. R. G.; Cairney, J. M. Elemental distributions within multiphase quaternary Pb chalcogenide thermoelectric materials determined through three-dimensional atom probe tomography. *Nano Energy* **2016**, *26*, 157−163.
(20) Wu, D.; Zhao, L.-D.; Zheng, F.; Jin, L.; Kanatzidis, M. G.; He, J. Understanding Nanostructuring Processes in Thermoelectrics and Their Effects on Lattice Thermal Conductivity. *Adv. Mater.* **2016**, *28*, 2737−2743. Wu, D.; Zhao, L.-D.; Tong, X.; Li, W.; Wu, L.; Tan, Q.; Pei, Y.; Huang, L.; Li, J.-F.; Zhu, Y.; et al. Superior Thermoelectric Performance in PbTe-PbS Pseudo-binary: Extremely Low Thermal Conductivity and Modulated Carrier. *Energy Environ. Sci.* **2015**, *8*, 2056−2068.
(21) Wang, L.-L.; Johnson, D. D. Ternary tetradymite compounds as topological insulators. *Phys. Rev. B: Condens. Matter Mater. Phys.* **2011**, *83*, No. 241309.
(22) Begum, A.; Hussain, A.; Rahman, A. Optical and Electrical Properties of Doped and Undoped Bi 2 S 3 -PVA Films Prepared by Chemical Drop Method. *Mater. Sci. Appl.* **2011**, *02*, 163−168.
(23) Michiardi, M.; Aguilera, I.; Bianchi, M.; de Carvalho, V. E.; Ladeira, L. O.; Teixeira, N. G.; Soares, E. A.; Friedrich, C.; Blügel, S.; Hofmann, P. Bulk band structure of Bi_2Te_3. *Phys. Rev. B: Condens. Matter Mater. Phys.* **2014**, *90*, No. 075105.
(24) Byrnes, J. B.; Gazder, A. A.; Yamini, S. A. Assessing phase discrimination via the segmentation of a n elemental energy dispersive X-ray spectroscopy map: a case study of Bi2Te3 and Bi2Te2S. *RSC Adv.* **2018**, *8*, 7457−7464.
(25) Cook, N. J.; Ciobanu, C. L.; Wagner, T.; Stanley, C. J. Minerals of the system Bi−Te−Se−S related to the tetradymite archetype: review of classification and compositional variation. *Can. Mineral.* **2007**, *45*, 665−708.
(26) Cava, R. J.; Ji, H.; Fuccillo, M. K.; Gibson, Q. D.; Hor, Y. S. Crystal structure and chemistry of topological insulators. *J. Mater. Chem. C* **2013**, *1*, 3176−3189.
(27) Harker, D. The Crystal Structure of the Mineral Tetradymite, Bi2Te2S. *Z. Kristallogr. - Cryst. Mater.* **1934**, *89*, 175−181.
(28) Pauling, L. The formula, structure, and chemical bonding of tetradymite, Bi14Te13S8, and the phase Bi14Te15S6. *Am. Mineral.* **1975**, *60*, 994−997. (acccessed 2/24/2022).
(29) Peng, J.; Witting, I.; Geisendorfer, N.; Wang, M.; Chang, M.; Jakus, A.; Kenel, C.; Yan, X.; Shah, R.; Snyder, G. J.; Grayson, M. 3D extruded composite thermoelectric threads for flexible energy harvesting. *Nat. Commun.* **2019**, *10*, 5590. Bao, D.; Chen, J.; Yu, Y.; Liu, W.; Huang, L.; Han, G.; Tang, J.; Zhou, D.; Yang, L.; Chen, Z.-G. Texture-dependent thermoelectric properties of nano-structured Bi2Te3. *Chem. Eng. J.* **2020**, *388*, No. 124295.
(30) Gibbs, Z. M.; Kim, H.-S.; Wang, H.; Snyder, G. J. Band gap estimation from temperature dependent Seebeck measurement—Deviations from the 2e|S|maxTmax relation. *Appl. Phys. Lett.* **2015**, *106*, No. 022112.

https://doi.org/10.1021/acsami.3c01956
ACS Appl. Mater. Interfaces 2023, 15, 19220−19229

(31) Lee, K. H.; Kim, S. I.; Mun, H.; Ryu, B.; Choi, S.-M.; Park, H. J.; Hwang, S.; Kim, S. W. Enhanced thermoelectric performance of n-type Cu0.008Bi2Te2.7Se0.3 by band engineering. *J. Mater. Chem. C* **2015**, *3*, 10604−10609. Rowe, D. M. *CRC Handbook of Thermoelectrics*; CRC Press LLC, 1995.
(32) Lebègue, S.; Björkman, T.; Klintenberg, M.; Nieminen, R. M.; Eriksson, O. Two-Dimensional Materials from Data Filtering and Ab Initio Calculations. *Phys. Rev. X* **2013**, *3*, No. 031002.
(33) Sumithra, S.; Takas, N. J.; Misra, D. K.; Nolting, W. M.; Poudeu, P. F. P.; Stokes, K. L. Enhancement in Thermoelectric Figure of Merit in Nanostructured Bi2Te3 with Semimetal Nanoinclusions. *Adv. Energy Mater.* **2011**, *1*, 1141−1147.
(34) Andrew, F.; May; Snyder, G. J. Introduction to Modeling Thermoelectric Transport at High Temperatures. In *Materials, Preparation and Characterisation in Thermoelectrics*; Rowe, D. M., Ed.; 2012; p 18. May, A. F.; Snyder, G. J. Introduction to Modeling Thermoelectric Transport at High Temperatures. In *Materials, Preparation and Characterisation in Thermoelectrics*; Rowe, D. M., Ed.; CRC Press: Boca Raton, FL, USA, 2012; p 18.
(35) Hori, T.; Shiomi, J. Tuning phonon transport spectrum for better thermoelectric materials. *Science and Technology of Advanced Materials* **2019**, *20*, 10−25. He, J.; Girard, S. N.; Kanatzidis, M. G.; Dravid, V. P. Microstructure-Lattice Thermal Conductivity Correlation in Nanostructured PbTe0.7S0.3 Thermoelectric Materials. *Adv. Funct. Mater.* **2010**, *20*, 764−772.
(36) Solomon, G.; Song, E.; Gayner, C.; Martinez, J. A.; Amouyal, Y. Effects of Microstructure and Neodymium Doping on Bi2Te3 Nanostructures: Implications for Thermoelectric Performance. *ACS Appl. Nano Mater.* **2021**, *4*, 4419−4431.

https://doi.org/10.1021/acsami.3c01956
ACS Appl. Mater. Interfaces 2023, 15, 19220−19229

ACS APPLIED ENERGY MATERIALS

www.acsaem.org Article

Thermoelectric Performance of n-Type Magnetic Element Doped Bi_2S_3

Raphael Fortulan, Sima Aminorroaya Yamini,* Chibuzor Nwanebu, Suwei Li, Takahiro Baba, Michael John Reece, and Takao Mori

Cite This: *ACS Appl. Energy Mater.* 2022, 5, 3845−3853 Read Online

ACCESS | Metrics & More | Article Recommendations | Supporting Information

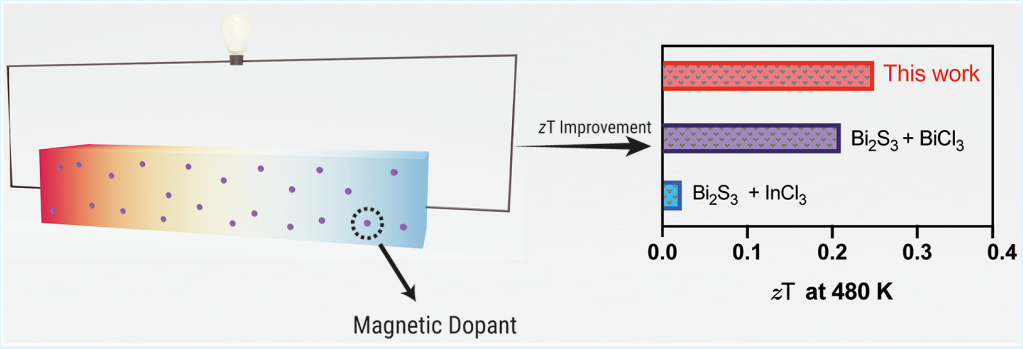

ABSTRACT: Thermoelectric technology offers great potential for converting waste heat into electrical energy and is an emission-free technique for solid-state cooling. Conventional high-performance thermoelectric materials such as Bi_2Te_3 and PbTe use rare or toxic elements. Sulfur is an inexpensive and nontoxic alternative to tellurium. However, achieving high efficiencies with Bi_2S_3 is challenging due to its high electrical resistivity that reduces its power factor. Here, we report Bi_2S_3 codoped with Cr and Cl to enhance its thermoelectric properties. An enhanced conductivity was achieved due to an increase in the carrier concentration by the substitution of S with Cl. High values of the Seebeck coefficients were obtained despite high carrier concentrations; this is attributed to an increase in the effective mass, resulting from the magnetic drag introduced by the magnetic Cr dopant. A peak power factor of 566 μW m^{-1} K^{-2} was obtained for a cast sample of $Bi_{2-x/3}Cr_{x/3}S_{3-x}Cl_x$ with x = 0.01 at 320 K, as high as the highest values reported in the literature for sintered samples. These results support the success of codoping thermoelectric materials with isovalent magnetic and carrier concentration tuning elements to enhance the thermoelectric properties of eco-friendly materials.

KEYWORDS: *thermoelectric, power factor, magnetic element, bismuth sulfide, chromium*

Downloaded via SHEFFIELD HALLAM UNIV on September 15, 2023 at 10:46:57 (UTC).
See https://pubs.acs.org/sharingguidelines for options on how to legitimately share published articles.

INTRODUCTION

Solid-state-based thermoelectric (TE) materials can directly and reversibly convert heat into electricity. The efficiency of thermoelectric materials is given by the figure of merit, $zT = (S^2T)/\rho\kappa_{total}$, where S is the Seebeck coefficient, T is the absolute temperature, ρ is the electrical resistivity, and κ_{total} is the thermal conductivity.

To increase zT, one needs to increase the power factor (S^2/ρ) and/or decrease κ_{total}. One of the most successful approaches to improve the figure of merit is reducing the lattice thermal conductivity, and over the years, various phonon engineering approaches have been used to enhance phonon scattering and decrease κ_L by taking advantage of nanoprecipitates,[1,2] alloying elements,[3,4] nanostructured grain boundaries,[5,6] and ionized impurities.[7,8]

A series of band structure engineering approaches have also been employed to improve the power factor of TE materials.[9−11] Strategies such as quantum confinement,[12] modulation doping,[13−15] and energy filtering[16,17] are being actively pursued.

Magnetic interactions have been proposed as a strategy to enhance the Seebeck coefficient in thermoelectric materials such as Bi_2Te_3.[18−23] Charge carriers interact with the local magnetic moments, effectively dragging the carriers, which results in an increased charge carrier effective mass, an increased Seebeck coefficient, and a decreased carrier mobility (μ). Overall, this has resulted in an increased power factor.[18−24]

Received: January 27, 2022
Accepted: February 22, 2022
Published: March 1, 2022

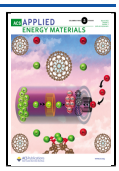

© 2022 American Chemical Society

https://doi.org/10.1021/acsaem.2c00295
ACS Appl. Energy Mater. 2022, 5, 3845−3853

Tellurium-based thermoelectric materials such as Bi_2Te_3 have been employed as power generators/refrigerators in lower-temperature applications (<500 K). However, tellurium is expensive and rare and can hinder the movement toward the mass adoption of TE generators. Sulfur, another element from group IV, is an inexpensive, nontoxic, and sustainable alternative. Bismuth sulfide (Bi_2S_3), in particular, has low thermal conductivity and a large Seebeck coefficient.[25,26] However, its high resistivity results in a low zT.[27] Several dopants have been used to optimize the electronic transport properties of Bi_2S_3, including $CuBr_2$,[28] Sb,[29] Cu,[30] Ag,[31] I,[32] Cl,[33] Se,[33,34] $InCl_3$,[35] $BiCl_3$,[36] and $NbCl_5$.[37] A lower thermal conductivity was also obtained in Bi_2S_3 by nanostructuring.[30,38−40]

The thermoelectric efficiency of pristine Bi_2S_3 was also increased to 0.11 from 0.09 at 623 K by texturing through hot forging and introducing sulfur vacancies.[41] $PbBr_2$ doping of bulk Bi_2S_3 has significantly improved its electrical conductivity by modulation doping and reduced the lattice thermal conductivity by introducing nanoprecipitates, resulting in a peak zT value of 0.8 at 673 K.[42]

It has been widely shown that the charge density is increased when halogen group elements (Cl, Br, and I) are doped at the sulfur sites.[28,32,33] Here, we doped bismuth sulfide with chromium chloride ($CrCl_3$) to obtain samples of $Bi_{2-x/3}Cr_{x/3}S_{3-x}Cl_x$ (x = 0.00, 0.005, 0.01, 0.015, 0.02). Doping with chlorine increases the number of free carriers in the material, leading to a reduction in the electrical resistivity, while the magnetic effect of chromium resulted in an increase in the carrier effective mass and, consequently, in the Seebeck coefficient.

EXPERIMENTAL SECTION

Sample Fabrication. Ultrahigh-purity bismuth pieces (99.999%, Sigma-Aldrich), sulfur pieces (99.9995%, Alfa Aesar Puratronic), and chromium chloride powder (99.99%, Sigma-Aldrich) were mixed stoichiometrically to obtain $Bi_{2-x/3}Cr_{x/3}S_{3-x}Cl_x$ (x = 0.00, 0.005, 0.01, 0.015, 0.02) in vacuum-sealed quartz ampules, prepared in an inert-atmosphere glovebox. The tubes were heated in a tube furnace to 1000 °C. After being quenched in cold water, the samples were annealed at 450 °C for 2 days.

The cylindrical ingot samples of 10 mm diameter were then cut into disk shapes of 10 mm diameter and ∼1.5 mm thickness for Hall effect measurements and bars of 2 × 2 × 10 mm^3 for electrical property measurements. The electrical resistivity and Seebeck coefficient were measured simultaneously under 0.1 bar of helium from room temperature to 483 K using an LSR-3 Linseis unit. Hall effect measurements were performed with an Ecopia HMS-3000 Hall Measurement System at room temperature. The density of the samples was determined from the bar-shaped samples using their dimensions and masses. All samples were then manually ground to fine powders by using an agate mortar and pestle. Three samples with x = 0, 0.005, and 0.01 were sintered in a 10 mm diameter graphite die under an axial pressure of 63 MPa at 723 K for 5 min under vacuum; the sample with x = 0.01 broke during sintering. To avoid this, the sintering temperature was reduced to 623 K for the samples with compositions of x = 0.015, 0.02. The measured densities of all samples are presented in Tables S1 and S2 in the Supporting Information.

Material Characterization. To investigate the electrical and thermal transport properties parallel and perpendicular to the sintering direction, the sintered samples were cut and polished into disks (10 mm diameter and ∼1.5 mm thickness, perpendicular to the pressing direction) and cuboids of 8 × 8 × 2 mm^3 parallel to the pressing direction for Hall effect and thermal diffusivity measurements and bars of 2 × 2 × 10 mm^3 (parallel and perpendicular to the pressing direction) for electrical property measurements. The total thermal conductivity (κ_{total}) was calculated from the thermal diffusivity (D), heat capacity (C_p) and density (ρ): $\kappa_{total} = DC_p\rho$. The temperature-dependent thermal diffusivity D was measured on disk-shaped samples by a laser flash diffusivity method using a Netzsch LFA-467 Hyperflash instrument. The temperature-dependent heat capacity was derived using a standard sample (Pyroceram-9060). The directions of measurement and sample shapes are illustrated in Figure 1. X-ray powder diffraction analysis was performed with a PANalytical X'Pert PRO instrument, using Cu Kα1 radiation (λ = 1.54059 Å) to identify the crystal structure of each sample. Rietveld refinement was performed using GSAS-II[43] to obtain the lattice parameters for all samples.

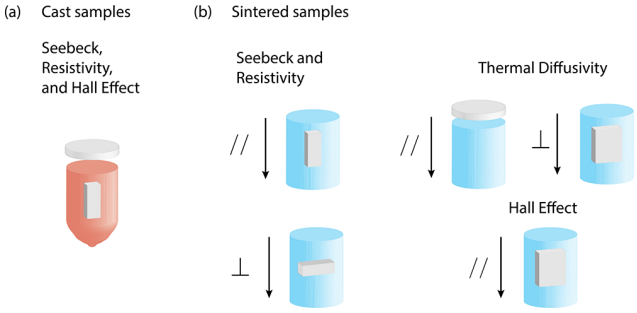

Figure 1. Measuring directions and sample shapes of the (a) cast samples and (b) sintered samples.

Electronic Structure Calculation. Density functional theory (DFT) calculations were employed to qualitatively study the electronic band structure of the doped sample. The Perdew−Burke−Ernzerhof (PBE) and generalized gradient approximation (GGA) exchange-correlation functionals were used[44] with the Quantum Espresso package.[45] A Monkhorst−Pack procedure was used to generate 12 × 12 × 12 k-points for the Brillouin zone.[46] The plane wave/pseudopotential approach was employed, with a kinetic energy cutoff of 45 Ry for the wave functions and 360 Ry for the electron density. Spin polarization was considered for the materials doped with Cr.

RESULTS AND DISCUSSION

Materials Characteristics. Figure 2 shows the XRD patterns of samples $Bi_{2-x/3}Cr_{x/3}S_{3-x}Cl_x$ (x = 0.00, 0.005, 0.01, 0.015, 0.02). All patterns confirm the presence of a single-phase Bi_2S_3, orthorhombic crystal structure with space group $Pnma$. The lattice parameters of all the samples were determined by the Rietveld refinement of the XRD patterns (Table S3 in the Supporting Information). No variation of the

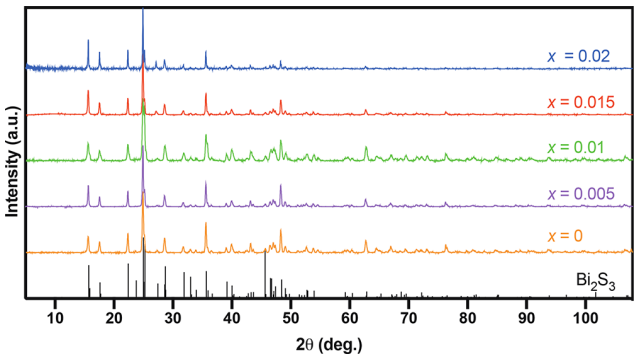

Figure 2. Powder XRD patterns of $Bi_{2-x/3}Cr_{x/3}S_{3-x}Cl_x$ (x = 0.00, 0.005, 0.01, 0.015, 0.02) samples in the range of 5−108°.

https://doi.org/10.1021/acsaem.2c00295
ACS Appl. Energy Mater. 2022, 5, 3845−3853

lattice parameters was detected, due to the comparable ionic radii of S^{2-} (1.84 Å) and Cl^{-} (1.81 Å).[47] Although there is a difference in the ionic radii of Bi^{3+} (1.03 Å) and Cr^{3+} (0.615 Å),[47] the amount of chromium introduced to the Bi_2S_3 is one-third of the chlorine atomic ratio, and therefore no noticeable difference was detected in the lattice parameters.

The lattice parameter values are consistent with the values reported in the literature (a = 11.269 Å, b = 3.972 Å, and c = 11.129 Å).[48]

The intensity of the {111} plane peaks for the x = 0.015 sample was higher than those for the other samples. This might be attributed to the preferred orientation, caused by nonuniform hand milling of the samples used for the XRD analysis.

An XRD analysis was also performed on the sintered samples (Figure S1 in the Supporting Information), and the lattice parameters were calculated by a Rietveld refinement (Table S4 in the Supporting Information). The lattice parameter values of $Bi_{2-x/3}Cr_{x/3}S_{3-x}Cl_x$ (x = 0.00, 0.005, 0.01, 0.015, 0.02) samples versus the dopant concentration (x) of cast and sintered samples are shown in Figure 3.

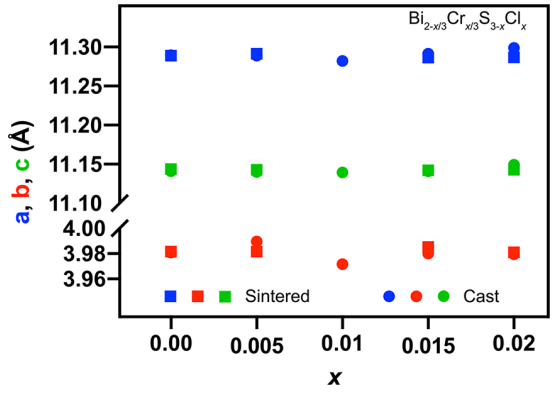

Figure 3. Rietveld refined lattice parameters of $Bi_{2-x/3}Cr_{x/3}S_{3-x}Cl_x$ (x = 0.00, 0.005, 0.01, 0.015, 0.02) samples as a function of the dopant concentration.

To understand the effect of dopants on the electronic band structure of Bi_2S_3, the band structures of Bi_2S_3 and the doped sample $Bi_{23}Cr_1S_{33}Cl_3$, for spin-up and -down states, were calculated (Figure 4a–c, respectively). The calculated band gap of the pristine material is ~1.25 eV, which is in good agreement with the reported experimental values of ~1.3 eV.[35,49,50] Both spin-up and spin-down states showed reduced values of ~0.6 and ~0.92 eV, respectively. The reduction in the band gap for the spin-up state was due to the presence of an additional impurity band. It is worth noting that the numerical results, presented in this calculation, should only be discussed qualitatively due to the rather high concentration of the dopant. The effective masses of electrons were calculated for both heavy and light bands in the spin-up (D point) and spin-down (Γ point) states of the electronic band structures, using the parabolic band approximation for the band extrema. The results are shown in Figure S2 in the Supporting Information. The electrons of both heavy and light bands show similar values of effective mass (m_{heavy}^* ≈ 0.48 and m_{light}^* ≈ 0.41 for the spin-up state and m_{heavy}^* ≈ 0.35 and m_{light}^* ≈ 0.21 for the spin-down state), indicating that the electronic band degeneracy plays an insignificant role in the transport properties of the material.

Electronic Transport Properties. The Seebeck coefficient, the electrical resistivity, and the carrier concentration of the cast samples of $Bi_{2-x/3}Cr_{x/3}S_{3-x}Cl_x$ (x = 0.00, 0.005, 0.01, 0.015, 0.02) and sintered samples of $Bi_{2-x/3}Cr_{x/3}S_{3-x}Cl_x$ (x = 0.00, 0.005, 0.015, 0.02) measured parallel to the direction of sintering are presented in Figure 5. The negative Seebeck coefficient indicates an n-type semiconductor behavior (Figure 5a,b). The Seebeck coefficient for the cast pristine Bi_2S_3 sample ranges from −96 μV K^{-1} at ~320 K to −135 μV K^{-1} at ~480 K. These values are considerably smaller than the reported values of −380 to 498 μV K^{-1} for Bi_2S_3 in the literature.[26,38] Following Mott's formula for the Seebeck coefficient,[51] $S = \frac{\pi^2 k_B^2 T}{3q}\left\{\frac{dn(E)}{dE}\frac{1}{n} + \frac{d\mu(E)}{dE}\frac{1}{\mu}\right\}_{E=E_F}$, the sharp decrease in the Seebeck coefficient can be explained by an increase in the charge carrier density in the material. This is supported by the electrical resistivity values for these samples, which varied from 3.16 mΩ cm at ~320 K to −4.82 mΩ cm at ~480 K (Figure 5c). These values, including for x = 0, are significantly smaller than the reported values of ~2400[41] and ~7460 mΩ cm[52] for the pristine sample of Bi_2S_3. These results can be explained by the volatile nature of sulfur during the sample fabrication. A single sulfur atom vacancy donates two free electrons to the bulk material. Atom vacancies in bismuth sulfide have been previously reported,[37,38] and they commonly occur in chalcogenides.[53,54] This is supported by the high charge carrier concentrations measured for both cast and sintered samples (Figure 5e,f). This also greatly reduces the

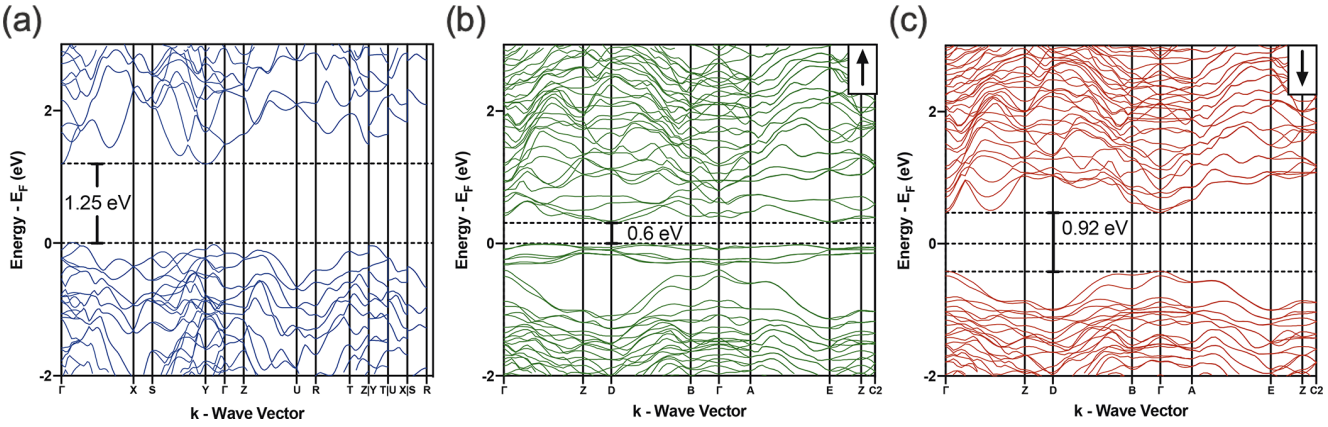

Figure 4. Electronic band structure of (a) Bi_2S_3, (b) $Bi_{23}Cr_1S_{33}Cl_3$ spin-up (↑) state, and (c) $Bi_{23}Cr_1S_{33}Cl_3$ spin-down (↓) state.

https://doi.org/10.1021/acsaem.2c00295
ACS Appl. Energy Mater. 2022, 5, 3845−3853

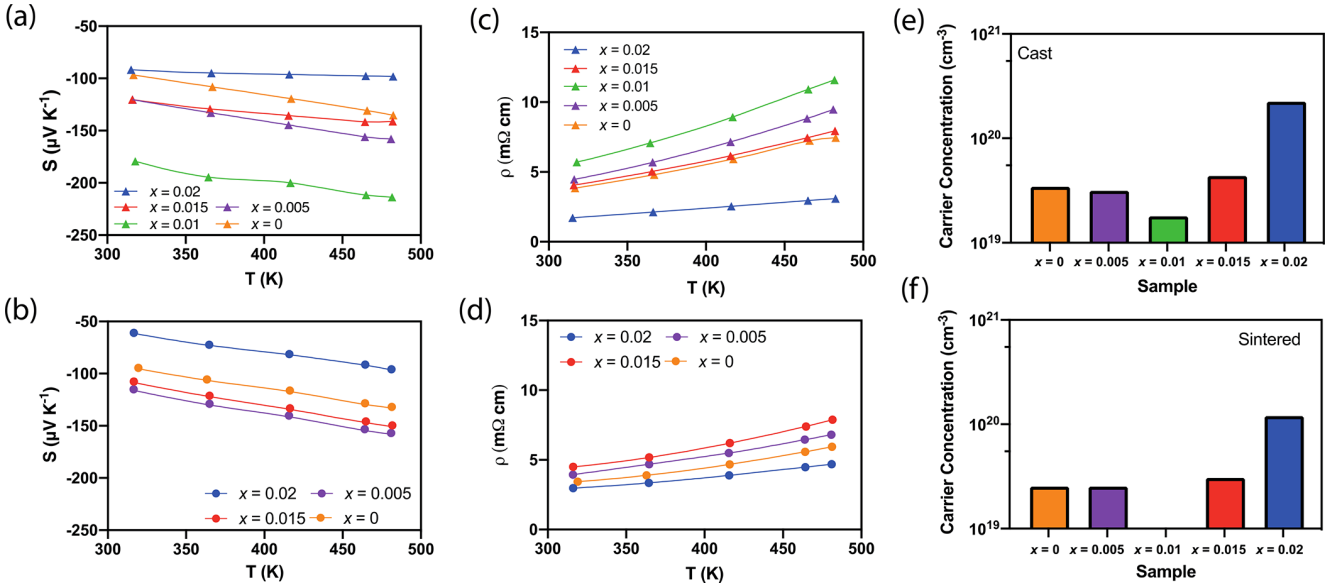

Figure 5. (a, b) Seebeck coefficients, (c, d) electrical resistivities, and (e, f) Hall carrier concentrations of cast $Bi_{2-x/3}Cr_{x/3}S_{3-x}Cl_x$ (x = 0.00, 0.005, 0.01, 0.015, 0.02) and sintered $Bi_{2-x/3}Cr_{x/3}S_{3-x}Cl_x$ (x = 0.00, 0.005, 0.015, 0.02), parallel to the direction of sintering as a function of temperature, respectively.

resistivity for the heavily doped samples, reaching 4.82 mΩ cm at ∼480 K for x = 0.02 in comparison to 7.46 mΩ cm for the pristine sample at room temperature. No significant difference was observed in the Seebeck coefficient values of sintered samples for both measurement directions. However, the electrical resistivity of the samples parallel to the direction of sintering is slightly lower than those perpendicular to the sintering direction (Figure S3 in the Supporting Information). The Seebeck coefficient values of sintered samples are very similar to the values obtained from ingots (Figure 5a,b), except for the Seebeck coefficient of the sample with x = 0.02, for which the Seebeck coefficient decreased from ∼−100 to ∼−60 μV K^{-1}. Overall, the electrical resistivities of the sintered samples are lower than those of their cast counterparts. This is attributed to the improved mechanical integrity of sintered samples relative to the cast samples. The sintered samples with x = 0.015, 0.02 showed a smaller reduction in resistivity in comparoson to those with x = 0, 0.005, due to the changes in the sintering conditions, which caused the former samples to be less dense than the latter (the sintering temperature was reduced from 723 to 623 K for the samples with x = 0.015, 0.02). The reproducibility of the results was verified by repeating the experiments several times (shown in Figure S5 in the Supporting Information).

The power factors (PFs; S^2/ρ) of the cast and sintered samples were measured parallel to the direction of sintering (Figure 6). The PF values of the doped samples are much higher than those of the pristine samples due to the optimization of the electrical conductivity and Seebeck coefficient. The cast Bi_2S_3 sample with moderate doping (x = 0.01) exhibited the highest PF value (∼566 μW m^{-1} K^{-2} at 320 K), which was about 2.3 times higher than that of the undoped Bi_2S_3 sample (about 243 μW m^{-1} K^{-2} at 320 K). However, the sintered sample with x = 0.01 was unavailable for measurement. The highest power factor for the sintered sample (x = 0.005, measured along the parallel direction to the sintering pressure) was ∼367 μW m^{-1} K^{-2} at 480 K (Figure 6b).

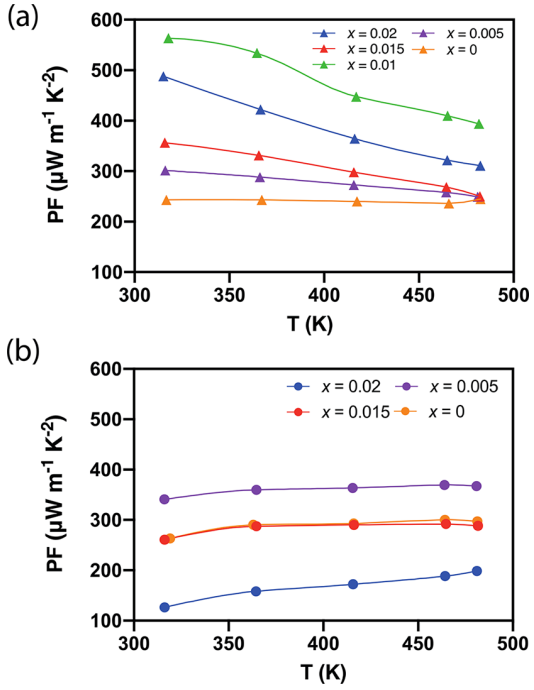

Figure 6. Power factors of (a) cast $Bi_{2-x/3}Cr_{x/3}S_{3-x}Cl_x$ (x = 0.00, 0.005, 0.01, 0.015, 0.02) and of (b) sintered $Bi_{2-x/3}Cr_{x/3}S_{3-x}Cl_x$ (x = 0.00, 0.005, 0.015, 0.02) along the parallel direction of the sintering pressure as a function of temperature.

The PFs obtained in this work are compared with the data reported in the literature (Figure 7). Our results are comparable with the highest values reported in the literature at the same temperature.

Since the samples in the current study have been codoped with Cr and Cl, the relation between the measured Seebeck coefficient and carrier concentration from the cast samples are compared with those of previous studies of Bi_2S_3 doped with $BiCl_3$,[36] $InCl_3$,[35] $LaCl_3$,[50] $CuBr_2$,[28] and Cl,[55] to illustrate the

https://doi.org/10.1021/acsaem.2c00295
ACS Appl. Energy Mater. 2022, 5, 3845−3853

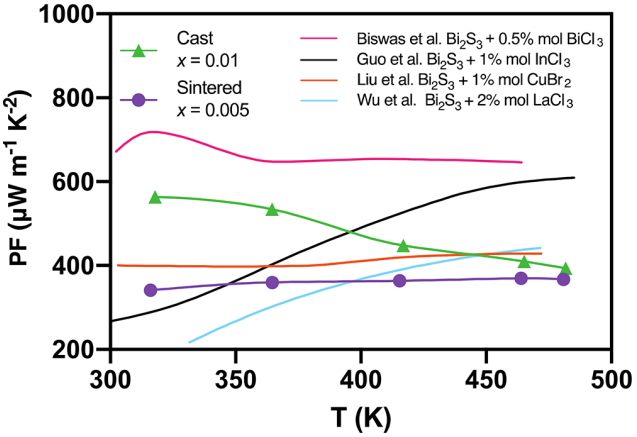

Figure 7. Power factor comparison of n-type Bi_2S_3 doped with 0.5% mol of $BiCl_3$,[36] 2% mol of $InCl_3$,[35] 2% of $LaCl_3$,[50] and 1% of $CuBr_2$[28] with sintered $Bi_{2-x/3}Cr_{x/3}S_{3-x}Cl_x$ (x = 0.005) and cast $Bi_{2-x/3}Cr_{x/3}S_{3-x}Cl_x$ (x = 0.01) as a function of temperature.

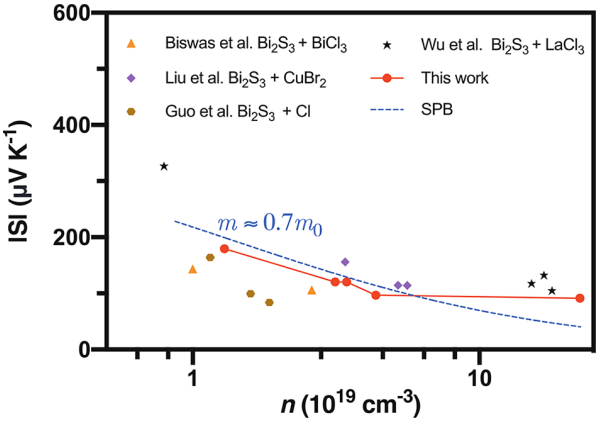

Figure 8. Hall carrier concentration dependence on the room-temperature Seebeck coefficient of n-type cast $Bi_{2-x/3}Cr_{x/3}S_{3-x}Cl_x$ compared to those reported in the literature of Bi_2S_3 doped with $BiCl_3$,[13] $LaCl_3$,[35] $CuBr_2$,[5] and Cl.[40]

effect of doping with chromium[56] (Figure 7). The effective mass was evaluated using the single parabolic band (SPB) model with acoustic phonon scattering.[57] The model uses a Fermi integral of[58,59]

$$F_j(\eta) = \int_0^\infty \frac{\varepsilon^j}{1 + e^{\varepsilon-\eta}}\,\mathrm{d}\varepsilon \tag{1}$$

where $\eta = E_F/(k_BT)$ is the reduced Fermi level and ε is the reduced energy of the electron state. The Seebeck coefficient and the carrier concentration are given by

$$S = \frac{k_B}{q}\left[\frac{2F_1(\eta)}{F_0(\eta)} - \eta\right] \tag{2}$$

$$n = \frac{(2m^*k_BT)^{3/2}}{3\pi^2\hbar^3}F_{1/2}(\eta) \tag{3}$$

where m^* is the effective mass.

For degenerate semiconductors, according to the Pisarenko relation,[60] the Seebeck coefficient is inversely proportional to the carrier concentration, n, with a dependence of $n^{-2/3}$. The experimental data of this study deviates from this ideal relationship, which indicates the changes in the electronic band structure of the material.[61] In particular, the Seebeck coefficient values of the current study are higher than values predicted by the SPB model and experimental data of samples doped only with Cl[35,36] (as seen in Figure 8). An increase in the Seebeck at a particular carrier concentration was observed in samples doped with La[35] (due to the presence of La nanoprecipitates) and $CuBr_2$ (due to the energy filtering effect[62]). It is worth noting that although Cu is not a magnetic element, it interacts with magnets.

The higher values of the Seebeck coefficient obtained in the current study might be attributed to a magnetic drag effect generated by the magnetic chromium dopant.[18−23] It has been shown, for example, in the case of magnetic materials that an additional contribution to the Seebeck coefficient is observed when the materials are subjected to a temperature gradient, due to the flux of magnons.[63,64] The interaction between magnons and carriers results in an overall increase in the effective mass and, consequently, in the Seebeck coefficient.[65] Similar Seebeck enhancement effects have been observed for nonmagnetic materials doped with magnetic elements, similarly to the present case.[18,19,21,24] In the present study, the effective mass of the cast samples increased significantly from $0.7m_0$ for the pristine sample to $2.1m_0$ for the sample with x = 0.02 (Table 1), where m_0 is the electron rest mass. This

Table 1. Carrier Concentration, Mobility, and Calculated Effective Mass of Cast $Bi_{2-x/3}Cr_{x/3}S_{3-x}Cl_x$

sample ($Bi_{2-x/3}Cr_{x/3}S_{3-x}Cl_x$)	n (10^{19} cm^{-3})	μ (cm^2 V^{-1} s^{-1})	m^*/m_0
x = 0	3.44	15.1	0.76
x = 0.005	3.14	28.2	0.79
x = 0.01	1.79	24.5	0.83
x = 0.015	4.35	16.7	0.75
x = 0.02	22.4	7.59	2.10

enhanced mass contributed to the higher Seebeck coefficient in comparison with materials doped only with Cl,[36,55] and it supports the hypothesis of carrier interactions with magnetic elements. The carrier mobilities also decreased with an increase in the concentration of chromium (Table 1). The reduction of charge carrier mobility is responsible for a decrease in the electrical conductivity.[66,67] However, the overall effect was an increase in the power factor for the lightly doped sample, given the enhanced Seebeck coefficient due to the increased effective mass.

For the sintered samples, the measured carrier concentrations were 2.54 × 10^{19}, 2.56 × 10^{19}, 3.08 × 10^{19}, and 1.2 × 10^{20} cm^{-3} and the mobilities were 60.4, 47.8, 40, and 53.3 cm^2 V^{-1} s^{-1} for sintered $Bi_{2-x/3}Cr_{x/3}S_{3-x}Cl_x$ (x = 0.00, 0.005, 0.015, 0.02), respectively.

The temperature dependences of κ_{total}, κ_e and κ_L for sintered $Bi_{2-x/3}Cr_{x/3}S_{3-x}Cl_x$ (x = 0.00, 0.005, 0.015, 0.02) samples measured parallel to the direction of sintering are presented in Figure 9. The total thermal conductivity is the sum of the electronic and lattice thermal conductivity $\kappa_L = \kappa_{total} - \kappa_e$.

The electronic thermal conductivity, κ_e, was obtained using the Wiedemann−Franz law, which is expressed as $\kappa_e = L\sigma T$. The Lorenz number (L) values as a function of temperature were estimated from the SPB model (Figure S4 in the Supporting Information):[57]

https://doi.org/10.1021/acsaem.2c00295
ACS Appl. Energy Mater. 2022, 5, 3845−3853

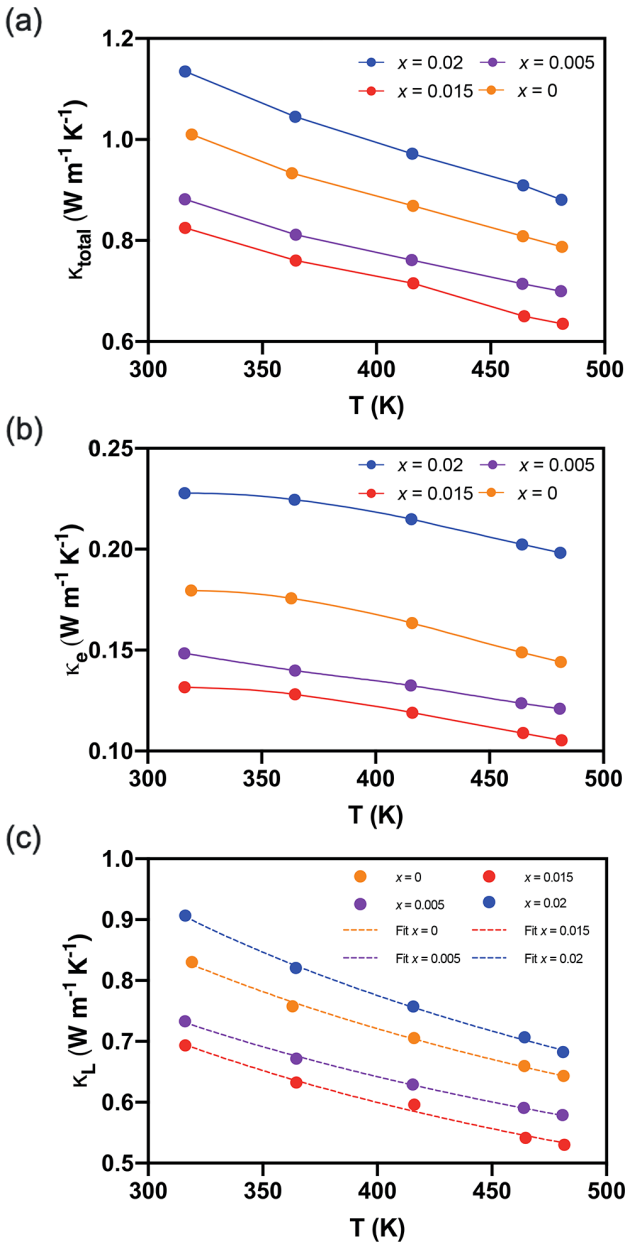

Figure 9. (a) Total thermal conductivity, (b) electronic thermal conductivity; (c) and lattice thermal conductivity (the dashed lines are the calculations based on the Debye−Callaway model) of sintered $Bi_{2-x/3}Cr_{x/3}S_{3-x}Cl_x$ (x = 0.00, 0.005, 0.015, 0.02) parallel to the direction of sintering as a function of temperature.

$$L = \left(\frac{k_B}{q}\right)^2 \left[\frac{3F_0(\eta)F_2(\eta) - 4F_1^2(\eta)}{F_0^2(\eta)}\right] \quad (4)$$

The values of the electronic thermal conductivity (Figure 9b) are larger for the doped samples. given their higher carrier concentrations (Figure 5f). The values of the lattice thermal conductivity for all samples are very close to the values of κ_{total} (Figure 8a,c), due to a small contribution of electronic thermal conductivity to the total thermal conductivity of Bi_2S_3.

The κ_{total} values of all the samples ranged from ∼0.8 to ∼1.1 W m^{-1} K^{-1} at 320 K and ranged from ∼0.6 to ∼0.8 W m^{-1} K^{-1} at 480 K (Figure 9a). The samples that were sintered at the lower temperature of 673 K (x = 0.015, 0.02) have greater thermal conductivity. Nevertheless, all samples have similar values of lattice thermal conductivity (Figure 9c). The reproducibility of the thermal diffusivity results was verified by repeating the experiment several times; the results are shown in the Figure S6 in the Supporting Information.

To further study this and the effect of the dopant on the scattering mechanism of phonons in these samples, the Debye−Callaway model was adopted to evaluate the thermal conductivity[68,69]

$$k_L = \frac{k_B}{2\pi^2 v_s}\left(\frac{k_B T}{\hbar}\right)^3 \int_0^{\theta_D/T} \frac{x^4 e^x}{\tau_C^{-1}(e^x - 1)^2}\,dx \quad (5)$$

where $x = \hbar\omega/k_B T$ is the reduced frequency, ω the phonon angular frequency, k_B the Boltzmann constant, v_s the speed of sound, $\hbar$ the reduced Planck constant, θ_D the Debye temperature, and τ_C the combined phonon relaxation time. The values of θ_D = 283 K and v_s = 2775 m s^{-1} were adopted from the literature.[70]

Four mechanisms of phonon scattering were considered: point impurities, a normal three-phonon process, an Umklapp process, and boundary scattering.[71] Matthiessen's rule[72] is employed to find the combined phonon relaxation time

$$\tau_C^{-1} = \tau_I^{-1} + \tau_N^{-1} + \tau_U^{-1} + \tau_B^{-1} = A\omega^4 + \beta\tau_U^{-1} + B_U T\omega^2 e^{-\theta_D/3T} + \frac{v_s}{L} \quad (6)$$

where τ_I, τ_N, τ_U, and τ_B are respectively the relaxation times for points impurity scattering, a normal three-phonon process, an Umklapp process, and boundary scattering, L is the average grain size, and the coefficients A, β, and B_U are fitting parameters. Table 2 presents the calculated parameters for all

Table 2. Calculated Parameters for the Debye−Callaway Model for Sintered $Bi_{2-x/3}Cr_{x/3}S_{3-x}Cl_x$ (x = 0.00, 0.005, 0.015, 0.02) Samples Parallel to the Direction of Sintering

x	A (10^{-41} s^3)	β	B_U (10^{-18} s K)	L (μm)
0	4.9	2.2	3.6	1.3
0.005	7.3	6.3	1.4	1.4
0.015	5.6	6.4	2.0	1.3
0.02	3.5	2.4	3.9	1.5

sintered samples parallel to the direction of sintering. The average grain size was obtained from the Rietveld refinement of XRD patterns obtained from samples. The fitted values are shown by dashed lines in Figure 9c.

The results show a noticeable increase in the scattering by point defects with increasing dopant concentration. In general, the thermal conductivity values of the sintered samples are similar for all samples. The changes in β and B_U indicate that the main mechanism causing these differences was due to changes in the phonon−phonon scattering.

Figure 10 shows the zT values for the sintered samples (measured parallel to the direction of sintering). The maximum zT value of ∼0.25 was achieved for the sample with x = 0.005 at 480 K. It is worth noting that the sample $Bi_{2-x/3}Cr_{x/3}S_{3-x}Cl_x$ (x = 0.01) with the potentially highest zT value was unavailable in the sintered form for measurement. Figure 10b compares the zT values of the samples in the current study samples with the largest values reported in the literature at the same temperature. There is a difference in the zT values obtained from measurements performed parallel and

https://doi.org/10.1021/acsaem.2c00295
ACS Appl. Energy Mater. 2022, 5, 3845−3853

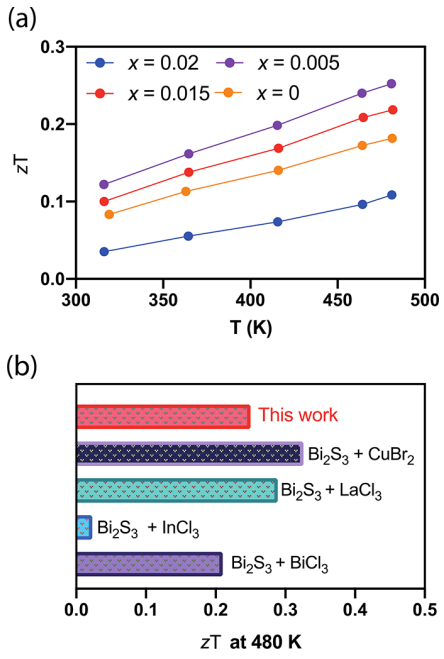

Figure 10. (a) zT values of sintered $Bi_{2-x/3}Cr_{x/3}S_{3-x}Cl_x$ (x = 0.00, 0.005, 0.015, 0.02) parallel to the direction of sintering as a function of temperature. (b) zT values of sintered $Bi_{2-x/3}Cr_{x/3}S_{3-x}Cl_x$ (x = 0.005) at 480 K in comparison to those of $BiCl_3$,[36] 2 mol % of $InCl_3$,[35] 2 mol % of $LaCl_3$,[50] and 1 mol % of $CuBr_2$.[28]

perpendicular to the direction of sintering, due to the crystal structure of Bi_2S_3 (Figure S3 in the Supporting Information).

CONCLUSIONS

Bi_2S_3 was successfully doped with $CrCl_3$ using a melting–annealing technique followed by sintering by the SPS. The electronic properties were measured for both the cast and sintered samples. In comparison to samples with nonmagnetic dopants, the Seebeck coefficient increased at the same carrier concentration, which was most likely due to the magnon drag effect, where the interaction between magnons and carriers effectively increases the effective mass of the carriers and consequently the Seebeck coefficient. The increase in the effective mass led to a decrease in the carrier mobility and the electrical conductivity of the samples with higher carrier concentration. Thermal conductivity measurements of the sintered samples showed similar values for all the samples, with differences arising from the carrier concentration and increased scattering due to impurities. The zT values of this work are comparable to the largest values reported in literature and provided experimental evidence that the presence of magnetic dopants can increase the overall efficiency of thermoelectric materials.

ASSOCIATED CONTENT

Supporting Information

The Supporting Information is available free of charge at https://pubs.acs.org/doi/10.1021/acsaem.2c00295.

Measured density of the samples, powder diffraction patterns and refined lattice parameters of sintered samples, transport properties and figure of merit of samples, perpendicular to the direction of sintering, heat capacity and Lorenz number used in the thermal conductivity calculations, additional measurements for the transport properties, and error analysis for the Seebeck coefficient and resistivity (PDF)

AUTHOR INFORMATION

Corresponding Author

Sima Aminorroaya Yamini − *Materials and Engineering Research Institute, Sheffield Hallam University, Sheffield S1 1WB, U.K.; Department of Engineering and Mathematics, Sheffield Hallam University, Sheffield S1 1WB, U.K.;* orcid.org/0000-0002-2312-8272; Email: S.Aminorroaya@shu.ac.uk

Authors

Raphael Fortulan − *Materials and Engineering Research Institute, Sheffield Hallam University, Sheffield S1 1WB, U.K.*

Chibuzor Nwanebu − *Materials and Engineering Research Institute, Sheffield Hallam University, Sheffield S1 1WB, U.K.*

Suwei Li − *School of Engineering and Material Science, Queen Mary University of London, London E1 4NS, U.K.*

Takahiro Baba − *International Center for Materials Nanoarchitectonics (WPI-MANA), National Institute for Materials Science, Tsukuba 305-0044, Japan; Graduate School of Pure and Applied Science, University of Tsukuba, Tsukuba 305-8577, Japan*

Michael John Reece − *School of Engineering and Material Science, Queen Mary University of London, London E1 4NS, U.K.;* orcid.org/0000-0002-2293-7123

Takao Mori − *International Center for Materials Nanoarchitectonics (WPI-MANA), National Institute for Materials Science, Tsukuba 305-0044, Japan; Graduate School of Pure and Applied Science, University of Tsukuba, Tsukuba 305-8577, Japan;* orcid.org/0000-0003-2682-1846

Complete contact information is available at: https://pubs.acs.org/10.1021/acsaem.2c00295

Author Contributions

The manuscript was written through contributions of all authors. All authors have given approval to the final version of the manuscript.

Notes

The authors declare no competing financial interest.

ACKNOWLEDGMENTS

The project has received funding from the European Union's Horizon 2020 research and innovation programme under the Marie Skłodowska-Curie grant agreement No. 801604. T.M. thanks the JST Mirai Program JPMJMI19A1 for support.

REFERENCES

(1) Delaire, O.; Ma, J.; Marty, K.; May, A. F.; McGuire, M. A.; Du, M. H.; Singh, D. J.; Podlesnyak, A.; Ehlers, G.; Lumsden, M. D.; Sales, B. C. Giant Anharmonic Phonon Scattering in PbTe. *Nat. Mater.* **2011**, *10* (8), 614−619.

(2) Hu, Y.; Zeng, L.; Minnich, A. J.; Dresselhaus, M. S.; Chen, G. Spectral Mapping of Thermal Conductivity through Nanoscale Ballistic Transport. *Nat. Nanotechnol* **2015**, *10* (8), 701−706.

(3) Hu, L.; Zhang, Y.; Wu, H.; Li, J.; Li, Y.; McKenna, M.; He, J.; Liu, F.; Pennycook, S. J.; Zeng, X. Entropy Engineering of SnTe: Multi-Principal-Element Alloying Leading to Ultralow Lattice Thermal Conductivity and State-of-the-Art Thermoelectric Performance. *Adv. Energy Mater.* **2018**, *8* (29), 1802116.

(4) Wei, P. C.; Liao, C. N.; Wu, H. J.; Yang, D.; He, J.; Biesold-McGee, G. V.; Liang, S.; Yen, W. T.; Tang, X.; Yeh, J. W.; Lin, Z.; He, J. H. Thermodynamic Routes to Ultralow Thermal Conductivity and High Thermoelectric Performance. *Adv. Mater.* **2020**, *32* (12), 1906457.
(5) Joshi, G.; Lee, H.; Lan, Y.; Wang, X.; Zhu, G.; Wang, D.; Gould, R. W.; Cuff, D. C.; Tang, M. Y.; Dresselhaus, M. S.; Chen, G.; Ren, Z. Enhanced Thermoelectric Figure-of-Merit in Nanostructured p-Type Silicon Germanium Bulk Alloys. *Nano Lett.* **2008**, *8* (12), 4670−4674.
(6) Lan, Y. C.; Minnich, A. J.; Chen, G.; Ren, Z. F. Enhancement of Thermoelectric Figure-of-Merit by a Bulk Nanostructuring Approach. *Adv. Funct Mater.* **2010**, *20* (3), 357−376.
(7) Wang, H.; Cao, X.; Takagiwa, Y.; Snyder, G. J. Higher Mobility in Bulk Semiconductors by Separating the Dopants from the Charge-Conducting Band − a Case Study of Thermoelectric PbSe. *Materials Horizons* **2015**, *2* (3), 323−329.
(8) Yu, B.; Zebarjadi, M.; Wang, H.; Lukas, K.; Wang, H.; Wang, D.; Opeil, C.; Dresselhaus, M.; Chen, G.; Ren, Z. Enhancement of Thermoelectric Properties by Modulation-Doping in Silicon Germanium Alloy Nanocomposites. *Nano Lett.* **2012**, *12* (4), 2077−2082.
(9) Heremans, J. P.; Jovovic, V.; Toberer, E. S.; Saramat, A.; Kurosaki, K.; Charoenphakdee, A.; Yamanaka, S.; Snyder, G. J. Enhancement of Thermoelectric Efficiency in PbTe by Distortion of the Electronic Density of States. *Science* **2008**, *321*, 554−557.
(10) Rhyee, J. S.; Lee, K. H.; Lee, S. M.; Cho, E.; Kim, S. I.; Lee, E.; Kwon, Y. S.; Shim, J. H.; Kotliar, G. Peierls Distortion as a Route to High Thermoelectric Performance in In(4)Se(3-Delta) Crystals. *Nature* **2009**, *459* (7249), 965−968.
(11) Zhou, J.; Yang, R.; Chen, G.; Dresselhaus, M. S. Optimal Bandwidth for High Efficiency Thermoelectrics. *Phys. Rev. Lett.* **2011**, *107* (22), 226601.
(12) Zeng, G.; Bowers, J. E.; Zide, J. M. O.; Gossard, A. C.; Kim, W.; Singer, S.; Majumdar, A.; Singh, R.; Bian, Z.; Zhang, Y.; Shakouri, A. ErAs:InGaAs/InGaAlAs Superlattice Thin-Film Power Generator Array. *Appl. Phys. Lett.* **2006**, *88* (11), 113502.
(13) Gu, Y.; Ai, W.; Zhao, Y.; Pan, L.; Lu, C.; Zong, P.; Hu, X.; Xu, Z.; Wang, Y. Remarkable Thermoelectric Property Enhancement in Cu2SnS3−CuCo2S4 Nanocomposites via 3D Modulation Doping. *J. Mater. Chem. A* **2021**, *9* (31), 16928−16935.
(14) Hou, Q. R.; Gu, B. F.; Chen, Y. B.; He, Y. J.; Sun, J. L. Enhancement of the Thermoelectric Power Factor of MnSi1.7 Film by Modulation Doping of Al and Cu. *Appl. Phys. a-Mater.* **2014**, *114* (3), 943−949.
(15) Zebarjadi, M.; Joshi, G.; Zhu, G.; Yu, B.; Minnich, A.; Lan, Y.; Wang, X.; Dresselhaus, M.; Ren, Z.; Chen, G. Power Factor Enhancement by Modulation Doping in Bulk Nanocomposites. *Nano Lett.* **2011**, *11* (6), 2225−2230.
(16) Kim, R.; Lundstrom, M. S. Computational Study of Energy Filtering Effects in One-Dimensional Composite Nano-Structures. *J. Appl. Phys.* **2012**, *111* (2), No. 024508.
(17) Cho, H.; Back, S. Y.; Yun, J. H.; Byeon, S.; Jin, H.; Rhyee, J. S. Thermoelectric Properties and Low-Energy Carrier Filtering by Mo Microparticle Dispersion in an n-Type (CuI)0.003Bi2(Te,Se)3 Bulk Matrix. *ACS Appl. Mater. Interfaces* **2020**, *12* (34), 38076−38084.
(18) Ahmed, F.; Tsujii, N.; Mori, T. Thermoelectric Properties of CuGa1−xMnxTe2: Power Factor Enhancement by Incorporation of Magnetic Ions. *Journal of Materials Chemistry A* **2017**, *5* (16), 7545−7554.
(19) Acharya, S.; Anwar, S.; Mori, T.; Soni, A. Coupling of Charge Carriers with Magnetic Entropy for Power Factor Enhancement in Mn Doped Sn1.03Te for Thermoelectric Applications. *Journal of Materials Chemistry C* **2018**, *6* (24), 6489−6493.
(20) Takaki, H.; Kobayashi, K.; Shimono, M.; Kobayashi, N.; Hirose, K.; Tsujii, N.; Mori, T. Thermoelectric Properties of a Magnetic Semiconductor CuFeS2. *Materials Today Physics* **2017**, *3*, 85−92.
(21) Mori, T. Novel Principles and Nanostructuring Methods for Enhanced Thermoelectrics. *Small* **2017**, *13* (45), 1702013.
(22) Tsujii, N.; Mori, T. High Thermoelectric Power Factor in a Carrier-Doped Magnetic Semiconductor Cufes2. *Applied Physics Express* **2013**, *6* (4), No. 043001.
(23) Tsujii, N.; Nishide, A.; Hayakawa, J.; Mori, T. Observation of Enhanced Thermopower Due to Spin Fluctuation in Weak Itinerant Ferromagnet. *Science Advances* **2019**, *5* (2), eaat5935.
(24) Vaney, J. B.; Yamini, S. A.; Takaki, H.; Kobayashi, K.; Kobayashi, N.; Mori, T. Magnetism-Mediated Thermoelectric Performance of the Cr-Doped Bismuth Telluride Tetradymite. *Mater. Today Phys.* **2019**, *9*, 100090.
(25) Liu, W.; Lukas, K. C.; McEnaney, K.; Lee, S.; Zhang, Q.; Opeil, C. P.; Chen, G.; Ren, Z. Studies on the Bi2Te3-Bi2Se 3-Bi2S3 System for Mid-Temperature Thermoelectric Energy Conversion. *Energy Environ. Sci.* **2013**, *6* (2), 552−560.
(26) Guo, Y.; Du, X.; Wang, Y.; Yuan, Z. Simultaneous Enhanced Performance of Electrical Conductivity and Seebeck Coefficient in Bi2−Sn S3 by Solvothermal and Microwave Sintering. *J. Alloys Compd.* **2017**, *717*, 177−182.
(27) Chen, B.; Uher, C.; Iordanidis, L.; Kanatzidis, M. G. Transport Properties of Bi2S3and the Ternary Bismuth Sulfides KBi6.33S10and K2Bi8S13. *Chem. Mater.* **1997**, *9* (7), 1655−1658.
(28) Liu, Z. H.; Pei, Y. L.; Geng, H. Y.; Zhou, J. C.; Meng, X. F.; Cai, W.; Liu, W. S.; Sui, J. H. Enhanced Thermoelectric Performance of Bi2S3 by Synergistical Action of Bromine Substitution and Copper Nanoparticles. *Nano Energy* **2015**, *13*, 554−562.
(29) Kawamoto, Y.; Iwasaki, H. Thermoelectric Properties of (Bi1−x Sb x)2S3 with Orthorhombic Structure. *Journal of Elec Materi* **2014**, *43* (6), 1475−1479.
(30) Ge, Z. H.; Zhang, B. P.; Liu, Y.; Li, J. F. Nanostructured Bi(2-x)Cu(x)S3 Bulk Materials with Enhanced Thermoelectric Performance. *Phys. Chem. Chem. Phys.* **2012**, *14* (13), 4475−4481.
(31) Yu, Y. Q.; Zhang, B. P.; Ge, Z. H.; Shang, P. P.; Chen, Y. X. Thermoelectric Properties of Ag-Doped Bismuth Sulfide Polycrystals Prepared by Mechanical Alloying and Spark Plasma Sintering. *Mater. Chem. Phys.* **2011**, *131* (1−2), 216−222.
(32) Yang, J.; Liu, G. W.; Yan, J. N.; Zhang, X. Z.; Shi, Z. Q.; Qiao, G. J. Enhanced the Thermoelectric Properties of N-Type Bi2S3 Polycrystalline by Iodine Doping. *J. Alloys Compd.* **2017**, *728*, 351−356.
(33) Du, X. L.; Cai, F. S.; Wang, X. W. Enhanced Thermoelectric Performance of Chloride Doped Bismuth Sulfide Prepared by Mechanical Alloying and Spark Plasma Sintering. *J. Alloys Compd.* **2014**, *587*, 6−9.
(34) Chen, Y.; Wang, D.; Zhou, Y.; Pang, Q.; Shao, J.; Wang, G.; Wang, J.; Zhao, L.-D. Enhancing the Thermoelectric Performance of Bi2S3: A Promising Earth-Abundant Thermoelectric Material. *Front Phys-Beijing* **2019**, *14* (1), 13.
(35) Guo, J.; Ge, Z. H.; Qian, F.; Lu, D. H.; Feng, J. Achieving High Thermoelectric Properties of Bi2S3 via InCl3 Doping. *J. Mater. Sci.* **2020**, *55* (1), 263−273.
(36) Biswas, K.; Zhao, L. D.; Kanatzidis, M. G. Tellurium-Free Thermoelectric: The Anisotropic n-Type Semiconductor Bi2S3. *Adv. Energy Mater.* **2012**, *2* (6), 634−638.
(37) Wang, Z. Y.; Guo, J.; Feng, J.; Ge, Z. H. Effects of NbCl5-Doping on the Thermoelectric Properties of Polycrystalline Bi2S3. *J. Solid State Chem.* **2021**, *297*, 122043.
(38) Zhang, L. J.; Zhang, B. P.; Ge, Z. H.; Han, C. G. Fabrication and Properties of Bi2S3-XSex Thermoelectric Polycrystals. *Solid State Commun.* **2013**, *162*, 48−52.
(39) Ge, Z. H.; Zhang, B. P.; Shang, P. P.; Li, J. F. Control of Anisotropic Electrical Transport Property of Bi2S3 Thermoelectric Polycrystals. *J. Mater. Chem.* **2011**, *21* (25), 9194−9200.
(40) Ge, Z.-H.; Zhang, B.-P.; Li, J.-F. Microstructure Composite-like Bi2S3 Polycrystals with Enhanced Thermoelectric Properties. *J. Mater. Chem.* **2012**, *22* (34), 17589.
(41) Zhao, L. D.; Zhang, B. P.; Liu, W. S.; Zhang, H. L.; Li, J. F. Enhanced Thermoelectric Properties of Bismuth Sulfide Polycrystals Prepared by Mechanical Alloying and Spark Plasma Sintering. *J. Solid State Chem.* **2008**, *181* (12), 3278−3282.

https://doi.org/10.1021/acsaem.2c00295
ACS Appl. Energy Mater. 2022, 5, 3845−3853

(42) Guo, J.; Zhang, Y. X.; Wang, Z. Y.; Zheng, F. S.; Ge, Z. H.; Fu, J. C.; Feng, J. High Thermoelectric Properties Realized in Earth-Abundant Bi2S3 Bulk via Carrier Modulation and Multi-Nano-Precipitates Synergy. *Nano Energy* **2020**, *78*, 105227.
(43) Toby, B. H.; Von Dreele, R. B. GSAS-II: The Genesis of a Modern Open-Source All Purpose Crystallography Software Package. *J. Appl. Crystallogr.* **2013**, *46* (2), 544−549.
(44) Perdew, J. P.; Burke, K.; Ernzerhof, M. Generalized Gradient Approximation Made Simple. *Phys. Rev. Lett.* **1996**, *77* (18), 3865−3868.
(45) Giannozzi, P.; Baseggio, O.; Bonfà, P.; Brunato, D.; Car, R.; Carnimeo, I.; Cavazzoni, C.; de Gironcoli, S.; Delugas, P.; Ferrari Ruffino, F.; Ferretti, A.; Marzari, N.; Timrov, I.; Urru, A.; Baroni, S. Quantum ESPRESSO toward the Exascale. *J. Chem. Phys.* **2020**, *152* (15), 154105.
(46) Monkhorst, H. J.; Pack, J. D. Special Points for Brillouin-Zone Integrations. *Phys. Rev. B* **1976**, *13* (12), 5188−5192.
(47) Pauling, L. *The Nature of the Chemical Bond and the Structure of Molecules and Crystals: An Introduction to Modern Structural Chemistry*, 3rd ed.; Cornell University Press: 1960.
(48) Lundegaard, L. F.; Makovicky, E. E.; Boffa-Ballaran, T.; Balic-Zunic, T. Crystal Structure and Cation Lone Electron Pair Activity of Bi2S3 between 0 and 10 GPa. *Phys. Chem. Miner* **2005**, *32* (8−9), 578−584.
(49) Ji, W.; Shi, X.-L.; Liu, W.-D.; Yuan, H.; Zheng, K.; Wan, B.; Shen, W.; Zhang, Z.; Fang, C.; Wang, Q.; Chen, L.; Zhang, Y.; Jia, X.; Chen, Z.-G. Boosting the Thermoelectric Performance of N-Type Bi2S3 by Hierarchical Structure Manipulation and Carrier Density Optimization. *Nano Energy* **2021**, *87*, 106171.
(50) Wu, Y.; Lou, Q.; Qiu, Y.; Guo, J.; Mei, Z. Y.; Xu, X.; Feng, J.; He, J. Q.; Ge, Z. H. Highly Enhanced Thermoelectric Properties of Nanostructured Bi2S3 Bulk Materials via Carrier Modification and Multi-Scale Phonon Scattering. *Inorg. Chem. Front* **2019**, *6* (6), 1374−1381.
(51) Jonson, M.; Mahan, G. D. Mott's Formula for the Thermopower and the Wiedemann-Franz Law. *Phys. Rev. B* **1980**, *21* (10), 4223−4229.
(52) Guo, J.; Lou, Q.; Qiu, Y.; Wang, Z.-Y.; Ge, Z.-H.; Feng, J.; He, J. Remarkably Enhanced Thermoelectric Properties of Bi2S3 Nanocomposites via Modulation Doping and Grain Boundary Engineering. *Appl. Surf. Sci.* **2020**, *520*, 146341.
(53) Tan, X. F.; Tan, X. J.; Liu, G. Q.; Xu, J. T.; Shao, H. Z.; Hu, H. Y.; Jin, M.; Jiang, H. C.; Jiang, J. Optimizing the Thermoelectric Performance of In-Cd Codoped SnTe by Introducing Sn Vacancies. *J. Mater. Chem. C* **2017**, *5* (30), 7504−7509.
(54) Chen, S.; Bai, H.; Li, J.; Pan, W.; Jiang, X.; Li, Z.; Chen, Z.; Yan, Y.; Su, X.; Wu, J.; Uher, C.; Tang, X. Vacancy-Based Defect Regulation for High Thermoelectric Performance in Ge9Sb2Te12-x Compounds. *ACS Appl. Mater. Interfaces* **2020**, *12* (17), 19664−19673.
(55) Guo, J.; Yang, J.; Ge, Z.-H.; Jiang, B.; Qiu, Y.; Zhu, Y.-K.; Wang, X.; Rong, J.; Yu, X.; Feng, J.; He, J. Realizing High Thermoelectric Performance in Earth-Abundant Bi2S3 Bulk Materials via Halogen Acid Modulation. *Adv. Funct. Mater.* **2021**, *31* (37), 2102838.
(56) Kang, S. D.; Snyder, G. J. Transport Property Analysis Method for Thermoelectric Materials: Material Quality Factor and the Effective Mass Model. *arXiv* 1710.06896 *[cond-mat]*, 2018.
(57) May, A. F.; Snyder, G. J. Introduction to Modeling Thermoelectric Transport at High Temperatures. In *Materials, Preparation, and Characterization in Thermoelectrics*; CRC Press: 2012.
(58) Pei, Y. Z.; LaLonde, A. D.; Wang, H.; Snyder, G. J. Low Effective Mass Leading to High Thermoelectric Performance. *Energ Environ. Sci.* **2012**, *5* (7), 7963−7969.
(59) Naithani, H.; Dasgupta, T. Critical Analysis of Single Band Modeling of Thermoelectric Materials. *ACS Appl. Energy Mater.* **2020**, *3* (3), 2200−2213.
(60) Ravich, Iu. I. *Semiconducting Lead Chalcogenides*; Springer: 1970; Monographs in Semiconductor Physics. DOI: 10.1007/978-1-4684-8607-0.
(61) Zou, T.; Qin, X.; Zhang, Y.; Li, X.; Zeng, Z.; Li, D.; Zhang, J.; Xin, H.; Xie, W.; Weidenkaff, A. Enhanced Thermoelectric Performance of β-Zn4Sb3 Based Nanocomposites through Combined Effects of Density of States Resonance and Carrier Energy Filtering. *Sci. Rep* **2015**, *5* (1), 17803.
(62) Liu, M.; Qin, X. Y. Enhanced Thermoelectric Performance through Energy-Filtering Effects in Nanocomposites Dispersed with Metallic Particles. *Appl. Phys. Lett.* **2012**, *101* (13), 132103.
(63) Costache, M. V.; Bridoux, G.; Neumann, I.; Valenzuela, S. O. Magnon-Drag Thermopile. *Nat. Mater.* **2012**, *11* (3), 199−202.
(64) Watzman, S. J.; Duine, R. A.; Tserkovnyak, Y.; Boona, S. R.; Jin, H.; Prakash, A.; Zheng, Y. H.; Heremans, J. P. Magnon-Drag Thermopower and Nernst Coefficient in Fe, Co, and Ni. *Phys. Rev. B* **2016**, *94* (14), 144407.
(65) Ang, R.; Khan, A. U.; Tsujii, N.; Takai, K.; Nakamura, R.; Mori, T. Thermoelectricity Generation and Electron-Magnon Scattering in a Natural Chalcopyrite Mineral from a Deep-Sea Hydrothermal Vent. *Angew. Chem., Int. Ed. Engl.* **2015**, *54* (44), 12909−12913.
(66) Ge, B.; Shi, Z.; Zhou, C.; Hu, J.; Liu, G.; Xia, H.; Xu, J.; Qiao, G. Enhanced Thermoelectric Performance of N-Type Eco-Friendly Material Cu1-XAgxFeS2 (X = 0−0.14) via Bandgap Tuning. *J. Alloys Compd.* **2019**, *809*, 151717.
(67) Xiao, Y.; Wang, D.; Zhang, Y.; Chen, C.; Zhang, S.; Wang, K.; Wang, G.; Pennycook, S. J.; Snyder, G. J.; Wu, H.; Zhao, L.-D. Band Sharpening and Band Alignment Enable High Quality Factor to Enhance Thermoelectric Performance in n -Type PbS. *J. Am. Chem. Soc.* **2020**, *142* (8), 4051−4060.
(68) He, J.; Girard, S. N.; Kanatzidis, M. G.; Dravid, V. P. Microstructure-Lattice Thermal Conductivity Correlation in Nanostructured PbTe0.7S0.3 Thermoelectric Materials. *Adv. Funct. Mater.* **2010**, *20* (5), 764−772.
(69) Callaway, J. Model for Lattice Thermal Conductivity at Low Temperatures. *Phys. Rev.* **1959**, *113* (4), 1046−1051.
(70) Koc, H.; Ozisik, H.; Deligöz, E.; Mamedov, A. M.; Ozbay, E. Mechanical, Electronic, and Optical Properties of Bi2S3 and Bi2Se3 Compounds: First Principle Investigations. *J. Mol. Model* **2014**, *20* (4), 2180.
(71) Ren, G.-K.; Lan, J.-L.; Ventura, K. J.; Tan, X.; Lin, Y.-H.; Nan, C.-W. Contribution of Point Defects and Nano-Grains to Thermal Transport Behaviours of Oxide-Based Thermoelectrics. *npj Comput. Mater.* **2016**, *2* (1), 1−9.
(72) Kittel, C. *Introduction to Solid State Physics*, 8th ed.; Wiley: 2004.

https://doi.org/10.1021/acsaem.2c00295
ACS Appl. Energy Mater. 2022, 5, 3845−3853

materials

MDPI

Review

Recent Progress in Multiphase Thermoelectric Materials

Raphael Fortulan [1] and Sima Aminorroaya Yamini [1,2,*]

[1] Materials and Engineering Research Institute, Sheffield Hallam University, Sheffield S1 1 WB, UK; b9044884@my.shu.ac.uk
[2] Department of Engineering and Mathematics, Sheffield Hallam University, Sheffield S1 1 WB, UK
* Correspondence: s.aminorroaya@shu.ac.uk

Abstract: Thermoelectric materials, which directly convert thermal energy to electricity and vice versa, are considered a viable source of renewable energy. However, the enhancement of conversion efficiency in these materials is very challenging. Recently, multiphase thermoelectric materials have presented themselves as the most promising materials to achieve higher thermoelectric efficiencies than single-phase compounds. These materials provide higher degrees of freedom to design new compounds and adopt new approaches to enhance the electronic transport properties of thermoelectric materials. Here, we have summarised the current developments in multiphase thermoelectric materials, exploiting the beneficial effects of secondary phases, and reviewed the principal mechanisms explaining the enhanced conversion efficiency in these materials. This includes energy filtering, modulation doping, phonon scattering, and magnetic effects. This work assists researchers to design new high-performance thermoelectric materials by providing common concepts.

Keywords: thermoelectric materials; multiphase; composite; energy filtering; magnetic effect; phonon scattering

check for updates

Citation: Fortulan, R.; Aminorroaya Yamini, S. Recent Progress in Multiphase Thermoelectric Materials. *Materials* **2021**, *14*, 6059. https://doi.org/10.3390/ma14206059

Academic Editor: Christof Schneider

Received: 31 August 2021
Accepted: 12 October 2021
Published: 14 October 2021

Publisher's Note: MDPI stays neutral with regard to jurisdictional claims in published maps and institutional affiliations.

Copyright: © 2021 by the authors. Licensee MDPI, Basel, Switzerland. This article is an open access article distributed under the terms and conditions of the Creative Commons Attribution (CC BY) license (https://creativecommons.org/licenses/by/4.0/).

1. Introduction

Thermoelectric (TE) materials have been attracting a great deal of interest because of their applications in energy recovery from industrial waste heat and high-efficiency cooling of next-generation integrated circuits [1]. The efficiency of TE materials is characterised by a dimensionless figure of merit $zT = S^2\sigma T/(\kappa_e + \kappa_l)$, where T, S, σ, κ_e and κ_l are the absolute temperature, Seebeck coefficient, electrical conductivity, and electronic and lattice components of the total thermal conductivity (κ_t), respectively. Most thermoelectric materials used in commercial applications have a zT of around 1 [2], which corresponds to an efficiency of roughly 10% in the medium temperature range [3]. To increase zT, one would need to increase S and σ and decrease κ_t. These parameters are interrelated though; the electronic thermal conductivity increases with the increase of electrical conductivity, and S and σ are inversely proportional [4]. Therefore, optimising these parameters is very challenging and the key to achieving higher efficiency.

One of the most successful approaches to improve the figure of merit is reducing the lattice thermal conductivity, and over the years, various phonon engineering approaches have been used to enhance phonon scattering and decrease κ_l by taking advantage of nanoprecipitates [5–7], alloying elements [8–10], nanostructured grain boundaries [11–14], ionised impurities [15,16], and superlattices [17].

A series of band structure engineering approaches have also been employed to improve the electronic properties [18–20]. Strategies such as quantum confinement [21,22], modulation doping [23–25], introducing resonance energy to the electronic density of states [26,27], and energy filtering [28] are being actively pursued. These strategies are adopted to modify the band structure and transport properties of the thermoelectric materials by either tuning the electrical conductivity and the Seebeck coefficient independently or by increasing them simultaneously. In practice, the best results were achieved with a

significant increase in one of these parameters and a slight decrease in the other, resulting in an increase in the power factor ($S^2\sigma$) and zT.

The development of highly efficient thermoelectric materials encountered a bottleneck when the exploration of single-phase alloys was exhausted. Therefore, investigating multiphase compounds is the most viable strategy to enhance the thermoelectric performance of bulk materials, where higher degrees of freedom are available to design new materials and tune their electronic transport properties [29–31]. Figure 1 presents the number of yearly publications on thermoelectric materials, indexed by the Scopus database, compared with the numbers of papers published on multiphase/composite thermoelectric materials, indicating an increasing interest of the research community on this topic over the last five years.

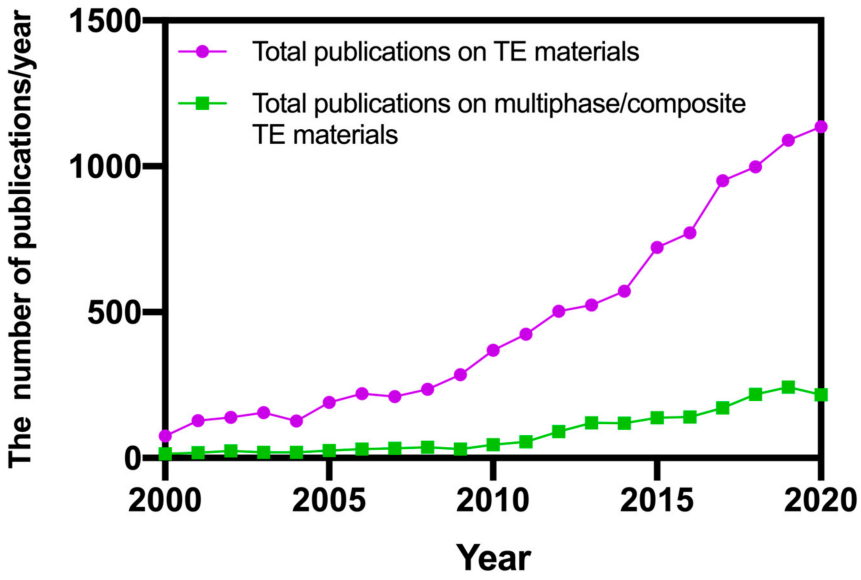

Figure 1. Yearly number of publications on thermoelectric materials, compared with publications on multiphase/composite thermoelectric materials.

The combination of several phases can improve the electrical conductivity, Seebeck coefficient, and thermal conductivity [32]. Here, we summarise the main strategies discovered to date to increase the thermoelectric efficiency in multiphase materials. This includes: (1) energy filtering, creating potential barriers in the electronic band structure of the main phase through interfaces with the secondary phases. This results in an increase in the overall Seebeck coefficient [33–35]; (2) modulation doping, where the heterojunctions between secondary phases with larger bandgaps and higher carrier concentrations than the matrix are used to greatly increase the electrical conductivity of the multiphase compounds [36–38]; (3) phonon scattering by interfaces, grain boundaries, and defects to reduce the lattice thermal conductivity [39–42]; and (4) magnetic effects, which utilises the magnon-drag mechanism in magnetic materials [43–45], semiconductors doped with magnetic elements [46–48], or semiconductors containing secondary magnetic phases [49,50] to improve the thermoelectric efficiency [51,52].

2. Energy Filtering

The concept of energy filtering in thermoelectric materials was first introduced and studied in the latter half of the last century [53]. The research on this field has been renewed and developed since the 1990s. In general, the Seebeck coefficient increases with an increase of the barrier height [54,55] while the electrical conductivity decreases [56–58]. In the presence of multiple potential barriers, the bipolar effect can be suppressed, decreasing the flow of minority charge carriers and reducing the decrease in the electrical conductivity [59–62].

Conventionally, the energy filtering effect could be understood by solving the Boltzmann transport equation (BTE) using the relaxation time approximation [63,64]. The BTE equation expresses all thermoelectric transport coefficients as a function of the energy-dependent relaxation times of the charge carriers $\tau(E)$ and the Fermi level E_F. The energy filtering effect can be readily verified considering the Seebeck coefficient expression [65]:

$$S = -\frac{1}{qT}\frac{\int (E - E_F)\sigma'(E)\mathrm{d}E}{\int \sigma'(E)\mathrm{d}E} \quad (1)$$

where T is the absolute temperature, E is the charge carrier energy, E_F is the Fermi level, and σ' is the differential conductivity. The Seebeck coefficient, as shown in Equation (1), is the energy average weighted by the electrical conductivity:

$$S = -\frac{1}{qT}\langle E - E_F \rangle_{\sigma'} \quad (2)$$

implying that an asymmetry between the density of states and the Fermi level can create higher Seebeck coefficients.

The implementation of energy barriers in thermoelectric materials is made in the form of either nanoparticles or grain boundary interfaces embedded in the bulk host matrix [66]. At these interfaces, the carriers with higher energy will pass the interface preferentially, while the carriers with lower energy are filtered out. A high density of the interfaces ensures the positive carrier filtering effect [67]. The band bending between the two materials creates an energy barrier that reflects the charge carrier [68,69]. Figure 2 illustrates the energy filtering effect: given the partial reflection of the lower energy electron waves, the high energy electrons mostly contribute to the Seebeck coefficient.

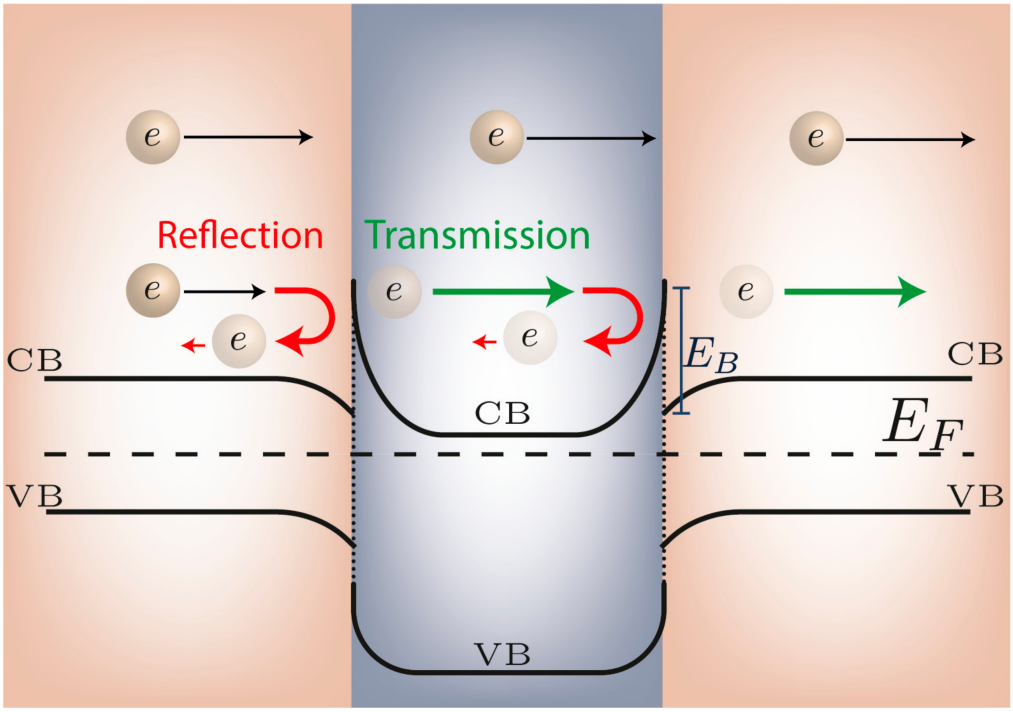

Figure 2. Energy filtering effect, showing that lower energy electrons are scattered by a potential barrier.

Multiphase materials present themselves as viable candidates to take advantage of energy filtering. Given the possibilities of tuning the electronic band structure of each phase, the band bending can noticeably enhance the energy filtering effect [70–77]. In the following sections, the energy filtering effect will be discussed in multiphase materials. A Schottky or ohmic barrier will appear at the interface with a metallic secondary phase,

while a heterojunction barrier will present at the interface of thermoelectric material with a semiconducting secondary phase.

2.1. Energy Filtering by Metal Secondary Phases

For metallic phases, the barrier height will be proportional to the work function of both the semiconductor and the metal and the electron affinity of the semiconductor. The work function, Φ, is defined as the minimum energy required to remove an electron from the surface of a material, and its value is equal to the energy difference between the vacuum and the Fermi level [78]. The electron affinity, χ, is the energy difference between the vacuum and the bottom of the conduction band. At the metal–semiconductor junction, the Schottky-Mott rule [79] defines the barrier height, E_B, to be the difference between the metals' work function, Φ_M, and the semiconductor electron affinity, χ_S:

$$E_B = \Phi_M - \chi_s \quad (3)$$

Small differences cause few restrictions on the movement of the electrons, and this barrier is known as ohmic. Both the work function and electron affinity depend on the surface impurity and the crystallographic orientation.

Theoretically, the presence of metals can strongly affect the carrier relaxation time and consequently affects both the electrical conductivity and the Seebeck coefficient [54,80,81]. The inclusion of metallic nanoparticles was shown to enhance the Seebeck coefficient mathematically [66]. The interface of *n*-type PbTe with metallic Pb nanoparticles, with a low work function, effectively scattered the electrons and increased both the Seebeck coefficient and electrical resistivity. This mechanism is illustrated schematically in Figure 3, where spherical metallic nanoparticles are randomly distributed in a host semiconductor.

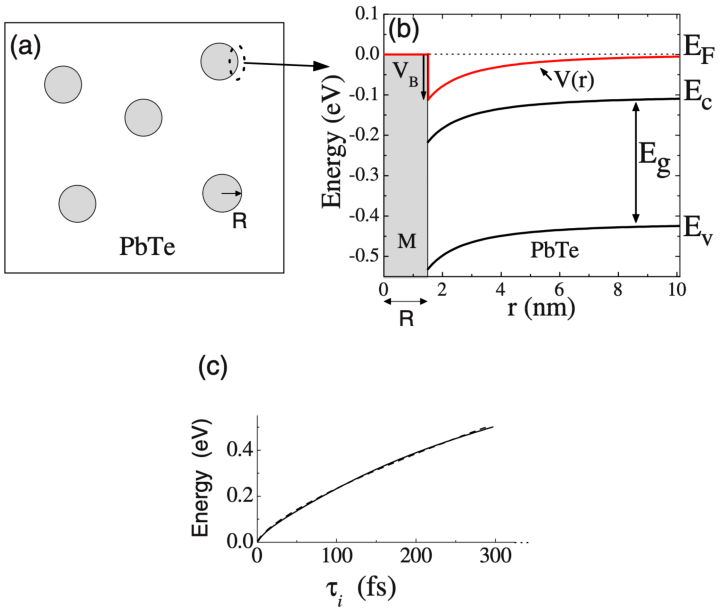

Figure 3. (**a**) Schematic of randomly distributed metallic Pb secondary phase in a PbTe matrix (**b**) Calculated potential V(r) and energy diagram for PbTe at 300 K, carrier concentration of 2.5 × 10^{19} cm^{-3}, barrier height of 0.11 eV, and radius of 1.5 nm, where E_F is the Fermi level, E_C is the energy at the bottom of the conduction band, E_g is the band gap, and E_V is the energy at the top of the valence band (**c**) Carriers' relaxation time as a function of their energy. Reprinted with permission from ref. [66]. Copyright 2008 Copyright American Physical Society.

Experimental results have proved this concept [82–84]: for instance, Pb precipitates in the matrix of *n*-type PbTe, intrinsically doped with excess Pb, increased the Seebeck coefficient and the average resistivity from −98 μV/K and 1.2 mΩ cm for $Pb_{1.03}Te$ to

−130 μV/K, and 3.2 mΩ cm for $Pb_{1.06}Te$ at 300 K, respectively [82]. The addition of metallic Sn and Cr to Cu_2O doubled the Seebeck coefficient from 700 μV/K to 1400 μV/K [84]. Platinum nanocrystals created energy barriers in *p*-type Sb_2T_3 thin films [83] and caused a large reduction in carrier mobility in about 2.5 orders of magnitude due to the additional scattering of charge carriers compared to Sb_2Te_3 films without Pt nanocrystals. The carrier concentration increased, possibly due to the overlapping of energy bands [66]. The band overlapping increases the distance between the Fermi energy level and the valence band maxima, thereby increasing the total concentration of holes in the semiconductor matrix.

Silver nanoparticles enhanced the Seebeck coefficient of CdO-Ag composites [85]—a potential barrier of E_B = 0.1 eV between the work function of Ag and the electron affinity of CdO increased the resistivity from 1.5 mΩ cm to 1.7 mΩ cm for a sample with 0.03% of Ag and increased the Seebeck coefficient from −120 μV/K for the pristine sample to −129 μV/K for the sample with 0.03% of Ag at 800 K.

2.2. Energy Filtering by Semiconducting Secondary Phases

For a semiconductor secondary phase, the difference between the bandgaps and Fermi levels of the two phases gives rise to a potential barrier at their junction [86]. The barrier height will be proportional to the difference between the electron affinity of the two semiconductors (χ_1, χ_2). Anderson's rule [78] allows a simple estimate of the barrier height at the conduction, E_{BC}, and valence, E_{BV}, bands:

$$E_{BC} = \chi_2 - \chi_1 \tag{4}$$

$$E_{BV} = (E_{g1} - E_{g2}) - E_{BC} \tag{5}$$

and it has been employed as a rough estimation to design multiphase materials. The actual curvature of the band bending can be found using Poisson's equation for the electric potential [87]:

$$-\nabla^2 V = \frac{\rho}{\varepsilon} = \frac{q(h - n + D)}{\varepsilon} \tag{6}$$

where ε is the permittivity of the material, h and n are the holes and electrons densities, respectively, and D is the concentration of ionised impurities (extrinsic dopant). The relation of the barrier height and conductivity is suggested as [88]:

$$\sigma \propto T^{-\frac{1}{2}} e^{-\frac{E_B}{k_B T}} \tag{7}$$

It should be noted that this equation was developed for homojunctions [89,90]. However, experimental data for heterojunctions fit this equation surprisingly well [91]. Experimental results show that energy filtering caused by dissimilar semiconducting phases can improve the power factor [92–95]. Silicon oxide particles in the $(Bi_2Te_3)_{0.2}(Sb_2Te_3)_{0.8}$ bulk alloy increased the Seebeck coefficient from 182 μV/K for the pristine sample to 218 μV/K for the sample with 1.1% volume of SiO_2 at room temperature [92]. Yttrium oxide (Y_2O_3) particles embedded in a $Bi_{0.5}Sb_{1.5}Te_3$ matrix increased the Seebeck coefficient significantly [96], deviated considerably from the ideal Pisarenko relation. The Seebeck coefficient is inversely proportional to the carrier concentration, n, by a rate of $n^{-2/3}$ for degenerate semiconductors, according to the Pisarenko relation [97]. The deviation from this ideal relationship has been used as an indication of changes in the electronic band structure of the material [98].

Randomly dispersed titanium dioxide nanoparticles (ranging from 10 to 25 nm) in a $Ba_{0.22}Co_4Sb_{12}$ matrix increased the Seebeck coefficient [99]. Although the bandgap for $Ba_{0.22}Co_4Sb_{12}$ was unknown, given the large bandgap of TiO_2 (3.2 eV [100]), some influence of the energy filtering was assumed. At 300 K, the electrical conductivity decreased from 2.9×10^5 S/K to 2.8×10^5 S/K, and the Seebeck coefficient increased from −105 μV/K for the pristine sample to −110 μV/K for the sample with 0.8% volume of TiO_2. The TiO_2 particles in Bi_2Se_3 based materials increased the overall power factor of the composite

from 0.75 × 10^{-3} W/m K to 1.07 × 10^{-3} W/m K for the sample with 10 wt.% of titanium dioxide [101]. The charge carrier concentration varied greatly with the concentration of TiO_2, possibly due to the formation of Ti^{2+} ions during hot pressing under the vacuum.

Interestingly, a double-filtering effect has been reported for a deposited TiO_2 on $TiC_{1-x}O_x$@TiO_y ($x < 1$, $1 < y < 2$) heterostructures (Figure 4) [102]. $TiC_{1-x}O_x$, with a narrow bandgap and high electrical conductivity, in combination with TiO_y and TiO_2 nanoparticles, with wide bandgaps, produced an effective barrier height for energy filtering. The Seebeck coefficient and resistivity of the samples increased where a larger amount of TiO_2 was deposited. The maximum value obtained for the Seebeck coefficient at 973 K was −156 μV/K, with an electrical conductivity of ~4 × 10^4 S/m.

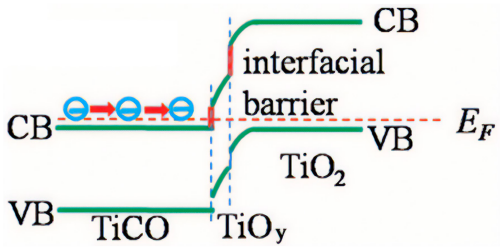

Figure 4. Band diagrams of the $TiC_{1-x}O_x$@TiO_y-TiO_2 heterostructured interface, where CB is the conduction band, VB is the valence band, and E_F is the Fermi level. Reprinted from [102].

Silicon-based materials, although not common in thermoelectricity, have also been shown to benefit from energy filtering [103–110]. For instance, heavily doped Si with B with nanoparticles of Si has shown an increased Seebeck coefficient and electrical conductivity in a particular range of dopant concentrations [111]. The increased Fermi level for the bulk material explains the increase of the electrical conductivity, and the energy filtering effect justifies the increased Seebeck coefficient.

A half-Heusler compound of $(Hf_{0.6}Zr_{0.4})NiSn_{0.99}Sb_{0.01}$, with added nanoparticles of tungsten (W), showed a maximum zT of 1.4 at 873 K and average zT of 0.9 in the temperature range of 300–973 K for the alloy with 5 wt.% tungsten nanoparticles [112].

Table 1 summarises the compositions and fabrication methods of recent studies that reported energy filtering effects in multiphase thermoelectric materials.

Table 1. Compositions, fabrication methods, and corresponding references of multiphase materials that benefited from the energy-filtering effect.

Composition	Fabrication Technique	Ref.
$Bi_{0.5}Sb_{1.5}Te$ + (0, 1.0, 2.0, 4.0, and 6.0 wt.%) nanoparticles of Sb_2O_3	Casting ($Bi_{0.5}Sb_{1.5}Te$) + ball milling of $Bi_{0.5}Sb_{1.5}Te$ and commercial powder of Sb_2O_3+ sintering	[113]
$Bi_2Te_{2.7}Se_{0.3}$ powder + ~2 nm layer of film of ZnO	Solution-based synthesis of Bi-Te-Se powder + atomic layer deposition of ZnO + hot pressing	[114]
$Bi_{1-x}Sb_x$ (x = 0, 0.10, 0.12, 0.13, 0.14, 0.2) + 3 wt.% carbon nanotubes	Ball milling + cold pressing + annealing	[115]
$Bi_{0.46}Sb_{1.54}Te_3$ + (0, 0.1, 0.2, and 0.3 wt.%) SiC	Ball milling + sintering	[70]
$Bi_{0.4}Sb_{1.6}Te_3$ + (0.1%, 0.2%, and 0.3 wt.%) $CuInTe_2$	Casting each phase separately + ball milling + sintering	[116]
$Lu_{0.1}Bi_{1.9}Te_3$ + (0, 0.0, 0.05, 1) wt.% carbon nanotubes	Hydrothermal synthesis + grinding + hot pressing	[117]
$Bi_{0.5}Sb_{1.5}Te_3$ + (0, 0.1, 0.2, 0.3, 0.4 wt.%) $BaTiO_3$	Hydrothermally synthesised $BaTiO_3$ + Commercial ingots of $Bi_{0.5}Sb_{1.5}Te_3$ were grinded and sintered	[74]
$Bi_{0.5}Sb_{1.5}Te_3$ + $SrTiO_3$	$Bi_{0.5}Sb_{1.5}Te_3$ films were grown on $SrTiO_3$ substrates by co-sputtering	[118]
Bi_2Te_3 + $Bi_{0.5}Sb_{1.5}Te_3$ thin films	Radio-frequency magnetron sputtering of Bi_2Te_3/$Bi_{0.5}Sb_{1.5}Te_3$ layers on a SiO_2/Si(001) substrate	[119]
$Bi_{0.4}Sb_{1.6}Te_3$ + (0, 0.2, 0.4, and 0.6 vol.%) $CuGaTe_2$	Vacuum melting + hot pressing	[120]
$Bi_{0.5}Sb_{1.5}Te_3$ + 2 wt.% (Gd_2O_3, $Gd_{1.98}Bi_{0.02}O_3$)	Powders for each phase were prepared by induction melting then mixed by spray pyrolysis + sintering	[121]
Bi_2Te_3 + (1, 2, and 5 wt.%) SnS	Commercial powders were mixed, cold pressed, and annealed	[122]
$Bi_{0.3}Sb_{1.7}Te_3$ + (0, 0.25, 0.50, and 0.75 wt.%) TiC	Ball milling + sintering	[123]
Bi_2Te_3 + ~4 wt.% of $Cu_{1.5}Te$	Solution-based synthesis (each phase separately) + hot pressing	[124]

Table 1. *Cont.*

Composition	Fabrication Technique	Ref.
Coated grains of SnTe with $CuInTe_2$	$CuInTe_2$ was formed by cation exchange of Sn by Cu and In on the surface of ball-milled SnTe powder	[125]
$Bi_{0.5}Sb_{1.5}Te_3$-$Cu_{0.07}$ + (0, 0.5, and 1.0 wt.%) HfO_2	Water atomisation + ball milling + sintering	[126]
SiGe + (2, 4, 6, 8, 10 wt.%) TiB_2	Ball milling + hot pressing	[108]

3. Modulation Doping

Modulation doping is a well-recognised concept to increase the conductivity in heterojunction devices [127]. The main idea behind modulation doping is to use the offset in the band structure between two semiconductors in combination with heavy doping of the material with a wider bandgap so that there is a transfer of carriers from the wide bandgap to the narrow bandgap material. The transferred carriers create two-dimensional electron gas, and they are essentially separated from the donor phase, which consequently increases the charge carrier mobility [128]. Conventionally, this strategy was employed to create *p*-channel devices, called modulation-doped field-effect transistors (MODFET) [129]. The difference between energy filtering and modulated doped samples is shown schematically in Figure 5. In the case of modulation doping, the secondary phase increases the conductivity by donating electrons to the host semiconductor, while in the case of energy filtering, the secondary phase scatters electrons and reduces mobility.

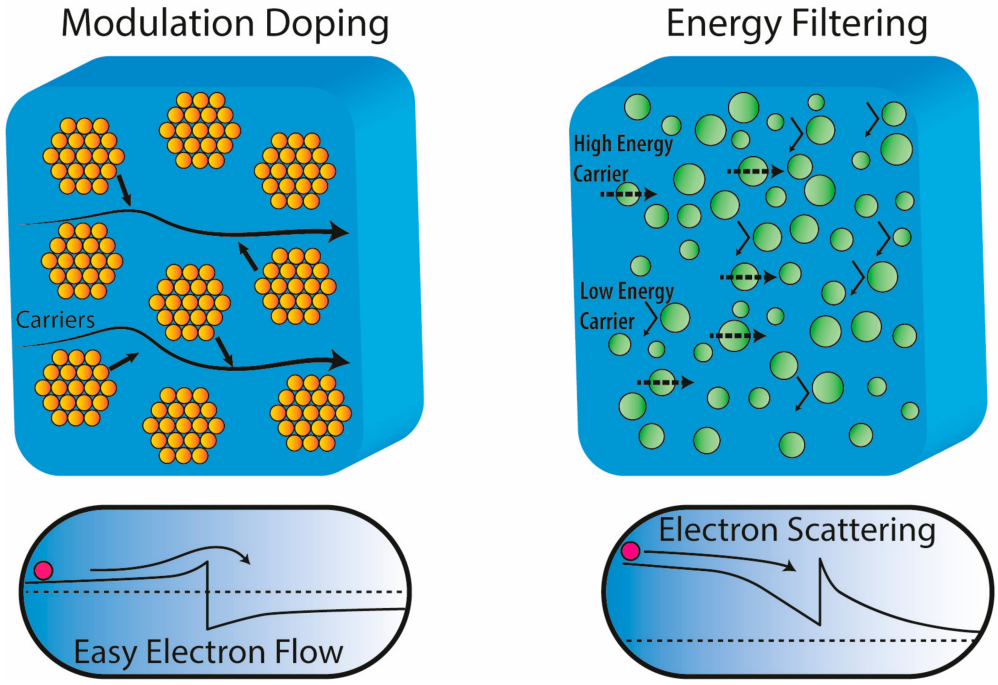

Figure 5. Comparison between a modulated doped semiconductor and a multiphase compound benefiting from energy filtering.

The thermoelectric research community has also used this mechanism to enhance the thermoelectric performance of materials [15,23,25,29,38]. For thermoelectric materials, a combination of two effects has enhanced the thermoelectric efficiency in the modulated doped materials: firstly, a large increase in the electrical conductivity and mobility of the charge carriers [130], and secondly, a reduction in the lattice thermal conductivity as a result of the scattering of phonons by nanostructuring [23,131].

Some attempts have also been made to explore the possibility of using modulation doping in structures similar to field-effect transistors (FETs) [129]. In this adopted structure,

the thermoelectric semiconductor nanowire (channel) is enclosed by the heavily doped layer (gate) [132–136]. A modest increase in the power factor was achieved by this approach.

Table 2 summarises the sample compositions, fabrication methods, and corresponding references of recent studies that employed modulation doping to enhance the thermoelectric performance of multiphase materials.

Table 2. Sample compositions and fabrication methods of references that employed modulation doping to enhance the thermoelectric performance of multiphase materials.

Composition	Fabrication Method	Ref.
$Ba_8(Al_xGa_{1-x})_{16}Ge_{30}$ (x = 0, 0.20, 0.23, 0.25, 0.33, 0.50, and 1)	Casting (each phase separately) + ball milling + sintering	[137]
$AgBiSe_2$ + Bi_4Se_3		[138]
Cu_2SnS_3 + (0, 1, 3, and 5% mol) $CuCo_2S_4$	Casting (each phase separately) + ball milling + sintering	[25,139]
$Si_a(Mg_2Si$ + x at. % $Bi)_{1-a}$ (a = 0.39, 0.50, 0.56, 0.59, and 0.67; x = 0.3, 0.8, 1.3, 1.8, 2.5)	Bi-doped Mg_2Si fabricated using induction melting + melt spinning si + sintering	[140]
p-type organic conducting polymer PEDOT:PSS + Ge	PEDOT:PSS coated with Ge layer	[141]
$(Ge_2Te_2)_x(CuInTe_2)_{1-x}$ (x = 98, 95, 90, 87.5, 85, 70, 30, and 10%)	Casting + hand milling + hot pressing	[142]
BiCuSeO + $Bi_{0.8}Pb_{0.2}Cu_{0.8}Ni_{0.2}SeO$	Each phase was fabricated by Mechanical alloying + ball milling of mixture + sintering	[143]
BiCuSeO + $Bi_{0.8}Er_{0.2}CuSeO$	Each phase was fabricated by ball milling + sintering. The final composition was obtained by ball milling + sintering	[144]
BiCuSeO + $Bi_{0.8}Ba_{0.2}CuSe_{0.8}Te_{0.2}O$	Each phase was fabricated by mechanical alloying + milling the mixture + sintering	[145]
$Pb_{(1-x)}Na_xTe_{0.65}S_{0.25}Se_{0.1}$ (x = 0.005, 0.01, 0.0015, 0.02, 0.025, and 0.03)	Casting PbSe and PbS + mixing stoichiometric amounts of PbSe, PbS, Pb, Te, and Na (casting) + sintering	[29]
$Pb_{0.97}Na_{0.03}Te_{(1-x)}S_x$ (x = 0.1, 0.15, 0.2, 0.25, 0.3, and 0.35)	Casting + hand milling + sintering	[146]

4. Phonon Scattering

When it comes to designing a thermoelectric material, the main goal is to maintain a high electrical conductivity while, at the same time, reduce the thermal conductivity to reach an amorphous solid [147]. In semiconductors, phonon transport plays a significant role in thermal conductivity [148,149]. Increasing phonon scattering has, therefore, proven to be a key strategy to improve the efficiency of thermoelectric materials [150]. This is mainly performed by nanostructuring of the material [151], introducing grains with sizes larger than the mean free path of the charge carriers but smaller than the mean free path of the phonons [152], alloy scattering with additional mass or strain fluctuation [153–155], nanocomposites [156–159], and embedding interfaces by creating texture between the two materials [160].

In thermoelectric materials, the phonon-scattering mechanisms are assessed using models for the total thermal conductivity. Traditional models are from Klemens [161], Holland [162], and Callaway [163]. Impurity scattering, boundary scattering, three-phonon normal process, and Umklapp process are considered in these models, and Matthiessen's rule is employed to determine the overall relaxation time.

The Klemens model has been successfully used to evaluate the contribution of each phase on the lattice thermal conductivity [164,165]. In this model, the thermal conductivity for each type of scattering mechanism is evaluated independently, and the overall thermal conductivity is given by [161]:

$$\kappa_{tot}^{-1} = \sum_i \kappa_i^{-1} \tag{8}$$

For phonon-point defects, the relaxation time is given by [161]:

$$\tau_I = \frac{\Gamma V}{4\pi v_s^3}\omega^4 \tag{9}$$

where v_s is the average sound speed on the material, V is the average atomic volume, and Γ is the mass-fluctuation, phonon-scattering parameter [166]:

$$\Gamma = \frac{\overline{\Delta M^2}}{\overline{M}^2} \tag{10}$$

where $\overline{M} = \frac{\sum_n c_n \sum_i f_{i,n} M_{i,n}}{\sum_n c_n}$, $\overline{\Delta M} = \frac{\sum_n c_n \sum_i f_{i,n} (M_{i,n} - \overline{M_n})^2}{\sum_n c_n}$, $\overline{M_n} = \sum_i f_{i,n} M_{i,n}$, c_n is the stoichiometry of the n-th component and $f_{i,n}$ is the fraction of the i-th element that is presented in the n-th component. Using this formulation, the effect of the material composition can be inferred from the lattice thermal conductivity.

Effective medium approximation, on the other hand, presents a more simplified version of the formula described above. The model incorporates an interface resistance, called Kapitza resistance (R_κ), in series with the inter grain resistance [167]. This model is further developed to consider the shapes, orientations, volume fractions, and thermal conductivities of the phases [160]. For instance, the thermal conductivity of a two-phase material with spherical inclusions is expressed by:

$$\kappa^* = \kappa_m \frac{\kappa_p(1+2\alpha) + 2\kappa_m + 2f\left[\kappa_p(1-\alpha) - \kappa_r\right]}{\kappa_p(1+2\alpha) + 2\kappa_m - f\left[\kappa_p(1-\alpha) - \kappa_r)\right]} \tag{11}$$

where κ_m is the thermal conductivity of the matrix, κ_p is the thermal conductivity of the secondary phase, and f is the volume fraction of the secondary phase. The non-dimensional parameter, α, is the ratio of the Kapitza length, L_κ, and the second phase radius, a:

$$\alpha = \frac{L_\kappa}{a} = \frac{\kappa_m R_\kappa}{a} \tag{12}$$

An even more simple model than that which has been used to describe the scattering in multiphase materials is impedance mismatch [152]. The specific acoustic impedance of a material is the analogue of the electrical impedance for electrical circuits. In this case, the acoustic impedance measures the opposition of a system when acoustic pressure is applied to it and its calculated as:

$$Z = \rho v \tag{13}$$

where ρ is the volumetric density of the medium and v_S is the speed of the sound in the medium. At the interface of two materials, the reflection (r) and transmission (t) energy coefficients are [168]:

$$r = \left[\frac{Z_2 - Z_1}{Z_2 + Z_1}\right]^2, \; t = \frac{4Z_1Z_2}{(Z_1 + Z_2)^2} \tag{14}$$

where Z_1 and Z_2 are the acoustic impedance of the two materials. Figure 6 illustrates phonon transmission and reflection between two dissimilar materials.

Experimentally, impedance mismatch between phases has been shown to reduce the thermal conductivity of the bulk material. The impedance mismatch between the PbTe and PbS rich phases in $(Pb_{0.95}Sn_{0.05}Te)_{1-x}(PbS)_x$ samples led to an inhibition of the heat flow, with the lattice thermal conductivity reaching 0.4 $W \cdot m^{-1} \cdot K^{-1}$ for the sample with 8% PbS, an 80% reduction in the reported values for the bulk material [169].

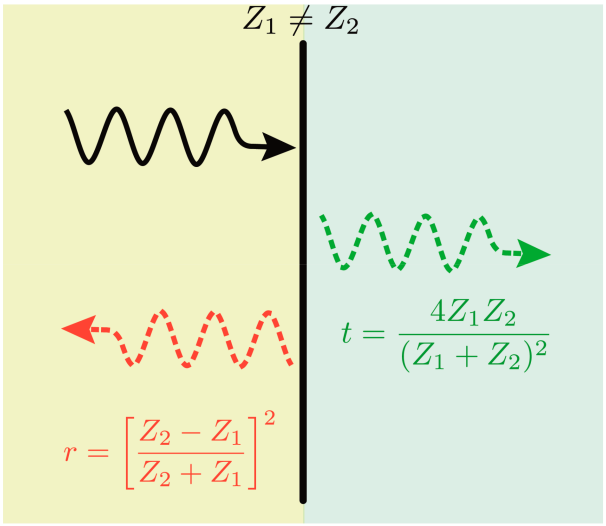

Figure 6. Phonon transmission and reflection due to impedance mismatch.

In general, phonon scattering has proven to be an effective strategy to reduce the lattice thermal conductivity in multiphase lead telluride-based materials [170–173] and bismuth telluride-based [174–176] materials. For instance, nano-engineered multiphase PbTe—x% InSb compounds showed an exceptionally low minimum lattice thermal conductivity of ~0.3 $W \cdot m^{-1} \cdot K^{-1}$ at ~770 K for 4% InSb and consequently a zT value of ~1.83 at 770 K [177]. Even higher zT values of ~2 were observed for $Pb_{(1-x)}Na_xTe_{0.65}S_{0.25}Se_{0.1}$ compounds [30,31], where the combined effects of phonon scattering at nanoprecipitates and the increase in the power factor due to heterogeneous distribution of dopants between phases were recognised to be responsible for the high TE efficiency. Nano and micro-sized precipitates in $Pb_{1-x}Ga_xTe$ (x = 0.01, 0.02, 0.03, and 0.04) compounds have shown a reduction in the lattice thermal conductivity, reaching 1.6 $W \cdot m^{-1} \cdot K^{-1}$. A larger fraction of a secondary phase with high thermal conductivity can increase the total thermal conductivity, reported for PbTe-Ge_x [178]. Five per cent of GeTe reduced the lattice thermal conductivity to 1.1 $W \cdot m^{-1} \cdot K^{-1}$, while a sample with x = 0.2 showed a lattice thermal conductivity similar to the pristine sample.

Adding a secondary phase of TiO_2 to a Bi_2Se_3 host increased the Seebeck coefficient by energy filtering and simultaneously reduced the lattice thermal conductivity by 45% [101]. The lattice thermal conductivity of multiphase half-Heusler $(Hf_{0.6}Zr_{0.4})NiSn_{0.99}Sb_{0.01}$ material was reduced from ~4.5 $W \cdot m^{-1} \cdot K^{-1}$ for the pristine sample to ~2.9 $W \cdot m^{-1} \cdot K^{-1}$ for the sample with 20wt.% of tungsten at 300 K [112]; the combined effects of phonon scattering and energy filtering due to the presence of metallic tungsten improved the zT by 55%.

The lattice thermal conductivity values of several single-phase chalcogenides are compared with their multiphase counterparts in Figure 7. The data for single-phase materials were manually extracted from the Materials Research Laboratory Energy Materials Datamining website [179,180]. This dataset contains information of 573 thermoelectric materials from various combinations of host materials and dopants along with several thermoelectric properties measured experimentally at 300 K, 400 K, and 700 K. Here, we have selected the lattice thermal conductivity of chalcogenides, measured at 300 K. Where the lattice thermal conductivity was not available, its value was evaluated using the Wiedemann–Franz law and the Sommerfeld limit for the Lorenz number [181]. Both the bar and boxplot show that the multiphase materials consistently present lower values of the lattice thermal conductivity. In particular, the boxplot shows that the multiphase materials have, on average, lower values of lattice thermal conductivity.

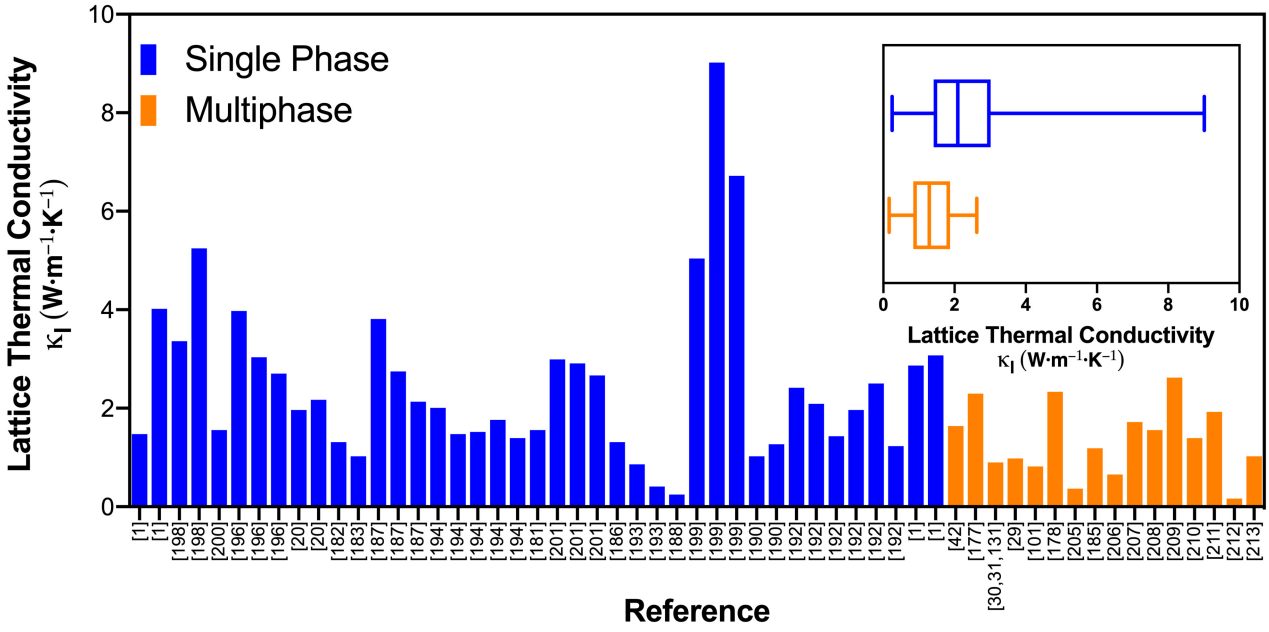

Figure 7. The lattice thermal conductivity of multiphase thermoelectric materials compared with single-phase counterparts; data extracted from [1,20,29–31,42,101,131,177,178,182–213]. The inset shows a boxplot of the same data.

5. Models to Estimate the Transport Properties

In general, multiphase materials can increase phonon scattering, increase the Seebeck coefficient due to energy filtering, and increase electrical conductivity due to modulation doping. These micro and nano effects clearly influence the material on a macroscale. It is, however, of interest to have simplified expressions to predict the behaviour of these materials from the composition and electronic band engineering perspectives. Regarding the thermal conductivity, the effective medium theory allows us to approximate the effective Seebeck coefficient and the electrical conductivity of multiphase materials [214]. There are two main equations to evaluate these properties. The most common equation is the one derived from the usual effective mean theory [215]:

$$\sum_i v_i \frac{\zeta_i - \zeta}{\zeta_i + 2\zeta} = 0 \tag{15}$$

where v_i and ζ_i are the volume fraction and property of phase i, respectively, and ζ is the effective material property. The electrical conductivity can be calculated by setting $\zeta = \sigma$, and the Seebeck coefficient can be calculated by setting $\zeta = S/\sigma$ [216]. The second equation is based on the generalised effective mean theory:

$$\sum_i v_i \frac{\zeta_i^{\frac{1}{t}} - \zeta^{\frac{1}{t}}}{\zeta_i^{\frac{1}{t}} + A \cdot \zeta^{\frac{1}{t}}} = 0 \tag{16}$$

where t is a measure of the grain structure and morphology, and $A = (1 - p_c)/p_c$, where p_c is the percolation threshold. Both parameters can be determined by fitting experimental data, and p_c is estimated from the lattice type and dimensions of the network [217]. The Seebeck coefficient and the conductivity are estimated similar to the previous equation [218].

Recently, models based on electrical networks have been introduced to estimate the electronic properties [214,219,220] and finite element analysis [221]. These latter models divide the material into pixels (for a 2D analysis) or voxels (for a 3D analysis) grids, where each node corresponds to a fraction of the total volume. Each voxel/pixel is required to be larger than the mean free paths of the carriers and phonons so that the transport is diffusive.

Each node is connected to its neighbours by a resistance that is an electric resistance (to calculate the electrical conductivity) and a thermal resistance (to calculate the thermal conductivity) in series with an interface resistance if needed. Following the construction of grids, a nodal analysis will be conducted [222] to determine the temperature and voltage profile of the grids. The Seebeck coefficient is estimated by assigning each node in the electric grid to a local voltage source in series, representing the local Seebeck voltage. By using a Norton equivalent of the voltage source [223], the usual nodal formulation can be applied, and the bulk Seebeck coefficient will be estimated. The general expression is presented as [220]:

$$0 = \sum_{k \neq l} V_{kl} G_{kl} + \sum_{k \neq l} I_{kl} \tag{17}$$

where $V_{k,l}$ is the voltage (or temperature) difference between nodes k and l, $I_{k,l}$ is the current flowing between nodes k and l, and $G_{k,l}$ is the conductivity between nodes k and l. The conductivity will be determined by the local thermoelectric properties of the voxels or pixels:

$$\sigma_{kl}^{-1} = \sigma_k^{-1} + \sigma_l^{-1},\ \kappa_{kl}^{-1} = \kappa_k^{-1} + \kappa_l^{-1} \tag{18}$$

where σ_k, σ_l is the electrical conductivity of nodes k and l, respectively, and κ_k, κ_l is the thermal resistivity of nodes k and l.

The main advantage of this approach is that this linear system of equations can easily be solved by electric circuit solvers, and the results can be directly interpreted by engineers. However, the quantum effects are not approximated by an effective medium theory in this model, and therefore, it provides similar accuracy to the more simple models described earlier [219]. Overall, from a design perspective, these equations suggest that the incorporation of highly conductive phases (both thermally and electrically) results in an overall increase in the conductivity of materials. This effect has been experimentally proven in several materials. Graphene, a zero-bandgap material [224], has been successfully used to create thermoelectric materials with high conductivity [225–227], the electrical conductivity of $CoSb_3$ reached 1.2×10^6 S/m, four times larger than the pristine sample at 300 K [226]. Copper telluride in $Bi_{0.5}Sb_{1.5}Te_3$ [228] and a composite of ZnSb matrix with minority phases of Zn_4Sb_3, Zn_3P_2, and Cu_5Zn_8 [229] have shown higher electrical conductivity. It should be noted that the values of electronic transport properties are greatly dependent on the fabrication methods [230], quality of the raw materials, and oxidisation of the material [231–233].

High-temperature, oxide-based thermoelectric materials have also been shown to benefit from the presence of secondary phases. A multiphase compound of $Ca_3Co_4O_9$, matrimid polymer + Ag, and carbon black [40] showed a reduction in the electrical conductivity compared to the porous $Ca_3Co_4O_9$, while the highly conductive phase of Ag reduced a significant deterioration of conductivity.

6. Magnetic Effects

The effects of magnetism on the performance of thermoelectric materials have been investigated for some time, but with less detailed analysis. The idea of spin-wave scattering and magnon drag was proposed in the middle of the last century, where magnon scattering was shown to contribute to an increase in the Seebeck coefficient [234]. Magnons are bosonic quasiparticles, the quanta associated with spin waves [235]. When a magnetic material is subjected to a temperature gradient, the hotter side contains a higher density of magnons that will diffuse towards the cooler side; this magnon flux "drags" the free charge carriers due to the electron–magnon collisions and gives rise to a second contribution to the Seebeck coefficient, called the magnon thermopower [236]. A hydrodynamical, Galilean based expression for the magnon thermopower is [237]

$$S_{md} = \frac{2}{3} \cdot \frac{C_m}{n_e e} \cdot \frac{1}{1 + \frac{\tau_{em}}{\tau_m}} \tag{19}$$

where C_m is the magnon specific heat capacity per unit volume, τ_m and τ_{em} are, respectively, the transport mean-free time for the electron and magnon–electron collision, e is carrier charge, and n_e is the charge carrier density.

When dealing with magnetism in semiconductors, three main strategies have been proposed to improve the thermoelectric efficiency: (1) optimise thermoelectric properties of magnetic materials using strategies known for non-magnetic materials [43–45,238,239]; (2) introduce a magnetic dopant in a non-magnetic material [46–48,240–243]; (3) introduce a magnetic secondary phase in a non-magnetic material [49,50].

6.1. Magnetic Semiconductors

Examples of magnetic semiconductors are $FeSb_2$ [244,245], MnTe [246–248], $Cr_2Ge_2Te_6$ [249], MgAgSb [250], MnSe [251], and FeSe [252]. Experimental results have shown their potential as thermoelectric materials; for instance, a massive Seebeck coefficient of ~27 mV/K has been reported for $FeSb_2$ (albeit at a low temperature of ~12 K) [253]. It is not easy, however, to establish a causal relationship between magnetism and the Seebeck coefficient. A common method is to check whether a heavily doped sample with a high carrier concentration shows a large value of the Seebeck coefficient [254], because this indicates a possible effect of electron–magnon scattering, which increases the Seebeck coefficient. Fitting mathematical models to the experimental data has also been proposed as a method to identify the magnetic thermopower [255]. Clearly, measuring the transport properties as a function of the magnetic field is the best method to determine the magnetic thermopower [236,256,257].

A spin-dependent Seebeck coefficient can occur in magnetic semiconductors [258]; since the Seebeck coefficients for the two spin channels of spin-up ($S^{\uparrow}$) and spin-down ($S^{\downarrow}$) are not equal, a spin current proportional to the difference between $S^{\uparrow}$ and $S^{\downarrow}$ flows through the magnetic material even in the absence of a charge current [259]. The literature refers to spintronics as the field of study that investigates devices that exploit the properties of electrons spins. In thermoelectricity, this is known as spin caloritronic [260]. This new field of research has attracted the interest of the thermoelectric research community [261–263].

6.2. Magnetic Dopants in Non-Magnetic Semiconductors

Doping non-magnetic thermoelectric materials with magnetic elements has improved the power factor. Magnetic doping of $CuGaTe_2$ with manganese ions (Mn^{2+}) increased the effective mass of the carriers due to the interaction of the magnetic ions and the charge carriers and, consequently, increased the Seebeck coefficient [264]. This effect has also been reported for a Chromium doped Bi_2Te_3 [265]. The negative side effect of magnetic ion dopants is the decrease in the charge carrier mobility that results in a reduction in the electrical conductivity. Overall, the power factor is shown to be increased [266–268].

6.3. Secondary Magnetic Phases

The natural extension of using magnetic elements is to include magnetic phases to enhance the performance of thermoelectric materials [264,269,270]. The magnetic particles of $BaFe_{12}O_{19}$ in $Ba_{0.3}In_{0.3}Co_4Sb_{12}$ formed a magnetic composite; $BaFe_{12}O_{19}$ nanoparticles trap electrons in the ferromagnetic phase due to the spiral motion of the electrons generated by non-uniform spherical magnetic fields. This effectively suppresses the deterioration of thermoelectric efficiency in the intrinsic excitation region [271]. In the paramagnetic phase (at temperatures above the Curie temperature), though, the nanoparticles release the trapped electrons to increase the carrier concentration in the intrinsic excitation. This effect enhances the overall performance of the thermoelectric material.

Coherent magnetic full-Heusler nanoparticles ($Ti(Ni_{4/3}Fe_{2/3})Sn$) in a half-Heusler matrix ($Ti_{0.25}Zr_{0.25}Hf_{0.5}NiSn_{0.975}Sb_{0.025}$) showed significant enhancements of both carrier mobility and the Seebeck coefficient [272]. The magnetic nanoparticles interact with the spin of itinerant carriers, leading to charge localisation (which consequently leads to a decrease in the charge density) and the formation of overlapping bound magnetic polarons (that leads to an increase in mobility).

Interestingly, some magnetic phenomena only occur when the particles are smaller than a certain size [273]. Nanoparticles provide a good platform to take advantage of these magnetic phenomena for the purpose of optimising the thermoelectric performance of materials. If the size of a ferromagnetic nanoparticle is small enough to have only several magnetic domains, it can be magnetised similar to a paramagnet under an external magnetic field, except with a much greater magnetisation. This mechanism is known as superparamagnetism (magnetisation of the nanoparticles can randomly flip direction under the influence of temperature, and they can be magnetised similar to a paramagnet under an external magnetic field [274]). Experimentally, soft magnet transition metals (Fe, Co, or Ni) nanoparticles were embedded in a $Ba_{0.3}In_{0.3}Co_4Sb_{12}$ matrix [275]. The superparamagnetism fluctuations of the nanoparticles gave rise to multiple scattering of electrons and enhanced phonon scattering. These effects increased the overall thermoelectric efficiency of the material.

In general, secondary magnetic phases introduce a new degree of freedom to enhance thermoelectric materials. The effects of magnetism in semiconductors are not fully understood yet, and general expressions for the contribution of the magnon-drag on the Seebeck coefficient are unavailable yet. The need for more experimental and theoretical investigation presents an opportunity for thermoelectricity.

Table 3 summarises the sample composition and fabrication techniques of recent studies that reported magnetic effects in thermoelectric materials.

Table 3. Sample composition, fabrication technique, and corresponding references which studied magnetic effects in thermoelectric materials.

System	Fabrication Method	Type	Ref.
$CuGa_{1-x}Mn_xTe_2$ (x = 0, 0.01, 0.02, and 0.03)	Casting + hand milling + sintering	Magnetic dopant	[264]
$Bi_{2-x}Cr_xTe_3$ (x = 0, 0.01, 0.02, 0.05, and 0.10)	Casting + hand milling + sintering	Magnetic dopant	[265]
$Fe_{3-x}Ti_xSn$ (x = 0, 0.25, 0.5, 0.75)	Casting	Magnetic material	[239]
$Sn_{1.03-x}Mn_xTe$ (x = 0, 0.05, 0.07, and 0.1)	Casting + cold pelletising	Magnetic dopant	[266]
$Ba_{0.3}In_{0.3}Co_4Sb_{12}$ +x $BaFe_{12}O_{19}$) (x = 0.15%, 0.25%, 0.35%, and 0.45%)	Ball milling + sintering	Magnetic phase	[271]
$Ti_{0.25}Zr_{0.25}Hf_{0.5}(Ni,Fe_x)Sn_{0.975}Sb_{0.025}$ (x = 0, 0.05, 0.01, 0.15)	Casting + hand milling + sintering	Magnetic phase	[272]
$Mn_{1-x}Na_xSe$ ($0 \leq x \leq 0.03$)	Ball milling + annealing + hot pressing	Magnetic material	[251]
$FeSb_2$	Hand milling + annealing + hot pressing	Magnetic material	[244]

Figure 8 compares the maximum zT values reported for several single chalcogenides with their multiphase counterparts. The data for single-phase materials were manually extracted from the Materials Research Laboratory Energy Materials Datamining website [179,180]. Both the bar and violin plot show that the multiphase materials consistently present larger values of zT. In particular, the violin plot shows that many single-phase materials have low zT, while the zT for multiphase materials is distributed towards larger values.

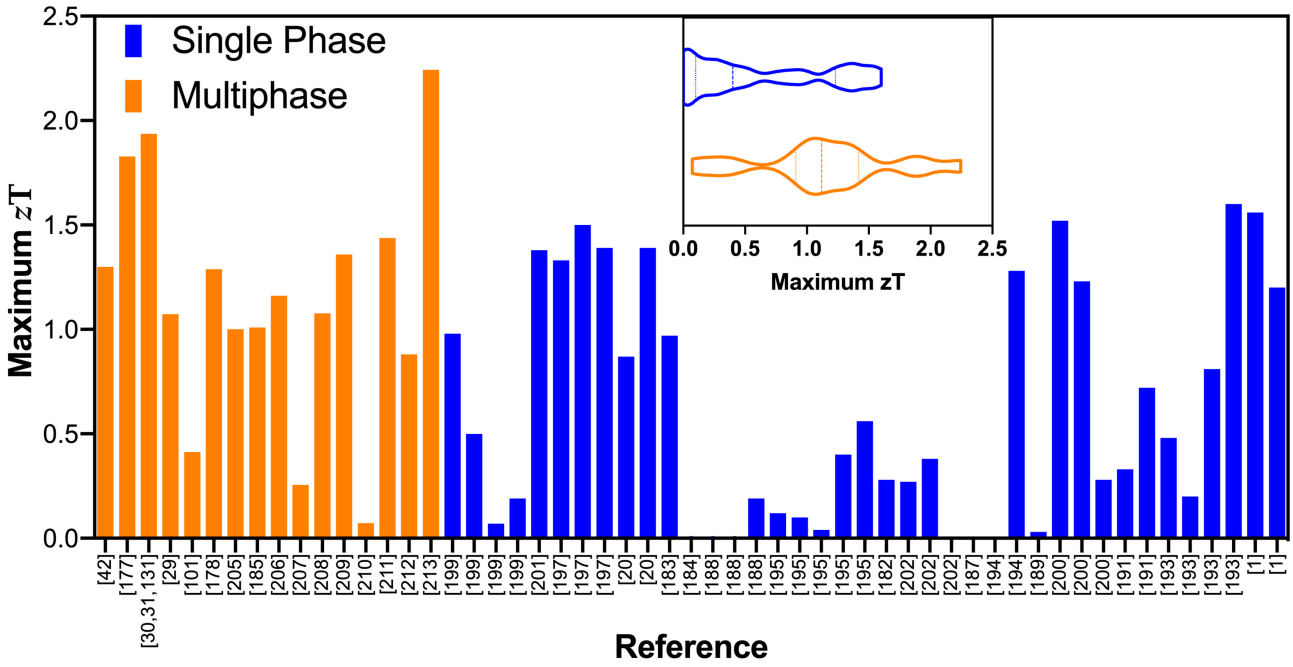

Figure 8. zT values of multiphase thermoelectric materials compared with single-phase counterparts; data extracted from [1,20,29–31,42,101,131,177,178,182–213]. The inset shows the truncated violin plot of the same data, where the dashed line represents the median and dotted lines represent the quartiles.

7. Summary and Outlook

Here, we have reviewed the principal mechanisms and strategies employed to enhance the thermoelectric efficiency of multiphase thermoelectric materials. The interfaces between phases in a material can be utilised to construct potential barriers in the electronic band structure and perform an energy filtering on the charge carriers, where the low energy charge carriers will be filtered/scattered. This can increase the average energy at which the electronic conduction occurs and consequently increase the Seebeck coefficient. The effect of the barrier height can be estimated from the relaxation time approximation from the Boltzmann equation. For a metallic secondary phase, the potential barrier height can be estimated from the work function of the metal and electron affinity of the semiconductor following Schottky's rule. For heterojunctions (two different semiconductors), the potential barrier is proportional to the difference of the electron affinities between the two materials and can be estimated from Anderson's rule. Experimental results have shown that the energy-filtering effect can increase the Seebeck coefficient while decreasing electrical conductivity. The overall result, however, is an increase in the power factor.

Modulation doping is a well-known technique for enhancing the conductivity of semiconductor devices. In this paper, we briefly reviewed the mechanism by which modulation doping is used in multiphase thermoelectric materials.

An increase in phonon scattering due to the presence of secondary phases improves the thermoelectric efficiency of these materials. Secondary phases decrease the relaxation time of the phonons. Traditional models can be employed to verify the effect of a secondary phase on the thermal conductivity of materials. The Klemens model has been used to theoretically explain the reduction in thermal conductivity. The effective medium approximation has been promising in describing the phonon scattering mechanisms of materials with simple structures, such as spherical particles. In an even more simplistic view, for some materials, the transmission and reflection coefficients determined based on the acoustic impedance of the primary and secondary phases can be readily used to evaluate the effect of multiple phases on the reduction of thermal conductivity. Experimentally, a large increase in the zT has been reported with the use of secondary phases.

Mathematical models based on effective medium theory and networks can also estimate the Seebeck coefficient and electrical conductivity of multiphase materials. These models can be used as a tool to evaluate and tune the properties of thermoelectric materials.

The incorporation of magnetic doping elements and secondary phases in thermoelectric materials has introduced new possibilities to enhance their efficiency. The scattering of electrons due to interactions between charge carriers and magnons can contribute to an increase in the Seebeck coefficient. A magnon flux generated from a temperature gradient "drags" the free carriers and contributes positively to the Seebeck coefficient—this effect is called the magnon thermopower. Experimentally, this has proven to be a promising strategy to enhance the thermoelectric properties of several materials.

Overall, multiphase materials have been shown to be instrumental in achieving high thermoelectric efficiency. Multiple phases allow for more degrees of freedom in the materials design as each phase can be finely tuned to improve selected properties of the multiphase material.

Author Contributions: Conceptualization, S.A.Y.; validation, S.A.Y. and R.F.; investigation, R.F.; resources, R.F.; writing—original draft preparation, R.F.; writing—review and editing, S.A.Y.; visualization, R.F.; supervision, S.A.Y.; project administration, S.A.Y.; funding acquisition, S.A.Y. All authors have read and agreed to the published version of the manuscript.

Funding: The work is partially funded by the DTA3 COFUND Marie Skłodowska-Curie PhD Fellowship programme No. 801604.

Institutional Review Board Statement: Not applicable.

Informed Consent Statement: Not applicable.

Acknowledgments: The authors would like to thank the DTA3 COFUND Marie Skłodowska-Curie PhD Fellowship programme for partially funding this work.

Conflicts of Interest: The authors declare no conflict of interest.

References

1. Biswas, K.; He, J.; Blum, I.D.; Wu, C.I.; Hogan, T.P.; Seidman, D.N.; Dravid, V.P.; Kanatzidis, M.G. High-Performance Bulk Thermoelectrics with All-Scale Hierarchical Architectures. *Nature* **2012**, *489*, 414–418. [CrossRef] [PubMed]
2. Vining, C.B. An Inconvenient Truth about Thermoelectrics. *Nat. Mater.* **2009**, *8*, 83–85. [CrossRef]
3. Tritt, T.M.; Boettner, H.; Chen, L. Thermoelectrics: Direct Solar Thermal Energy Conversion. *MRS Bull.* **2008**, *33*, 366–368. [CrossRef]
4. Cutler, M.; Mott, N.F. Observation of Anderson Localization in an Electron Gas. *Phys. Rev.* **1969**, *181*, 1336–1340. [CrossRef]
5. Siemens, M.E.; Li, Q.; Yang, R.; Nelson, K.A.; Anderson, E.H.; Murnane, M.M.; Kapteyn, H.C. Quasi-Ballistic Thermal Transport from Nanoscale Interfaces Observed Using Ultrafast Coherent Soft X-Ray Beams. *Nat. Mater.* **2010**, *9*, 26–30. [CrossRef]
6. Delaire, O.; Ma, J.; Marty, K.; May, A.F.; McGuire, M.A.; Du, M.H.; Singh, D.J.; Podlesnyak, A.; Ehlers, G.; Lumsden, M.D.; et al. Giant Anharmonic Phonon Scattering in PbTe. *Nat. Mater.* **2011**, *10*, 614–619. [CrossRef] [PubMed]
7. Hu, Y.; Zeng, L.; Minnich, A.J.; Dresselhaus, M.S.; Chen, G. Spectral Mapping of Thermal Conductivity through Nanoscale Ballistic Transport. *Nat. Nanotechnol.* **2015**, *10*, 701–706. [CrossRef]
8. Hu, L.; Zhang, Y.; Wu, H.; Li, J.; Li, Y.; McKenna, M.; He, J.; Liu, F.; Pennycook, S.J.; Zeng, X. Entropy Engineering of SnTe: Multi-Principal-Element Alloying Leading to Ultralow Lattice Thermal Conductivity and State-of-the-Art Thermoelectric Performance. *Adv. Energy Mater.* **2018**, *8*, 1802116. [CrossRef]
9. Fan, Z.; Wang, H.; Wu, Y.; Liu, X.J.; Lu, Z.P. Thermoelectric High-Entropy Alloys with Low Lattice Thermal Conductivity. *RSC Adv.* **2016**, *6*, 52164–52170. [CrossRef]
10. Wei, P.C.; Liao, C.N.; Wu, H.J.; Yang, D.; He, J.; Biesold-McGee, G.V.; Liang, S.; Yen, W.T.; Tang, X.; Yeh, J.W.; et al. Thermodynamic Routes to Ultralow Thermal Conductivity and High Thermoelectric Performance. *Adv. Mater.* **2020**, *32*, e1906457. [CrossRef]
11. Joshi, G.; Lee, H.; Lan, Y.; Wang, X.; Zhu, G.; Wang, D.; Gould, R.W.; Cuff, D.C.; Tang, M.Y.; Dresselhaus, M.S.; et al. Enhanced Thermoelectric Figure-of-Merit in Nanostructured p-Type Silicon Germanium Bulk Alloys. *Nano Lett.* **2008**, *8*, 4670–4674. [CrossRef]
12. Wang, X.W.; Lee, H.; Lan, Y.C.; Zhu, G.H.; Joshi, G.; Wang, D.Z.; Yang, J.; Muto, A.J.; Tang, M.Y.; Klatsky, J.; et al. Enhanced Thermoelectric Figure of Merit in Nanostructured N-Type Silicon Germanium Bulk Alloy. *Appl. Phys. Lett.* **2008**, *93*, 193121. [CrossRef]
13. Lan, Y.C.; Minnich, A.J.; Chen, G.; Ren, Z.F. Enhancement of Thermoelectric Figure-of-Merit by a Bulk Nanostructuring Approach. *Adv. Funct. Mater.* **2010**, *20*, 357–376. [CrossRef]

14. Ren, Z.; Poudel, B.E.D.; Chen, G.; Lan, Y.; Wang, D.; Hao, Q.; Dresselhaus, M.; Ma, Y.I.; Yan, X.; Chen, X.; et al. Methods for High Figure-of-Merit in Nanostructured Thermoelectric Materials. U.S. Patent 8865995B2, 21 October 2014.
15. Yu, B.; Zebarjadi, M.; Wang, H.; Lukas, K.; Wang, H.; Wang, D.; Opeil, C.; Dresselhaus, M.; Chen, G.; Ren, Z. Enhancement of Thermoelectric Properties by Modulation-Doping in Silicon Germanium Alloy Nanocomposites. *Nano Lett.* **2012**, *12*, 2077–2082. [CrossRef]
16. Wang, H.; Cao, X.; Takagiwa, Y.; Snyder, G.J. Higher Mobility in Bulk Semiconductors by Separating the Dopants from the Charge-Conducting Band—A Case Study of Thermoelectric PbSe. *Mater. Horiz.* **2015**, *2*, 323–329. [CrossRef]
17. Thesberg, M.; Pourfath, M.; Kosina, H.; Neophytou, N. The Influence of Non-Idealities on the Thermoelectric Power Factor of Nanostructured Superlattices. *J. Appl. Phys.* **2015**, *118*, 224301. [CrossRef]
18. Rhyee, J.S.; Lee, K.H.; Lee, S.M.; Cho, E.; Kim, S.I.; Lee, E.; Kwon, Y.S.; Shim, J.H.; Kotliar, G. Peierls Distortion as a Route to High Thermoelectric Performance in In(4)Se(3-Delta) Crystals. *Nature* **2009**, *459*, 965–968. [CrossRef] [PubMed]
19. Zhou, J.; Yang, R.; Chen, G.; Dresselhaus, M.S. Optimal Bandwidth for High Efficiency Thermoelectrics. *Phys. Rev. Lett.* **2011**, *107*, 226601. [CrossRef] [PubMed]
20. Heremans, J.P.; Jovovic, V.; Toberer, E.S.; Saramat, A.; Kurosaki, K.; Charoenphakdee, A.; Yamanaka, S.; Snyder, G.J. Enhancement of Thermoelectric Efficiency in PbTe by Distortion of the Electronic Density of States. *Science* **2008**, *321*, 554–557. [CrossRef]
21. Mao, J.; Liu, Z.; Ren, Z. Size Effect in Thermoelectric Materials. *npj Quant. Mater.* **2016**, *1*, 16028. [CrossRef]
22. Zeng, G.; Bowers, J.E.; Zide, J.M.O.; Gossard, A.C.; Kim, W.; Singer, S.; Majumdar, A.; Singh, R.; Bian, Z.; Zhang, Y.; et al. ErAs:InGaAs/InGaAlAs Superlattice Thin-Film Power Generator Array. *Appl. Phys. Lett.* **2006**, *88*, 113502. [CrossRef]
23. Zebarjadi, M.; Joshi, G.; Zhu, G.; Yu, B.; Minnich, A.; Lan, Y.; Wang, X.; Dresselhaus, M.; Ren, Z.; Chen, G. Power Factor Enhancement by Modulation Doping in Bulk Nanocomposites. *Nano Lett.* **2011**, *11*, 2225–2230. [CrossRef] [PubMed]
24. Hou, Q.R.; Gu, B.F.; Chen, Y.B.; He, Y.J.; Sun, J.L. Enhancement of the Thermoelectric Power Factor of MnSi1.7 Film by Modulation Doping of Al and Cu. *Appl. Phys. A Mater.* **2014**, *114*, 943–949. [CrossRef]
25. Gu, Y.; Ai, W.; Zhao, Y.; Pan, L.; Lu, C.; Zong, P.; Hu, X.; Xu, Z.; Wang, Y. Remarkable Thermoelectric Property Enhancement in Cu_2SnS_3–$CuCo_2S_4$ Nanocomposites via 3D Modulation Doping. *J. Mater. Chem. A* **2021**, *9*, 16928–16935. [CrossRef]
26. Wu, L.H.; Li, X.; Wang, S.Y.; Zhang, T.S.; Yang, J.; Zhang, W.Q.; Chen, L.D.; Yang, J.H. Resonant Level-Induced High Thermoelectric Response in Indium-Doped GeTe. *NPG Asia Mater.* **2017**, *9*, e343. [CrossRef]
27. Zhang, Q.Y.; Wang, H.; Liu, W.S.; Wang, H.Z.; Yu, B.; Zhang, Q.; Tian, Z.T.; Ni, G.; Lee, S.; Esfarjani, K.; et al. Enhancement of Thermoelectric Figure-of-Merit by Resonant States of Aluminium Doping in Lead Selenide. *Energy Environ. Sci.* **2012**, *5*, 5246–5251. [CrossRef]
28. Kim, R.; Lundstrom, M.S. Computational Study of Energy Filtering Effects in One-Dimensional Composite Nano-Structures. *J. Appl. Phys.* **2012**, *111*, 024508. [CrossRef]
29. Yamini, A.; Li, T.; Mitchell, D.R.G.; Cairney, J.M. Elemental Distributions within Multiphase Quaternary Pb Chalcogenide Thermoelectric Materials Determined through Three-Dimensional Atom Probe Tomography. *Nano Energy* **2016**, *26*, 157–163. [CrossRef]
30. Aminorroaya Yamini, S.; Mitchell, D.R.; Avdeev, M. In Situ Characterisation of Nanostructured Multiphase Thermoelectric Materials at Elevated Temperatures. *Phys. Chem. Chem. Phys.* **2016**, *18*, 32814–32819. [CrossRef]
31. Byrnes, J.; Mitchell, D.R.G.; Yamini, S.A. Thermoelectric Performance of Thermally Aged Nanostructured Bulk Materials-a Case Study of Lead Chalcogenides. *Mater. Today Phys.* **2020**, *13*, 100190. [CrossRef]
32. Gao, Y.-H.; Chen, H.; Liu, N.; Zhang, R.-Z. Criteria for Power Factor Improvement in Thermoelectric Composite. *Results Phys.* **2018**, *11*, 915–919. [CrossRef]
33. Hu, Q.; Qiu, W.; Chen, L.; Chen, J.; Yang, L.; Tang, J. Realize High Thermoelectric Properties in N-Type $Bi_2Te_{2.7}Se_{0.3}/Y_2O_3$ Nanocomposites by Constructing Heterointerfaces. *ACS Appl. Mater. Interfaces* **2021**, *13*, 38526–38533. [CrossRef] [PubMed]
34. Pham, A.T.T.; Vo, P.T.N.; Ta, H.K.T.; Lai, H.T.; Tran, V.C.; Doan, T.L.H.; Duong, A.T.; Lee, C.T.; Nair, P.K.; Zulueta, Y.A.; et al. Improved Thermoelectric Power Factor Achieved by Energy Filtering in ZnO: Mg/ZnO Hetero-Structures. *Thin Solid Films* **2021**, *721*, 138537. [CrossRef]
35. Park, W.; Hwang, H.; Kim, S.; Park, S.; Jang, K.-S. Optimized Thermoelectric Performance of Carbon Nanoparticle–Carbon Nanotube Heterostructures by Tuning Interface Barrier Energy. *ACS Appl. Mater. Interfaces* **2021**, *13*, 7208–7215. [CrossRef] [PubMed]
36. Lee, M.H.; Yun, J.H.; Kim, G.; Lee, J.E.; Park, S.-D.; Reith, H.; Schierning, G.; Nielsch, K.; Ko, W.; Li, A.-P.; et al. Synergetic Enhancement of Thermoelectric Performance by Selective Charge Anderson Localization–Delocalization Transition in n-Type Bi-Doped PbTe/Ag_2Te Nanocomposite. *ACS Nano* **2019**, *13*, 3806–3815. [CrossRef]
37. Wang, C.; Lin, S.; Chen, H.; Zhao, Y.; Zhao, L.; Wang, H.; Huo, D.; Chen, X. Thermoelectric Performance of $Si_{80}Ge_{20-x}Sb_x$ Based Multiphase Alloys with Inhomogeneous Dopant Distribution. *Energy Convers. Manag.* **2015**, *94*, 331–336. [CrossRef]
38. Wu, D.; Pei, Y.; Wang, Z.; Wu, H.; Huang, L.; Zhao, L.-D.; He, J. Significantly Enhanced Thermoelectric Performance in N-Type Heterogeneous BiAgSeS Composites. *Adv. Funct. Mater.* **2014**, *24*, 7763–7771. [CrossRef]
39. Ahmad, K.; Wan, C.; Al-Eshaikh, M.A.; Kadachi, A.N. Enhanced Thermoelectric Performance of Bi_2Te_3 Based Graphene Nanocomposites. *Appl. Surf. Sci.* **2019**, *474*, 2–8. [CrossRef]
40. Wolf, M.; Menekse, K.; Mundstock, A.; Hinterding, R.; Nietschke, F.; Oeckler, O.; Feldhoff, A. Low Thermal Conductivity in Thermoelectric Oxide-Based Multiphase Composites. *J. Electron. Mater.* **2019**, *48*, 7551–7561. [CrossRef]

41. Manimozhi, T.; Kavirajan, S.; Harish, S.; Archana, J.; Kamala Bharathi, K.; Senthil Kumar, E.; Navaneethan, M. Anharmonicity and Low-Thermal Conductivity in the Multi-Phase Composition of $Cu_3Bi_{0.75}Sb_{0.25}S_3$. *Mater. Lett.* **2021**, *304*, 130399. [CrossRef]
42. Wang, Z.; Wang, G.; Wang, R.; Zhou, X.; Chen, Z.; Yin, C.; Tang, M.; Hu, Q.; Tang, J.; Ang, R. Ga-Doping-Induced Carrier Tuning and Multiphase Engineering in n-Type PbTe with Enhanced Thermoelectric Performance. *ACS Appl. Mater. Interfaces* **2018**, *10*, 22401–22407. [CrossRef]
43. Sun, P.; Oeschler, N.; Johnsen, S.; Iversen, B.B.; Steglich, F. Thermoelectric Properties of the Narrow-Gap Semiconductors $FeSb_2$ and $RuSb_2$: A Comparative Study. *J. Phys. Conf. Ser.* **2009**, *150*, 012049. [CrossRef]
44. Sun, Y.; Canulescu, S.; Sun, P.J.; Steglich, F.; Pryds, N.; Schou, J.; Iversen, B.B. Growth and Thermoelectric Properties of $FeSb_2$ Films Produced by Pulsed Laser Deposition. *Appl. Phys. A Mater.* **2011**, *104*, 883–887. [CrossRef]
45. Tsujii, N.; Mori, T.; Isoda, Y. Phase Stability and Thermoelectric Properties of $CuFeS_2$-Based Magnetic Semiconductor. *J. Electron. Mater.* **2014**, *43*, 2371–2375. [CrossRef]
46. Motohashi, T.; Naujalis, E.; Ueda, R.; Isawa, K.; Karppinen, M.; Yamauchi, H. Simultaneously Enhanced Thermoelectric Power and Reduced Resistivity of $NaxCo_2O_4$ by Controlling Na Nonstoichiometry. *Appl. Phys. Lett.* **2001**, *79*, 1480–1482. [CrossRef]
47. Wen, Q.; Chang, C.; Pan, L.; Li, X.T.; Yang, T.; Guo, H.H.; Wang, Z.H.; Zhang, J.; Xu, F.; Zhang, Z.D.; et al. Enhanced Thermoelectric Performance of BiCuSeO by Increasing Seebeck Coefficient through Magnetic Ion Incorporation. *J. Mater. Chem. A* **2017**, *5*, 13392–13399. [CrossRef]
48. Xiao, C.; Li, K.; Zhang, J.J.; Tong, W.; Liu, Y.W.; Li, Z.; Huang, P.C.; Pan, B.C.; Su, H.B.; Xie, Y. Magnetic Ions in Wide Band Gap Semiconductor Nanocrystals for Optimized Thermoelectric Properties. *Mater. Horiz.* **2014**, *1*, 81–86. [CrossRef]
49. Liu, K.G.; Li, J. Thermoelectric Properties of Bulk $FeSb_2$ and the Composite of $FeSb_2$ and $CoSb_3$ Prepared by Sintering. *Appl. Mech. Mater.* **2011**, *71–78*, 3741–3744. [CrossRef]
50. Tan, G.; Shi, F.; Hao, S.; Chi, H.; Bailey, T.P.; Zhao, L.D.; Uher, C.; Wolverton, C.; Dravid, V.P.; Kanatzidis, M.G. Valence Band Modification and High Thermoelectric Performance in SnTe Heavily Alloyed with MnTe. *J. Am. Chem. Soc.* **2015**, *137*, 11507–11516. [CrossRef] [PubMed]
51. Hébert, S.; Daou, R.; Maignan, A.; Das, S.; Banerjee, A.; Klein, Y.; Bourgès, C.; Tsujii, N.; Mori, T. Thermoelectric Materials Taking Advantage of Spin Entropy: Lessons from Chalcogenides and Oxides. *Sci. Technol. Adv. Mater.* **2021**, *22*, 583–596. [CrossRef] [PubMed]
52. Xing, L.; Cui, W.; Sang, X.; Hu, F.; Wei, P.; Zhu, W.; Nie, X.; Zhang, Q.; Zhao, W. Enhanced Thermoelectric Performance and Atomic-Resolution Interfacial Structures in BiSbTe Thermo-Electro-Magnetic Nanocomposites Incorporating Magnetocaloric LaFeSi Nanoparticles. *J. Mater.* **2021**, *7*, 998–1006. [CrossRef]
53. Ioffe, A.F.; Stil'bans, L.S.; Iordanishvili, E.K.; Stavitskaya, T.S.; Gelbtuch, A.; Vineyard, G. Semiconductor Thermoelements and Thermoelectric Cooling. *Phys. Today* **1959**, *12*, 42. [CrossRef]
54. Popescu, A.; Woods, L.M.; Martin, J.; Nolas, G.S. Model of Transport Properties of Thermoelectric Nanocomposite Materials. *Phys. Rev. B* **2009**, *79*, 205302. [CrossRef]
55. Medlin, D.L.; Snyder, G.J. Interfaces in Bulk Thermoelectric Materials: A Review for Current Opinion in Colloid and Interface Science. *Curr. Opin. Colloid Interface Sci.* **2009**, *14*, 226–235. [CrossRef]
56. Heremans, J.P.; Thrush, C.M.; Morelli, D.T. Thermopower Enhancement in Lead Telluride Nanostructures. *Phys. Rev. B* **2004**, *70*, 115334. [CrossRef]
57. Kishimoto, K.; Yamamoto, K.; Koyanagi, T. Influences of Potential Barrier Scattering on the Thermoelectric, Properties of Sintered n-Type PbTe with a Small Grain Size. *Jpn. J. Appl. Phys.* **2003**, *42*, 501–508. [CrossRef]
58. Hu, Q.J.; Zhang, Y.; Zhang, Y.W.; Li, X.J.; Song, H.Z. High Thermoelectric Performance in Cu_2Se/CDs Hybrid Materials. *J. Alloy. Compd.* **2020**, *813*, 152204. [CrossRef]
59. Shakouri, A.; Lee, E.Y.; Smith, D.L.; Narayanamurti, V.; Bowers, J. Thermoelectric Effects in Submicron Heterostructure Barriers. *Microscale Thermophys. Eng.* **1998**, *2*, 37–47. [CrossRef]
60. Bahk, J.H.; Bian, Z.X.; Shakouri, A. Electron Energy Filtering by a Nonplanar Potential to Enhance the Thermoelectric Power Factor in Bulk Materials. *Phys. Rev. B* **2013**, *87*, 075204. [CrossRef]
61. Rowe, D.M.; Min, G. Multiple Potential Barriers as a Possible Mechanism to Increase the Seebeck Coefficient and Electrical Power Factor. *AIP Conf. Proc.* **1994**, *316*, 339–342.
62. Whitlow, L.W.; Hirano, T. Superlattice Applications to Thermoelectricity. *J. Appl. Phys.* **1995**, *78*, 5460–5466. [CrossRef]
63. Zianni, X.; Narducci, D. Parametric Modeling of Energy Filtering by Energy Barriers in Thermoelectric Nanocomposites. *J. Appl. Phys.* **2015**, *117*, 035102. [CrossRef]
64. Ziman, J.M. *Electrons and Phonons: The Theory of Transport Phenomena in Solids*; Oxford University Press: Oxford, UK, 2001; ISBN 978-0-19-170993-7.
65. Jeong, C.; Kim, R.; Luisier, M.; Datta, S.; Lundstrom, M. On Landauer versus Boltzmann and Full Band versus Effective Mass Evaluation of Thermoelectric Transport Coefficients. *J. Appl. Phys.* **2010**, *107*, 023707. [CrossRef]
66. Faleev, S.V.; Leonard, F. Theory of Enhancement of Thermoelectric Properties of Materials with Nanoinclusions. *Phys. Rev. B* **2008**, *77*, 214304. [CrossRef]
67. Gayner, C.; Amouyal, Y. Energy Filtering of Charge Carriers: Current Trends, Challenges, and Prospects for Thermoelectric Materials. *Adv. Funct. Mater.* **2019**, *30*, 1901789. [CrossRef]

68. Singha, A.; Muralidharan, B. Incoherent Scattering Can Favorably Influence Energy Filtering in Nanostructured Thermoelectrics. *Sci. Rep.* **2017**, *7*, 7879. [CrossRef] [PubMed]
69. Narducci, D.; Selezneva, E.; Cerofolini, G.; Frabboni, S.; Ottaviani, G. Impact of Energy Filtering and Carrier Localization on the Thermoelectric Properties of Granular Semiconductors. *J. Solid State Chem.* **2012**, *193*, 19–25. [CrossRef]
70. Zhang, D.; Lei, J.; Guan, W.; Ma, Z.; Wang, C.; Zhang, L.; Cheng, Z.; Wang, Y. Enhanced Thermoelectric Performance of BiSbTe Alloy: Energy Filtering Effect of Nanoprecipitates and the Effect of SiC Nanoparticles. *J. Alloys Compd.* **2019**, *784*, 1276–1283. [CrossRef]
71. Liu, S.Q.; Kong, J.H.; Chen, H.M.; He, C.B. Interfacial Energy Barrier Tuning for Enhanced Thermoelectric Performance of PEDOT Nanowire/SWNT/PEDOT:PSS Ternary Composites. *ACS Appl. Energy Mater.* **2019**, *2*, 8843–8850. [CrossRef]
72. Jiang, X.Y.; Zhang, Q.K.; Deng, S.P.; Zhou, B.; Wang, B.; Chen, Z.Q.; Qi, N.; Tang, X.F. Enhanced Thermoelectric Performance of Polythiophene/Carbon Nanotube-Based Composites. *J. Electron. Mater.* **2020**, *49*, 2371–2380. [CrossRef]
73. An, H.; Pusko, M.; Chun, D.; Park, S.; Moon, J. In-Situ Synthesis of Flexible Hybrid Composite Films for Improved Thermoelectric Performance. *Chem. Eng. J.* **2019**, *357*, 547–558. [CrossRef]
74. Zhang, Z.; Zhao, W.; Zhu, W.; Ma, S.; Li, C.; Mu, X.; Wei, P.; Nie, X.; Zhang, Q.; Zhao, W. Preparation and Thermoelectric Performance of $BaTiO_3/Bi_{0.5}Sb_{1.5}Te_3$ Composite Materials. *J. Electron. Mater.* **2020**, *49*, 2794–2801. [CrossRef]
75. Jiang, Q.; Li, S.; Luo, Y.; Xin, J.; Li, S.; Li, W.; Zhao, G.; Yang, J. Ecofriendly Highly Robust Ag_8SiSe_6-Based Thermoelectric Composites with Excellent Performance Near Room Temperature. *ACS Appl. Mater. Interfaces* **2020**, *12*, 54653–54661. [CrossRef] [PubMed]
76. Cho, H.; Back, S.Y.; Yun, J.H.; Byeon, S.; Jin, H.; Rhyee, J.S. Thermoelectric Properties and Low-Energy Carrier Filtering by Mo Microparticle Dispersion in an n-Type $(CuI)_{0.003}Bi_2(Te,Se)_3$ Bulk Matrix. *ACS Appl. Mater. Interfaces* **2020**, *12*, 38076–38084. [CrossRef] [PubMed]
77. Li, X.X.; Yu, Z.K.; Zhou, H.B.; Yang, F.; Zhong, F.; Mao, X.H.; Li, B.Z.; Xin, H.; Gao, C.M.; Wang, L. Promoting the Thermoelectric Performance of Single-Walled Carbon Nanotubes by Inserting Discotic Liquid-Crystal Molecules. *ACS Sustain. Chem. Eng.* **2021**, *9*, 1891–1898. [CrossRef]
78. Davies, J.H. *The Physics of Low-Dimensional Semiconductors: An Introduction*, 1st ed.; Cambridge University Press: Cambridge, UK, 1997; ISBN 978-0-521-48148-9.
79. Liu, Y.; Guo, J.; Zhu, E.; Liao, L.; Lee, S.J.; Ding, M.; Shakir, I.; Gambin, V.; Huang, Y.; Duan, X. Approaching the Schottky-Mott Limit in van Der Waals Metal-Semiconductor Junctions. *Nature* **2018**, *557*, 696–700. [CrossRef]
80. Vashaee, D.; Shakouri, A. Improved Thermoelectric Power Factor in Metal-Based Superlattices. *Phys. Rev. Lett.* **2004**, *92*, 106103. [CrossRef]
81. Liu, M.; Qin, X.Y. Enhanced Thermoelectric Performance through Energy-Filtering Effects in Nanocomposites Dispersed with Metallic Particles. *Appl. Phys. Lett.* **2012**, *101*, 132103. [CrossRef]
82. Heremans, J.P.; Thrush, C.M.; Morelli, D.T. Thermopower Enhancement in PbTe with Pb Precipitates. *J. Appl. Phys.* **2005**, *98*, 063703. [CrossRef]
83. Ko, D.K.; Kang, Y.; Murray, C.B. Enhanced Thermopower via Carrier Energy Filtering in Solution-Processable Pt-Sb_2Te_3 Nanocomposites. *Nano Lett.* **2011**, *11*, 2841–2844. [CrossRef]
84. Zhou, Y.; Zhang, M.Y.; Liang, S. Improved Thermoelectric Performance of Cu_2O-Cr/Sn Composite Powder. *Chem. Phys. Lett.* **2021**, *777*, 138722. [CrossRef]
85. Gao, L.; Wang, S.; Liu, R.; Zha, X.; Sun, N.; Wang, S.; Wang, J.; Fu, G. Enhanced Thermoelectric Performance of CdO: Ag Nanocomposites. *Dalton Trans.* **2016**, *45*, 12215–12220. [CrossRef] [PubMed]
86. Milnes, A.G.; Feucht, D.L. *Heterojunctions and Metal Semiconductor Junctions*; Elsevier: Amsterdam, The Netherlands, 1972; ISBN 978-0-12-498050-1.
87. Mayergoyz, I.D. Solution of the Nonlinear Poisson Equation of Semiconductor Device Theory. *J. Appl. Phys.* **1986**, *59*, 195–199. [CrossRef]
88. Wu, H.J.; Carrete, J.; Zhang, Z.Y.; Qu, Y.Q.; Shen, X.T.; Wang, Z.; Zhao, L.D.; He, J.Q. Strong Enhancement of Phonon Scattering through Nanoscale Grains in Lead Sulfide Thermoelectrics. *NPG Asia Mater.* **2014**, *6*, e108. [CrossRef]
89. Seto, J.Y.W. The Electrical Properties of Polycrystalline Silicon Films. *J. Appl. Phys.* **1975**, *46*, 5247–5254. [CrossRef]
90. Taylor, W.E.; Odell, N.H.; Fan, H.Y. Grain Boundary Barriers in Germanium. *Phys. Rev.* **1952**, *88*, 867–875. [CrossRef]
91. Zhou, Z.W.; Yang, J.Y.; Jiang, Q.H.; Zhang, D.; Xin, J.W.; Li, X.; Ren, Y.Y.; He, X. Thermoelectric Performance of SnTe with ZnO Carrier Compensation, Energy Filtering, and Multiscale Phonon Scattering. *J. Am. Ceram. Soc.* **2017**, *100*, 5723–5730. [CrossRef]
92. Dou, Y.C.; Qin, X.Y.; Li, D.; Li, L.L.; Zou, T.H.; Wang, Q.Q. Enhanced Thermopower and Thermoelectric Performance through Energy Filtering of Carriers in $(Bi_2Te_3)_{(0.2)}(Sb_2Te_3)_{(0.8)}$ Bulk Alloy Embedded with Amorphous SiO_2 Nanoparticles. *J. Appl. Phys.* **2013**, *114*, 7. [CrossRef]
93. Fang, T.; Li, X.; Hu, C.; Zhang, Q.; Yang, J.; Zhang, W.; Zhao, X.; Singh, D.J.; Zhu, T. Complex Band Structures and Lattice Dynamics of Bi_2Te_3-Based Compounds and Solid Solutions. *Adv. Funct. Mater.* **2019**, *29*, 1900677. [CrossRef]
94. Li, Y.; Dou, Y.; Qin, X.; Zhang, J.; Xin, H.; Li, D.; Song, C.; Zou, T.; Liu, Y.; Li, C. Enhanced Thermoelectric Figure of Merit in P-Type β-$Zn_4Sb_3/Bi_{0.4}Sb_{1.6}Te_3$ Nanocomposites. *RSC Adv.* **2016**, *6*, 12243–12248. [CrossRef]
95. Nguyen, T.H.; Enju, J.; Ono, T. Enhancement of Thermoelectric Properties of Bismuth Telluride Composite with Gold Nano-Particles Inclusions Using Electrochemical Co-Deposition. *J. Electrochem. Soc.* **2019**, *166*, D508. [CrossRef]

96. Madavali, B.; Kim, H.S.; Lee, K.H.; Hong, S.J. Enhanced Seebeck Coefficient by Energy Filtering in Bi-Sb-Te Based Composites with Dispersed Y_2O_3 Nanoparticles. *Intermetallics* **2017**, *82*, 68–75. [CrossRef]
97. Ravich, I.I. *Semiconducting Lead Chalcogenide*; Monographs in Semiconductor Physics; Springer: New York, NY, USA, 1970; ISBN 978-1-4684-8609-4.
98. Zou, T.; Qin, X.; Zhang, Y.; Li, X.; Zeng, Z.; Li, D.; Zhang, J.; Xin, H.; Xie, W.; Weidenkaff, A. Enhanced Thermoelectric Performance of β-Zn_4Sb_3 Based Nanocomposites through Combined Effects of Density of States Resonance and Carrier Energy Filtering. *Sci. Rep.* **2015**, *5*, 17803. [CrossRef] [PubMed]
99. Xiong, Z.; Chen, X.; Zhao, X.; Bai, S.; Huang, X.; Chen, L. Effects of Nano-TiO_2 Dispersion on the Thermoelectric Properties Offilled-Skutterudite $Ba_{0.22}Co_4Sb_{12}$. *Solid State Sci.* **2009**, *11*, 1612–1616. [CrossRef]
100. Dette, C.; Perez-Osorio, M.A.; Kley, C.S.; Punke, P.; Patrick, C.E.; Jacobson, P.; Giustino, F.; Jung, S.J.; Kern, K. TiO_2 Anatase with a Bandgap in the Visible Region. *Nano Lett.* **2014**, *14*, 6533–6538. [CrossRef]
101. Yang, Y.-X.; Wu, Y.-H.; Zhang, Q.; Cao, G.-S.; Zhu, T.-J.; Zhao, X.-B. Enhanced Thermoelectric Performance of Bi_2Se_3/TiO_2 Composite. *Rare Met.* **2020**, *39*, 887–894. [CrossRef]
102. Ou, C.; Hou, J.; Wei, T.-R.; Jiang, B.; Jiao, S.; Li, J.-F.; Zhu, H. High Thermoelectric Performance of All-Oxide Heterostructures with Carrier Double-Barrier Filtering Effect. *NPG Asia Mater.* **2015**, *7*, e182. [CrossRef]
103. Yang, X.; Chen, S.; Zhang, H.; Lv, F.; Fan, W.; Wang, W.; Munir, Z.A. Thermoelectric Properties and Transport Mechanism of Pure and Bi-Doped SiNWs-Mg_2Si. *Phys. Status Solidi A Appl. Mater. Sci.* **2018**, *215*, 1700742. [CrossRef]
104. Hu, Q.; Wang, K.; Zhang, Y.; Li, X.; Song, H. Enhanced Thermoelectric Properties of Nano SiC Dispersed $Bi_2Sr_2Co_2Oy$ Ceramics. *Mater. Res. Express* **2018**, *5*, 045510. [CrossRef]
105. Zhou, Z.; Li, J.; Fan, Y.; Zhang, Q.; Lu, X.; Fan, S.; Kikuchi, K.; Nomura, N.; Kawasaki, A.; Wang, L.; et al. Uniform Dispersion of SiC in Yb-Filled Skutterudite Nanocomposites with High Thermoelectric and Mechanical Performance. *Scr. Mater.* **2019**, *162*, 166–171. [CrossRef]
106. Zhang, W.; Zhu, K.; Liu, J.; Wang, J.; Yan, K.; Liu, P.; Wang, Y. Enhanced Thermoelectric Properties of Nano-SiC Dispersed $NaCo_2O_4$ Composites. *Funct. Mater. Lett.* **2019**, *12*, 1950009. [CrossRef]
107. Xia, Y.; Park, J.; Zhou, F.; Ozoliņš, V. High Thermoelectric Power Factor in Intermetallic CoSi Arising from Energy Filtering of Electrons by Phonon Scattering. *Phys. Rev. Appl.* **2019**, *11*, 024017. [CrossRef]
108. Ahmad, S.; Basu, R.; Sarkar, P.; Singh, A.; Bohra, A.; Bhattacharya, S.; Bhatt, R.; Meshram, K.N.; Samanta, S.; Bhatt, P.; et al. Enhanced Thermoelectric Figure-of-Merit of p-Type SiGe through TiO_2 Nanoinclusions and Modulation Doping of Boron. *Materialia* **2018**, *4*, 147–156. [CrossRef]
109. Felizco, J.C.; Uenuma, M.; Fujii, M.N.; Uraoka, Y. Improved Thermoelectric Power Factor of InGaZnO/SiO Thin Film Transistor via Gate-Tunable Energy Filtering. *IEEE Electron Device Lett.* **2021**, *42*, 1236–1239. [CrossRef]
110. Solá, F.; Dynys, F.W. Probing the Mechanical Properties and Microstructure of WSi2/SixGe1−x Multiphase Thermoelectric Material by Nanoindentation, Electron and Focused Ion Beam Microscopy Methods. *J. Alloy. Compd.* **2015**, *633*, 165–169. [CrossRef]
111. Neophytou, N.; Zianni, X.; Kosina, H.; Frabboni, S.; Lorenzi, B.; Narducci, D. Simultaneous Increase in Electrical Conductivity and Seebeck Coefficient in Highly Boron-Doped Nanocrystalline Si. *Nanotechnology* **2013**, *24*, 205402. [CrossRef] [PubMed]
112. Kang, H.B.; Poudel, B.; Li, W.; Lee, H.; Saparamadu, U.; Nozariasbmarz, A.; Kang, M.G.; Gupta, A.; Heremans, J.J.; Priya, S. Decoupled Phononic-Electronic Transport in Multi-Phase n-Type Half-Heusler Nanocomposites Enabling Efficient High Temperature Power Generation. *Mater. Today* **2020**, *36*, 63–72. [CrossRef]
113. Pakdel, A.; Guo, Q.; Nicolosi, V.; Mori, T. Enhanced Thermoelectric Performance of Bi-Sb-Te/Sb_2O_3 Nanocomposites by Energy Filtering Effect. *J. Mater. Chem. A* **2018**, *6*, 21341–21349. [CrossRef]
114. Li, S.; Liu, Y.; Liu, F.; He, D.; He, J.; Luo, J.; Xiao, Y.; Pan, F. Effective Atomic Interface Engineering in $Bi_2Te_{2.7}Se_{0.3}$ Thermoelectric Material by Atomic-Layer-Deposition Approach. *Nano Energy* **2018**, *49*, 257–266. [CrossRef]
115. Güneş, E.; Wickleder, M.S.; Müller, E.; Elm, M.T.; Klar, P.J. Improved Thermoelectric Properties of Nanostructured Composites out of $Bi_{1-x}Sb_x$ Nanoparticles and Carbon Phases. *AIP Adv.* **2018**, *8*, 075319. [CrossRef]
116. Wang, Y.S.; Huang, L.L.; Li, D.; Zhang, J.; Qin, X.Y. Enhanced Thermoelectric Performance of $Bi_{0.4}Sb_{1.6}Te_3$ Based Composites with $CuInTe_2$ Inclusions. *J. Alloys Compd.* **2018**, *758*, 72–77. [CrossRef]
117. Cao, R.; Zhu, Z.; Li, X.-J.; Hu, X.; Song, H. Enhanced Thermoelectric Properties of the Lu-Doped and CNT-Dispersed Bi_2Te_3 Alloy. *Appl. Phys. A Mater. Sci. Process.* **2019**, *125*. [CrossRef]
118. Wan, X.; Liu, Z.; Sun, L.; Jiang, P.; Bao, X. Synergetic Enhancement of Thermoelectric Performance in a $Bi_{0.5}Sb_{1.5}Te_3/SrTiO_3$ Heterostructure. *J. Mater. Chem. A* **2020**, *8*, 10839–10844. [CrossRef]
119. Park, N.-W.; Lee, W.-Y.; Yoon, Y.-S.; Kim, G.-S.; Yoon, Y.-G.; Lee, S.-K. Achieving Out-of-Plane Thermoelectric Figure of Merit ZT = 1.44 in a p-Type $Bi_2Te_3/Bi_{0.5}Sb_{1.5}Te_3$ Superlattice Film with Low Interfacial Resistance. *ACS Appl. Mater. Interfaces* **2019**, *11*, 38247–38254. [CrossRef] [PubMed]
120. Li, Y.; Wang, X.; Liu, G.; Shin, B.; Shan, F. High Thermoelectric Efficiency of P-Type BiSbTe-Based Composites with $CuGaTe_2$ Nanoinclusions. *Scr. Mater.* **2019**, *172*, 88–92. [CrossRef]
121. Lwin, M.L.; Dharmaiah, P.; Min, B.H.; Song, G.; Jung, K.Y.; Hong, S.-J. Tuning of Thermoelectric Transport Properties via the Formation of Hierarchical Structures in Bi-Doped $Gd_2O_3/Bi_{0.5}Sb_{1.5}Te_3$ Nanocomposites. *Int. J. Energy Res.* **2021**. [CrossRef]

122. Ahmad, M.; Kodan, N.; Ghosh, A.; Mehta, B.R. The Nature of 2D:3D SnS:Bi_2Te_3 Interface and Its Effect on Enhanced Electrical and Thermoelectric Properties. *J. Alloy. Compd.* **2020**, *847*, 156233. [CrossRef]
123. Zhao, L.; Qiu, W.; Sun, Y.; Chen, L.; Deng, H.; Yang, L.; Shi, X.; Tang, J. Enhanced Thermoelectric Performance of $Bi_{0.3}Sb_{1.7}Te_3$ Based Alloys by Dispersing TiC Ceramic Nanoparticles. *J. Alloy. Compd.* **2021**, *863*, 158376. [CrossRef]
124. Zhang, Y.; Xing, C.; Liu, Y.; Li, M.; Xiao, K.; Guardia, P.; Lee, S.; Han, X.; Ostovari Moghaddam, A.; Josep Roa, J.; et al. Influence of Copper Telluride Nanodomains on the Transport Properties of N-Type Bismuth Telluride. *Chem. Eng. J.* **2021**, *418*, 129374. [CrossRef]
125. Hwang, J.; Lee, M.; Yu, B.-K.; Han, M.-K.; Kim, W.; Kim, J.; Al Rahal Al Orabi, R.; Wang, H.; Acharya, S.; Kim, J.; et al. Enhancement of Thermoelectric Performance in a Non-Toxic $CuInTe_2$/SnTe Coated Grain Nanocomposite. *J. Mater. Chem. A* **2021**, *9*, 14851–14858. [CrossRef]
126. Dharmaiah, P.; Nagarjuna, C.; Sharief, P.; Hong, S.-J. Synergetic Effects of Co-Dispersed Cu and Insulating HfO_2 Nanoparticles Enabled High Thermoelectric Figure of Merit in $Bi_{0.5}Sb_{1.5}Te_3$ Composites. *Appl. Surf. Sci.* **2021**, *556*, 149783. [CrossRef]
127. Pei, Y.L.; Wu, H.; Wu, D.; Zheng, F.; He, J. High Thermoelectric Performance Realized in a BiCuSeO System by Improving Carrier Mobility through 3D Modulation Doping. *J. Am. Chem. Soc.* **2014**, *136*, 13902–13908. [CrossRef]
128. Dingle, R.; Störmer, H.L.; Gossard, A.C.; Wiegmann, W. Electron Mobilities in Modulation-doped Semiconductor Heterojunction Superlattices. *Appl. Phys. Lett.* **1978**, *33*, 665–667. [CrossRef]
129. Mimura, T.; Hiyamizu, S.; Fujii, T.; Nanbu, K. A New Field-Effect Transistor with Selectively Doped GaAs/n-$Al_xGa_{1-x}As$ Heterojunctions. *Jpn. J. Appl. Phys.* **1980**, *19*, L225–L227. [CrossRef]
130. Pfeiffer, L.; West, K.W.; Stormer, H.L.; Baldwin, K.W. Electron Mobilities Exceeding 10^7 cm^2/V s in Modulation-doped GaAs. *Appl. Phys. Lett.* **1998**, *55*, 1888. [CrossRef]
131. Yamini, S.A.; Mitchell, D.R.G.; Gibbs, Z.M.; Santos, R.; Patterson, V.; Li, S.; Pei, Y.Z.; Dou, S.X.; Snyder, G.J. Heterogeneous Distribution of Sodium for High Thermoelectric Performance of P-Type Multiphase Lead-Chalcogenides. *Adv. Energy Mater.* **2015**, *5*, 1501047. [CrossRef]
132. Tian, Y.; Sakr, M.R.; Kinder, J.M.; Liang, D.; MacDonald, M.J.; Qiu, R.L.J.; Gao, H.-J.; Gao, X.P.A. One-Dimensional Quantum Confinement Effect Modulated Thermoelectric Properties in InAs Nanowires. *Nano Lett.* **2012**, *12*, 6492–6497. [CrossRef] [PubMed]
133. Moon, J.; Kim, J.-H.; Chen, Z.C.Y.; Xiang, J.; Chen, R. Gate-Modulated Thermoelectric Power Factor of Hole Gas in Ge-Si Core-Shell Nanowires. *Nano Lett.* **2013**, *13*, 1196–1202. [CrossRef]
134. Liang, W.; Hochbaum, A.I.; Fardy, M.; Rabin, O.; Zhang, M.; Yang, P. Field-Effect Modulation of Seebeck Coefficient in Single PbSe Nanowires. *Nano Lett.* **2009**, *9*, 1689–1693. [CrossRef] [PubMed]
135. Curtin, B.M.; Codecido, E.A.; Krämer, S.; Bowers, J.E. Field-Effect Modulation of Thermoelectric Properties in Multigated Silicon Nanowires. *Nano Lett.* **2013**, *13*, 5503–5508. [CrossRef] [PubMed]
136. Neophytou, N.; Thesberg, M. Modulation Doping and Energy Filtering as Effective Ways to Improve the Thermoelectric Power Factor. *J. Comput. Electron.* **2016**, *15*, 16–26. [CrossRef]
137. Zhang, Y.; Brorsson, J.; Qiu, R.; Palmqvist, A.E.C. Enhanced Thermoelectric Performance of $Ba_8Ga_{16}Ge_{30}$ Clathrate by Modulation Doping and Improved Carrier Mobility. *Adv. Electron. Mater.* **2021**, *7*, 2000782. [CrossRef]
138. Rathore, E.; Guin, S.N.; Biswas, K. Enhancement of Thermoelectric Performance of N-Type $AgBi_{1+x}Se_2$ via Improvement of the Carrier Mobility by Modulation Doping. *Bull. Mater. Sci.* **2020**, *43*, 315. [CrossRef]
139. Peng, Y.; Lai, H.; Liu, C.; Gao, J.; Kurosawa, M.; Nakatsuka, O.; Takeuchi, T.; Zaima, S.; Tanemura, S.; Miao, L. Realizing High Thermoelectric Performance in P-Type Si_{1-x}-YGexSny Thin Films at Ambient Temperature by Sn Modulation Doping. *Appl. Phys. Lett.* **2020**, *117*, 053903. [CrossRef]
140. Souda, D.; Shimizu, K.; Ohishi, Y.; Muta, H.; Yagi, T.; Kurosaki, K. High Thermoelectric Power Factor of Si–Mg_2Si Nanocomposite Ribbons Synthesized by Melt Spinning. *ACS Appl. Energy Mater.* **2020**, *3*, 1962–1968. [CrossRef]
141. Lee, D.; Zhou, J.; Chen, G.; Shao-Horn, Y. Enhanced Thermoelectric Properties for PEDOT:PSS/Undoped Ge Thin-Film Bilayered Heterostructures. *Adv. Electron. Mater.* **2019**, *5*, 1800624. [CrossRef]
142. Hui, S.; Gao, W.; Lu, X.; Panda, A.; Bailey, T.P.; Page, A.A.; Forrest, S.R.; Morelli, D.T.; Pan, X.; Pipe, K.P.; et al. Engineering Temperature-Dependent Carrier Concentration in Bulk Composite Materials via Temperature-Dependent Fermi Level Offset. *Adv. Energy Mater.* **2017**, *8*, 1701623. [CrossRef]
143. Feng, B.; Li, G.; Pan, Z.; Hu, X.; Liu, P.; He, Z.; Li, Y.; Fan, X. Enhanced Thermoelectric Properties in BiCuSeO Ceramics by Pb/Ni Dual Doping and 3D Modulation Doping. *J. Solid State Chem.* **2019**, *271*, 1–7. [CrossRef]
144. Feng, B.; Li, G.; Pan, Z.; Hu, X.; Liu, P.; Li, Y.; He, Z.; Fan, X. Enhanced Thermoelectric Performances in BiCuSeO Oxyselenides via Er and 3D Modulation Doping. *Ceram. Int.* **2019**, *45*, 4493–4498. [CrossRef]
145. Feng, B.; Li, G.; Pan, Z.; Hu, X.; Liu, P.; He, Z.; Li, Y.; Fan, X. Enhanced Thermoelectric Performance in BiCuSeO Oxyselenides via Ba/Te Dual-Site Substitution and 3D Modulation Doping. *J. Solid State Chem.* **2018**, *266*, 297–303. [CrossRef]
146. Wu, D.; Zhao, L.-D.; Tong, X.; Li, W.; Wu, L.; Tan, Q.; Pei, Y.; Huang, L.; Li, J.-F.; Zhu, Y.; et al. Superior Thermoelectric Performance in PbTe–PbS Pseudo-Binary: Extremely Low Thermal Conductivity and Modulated Carrier Concentration. *Energy Environ. Sci.* **2015**, *8*, 2056–2068. [CrossRef]
147. Rowe, D.M. (Ed.) *Thermoelectrics Handbook*, 1st ed.; CRC Press: Boca Raton, FL, USA, 2006; ISBN 978-1-4200-3890-3.

148. Hong, M.; Wang, Y.; Feng, T.; Sun, Q.; Xu, S.; Matsumura, S.; Pantelides, S.T.; Zou, J.; Chen, Z.G. Strong Phonon-Phonon Interactions Securing Extraordinary Thermoelectric Ge1- XSb XTe with Zn-Alloying-Induced Band Alignment. *J. Am. Chem. Soc.* **2019**, *141*, 1742–1748. [CrossRef]
149. Bao, D.Y.; Chen, J.; Yu, Y.; Liu, W.D.; Huang, L.S.; Han, G.; Tang, J.; Zhou, D.L.; Yang, L.; Chen, Z.G. Texture-Dependent Thermoelectric Properties of Nano-Structured Bi_2Te_3. *Chem. Eng. J.* **2020**, *388*, 124295. [CrossRef]
150. Alam, H.; Ramakrishna, S. A Review on the Enhancement of Figure of Merit from Bulk to Nano-Thermoelectric Materials. *Nano Energy* **2013**, *2*, 190–212. [CrossRef]
151. Dresselhaus, M.S.; Chen, G.; Tang, M.Y.; Yang, R.G.; Lee, H.; Wang, D.Z.; Ren, Z.F.; Fleurial, J.P.; Gogna, P. New Directions for Low-Dimensional Thermoelectric Materials. *Adv. Mater.* **2007**, *19*, 1043–1053. [CrossRef]
152. Chen, X.; Parker, D.; Singh, D.J. Acoustic Impedance and Interface Phonon Scattering in Bi_2Te_3 and Other Semiconducting Materials. *Phys. Rev. B* **2013**, *87*, 045317. [CrossRef]
153. Yang, J.; Meisner, G.P.; Chen, L. Strain Field Fluctuation Effects on Lattice Thermal Conductivity of ZrNiSn-Based Thermoelectric Compounds. *Appl. Phys. Lett.* **2004**, *85*, 1140–1142. [CrossRef]
154. Yan, X.; Liu, W.S.; Wang, H.; Chen, S.; Shiomi, J.; Esfarjani, K.; Wang, H.Z.; Wang, D.Z.; Chen, G.; Ren, Z.F. Stronger Phonon Scattering by Larger Differences in Atomic Mass and Size in P-Type Half-Heuslers Hf1-XTixCoSb$_{0.8}$Sn$_{0.2}$. *Energy Environ. Sci.* **2012**, *5*, 7543–7548. [CrossRef]
155. Xie, H.; Wang, H.; Fu, C.; Liu, Y.; Snyder, G.J.; Zhao, X.; Zhu, T. The Intrinsic Disorder Related Alloy Scattering in ZrNiSn Half-Heusler Thermoelectric Materials. *Sci. Rep.* **2014**, *4*, 6888. [CrossRef] [PubMed]
156. Bhattacharya, S.; Skove, M.J.; Russell, M.; Tritt, T.M.; Xia, Y.; Ponnambalam, V.; Poon, S.J.; Thadhani, N. Effect of Boundary Scattering on the Thermal Conductivity of TiNiSn-Based Half-Heusler Alloys. *Phys. Rev. B* **2008**, *77*, 184203. [CrossRef]
157. Bhattacharya, S.; Tritt, T.M.; Xia, Y.; Ponnambalam, V.; Poon, S.J.; Thadhani, N. Grain Structure Effects on the Lattice Thermal Conductivity of Ti-Based Half-Heusler Alloys. *Appl. Phys. Lett.* **2002**, *81*, 43–45. [CrossRef]
158. Yan, X.; Joshi, G.; Liu, W.; Lan, Y.; Wang, H.; Lee, S.; Simonson, J.W.; Poon, S.J.; Tritt, T.M.; Chen, G.; et al. Enhanced Thermoelectric Figure of Merit of P-Type Half-Heuslers. *Nano Lett.* **2011**, *11*, 556–560. [CrossRef]
159. Joshi, G.; Yan, X.; Wang, H.; Liu, W.; Chen, G.; Ren, Z. Enhancement in Thermoelectric Figure-Of-Merit of an N-Type Half-Heusler Compound by the Nanocomposite Approach. *Adv. Energy Mater.* **2011**, *1*, 643–647. [CrossRef]
160. Jiang, P.; Lindsay, L.; Huang, X.; Koh, Y.K. Interfacial Phonon Scattering and Transmission Loss in >1 Mm Thick Silicon-on-Insulator Thin Films. *Phys. Rev. B* **2018**, *97*, 195308. [CrossRef]
161. Klemens, P.G.; Simon, F.E. The Thermal Conductivity of Dielectric Solids at Low Temperatures (Theoretical). *Proc. R. Soc. Lond. Ser. A Math. Phys. Sci.* **1951**, *208*, 108–133. [CrossRef]
162. Holland, M.G. Analysis of Lattice Thermal Conductivity. *Phys. Rev.* **1963**, *132*, 2461–2471. [CrossRef]
163. Callaway, J. Model for Lattice Thermal Conductivity at Low Temperatures. *Phys. Rev.* **1959**, *113*, 1046–1051. [CrossRef]
164. Limarga, A.M.; Shian, S.; Leckie, R.M.; Levi, C.G.; Clarke, D.R. Thermal Conductivity of Single- and Multi-Phase Compositions in the ZrO_2-Y_2O_3-Ta_2O_5 System. *J. Eur. Ceram. Soc.* **2014**, *34*, 3085–3094. [CrossRef]
165. Zhao, H.Z.; Pokheral, M.; Zhu, G.H.; Chen, S.; Lukas, K.; Jie, Q.; Opeil, C.; Chen, G.; Ren, Z.F. Dramatic Thermal Conductivity Reduction by Nanostructures for Large Increase in Thermoelectric Figure-of-Merit of $FeSb_2$. *Appl. Phys. Lett.* **2011**, *99*, 163101. [CrossRef]
166. Gurunathan, R.; Hanus, R.; Jeffrey Snyder, G. Alloy Scattering of Phonons. *Mater. Horiz.* **2020**, *7*, 1452–1456. [CrossRef]
167. Nan, C.-W.; Birringer, R. Determining the Kapitza Resistance and the Thermal Conductivity of Polycrystals: A Simple Model. *Phys. Rev. B* **1998**, *57*, 8264–8268. [CrossRef]
168. Kinsler, L.E.; Frey, A.R.; Coppens, A.B.; Sanders, J.V. *Fundamentals of Acoustics*, 4th ed.; Wiley: Hoboken, NJ, USA, 1999.
169. James, D.; Lu, X.; Nguyen, A.C.; Morelli, D.; Brock, S.L. Design of Lead Telluride Based Thermoelectric Materials through Incorporation of Lead Sulfide Inclusions or Ligand Stripping of Nanosized Building Blocks. *J. Phys. Chem. C* **2015**, *119*, 4635–4644. [CrossRef]
170. Ahmad, K.; Almutairi, Z.; Wan, C. Thermoelectric Properties of PbTe-Based Graphene Nanocomposite. *J. Mater. Sci. Mater. Electron.* **2020**, *31*, 20996–21004. [CrossRef]
171. Aminorroaya Yamini, S.; Wang, H.; Gibbs, Z.M.; Pei, Y.; Mitchell, D.R.G.; Dou, S.X.; Snyder, G.J. Thermoelectric Performance of Tellurium-Reduced Quaternary p-Type Lead–Chalcogenide Composites. *Acta Mater.* **2014**, *80*, 365–372. [CrossRef]
172. Falkenbach, O.; Hartung, D.; Klar, P.J.; Koch, G.; Schlecht, S. Thermoelectric Properties of Nanostructured Bismuth-Doped Lead Telluride $Bi_x(PbTe)_{1-x}$ Prepared by Co-Ball-Milling. *J. Electron. Mater.* **2013**, *43*, 1674–1680. [CrossRef]
173. Falkenbach, O.; Schmitz, A.; Hartung, D.; Dankwort, T.; Koch, G.; Kienle, L.; Klar, P.J.; Mueller, E.; Schlecht, S. Effect of Preparation Procedure and Nanostructuring on the Thermoelectric Properties of the Lead Telluride-Based Material System $AgPb_mBiTe_{2+m}$ (BLST-m). *J. Appl. Phys.* **2016**, *119*, 214310. [CrossRef]
174. Keshavarz, M.K.; Vasilevskiy, D.; Masut, R.A.; Turenne, S. Synthesis and Characterization of Bismuth Telluride-Based Thermoelectric Nanocomposites Containing MoS_2 Nano-Inclusions. *Mater. Charact.* **2014**, *95*, 44–49. [CrossRef]
175. Trawiński, B.; Bochentyn, B.; Gostkowska, N.; Łapiński, M.; Miruszewski, T.; Kusz, B. Structure and Thermoelectric Properties of Bismuth Telluride—Carbon Composites. *Mater. Res. Bull.* **2018**, *99*, 10–17. [CrossRef]

176. Yang, G.; Sang, L.; Yun, F.F.; Mitchell, D.R.G.; Casillas, G.; Ye, N.; See, K.; Pei, J.; Wang, X.; Li, J.; et al. Significant Enhancement of Thermoelectric Figure of Merit in BiSbTe-Based Composites by Incorporating Carbon Microfiber. *Adv. Funct. Mater.* **2021**, *31*, 2008851. [CrossRef]
177. Zhang, J.; Wu, D.; He, D.; Feng, D.; Yin, M.; Qin, X.; He, J. Extraordinary Thermoelectric Performance Realized in N-Type PbTe through Multiphase Nanostructure Engineering. *Adv. Mater.* **2017**, *29*, 1703148. [CrossRef]
178. Sootsman, J.R.; He, J.Q.; Dravid, V.P.; Li, C.P.; Uher, C.; Kanatzidis, M.G. High Thermoelectric Figure of Merit and Improved Mechanical Properties in Melt Quenched PbTe-Ge and PbTe-$Ge_{1-x}Si_x$ Eutectic and Hypereutectic Composites. *J. Appl. Phys.* **2009**, *105*, 083718. [CrossRef]
179. Gaultois, M.W.; Sparks, T.D.; Borg, C.K.H.; Seshadri, R.; Bonificio, W.D.; Clarke, D.R. Data-Driven Review of Thermoelectric Materials: Performance and Resource Considerations. *Chem. Mater.* **2013**, *25*, 2911–2920. [CrossRef]
180. Gaultois, M.W.; Sparks, T.D.; Borg, C.K.H.; Seshadri, R.; Bonificio, W.D.; Clarke, D.R. Energy Materials Datamining. Available online: http://www.mrl.ucsb.edu:8080/datamine/about.jsp (accessed on 23 August 2021).
181. Kittel, C. *Introduction to Solid State Physics*, 8th ed.; John Wiley & Sons: New York, NY, USA, 2018; ISBN 978-1-119-45620-9.
182. Chung, D.Y.; Hogan, T.; Brazis, P.; Rocci-Lane, M.; Kannewurf, C.; Bastea, M.; Uher, C.; Kanatzidis, M.G. $CsBi_4Te_6$: A High-Performance Thermoelectric Material for Low-Temperature Applications. *Science* **2000**, *287*, 1024–1027. [CrossRef] [PubMed]
183. Chung, D.-Y.; Choi, K.-S.; Iordanidis, L.; Schindler, J.L.; Brazis, P.W.; Kannewurf, C.R.; Chen, B.; Hu, S.; Uher, C.; Kanatzidis, M.G. High Thermopower and Low Thermal Conductivity in Semiconducting Ternary K−Bi−Se Compounds. Synthesis and Properties of β-$K_2Bi_8Se_{13}$ and $K_{2.5}Bi_{8.5}Se_{14}$ and Their Sb Analogues. *Chem. Mater.* **1997**, *9*, 3060–3071. [CrossRef]
184. Gascoin, F.; Maignan, A. Order-Disorder Transition in $AgCrSe_2$: A New Route to Efficient Thermoelectrics. *Chem. Mater.* **2011**, *23*, 2510–2513. [CrossRef]
185. Hsu, K.F.; Loo, S.; Guo, F.; Chen, W.; Dyck, J.S.; Uher, C.; Hogan, T.; Polychroniadis, E.K.; Kanatzidis, M.G. Cubic $AgPb_{(m)}SbTe_{(2+m)}$: Bulk Thermoelectric Materials with High Figure of Merit. *Science* **2004**, *303*, 818–821. [CrossRef]
186. Jungwirth, T.; Wunderlich, J.; Olejnik, K. Spin Hall Effect Devices. *Nat. Mater.* **2012**, *11*, 382–390. [CrossRef]
187. Kanatzidis, M.G.; McCarthy, T.J.; Tanzer, T.A.; Chen, L.-H.; Iordanidis, L.; Hogan, T.; Kannewurf, C.R.; Uher, C.; Chen, B. Synthesis and Thermoelectric Properties of the New Ternary Bismuth Sulfides $KBi_{6.33}S_{10}$ and $K_2Bi_8S_{13}$. *Chem. Mater.* **1996**, *8*, 1465–1474. [CrossRef]
188. Kurosaki, K.; Kosuga, A.; Yamanaka, S. Thermoelectric Properties of Chevrel Phase Mo6Te8-XSx. *J. Alloys Compd.* **2003**, *351*, 208–211. [CrossRef]
189. Kurosaki, K.; Kosuga, A.; Muta, H.; Uno, M.; Yamanaka, S. Ag_9TlTe_5: A High-Performance Thermoelectric Bulk Material with Extremely Low Thermal Conductivity. *Appl. Phys. Lett.* **2005**, *87*, 061919. [CrossRef]
190. Larouche, S.; Tsai, Y.J.; Tyler, T.; Jokerst, N.M.; Smith, D.R. Infrared Metamaterial Phase Holograms. *Nat. Mater.* **2012**, *11*, 450–454. [CrossRef] [PubMed]
191. Liu, H.; Shi, X.; Xu, F.; Zhang, L.; Zhang, W.; Chen, L.; Li, Q.; Uher, C.; Day, T.; Snyder, G.J. Copper Ion Liquid-like Thermoelectrics. *Nat. Mater.* **2012**, *11*, 422–425. [CrossRef] [PubMed]
192. Martin, C.D.; Costa, A.; Dering, B.; Hoshino, N.; Wu, Y.J.; Thierry, G. Effects of Speed of Word Processing on Semantic Access: The Case of Bilingualism. *Brain Lang.* **2012**, *120*, 61–65. [CrossRef]
193. May, A.F.; Flage-Larsen, E.; Snyder, G.J. Electron and Phonon Scattering in the High-Temperature Thermoelectric $La_3Te_{4-z}M_z$ (M = Sb,Bi). *Phys. Rev. B* **2010**, *81*, 125205. [CrossRef]
194. McGuire, M.A.; Reynolds, T.K.; DiSalvo, F.J. Exploring Thallium Compounds as Thermoelectric Materials: Seventeen New Thallium Chalcogenides. *Chem. Mater.* **2005**, *17*, 2875–2884. [CrossRef]
195. Ohta, M.; Yamamoto, A.; Obara, H. Thermoelectric Properties of Chevrel-Phase Sulfides M_x Mo_6S_8 (M: Cr, Mn, Fe, Ni). *J. Electron. Mater.* **2010**, *39*, 2117–2121. [CrossRef]
196. Orava, J.; Greer, A.L.; Gholipour, B.; Hewak, D.W.; Smith, C.E. Characterization of Supercooled Liquid Ge2Sb2Te5 and Its Crystallization by Ultrafast-Heating Calorimetry. *Nat. Mater.* **2012**, *11*, 279–283. [CrossRef] [PubMed]
197. Pei, Y.; Shi, X.; LaLonde, A.; Wang, H.; Chen, L.; Snyder, G.J. Convergence of Electronic Bands for High Performance Bulk Thermoelectrics. *Nature* **2011**, *473*, 66–69. [CrossRef] [PubMed]
198. Rogers, E.T.; Lindberg, J.; Roy, T.; Savo, S.; Chad, J.E.; Dennis, M.R.; Zheludev, N.I. A Super-Oscillatory Lens Optical Microscope for Subwavelength Imaging. *Nat. Mater.* **2012**, *11*, 432–435. [CrossRef] [PubMed]
199. Scherrer, S.; Scherrer, H.; Rowe, D. Bismuth Telluride, Antimony Telluride, and Their Solid Solutions. In *CRC Handbook of Thermoelectrics*; CRC Press: Boca Raton, FL, USA, 1995.
200. Sharp, J.W.; Sales, B.C.; Mandrus, D.G.; Chakoumakos, B.C. Thermoelectric Properties of Tl_2SnTe_5 and Tl_2GeTe_5. *Appl. Phys. Lett.* **1999**, *74*, 3794–3796. [CrossRef]
201. Skrabek, E.; Trimmer, D.; Rowe, D. Properties of the General TAGS System. In *CRC Handbook of Thermoelectrics*; CRC Press: Boca Raton, FL, USA, 1995.
202. Wan, C.; Wang, Y.; Wang, N.; Koumoto, K. Low-Thermal-Conductivity $(MS)_{1+x}(TiS_2)_2$ (M = Pb, Bi, Sn) Misfit Layer Compounds for Bulk Thermoelectric Materials. *Materials* **2010**, *3*, 2606–2617. [CrossRef]
203. Wang, W.H. Metallic Glasses: Family Traits. *Nat. Mater.* **2012**, *11*, 275–276. [CrossRef]
204. Warren, S.C.; Perkins, M.R.; Adams, A.M.; Kamperman, M.; Burns, A.A.; Arora, H.; Herz, E.; Suteewong, T.; Sai, H.; Li, Z.; et al. A Silica Sol-Gel Design Strategy for Nanostructured Metallic Materials. *Nat. Mater.* **2012**, *11*, 460–467. [CrossRef]

205. Cui, J.L.; Xue, H.F.; Xiu, W.J. Preparation and Thermoelectric Properties of P-Type $(Ga_2Te_3)x–(Bi_{0.5}Sb_{1.5}Te_3)_{1-x}$ (X = 0–0.2) Alloys Prepared by Spark Plasma Sintering. *Intermetallics* **2007**, *15*, 1466–1470. [CrossRef]
206. Gayner, C.; Nandihalli, N. Enhancement of Thermoelectric Performance of PbTe by Embedding NaCl. *Materialia* **2020**, *14*, 100912. [CrossRef]
207. Chang, C.-C.; Liu, C.-H.; Wu, C.-C.; Bag, P.; Kuo, Y.-K. Thermoelectric Properties of $(HgTe)_{0.55}(PbTe)_{0.45}$ Eutectic Composite with In Doping. *Mater. Res. Bull.* **2020**, *129*, 110916. [CrossRef]
208. Nandihalli, N.; Pai, Y.-H.; Liu, C.-J. Thermoelectric Properties of $Pb_{0.833}Na_{0.017}(Zn_{0.85}Al_{0.15})_{0.15}$Te-Te Composite. *Ceram. Int.* **2020**, *46*, 18683–18689. [CrossRef]
209. Zhu, C.; Zhang, J.; Ming, H.; Lou, X.; Huang, L.; Chen, T.; Zhang, B.; Li, D.; Xin, H.; Qin, X. Enhanced Thermoelectric Performance of PbTe Based Materials by Bi Doping and Introducing MgO Nanoparticles. *Appl. Phys. Lett.* **2020**, *117*, 042105. [CrossRef]
210. Yang, Z.-R.; Liu, C.-J. Thermoelectric Transport in P-Type $(Pb_{0.98}Na_{0.02}Te)_{1-x}(Zn_{0.85}Al_{0.15}Te)_x$-Te Composites Fabricated Using a Combination of Hydrothermal Synthesis and Evacuating-and-Encapsulating Sintering. *J. Electron. Mater.* **2020**, *49*, 2954–2961. [CrossRef]
211. Zhu, T.; Xie, H.; Zhang, C.; Cheng, X.; Zhang, J.; Poudeu, P.F.P.; Tan, G.; Yan, Y.; Liu, W.; Su, X.; et al. Enhanced Mechanical Properties of $Na_{0.02}Pb_{0.98}Te/MoTe_2$ Thermoelectric Composites Through in-Situ-Formed $MoTe_2$. *ACS Appl. Mater. Interfaces* **2019**, *11*, 41472–41481. [CrossRef]
212. Gao, J.; Mao, T.; Lv, T.; Li, Z.; Xu, G. Thermoelectric Performance of N-Type $(PbTe)_{1-x}(CoTe)_x$ Composite Prepared by High Pressure Sintering Method. *J. Mater. Sci. Mater. Electron.* **2018**, *29*, 5327–5336. [CrossRef]
213. Ginting, D.; Lin, C.-C.; Rathnam, L.; Hwang, J.; Kim, W.; Al Orabi, R.A.r.; Rhyee, J.-S. Dataset on the Electronic and Thermal Transport Properties of Quaternary Compounds of $(PbTe)_{0.95-x}(PbSe)_x(PbS)_{0.05}$. *Data Brief* **2017**, *13*, 233–241. [CrossRef] [PubMed]
214. Rösch, A.G.; Giunta, F.; Mallick, M.M.; Franke, L.; Gall, A.; Aghassi-Hagmann, J.; Schmalian, J.; Lemmer, U. Improved Electrical, Thermal, and Thermoelectric Properties Through Sample-to-Sample Fluctuations in Near-Percolation Threshold Composite Materials. *Adv. Simul.* **2021**, *4*, 2000284. [CrossRef]
215. Bruggeman, D.A.G. Berechnung Verschiedener Physikalischer Konstanten von Heterogenen Substanzen. I. Dielektrizitätskonstanten Und Leitfähigkeiten Der Mischkörper Aus Isotropen Substanzen. *Ann. Physik* **1935**, *416*, 636–664. [CrossRef]
216. Landauer, R. The Electrical Resistance of Binary Metallic Mixtures. *J. Appl. Phys.* **1952**, *23*, 779–784. [CrossRef]
217. Vaney, J.B.; Piarristeguy, A.; Ohorodniichuck, V.; Ferry, O.; Pradel, A.; Alleno, E.; Monnier, J.; Lopes, E.B.; Goncalves, A.P.; Delaizir, G.; et al. Effective Medium Theory Based Modeling of the Thermoelectric Properties of Composites: Comparison between Predictions and Experiments in the Glass-Crystal Composite System $Si_{10}As_{15}Te_{75}$-$Bi_{0.4}Sb_{1.6}Te_3$. *J. Mater. Chem. C* **2015**, *3*, 11090–11098. [CrossRef]
218. Sonntag, J. Comment on Effective Medium Theory Based Modeling of the Thermoelectric Properties of Composites: Comparison between Predictions and Experiments in the Glass–Crystal Composite System $Si_{10}As_{15}Te_{75}$-$Bi_{0.4}Sb_{1.6}Te_3$ by J.-B. Vaney et al., J. Mater. Chem. C, **2015**, *3*, 11090. *J. Mater. Chem. C* **2016**, *4*, 10973–10976. [CrossRef]
219. Angst, S.; Wolf, D.E. Network Theory for Inhomogeneous Thermoelectrics. *New J. Phys.* **2016**, *18*, 043004. [CrossRef]
220. Gather, F.; Heiliger, C.; Klar, P.J. NeMo: A Network Model Program for Analyzing the Thermoelectric Properties of Meso and Nanostructured Composite Materials. *Prog. Solid State Chem.* **2011**, *39*, 97–107. [CrossRef]
221. Aboudi, J.; Haj-Ali, R. A Fully Coupled Thermal–Electrical–Mechanical Micromodel for Multi-Phase Periodic Thermoelectrical Composite Materials and Devices. *Int. J. Solids Struct.* **2016**, *80*, 84–95. [CrossRef]
222. Monticelli, A. *State Estimation in Electric Power Systems: A Generalized Approach*, 1st ed.; Springer Science & Business Media: Berlin/Heidelberg, Germany, 1999.
223. Razavi, B. *Fundamentals of Microelectronics*, 2nd ed.; Wiley: Hoboken, NJ, USA, 2013; ISBN 978-1-118-15632-2.
224. Roche, S. Graphene Gets a Better Gap. *Nat. Nanotechnol.* **2010**, *6*, 8–9. [CrossRef]
225. Suh, D.; Lee, S.; Mun, H.; Park, S.H.; Lee, K.H.; Kim, S.W.; Choi, J.Y.; Baik, S. Enhanced Thermoelectric Performance of Bi0.5Sb1.5Te3-Expanded Graphene Composites by Simultaneous Modulation of Electronic and Thermal Carrier Transport. *Nano Energy* **2015**, *13*, 67–76. [CrossRef]
226. Yadav, S.; Chaudhary, S.; Pandya, D.K. Effect of 2D MoS_2 and Graphene Interfaces with $CoSb_3$ Nanoparticles in Enhancing Thermoelectric Properties of 2D MoS_2-$CoSb_3$ and Graphene-$CoSb_3$ Nanocomposites. *Ceram. Int.* **2018**, *44*, 10628–10634. [CrossRef]
227. Zhang, Y.; Ma, H.; Sun, B.; Liu, B.; Liu, H.; Kong, L.; Liu, B.; Jia, X.; Chen, X. Thermoelectric Performance of Graphene Composited BiSbTe Bulks by High Pressure Synthesis. *J. Alloys Compd.* **2017**, *715*, 344–348. [CrossRef]
228. He, Y.; Zhang, T.S.; Shi, X.; Wei, S.H.; Chen, L.D. High Thermoelectric Performance in Copper Telluride. *NPG Asia Mater.* **2015**, *7*, e210. [CrossRef]
229. Sottmann, J.; Valset, K.; Karlsen, O.B.; Tafto, J. Synthesis and Measurement of the Thermoelectric Properties of Multiphase Composites: ZnSb Matrix with Zn_4Sb_3, Zn_3P_2, and Cu_5Zn_8. *J. Electron. Mater.* **2013**, *42*, 1820–1826. [CrossRef]
230. Yamini, S.A.; Brewis, M.; Byrnes, J.; Santos, R.; Manettas, A.; Pei, Y.Z. Fabrication of Thermoelectric Materials—Thermal Stability and Repeatability of Achieved Efficiencies. *J. Mater. Chem. C* **2015**, *3*, 10610–10615. [CrossRef]
231. Aminorroaya Yamini, S.; Mitchell, D.R.G.; Wang, H.; Gibbs, Z.M.; Pei, Y.; Dou, S.X.; Snyder, G.J. Origin of Resistivity Anomaly in P-Type Leads Chalcogenide Multiphase Compounds. *AIP Adv.* **2015**, *5*, 053601. [CrossRef]

232. Shen, J.J.; Hu, L.P.; Zhu, T.J.; Zhao, X.B. The Texture Related Anisotropy of Thermoelectric Properties in Bismuth Telluride Based Polycrystalline Alloys. *Appl. Phys. Lett.* **2011**, *99*, 124102. [CrossRef]
233. Zhao, X.B.; Ji, X.H.; Zhang, Y.H.; Zhu, T.J.; Tu, J.P.; Zhang, X.B. Bismuth Telluride Nanotubes and the Effects on the Thermoelectric Properties of Nanotube-Containing Nanocomposites. *Appl. Phys. Lett.* **2005**, *86*, 062111. [CrossRef]
234. Bailyn, M. Maximum Variational Principle for Conduction Problems in a Magnetic Field, and the Theory of Magnon Drag. *Phys. Rev.* **1962**, *126*, 2040–2054. [CrossRef]
235. Hirohata, A.; Yamada, K.; Nakatani, Y.; Prejbeanu, I.L.; Dieny, B.; Pirro, P.; Hillebrands, B. Review on Spintronics: Principles and Device Applications. *J. Magn. Magn. Mater.* **2020**, *509*, 166711. [CrossRef]
236. Costache, M.V.; Bridoux, G.; Neumann, I.; Valenzuela, S.O. Magnon-Drag Thermopile. *Nat. Mater.* **2011**, *11*, 199–202. [CrossRef]
237. Watzman, S.J.; Duine, R.A.; Tserkovnyak, Y.; Boona, S.R.; Jin, H.; Prakash, A.; Zheng, Y.H.; Heremans, J.P. Magnon-Drag Thermopower and Nernst Coefficient in Fe, Co, and Ni. *Phys. Rev. B* **2016**, *94*, 144407. [CrossRef]
238. Saito, T.; Nishio-Hamane, D. Magnetic and Thermoelectric Properties of Co_2MnT (T = Ga, Si) Heusler Compounds. *Phys. B Condens. Matter* **2021**, *603*. [CrossRef]
239. Saito, T.; Kamishima, S. Magnetic and Thermoelectric Properties of Fe–Ti–Sn Alloys. *IEEE Trans. Magn.* **2019**, *55*, 2900104. [CrossRef]
240. Vikram, F.; Johnson, D.D.; Alam, A. Enhanced Thermoelectric Performance of $Mg_2Si_{1-x}Sn_x$ Codoped with Bi and Cr. *Phys. Rev. B* **2018**, *98*, 115204. [CrossRef]
241. Solomon, G.; Song, E.; Gayner, C.; Martinez, J.A.; Amouyal, Y. Effects of Microstructure and Neodymium Doping on Bi_2Te_3 Nanostructures: Implications for Thermoelectric Performance. *ACS Appl. Nano Mater.* **2021**, *4*, 4419–4431. [CrossRef]
242. Jena, A.; Lee, S.-C.; Bhattacharjee, S. Tuning the Lattice Thermal Conductivity in Bismuth Telluride via Cr Alloying. *Phys. Rev. Appl.* **2021**, *15*, 064023. [CrossRef]
243. Das, S.; Valiyaveettil, S.M.; Chen, K.-H.; Suwas, S.; Mallik, R.C. Thermoelectric Properties of Mn Doped BiCuSeO. *Mater. Res. Express* **2019**, *6*, 086305. [CrossRef]
244. Diakhate, M.S.; Hermann, R.P.; Mochel, A.; Sergueev, I.; Sondergaard, M.; Christensen, M.; Verstraete, M.J. Thermodynamic, Thermoelectric, and Magnetic Properties of $FeSb_2$: A Combined First-Principles and Experimental Study. *Phys. Rev. B* **2011**, *84*, 125210. [CrossRef]
245. Sun, P.; Oeschler, N.; Johnsen, S.; Iversen, B.B.; Steglich, F. Narrow Band Gap and Enhanced Thermoelectricity in $FeSb_2$. *Dalton Trans.* **2010**, *39*, 1012–1019. [CrossRef] [PubMed]
246. Franzen, H.; Sterner, C. The X-Ray Photoelectron Spectra of MnS, MnSe, and MnTe. *J. Solid State Chem.* **1978**, *25*, 227–230. [CrossRef]
247. Podgorny, M.; Oleszkiewicz, J. Electronic Structure of Antiferromagnetic MnTe. *J. Phys. C Solid State Phys.* **1983**, *16*, 2547–2557. [CrossRef]
248. Wasscher, J.D.; Haas, C. Contribution of Magnon-Drag to the Thermoelectric Power of Antiferromagnetic Mn Te. *Phys. Lett.* **1964**, *8*, 302–304. [CrossRef]
249. Peng, C.; Zhang, G.; Wang, C.; Yan, Y.; Zheng, H.; Wang, Y.; Hu, M. Improvement of Thermoelectricity Through Magnetic Interactions in Layered $Cr_2Ge_2Te_6$. *Phys. Status Solidi RRL Rapid Res. Lett.* **2018**, *12*, 1800172. [CrossRef]
250. Kirkham, M.J.; dos Santos, A.M.; Rawn, C.J.; Lara-Curzio, E.; Sharp, J.W.; Thompson, A.J. Abinitio Determination of Crystal Structures of the Thermoelectric Material MgAgSb. *Phys. Rev. B* **2012**, *85*, 144120. [CrossRef]
251. Zheng, L.; Li, J.; Zhou, B.; Liu, H.; Bu, Z.; Chen, B.; Ang, R.; Li, W. Thermoelectric Properties of P-Type MnSe. *J. Alloys Compd.* **2019**, *789*, 953–959. [CrossRef]
252. Shimizu, S.; Shiogai, J.; Takemori, N.; Sakai, S.; Ikeda, H.; Arita, R.; Nojima, T.; Tsukazaki, A.; Iwasa, Y. Giant Thermoelectric Power Factor in Ultrathin FeSe Superconductor. *Nat. Commun.* **2019**, *10*, 825. [CrossRef]
253. Takahashi, H.; Okazaki, R.; Ishiwata, S.; Taniguchi, H.; Okutani, A.; Hagiwara, M.; Terasaki, I. Colossal Seebeck Effect Enhanced by Quasi-Ballistic Phonons Dragging Massive Electrons in $FeSb_2$. *Nat. Commun.* **2016**, *7*, 12732. [CrossRef]
254. Tsujii, N.; Mori, T. High Thermoelectric Power Factor in a Carrier-Doped Magnetic Semiconductor $CuFeS_2$. *Appl. Phys. Express* **2013**, *6*, 043001. [CrossRef]
255. Ang, R.; Khan, A.U.; Tsujii, N.; Takai, K.; Nakamura, R.; Mori, T. Thermoelectricity Generation and Electron-Magnon Scattering in a Natural Chalcopyrite Mineral from a Deep-Sea Hydrothermal Vent. *Angew. Chem. Int. Ed. Engl.* **2015**, *54*, 12909–12913. [CrossRef]
256. Kikkawa, T.; Reitz, D.; Ito, H.; Makiuchi, T.; Sugimoto, T.; Tsunekawa, K.; Daimon, S.; Oyanagi, K.; Ramos, R.; Takahashi, S.; et al. Observation of Nuclear-Spin Seebeck Effect. *Nat. Commun.* **2021**, *12*, 4356. [CrossRef] [PubMed]
257. Uchida, K.; Takahashi, S.; Harii, K.; Ieda, J.; Koshibae, W.; Ando, K.; Maekawa, S.; Saitoh, E. Observation of the Spin Seebeck Effect. *Nature* **2008**, *455*, 778–781. [CrossRef] [PubMed]
258. Wang, Y.; Rogado, N.S.; Cava, R.J.; Ong, N.P. Spin Entropy as the Likely Source of Enhanced Thermopower in $Na(x)Co_2O_4$. *Nature* **2003**, *423*, 425–428. [CrossRef]
259. Bauer, G.E.; Saitoh, E.; van Wees, B.J. Spin Caloritronics. *Nat. Mater.* **2012**, *11*, 391–399. [CrossRef] [PubMed]
260. Yu, H.M.; Brechet, S.D.; Ansermet, J.P. Spin Caloritronics, Origin and Outlook. *Phys. Lett. A* **2017**, *381*, 825–837. [CrossRef]
261. Erekhinsky, M.; Casanova, F.; Schuller, I.K.; Sharoni, A. Spin-Dependent Seebeck Effect in Non-Local Spin Valve Devices. *Appl. Phys. Lett.* **2012**, *100*, 212401. [CrossRef]

262. Marchal, N.; da Camara Santa Clara Gomes, T.; Abreu Araujo, F.; Piraux, L. Large Spin-Dependent Thermoelectric Effects in NiFe-Based Interconnected Nanowire Networks. *Nanoscale Res. Lett.* **2020**, *15*, 137. [CrossRef]
263. Yamanoi, K.; Yafuso, M.; Miyazaki, K.; Kimura, T. Signature of Spin-Dependent Seebeck Effect in Dynamical Spin Injection of Metallic Bilayer Structures. *J. Phys. Mater.* **2019**, *3*, 014005. [CrossRef]
264. Ahmed, F.; Tsujii, N.; Mori, T. Thermoelectric Properties of $CuGa_{1-x}Mn_xTe_2$: Power Factor Enhancement by Incorporation of Magnetic Ions. *J. Mater. Chem. A* **2017**, *5*, 7545–7554. [CrossRef]
265. Vaney, J.B.; Yamini, S.A.; Takaki, H.; Kobayashi, K.; Kobayashi, N.; Mori, T. Magnetism-Mediated Thermoelectric Performance of the Cr-Doped Bismuth Telluride Tetradymite. *Mater. Today Phys.* **2019**, *9*, 100090. [CrossRef]
266. Acharya, S.; Anwar, S.; Mori, T.; Soni, A. Coupling of Charge Carriers with Magnetic Entropy for Power Factor Enhancement in Mn Doped $Sn_{1.03}Te$ for Thermoelectric Applications. *J. Mater. Chem. C* **2018**, *6*, 6489–6493. [CrossRef]
267. Li, W.; Chen, Z.W.; Lin, S.Q.; Chang, Y.J.; Ge, B.H.; Chen, Y.; Pei, Y.Z. Band and Scattering Tuning for High Performance Thermoelectric $Sn_{1-x}Mn_xTe$ Alloys. *J. Mater.* **2015**, *1*, 307–315. [CrossRef]
268. He, J.; Tan, X.; Xu, J.; Liu, G.-Q.; Shao, H.; Fu, Y.; Wang, X.; Liu, Z.; Xu, J.; Jiang, H.; et al. Valence Band Engineering and Thermoelectric Performance Optimization in SnTe by Mn-Alloying via a Zone-Melting Method. *J. Mater. Chem. A* **2015**, *3*, 19974–19979. [CrossRef]
269. Graf, T.; Barth, J.; Blum, C.G.F.; Balke, B.; Felser, C.; Klaer, P.; Elmers, H.-J. Phase-Separation-Induced Changes in the Magnetic and Transport Properties of the Quaternary Heusler Alloy $Co_2Mn_{1-x}Ti_xSn$. *Phys. Rev. B* **2010**, *82*, 104420. [CrossRef]
270. Liu, Z.; Zhu, J.; Wei, P.; Zhu, W.; Zhao, W.; Xia, A.; Xu, D.; Lei, Y.; Yu, J. Candidate for Magnetic Doping Agent and High-Temperature Thermoelectric Performance Enhancer: Hard Magnetic M-Type $BaFe_{12}O_{19}$ Nanometer Suspension. *ACS Appl. Mater. Interfaces* **2019**, *11*, 45875–45884. [CrossRef]
271. Zhao, W.; Liu, Z.; Wei, P.; Zhang, Q.; Zhu, W.; Su, X.; Tang, X.; Yang, J.; Liu, Y.; Shi, J.; et al. Magnetoelectric Interaction and Transport Behaviours in Magnetic Nanocomposite Thermoelectric Materials. *Nat. Nanotechnol.* **2017**, *12*, 55–60. [CrossRef]
272. Lu, R.; Lopez, J.S.; Liu, Y.; Bailey, T.P.; Page, A.A.; Wang, S.; Uher, C.; Poudeu, P.F.P. Coherent Magnetic Nanoinclusions Induce Charge Localization in Half-Heusler Alloys Leading to High-Tc Ferromagnetism and Enhanced Thermoelectric Performance. *J. Mater. Chem. A* **2019**, *7*, 11095–11103. [CrossRef]
273. Vandendriessche, S.; Brullot, W.; Slavov, D.; Valev, V.K.; Verbiest, T. Magneto-Optical Harmonic Susceptometry of Superparamagnetic Materials. *Appl. Phys. Lett.* **2013**, *102*, 161903. [CrossRef]
274. Marghussian, V. Magnetic Properties of Nano-Glass Ceramics. In *Nano-Glass Ceramics*; Elsevier: Amsterdam, The Netherlands, 2015; pp. 181–223, ISBN 978-0-323-35386-1.
275. Zhao, W.; Liu, Z.; Sun, Z.; Zhang, Q.; Wei, P.; Mu, X.; Zhou, H.; Li, C.; Ma, S.; He, D.; et al. Superparamagnetic Enhancement of Thermoelectric Performance. *Nature* **2017**, *549*, 247–251. [CrossRef] [PubMed]